CWP-137

— Project Review —

Consortium Project on
Seismic Inverse Methods for Complex Structures

Breckenridge, Colorado
May 11-14, 1993

prepared by

CWP Students and Faculty:

Mohammed Alfaraj
Tariq Alkhalifah
John Anderson
Craig Artley
Norm Bleistein
Tong Chen
Jack K. Cohen
Hongling Deng
Tong Fei
Wenceslau Gouveia
Ken Larner
Zhenyue Liu
Boyi Ou
Andreas Rüeger
John A. Scales
John W. Stockwell
Timo Tjan
Ilya Tsvankin
Omar Uzcategui
Meng Xu
Michael Zhdanov

CWP Staff:

Jo Ann Fink
Administrative Assistant

Barbara McLenon
Publications Manager

Center for Wave Phenomena
Colorado School of Mines
Golden, Colorado 80401

CONTENTS

Acknowledgments iii

Introduction 1

Transformation to zero offset for mode-converted waves by Fourier transform
Mohammed Alfaraj 5

Efficient synthetic seismograms for transversely isotropic media with constant velocity gradient
Tariq Alkhalifah 39

Migration error in transversely isotropic media
Tariq Alkhalifah and Ken Larner 63

Gaussian beam migration for anisotropic media
Tariq Alkhalifah 87

Parabolic and linear 2-D τ-p transforms using the generalized radon transform
John E. Anderson 109

Three-dimensional dip moveout for depth-variable velocity
Craig Artley, Patrick Blondel, Alexander M. Popovici, and Matthias Schwab 123

Expanded Abstract: Fundamentals of the discrete wavelet transform for seismic data processing
Jack K. Cohen and Tong Chen 133

Elimination of dispersion in finite-difference modeling and migration
Tong Fei 155

Seismic modeling in anisotropic media
Tong Fei 177

A study on distributed genetic algorithms
Wenceslau Gouveia 199

A Kirchhoff approach to seismic modeling and prestack depth migration
Zhenyue Liu 217

Velocity analysis by perturbation 241
Zhenyue Liu and Norman Bleistein

Application of dynamic ray tracing in triangulated subsurface models 261
Andreas Rüger

Inverse calculations with realistic *a priori* information 291
John A. Scales, Boyi Ou and Albert Tarantola

2.5-D full-waveform modeling 311
John W. Stockwell, Jr.

Analytic description of dip moveout in anisotropic media 327
I. Tsvankin

Body-wave radiation patterns and AVO in anisotropic media 355
I. Tsvankin

2-D depth migration in transversely isotropic media using explicit operators 377
Omar Uzcategui

Migration by analytic continuation through a variable background medium 399
Michael Zhdanov and Timo Tjan

Tutorial: Regularization in inversion theory, Expanded Abstract 417
Michael Zhdanov

CWP Biographies 421

Sponsors Mailing List 429

Index 431

ACKNOWLEDGMENTS

This project review is prepared for the sponsors of the Consortium Project at the Center for Wave Phenomena. This project provides substantial funding for the overall research and educational program at the Center. We also receive funds from the Department of Energy and the Office of Naval Research for research that is integrated into our program and reported on in this document. We are extremely grateful to our consortium sponsors (listed on page 429) and our government sponsors for their support.

INTRODUCTION

This book is a review of the research program at the Center for Wave Phenomena (CWP) for the 1992-93 academic year. The scope of research at CWP broadened dramatically this year with the addition to the faculty of two outstanding young scientists, John A. Scales and Ilya D. Tsvankin. Both John and Ilya come to CWP from Amoco where John was a research scientist and Ilya served as a consultant to the Geophysical Research Department.

John gives CWP strength in the "other" kind of inversion—inversion as a kind of constrained optimization problem—that complements the asymptotic inversion theories of the founding members of CWP, Norman Bleistein and Jack Cohen. John's special interests are in developing a sound statistical underpinning for the inversion problem and incorporating detailed geological and other prior information into the calculations. His influence in CWP is seen in this volume in his co-authored paper with Boyi Ou on inverse problems and in the paper by Wenceslau Gouveia on genetic algorithms. John's expertise in diverse areas of the geosciences brings him many visitors both inside and outside CWP. In this, his first semester at Colorado School of Mines, John also authored a comprehensive set of notes for his seismic migration course.

In last year's Project Review, Ken Larner presented several papers on the problem of appraising the importance of errors in seismic imaging caused by neglect of anisotropy. With the addition of Ilya Tsvankin's penetrating research in the area of anisotropy, CWP becomes a substantial player in the investigation of this important area of exploration geophysics. Ilya is represented in this volume by two papers devoted to the influence of anisotropy on dip moveout and amplitude-versus-offset analysis. Analytic and numerical developments in these papers lead to a methodology for doing DMO and analysis of issues in AVO in such media. Both Ilya's and Ken's work are further seen in the papers by Tariq Alkhalifah on migration error, modeling, and migration in inhomogeneous, transversely isotropic media.

Michael Zhdanov, on leave from the Institute of the Physics of the Earth, Moscow, continues his two-year visit to CWP. A renowned researcher in electromagnetic methods, Michael's work is represented in this Project Review by his paper with Timo Tjan on their "analytic continuation" migration method, which accounts for downward traveling energy for imaging of multiples. Also included in this book is Michael's abstract for a tutorial on regularization in inversion theory. With their keen interest in applying techniques in the field, it is natural that both Ilya and Michael have also established close contacts with Tom Davis's field study consortium at CSM.

John Anderson, of Mobil, is on campus for two years as Mobil's Visiting Scientist. John has devoted a substantial block of his time to interacting with CWP faculty and students, enhancing our efforts with his formidable experience with "real world" data

[1]We acknowledge John Scales, Craig Artley, and our publications specialist Barbara McLenon, for their contributions to the production of this book's new format.

processing techniques. He is represented by a short paper on a state-of-the-art code for doing discrete radon transforms, which he wrote while simultaneously learning the NeXT operating system, the C language, the CWP library routines, and LaTeX.

Our students continue to produce high-quality work, and CWP is exceptionally proud of them. Members of our faculty and students made a strong showing in their presentations at the 1992 SEG meeting in New Orleans, and we anticipate a favorable response to the nine talks planned for the upcoming 1993 meeting in Washington, D.C. (The collected expanded abstracts submitted for that meeting are available from the CWP office.)

During the past year sponsors have received a number of published research reports, as well as the following proprietary computer codes:

- U16, Docherty, P., CWELL: 2.5 dimensional crosswell modeling program. Proprietary: 8/24/95.
- U17, Hale, D., SUMIGGBZO: A zero offset migration code using Gaussian beams. Proprietary: 5/26/95.
- U19, Artley, C., SUDMOVZ: Depth-variable velocity DMO programs SUDMOVZ and DMOIR. Proprietary: 1/25/86.

In addition, three CWP students are scheduled to complete their thesis work in the near future: Tariq Alkhalifah, M.Sc., Migration error in transversely isotropic media; Andreas Rüeger, M.Sc., Application of dynamic ray tracing in triangulated subsurface models; and Mohammed Alfaraj, Ph.D., Transformation to zero offset for mode-converted waves.

We believe that the breadth and quality of research within CWP, represented in this book, is currently at the highest point of its nine-year history.

CWP-132

Transformation to zero offset for mode-converted waves by Fourier transform

Mohammed Alfaraj

Excerpt from

— Doctoral Thesis —

Transformation to zero offset for mode-converted waves by Fourier transform

Mohammed Alfaraj

ABSTRACT

A frequency-wavenumber (f–k) method for doing transformation to zero-offset (TZO) for mode-converted waves is thoroughly investigated here. The method requires only slight modification to the existing Hale's TZO method for ordinary p-waves. To modify Hale's TZO method to mode conversion, one needs to know only the velocity ratio. The TZO operator here differs from the elliptical p-wave operator in two aspects. First, the operator is a pseudo-ellipse; its deviation from being an ellipse is controlled solely by the velocity ratio which squeezes one side of the operator and stretches the other, depending on the mode of conversion. Second, the operator is laterally shifted, and in a time-varying manner, so that it closely resembles the behavior of the theoretical operator for mode-converted waves. Using a modified version of Hale and Artley's squeezing trick, the method is readily extendible to approximately handle velocity variations with depth.

Tests on synthetic data show that the method is capable, to a great extent, of transforming mode-converted data to zero offset. Although not too sensitive to the choice of velocity ratio, the TZO process must account for mode conversion when dealing with mode-converted data. Not only can the mode-converted TZO method correct reflections from dipping reflectors, but also from horizontal ones, in which case reflections are simply shifted laterally to their appropriate, zero-offset locations. As for dipping reflectors, reflections are properly TZO-corrected regardless of the sign of dip.

Finally, I have tested the method on two field (p–sv) data sets acquired in the same area, but shot in opposite directions. Because of poor signal quality, the results obtained after applying mode-converted TZO were not as dramatic as those seen in the synthetic data. Nevertheless, the stacking velocity, obtained after mode-converted TZO has been applied, is dip-independent—a result both conventional processing (no TZO) and conventional TZO (ignoring mode conversion) have failed to achieve. Furthermore, I show that the method may be used to qualitatively infer information about the velocity ratio from field data. I also derive an expression for quantitatively estimating the velocity ratio from the two mode-converted data sets; the expression makes use of the relative shift between the stacks from each set, among other things.

INTRODUCTION

A formulation for the transformation to zero-offset (TZO) for mode-converted waves in the t–x domain (Kirchhoff implementation) was introduced by Harrison (1990). Den Rooijen (1991) applied the formulation to mode-converted seismic data; his synthetic tests showed that the TZO operator yielded aliased results, though not too severely. Alfaraj and Larner (1992) and Alfaraj (1992) described a method for doing mode-converted TZO in a nonphysical domain; this method is, in principle, exact for constant-velocity media, and requires knowledge of only the velocity ratio. Unfortunately, Alfaraj and Larner's method, due to intrinsic problems, fell short of achieving its TZO goal; it can be used only for obtaining dip-independent velocity functions.

Here, I describe and implement a practical, frequency-wavenumber (f–k) TZO method that deals with mode-converted waves. The method is practical because it requires only slight modification to the existing Hale's (1984) TZO method developed for ordinary p-waves. The modification, in turn, requires only knowledge of the velocity ratio. Furthermore, the mode-converted f–k TZO method, as with Hale's method, is readily extendible to approximately handle the more practical situation wherein the velocity varies with depth.

I test the method on both synthetic and field mode-converted (p–sv) data. Results from synthetic data reveal that the method is capable, to a great extent, of transforming mode-converted data to zero offset. The method corrects data from both dipping reflectors regardless of the sign of dip, and from horizontal reflectors by laterally shifting reflections to their appropriate zero-offset locations. Although the method is not too sensitive to the choice of velocity ratio, tests show that it is essential to to take mode conversion into account when dealing with mode-converted waves.

Results from two field data sets show that the dip influence on stacking velocity has significantly decreased after application of mode-converted TZO, a result that conventional TZO (ignoring mode conversion) has failed to produce. Additionally, I show that the method can be used to infer information about the velocity ratio from seismic data. Also, with the availability of two data sets shot in opposite direction (as the field example here), one can make use of the relative lateral shift between their stacks to estimate a velocity ratio.

TZO FOR CONVERTED WAVES BY FOURIER TRANSFORM

Review

Following is a review of the formulation for the mode-converted f–k TZO method. For a detailed analysis, see Alfaraj (1993).

Assuming a constant-velocity medium, the f–k zero-offset seismogram for mode-

converted waves is given in terms of the NMO-corrected seismogram p_n as

$$P_0(\omega,k,h) = \int dt_n\, A^{-1}\, e^{i\omega A t_n}\, e^{iBk} \int dy\, e^{-iky}\, p_n(t_n,y,h), \tag{1}$$

where A is given by

$$A \equiv \frac{dt_n}{dt_0} = \sqrt{1+\frac{4\gamma h^2 k^2}{(1+\gamma)^2 t_n^2 \omega^2}}, \tag{2}$$

the quantity B is a constant given by

$$B = \frac{\gamma-1}{\gamma+1}h. \tag{3}$$

In the above relations, h is half-offset between source and receiver, t_n and t_0 are NMO-corrected and zero-offset times, respectively, y denotes midpoint, and γ is the velocity ratio. The fact that B is a constant (for a constant offset $2h$) implies a linear spatial phase shift, i.e. e^{iBk}, in the Fourier domain. This linear phase shift, in turn, corresponds to a constant lateral shift in the space domain. Specifically, this constant shift is the asymptotic approximation (offset small compared with depth) for the spatial location of the conversion point for a horizontal reflector (Sword, 1984).

Finally, 2-D inverse transformation of equation (1) yields the desired TZO data, i.e., $p_0(t_0,y,h)$, as follows

$$p_0(t_0,y,h) = \frac{1}{(2\pi)^2}\int d\omega\, e^{-i\omega t_0} \int dk\, e^{iky}\, P_0(\omega,k,h).$$

The impulse response

The corresponding TZO operator in the t–y domain is obtained by finding the inverse Fourier transform of $P_0(\omega,k,h)$ when $p_n(t_n,y,h)$ is an impulse. This is accomplished by applying the method of stationary phase to equation (1) (see, for example, Bleistein, 1984; and Liner, 1988). The TZO operator in the t–y domain is found to be an ellipse, given by

$$\left(\frac{t_0}{t_n}\right)^2 + \left(\frac{Y_0}{H}\right)^2 = 1. \tag{4}$$

The quantity H is a scaled version of half-offset h, given by

$$H = \frac{2\sqrt{\gamma}}{1+\gamma}h. \tag{5}$$

Equation (5) implies that the TZO impulse response for mode-converted waves is a *squeezed* version of that for ordinary p-waves. The quantity Y_0 is the location of the output zero-offset trace; it is shifted from the output location for ordinary p-waves, y_0, and is given by

$$Y_0 = y_0 - \frac{1-\gamma}{1+\gamma}h. \tag{6}$$

When $\gamma = 1$ (no mode conversion), equation (4) reduces to the well-known dip-moveout (DMO) ellipse for ordinary p-waves.

The offset scaling as implied by (5), and the shift in the output zero-offset trace as suggested by (6), are equivalent to the transformation introduced by Sword (1984). Sword suggested that each prestack seismic trace, in the time-space domain, be given a new midpoint location and a new offset, consistent with equations (5) and (6), prior to any processing. The TZO approach introduced here, on the other hand, accounts for the location of the new midpoints, as suggested by Sword, without having to deal with trace interpolation in the time-space domain; each trace is simply shifted to the desired location by introducing a spatial phase shift in the f–k domain, as suggested by the transform in equation (1).

The above f–k TZO formulation was based on a truncated power series for the traveltime for mode-converted waves (Alfaraj, 1993). One result of the truncation of the power series was that the phase shift obtained in (1) was constant and time-invariant. The actual spatial shift of the conversion point for a horizontal reflector, however, is known to vary with reflection depth, or time (Tessmer and Behle, 1988). Figure (1) shows the theoretical impulse response (solid), along with the derived,

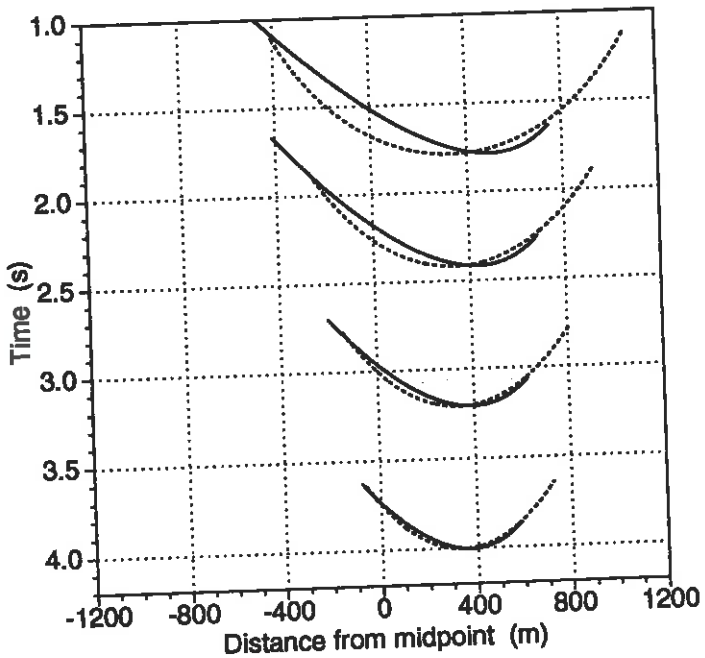

FIG. 1. Theoretical (solid) and approximate (dotted) TZO impulse responses for four input impulses (1.75, 2.4, 3.2, and 4.0 s) at midpoint 0. The approximate operator has a constant (time-invariant) lateral shift, as opposed to the time-variant shift for the theoretical TZO operator. The offset is 2000 m. The downgoing and upgoing velocities are 2000 and 1000 m/s, respectively.

approximate impulse response assuming four input impulses. The lateral shifts of the apexes of the theoretical operators are clearly time-variant; the apexes correspond to

horizontal reflections, i.e., zero dip. From the figure, it is also clear that the lateral, constant shift of the derived TZO operator needs to be adjusted (increased in this case), in a time-varying manner, so as to obtain a better match of the two operators near the vicinity of their apexes.

IMPROVING THE TZO OPERATOR

In this section, we attempt to improve the derived, approximate TZO operator in two different ways. First, the constant, spatial shift of the operator will be modified to better resemble the behavior of the conversion point for a horizontal reflector. This modification is achieved by altering the phase of the TZO transform to be time variant. Second, a squeeze/stretch technique is applied to the operator to make it better match the theoretical one.

Time-variant phase shift

It is easy to embed time-variance of the conversion point into the phase-shift term of the transform in (1), and thus partially alleviate errors arising from truncating the series. Let us call the lateral position of the conversion point b, relative to the midpoint. With D denoting the depth of a horizontal reflector, the relationship between D and b (Alfaraj, 1993) is given by

$$D^2 = -\frac{(h^2 - b^2)^2}{h^2 + 2\alpha hb/\beta + b^2}\,, \tag{7}$$

where α and β are constants depending only on the velocity ratio γ. In terms of normalized quantities $\tilde{D} = D/h$ and $\tilde{b} = b/h$, equation (7) can be written as

$$\tilde{D}^2 = -\frac{(1 - \tilde{b}^2)^2}{1 + 2\alpha\tilde{b}/\beta + \tilde{b}^2}\,, \tag{8}$$

showing that the relation between $\tilde{D}$ and $\tilde{b}$ is totally determined if the velocity ratio γ is known. Naturally, we would prefer to find b as a function of D using equation (7); this, however, requires solving a quartic equation in b. Rather, we directly calculate $\tilde{D}$ as a function of $\tilde{b}$ using equation (8), thus building a table of $[\tilde{D}, \tilde{b}(\tilde{D})]$ pairs for any given velocity ratio. Making use of a table constructed in this way aids the efficiency of the TZO process since such a table needs to be calculated only once (the only required parameter is the velocity ratio). Figure 2 shows an example of normalized b as a function of normalized depth for different velocity ratios. In the TZO process itself, both $\tilde{D}$ and $\tilde{b}$ are translated, respectively, into NMO-corrected time t_n and actual lateral shift b, using velocity and half-offset information. In other words, the pairs $[\tilde{D}, \tilde{b}(\tilde{D})]$ in the original table are trivially converted into pairs $[t_n, b(t_n)]$. Then, we use this time-variant $b(t_n)$ in the phase shift of the transform given by (1), instead of the time-invariant B given by equation (3). Figure 3 shows impulses and TZO impulse responses for TZO constructed in this way.

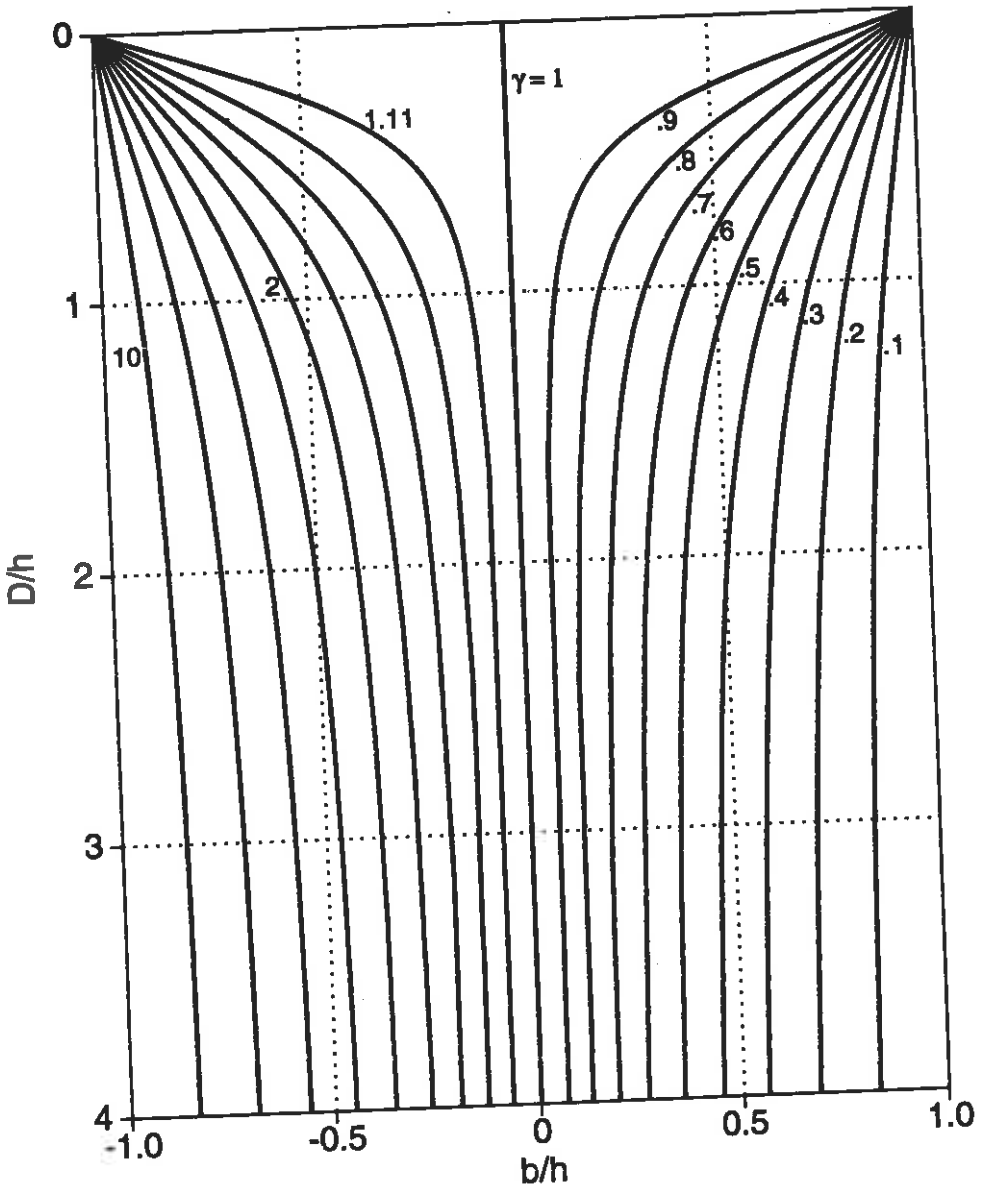

FIG. 2. Behavior of the conversion point in a homogeneous medium, as dictated by equation (8). Here, for different velocity ratios, normalized depth (D/h) of the conversion point is plotted against the normalized, lateral position (b/h) for a horizontal reflector. The numbers shown on the plots are values of γ. Note that plots for γ and $1/\gamma$ are symmetric about the vertical line $b/h = 0$.

Figure 3a shows ten impulses on a common-offset ($2h$ = 5000 m) section. Assuming a p–sv mode conversion with velocity ratio $\gamma = 0.5$, the response of the

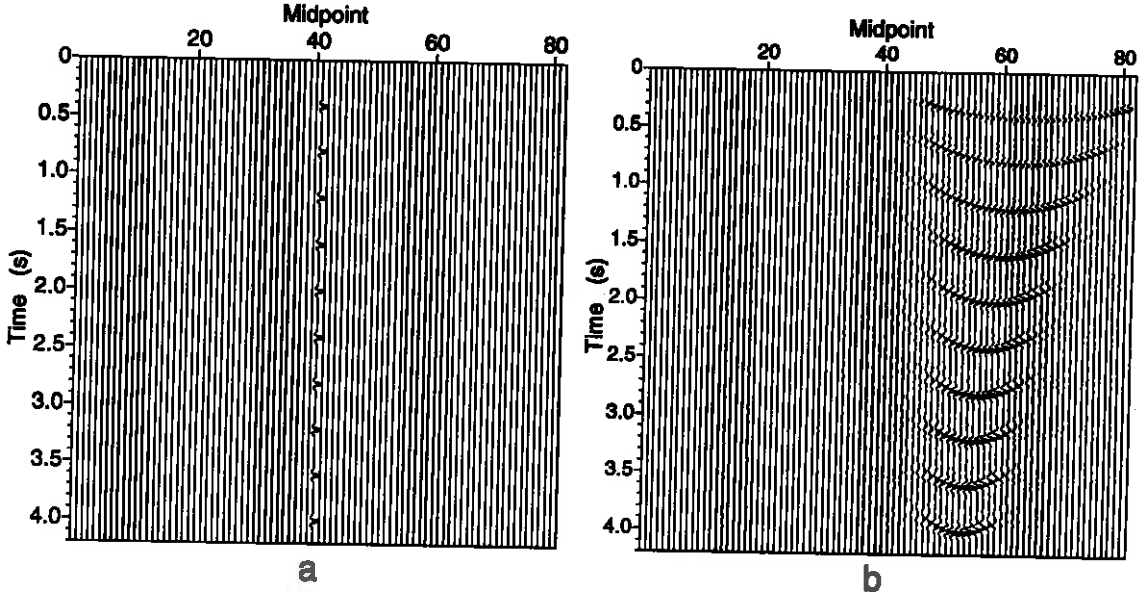

FIG. 3. Ten impulses in a constant-offset section (a) used to test the response of the TZO operator for mode-converted waves (b). The offset here, 5000 m, is chosen large to emphasize the time-variant lateral shifts seen in the impulse responses in (b). The midpoint spacing is 100 m.

modified TZO operator to those impulses is as shown in Figure 3b. Each impulse response is an ellipse that has now been squeezed, relative to that for ordinary p-waves, in the sense that its horizontal axis, when extended to the surface, spans a distance $2H$ (see equation [5]) that is smaller than offset $2h$. Furthermore, each squeezed ellipse has been laterally shifted, in a time-varying manner, in such a way that the apex now corresponds to the conversion point for a horizontal reflector.

Squeezing and stretching the TZO operator

While proper, time-variant shift has been introduced, the elliptical shape of the TZO operator, as Figure 1 clearly shows, is still wrong. Squeezing (or stretching) the operator is a practical way to modifying its response to a nonelliptical shape that is closer to the correct one. Hale and Artley (1991) introduced a *squeeze factor* that would squeeze the elliptical DMO response for ordinary p-waves. Although their squeeze factor was used primarily to tune the elliptical DMO response to better handle steep reflections for depth-variable velocity, the same squeeze concept may also be used even when velocity is constant. Specifically, Hale and Artley have empirically found that a squeeze factor of 0.62 is sufficient to improve the accuracy of constant-velocity DMO if the Fourier-transform approximation introduced by Notfors and Godfrey (1987) is used. I find that this squeeze concept is also beneficial in

improving the f–k TZO process for mode-converted waves. I adopt Hale and Artley's squeeze idea here to distort the shape of the approximate, mode-converted TZO operator. As we will see, TZO based on the resulting shape, which is closer to the correct one than that without distortion, yields better alignment of reflections in CRP gathers.

Figure 4a shows the shapes of four impulse responses of TZO (dashed), where only

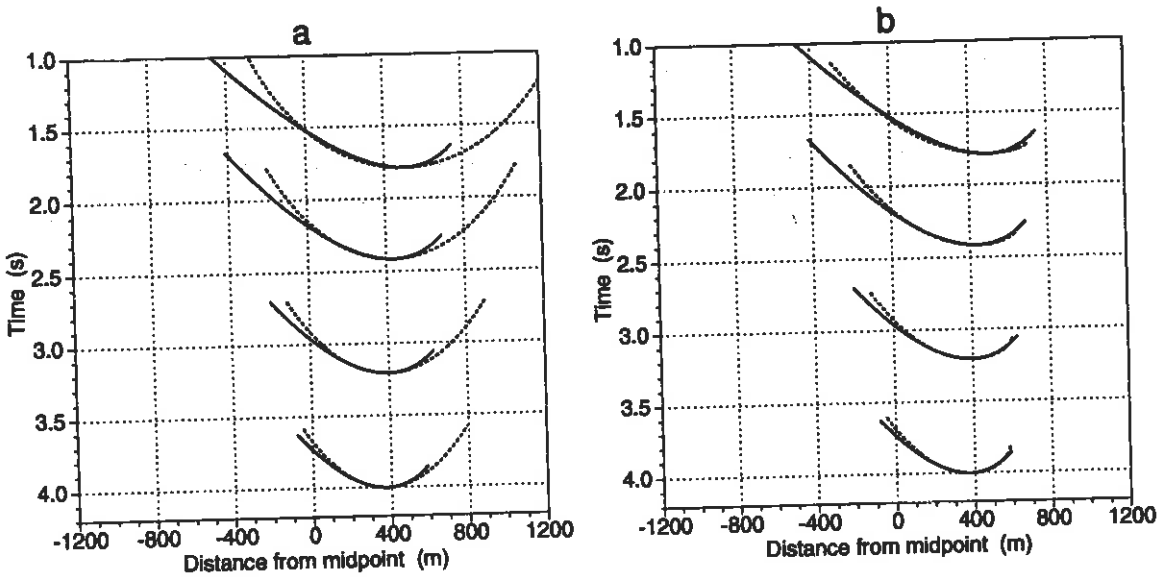

FIG. 4. Shapes of approximate TZO response (dashed) to four impulses, along with those of the correct responses (solid lines). Proper, time-variant lateral shifts have been applied in (a). The result in (a) after squeezing/stretching is shown in (b); the squeeze and stretch factors are, respectively, 0.05 and 5.0. A p–sv mode conversion ($\gamma = 0.5$) is assumed here. Offset is 2000 m. Input impulses are the same as those for Figure 1.

proper, time-variant lateral shifts have been applied. For comparison, the correct responses (solid) are also shown in the figure. Negative zero-offset slopes correspond to the right segments of each curve, whereas positive zero-offset slopes correspond to the left segments. As Figure 4a suggests, to achieve a response that is closer to the correct one, negative slopes need to be squeezed, and positive slopes need to be stretched. In other words, for the p–sv mode conversion shown in Figure 4a, the *sign* of the slope, alone, determines whether stretching or squeezing should be applied. Figure 4b exhibits a squeezed/stretched version of the responses shown in Figure 4a. Figure 5 shows the response of an actual TZO algorithm without and with stretching/squeezing applied, for six input impulses.

The empirical process of squeezing or stretching would have little practical value if it were dependent on either dip or time. Moreover, the stretch and squeeze factors must not depend too sensitively on γ. Although the stretched/squeezed curves could be made to fit the correct ones if the stretch/squeeze factors were allowed to vary with time and dip, I choose stretch and squeeze factors here that depend only on the

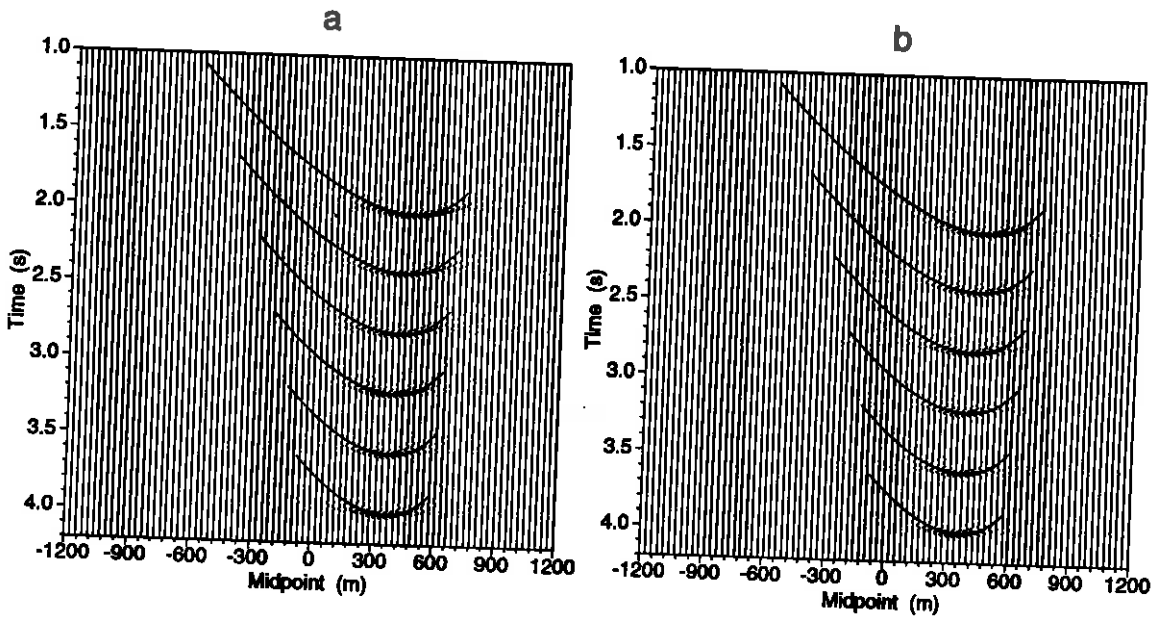

FIG. 5. Response of a TZO algorithm to six impulses, along with the correct responses (solid lines). (a) No squeezing/stretching, (b) Stretch and squeeze factors of 5.0 and 0.05, respectively, have been applied. The responses in (b) are closer to the correct shapes. A p–sv mode conversion ($\gamma = 0.5$) is assumed here. Offset is 2000 m. Input impulses were originally at midpoint 0.

velocity ratio, γ, and yield Hale and Artley's squeeze factor when $\gamma = 1$. Because the stretch/squeeze factors here depend on the velocity ratio only, the match between a stretched/squeezed curve and its theoretical counterpart is imperfect, but, as we shall see, yields quite acceptable moveout correction. The TZO operator is thus either squeezed or stretched, depending on the sign of the zero-offset slope as well as on the mode of conversion (p–sv or sv–p). I empirically determine this factor by comparing squeezed/stretched TZO impulse responses, using different velocity ratios, to correct theoretical impulse responses (Alfaraj, 1993).

For convenience, let us define $S1$ as a parameter that achieves either squeezing or stretching and apply it to the *positive* zero-offset slopes, i.e. the left segment of the TZO operator, regardless of the mode of conversion (p–sv or sv–p). By the same token, we define $S2$ as a parameter differing from $S1$ in that (1) $S2$ is always associated with the *negative* zero-offset slopes, and (2) $S2$ performs the opposite action of $S1$ (e.g., if the action of $S1$ is squeezing, then that of $S2$ is stretching). With this convention, and assuming p–sv mode conversion, the stretch and squeeze factors, $S1$ and $S2$, respectively, may be approximated using the following relations

$$S1 \;=\; 0.620 + 0.633 \left[\left(\frac{1}{\gamma} \right)^3 - 1 \right],$$

$$S2 = 0.620 + 0.615\left[\left(\frac{1}{2-\gamma}\right)^7 - 1\right], \tag{9}$$

which were empirically determined using a least-square fit on experimental data. For sv–p mode conversion, the empirical squeeze and stretch factors, $S1$ and $S2$, respectively, are given by

$$\begin{aligned} S1 &= 0.620 + 0.615\left[\left(\frac{1}{2-1/\gamma}\right)^7 - 1\right], \\ S2 &= 0.620 + 0.633(\gamma^3 - 1). \end{aligned} \tag{10}$$

In general, any of these four expressions achieves squeezing when its value is less than 1, stretching if the value exceeds 1, and does nothing to the TZO operator when it is equal to 1.

Neither relation for $S1$ and $S2$, however, yields a value of unity when the velocity ratio is 1; they both give a value of 0.62 which implies squeezing of both positive and negative slopes. As shown by Liner (1990), the Fourier-transform approximation (Notfors and Godfrey, 1987), which we assume is used here, results in a stretched impulse response that is wider than the theoretical constant-velocity DMO ellipse. The squeeze factor 0.62 compensates for this stretching (Hale and Artley, 1991).

I shall refer to the improved method (with time-varying shift and stretch/squeeze) as the *mode-converted TZO method* and use it for the remainder of this paper.

DEPTH-VARIABLE VELOCITY

The mode-converted TZO method is able, to a great extent, to correct mode-converted seismic data when the medium velocity is assumed constant (results not shown). We now investigate the situation when the velocity function varies with depth. We begin by showing that the proposed, constant-velocity TZO method can be modified, in a simple and a practical way, to handle velocity variations with depth. The modification here is simply achieved by further *squeezing* the derived (stretched/squeezed) TZO operator. We then apply the modified TZO method to synthetic, mode-converted seismic data, assuming a velocity function that varies linearly with depth.

TZO operator for depth-variable velocity

To approximately handle velocity variations with depth for ordinary p-waves, Hale and Artley (1991) proposed the concept of squeezed DMO, an efficient method that yields reasonably accurate results. We have already made use of their squeeze concept in the previous section. There, the TZO operator for mode-converted waves was squeezed/stretched to better resemble the theoretical operator in a constant-velocity medium. Here, we use Hale and Artley's squeeze concept, once more, but the aim now

is to allow the constant-velocity TZO operator for mode-converted waves to better handle velocity variations with depth.

To study TZO when velocity varies with depth, I empirically analyze synthetic, mode-converted seismic data, assuming a linear velocity function with depth, given by

$$v(z) = v_0 + G\,z,$$

where v is the downgoing velocity as a function of depth z, v_0 is the downgoing velocity at the surface, and $G = \Delta v/\Delta z$ denotes the downgoing-velocity gradient with respect to depth. I then apply a slightly modified version of Hale and Artley's squeeze idea to the data. The modification is solely that I choose a different squeeze factor than theirs, keeping in mind that this squeezing action is in addition to the modifications (squeezing/stretching) already incorporated into the TZO operator developed in the previous section. The additional squeeze factor here, which I also choose as a function of only the velocity ratio, is just to make the constant-velocity TZO operator better cope with situations when velocities vary with depth.

For ordinary p-waves, Hale and Artley found that an additional squeeze factor $A = 0.6$ is sufficient to make the constant-velocity TZO approximately handle velocity variations with depth. Applying the constant-velocity TZO to vertically inhomogeneous media, therefore, requires an overall squeeze factor given by

$$\tilde{S} = A\,S,$$

where we recall from the previous section that $S = 0.62$ is a squeeze factor Hale and Artley applied even when velocity is a constant. For mode-converted waves in homogeneous media, however, we needed two factors, $S1$ and $S2$ in equations (9) and (10), to tailor the TZO operator to better resemble the theoretical one. Consequently, we deal with two overall factors, $\tilde{S}1$ and $\tilde{S}2$, when velocity changes with depth for mode-converted waves.

Numerical results of tests with different velocity ratios and different velocity gradients show that the required overall factors for mode-converted waves can be estimated from the following relations

$$\begin{aligned} \tilde{S}1 &= \gamma\,A\,S1, \\ \tilde{S}2 &= \gamma\,A\,S2, \end{aligned} \tag{11}$$

where $A = 0.6$ is the additional squeeze factor given by Hale and Artley (1991) for ordinary p-waves ($\gamma = 1$) when velocity varies with depth. From equation (11), the additional squeeze factor needed for depth-variable velocity for mode-converted waves is thus γA, which reduces to A, Hale and Artley's additional squeeze factor for ordinary p-waves ($\gamma = 1$).

Figure 6 shows four examples of common-reflection-point (CRP) gathers processed using overall stretch/squeeze factors calculated from equation (11), assuming different velocity gradients (0.4, 0.5, 0.6, and 0.8 s^{-1}). Each CRP gather contains reflections

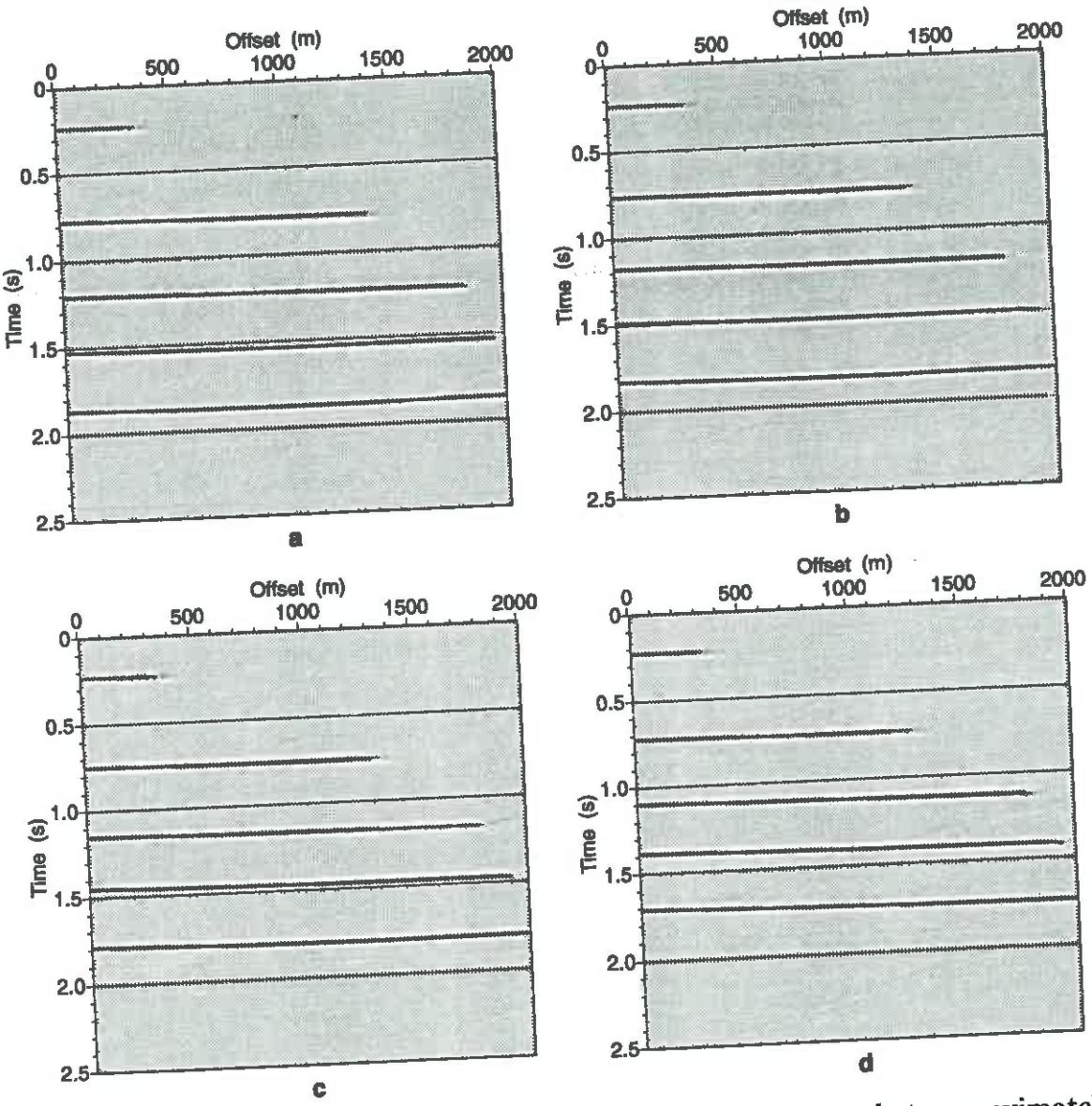

FIG. 6. CRP gathers processed with a squeezed TZO operator that approximately handles velocity variations with depth. The velocity gradients used in generating the data in (a), (b), (c), and (d) are, respectively, 0.4, 0.5, 0.6, and 0.8 s^{-1}. The velocity ratio and the downgoing velocity at the surface are 0.5 and 2500 m/s, respectively. The overall stretch and squeeze factors used here are $\tilde{S}1 = 1.5$ and $\tilde{S}2 = 0.01$, calculated from equation (11).

from five reflectors, with negative reflector dips ranging from zero (shallowest) to 80 degrees (deepest), in increments of 20 degrees. In each model, p–sv mode conversion is assumed, with $\gamma = 0.5$, and the downgoing velocity at the surface is 2500 m/s.

The good alignment in the results of Figure 6 suggests that the squeezed TZO approach for mode-converted waves provides a natural and efficient method of TZO correction for depth-variable velocity. The empirical relation for the squeeze factor given by equation (11) therefore provides an extension, to mode conversion, of the concept of squeezed DMO for depth-variable velocity introduced by Hale and Artley (1991) for ordinary p-waves. Next, I show, more fully, implementation of squeezed TZO on mode-converted seismic data, using relation (11), for a velocity function that varies linearly with depth.

Depth-variable velocity: synthetic examples

Here, we consider a depth model consisting of five reflectors with negative dips. The shallowest reflector is horizontal, the deepest dips at 80 degrees, and the dip increment is 20 degrees. We assume a downgoing velocity v that increases linearly with depth z, i.e.,

$$v(z) = v_0 + G\,z, \tag{12}$$

where the downgoing velocity at the surface $v_0 = 2500$ m/s, and the gradient of the downgoing velocity $G = 0.7\ \mathrm{s}^{-1}$. We assume p–sv mode conversion, with a velocity ratio of 0.5. The zero-offset section associated with this depth model is exhibited in Figure 7. Note that, since velocity varies with depth, the reflections from the various flat, dipping reflectors are slightly curved. We shall use the middle midpoint at 500 m as a test point to study various output results. The synthetic data here consist of 126 CMP gathers, each with 125 traces. Spacing between CMP gathers is 8 m. A zero-phase wavelet is assumed, with a dominant frequency of 25 Hz.

The CMP gather corresponding to the test point of the model is shown in Figure 8a. As with the constant-velocity case (results not shown), the moveout curves are nonhyperbolic, and their apexes are not located at zero-offset. The CMP gather exhibits reverse moveout for dipping reflections, as in the constant-velocity case.

To perform the NMO correction for this depth-variable velocity, we use a root-mean-square (RMS) velocity, V_{nmo}, which is an extension of v_{nmo} given by Alfaraj (1993) for the constant-velocity case. We replace the constant downgoing velocity v by the corresponding RMS velocity, v_{rms}, since the medium velocity is no longer a constant. That is, for depth-variable velocity the NMO velocity for mode-converted waves, V_{nmo}, is given by

$$V_{nmo}^2 = \gamma\, v_{rms}^2, \tag{13}$$

where the RMS velocity v_{rms} is calculated based on the downgoing velocity function $v(z)$ given in equation (12).

The NMO-corrected gather corresponding to Figure 8a is shown in Figure 8b. In that figure, only the horizontal reflections (shallowest) are correctly aligned. In addi-

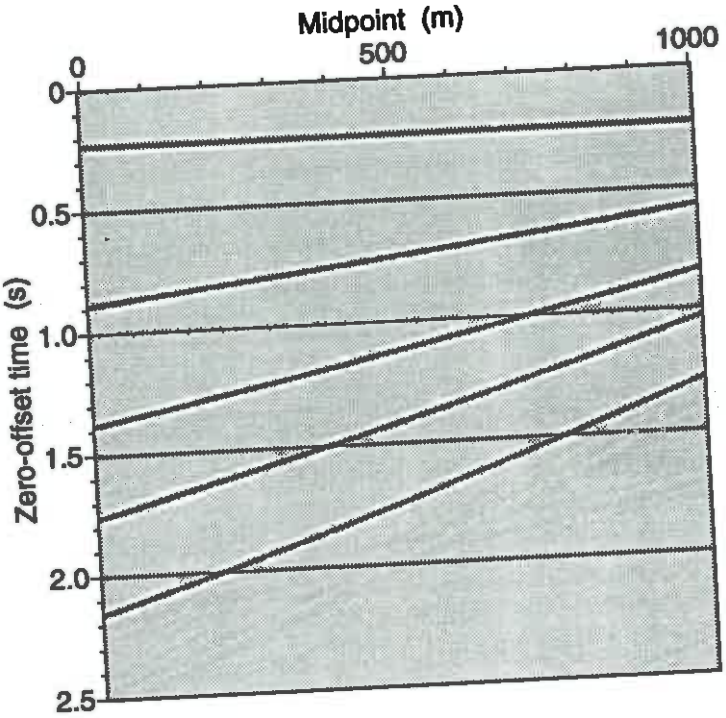

FIG. 7. Zero-offset model used to generate synthetic p–sv data. The model shows zero-offset reflections from five reflectors in a medium where velocity varies linearly with depth. The downgoing velocity at the surface and the gradient of the downgoing velocity are 2500 m/s and 0.7 s^{-1}, respectively, and the sv–p velocity ratio is 0.5. The shallowest reflector is horizontal, the deepest reflector dips at 80 degrees, and the dip increment is 20 degrees.

tion, dipping reflections are now severely overcorrected. Obviously, NMO correction alone is not enough to produce a good stack since reflections from dipping reflectors are present.

Let us emphasize the negative consequence of erroneously TZO-processing the mode-converted data by ignoring mode conversion. Figure 9a shows a CRP gather corresponding to the NMO-corrected gather of Figure 8b, resulting from application of Hale's f–k TZO method. TZO applied erroneously by ignoring mode conversion *fails* to correct the data. CRP gathers processed in this way, therefore, will produce a poor stack.

Figure 9b shows the same CRP gather, but processed now using the mode-converted TZO method. For this CRP gather, the overall stretch and squeeze factors, $\tilde{S}1 = 1.50$ and $\tilde{S}2 = 0.01$, were calculated using equation (11). Alignments of reflections are much improved.

Stacks of the processed data from both the conventional and the mode-converted TZO methods are shown in Figure 10. While dipping events are almost completely wiped out in the stack of the conventional-TZO data, the mode-converted TZO

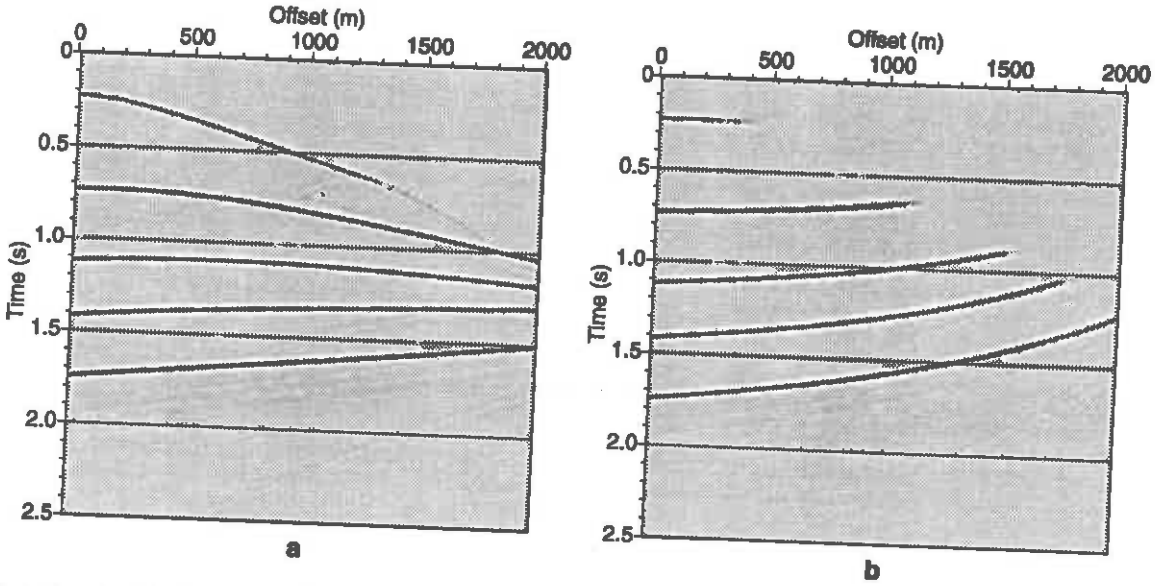

FIG. 8. Synthetic p–sv CMP gather (a), and (b) after applying NMO correction. Both gathers correspond to the middle midpoint of Figure 7. The downgoing velocity at the surface and the downgoing-velocity gradient are 2500 m/s and 0.7 s^{-1}, respectively; the velocity ratio is 0.5.

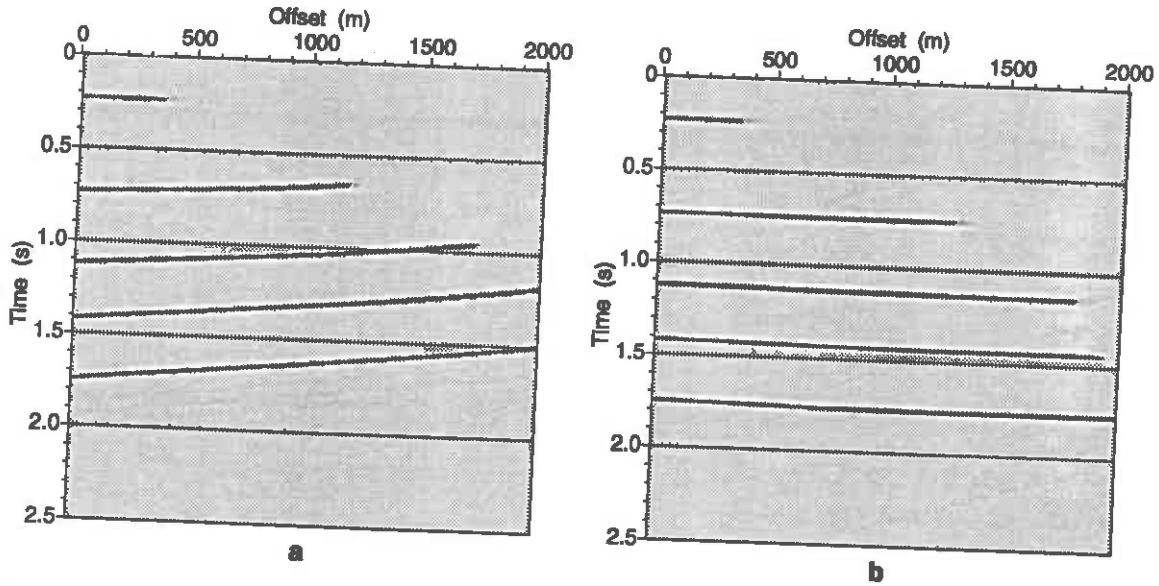

FIG. 9. CRP gathers corresponding to the NMO-corrected gather of Figure 8b. (a) is obtained by processing the mode-converted data with a conventional TZO algorithm that ignores mode conversion. Only the horizontal reflection (shallowest) is properly aligned. (b) is the same gather obtained by applying the mode-converted TZO method.

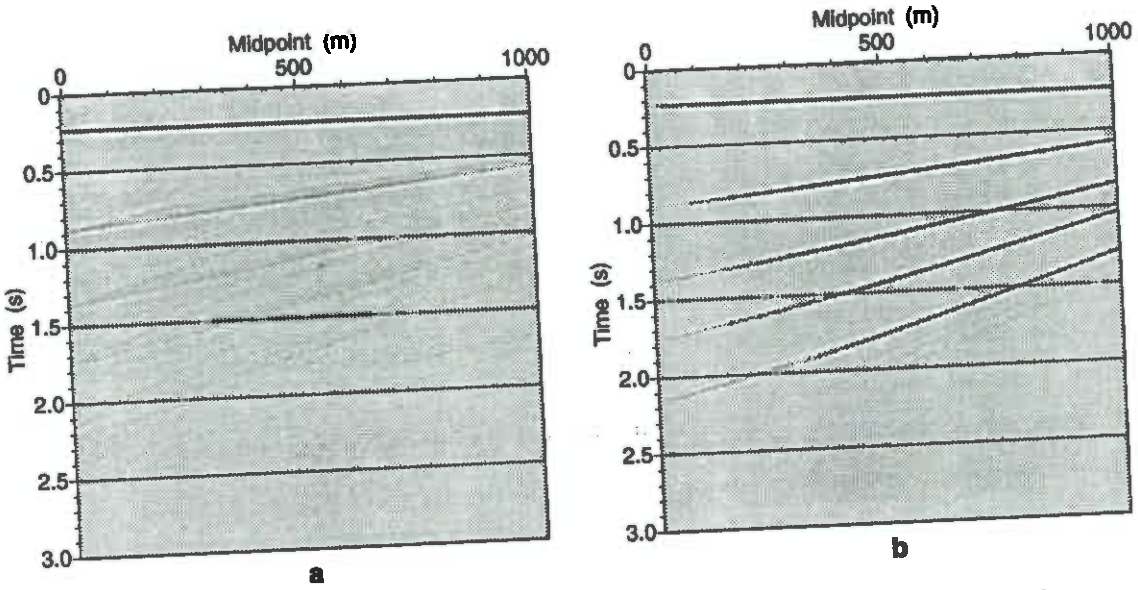

FIG. 10. Stacks of CRP gathers. The data in (a) were processed by ignoring mode conversion; those in (b) were processed using the mode-converted TZO method. Reflections from only the horizontal reflector (shallowest) stack properly when mode conversion is ignored (a). The mode-converted TZO method produces a stack that has the same structure as that of the zero-offset model depicted in Figure 7.

method was able to produce the same structure as that of the zero-offset model (Figure 7). The weak amplitude at lower midpoints in Figure 10b is due to the tendency of the mode-converted TZO operator to move energy toward the right (receivers are situated to right of source, with p–sv mode conversion).

Finally, I note that the mode-converted TZO method is not highly sensitive to the choice of the overall stretch/squeeze factors (results not shown).

APPLICATION TO FIELD DATA

Introduction

Here, we discuss results of processing two field data sets consisting of mode-converted (p–sv) reflections. The data, acquired in the southern San Joaquin Valley of California, are courtesy of Chevron Oil Field Research Company. The two data sets were recorded over the same area, but shot in different directions. I shall refer to the data set whose receivers are located on the right of the source as Line 1, and to the other set (receivers on the left of source) as Line 2.

For comparison, I process the data in different ways: (1) processing with no regard to TZO; that is, the data are stacked using conventional stacking velocity; (2) processing with conventional TZO that does not honor mode conversion; and (3) processing with mode-converted TZO. I compare stacking velocities for all cases.

To apply mode-converted TZO, I start by estimating a velocity ratio that would be

suitable for processing the entire data. I achieve this by conducting both qualitative and quantitative analyses on the data. Based on both approaches, as we shall see, any velocity ratio γ in the range 0.4–0.5 (corresponding to Poisson's ratios $\sigma_P = 0.4$–0.3) is a reasonable estimate for the data here. I choose to use $\gamma = 0.4$ in applying mode-converted TZO to the two lines.

Field geometry and preprocessing

Each data set consists of 188 shot gathers, each gather has 60 receivers, covering a total surface distance of about 26000 ft. Within each shot gather, the nearest receiver is located 1080-ft from the source, and the receiver spacing is 120 ft, thus yielding a maximum source-receiver offset of 8160 ft. The recorded time is 6 s.

The source is a vertical-motion vibrator; the horizontal-component geophones are oriented so as to detect radial (horizontal, in-line) particle motion. Thus, we assume that the recorded reflections are dominated by mode-converted (p–sv) waves.

Preprocessing consists of applying residual-statics correction (provided by Chevron), muting of early times, gain, and filtering. Two forms of gain were applied to the data, trace balancing and automatic gain control (AGC). The AGC time window was 0.5 s. The filter is trapezoidal bandpass, with corner frequencies of 5, 10, 30, and 50 Hz.

The preprocessed data were sorted into 444 common-midpoint (CMP) gathers for each data set. These CMP gathers are used as inputs to the subsequent processing.

Conventional processing

In this section, I discuss data processed with no regard to TZO. I first perform velocity analysis on the preprocessed CMP gathers, and then use the velocity functions so-obtained to NMO-correct the data. The stacks of the NMO-corrected gathers for both Line 1 and 2 are shown in Figures 11 and 12, respectively.

The receivers are situated to the right of the source for Line 1, and to the left of the source for Line 2. With this, and since we are dealing with p–sv mode conversion, we expect to see events in Line 2 shift to the right relative to those in Line 1. A close examination of the two stacks reveals that the events are indeed shifted in accordance with the above assertion. Take, for example, the portion of the anticline at 4 s in Line 1, just to the left of the broad horizontal region (about midpoint 245). Now, the same feature in Line 2 intersects 4 s at about midpoint 215, resulting in a total relative shift to the right of $245 - 215 = 30$ midpoints. Allowing ± 5 midpoints for error tolerance, and recalling that the midpoint spacing is 60 ft, the total relative shift is thus $(30 \pm 5) \cdot 60 = 1800 \pm 300$ ft, a quantity I will later use to estimate the velocity ratio.

In Line 1 (Figure 11), note that the signal-to-noise ratio is poor on the right portion of the section, particularly after 2 s; Line 2 (Figure 12) has a better data quality in the same region, though still poor. In other regions, the data quality of

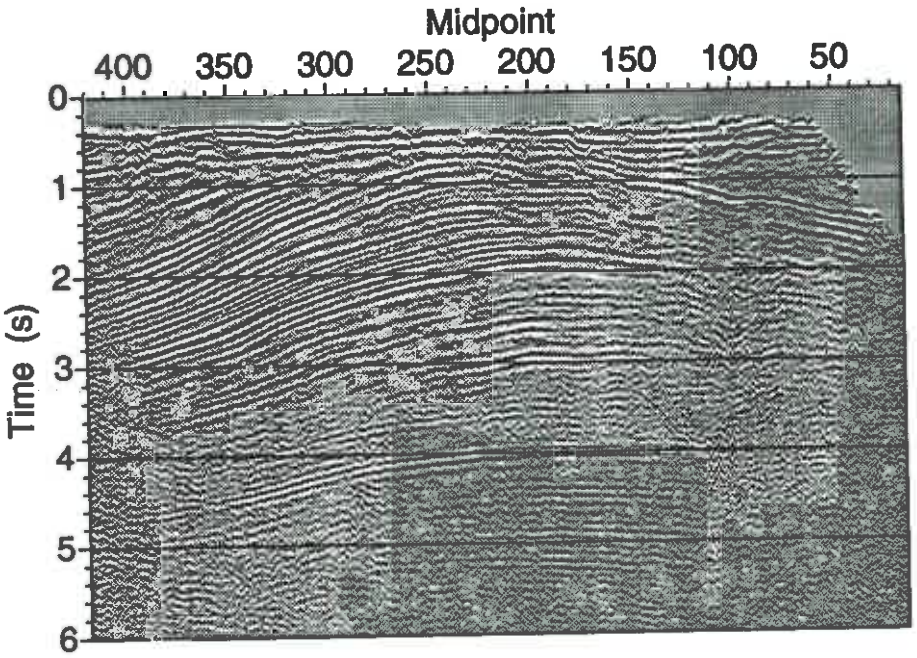

FIG. 11. Conventional stack of Line 1 with no TZO. In the acquisition of the data here, the receivers are situated to the right of the source.

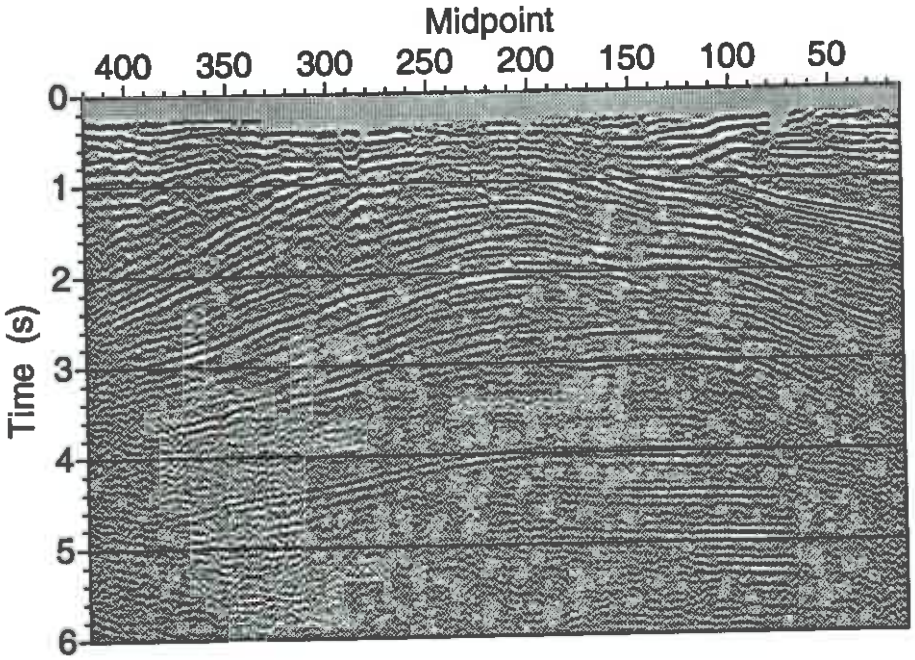

FIG. 12. Conventional stack of Line 2 with no TZO. In the acquisition of the data here, the receivers are situated to the left of the source.

Line 1 is, in general, better than that of Line 2. Compare, for example, the sloping reflections on the left of both sections, between 1 and 3 s. Also, it is obvious from the two stacks that there are no conflicting dips present in the subsurface (e.g., fault-plane reflections). Conflicting dips would have further aided in the assessment of results after applying mode-converted TZO to the two data sets. Below, I compare these sections to their counterparts when mode-converted TZO is performed.

The maximum reflection slope in the data is about 0.2 ms/ft, seen in Figure 11 at about 2 s and midpoint 350. This corresponds to a maximum dip angle of about 25 degrees (Alfaraj, 1993). This is a modest dip value when attempting to assess the value of TZO; therefore we should not expect TZO to have a dramatic influence on the imaging of the data in these lines.

Estimation of velocity ratio

Qualitative analysis.—Here, I compare TZO-corrected data resulting from use of different velocity ratios. I have tested eight ratios, from 0.3 to 1.0, in increments of 0.1. We first look at unstacked gathers from Line 1, at midpoints 100 and 275. To compare CRP (TZO-corrected) gathers with CMP gathers, I have removed the NMO correction from the CRP gathers. The gathers shown in Figure 13 pertain to midpoint 100 of Line 1. Figure 13a shows the CMP gather with only preprocessing applied. Figure 13b is a CRP gather after applying conventional TZO ($\gamma = 1$). Figures 13c, 13d, and 13e show CRP gathers after applying mode-converted TZO assuming velocity ratios of 0.6, 0.5, and 0.4, respectively. In the unstacked gathers of the two mode-converted data sets, the signal-to-noise ratio is poor compared to that of conventional p-wave data from the same area (not shown).

In terms of reflection continuity, I judge CRP gather 13e, with $\gamma = 0.4$, to be the best among the CRP gathers shown, including 13b which assumes conventional TZO. Compare, for example, the shallow event at 1.2 s, and the events just below 2 s in all gathers. Midpoint 100 is, of course, in the poor-signal portion of the section. The unstacked gathers for midpoint 275, over a better-signal part of the line, is shown in Figure 14. Again in terms of reflection continuity, the CRP gather with $\gamma = 0.4$ or 0.5 appear to be best among other gathers, although the reflections quality is far from ideal in any of the panels. Any of the choices, $\gamma = 0.4$–0.6, gives better reflection continuity than that in either the original data or the TZO-corrected data with $\gamma = 1$. However, as we recall from the study of the conversion point (Figure 2), the choice of velocity ratio also controls the time-varying lateral shift of reflections imposed by the TZO operator. Since the magnitude of shift depends on the choice of velocity ratio, only those choices of ratio that are close to the actual one in the subsurface will eventually place reflections in their correct positions. Hence, we can expect that reflector continuity might improve with those choices of velocity ratio that are close to the actual one. The conclusion here, that γ =0.4–0.5 for the data, was also supported by results from analyzing constant-velocity stacks (results not shown).

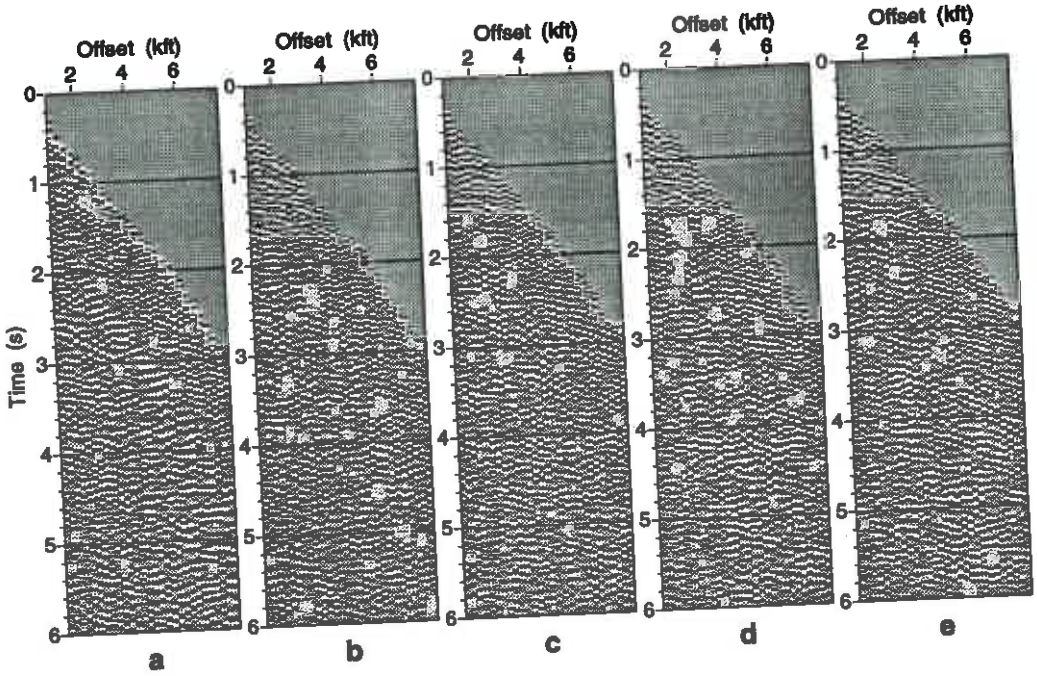

FIG. 13. Unstacked gathers corresponding to midpoint 100 of Line 1. The CMP gather with only preprocessing applied is shown in (a). CRP gathers, after undoing the NMO correction, are shown in (b), (c), (d), and (e), with velocity ratios 1.0, 0.6, 0.5, and 0.4, respectively.

Pleasing as it is to see the best continuity in the gathers produced by mode-converted TZO, one could ask whether that result is to be expected. From the synthetic data in Figure 9, we saw that mode-converted TZO altered moveouts, but it did not actually change reflection continuity.

Quantitative analysis.—To further support the qualitative assertion made above, that a velocity ratio $\gamma = 0.4$–0.5 is a reasonable choice, here I estimate the ratio based on measurements from the data.

Alfaraj (1993) gives an expression for zero-offset time for mode-converted waves. We start by splitting that relation into two parts, namely

$$\frac{\sigma^2}{\alpha h + \beta b} = a, \tag{14}$$

and

$$a = \frac{2h}{t^2}\left[\frac{t_0^2}{h^2 - b^2} + \left(\frac{2}{v_a}\right)^2\right]. \tag{15}$$

Quantities σ, α, and β depend on only the velocity ratio. The reason for the above splitting, as equation (15) implies, is to express a in terms of quantities that can be measured from seismic data (including the lateral shift b). With quantities b and a

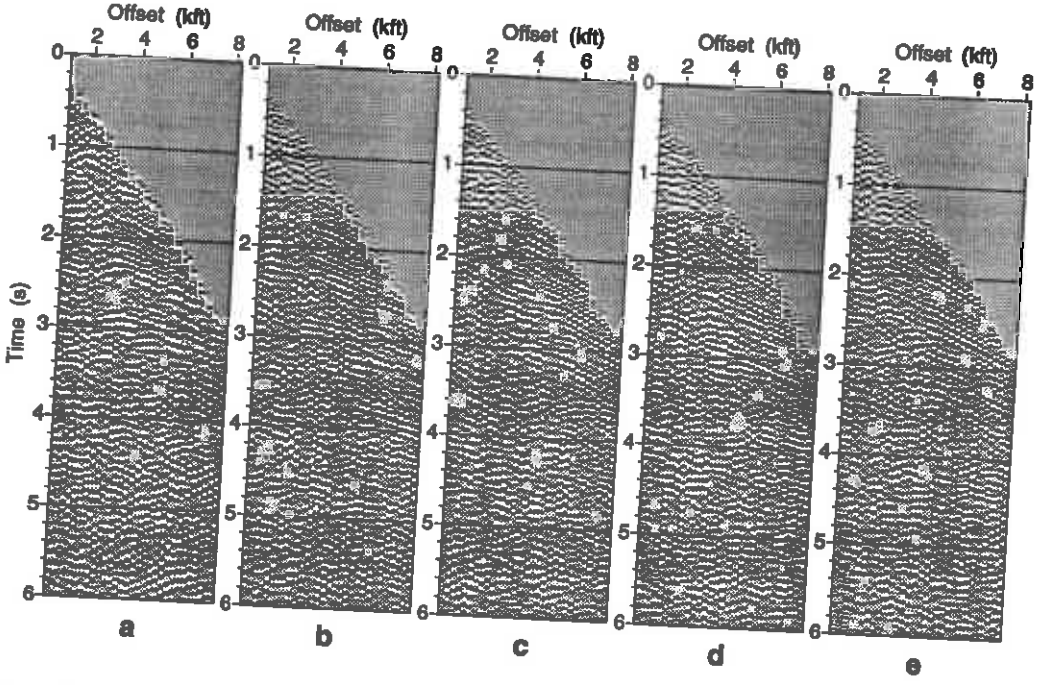

FIG. 14. Unstacked gathers corresponding to midpoint 275 of Line 1. The CMP gather with only preprocessing applied is shown in (a). CRP gathers, after undoing the NMO correction, are shown in (b), (c), (d), and (e), with velocity ratios 1.0, 0.6, 0.5, and 0.4, respectively.

known, we can then solve for γ from equation (14). Solving for γ from that equation, and simplifying, we get

$$\gamma = \frac{a(h-b)-1}{1-\sqrt{2ah-a^2(h^2-b^2)}}. \tag{16}$$

For simplicity here, we shall take v_a as the stacking velocity v_s, and t can be simply found from the expression

$$t^2 = t_0^2 + \frac{4h^2}{v_s^2}.$$

Also for simplicity, we shall assume near-horizontal reflectors, implying $b = 0$ for conventional p-waves.

The quantity b can be estimated from two stacked sections shot in two different directions, e.g., Lines 1 and 2 discussed earlier. We recall that the relative shift between the two sections at 4 s was 1800 $\pm$ 300 ft, corresponding to $b = 900 \pm 150$ ft (half the relative shift between the two sections). Since we are dealing with stacked data, the question now is: what value of half-offset h shall we use in the above relations? I choose to pick half the maximum h present in the data; i.e., $h = 2040$ ft—an average value that, I believe, is fairly representative of all half-offsets. As for velocity at 4 s between midpoints 248 and 215 (the vicinity of the shift

under investigation), I choose a value of 4500 ft/s, a reasonable value as we shall see when I analyze velocities.

With the above assumptions, relation (15) yields the range $a = 0.00113$–0.00132 ft^{-1}. Equation (16) then gives the corresponding range of velocity ratio $\gamma = 0.41$–0.52. A similar calculation at 2 s (peak of anticline at midpoint 180 in Line 1 shifts to midpoint 140 in Line 2) gives $a = 0.00126$–0.00159 ft^{-1}, and $\gamma = 0.40$–0.53. Both ranges of velocity ratio are consistent with that ($\gamma = 0.4$–0.5) from the qualitative analysis.

From the above analysis, and since TZO is not too sensitive to the choice of velocity ratio, I choose $\gamma = 0.4$ in the TZO processing of the two data sets.

Application of TZO

I now apply TZO to both data sets assuming $\gamma = 0.4$. For comparison, I also show the same data processed with conventional TZO. The processing sequence for the stacked sections to come is as follows

1. NMO-correct preprocessed CMP gathers;
2. sort into common-offset gathers;
3. apply TZO;
4. sort into CMP gathers;
5. remove NMO correction (applied in Step 1) from data in Step 4;
6. perform velocity analysis;
7. use velocity function from Step 6 to NMO-correct and stack the data in Step 5.

Next, I show results of velocity analysis (Step 6), and compare them to their counterparts when TZO is not performed.

Figures 15 and 16 show stacks of TZO-corrected data for Lines 1 and 2, respectively, assuming $\gamma = 0.4$. Ideally, the two sections should display the same subsurface image, with no lateral shift of reflections. Let us compare these two sections to one another, and then compare each one to its counterpart when conventional processing (no TZO) is performed.

At first glance, it seems as though there is a prominent lateral shift of reflections between the two stacks on the left of the sections (midpoint 400) between 2 and 3 s (Figures 15 and 16). However, a closer look shows that this is not the case; instead the major difference here is that amplitudes of events on the left end of Line 1 are weaker than those in Line 2. This can be attributed to the fact that the two lines were shot in opposite directions, resulting in each line having a different (shifted)

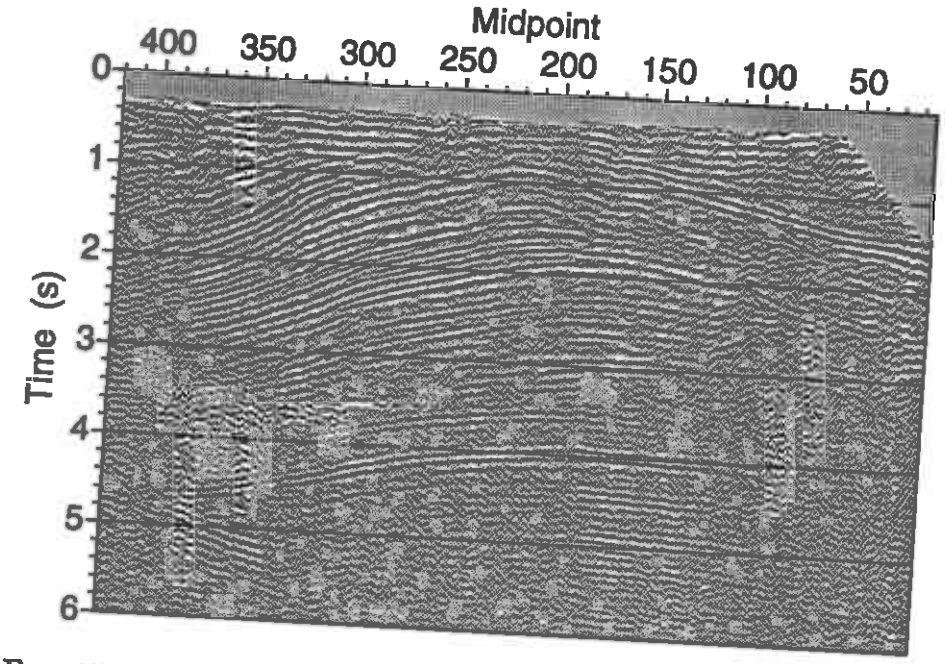

FIG. 15. Stack of TZO-corrected data of Line 1, assuming $\gamma = 0.4$.

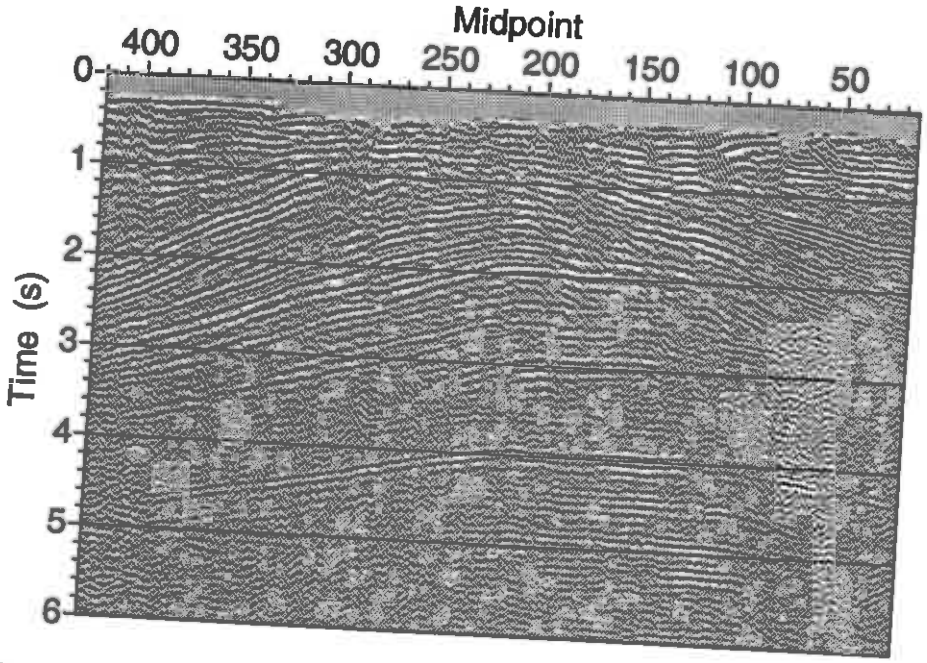

FIG. 16. Stack of TZO-corrected data of Line 2, assuming $\gamma = 0.4$.

subsurface *coverage* at the left and right ends of the section. This also explains the weakened amplitudes seen on the right end of Line 2.

I have asked several colleagues to compare the two stacks on a workstation. Not knowing my personal bias, and not knowing how the data were processed, most of them confirmed that the major difference between the two sections was in their amplitudes, and not in their shifts. Elsewhere in the two sections, locations of events generally match each other, although differences between the two sections are present (due to data quality and independently chosen stacking velocities). Take, for example, the anticline that intersects 4 s; in both sections, the intersection takes place at about midpoint 230. Another example is the anticline intersecting 2 s at midpoint 235 in both stacks.

We now compare the TZO-corrected stacks with conventional stacks for both lines. For Line 1, we note an improvement (flattening) of the dipping shallow reflector (Figure 15, midpoint 100, 1.2 s), as compared with its counterpart when conventional stack was used (Figure 11). Also, among other differences between the two stacks of Line 1, notice how the reflector at midpoint 175 and 3 s is smoother in the TZO-corrected section. In addition, dipping reflections below 5 s at midpoint 350 are present only in the TZO-corrected section. Note, also, that the reflections here have been shifted to the right; this is most prominent up shallow (compare, for example, the dipping reflections around 2 s between midpoints 350 and 400).

As expected for Line 2, the relative shift of events between the conventional stack (Figure 12) and the TZO-corrected stack (Figure 16) is opposite to that seen in the stacks of Line 1. That is, events in the TZO-corrected section are now shifted to the left, relative to those in the conventional stack. This opinion is shared, again, by colleagues with no knowledge as to how the data were processed. As for data quality, reflector continuity has improved on the left of the TZO-corrected section (between midpoints 350–400, 1.5–3 s). Meanwhile, data in the shallow part of the conventional stack have better quality than those in the TZO-corrected section.

For comparison, I show the same lines but now processed with conventional TZO ($\gamma = 1$). Figure 17 shows the stack of Line 1, and Figure 18 shows that of Line 2. The stack with conventional TZO for Line 1 (Figure 17) shows poorer reflectors continuity than when $\gamma = 0.4$ (Figure 15). For instance, compare the continuity of the reflector at midpoint 350 and 4.6 s in Figures 15 and 17. As for Line 2, the continuity of reflectors on the right of the section seems better in the stack with conventional TZO (Figure 18) than that with mode-converted TZO (Figure 16). However, data quality on the left of Line 2 is far superior with mode-converted TZO.

Unfortunately, but unsurprisingly, the data comparisons here are much less dramatic demonstrations of the effectiveness of mode-converted TZO than were the synthetic data examples. Given the sensitivity of any stack section to the choice of velocities for NMO correction, a look at the velocities used and the influence of velocity on these stacks may further help in assessment of the results.

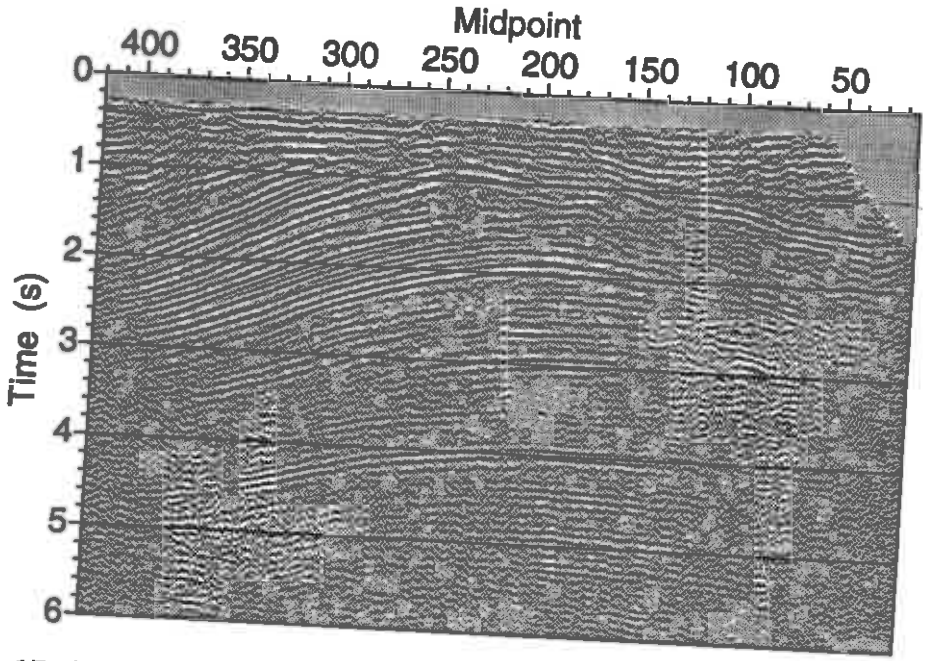

FIG. 17. Stack of TZO-corrected data of Line 1 assuming $\gamma = 1$ (no mode conversion).

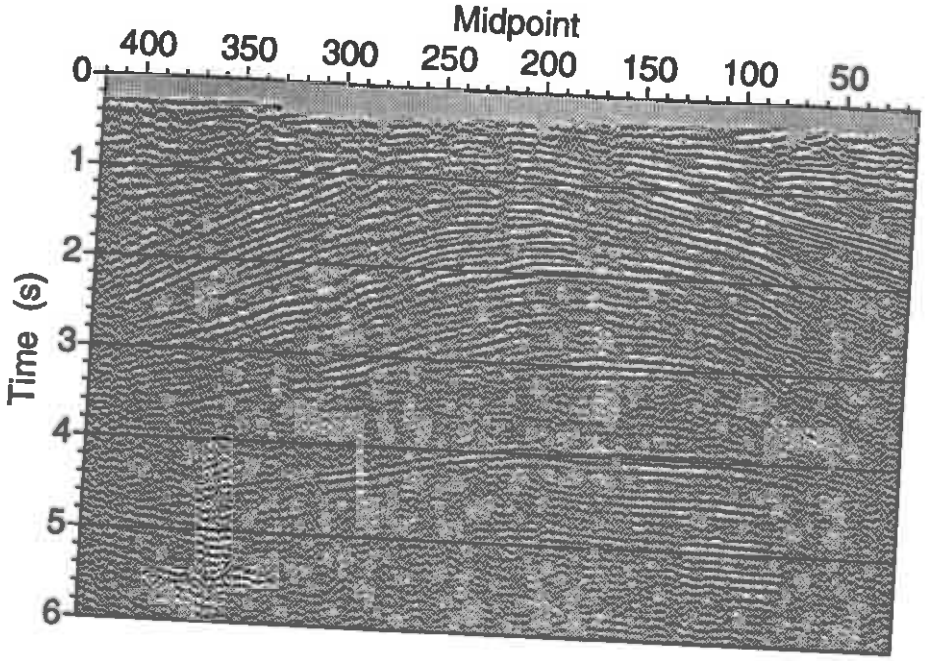

FIG. 18. Stack of TZO-corrected data of Line 2 assuming $\gamma = 1$ (no mode conversion).

Velocity analysis

We now look at stacking velocities for both lines, obtained before and after TZO has been applied. For data after TZO correction, I show stacking velocities for both mode-converted TZO and conventional TZO.

For Line 1, contours of stacking velocities, v_s, are shown in Figure 19. The conventional stacking velocities (no TZO) are shown in Figure 19a. Note the general decrease in velocity from left to right. This velocity trend is consistent with observations discussed by Alfaraj (1993)—that not only does the stacking velocity for mode-converted waves depend on dip, but also on the sign of dip. More specifically, the stacking velocity *increases* when the shooting is updip from source to receivers; the increase is relative to when the reflector is horizontal. On the other hand, when the shooting is downdip, the stacking velocity *decreases*. (The stacking velocity for ordinary p-waves always increases with dip, regardless of the sign of dip.)

Recall that the shooting in Line 1 was from left to right. Given the anticlinal features present in the subsurface for this case, the shooting from left (midpoint 400) to right (midpoint 200) is then seen in the updip direction from source to receivers. Hence, the stacking velocity in this region (Figure 19a) is, as expected, relatively higher than that on the right portion of the section (midpoints 50–200) where shooting is now downdip.

The velocity contours for Line 1 after applying mode-converted TZO are shown in Figure 19b. Note that the velocities are consistent across the section, and are generally structure-independent. This indicates that mode-converted TZO has removed the influence of dip on stacking velocity, as one would hope.

For comparison, I show velocity contours for the same data but now processed with conventional TZO (Figure 19c). The general trend here is similar to that with no TZO (Figure 19a), implying that conventional TZO did not remove the dip influence from stacking velocity; this is not surprising. Since we are dealing with mode conversion, we should not expect conventional TZO (ignoring mode conversion) to correct mode-converted data as effectively as does mode-converted TZO.

As for Line 2, results of velocity contours are shown in Figure 20. The shooting geometry here is the reverse of that for Line 1. Hence, what was updip shooting for Line 1 is now downdip shooting here, and visa versa. As a result, the velocity trend in the conventional stack (Figure 20a) is now the reverse of that from Line 1 (Figure 19a). The velocities after mode-converted TZO has been applied are shown in Figure 20b. Clearly by comparing Figures 20a and 20b, mode-converted TZO has significantly lessened the dip influence on stacking velocity. Velocities from conventional TZO are shown in Figure 20c; again, the trend here is similar to that with no TZO shown in Figure 20a.

The differences in stacking velocity seen in Figures 19 and 20 are significant in terms of their influence on the quality of the stacked data. To see this, Figure 21 shows a stack of conventional CMP gathers (Line 1), but the velocity function used

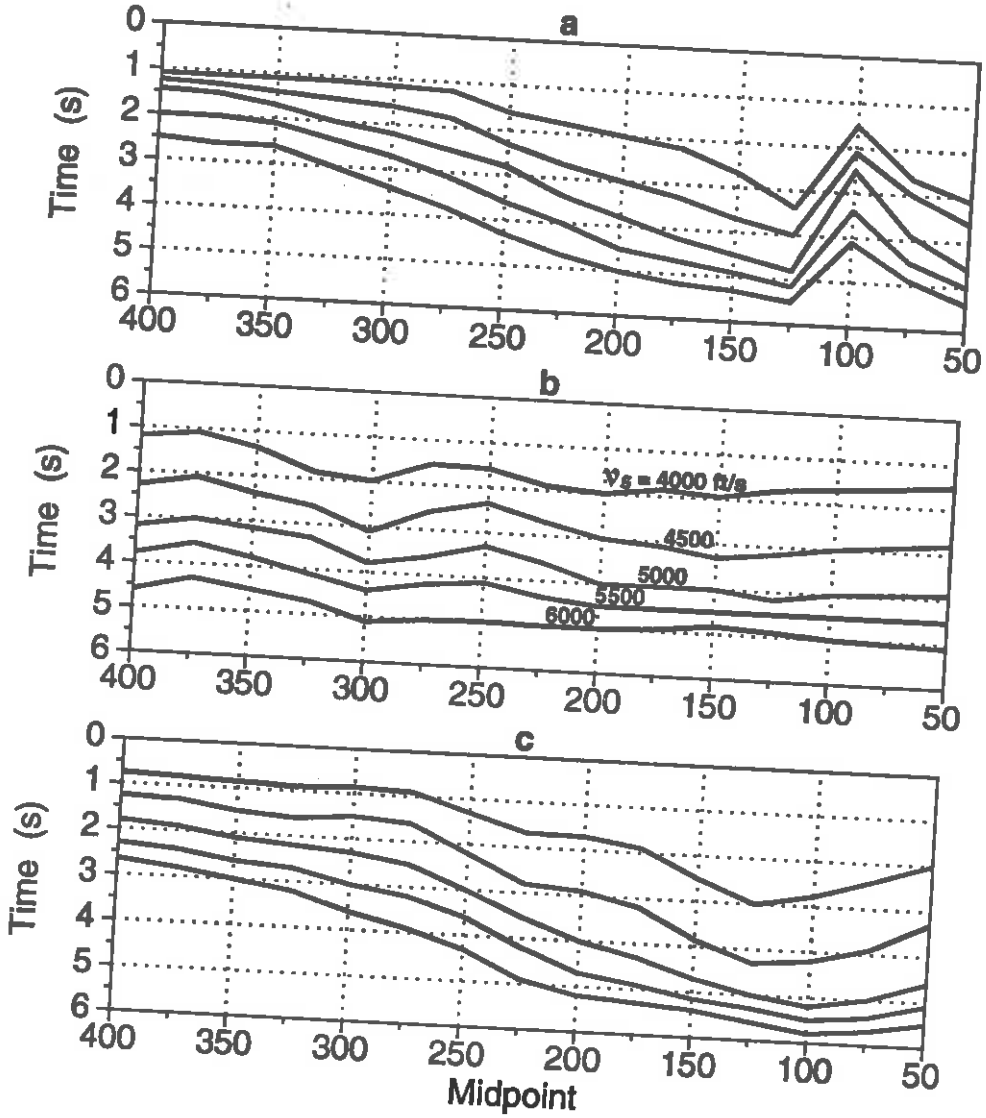

FIG. 19. Contours of stacking velocities for Line 1. (a) processing with no TZO; (b) mode-converted TZO; (c) conventional TZO.

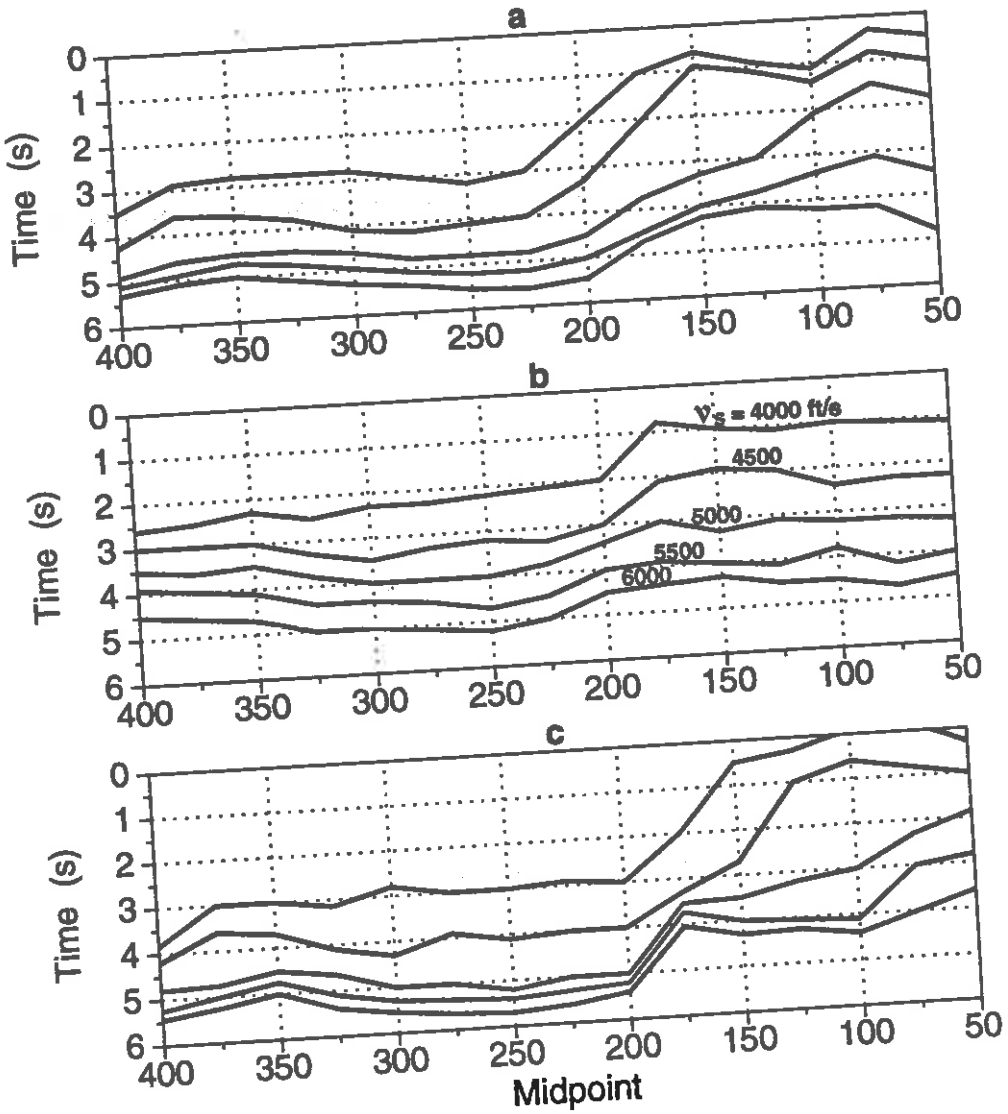

FIG. 20. Contours of stacking velocities for Line 2. (a) processing with no TZO; (b) mode-converted TZO; (c) conventional TZO.

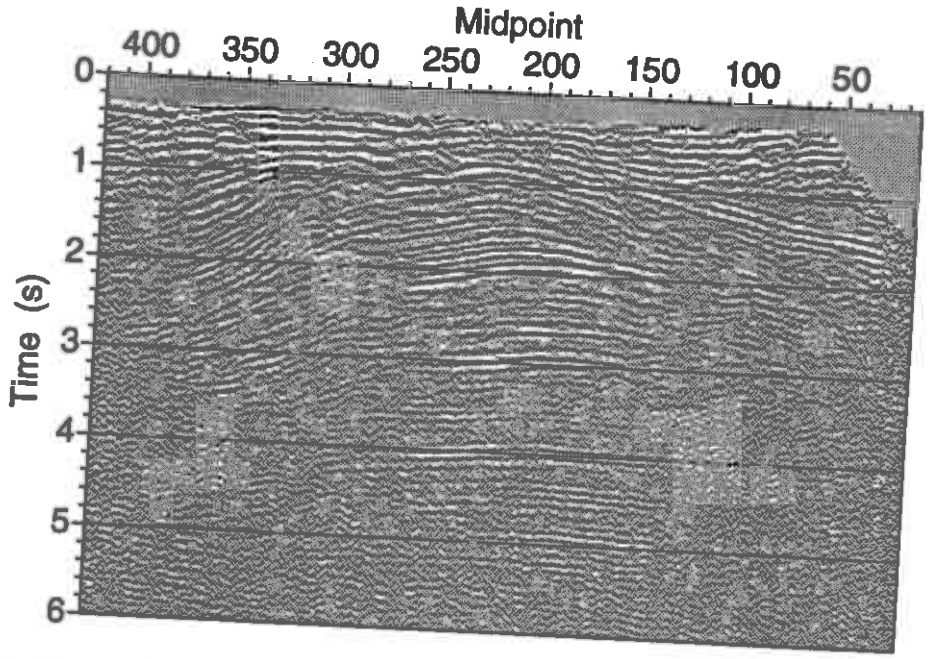

FIG. 21. Stack of conventional CMP gathers (Line 1), but using NMO velocity obtained after mode-converted TZO has been applied.

to NMO-correct these data is that (Figure 19b) obtained after mode-converted TZO has been applied. The stack here is much poorer in reflection quality than either the TZO-corrected stack (Figure 15) or the conventional stack (Figure 11). The same observation holds for Line 2; the stack of conventional CMP gathers, using NMO velocity after mode-converted TZO has been applied (Figure 22) is much poorer than that in Figure 12.

The central point in the "improper" stacks in Figures 21 and 22 is that the stack quality deteriorated when the rather stable, dip-independent NMO-correction velocities, as opposed to the dip-corrected velocities, were applied to the data. The conventional stacks were aided by the option to pick dip-dependent stacking velocity. That option would not have been available if the unmigrated data had contained crossing reflections having widely differing dips. We should not be surprised, therefore, that for these data, the mode-converted TZO, stacked data in Figures 15 and 16 were not dramatically superior to the conventionally stacked data in Figures 11 and 12.

I conclude from the analysis of the San Joaquin Valley data that, despite its poor signal quality and consequent difficulties in picking stacking velocities, and despite the fact that the data do not contain steep reflectors or conflicting slopes, the diagnostic results support the conclusion that mode-converted TZO yielded the best-processed results, (results that are most consistent on the two reversed lines), and did so with stacking velocities that were essentially independent of dip.

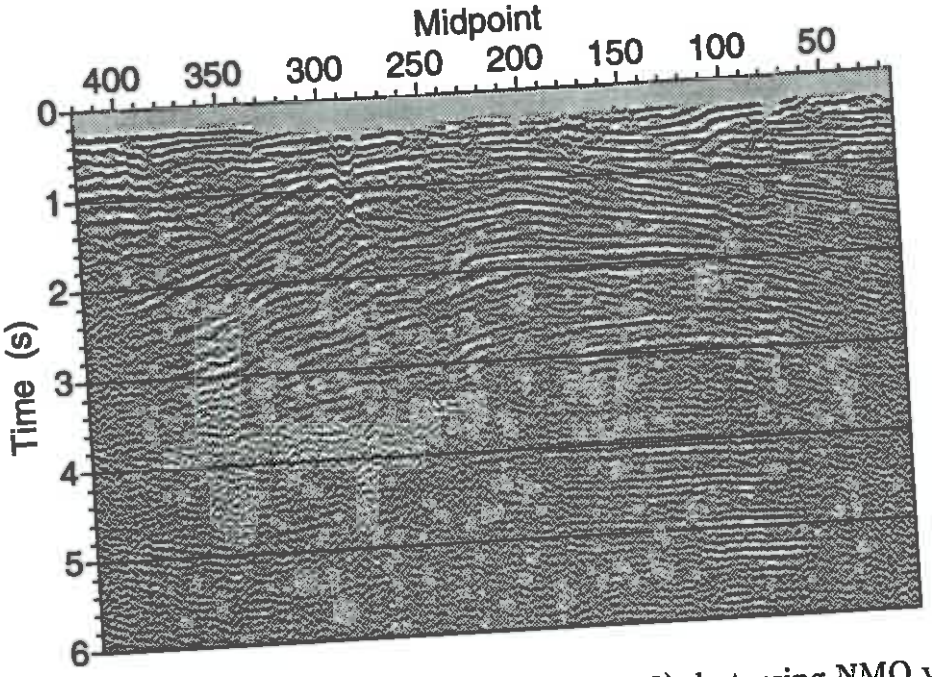

FIG. 22. Stack of conventional CMP gathers (Line 2), but using NMO velocity obtained after mode-converted TZO has been applied.

CONCLUSION

The f–k TZO approach for mode-converted waves, though approximate, is straightforward and easy to implement. Its implementation requires only slight modification to an existing algorithm—the Hale's f–k TZO algorithm used in processing ordinary p-waves. The mode-converted TZO operator differs from the well-known, elliptical p-wave operator in two aspects. First, its non-elliptical shape is controlled solely by the velocity ratio which, depending on the mode of conversion, squeezes one side of the operator and stretches the other. Second, the operator is laterally shifted, and in a time-varying manner. Furthermore, when the velocity ratio is unity (no mode conversion) the mode-converted TZO operator reduces to the conventional operator. As with conventional TZO, Hale and Artley's squeezing trick is readily extended to mode conversion so that mode-converted TZO can approximately handle velocity variations with depth.

Although the method is not too sensitive to the choice of velocity ratio, tests on synthetic data show that it is essential to take mode conversion into account when applying TZO. Application of this mode-converted f–k TZO method to synthetic seismic data reveals that the method is capable, to a great extent, of transforming data to zero offset. The method corrects data from both dipping reflectors regardless of the sign of dip, and from horizontal reflectors by laterally shifting reflections to their appropriate zero-offset locations.

Results from two field data sets show that the dip influence on stacking velocity

has significantly decreased after application of mode-converted TZO, a result that conventional TZO has failed to produce. Furthermore, this method can be used, in conjunction with velocity analysis, to qualitatively estimate a velocity ratio γ from field data (since the mode-converted TZO method is not too sensitive to the choice of γ, one would actually be able to estimate a range of γ, rather than a single, precise value of γ). Also, with the availability of two data sets shot over the same area but in opposite directions (as the field example in this paper), one can make use of the relative lateral shift between their two stacks to estimate a velocity ratio.

Finally, I recommend that this f–k TZO method for mode-converted waves be further modified to handle the more general situation wherein the velocity ratio varies with depth. The influence of anisotropy on this mode-converted TZO process could also be investigated. More specifically, I recommend that the work by Larner (1993), on TZO error due to anisotropy for ordinary p-waves, be extended to mode conversion. Such a study on synthetic data would provide insight as to how mode-converted TZO would behave in transversely isotropic media.

ACKNOWLEDGEMENTS

I thank Ken Larner for monitoring and reviewing my thesis (this paper is an excerpt from my thesis). He suggested this research, and provided valuable suggestions, beautiful ideas, and many *inserts* into the text of this paper. I am grateful to Ken for all that. Thanks are due to Saudi Aramco, Saudi Arabia, for their financial support. Finally, Clint Frasier, Chevron Oil Research Company, provided the field data; thanks to Clint and Chevron.

REFERENCES

Alfaraj, M., and Larner, K., 1992, Transformation to zero offset for mode-converted waves: Geophysics, **57**, 474–477.

Alfaraj, M., 1992, Transformation to zero offset for mode-converted waves in the k–t_1 domain: Colorado School of Mines, CWP Report 121.

Alfaraj, M., 1993, Transformation to zero offset for mode-converted waves: Ph.D. Thesis, Colorado School of Mines.

Bleistein, N., 1984, Mathematical methods for wave phenomena: Academic Press.

Den Rooijen, H. P. G. M., 1991, Stacking of p–sv reflection data using dip moveout: Geophysical Prospecting, **39**, 585–598.

Hale, D., 1984, Dip-moveout by Fourier transform: Geophysics, **49**, 741–757.

Hale, D., and Artley, C., 1991, Squeezing dip moveout for depth-variable velocity: Colorado School of Mines, CWP Report 112.

Harrison, M., 1990, Converted wave DMO: Presented at the 60th Ann. Internat. Mtg., Soc. Expl. Geophys., Expanded Abstracts, 1370–1373.

Larner, K., 1993, Dip-moveout error in transversely isotropic media with linear velocity: Geophysics, **58**.

Liner, C., 1988, General theory and comparative anatomy of dip moveout: Colorado School of Mines, CWP Report 073R.

Liner, C., 1990, General theory and comparative anatomy of dip moveout: Geophysics, **55**, 595–607.

Notfors, C. D., and Godfrey, R. J., 1987, Dip moveout in the frequency-wavenumber domain: Geophysics, **52**, 1718–1721.

Sword, C., 1984, Approximating the kinematics of converted waves: Stanford Exploration Project Report **41**, 347–368, Stanford University.

Tessmer, G., and Behle, A., 1988, Common reflection point data-stacking technique for converted waves: Geophysical Prospecting, **36**, 671–688.

CWP-129

Efficient synthetic seismograms for transversely isotropic media with constant velocity gradient

Tariq Alkhalifah

Efficient synthetic seismograms for transversely isotropic media with constant velocity gradient

Tariq Alkhalifah

ABSTRACT

Hale, in 1991, developed an efficient Kirchhoff-summation-based Seismic Unix (SU) program to generate synthetic seismograms in isotropic media with constant velocity gradient. Here, I extend his method to work for inhomogeneous transversely isotropic (TI) media with tilted axis of symmetry, using the analytic equations developed by Shearer and Chapman (1988) for raypaths in factorized TI (FTI) media with constant velocity gradient. Furthermore, I derive an analytical equation for geometrical spreading in FTI media that aids in preserving program efficiency. I then generalize this program to treat TI media that are not factorized anisotropic inhomogeneous by perturbing the FTI traveltimes, following the perturbation ideas of Červený and Filho (1991). For the type of velocity models treated, the program is much more efficient (at least an order of magnitude faster) than finite-difference and general ray-trace modeling techniques.

INTRODUCTION

Efficient seismic modeling programs are useful for testing the performance of algorithms for various processing needs such as dip-moveout and migration. For generating zero-offset synthetic seismograms, ray-tracing approaches generally offer substantially better performance than do finite-difference methods when the model is assumed to have simple velocity structure, such as constant velocity or constant velocity gradient. In 1991, Dave Hale developed a particularly efficient Kirchhoff-summation-based approach that exploited analytic expressions for raypaths and traveltimes in isotropic media with constant velocity gradient.

For modeling data from generally inhomogeneous, transversely isotropic (TI) media, ray tracing is computationally costly, so, again, some simplification of the velocity structure is needed to bring about desired computational efficiency. Although the tidy analytic expressions that arise for isotropic media with constant velocity gradient are no longer available for TI media, I find Hale's isotropic algorithm to be an ideal starting point for extending to efficient synthetic-seismogram computation for inhomogeneous TI media.

I first establish a ray-tracing algorithm for computing time and amplitude in a *factorized* TI (FTI) medium (i.e., TI medium in which all *ratios* among the elastic coefficients for TI media are independent of position). The constant-velocity-gradient restriction is essential in establishing analytic solutions for raypaths. Then, I use the time-perturbation equations developed by Červený and Filho (1991) to extend from FTI to general, inhomogeneous TI media with tilted symmetry axis. After developing the perturbation approach, I show sample synthetic data and demonstrate the efficiency of the approach.

RAY-TRACING EQUATIONS

I consider only 2-D wave propagation; that is, raypaths are confined to the vertical plane containing the axis of symmetry and the velocity gradient vector. The ray tracing is for a P-wave traveling in FTI media with linear velocity variation in space. With these assumptions, raypaths and amplitudes can be obtained by analytic solution.

Raypath and traveltime

The eigenvalues that describe the raypath (eikonal equation) and the eigenvectors that describe the amplitudes of the various waves in inhomogeneous media are based on a high-frequency approximation. The eigenvalues are calculated from the following relation (Červený, 1972)

$$\mathrm{Det}(\Gamma_{jk} - G_m \delta_{jk}) = 0,$$

where Γ_{jk} are components of a 3×3 matrix Γ given by the relation

$$\Gamma_{ik}(x_s, p_s) = a_{ijkl}(x_s) p_j p_l,$$

where I am using the summation convention for repeated subscripts,
$p_s = \partial\tau/\partial x_s$, $a_{ijkl} = c_{ijkl}/\rho$,

τ	is the traveltime along the ray,
ρ	is the density,
x_s	is the position, s=1,2,3, and
c_{ijkl}	are the elastic coefficients; in general, functions of x_s.

The G_m are the three eigenvalues representing the eikonal equation for the quasi P-wave when m=1, for the quasi SV-wave when m=2, and for the quasi SH-wave when

m=3. For P-waves (I shall drop the "quasi" modifier in the following),

$$G_1(x_s, p_s) = 1. \tag{1}$$

For isotropic media, $G_1 = \alpha^2(x_s)p_i p_i$, where $\alpha(x_s)$ is the P-wave velocity.

In a factorized anisotropic inhomogeneous (FAI) medium

$$a_{ijkl}(x_s) = f^2(x_s)A_{ijkl},$$

where $A_{ijkl} \equiv \frac{a_{ijkl}(x_s)}{a_{3333}(x_s)}$ are *position-independent* ratios of the density-normalized elastic coefficient, and $f(x_s) = [a_{3333}(x_s)]^{\frac{1}{2}}$ is the velocity in the direction parallel to the symmetry axis at position x_s. Equation (1) then becomes

$$G_1(x_s, p_s) = f^2(x_s)G_1^o(p_s) = 1, \tag{2}$$

where $G_1^o(p_i)$ is P-wave eigenvalue expression (1) with the $a_{ijkl}(x_s)$ replaced by the A_{ijkl}.

For a constant velocity gradient,

$$f(x_s) = A_s x_s, \tag{3}$$

where A_s is the gradient in the x_s direction. For such inhomogeneity, Shearer and Chapman (1988) showed the following simple relation between the slowness vector and the position vector.

$$p_i x_i = 0. \tag{4}$$

For 2-D, substituting equations (3) and (4) into equation (2) results in the *raypath equation* for a generally anisotropic medium with constant velocity gradients in the x_1 and x_3 directions,

$$(A_3 p_1 - A_1 p_3)^2 G_1^o(x_3, -x_1) = 1. \tag{5}$$

Note that, for media with constant velocity gradient, the factor $A_3 p_1 - A_1 p_3$ is independent of position along a ray.

For the special case of a transversely isotropic medium, the position-independent eigenvalue for the P-wave is given by (White, 1983)

$$G_1^o(p_1, p_3) = 0.5\{(a+l)p_1^2 + (c+l)p_3^2 + \{[(a-l)p_1^2 - (c-l)p_3^2]^2 + 4(f+l)^2 p_1^2 p_3^2\}^{\frac{1}{2}}\}, \tag{6}$$

where $a = A_{1111}$, $c = A_{3333}$, $f = A_{1133}$, and $l = A_{1313}$.

For axis of symmetry in the x_3 (vertical) direction, equation (6), along with equation (4), gives (Larner, 1993)

$$G_1^o(x_3, -x_1) = 0.5\{(a+l)x_3^2 + (c+l)x_1^2 + \{[(a-l)x_3^2 - (c-l)x_1^2]^2 + 4(f+l)^2 x_3^2 x_1^2\}^{\frac{1}{2}}\}. \tag{7}$$

Now, equation (4) gives

$$p_3(p_1) = -\frac{x_1}{x_3} p_1,$$

which, for later purposes, I use in defining the distance

$$r_0 = r_0[p_1(\xi_0)] \equiv \frac{1}{A_3 p_1(\xi_0) - A_1 p_3[p_1(\xi_0)]}, \tag{8}$$

where ξ is a running parameter that monotonically increases along the ray, with $\xi = \xi_0$ at the starting point of the ray (see Figure 1). Specifically,

$$d\xi = \frac{1}{f(x_i)} d\tau.$$

The value of the ray parameter $p_1(\xi_0)$ at ξ_0 defines the particular raypath. Then, distance r_0, defined in terms of the ray parameter at the starting point, $p_1(\xi_0)$, is shown in Figure 1.

In an isotropic medium with constant velocity gradient, all raypaths are circles. Consider an isotropic medium with velocity $f(x_i)$ identical to the vertical velocity in the constant-gradient FTI medium. Then, r_0, as defined in equation (8), is the radius of the circular raypath whose center is at the origin ($x_1 = 0, x_3 = 0$) and goes through point b, in Figure 1, associated with the raypath for the TI medium. Substituting equation (8) into equation (5) gives

$$G_1^o(x_3, -x_1) = r_0^2,$$

which, along with (7), results in the quadratic raypath equation for the TI medium

$$\alpha x_1^4 + \beta(r_0, x_3^2) x_1^2 + \gamma(r_0, x_3^2) = 0,$$

for $x_1[x_3, r_0]$. Here the coefficient α is a function of only the elasticity coefficients, and the coefficients β and α have the additional dependencies shown.

Following Červený (1989), for constant velocity gradient [equation (3)],

$$\begin{aligned} f(x_1, x_3) &= A_1 x_1 + A_3 x_3, \\ p_1(\xi) &= p_1(\xi_0) - A_1(\xi - \xi_0), \\ p_3(\xi) &= p_3(\xi_0) - A_3(\xi - \xi_0). \end{aligned}$$

Then, traveltime along the ray is given by

$$\tau(\xi) = \tau(\xi_0) + \int_{\xi_0}^{\xi} [G^o(p_1, p_3)]^{-\frac{1}{2}} d\xi.$$

Geometric spreading

Although geometric spreading in an isotropic medium with constant velocity gradient can be expressed analytically, the situation is not that simple for FTI media, which require dealing with the distinction between group and phase velocities. I use

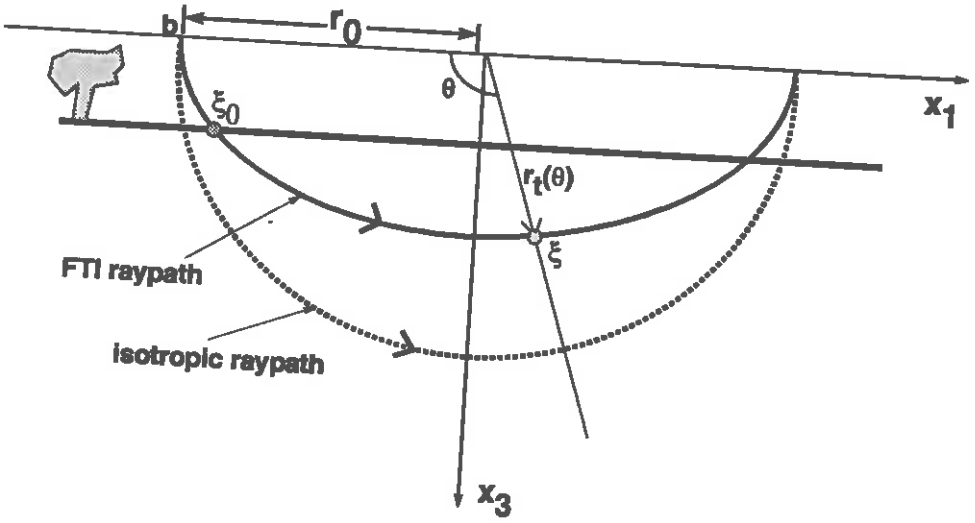

FIG. 1. Raypaths in a constant-gradient, transversely isotropic medium and in its isotropic counterpart. The velocity $f(x_s)$ in the isotropic medium is identical to the vertical velocity in the FTI medium.

a scaling technique to get an approximate expression for the geometric spreading in such a medium.

First, consider the geometric spreading function q,

$$q = \int_{s_0}^{s} v(s)ds = kl, \tag{9}$$

where $v(s)$ is the velocity and s is the arclength along a computed ray— the *central* ray. The parameter q is seen to be proportional to the distance l between the central ray and a nearby paraxial ray, with proportionality constant k. A paraxial ray is a ray (not actually traced) in the vicinity of the central ray, its normal distance from the central ray describing the geometrical spreading (Červený, 1981) along the central ray. Figure 2 shows a central and paraxial ray for a transversely isotropic medium, and Figure 3 shows the two rays for its isotropic counterpart. Note, in Figure 3, that although the paraxial ray, like the central ray, is circular, the distance r_p from the center *of the central ray* to the paraxial raypath depends on the angle from horizontal.

In an isotropic, constant-gradient medium, equation (9) becomes

$$q = r_0 x \sqrt{A_1^2 + A_3^2}, \tag{10}$$

where $r_0 = (x_1^2 + x_3^2)^{\frac{1}{2}}$ is the same r_0 given in equation (8), and x is the distance, measured along the normal to the gradient direction, between the ray takeoff point

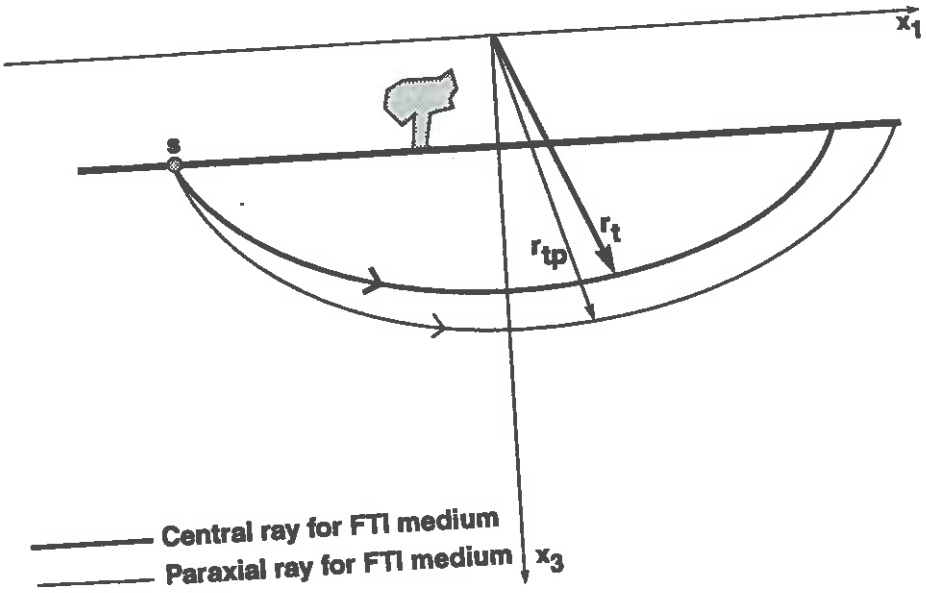

FIG. 2. A central ray and nearby paraxial ray for a transversely isotropic medium.

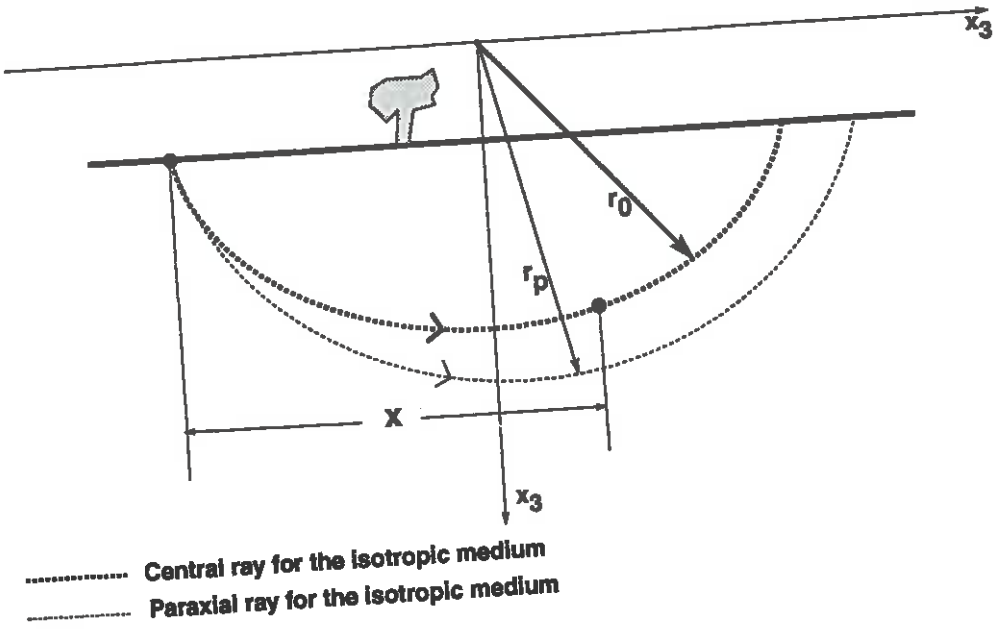

FIG. 3. A central ray and nearby paraxial ray for the isotropic counterpart of the medium in Figure 2.

and the point along the ray where q is measured. We now seek a comparably simple, approximate expression for the geometric spreading function q_t for FTI media.

The keys to estimating q_t are scaling relationships, the first of which is that underlying the similarity between the ray equation (5) and the slowness equation (2) for FTI media. That similarity is shown graphically in a comparison of the raypaths shown in Figure 1 and the slowness curves in Figure 4. The raypaths for both the FTI and isotropic media are scaled, 90-degree rotated versions of the slowness curves. Now, define the distance from the origin to a point ξ along the raypath as $r_t(\theta) \equiv \sqrt{x_1^2[\xi(\theta)] + x_3^2[\xi(\theta)]}$, where θ is the angle between the line connecting these two points and the horizontal axis, as shown in Figure 1. Also, as shown in Figure 4, define the slowness of the ray at that same point ξ as $p(\theta) \equiv \sqrt{p_1^2[\xi(\theta)] + p_3^2[\xi(\theta)]}$, where the angle θ is now seen to be the angle of the slowness vector with the vertical slowness axis (axis of symmetry, here). Consider $r_0 = x_1(\xi)$ where $x_3(\xi) = 0$, and $p_0 = p_3(\xi)$ where $p_1(\xi) = 0$, as reference values for position and slowness, respectively. From the similarity of the FTI curves in Figures 1 and 4,

$$r_t(\theta) = \frac{p(\theta)}{p_0} r_0. \tag{11}$$

But r_0 and p_0 are just the radii of the circular raypath and slowness curve for the isotropic counterpart of the FTI medium, shown in Figures 1 and 4. Therefore, equation (11) is a scaling relationship between the distance $r_t(\theta)$ and r_0 for the two media.

Exploiting this scaling relationship, I can establish an equation for the geometrical spreading function q_t in FTI media. The scaling relationship given by equation (11) pertains to the central ray. For the paraxial rays this relationship is only approximate because I am using the origin for the central rays in describing the paraxial rays. I assert that the following *approximate* relationship holds for paraxial rays of the TI and isotropic media.

$$r_{tp}(\theta) \doteq \frac{p(\theta)}{p_0} r_p(\theta), \tag{12}$$

where

- r_p is the distance from the origin to the paraxial ray for the isotropic medium, and
- r_{tp} is the distance from the origin to the paraxial ray for the FTI medium.

This approximate relationship holds the difference in takeoff angle for the central ray and the paraxial ray is small (see Figures 2 and 3). From equation (9),

$$q_t = k l_t, \tag{13}$$

where l_t is the distance between the central ray and a paraxial ray for the FTI medium. But, from Figure 5

$$l_t(\theta) = [r_{tp}(\theta) - r_t(\theta)] \cos\phi, \tag{14}$$

where ϕ, the angle between the group-velocity direction and the phase-velocity direction, is given by

$$\phi = \tan^{-1}[p(\theta)\frac{d\frac{1}{p(\theta)}}{d\theta}].$$

The $\cos\phi$ factor in equation (14) is necessary because the raypath in the FTI medium, unlike that in the isotropic medium, is not perpendicular to the line from the origin.

Inserting equation (14) into equation (13) and using equations (11) and (12), we get

$$q_t = k[r_p(\theta) - r_0]\frac{p(\theta)}{p_0}\cos\phi. \tag{15}$$

But for the isotropic medium

$$q = kl = k[r_p(\theta) - r_0],$$

so equation (15) becomes

$$q_t = \frac{p(\theta)}{p_0}q\cos\phi = \frac{r_t(\theta)}{r_0}q\cos\phi. \tag{16}$$

The second equality here follows from equation (11).

Substituting equation (10) into equation (16) gives the geometric spreading function in the FTI medium,

$$q_t = r_t x\sqrt{A_1^2 + A_3^2}\cos\phi.$$

Ray tracing between two points

I now use the scaling technique once again, this time to iteratively find the angle θ_0 for the ray originating at source position $[x_1(\xi_0), x_3(\xi_0)]$ and ending at diffractor position $[x_1(\xi_1), x_3(\xi_1)]$ in an FTI medium with general velocity gradient direction.

The non-vertical, constant-velocity gradient has magnitude

$$g = \sqrt{A_1^2 + A_3^2},$$

and angle from vertical

$$\varphi = \tan^{-1}\frac{A_1}{A_3}.$$

As shown in Figure 6, the distance from the origin to the reference position (starting point), measured along the gradient direction, is

$$z_g = \frac{v_0}{g},$$

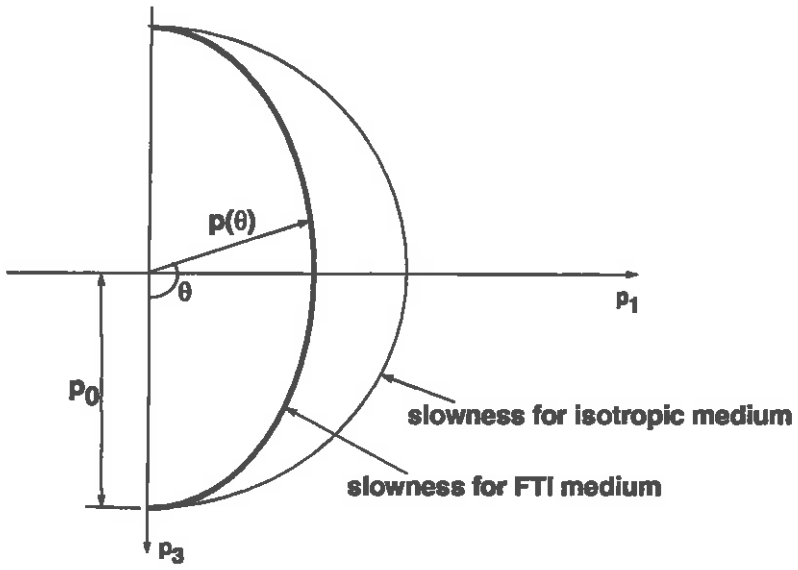

FIG. 4. The slowness curve for an FTI medium and its isotropic counterpart.

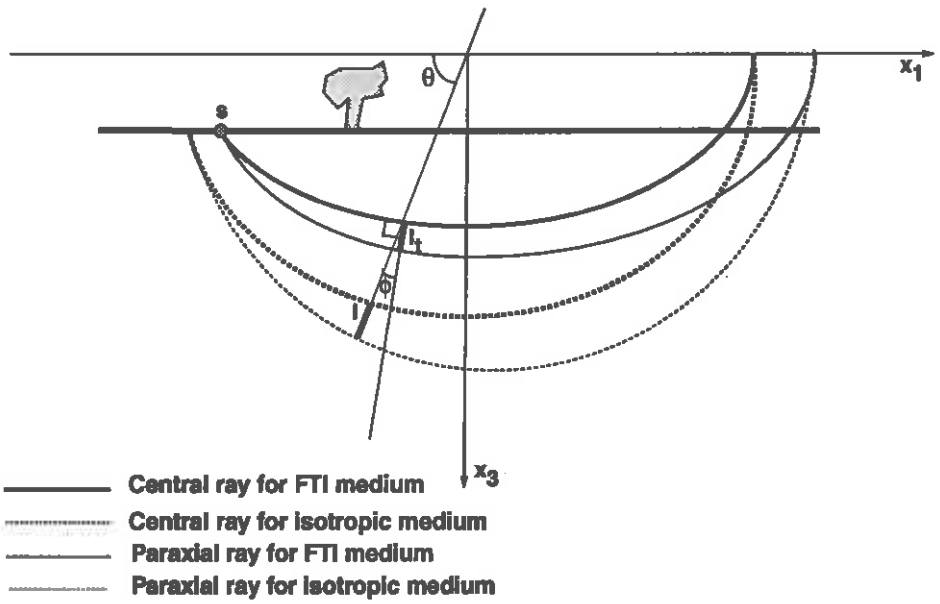

FIG. 5. The scaling relations that exists between a ray traveling in a constant-gradient FTI medium and its isotropic counterpart.

where v_0 is the velocity in the vertical direction at the starting point. I use

$$\cos\varphi = \frac{A_3}{\sqrt{A_1^2 + A_3^2}}$$

and

$$\sin\varphi = \frac{A_1}{\sqrt{A_1^2 + A_3^2}}$$

to rotate the coordinates x_1 and x_3 to new coordinates x_1^T and x_3^T, where x_3^T is along the gradient vector direction. Consider the distance in the x_3^T direction between position $[x_1(\xi_0), x_3(\xi_0)]$ and position $[x_1(\xi_1), x_3(\xi_1)]$,

$$\Delta x_3^T \equiv x_3^T(\xi_1) - x_3^T(\xi_0),$$

which I use to define

$$z \equiv \Delta x_3^T + z_g,$$

as the distance in the x_3^T direction from the origin to position$[x_1(\xi_1), x_3(\xi_1)]$.

Using scaling relationship (11) once for angle θ_0 at ξ_0 and again for angle θ_1 at ξ_1 along the ray (see Figure 6), gives

$$r_t(\theta_1) = \frac{p(\theta_1)}{p(\theta_0)} r_t(\theta_0). \tag{17}$$

From Figure 6,

$$r_t(\theta_1) = \frac{z}{\sin\psi_1} \tag{18}$$

and

$$r_t(\theta_0) = \frac{z_g}{\sin\psi_0}, \tag{19}$$

where ψ_0 and ψ_1 are angles from the x_1^T axis to lines connecting the origin with ξ_0 and ξ_1, respectively. Also from Figure 6,

$$\psi_0 = \theta_0 - \varphi$$

and

$$\psi_1 = \theta_1 - \varphi.$$

Substituting equations (18) and (19) into equation (17) gives

$$\frac{z}{\sin\psi_1} = \frac{p(\psi_1 + \varphi)}{p(\psi_0 + \varphi)} \frac{z_g}{\sin\psi_0}. \tag{20}$$

equation (20) has two unknowns, ψ_1 and ψ_0. The known value of Δx_1^T satisfies

$$\Delta x_1^T = x_1^T(\xi_1) - x_1^T(\xi_0) = \frac{x_3^T(\xi_1)}{\tan\psi_1} - \frac{x_3^T(\xi_0)}{\tan\psi_0},$$

which gives

$$\psi_1(\psi_0) = \tan^{-1} \frac{x_3^T(\xi_1) \tan \psi_0}{x_3^T(\xi_0) + \Delta x_1^T \tan \psi_0}. \tag{21}$$

Combining equations (20) and (21) yields a single transcendental equation for ψ_0, the takeoff phase-velocity angle from x_1^T for the two-point ray-tracing problem. A root-finding algorithm (e.g., the Newton-Raphson method or the secant method) is used to solve for ψ_0.

The scaling approach is an alternative to the general raypath equation for two-point ray tracing. It gives a simpler way of treating rotation in the gradient direction; rotation of the raypath equation is relatively complicated.

For arbitrary orientation of symmetry axis, a rotation of the coordinate axes is done in the program such that x_3 is always in the direction of the axis of symmetry for the FTI medium. This rotation is simpler than the rotation used in the two-point ray-tracing because it involves a rotation of the whole problem.

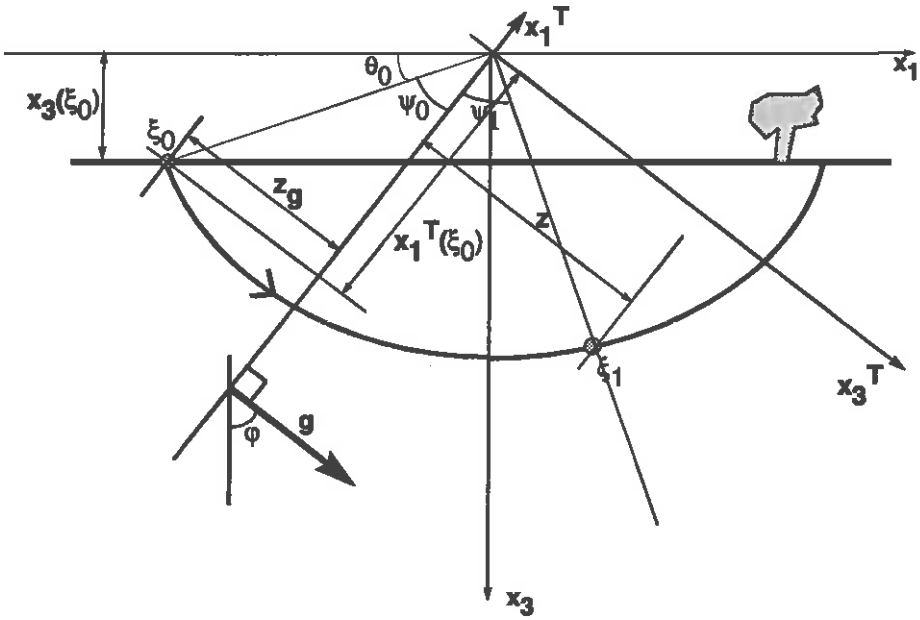

FIG. 6. Parameters that correspond to the case of non-vertical velocity gradient.

From FTI to general anisotropy

The anisotropy condition can be generalized without jeopardizing the analytic solutions through perturbation of the traveltimes and geometric spreading for the FTI medium.

Consider two media, a background medium (unperturbed), possibly anisotropic and inhomogeneous, in which we do our general ray tracing, and a perturbed medium,

that may also be anisotropic and inhomogeneous, in which we wish to calculate traveltime and amplitude. The traveltime in the perturbed medium $T(a,b)$ along a ray traveling from point a to point b is calculated from the traveltime in the background medium $T^0(a,b)$ traveling between the same two points. I seek an efficient scheme for computing the time perturbation $\delta T(a,b)$, given $T^0(a,b)$ and relationships between the parameters of the background and perturbed media.

$$T(a,b) = T^0(a,b) + \delta T(a,b). \tag{22}$$

Differences between the density-normalized elastic parameters in the background medium a^0_{ijkl} and those in the perturbed medium a_{ijkl} define the degree of perturbation δa_{ijkl} as follows

$$a_{ijkl} = a^0_{ijkl} + \delta a_{ijkl}.$$

Following Červený and Filho (1991), for a generally anisotropic inhomogeneous background,

$$\delta T_P(a,b) = -\frac{1}{2}\int_a^b \delta a_{ijkl} p_i p_l m_j m_k dT, \tag{23}$$

where m_i are the components of the eigenvector $\mathbf{m}$ (the direction of the particle motion), here for the P-wave. The integration in equation (23) is performed along a ray L_0 computed in the background medium, and quantities p_i, p_l, m_j, m_k and dT pertain to the background medium.

Take the integrand in equation (23) as *the anisotropy perturbation factor* F for the homogeneous, isotropic segment,

$$F = -\frac{1}{2}\delta a_{ijkl} p_i p_l m_j m_k.$$

Consider the geometric spreading function q along the ray in the background medium (e.g., in a homogeneous isotropic medium, $q = \alpha^2 T^o$). Then, the first-order perturbation of the geometrical spreading for the raypath between point a and point b (Alkhalifah, 1993), is given by

$$\delta q(a,b) = \int_a^b -F dq,$$

where F and dq pertain to the background medium, and $F \ll 1$.

UPGRADING SUSYNLV

SUSYNLV— SYNthetic seismogram for Linear Velocity model— is a Seismic Unix (SU) program, authored by Dave Hale in 1991, that generates synthetic seismograms for a linear velocity function in an isotropic medium. I use the ray-tracing equations derived in the previous sections to modify Hale's program to generate synthetic seismograms for constant-gradient TI media.

The modification includes adding a subroutine that calculates traveltimes, ray angles, and geometrical spreading for a linear velocity function in an FTI medium. In a second modification, I use the necessary time-perturbation equation to generalize the FTI application to work for a general TI medium. The modified program thus now has options for both isotropic and TI media.

Computation of seismograms in this program is based on Huygen's principle, in which every segment along a reflector acts as a diffractor, sending rays in all directions. The net result of the superposition of the arrivals from the scatterers along an interface is the seismogram synthesized at each geophone location. In a transversely isotropic medium, where the calculation of reflection angles is relatively complicated (i.e., it requires iteration), Huygen's principle is a useful tool that obviates the need for explicit computation of reflection angles.

For arbitrary orientation of the symmetry axis, a rotation of the coordinate axes is done in the program such that x_3 is always in the direction of the symmetry axis for the FTI medium.

The program as developed by Hale generates synthetic seismograms for a smoothly or linearly interpolated reflector shape beneath a homogeneous or constant-gradient medium. The data may be nonzero-offset, and options exist for various source definition (e.g., exploding reflectors). These features remain in the modified program, now for computation of synthetic seismograms for general TI media with constant velocity gradient.

SYNTHETIC DATA EXAMPLES

I will use a single TI medium to show synthetic data generated by this modelling program. The Wills Point shale with Thomsen's anisotropy parameters $\delta = 0.315$ and $\epsilon = 0.215$ (Thomsen, 1986) is considered to be a relatively strongly anisotropic medium. Positive angle between the symmetry axis and the vertical, ψ, corresponds to symmetry axis rotated clockwise from the vertical, where negative ψ is just the opposite.

Figure 7 shows synthetic seismograms resulting from modeling two point scatters located at midpoint 2.5 km, and depths 1 and 3 km. The vertical velocities for all the models $v(x_3)$=2.0+0.6 x_3 km/s. Figure 7a shows the diffraction curves for an isotropic medium; 7b for a Wills Point shale FTI medium with a vertical axis of symmetry ($\psi = 0$); 7c for the same FTI medium with $\psi = 30$ degrees; and 7d for the same FTI medium with lateral as well as vertical velocity variation, $v(x_1, x_3)$=2.0+0.6 x_3+ 0.1 x_1 km/s, and with $\psi = -40$ degrees. Note that for Figure 7a and 7b the diffraction curves, as expected, are symmetric; however, in Figure 7c and 7d they are non-symmetric and laterally shifted. In 7c, nonsymmetry and shift are due solely to the tilt of the symmetry axis. In 7d, both the lateral velocity variations and the nonvertical symmetry axis contribute (oppositely, here) to the nonsymmetry and shift.

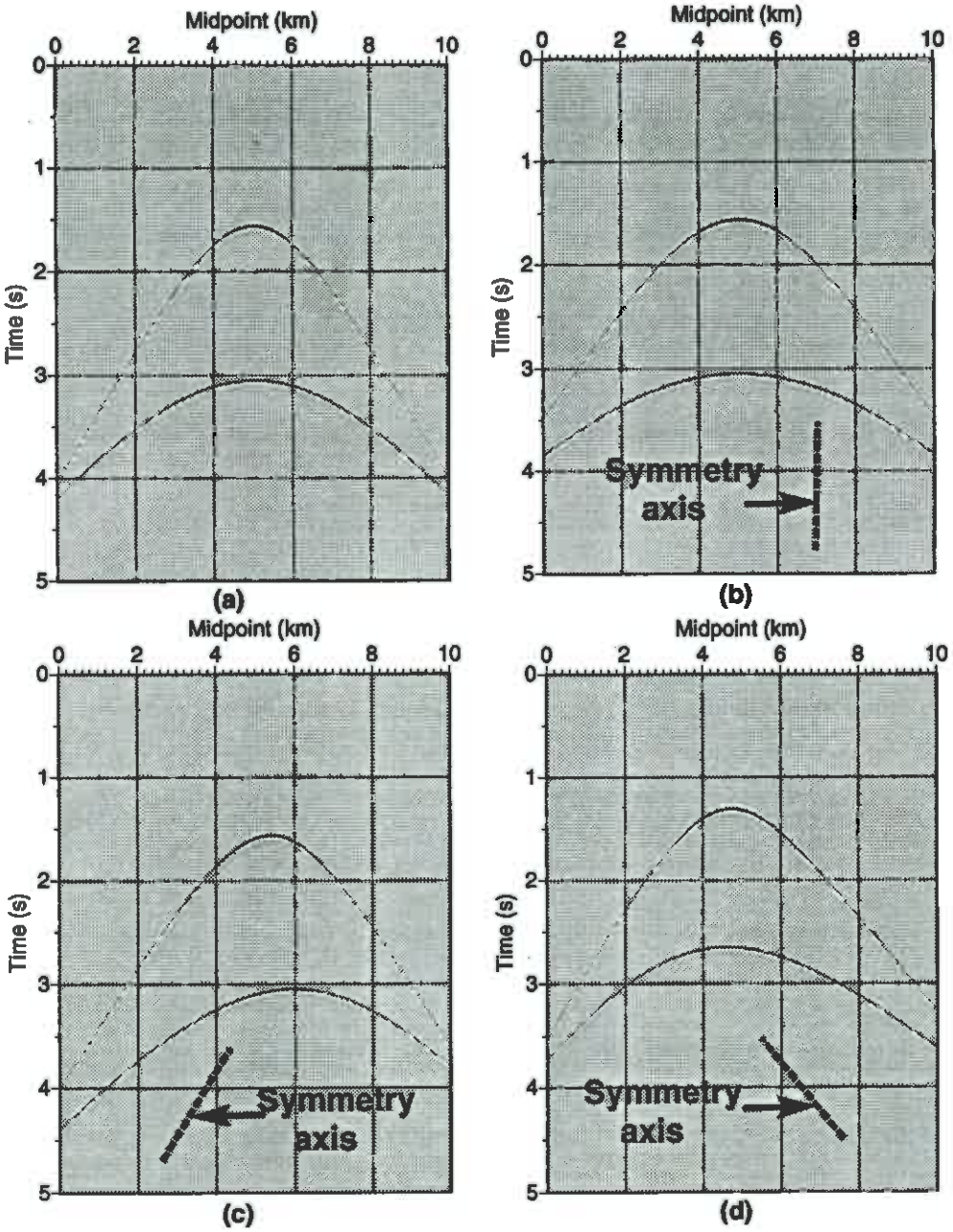

FIG. 7. Zero-offset synthetic seismograms of two diffractor points for (a) an isotropic medium, (b) Wills Point shale FTI medium with vertical axis of symmetry ($\psi = 0$), (c) the same FTI medium with $\psi = 30$ degrees, and (d) the same FTI medium with $\psi = -40$ degrees and velocity $v(x_1, x_3)$=2.0+0.6 x_3+ 0.1 x_1 km/s. The velocity in (a), (b) and (c) is $v(x_3)$=2.0+0.6 x_3 km/s.

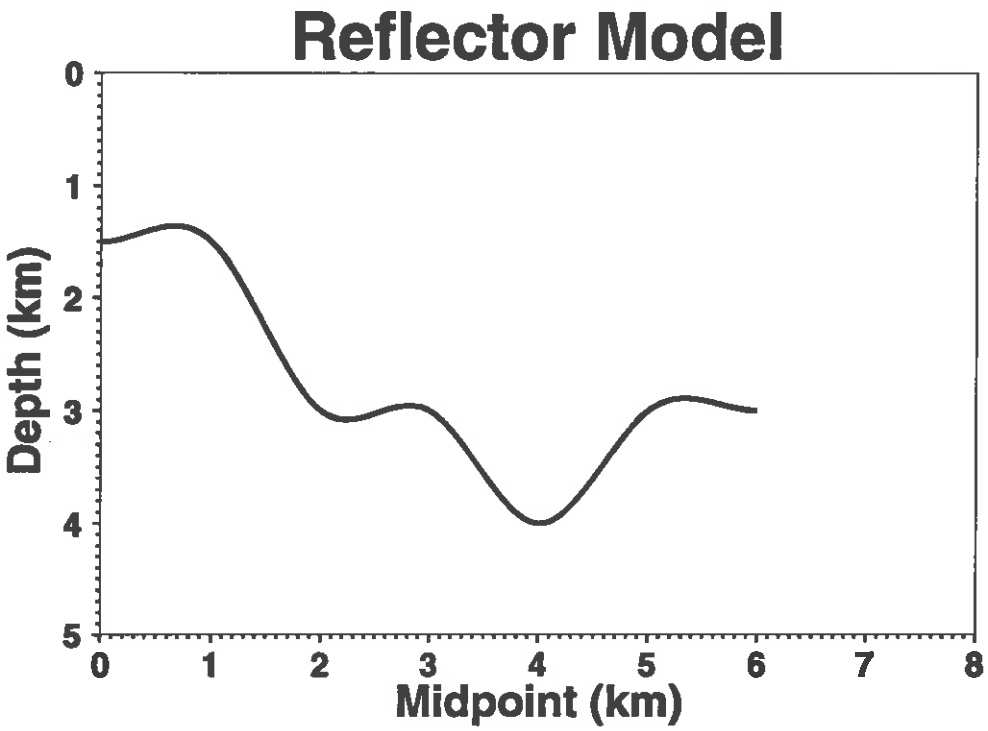

FIG. 8. Reflector model.

The lateral shift in Figure 7c implies that migration that ignores the tilted symmetry axis, such as conventional isotropic migration, will yield lateral mispositioning of reflectors, even horizontal ones, just as happens in media with lateral varying overburden, even though the medium here has no lateral variation.

Figure 8 shows an undulating reflector model, and Figure 9 shows synthetic seismograms corresponding to that model. The vertical velocity this time is held at $v(x_3)$=3.0+0.5 x_3 km/s. Figure 9a corresponds to an isotropic medium; 9b to the Wills Point shale FTI medium with $\psi = 0$ degrees; 9c to the same FTI medium with $\psi = -30$ degrees; and 9d to the same FTI medium with lateral and vertical velocity variation, $v(x_1, x_3)$=3.0+0.5 x_3+ 0.5 x_1 km/s, with $\psi = -40$ degrees. Nonsymmetry and shift, such as that mentioned above, is observed here, as well. The reflector shown in Figure 8 is just a summation of scattering points, and the reflector response in Figure 9 is a superposition of diffraction curves such as those in Figure 7.

Figure 10 shows more synthetic seismograms generated for the reflector model in Figure 8. This time, the velocity structure $v(x_3) = 4.0-0.1\, x_3$ km/s, corresponding to a *decrease* in the vertical velocity with depth, a situation not generally encountered in practice. Figure 10a corresponds to the Wills Point shale with $\psi = 0$ degrees, and 10b with $\psi = -30$ degrees. Clearly, the program is not restricted to modeling velocities that only increase with depth.

Next, I lift the restriction that the medium be factorized anisotropic. Figure 11 shows synthetic seismograms for (a) the same two diffractors used in generating Fig-

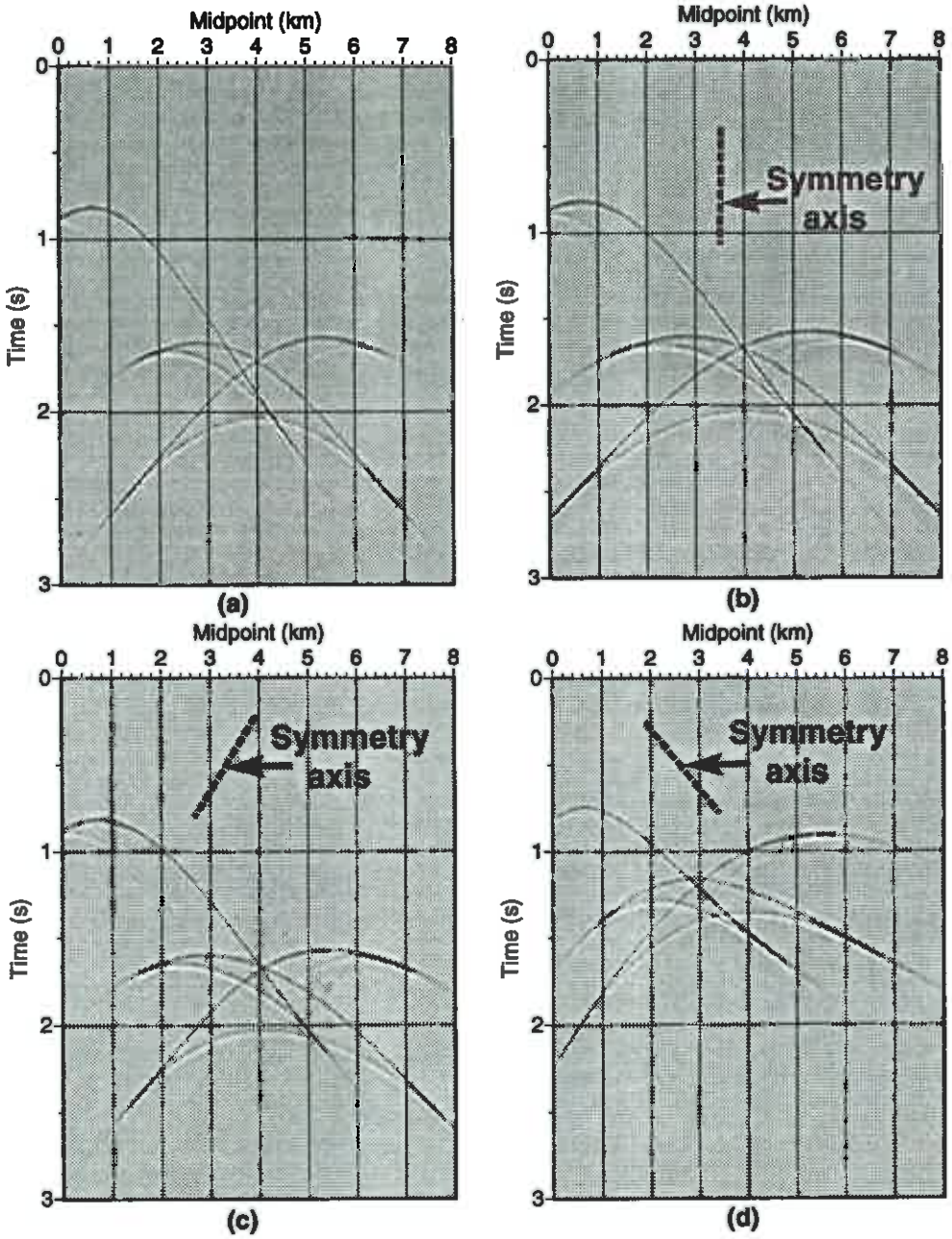

FIG. 9. Zero-offset synthetic seismograms corresponding the reflector model in Figure 8 for (a) an isotropic medium, (b) Wills Point shale FTI medium with vertical axis of symmetry ($\psi = 0$ degrees), (c) the same FTI medium with $\psi = 30$ degrees, and (d) the same FTI medium with $\psi = -40$ degrees and velocity $v(x_1, x_3)$=3.0+0.5 x_3+0.5 x_1 km/s. The velocity in (a), (b) and (c) is $v(x_3)$=3.0+0.5 x_3 km/s.

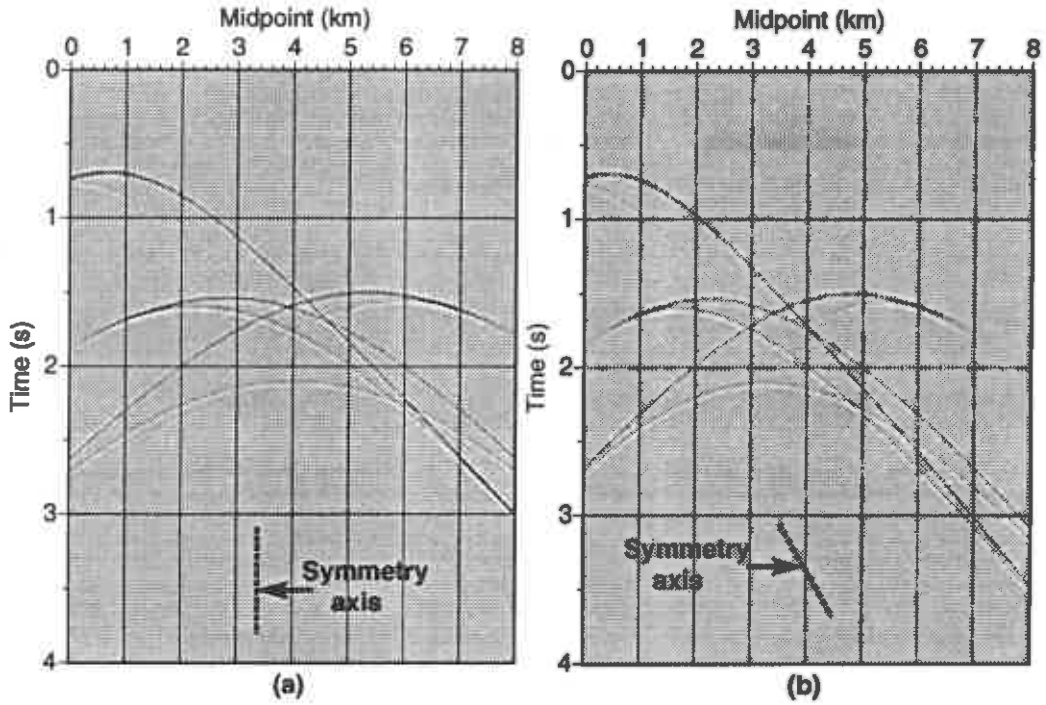

FIG. 10. Zero-offset synthetic seismograms corresponding the reflector model in Figure 8 for (a) the Wills Point shale FTI medium with vertical axis of symmetry ($\psi = 0$), and (b) the same FTI medium with $\psi = -30$ degrees. The velocity structure here is $v(x_3) = 4.0 - 0.1\,x_3$ km/s.

ure 7, and (b) the reflector model in Figure 8, but these seismograms were generated for a TI medium using the time-perturbation feature. The time perturbation is from the FTI Wills Point shale, to another anisotropic medium, a general TI medium, in which δ and ϵ change with depth. Specifically, the perturbation includes the following changes of elastic coefficients: $\frac{dl}{dx_3} = 0.05$ and $\frac{da}{dx_3} = 0.1$, where l and a are the coefficient ratios given in equation (6), and $\delta = 0.315$ and $\epsilon = 0.215$ at the surface. Comparing Figure 11a with Figures 7a and 7b, note that 11a suggests more extreme anisotropy than does 7b; that is, the diffraction curves in 11a show more departure from those for the isotropic medium than do the curves in Figure 7b, despite the fact that all models have the same vertical root-mean-square velocity. I attribute this behavior to the increase in size of the anisotropy parameters with depth.

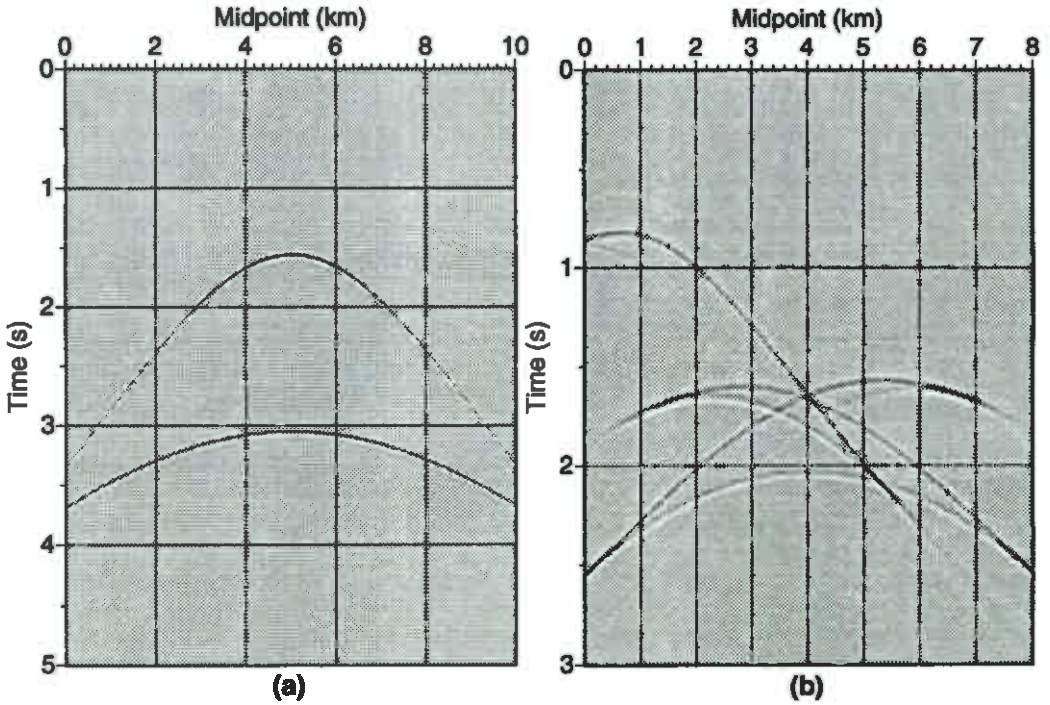

FIG. 11. Zero-offset synthetic seismograms corresponding to (a) the two diffraction points used in Figure 7, and (b) the reflector model used in Figure 9b. Here, time perturbation is used with $\frac{dl}{dx_3} = 0.05$ and $\frac{da}{dx_3} = 0.1$ for both plots. The symmetry axis is vertical.

EFFICIENCY

The primary objective of constructing the original isotropic modeling program was efficiency in generating synthetic data. Similarly my goal was to preserve that essential efficiency while extending to inhomogeneous TI media. Previously, generating synthetic data for such media has usually been slow and costly (using either finite-difference or general ray tracing). For ray tracing approaches, speed has been slowed down primarily by the time needed to perform ray tracing between two points using numerical integration to compute the raypath in every iteration.

The synthetic data generated for Figure 7 and Figure 11b contain 201 common midpoints at an interval of 0.05 km, and 401 time samples with a time interval of 0.01 s. The peak frequency used is 15 Hz. Table 1 shows CPU times, on the IBM RS/6000 Model 520 workstation, needed to generate these synthetic seismograms. For the FTI time shown in Table 1, I chose the largest of the times for the three FTI cases in Figure 7. The technique labeled "FD" in Table 1 and 2 pertains to a generic finite-difference method using the full elastic-wave equation for transversely isotropic media with vertical symmetry axis. The CPU time for FD was not based on any specific test, but I believe it to be a considerable underestimate.

Technique	*CPU time* (s)
Isotropic (Figure 7)	0.6
FTI (Figure 7)	1.5
general TI (Figure 11a)	2.1
FD	> 1800

Table 1. Compute times for various two-diffractor tests.

The synthetic data generated in Figure 9 and Figure 11b contain 201 common midpoints at an interval of 0.05 km, and 501 time samples at 0.01-s time interval. The peak frequency is again 15 Hz. Table 2 shows the CPU times needed to generate those data.

Technique	*CPU time* (s)
Isotropic (Figure 9)	5.6
FTI (Figure 9)	36.9
general TI (Figure 11b)	52.0
FD	> 1800

Table 2. Compute times for various tests with the reflector model in Figure 8.

The ray-trace times in Table 2 are much larger than those in Table 1 because seismogram computation for the model in Figure 8 required summation of contributions from 246 diffraction points along the reflector, whereas only two diffractors were used for the tests in Figure 7 and 11a. While, the time needed for FD is not influenced by

the complexity of the reflector shape, it is dependent on the dominant wavelength in the data. For the class of models allowed in this program, the efficiency demonstrated here far exceeds that of either general ray tracing (Červený, 1989) or FD techniques.

CONCLUSION

The modeling program for FTI and general TI media should be useful for applications such as algorithm testing in TI inhomogeneous media, migration and dip-moveout studies, and amplitude-versus-offset (AVO) studies. Alkhalifah (1993), for example, used synthetic data generated by this program in tests of Gaussian beam migration for FTI media. Whereas, for FTI media, the ray-trace solutions here are nearly exact, when applying time perturbation to generalize the anisotropy condition, errors arise that depend on the amount of perturbation. Alkhalifah (1993), however, shows that the errors are negligible when the perturbation is less than about 20 percent.

The key characteristic of this program is the efficiency with which it generates seismograms. This efficiency is brought about by the analytical equation for geometrical spreading, derived here. This geometrical spreading equation for FTI media could have other applications such as in study of AVO dependency on TI parameters in inhomogeneous media.

ACKNOWLEDGMENTS

I thank Professor Ken Larner for his critical suggestions and review of this paper. Ken Larner also gave me the idea for this study. I also thank V. Cerveny for helping me understand some practical issues in ray tracing. In addition, I thank Mohammed Alfaraj for his time in introducing me to the Center for Wave Phenomena (CWP) environment. Thanks are due to KACST, Saudi Arabia, for its financial support.

REFERENCES

Alkhalifah, T., 1993, Gaussian beam migration for anisotropic media: CWP Annual Report, CWP, Colorado School of Mines.

Červený, V., 1972, Seismic rays and ray intensities in inhomogeneous anisotropic media: Geophys. J. R.astr. Soc., **29**, 1–13.

Červený, V., 1981, Computation of geometrical spreading by dynamic ray tracing: Stanford Exploration Project, **28**, 49–59.

Červený, V., and Simoes-Filho, I. A., 1991, The traveltime perturbations for seismic body waves in factorized anisotropic inhomogeneous media: Geophys. J. Int., **107**, 219–229.

Červený, V., 1989, Ray tracing in factorized anisotropic inhomogeneous media: Geophys. J. Int., **94**, 575–580.

Larner, K., 1993, Dip-moveout error in transversely isotropic media with linear velocity variation in depth: Geophysics, in press.

Shearer, P. M. and Chapman, C. H., 1988, Ray tracing in anisotropic media with linear velocity gradient: Geophys.J. Int., **94**, 575–580.

Thomsen, L., 1986, Weak elastic anisotropy: Geophysics, **51**, 1954–1966.

White, J. E., 1983, Underground sound: Application of sound waves: Elsevier, 253 p.

CWP-133

Migration error in transversely isotropic media

Tariq Alkhalifah and Ken Larner

Migration error in transversely isotropic media

Tariq Alkhalifah and Ken Larner

ABSTRACT

Most migration algorithms today are based on the assumption that the Earth is isotropic, an approximation that is often not valid and thus can lead to position errors on migrated images. Here, we compute curves of such position error as a function of reflector dip for transversely isotropic (TI) media characterized by Thomsen's anisotropy parameters δ and ϵ. Depending on whether the migration velocity is derived from stacking velocity or vertical root-mean-square (rms) velocity, we find quite contrary sensitivities of the error behavior to the values of δ and ϵ. Likewise error-versus-dip behavior depends in a complicated way on vertical velocity gradient and vertical time, as well as orientation of the symmetry axis. Moreover, error behavior is quite dependent on just how δ and ϵ vary with depth. In addition to presenting such error curves, we show migrations of synthetic data that exemplify the mispositioning that results from ignoring anisotropy.

When the stacking velocity is used in migration and when medium velocity increases with depth at rates typically encountered in practice, δ alone is sufficient to describe the position error. This is fortunate since the value of δ, unlike ϵ, can be obtained from VSP and surface seismic data. In contrast, when the migration velocity is obtained from the vertical rms velocity, the position errors depend highly on ϵ, suggesting the importance of having an accurate estimate of ϵ when using an anisotropic migration algorithm.

INTRODUCTION

Invariably, the Earth's crust is anisotropic. The degree of anisotropy varies from weak, having hardly any effect on seismic wave propagation, to strong, causing major influence on raypaths and on reflection times and amplitudes.

Through the years, processing of seismic data has seldom taken anisotropy into consideration. Conventional processing seemed to work well; taking anisotropy into consideration was thought to be complicated, slow, and costly. It is likely, however, that ignoring anisotropy probably has lead to errors that have been either unrecognized or attributed to acquisition and processing problems. Such errors are usually left unmeasured and untreated.

Larner and Cohen (1993) have studied the mispositioning of imaged reflectors that results when, as is typically done in practice, data from transversely isotropic (TI) media are migrated with an algorithm that ignores anisotropy. The media they studied had linear variation with depth, had vertical symmetry axis for the transverse isotropy, and were factorized anisotropic inhomogeneous (FAI; Červený, 1989). That is, all ratios among the various elasticity parameters were independent of position. Moreover, they limited their study to the four examples of TI media studied by Levin (1990). They found highly variable dependence of the behavior of lateral position error versus reflector dip upon the velocity gradient and vertical reflection time.

While their curves were interesting and might qualitatively explain apparent accuracy of migration in practice, those results have no ready explanation in terms of current knowledge about anisotropy. Moreover, while more general than those studied in the past, the model used by Larner and Cohen had a number of limitations that we lift in our follow-up study, here. While retaining the restriction that the medium be TI, here we allow the symmetry axis to be tilted from vertical, and we consider departures from FAI media. Also, rather than limit study to four specific media, we characterize the anisotropy of the media more generally in terms of the Thomsen (1986) parameters δ and ϵ (see equations [1] and [2], below), and $\frac{V_s}{V_p}$, where V_p and V_s are the P-wave and S-wave velocity along the symmetry-axis direction. We find that errors are quite insensitive to $\frac{V_s}{V_p}$, even for media not considered weakly anisotropic. With this parameterization, we can gain understanding of the results for the four media studied by Larner and Cohen in terms of the δ and ϵ values for those media. Also, with this parameterization, we can efficiently study media having a wide range of anisotropy.

Following the general study of error-versus-dip curves, we generate synthetic data for TI models with steep reflectors, and see the action of isotropic time migration on those data. Such sample migration tests highlight the dependence of position error on symmetry-axis direction, as well as difficulties in assessing migration error in practice.

Paralleling Larner and Cohen (1993), we first generate two-way traveltimes corresponding to zero-offset P-wave data from point scatterers, by ray tracing in a TI medium with constant velocity gradient (Alkhalifah, 1993). Larner and Cohen considered only FAI, TI media with constant velocity gradient so as to take advantage of the analytic solution of Shearer and Chapman (1988) for ray tracing in such media. We generalize to TI media that are not factorized anisotropic inhomogeneous by perturbing the FAI traveltimes (Alkhalifah, 1993), patterned after the perturbation ideas of Červený and Filho (1991). Once we have generated the diffraction curves, we then simulate migration of points along these diffraction curves with an algorithm that computes diffraction times for an isotropic medium with velocity variation equal to that for the vertical velocity in the TI medium. The only source of error in the simulated migration should be the failure to honor anisotropy in the migration.

Following Larner and Cohen (1993), we study the dimensionless lateral distance $\Delta\tilde{y}$ between the incorrectly imaged reflector position and the true position of the

reflector,

$$\Delta\tilde{y} = \frac{\Delta y}{\lambda_d},$$

where Δy is the error in horizontal distance, and λ_d is the horizontal wavelength

$$\lambda_d = \frac{1}{f_d p},$$

with f_d a selected "dominant" frequency, and p the slope of the unmigrated reflection. Positive position errors imply undermigration, and negative position errors imply overmigration. The reference dominant frequency used throughout, here, is 30 Hz.

Repeating, here we consider only a velocity gradient in the vertical direction, and only 2-D propagation in the vertical plane perpendicular to strike, but allow general orientation ψ of the symmetry axis within the propagation plane. The velocity gradient used in most tests is 0.6 s^{-1}, which we judge to be sufficiently representative value for the subsurface, considering that the constant gradient is itself a simplification. Also, in most of the tests, the depth D of the reflection point is 3000 m, and the vertical root-mean-square (rms) velocity V_{rms} to that point at 3000 m/s; thus the vertical (migrated) time to the reflection point is $t_m = \frac{2D}{V_{rms}} = 2$ s. Except for the vertical time, these are values generally used by Larner and Cohen (1993) in their study of migration error for vertical axis of symmetry. In all cases where migration velocity is based on the stacking velocity, the $T^2 - X^2$ analysis is done over a spreadlength X equal depth D to an assumed horizontal reflector. We also consider, at first, just factorized transversely isotropic (FTI) media; that is media in which all ratios among the elastic coefficients for TI media (therefore, $\frac{V_s}{V_p}$, δ, and ϵ) are independent of position. Later, we lift this restriction.

Medium	$\frac{V_s}{V_p}$	δ	ε
Shale-limestone	0.55	0.0	0.134
Cotton Valley shale	0.61	0.205	0.135
Berea sandstone	0.63	0.02	0.002
Pierre shale	0.44	0.06	0.015
Taylor sandstone	0.54	-0.035	0.110

Table 3. Thomsen's parameters δ and ε, along with the S-wave velocity to P-wave velocity ratio $\frac{V_s}{V_p}$, for five TI media. The top four media listed are the same as those studied by Levin (1990); the Taylor sandstone was studied by Thomsen (1986).

VELOCITY

Migration velocity

Commonly, the interval velocities required to migrate field data are derived from stacking velocity. In isotropic media, the stacking velocity usually approximates the

vertical rms velocity with acceptable accuracy. This is not so, however, for anisotropic media. The velocity variation as a function of direction causes the best-fit stacking velocity obtained from conventional velocity analysis to differ from the vertical rms velocity. These differences are highlighted by Thomsen (1986) for homogeneous TI media, and by Larner and Cohen (1993) for TI media with a vertical axis symmetry and constant vertical velocity gradient. Larner and Cohen showed that position errors are smaller when stacking velocity, as opposed to vertical rms velocity, is used to obtain velocities for isotropic time migration, as is typically done in practice.

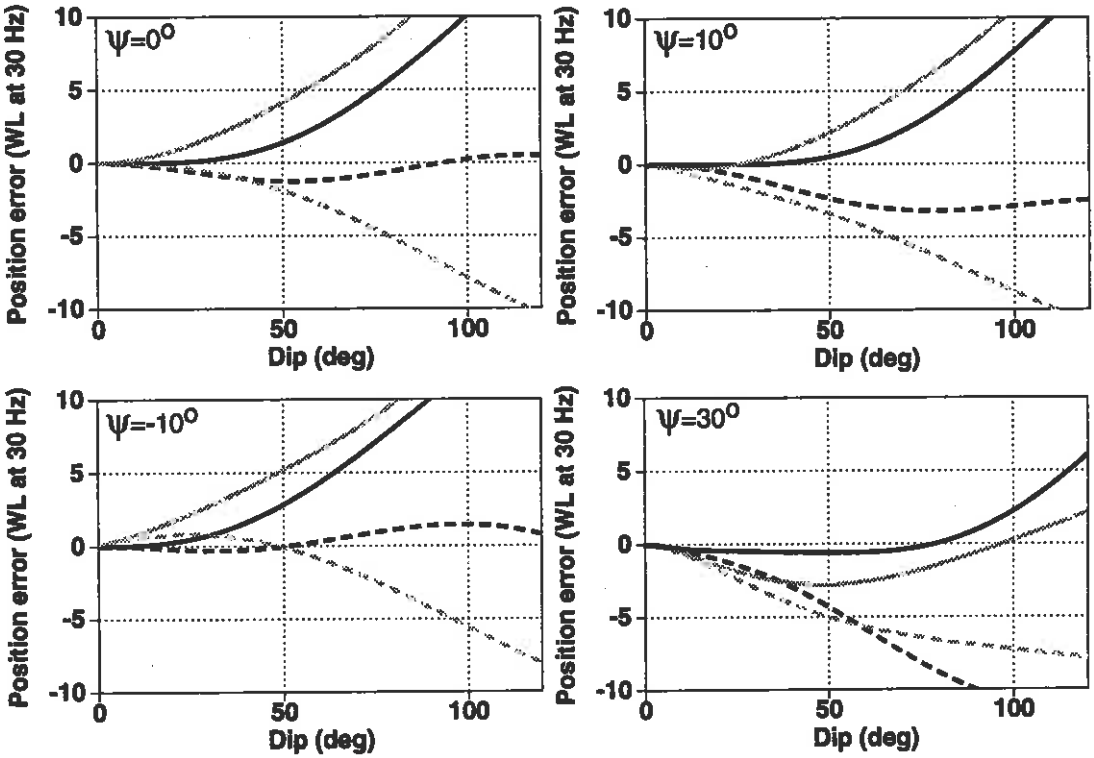

FIG. 1. Lateral position error as a function of reflector dip. ψ denotes the angle that the symmetry axis makes with the vertical. Black lines are for shale-limestone, and gray ones are for Cotton Valley shale (see Table 1). The solid lines show the error when migration velocity is based on the vertical rms velocity, and the dashed lines show the error when it is based on the best-fit stacking velocity. Vertical velocity gradient= 0.6 s^{-1}, here and throughout the paper, unless otherwise stated.

Figure 1 shows the dip-dependence of the lateral position error for four angles ψ of the symmetry axis with the vertical, using for the migration either the vertical rms velocity (solid lines) and the stacking velocity (dashed lines). Positive ψ corresponds to axis of symmetry tilted toward the normal to the dipping reflector, and negative ψ means that it is tilted away from the normal. Here, for both shale-limestone (black

lines) and Cotton Valley shale (gray lines), migration errors for $\psi = 30$ degrees were smaller when migration velocity was derived from vertical rms velocity than when it was derived from the stacking velocity. We attribute this to the asymmetric and laterally shifted diffraction curves when the symmetry axis departs from vertical. In an isotropic medium, lateral velocity variation is needed in order for diffraction curves to be asymmetric and shifted. However, where velocity varies with depth only, moveout in common-midpoint (CMP) gathers is symmetric for any anisotropic medium, and no change from one gather to another will be detected. Thus, we cannot expect a good fit of the diffraction curve for isotropic medium to that of a TI medium with tilted symmetry axis, so we have no reason to expect stacking velocity to be a better source of migration-velocity information than is vertical rms velocity.

Velocity Analysis

To obtain stacking velocity, we usually attempt either to apply velocity analysis to CMP gathers that contain horizontal reflectors or to account for the dipping reflectors (by either including an appropriate "dip-correction" factor or performing velocity analysis on dip-moveout-processed data). Thomsen's (1986) relationship for the ratio of small-offset stacking velocity to vertical rms velocity pertains to so-called *weak anisotropy* in a homogeneous TI medium with vertical axis of symmetry. Larner and Cohen (1993) computed such ratios for constant vertical velocity gradient in four TI media using different spreadlength-to-depth ratios ($\frac{X}{D}$). They showed that as spreadlength-to-depth ratio goes to zero, the stacking velocities for the homogeneous medium and a vertically inhomogeneous medium are the same when both media have the same vertical rms velocity.

Medium	$\frac{V_{sh}}{V_{rms}}(0)$	$\frac{V_{stack}}{V_{rms}}(0)$	$\frac{V_{stack}}{V_{rms}}(10)$	$\frac{V_{stack}}{V_{rms}}(20)$	$\frac{V_{stack}}{V_{rms}}(30)$	$\frac{V_{stack}}{V_{rms}}(45)$
Shale-limestone	1.00	1.07	1.08	1.09	1.10	1.07
Cotton Valley shale	1.19	1.17	1.15	1.11	1.06	0.99
Berea sandstone	1.02	1.02	1.02	1.01	1.01	1.00
Pierre shale	1.06	1.05	1.04	1.03	1.01	0.99
Taylor sandstone	0.96	1.04	1.05	1.08	1.10	1.08

Table 4. Dependence of the ratio of the stacking to vertical rms velocity on the orientation of the symmetry axis for TI media. The spreadlength-to-depth ratio $\frac{X}{D} = 1.0$. V_{stack} is the stacking velocity corresponding to a $k = 0.6\ s^{-1}$ velocity gradient; the values for the ratio, $\frac{V_{sh}}{V_{rms}}(0)$, pertaining to homogeneous media, are those of Thomsen (1986) for $\frac{X}{D} \rightarrow 0$; and the number in parentheses denotes the angle between the vertical axis and the axis of symmetry.

Table 2 contains the ratio of the stacking velocity to the vertical rms velocity ($\frac{V_{stack}}{V_{rms}}$) for the same TI media shown in Table 1, but here the axis of symmetry is not limited to the vertical. Given the symmetries associated with CMP gathers, the sign of the angle of the symmetry axis is immaterial. Note, in Table 2, that the

angle-dependence of this ratio is greatest for the Cotton Valley shale, whereas it is quite small for the shale-limestone. These differences are related to a large value of the Thomsen parameter δ, for the Cotton Valley shale, whereas it is zero for the shale-limestone (see Table 1).

MIGRATION ERRORS

Rather than study errors for specific media (i.e., Cotton Valley shale) as Larner and Cohen (1993) did, hereafter we use Thomsen's (1986) parameters to identify the TI media. As we shall see, error behavior is well characterized by certain of these parameters. The two key Thomsen parameters for P-waves are δ, which describes near-vertical velocity variation, and ϵ, which involves just the ratio of the horizontal to vertical velocity. In terms of the elastic coefficients c_{ijkl}, these two dimensionless parameters are

$$\delta = \frac{(c_{1133} + c_{1313})^2 - (c_{3333} - c_{1313})^2}{2c_{3333}(c_{3333} - c_{1313})}, \tag{1}$$

$$\varepsilon = \frac{c_{1111} - c_{3333}}{2c_{3333}}, \tag{2}$$

where the subscript 3 refers to the symmetry-axis direction, and 1 to the normal to that direction, within the propagation plane. These parameters, along with the P-wave velocity V_p and S-wave velocity V_s in the symmetry-axis direction are sufficient to describe anisotropic behavior in a TI medium. Negative δ implies that the velocity will initially decrease away from the symmetry direction. In contrast, negative ϵ describes a medium where velocity in the symmetry direction exceeds that in the normal direction, a rare occurrence.

Dependence on anisotropy

Figure 2 shows lateral position error as a function of reflector dip keeping $\delta = .1$, $\epsilon = .2$ for the left plot, and $\delta = .1$, $\epsilon = 1.5$ for the right plot, and using the same $V_p(z)$ for all the curves, where z is depth. The only parameter changed from one curve to another within each plot is the S-wave velocity, V_s, such that $\frac{V_s}{V_p}$ ranges from 0.3 to 0.7, a wide range that covers all cases of practical interest. Differences among the curves are insignificant up to about 80-degree reflector dip. Rays must pass the turning point before any differences of significance are realized for even strongly anisotropic media (e.g., $\epsilon = 1.5$). For relatively moderate anisotropy (e.g., $\epsilon = 0.2$) the position errors are relatively small (less than four wavelengths at 120-degree dip), and differences among the curves are insignificant up to 120 degrees. Similar behavior holds for the range of practical choices for δ (not shown here). Therefore, for P-waves, the two parameters, δ and ϵ, are sufficient to characterize most TI media (Tsvankin and Thomsen [1993] found the same behavior for homogeneous media). Also, here, as elsewhere Thomsen's parameters are a convenient set for characterizing even TI media that are not necessarily "weakly anisotropic."

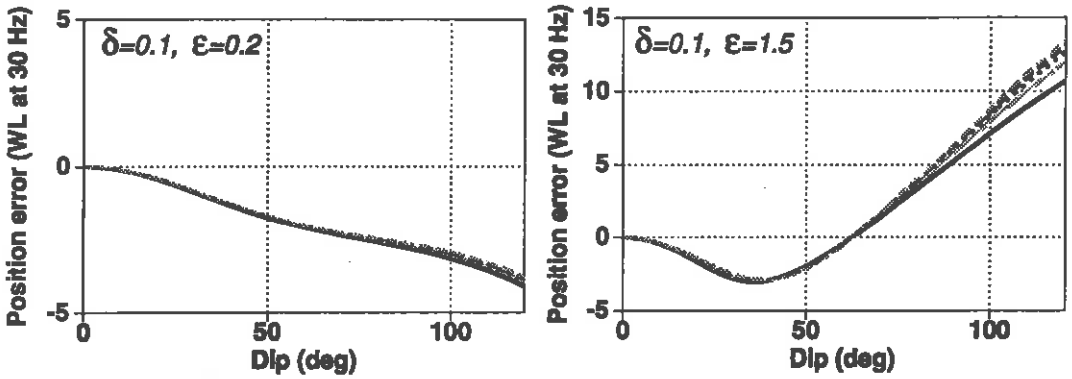

FIG. 2. Lateral position error as a function of reflector dip for two pairs of values for δ and ϵ. The vertical P-wave velocity function is the same for all the curves, but the velocity ratio $\frac{V_s}{V_p}$ ranges from 0.3 to 0.7 in each figure.The symmetry axis is vertical (i.e., $\psi = 0$).

Figure 3 shows lateral position error as a function of reflector dip for a wide range of TI media represented by different combinations of δ and ϵ, with vertical velocity gradient 0.6 s^{-1} and vertical axis of symmetry. The reflector depth D and vertical rms velocity V_{rms} are chosen so that the reflection point is at a migrated time $t_m = \frac{2D}{V_{rms}} = 2$ s. Here, following Larner and Cohen (1993), we use the stacking velocity to derive migration velocity. As a result, the position errors are not zero when $\delta = \epsilon = 0$ (isotropic medium). Recall that the stacking velocity for horizontal reflectors in a vertically inhomogeneous medium is only an approximation to the vertical rms velocity. It cannot exactly characterize moveout.

Figure 3 shows that when using the stacking velocity in the migration process, the influence of δ on the position error is insignificant for dip less than 50 degrees, but is considerably greater than that of ϵ, for steep reflectors. This is evident in the closeness of curves within each of the left-column plots of Figure 3, as opposed to the branching out of curves in the right column of Figure 3. When stacking velocity, as opposed to rms velocity, is used to derive velocity for migration in a TI medium, we expect that we have corrected for the influence that δ (which controls near-vertical propagation velocities) has on the traveltime. This expectation seems to be satisfied for dip less than 50 degrees.

Also, as Figure 3 suggests, when using stacking velocity in migrating seismic data, δ controls the sign of the position error for steep reflectors. For negative δ, steep reflectors will generally be undermigrated; for positive δ, they will generally be overmigrated. This observation, however, cannot be generalized to vertical migrated time other than $t_m = 2$ s (see Figure 6). This sensitivity of error to δ implies that δ largely governs the expected position error for steep reflectors. This is fortunate since the value δ, unlike ϵ, can be obtained with relatively good accuracy from seismic

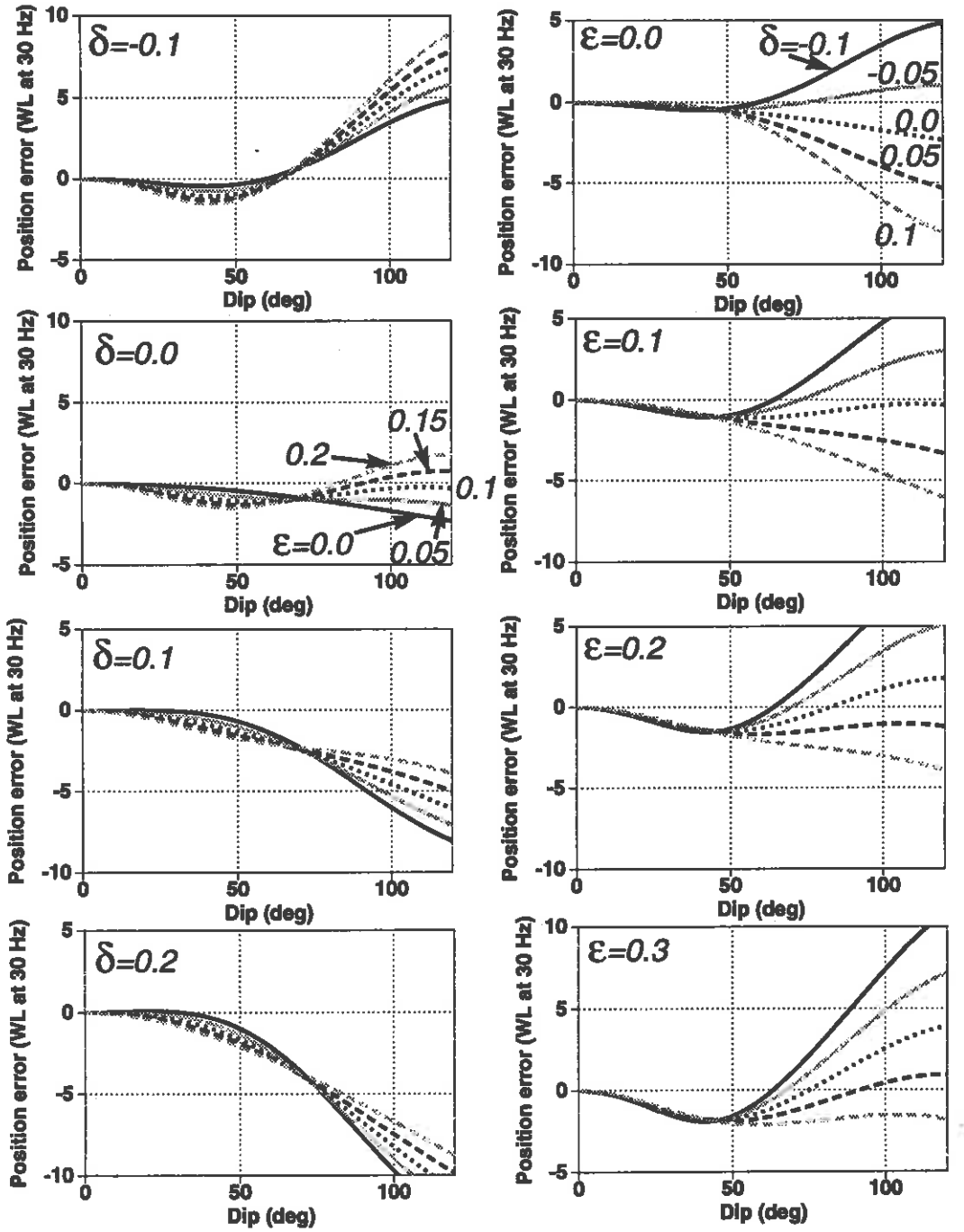

FIG. 3. Lateral position error as a function of reflector dip, for different combinations of ϵ and δ. Migration velocity is derived from the best-fit stacking velocity, and the axis of symmetry is vertical. The vertical velocity gradient $k = 0.6\ s^{-1}$, and the reflection point is positioned at vertical migrated time $t_m = 2$ s.

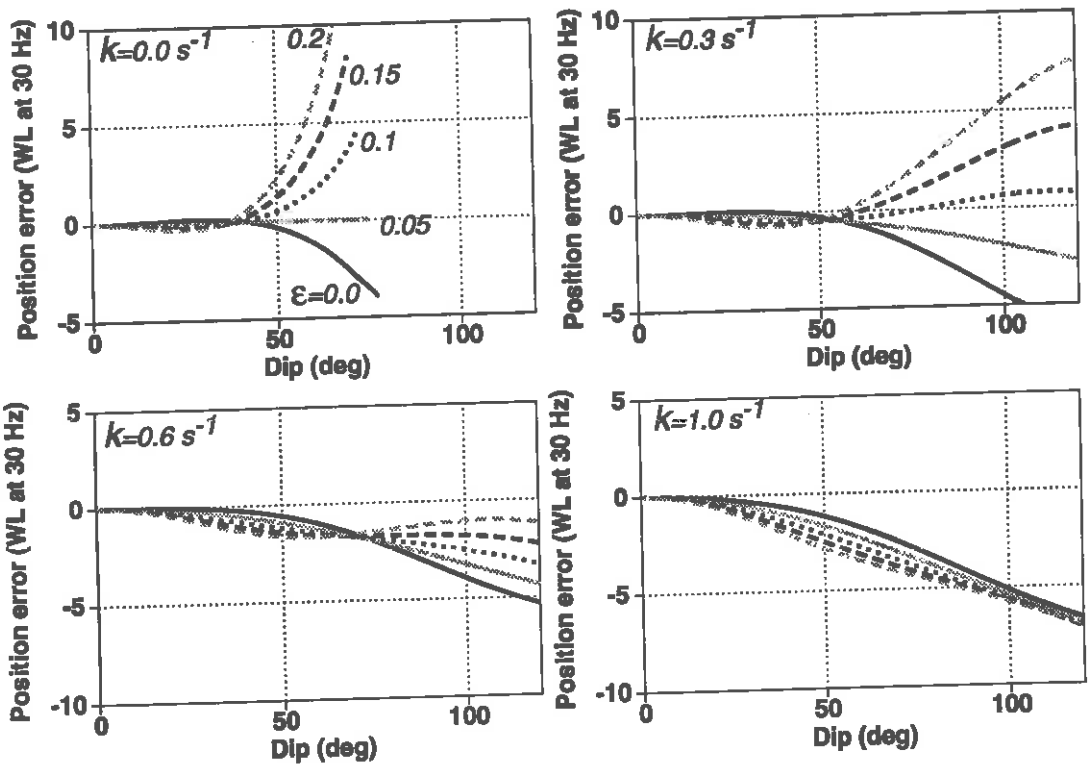

FIG. 4. Lateral position error as a function of reflector dip and ϵ for different values of vertical velocity gradient, k. Here $\delta = 0.05$, and the symmetry axis is vertical.

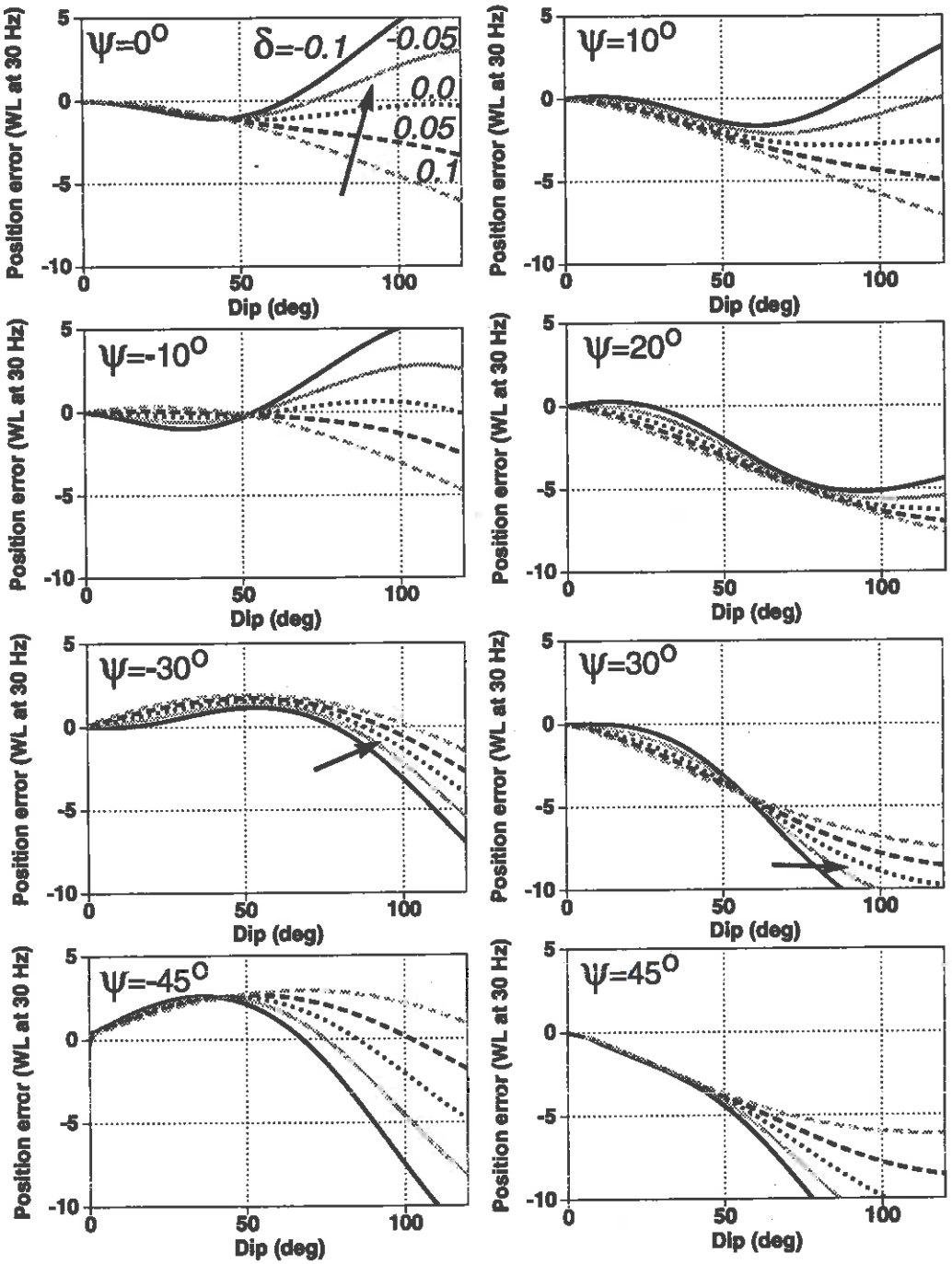

FIG. 7. Position error as a function of reflector dip and δ, for different orientations ψ of symmetry axis. Throughout, $\epsilon = 0.1$. In anticipation of Figure 11, the arrows point to approximately the position error for a reflector dip of 90 degrees in Taylor sandstone ($\delta = -0.035$ and $\epsilon = 0.11$).

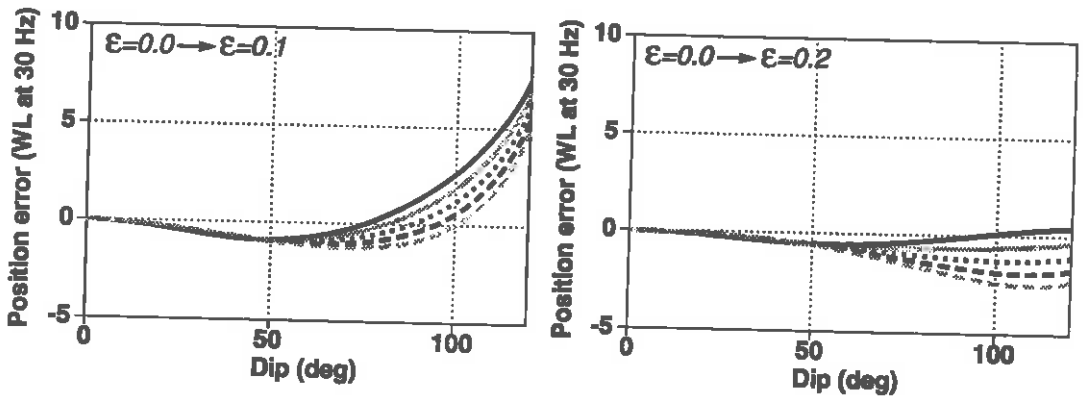

FIG. 8. Position errors as a function of reflector dip for a medium where ϵ and δ vary with depth. At the surface the medium is isotropic, $\delta = \epsilon = 0$; at the reflector the medium is TI with $\epsilon = 0.1$ for the left plot, $\epsilon = 0.2$ for the right plot, and δ has the same values shown in Figure 6. Here, $\psi = 0$, and the gradient in vertical velocity is k=0.6 s^{-1}.

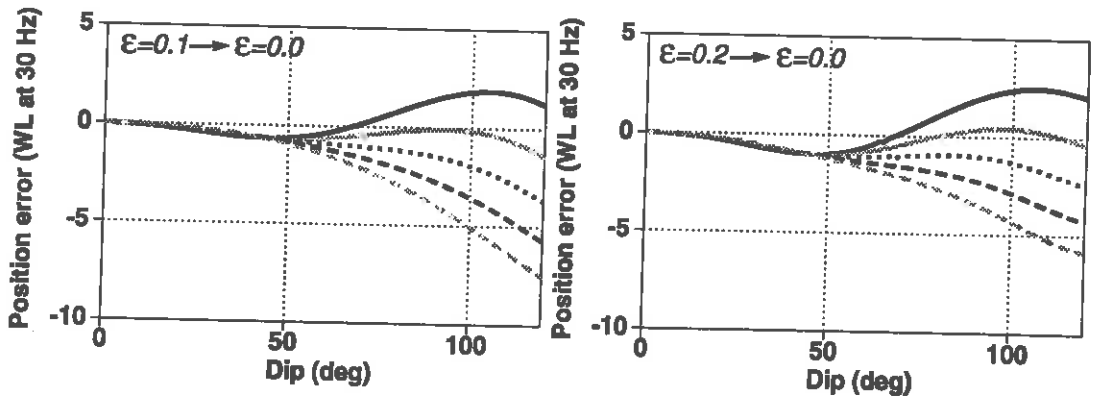

FIG. 9. Same as Figure 8, but this time the medium varies from being TI at the surface to isotropic at the reflector. Again k=0.6 s^{-1}.

Again, differences in the behavior of the error curves in Figures 8 and 9 are controlled largely by the size vertical velocity gradient (k=0.6 s^{-1} in these figures). For smaller gradient the two figures would show smaller difference.

SYNTHETIC DATA EXAMPLES

To this point, we have been showing curves of position error for a wide variety of situations. Let us now see how these errors are manifested in the imaging of synthetic data. We use here the time-wavenumber (t-k) migration algorithm of Hale (1991). This isotropic time migration algorithm was chosen largely because it preserves the amplitudes of the vertical reflectors in isotropic media.

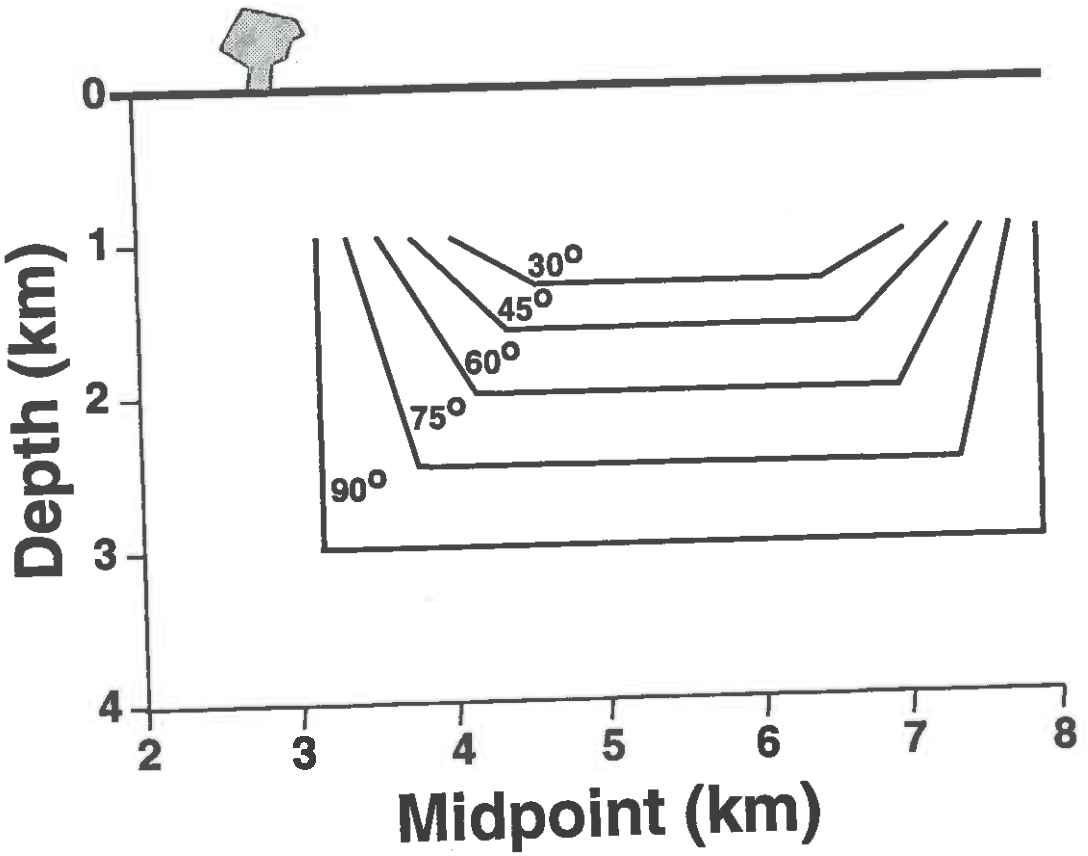

FIG. 10. Model consisting of horizontal reflectors with segments having dips ranging from 30 to 90 degrees on both sides.

Figure 10 shows a model containing horizontal reflectors with dipping segments having dips ranging from 30 to 90 degrees on both sides. The medium has the properties of Taylor sandstone ($\delta = -0.035$ and $\epsilon = 0.11$) with a vertical velocity $v(z)$=2000+0.6z m/s. Figure 11 shows three sections, all migrated using the isotropic t-k algorithm of Hale, with velocities calculated from the stacking velocity. In (a) the

medium is isotropic, so the migration is accurate for all dips, with only a slight overmigration related to the small difference between the stacking velocity and the actual vertical rms velocity in a vertically inhomogeneous medium. In contrast, the steep portions are erroneously migrated for the Taylor sandstone TI medium, with errors largely influenced by the orientation of the symmetry axis. The arrows in Figure 7 point to the approximate errors expected for the Taylor sandstone having the symmetry-axis directions used in Figure 11. The differences in ϵ (0.11 for the Taylor sandstone and 0.1 in Figure 7) are insignificant since, as seen above, ϵ has little influence on position error when stacking velocity is used. At migrated time $t_m = 2$ s in Figure 11, the horizontal position errors reflect, in general, the results obtained from the curves in Figure 7. However, those curves could not show some the artifacts near the reflector corners. Note also that the 90-degree reflector in (c) appears overturned. Also, the horizontal segments are shifted slightly to the right, consistent with expectation from the modeling results in Alkhalifah (1993).

Figure 11 is representative of fault-like structures, where the dip changes abruptly at the fault. In this circumstance, anisotropy-generated errors are clearly observed, and practical measures can be taken to correct for the errors; e.g., the migration velocity function can be altered to improve the "look" of the data, or perhaps an anisotropic migration algorithm can be used. However, often errors due to ignoring anisotropy can pass unnoticed. An example of this problem is the situation where reflectors have continuously varying dip similar to that in bedding upturned against a steep salt-dome flank, as depicted in Figure 12. Figure 12 shows migrated sections for TI media with (a) $\delta = 0.1$, $\epsilon = 0.15$ and $\psi = 0$, and (b) $\delta = -0.1$, $\epsilon = 0.1$ and $\psi = 0$. The dotted line is the true location of the salt-dome flank. With anisotropy ignored, the migrated images look plausible in both cases (i.e., little or no crossing of reflections), yet both are incorrect and differ substantially from one another.

Another type of position error can arise in the imaging of TI media. Because stacking velocity differs from vertical rms velocity, conversion from time to depth based on stacking velocity will be erroneous. This error, which distorts depths throughout the section, results in vertical shifts

$$D_{shift} \simeq (\frac{V_{stack}}{V_{rms}} - 1)D,$$

where D is the true depth of the reflector. Such errors can be avoided by obtaining an estimate of δ for the medium. Then, the vertical rms velocity can be calculated from the limiting stacking velocity as $\frac{X}{D} \rightarrow 0$ (Thomsen, 1986). In a $v(z)$, medium depth migration is equivalent to time migration followed by a time-to-depth conversion. Therefore, the depth error resulting from using the stacking velocity in the conversion is the same as that when depth migration is done with the stacking velocity. (Depth migration would have the same lateral position errors described in the curves.) The depth-shift problem is similar to that described by Verwest (1989) for migration in elliptically anisotropic media, and could be similarly corrected with use, in effect, of different velocities for the migration and for the depth conversion.

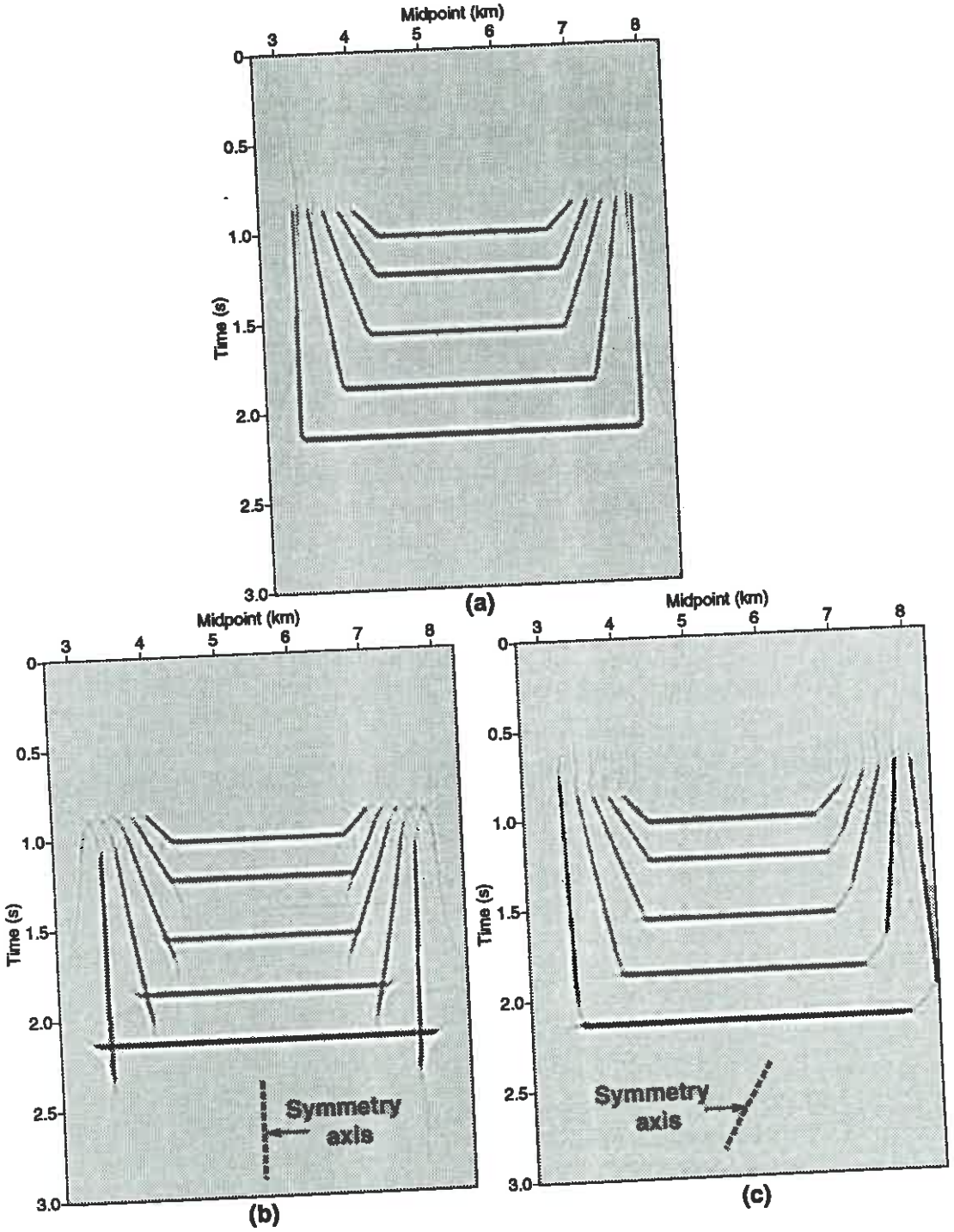

FIG. 11. Isotropic time migration of the model in Figure 10. (a): isotropic medium. (b) and (c): Taylor sandstone medium, with $\delta = -0.035$ and $\epsilon = 0.11$. In (b) the symmetry axis is vertical, and in (c) it is 30 degrees from the vertical. The vertical velocity $v(z)$=2000+0.6z m/s.

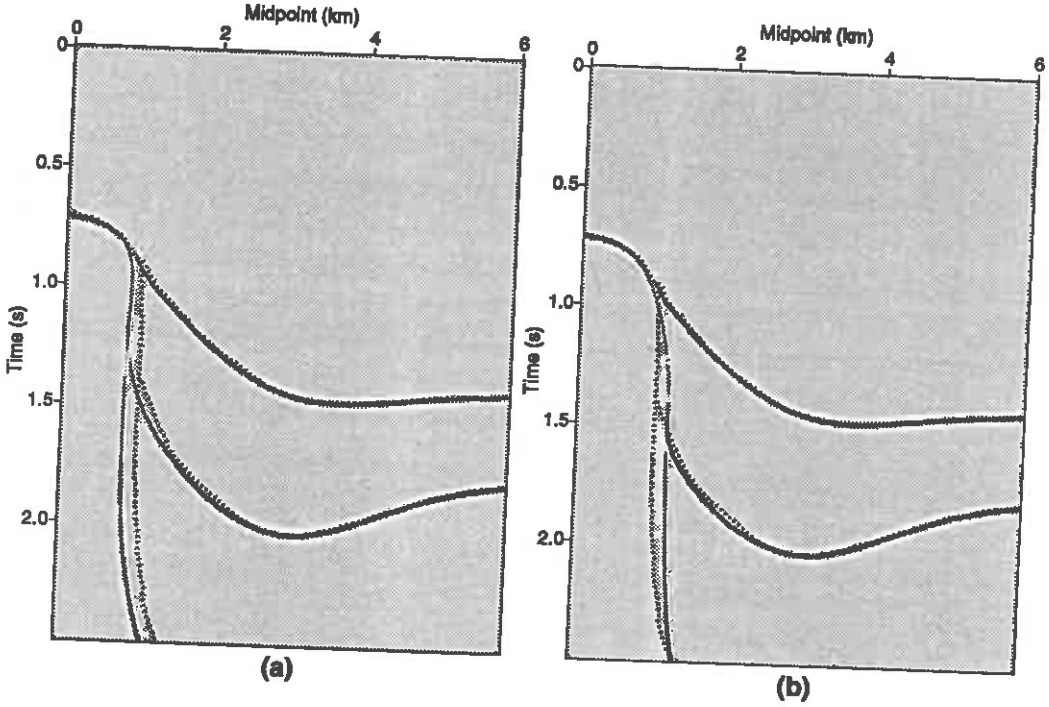

FIG. 12. Isotropic time migration of a simulated case of sedimentary beds upturned against the flank of a salt dome, where the medium is TI with (a) $\delta = 0.1$, $\epsilon = 0.15$ and $\psi = 0$, and (b) $\delta = -0.1$, $\epsilon = 0.1$ and $\psi = 0$. Both media have vertical velocity $v(z)$=2000+0.6z m/s. The correct reflector positions are represented by the dotted line.

Figure 13 shows a migrated image using an isotropic depth-migration algorithm for the model in Figure 10. The medium is Taylor sandstone, and the vertical velocity is $v(z)$=2000+0.6 z m/s. Because the velocity used in the migration process is the stacking velocity, all reflectors, but most obviously the horizontal ones, are imaged too deep (compare with Figure 10). In field data, these depth errors might not be recognized without some assessment of the anisotropy of the medium.

CONCLUSION

For the ranges of δ and ϵ studied here, we believe that an isotropic time migration using the stacking velocity would result in acceptable images for reflector dip less than 50 degrees in laterally homogeneous media.

Depending on whether the migration velocity is derived from stacking velocity or vertical rms velocity, we find quite contrary sensitivities of the error behavior to the values of δ and ϵ. In media with typical vertical velocity gradient (0.5 s^{-1} or greater) and $\psi = 0$, the value of δ largely governs the position errors for steep reflectors (dips greater than 50 degrees) when using the stacking velocity in migration. This is convenient, since δ is the anisotropy parameter most readily obtainable from seismic data. In addition, most of the errors associated with TI media, when stacking velocity is used for the migration, are associated with steep reflectors.

Interestingly, when the vertical rms velocity, which is independent of values of δ and ϵ, is used in the migration process, the value of ϵ largely governs the position errors, especially for steep reflectors and velocity gradient 0.5 s^{-1} or greater. Given the large sensitivity of position error to ϵ when the vertical rms velocity is used in isotropic migration, we infer that one should not go to the effort of using a migration algorithm that honors anisotropy unless ϵ is properly estimated. This contention further suggests that the practice of equating ϵ to δ and doing migration based on elliptical anisotropy, as is often done when the actual value of ϵ is unknown, might lead to erroneous migration, especially for reflector dip greater than about 50 degrees. For vertical velocity gradients of 0.5 s^{-1} or more, if the value of ϵ is not well known, we believe it is better to use the stacking velocity in isotropic migration and use the value of δ to estimate the errors than to do migration based on an anisotropic algorithm.

The above conclusions pertain to media with vertical symmetry axis. Tilting of the axis adds yet more complication to migration-error behavior. Tilt in the orientation of the symmetry axis results in lateral shifts of imaged horizontal reflectors from their true positions, much as happens when time migration is used where overburden velocity varies laterally.

Clearly, models with constant velocity gradient and FTI are simplifications of the true subsurface. The limitation to constant velocity gradient could readily be relaxed by a perturbation method similar to that used in going from FTI to general TI media. Despite the limitations of the models used here, analysis of position errors for these

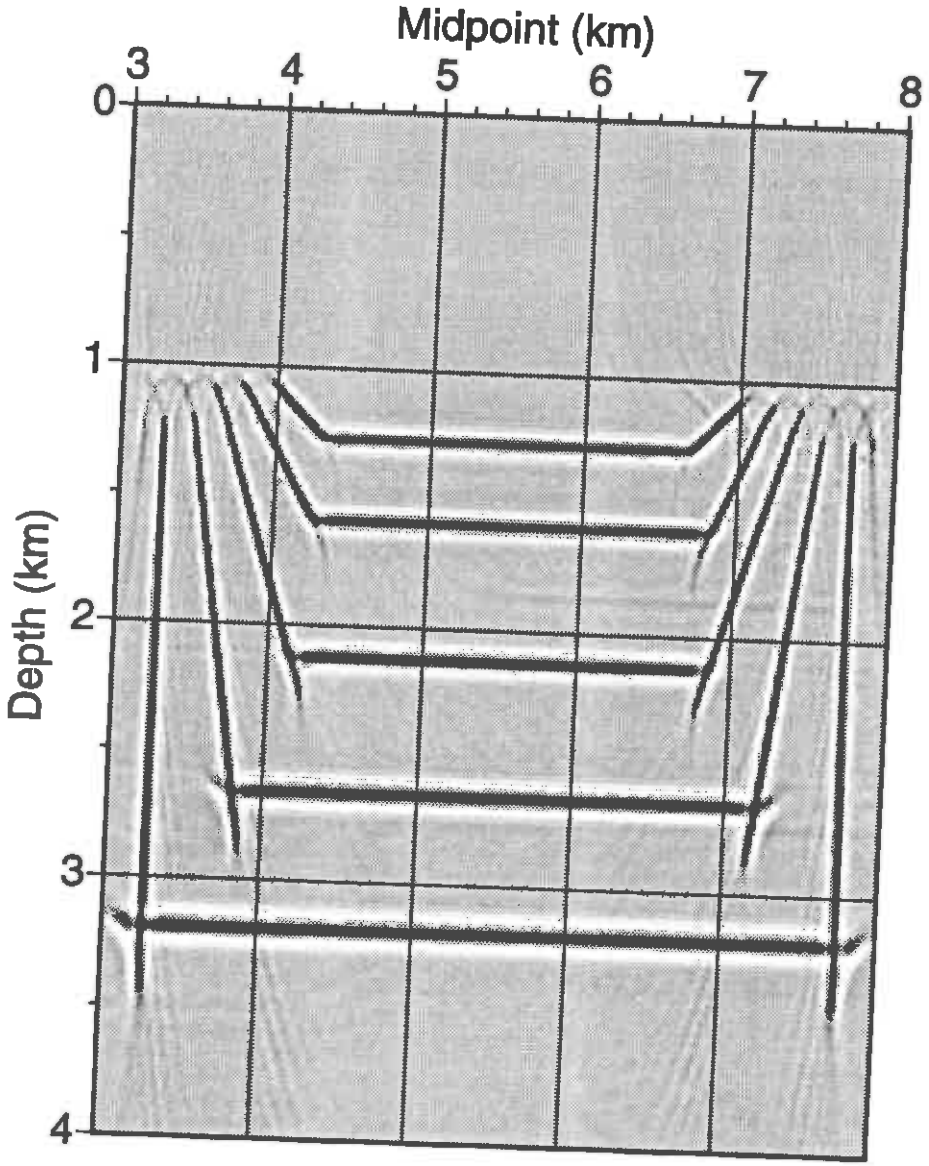

FIG. 13. Depth migration of the reflector model in Figure 10. The medium is Taylor sandstone, with $\delta = -0.035$ and $\epsilon = 0.11$, where the axis of symmetry is vertical. The vertical velocity is $v(z)$=2000+0.6z m/s.

models should aid in understanding accuracy limitations in anisotropic media.

Unless we are imaging a fault or structure with sharp edges, many errors due to anisotropy pass by unnoticed, particularly given the latitude often exercised in choosing migration velocity, in practice. Clearly, the key to success in migration in the presence of anisotropy is the use of an algorithm that not only honors anisotropy, but also uses good estimates of the anisotropy parameters, δ and ϵ.

ACKNOWLEDGMENTS

We thank Ilya Tsvankin for his useful insights at critical stages of this study, especially his suggestion to parameterize the TI media in terms of Thomsen's parameters.

REFERENCES

Alkhalifah, T., 1993, Efficient synthetic seismograms for transversely isotropic media with constant velocity gradient: CWP Annual Report, CWP-128, Colorado School of Mines.

Červený, V., 1989, Ray tracing in factorized anisotropic inhomogeneous media: Geophys. J. Int., **94**, 575–580.

Červený, V., and Simoes-Filho, I. A., 1991, The traveltime perturbations for seismic body waves in factorized anisotropic inhomogeneous media: Geophys. J. Int., **107**, 219–229.

Hale, D., 1991, Migration in the Time-Wavenumber Domain: Project Review, CWP-107, Colorado School of Mines.

Larner, K. and Cohen, J., 1993, Migration error in factorized transversely isotropic media with linear velocity variation with depth: Geophysics, in press.

Levin, F., 1990, Reflection from a dipping plane—Transversely isotropic solid: Geophysics, **55**, 851–855.

Shearer, P. M. and Chapman, C. H., 1988, Ray tracing in anisotropic media with linear velocity gradient: Geophys. J. Int., **94**, 575–580.

Thomsen, L., 1986, Weak elastic anisotropy: Geophysics, **51**, 1954–1966.

Tsvankin, I., and Thomsen, L., 1993, Nonhyperbolic reflection moveout and the inverse problem for transversely isotropic media: submitted to Geophysics.

Verwest, B. J., 1989, Seismic migration in elliptically anisotropic media: Geophysical Prospecting, **37**, 149–166.

CWP-134

Gaussian beam migration for anisotropic media

Tariq Alkhalifah

Gaussian beam migration for anisotropic media

Tariq Alkhalifah

ABSTRACT

Gaussian beam migration (GBM), as it is implemented today, efficiently handles isotropic inhomogeneous media. The approach is based on the solution of the wave equation in ray-centered coordinates (s, n). However, for anisotropic media, the wave equation in (s, n) coordinates is complicated and cumbersome to work with. An alternative that circumvents the complexity is to perturb the traveltimes in the GBM method, from those for a background isotropic medium to those for the desired anisotropic medium. Although the perturbation technique is exemplified here for GBM, it just as well could be implemented for either Kirchhoff or slant stack migration. However, it is particularly cost efficient to use it for GBM; anisotropic GBM is slower than its isotropic counterpart by only 10%. The performance of this method is demonstrated on synthetic examples that show successful migration for reflector dips up to and beyond 90 degrees.

INTRODUCTION

Although modern migration algorithms now can treat 3-D data from areas of relatively complex structure, and can accommodate turning waves associated with dip beyond 90 degrees, only recently has anisotropy been taken into account. Anisotropy may cause considerable departure of traveltime curves from those expected in comparable isotropic media. Such departures will influence the accuracy of both migration and velocity analysis. For some transversely isotropic (TI) media, for example, large position errors could arise for steep reflectors when anisotropy is ignored in poststack migration.

Migration algorithms for special cases of anisotropy have been developed in the past few years. Verwest (1989) developed a seismic migration algorithm for elliptically anisotropic media; however, this type of anisotropy is usually a poor approximation for P-waves. Uren, Gardner and McDonald (1990) found a migrator equation for anisotropic homogeneous media that works in the frequency-wavenumber (f-k) domain. However, that approach requires that analytical expressions for the phase velocity to be solved for angle of the plane wave propagation direction; such expressions for anisotropic media are rather complicated.

Gaussian beam migration (GBM) has emerged in the past few years as a desirable method for subsurface imaging. Among its features are computational efficiency, robustness with respect to ray caustics and shadows, the ability to image reflector dips greater than 90 degrees with turning waves, and straightforward extensions for migration of nonzero-offset sections and 3-D data (Hale, 1992).

Here, I use time-perturbation equations developed by Červený and Firbas (1982) for general anisotropic media, and by Červený and Filho (1991) for factorized anisotropic inhomogeneous (FAI) media, along with newly developed perturbation-corrected parameters for amplitude and velocity, to modify GBM to treat generally anisotropic media.

THE FIRST-ORDER TIME PERTURBATION

Ray equations

The eigenvalues that describe the raypath (eikonal equation) and the eigenvectors that describe the amplitudes of the various waves in inhomogeneous media are based on a high-frequency approximation. The eigenvalues are calculated from the following relation (Červený, 1972):

$$Det(\Gamma_{jk} - G_m \delta_{jk}) = 0,$$

where Γ_{jk} are components of a 3×3 matrix $\mathbf{\Gamma}$ given by the relation

$$\Gamma_{ik}(x_s, p_i) = a_{ijkl}(x_s) p_j p_l,$$

with

$$p_i = \frac{\partial \tau}{\partial x_i},$$

$$a_{ijkl} = c_{ijkl}/\rho,$$

and

τ	is the traveltime along the ray,
ρ	is bulk density,
x_s	are the cartesian coordinates for position along the ray, s=1,2,3, and
c_{ijkl}	are elastic coefficients; in general, functions of x_s.

The G_m are the three eigenvalues representing the eikonal equation for the quasi P-wave when m=1, for the quasi SV-waves when m=2, and for the quasi SH-waves when m=3. For P-waves (I shall drop the "quasi" modifier in the following),

$$G_1(x_s, p_s) = 1. \tag{1}$$

For isotropic media, $G_1 = \alpha^2(x_s)p_ip_i$, where $\alpha(x_s)$ is the P-wave velocity.

In a factorized anisotropic inhomogeneous (FAI) medium

$$a_{ijkl}(x_s) \equiv f^2(x_s)A_{ijkl}, \tag{2}$$

where $A_{ijkl} \equiv a_{ijkl}(x_s)/a_{3333}(x_s)$ are the *position-independent* density-normalized elastic coefficient ratios, and $f(x_s) = \sqrt{a_{3333}(x_s)}$ represents the velocity in the depth direction x_3 at a position x_s. Equation (1) then becomes

$$G_1(x_s, p_s) \equiv f^2(x_s)G_1^o(p_s) = 1, \tag{3}$$

where $G_1^o(p_i)$ is the position-independent eigenvalue of the P-wave.

Perturbation parameters

Consider two media, a background medium (unperturbed), possibly anisotropic and inhomogeneous, in which we do our general ray tracing, and a perturbed medium, which may also be anisotropic and inhomogeneous, in which we wish to calculate traveltime and amplitude. The traveltime $T(a,b)$ in the perturbed medium of the ray traveling from point a to point b is calculated from the traveltime in the background medium $T^0(a,b)$ of the ray traveling between the same two points. Specifically, we seek an efficient scheme for computing the time perturbation $\delta T(a,b)$, given $T^0(a,b)$ and relationships between the parameters of the background and perturbed media.

$$T(a,b) = T^0(a,b) + \delta T(a,b). \tag{4}$$

Differences between the density-normalized elastic parameters in the background medium a^0_{ijkl} and those in the perturbed medium a_{ijkl} define the degree of perturbation δa_{ijkl}.

$$a_{ijkl} = a^0_{ijkl} + \delta a_{ijkl}.$$

In an FAI medium, the vertical velocity $f^0(x_i)$ in the background medium and $f(x_i)$ in the perturbed medium are related as follows

$$f(x_i) = f^0(x_i) + \delta f(x_i). \tag{5}$$

Likewise for the ratios of elastic coefficients,

$$A_{ijkl} = A^0_{ijkl} + \delta A_{ijkl}. \tag{6}$$

Time perturbation

Following Červený and Firbas (1982), for a generally anisotropic inhomogeneous background,

$$\delta T(a,b) = -\frac{1}{2}\int_a^b \delta a_{ijkl}p_ip_lg_jg_k dT, \tag{7}$$

where g_i are the components of the eigenvector $\mathbf{g}$ (the direction of particle motion), here for the P-wave. The integration in equation (7) is performed along ray L_0 computed in the background medium, and quantities p_i, p_l, g_j, g_k and dT correspond to the background medium. Hanyga (1982) showed that the relation between $\delta T(a,b)$ and δa_{ijkl} is linearized.

For an isotropic background medium, $\mathbf{g} = \mathbf{N}$, the normal to the wavefront for the isotropic background, and $\mathbf{p} = \mathbf{N}/\alpha$. Equation (7) then yields

$$\delta T(a,b) = -\frac{1}{2}\int_a^b \delta a_{ijkl} N_i N_l N_j N_k \alpha^{-2} dT, \tag{8}$$

where $\alpha = f^0(x_i)$ is the velocity of the P-wave in the background medium, and $dT = ds/\alpha$, with s the arclength along the ray L_0.

For FAI media, using equations (2), (5), and (6) in equation (7) yields (Červený and Filho, 1991)

$$\delta T(a,b) = -\int_a^b \frac{\delta f(x_i)}{f^o(x_i)} dT - \frac{1}{2}\delta A_{ijkl}\int_a^b f^{o^2}(x_i) p_i p_l g_j g_k dT, \tag{9}$$

where the first integral corresponds to structural perturbations and the second integral corresponds to anisotropy perturbations. For an isotropic background, equation (9) becomes (Červený and Filho, 1991)

$$\delta T(a,b) = -\int_a^b \frac{\delta f(x_i)}{\alpha(x_i)} dT - \frac{1}{2}\delta A_{ijkl}\int_a^b N_i N_l N_j N_k dT. \tag{10}$$

Amplitude and velocity perturbations

Amplitude decay due to geometrical spreading in the perturbed medium can be estimated from the background medium by a similar perturbation approach. Consider q, the geometrical spreading function for velocity variation with depth, given by

$$q = \int_{t_0}^{t} v^2(\tau) d\tau, \tag{11}$$

where $v(\tau)$ is the velocity and $\tau = \int \frac{ds}{v(s)}$ is the time along the ray. I now define the amplitude perturbation δq as

$$q = q^o + \delta q,$$

where q^o is the geometrical spreading in the background medium, and q is the geometrical spreading in perturbed medium.

Consider a segment of the raypath that is so short that velocity can be taken as constant. Then, from equation (11) the geometrical spreading in this segment from point a_0 to point b_0 ($l \equiv |a_0 - b_0| << 1$) is

$$q^o = v^2 T^o = \frac{l^2}{T^o}.$$

For a ray traveling in the perturbed media between the same two points, the approximate geometrical spreading is

$$q^o + \delta q = \frac{l^2}{T^o + \delta T}.$$

Take the integrand in equation (8) as *the anisotropy perturbation factor* F for the homogeneous, isotropic segment,

$$F = -\frac{1}{2}\delta a_{ijkl} N_i N_l N_j N_k \alpha^{-2}$$

and

$$\delta T = F T^o.$$

Then

$$q^o + \delta q = \frac{l^2}{T^o(1+F)} = \frac{q^o}{1+F},$$

so

$$\delta q = -\frac{F}{1+F} q^o \approx -F q^o.$$

A summation of these segments will provide the first-order perturbation of the geometrical spreading for the raypath between point a and point b,

$$\delta q(a,b) = \int_a^b -F dq,$$

where F and dq correspond to the background medium and $F << 1$.

Based on a similar argument, the perturbation of the ray velocity is given by

$$\delta v(a,b) = \int_a^b \frac{-F}{1+F} dv \cong \int_a^b -F dv.$$

I use the amplitude and velocity perturbations, along with the time perturbation of equation (10) to modify Hale's GBM program (which previously could be considered to have been operating in the background medium) to work for a generally anisotropic medium. These perturbations could be implemented in either Kirchhoff or slant stack migration, just as well in GBM.

Traveltime calculation along the beam

Up to this point, all the perturbations mentioned above deal with the central ray. However, in GBM another parameter must be considered— the distance n along the normal to the ray. The traveltime as a function of position in (s,n) coordinates in an isotropic medium can be estimated by Taylor series expansion (Červený and Pšenčík, 1984).

$$T^0(s,n) \cong T^0(s) + 0.5\frac{\partial^2 T^0(s)}{\partial n^2} n^2, \qquad (12)$$

where $T^0(s)$ is the time along the central ray in the isotropic background medium, and the $\frac{\partial T^0(s)}{\partial n}$ term in this Taylor's series expansion equals zero because the wavefront is normal to the raypath in an isotropic media. The perturbed time, as shown before, is

$$T(s,n) = T^0(s,n) + \delta T(s,n),$$

where the expansion of the perturbation time along n is

$$\delta T(s,n) \cong \delta T(s) + \frac{\partial \delta T(s)}{\partial n} n + 0.5 \frac{\partial^2 \delta T(s)}{\partial n^2} n^2, \tag{13}$$

and $\delta T(s)$ is the perturbation time along the central ray. Considering only the first term of the expansion and ignoring the rest, such as where the time perturbation is rather small relative to the actual time, might be thought to be an acceptable approximation for most anisotropy

$$\delta T(s,n) = \delta T(s). \tag{14}$$

This approximation gives accurate results when a large initial beam width is used. A large initial beam width implies that the traveltime Taylor series expansion is applied primarily for plane waves, where the other terms in the expansion go to zero. However, this expansion will yield an erroneous loss of amplitude for spherical waves. This amplitude loss results from the out-of-phase superposition of the spherical beams that contribute to a point in the depth section.

Hale (1992) showed that GBM is a weighted combination of Kirchhoff (spherical-wave) and slant stack (planar-wave) migrations. The weighting is controlled somewhat by the initial beam width. A large initial beam width implies that most of the expansion in equation (14) will be applied along plane waves. For perturbation to an anisotropic medium, this choice gives the most accurate expansion. From my tests, I find good results for initial beam width that exceeds the width predicted by Hill (1991) by about 30 percent. Choosing the appropriate value for the initial beam width is largely a judgement call. Hill (1991) showed the shortcomings of using too large an initial beam width; he also showed that considerable latitude is allowed in the choice of beam width. The approximation in equation (14) primarily influences amplitudes, with small influence on traveltimes.

An alternative is to attempt the expansion in equation (13). This choice would somewhat slow the program; however, it should correct for the out-of-phase superposition problem. Evaluating the derivatives in equation 13,

$$\frac{\partial \delta T(s)}{\partial n} = \frac{d\delta T(s)}{d\theta} \frac{\partial \theta}{\partial n},$$

and

$$\frac{\partial^2 \delta T(s)}{\partial n^2} = \frac{d^2 \delta T(s)}{d\theta^2} (\frac{\partial \theta}{\partial n})^2 + \frac{d\delta T(s)}{d\theta} \frac{\partial^2 \theta}{\partial n^2},$$

where θ is the ray angle with the vertical in the isotropic background medium, and n is independent of s. The above two equations are evaluated in the background medium, where the $\frac{\partial^2\theta}{\partial n^2}$ term can be neglected. This term requires higher-order solutions of the traveltime equation in the ray-centered coordinates, terms that can be neglected. Given

$$\frac{p}{q} = \frac{\sin d\theta}{vq} \approx \frac{1}{v}\frac{d\theta}{dn}.$$

Then,

$$\frac{\partial\theta}{\partial n} = \frac{pv}{q},$$

where p and q correspond to the background medium, and satisfy the following equations (Červený, 1981)

$$\frac{dq}{dt} = v^2 p \qquad \frac{dp}{dt} = -\frac{v_{,nn}}{v}q.$$

Given, for 2-D that is $N_1 = \sin\theta$ and $N_3 = \cos\theta$,

$$\frac{dN_1}{d\theta} = N_3 \qquad \frac{dN_3}{d\theta} = -N_1,$$

so

$$\frac{d\delta T(s)}{d\theta} = -2\delta A_{1111}\int_a^b N_1^3 N_3 dT - 2(\delta A_{1133} + \delta A_{1313})\int_a^b (N_1 N_3^3 - N_1^3 N_3)dT$$

$$-6(\delta A_{1113} + \delta A_{3313})\int_a^b N_1^2 N_3^2 dT + 2\delta A_{1113}\int_a^b N_1^4 dT - 2\delta A_{3313}\int_a^b N_3^4 dT.$$

$d^2\delta T(s)/d\theta^2$ could be derived in a similar way. Inserting these values in equation (13) would give the more accurate expansion for the perturbed TI media. However, I have not yet implemented this expansion.

This expansion could also be used as a paraxial expansion along the ray for anisotropic media considering an isotropic ray path. Actual expansions for anisotropic media would have been rather complicated, and probably unsolvable.

GAUSSIAN BEAM MIGRATION

Gaussian beam migration (GBM) is an efficient way of doing migration in a generally inhomogeneous, isotropic medium. Here, I describe how the above perturbation approach can be applied to modify GBM to work for general anisotropic media. For simplicity, I will demonstrate this for 2-D migration in an FAI medium.

Consider an inhomogeneous, isotropic background and an FAI medium with vertical velocity function equal to the velocity function of the isotropic background.

Then $\delta f(x_i) = 0$; and $\delta A_{3333} = 0$. Equation (10) becomes

$$\delta T(a,b) = -\frac{1}{2}\delta A_{1111}\int_a^b N_1^4(T)dT - (\delta A_{1133} + \delta A_{1313})\int_a^b N_1^2(T)N_3^2(T)dT$$
$$- 2\delta A_{1113}\int_a^b N_1^3(T)N_3(T)dT - 2\delta A_{3313}\int_a^b N_1(T)N_3^3(T)dT, \qquad (15)$$

where N_1, N_3 and dT correspond to the background medium.

As a result, the GBM algorithm of Hale (1992) becomes

Gaussian beam migration for anisotropic medium:

for all points (x_1, x_3) {
    $g(x_1, x_3) = 0$
}

for all $x_{1j} = j\Delta$ *(all beam center locations)* {
    compute $f_j(t, x_1)$ *by shifting and tapering data* $f(t, x_1)$
    compute filtered slant stack $b_j(\tau, p_1)$ *of* $f_j(t, x_1)$
    for all p_1 *(all reflection slopes)* {
        for all points (x_1, x_3) *within beam* {
            compute complex-valued $\tau_j(p_1, x_1, x_3)$ + "$\delta T(p_1, x_1, x_3)$"
            compute complex-valued "$A_j(p_1, x_1, x_3, q^o + \delta q)$"
            accumulate contribution to $g(x_1, x_3)$ *of* $b_j(\tau, p_1)$
        }
    }
}

where

$g(x_1, x_3)$	is the subsurface image,
$f(t, x_1)$	is the recorded seismic data,
$b(\tau, p_1)$	is the filtered slant stack,
A, τ	are the amplitude and traveltime of the seismic wave,

and the only changes to the algorithm are enclosed in quotes. Both δT and δq, as given above, have real values.

These changes do not limit GBM in any way. Specifically, it is still extendable to 3-D and its efficiency is unchanged; relative to the cost of the migration, the cost

of computing δT and δq is insignificant. The GBM is particularly suited for this perturbation approach because it already calculates traveltimes and amplitudes in an isotropic inhomogeneous media, the background medium.

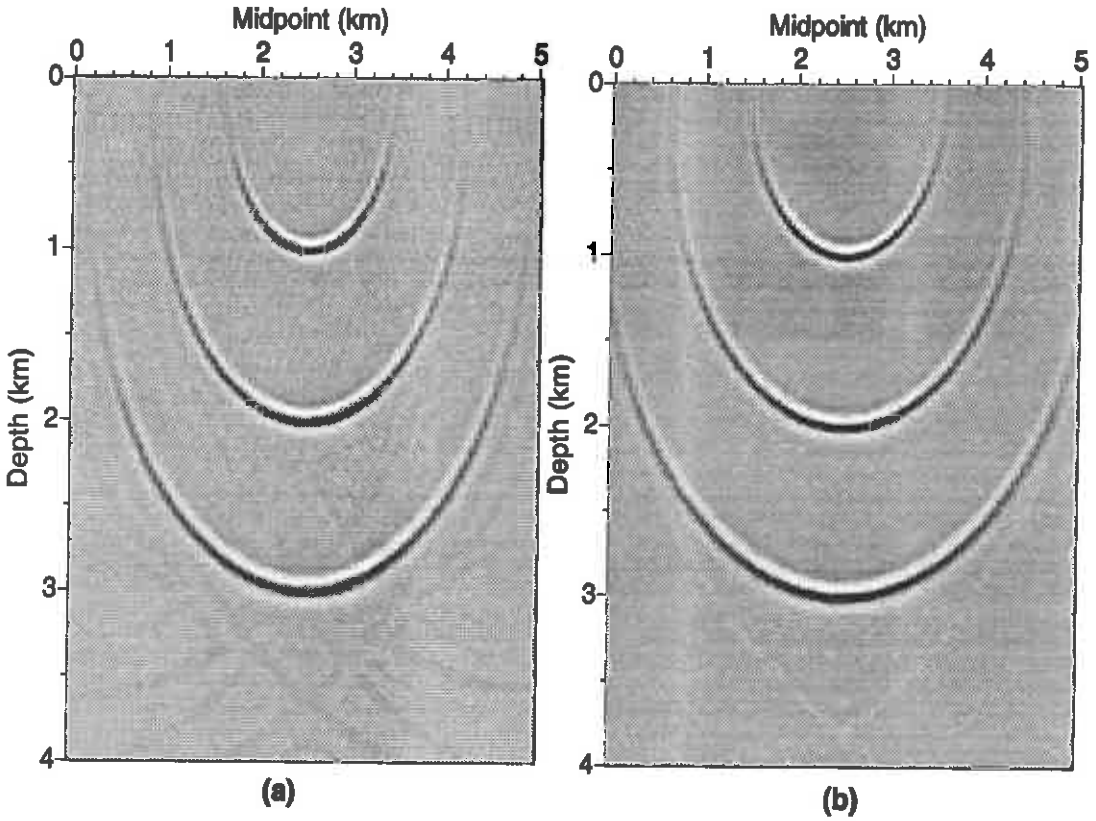

FIG. 1. GBM impulse responses for (a) isotropic, and (b) shale-limestone with vertical axis of symmetry. Both media have the same vertical velocity $v(x_3) = 3306 + 0.5\,x_3$ m/s.

Figure 1 shows the response of GBM to impulses at depths 1, 2, and 3 km for vertical velocity variation $v(x_3) = 3306 + 0.5\,x_3$ m/s in (a) an isotropic medium and (b) a thin-bedded system of horizontal layers of shale and limestone (factorized transversely isotropic inhomogeneous [FTI] medium with vertical axis of symmetry). The shale-limestone FTI medium has the following anisotropy parameters at the surface (Thomsen, 1986)

$\sqrt{C/\rho} = 3306$ m/s, $\sqrt{A/\rho} = 3721$ m/s,
$\sqrt{F/\rho} = 2076$ m/s, $\sqrt{L/\rho} = 1819$ m/s,
$\delta = 0.0$, $\epsilon = 0.134$,

where A, C, F, and L are the elastic coefficients used by White (1983) to describe

a TI medium, and δ and ϵ are Thomsen's anisotropy parameters (see equations [18] and [19], below). The essential difference between the two results in Figure 2 is that the impulse responses for the TI case are wider due to the higher ray velocities away from the vertical direction.

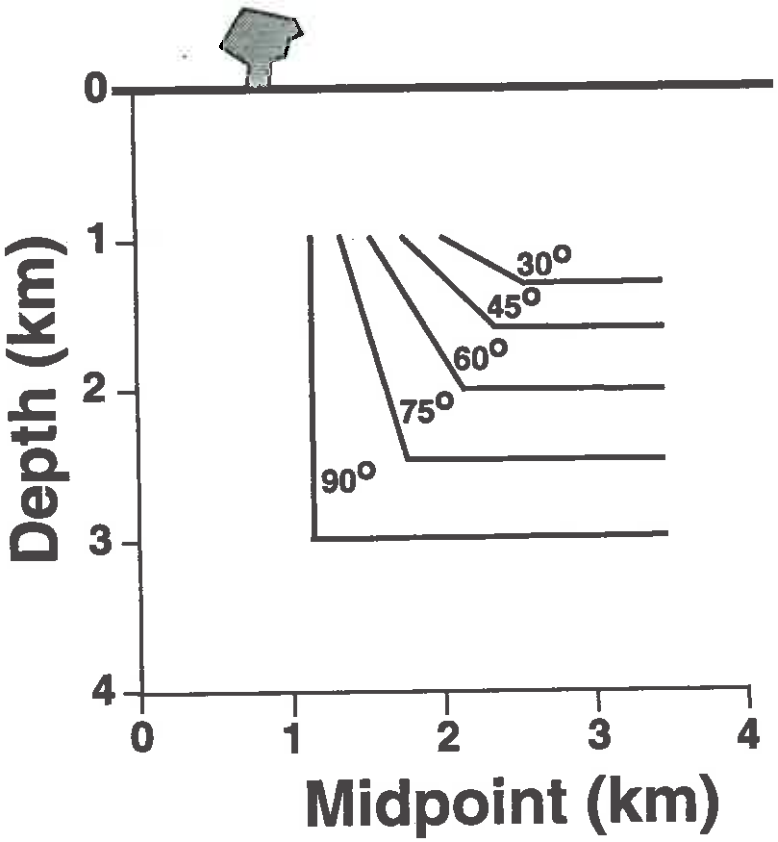

FIG. 2. Model of reflectors with dips of 0, 30, 45, 60, 75, 90 degrees. Note that the vertical reflector is at 1.2-km midpoint position.

Now, consider the reflector model shown in Figure 2. It consists of five reflectors, each of which has a horizontal segment and a dipping one. Figure 3 shows the synthetic zero-offset seismograms for this model in (a) the isotropic medium (b) the shale-limestone TI medium, described above. Figure 3a was generated using a Kirchhoff modeling program for an isotropic medium with a linear velocity increase. Figure 3b was generated using a modified version of that modeling program that treats FTI media (Alkhalifah, 1993). Figure 4 shows migrations of the data in Figure 3b using (a) standard, isotropic GBM and (b) GBM modified for anisotropic media. The velocity used to derive medium velocities for standard GBM is the best-fit stacking velocity for horizontal reflectors. Clearly the image in 4b is superior to that in 4a. The image from migration that ignores anisotropy, 4a, not only is undermigrated, it is placed at too great a depth because stacking velocity exceeds the vertical rms ve-

locity. In contrast, the reflector locations have been correctly imaged by the modified GBM, 4b, but the amplitudes for the near-vertical reflectors are low, as a result of the superposition problems for the traveltime calculations along the beams, discussed above.

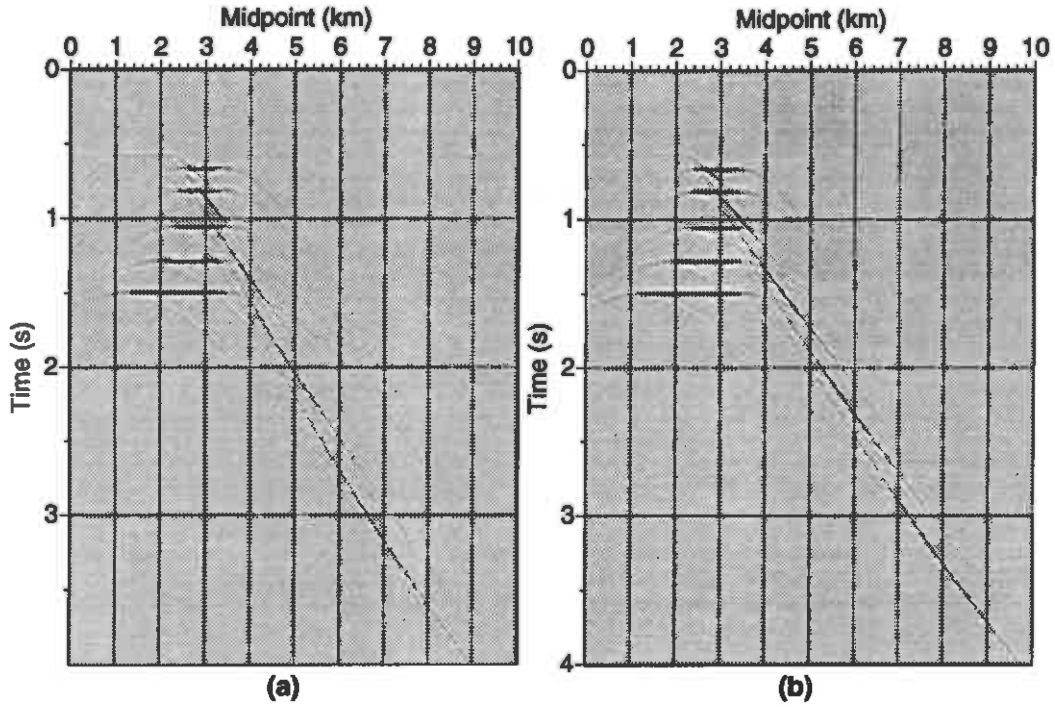

FIG. 3. Synthetic zero-offset seismograms for the structural model in Figure 2, for (a) an isotropic medium, and (b) a shale-limestone, transversely-isotropic medium. Both media have vertical velocity $v(x_3) = 3306 + 0.5\,x_3$ m/s and reflector dips ranging from 0 to 90 degrees.

Figure 5 shows isotropic GBM and perturbed, anisotropic GBM for the Cotton Valley shale FTI medium of Levin (1993), with anisotropy parameters

$\sqrt{C/\rho} = 4721$ m/s, $\sqrt{A/\rho} = 3095$ m/s,
$\sqrt{F/\rho} = 5320$ m/s, $\sqrt{L/\rho} = 2890$ m/s,
$\delta = 0.205$, $\epsilon = 0.135$,

and $v(x_3) = 4721 + 0.5\,x_3$ m/s. Following Larner and Cohen (1992), I used the best-fit stacking velocity (for horizontal reflectors) to minimize the position errors. The isotropic GBM not only yielded a considerably overmigrated image, it also re-

sulted in large vertical shifts in the reflector position. The depth error is caused by using the wrong velocity, namely stacking velocity in a TI medium, for the vertical traveltime-to-depth conversion. In contrast, the modified GBM gave the much more accurate image, with only a small overmigration of the vertical reflector.

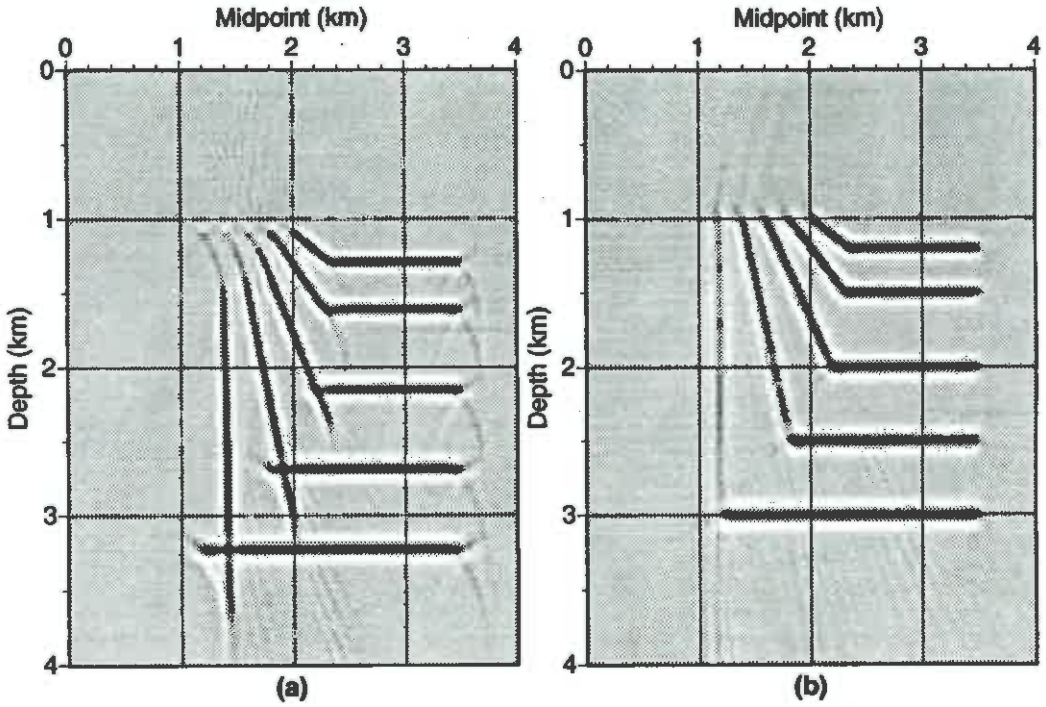

FIG. 4. Migration of the data in Figure 4b using (a) the isotropic GBM algorithm (b) perturbed GBM, for the shale-limestone TI medium.

For both anisotropic media — shale-limestone and Cotton Valley shale — the anisotropic GBM gave a substantially better image of the reflector position than did the GBM that ignores anisotropy.

Figure 6 shows a migration for the Mesaverde shale FTI medium ($\delta = 0.078$, $\epsilon = 0.128$) where turning waves were needed to migrate the model at the top of the figure. Mesaverde shale has parameters shown in Table 1, given by Thomsen (1986).

VELOCITY AND MOVEOUT EQUATIONS

Accurate estimation of velocities is essential to obtaining accurate migrations. Whereas isotropic time migration works best with the use of stacking, as opposed to

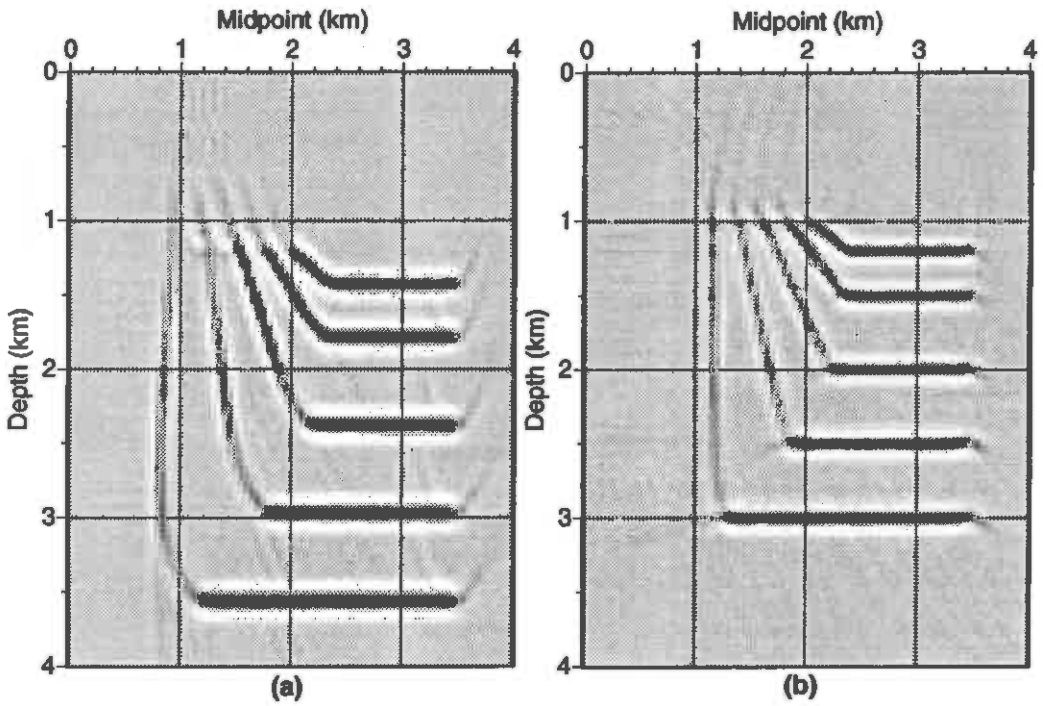

FIG. 5. Migration of data from the structural model shown in Figure 3 for Cotton Valley shale with $v(x_3) = 4721 + 0.5\,x_3$ m/s, using (a) isotropic GBM and (b) anisotropic GBM.

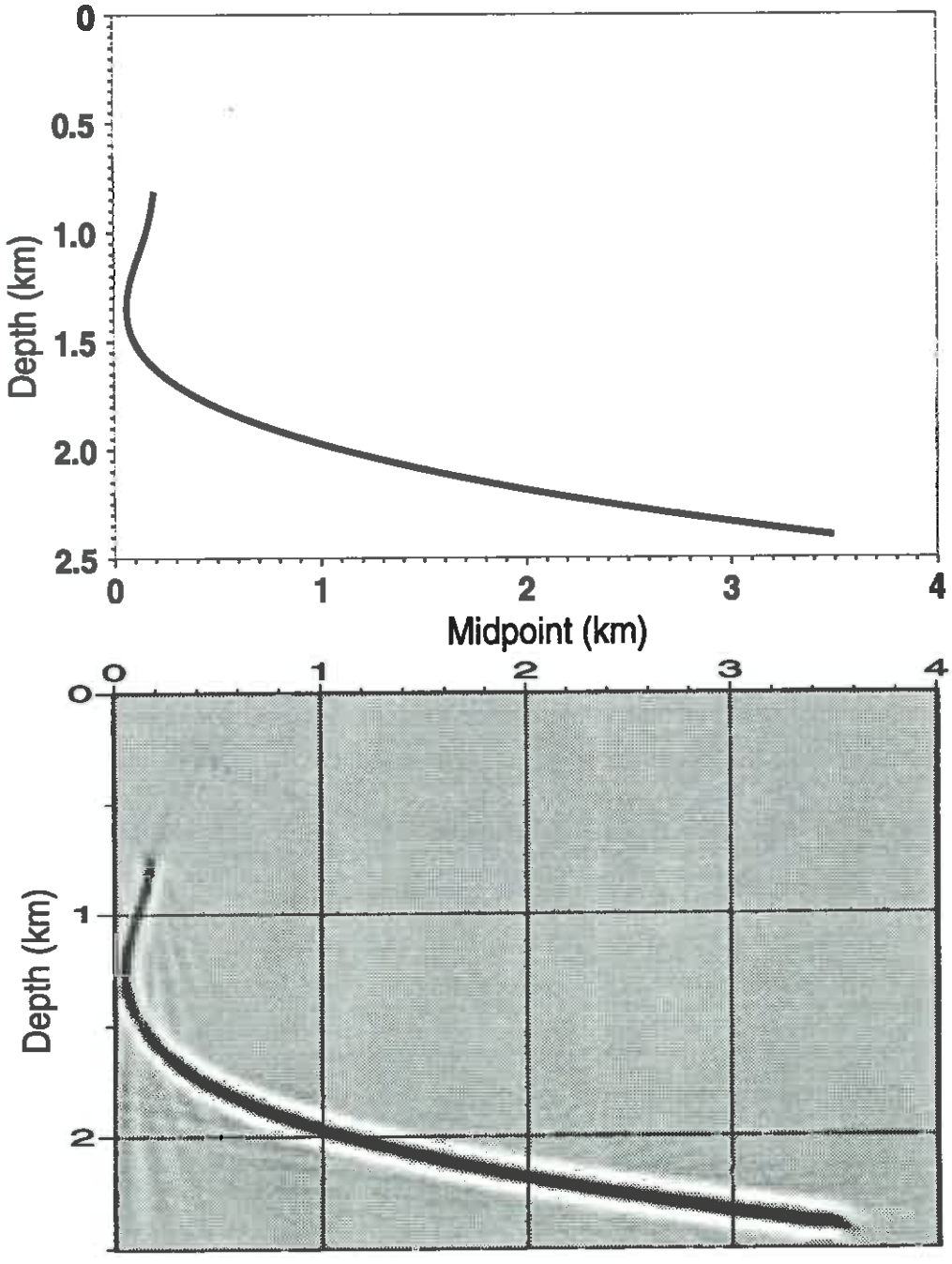

FIG. 6. Top: Model containing reflector with dip as large as 120 degrees. Bottom: Anisotropic GBM of data from the above structural model for Mesaverde shale, with $v(x_3) = 3749 + 1.0\,x_3$ m/s.

rms, velocity (Larner and Cohen, 1993), the modified GBM uses vertical rms velocity, based on the velocity of the background medium. (In all the tests, the vertical velocity of the TI medium is identical to the velocity of the isotropic background medium.) In practice, the vertical velocity could be obtained from various methods, such as vertical seismic profiling or check-shot velocity surveying.

For perturbation away from traveltime in an isotropic, homogeneous background, equation (10) becomes

$$\delta T(a,b) = [-\frac{1}{2}\delta A_{1111}N_1^4 - (\delta A_{1133}+\delta A_{1313})N_1^2N_3^2 - 2A_{1113}N_1^3N_3 - 2A_{3313}N_3^3N_1]T^0(a,b),$$

in which $T^0(a,b) = \sqrt{t_0^2 + 4h^2/v^2}$ is the hyperbolic moveout (diffraction pattern) for a homogeneous, isotropic medium, and

$$N_1 = \frac{2h/v}{\sqrt{t_0^2 + 4h^2/v^2}},$$

and

$$N_3 = \frac{t_0}{\sqrt{t_0^2 + 4h^2/v^2}}.$$

N_1, N_3 and $T^0(a,b)$ again correspond to the background medium, h is the half-offset between source and receiver, t_0 is the two-way vertical traveltime, and v is the rms velocity in the isotropic background medium, which equals the vertical rms velocity in the TI medium. The normal-moveout equation, based on the time-perturbation method, is given by

$$t_{pert}(h) = \sqrt{t_0^2 + 4\frac{h^2}{v^2}} + \delta T(a,b), \tag{16}$$

Tsvankin and Thomsen (1992) derived the exact coefficients for the expansion of the moveout equation up to fourth order for a TI medium with vertical axis of symmetry (TI expansion).

$$t_{exp}^2(h) = t_0^2 + 4A_2h^2 + \frac{A_4x^4}{1 + (x/(vt_0))^2}, \tag{17}$$

where

$$A_2 = \frac{1}{v^2(1+2\delta)},$$

and

$$A_4 = -\frac{2(\varepsilon-\delta)}{t_0^2v^4}\frac{1+\frac{2\delta}{1-v_s^2/v^2}}{(1+2\delta)^4}.$$

v_s is the shear-wave velocity, and δ and ε are given by Thomsen (1986)

$$\delta = \frac{(A_{1133}+A_{1313})^2 - (A_{3333}-A_{1313})^2}{2A_{3333}(A_{3333}-A_{1313})}, \tag{18}$$

$$\varepsilon = \frac{A_{1111} - A_{3333}}{2A_{3333}}. \tag{19}$$

Figure 7 compares moveouts t_{pert} and t_{exp} with the numerically calculated, exact

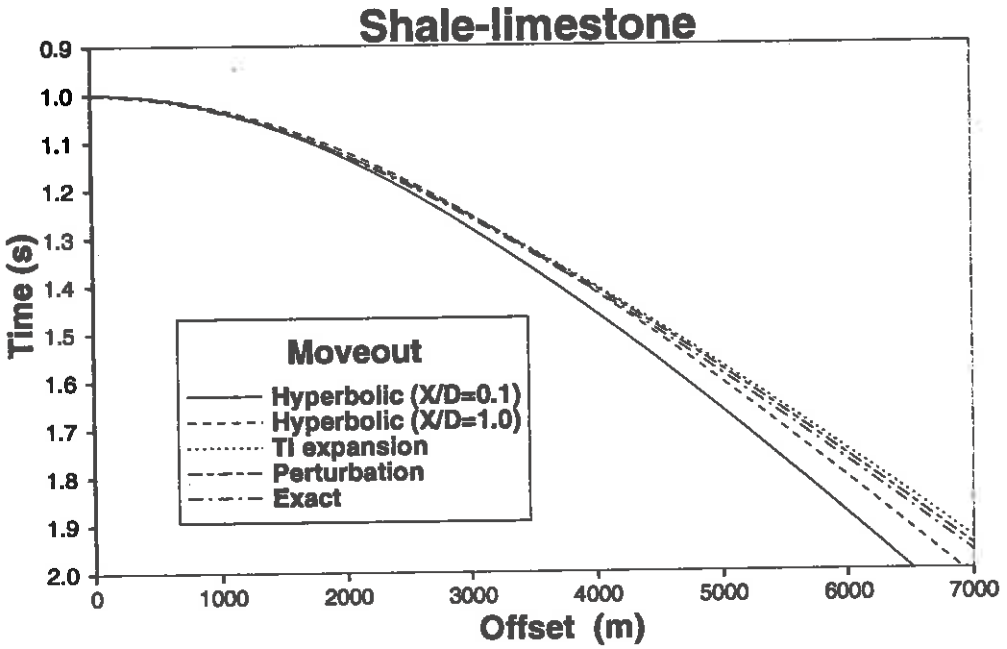

FIG. 7. Moveout curves for the same vertical rms velocity $v_{rms} = 3766$ m/s, and reflector depth of 1883 m.

moveout and the best-fit hyperbolic moveouts for offset-depth ratios $(\frac{X}{D})$ of 0.1 and 1.0. The medium is the shale-limestone FTI medium with vertical velocity $v(x_3) = 3306 + 0.5\,x_3$ m/s. Note that the moveouts of the time perturbation and TI expansion compare favorably with the exact moveout out to large offset X (for Figure 7, up to 7000 m).

DEGREE OF ANISOTROPY

Commonly, the degree of anisotropy of a specific medium is described by the ratio of the horizontal to vertical velocity, concentrating on two elastic coefficients a_{1111} and a_{3333}, ignoring the rest. Thomsen (1986) showed that traveltimes for P-waves are largely dependent on three parameters, —the vertical P-wave velocity $(\sqrt{a_{3333}})$, δ and ε. These three parameters are sufficient to evaluate the anisotropy of a medium and give a good understanding of the variation of velocity with direction. δ describes the velocities near the vertical axis, whereas ε describes the relation between a_{1111} and a_{3333}. The condition $\delta = \varepsilon = 0$ implies that the medium is isotropic, and $\delta = \epsilon$ in general for elliptically anisotropic media. However, these parameters do not indicate the overall sensitivity of the traveltime to a particular anisotropy. For example both

parameters δ and ε may have large values and yet represent a weak anisotropy (see Table 1).

Alternatively, time-perturbation equation (15) gives a direct expression for the sensitivity of the traveltime to the various elastic coefficients. Consider an isotropic background medium

$$A^0_{1111} = A^0_{3333} = A^0_{1133} + 2A^0_{1313}$$

where $A^0_{3333} = A_{3333}$, and

$$A^0_{1113} = A^0_{3313} = 0.$$

To keep the perturbations small, A^0_{1133} and A^0_{1313} are chosen such that

$$\frac{A^0_{1133}}{A^0_{1313}} \simeq \frac{A_{1133}}{A_{1313}}.$$

From equation (15), ignoring angle dependency (i.e., the integrals in equation [15]), I define the *percentage anisotropy* D as

$$D \equiv (\frac{1}{2} \mid \delta A_{1111} \mid + \mid \delta A_{1133} \mid + \mid \delta A_{1313} \mid + 2 \mid \delta A_{1113} \mid + 2 \mid \delta A_{3313} \mid) \times 100.$$

Although it ignores angle dependencies, this measure of anisotropy seems to serve acceptably as a single-parameter measure of the extent to which anisotropy influences traveltime. Therefore, it can be a useful tool in evaluating the performance of anisotropic GBM.

Table 1 lists the percentage anisotropy D and the three measures of anisotropy, described above, for the four media used by Levin (1990), as well as the Taylor sandstone and Mesaverde shale studied by Thomsen (1986).

Medium	V_p(m/s)	V_s(m/s)	δ	ε	V_A/V_C	D(%)
Shale-limestone	3306	1819	0.0	0.134	1.126	14
Cotton Valley shale	4721	2890	0.205	0.135	1.127	25
Berea sandstone	4206	2664	0.02	0.002	1.001	1.4
Pierre shale	2202	969	0.06	0.015	1.015	5.4
Taylor sandstone	3368	1829	-0.035	0.110	1.105	29
Mesaverde shale	3749	2621	0.078	0.128	1.121	17

Table 5. Different measures of anisotropy: Thomsen's parameters (δ and ε), the horizontal-to-vertical velocity ratio (V_A/V_C), and the percentage anisotropy D. V_A and V_C are the velocities of the P-wave in the horizontal and vertical direction, respectively. V_p and V_s are the vertical velocities for the P-wave and S-wave. ($V_C = V_p$.)

The percentage anisotropy, D, seems to be a reliable indicator of how well anisotropic GBM will perform in various anisotropic media. For example, as seen in Figure 5b and 6b, anisotropic GBM for shale-limestone TI media (D=14%) resulted in more

accurate reflector imaging than did that for Cotton Valley shale (D=25%). Anisotropic GBM produces accurate reflector positions for all dips in media with D less than 20%. It produces relatively good positioning for anisotropy with D less than 30%. Even when using the modified GBM for percentage anisotropy D higher than 30% (not shown here), the migration errors in general are considerably less than when using the standard GBM.

The errors that result from using time-perturbation equations are directly dependent on the amount of perturbation from the background to the desired medium. For $\delta a_{ijkl} = 0$ (isotropic medium), for example, the error should be zero.

CONCLUSION

Because of the sensitivity of migration to velocity, anisotropy could have a large influence on the accuracy of migrated images. Use of the modified GBM with correct velocity information can substantially reduce errors that arise when anisotropy is ignored and thus provide improved images. Modified GBM, like standard GBM, can be extended to 3-D by simply using the 3-D version of the time-perturbation equation.

The anisotropic GBM, although designed for weak anisotropy, can handle a wide range of anisotropy. The percentage of anisotropy, D, seems to be a reliable indicator of how well the anisotropic GBM will perform in different anisotropic media. It also could be used generally to describe the anisotropy level in a particular medium.

ACKNOWLEDGMENTS

I thank Professor Ken Larner for his critical input and review of this paper. Thanks are also due to KACST, Saudi Arabia, for its financial support.

REFERENCES

Alkhalifah, T., 1993, Synthetic seismograms for transversely isotropic constant velocity gradient media: CWP Annual Report.

Červený, V., 1972, Seismic rays and ray intensities in inhomogeneous anisotropic media: Geophys. J. R. Astr. Soc., **29**, 1–13.

Červený, V., 1981, Computation of geometrical spreading by dynamic ray tracing: Stanford Exploration Project, **28**, 49–59.

Červený, V., and Firbas, P., 1982, Numerical modeling and inversion of traveltimes of seismic body waves in inhomogeneous anisotropic media: Geophys. J. R. Astr. Soc., **76**, 41–51.

Červený, V., and Pšenčík, I., 1984, Gaussian beams in elastic 2-D laterally varying layered structures: Geophys. J. R. Astr. Soc., **78**, 65–91.

Červený, V., 1989, Ray tracing in factorized anisotropic inhomogeneous media: Geophys. J. Int., **94**, 575–580.

Červený, V., and Simoes-Filho, I. A., 1991, The traveltime perturbations for seismic body waves in factorized anisotropic inhomogeneous media: Geophys. J. Int., **107**, 219–229.

Hale, D., 1992, Migration by the Kirchhoff, slant stack, and Gaussian beam methods: CWP,1992 Report 121, Colorado School of Mines.

Hanyga, A., 1982, The kinematic inverse problem for weakly laterally inhomogeneous anisotropic media: Tectonophysics, **90**, 253–262.

Hill, N. R., 1990, Gaussian beam migration: Geophysics, **55**, 1416–1428.

Larner, K., and Cohen, J., 1993, Migration error in factorized transversely isotropic media with linear velocity variation with depth: Geophysics, in press.

Levin, F., 1990, Reflection from a dipping plane—Transversely isotropic solid: Geophysics, **55**, 851–855.

Thomsen, L., 1986, Weak elastic anisotropy: Geophysics, **51**, 1954–1966.

Tsvankin, I., and Thomsen, L., 1992, Nonhyperbolic reflection moveout and the inverse problem for transversely isotropic media: Presented at the 62nd Ann. Internat. Mtg. Soc. Expl. Geophys., Expanded Abstracts, 1348–1351.

Uren, N., F., Gardner, G., H., F., and McDonald, J., A., 1990, The migrator's equation for anisotropic media: Geophysics, **55**, 1429–1434.

Verwest, B. J., 1989, Seismic migration in elliptically anisotropic media: Geophysical Prospecting, **37**, 149–166.

White, J. E., 1983, Underground sound: Application of sound waves: Elsevier, 253 p.

Parabolic and linear 2-D $\tau - p$ transforms using the generalized radon transform

John Anderson

Parabolic and linear 2-D τ-p transforms using the generalized radon transform

John E. Anderson

ABSTRACT

The parabolic and linear τ-p transforms can be cast as a least-squares problem in the frequency-space domain and solved using a complex form of Levinson recursion.

This paper briefly documents the algorithms coded in routines **suradon** and **suiradon.**

INTRODUCTION

There is a rich lore of papers invoking slant stack and velocity stack methods (Thorson, 1984). The mathematical foundation for the discrete Radon transform appears in Beylkin (1987). Dan Hampson (1986) won the Canadian SEG Best Paper award based on his work using the parabolic Radon transform for multiple elimination. Hampson's method removes multiples from the near-offset traces on a common midpoint gather more effectively and with fewer edge-effect artifacts than does the traditional F-K filtering approach. Traditional F-K filtering works well on intermediate-offset and long-offset traces where Hampson's method may encounter aliasing problems. Kostov (1989) presented his work as part of the Stanford Exploration Project demonstrating that the Radon transform inversions could be computed using a complex form of Levinson recursion. Several companies had discovered this independently (Anderson, 1988; Bednar, 1988) but delayed publishing their results. In 1990, many papers were presented at the SEG meeting covering variations on this topic as corporations released their internal work in anticipation of Kostov's paper. Those authors include Darche (1990), Foster and Mosher (1990), Gulunay(1990), Johnston (1990), Kostov (1990), and Sullivan, Schneider, and Shurtleff (1990).

Traditional 2-D τ-p methods discretize equations derived using continuous function theory (Chapman, 1981). Finite aperture, finite sampling, and aliasing distort the numerical solution obtained. The discrete Radon transform approach works effectively for transforms based on temporally shift-invariant operators. Operators that fit the discrete Radon transform theory well include those for the parabolic and linear τ-p transforms since the shapes of their characteristic curves do not change with time.

NMO operators do not fit the theory well since the shapes of NMO curves do vary with time. In the first step for a discrete Radon transform, data are transformed to the frequency domain. Radon transforms are defined in terms of forward and inverse matrix operators to be applied to the data for each frequency component. Least-squares inverses are used when an exact inverse does not exist. The least-squares inverse is often different from the discretized version of the continuous inverse function. The least-squares approach takes note of the aperture and sampling of the data and does a least-squares correction to minimize their influence. Aliasing remains a problem that shows up in the form of instabilities in the least-squares inverse.

The approach taken here is to first define a transform that takes data from the "slowness" domain for linear τ-p back to the x domain. The transform of the original data to the slowness domain will be accomplished using the least-squares inverse to that transform. This allows one to model the data as a sum of slowness components. One can use this high-resolution slowness model for any purpose requiring a linear 2-D τ-p transform. In particular, based on this model, one can interpolate the original data or subtract slowness components identified as noise. The least-squares algorithm ensures that amplitudes estimated for the model are properly balanced relative to the original data. The algorithm for the parabolic transform will be defined and used in an analogous manner except that a new parameter defining parabola shape should be substituted for slowness. Typically, multiple removal is accomplished by subtracting from normal-move-out corrected common-midpoint gathers any model parabolas identified by a seismic processor as multiples.

In this paper, I derive the least-squares equations for the discrete Radon transform and show that under certain fairly general assumptions they form a Hermitian Toeplitz system solvable by a complex form of Levinson recursion. Levinson recursion requires a computational effort proportional to n^2 and thus is far more computationally efficient than is standard matrix inversion which requires an effort proportional to n^3. The derivation will apply to either the parabolic transform, as described by Hampson, or to 2-D linear τ-p methods. This derivation adds no new knowledge on the topic beyond that in the literature. It does provide a concise overview and an introduction to the algorithm in the routine **suradon**.

DEFINING THE TRANSFORM IN TERMS OF THE LEAST-SQUARES EQUATIONS

Consider a transform of the form

$$f(x,\omega) \equiv \sum_{k=0}^{n_p-1} F(p_k,\omega) e^{i\omega p_k g(x)}.$$

This can be rewritten in the matrix form $BF = f$, where the transformation matrix B is defined as $B_{kl} = e^{i\omega p_k g(x_l)}$. The vector $f(x,\omega)$ is provided from the input data. The goal is to find a least-squares representation of $F(p,\omega)$.

The general least-squares solution can be written in the form of the normal equations as $(B^\dagger B)^{-1}(B^\dagger B)F = (B^\dagger B)^{-1}B^\dagger f$ which reduces to $F = (B^\dagger B)^{-1}B^\dagger f$. Here the $\dagger$ symbol is used to denote the adjoint or complex conjugate transpose.

Now, restrict the generalized slowness parameter p to be of the form

$$p = p_{\min} + k \cdot \delta p$$

Under that restriction, the matrix $B^\dagger B$ is Hermitian Toeplitz. To see this, first note that for any matrix B, $B^\dagger B$ is Hermitian. That is, $(B^\dagger B)^\dagger = B^\dagger B$. Now, study the matrix $C = B^\dagger B$ for our choice of B. The components of C are

$$C_{mk} = \sum_{l=0}^{nx-1} B^\dagger_{lm} B_{lk}$$

$$C_{mk} = \sum_{l=0}^{nx-1} e^{-i\omega p_m g(x_l)} e^{i\omega p_k g(x_l)} = \sum_{l=0}^{nx-1} e^{i\omega(p_k - p_m)g(x_l)}$$

Note that the quantity $p_k - p_m = (k-m)\cdot\delta p$. Therefore,

$$C_{mk} = \sum_{l=0}^{nx-1} e^{i\omega(k-m)\delta p g(x_l)}$$

Note also that $C_{mk} = R_{k-m}$, so C is Toeplitz in form, with the same elements going down each diagonal. This fact allows us to use Levinson recursion to solve the systems $CF = B^\dagger f$ for each frequency component. This derivation did not require regular spacing in x or even a particular form for $g(x)$. We set $g(x)$ equal to x for 2-D linear τ-p transforms or equal to x^2 for parabolic transforms. Foster and Mosher (1992) set $g(x)$ equal to $\sqrt{x^2 + z_{\text{ref}}^2} - z_{\text{ref}}$ in attempt to more closely fit multiple events to hyperbolas rather than to parabolas.

STABILITY

A good overview of the stability issues is given by Gulunay (1990). For some frequency components such as 0 Hz, or at frequencies where aliasing artifacts occur, the matrix inversion cannot successfully determine F, as the problem is clearly underdetermined. At 0 Hz, all values of the Toeplitz matrix have the same amplitude so the matrix is clearly not diagonally dominant or invertible. A similar matrix form can occur at higher frequencies when there is a spatial aliasing problem. For these frequencies, a large white-noise parameter is required to stabilize the result. The limiting case, where an infinitely large white-noise parameter is used, completely diagonalizes the matrix C and provides a solution identical to that obtained with a classical τ-p inversion based only on the conjugate operator $B^\dagger$. More accurate inverses are computed using small values of white noise. Ideally, the white-noise parameter would vary frequency-by-frequency and be set at the smallest level required

to ensure stability. **Suradon** applies a single white-noise factor to all frequencies. As the white-noise level is increased, the advantage of the matrix inversion is lost and the solution moves toward that of traditional conjugate operator methods. Conversely, as the white-noise level is decreased, a point is reached beyond which results become unstable.

Gulunay also points out that in the limit as the aperture becomes large and the trace spacing becomes small, the solution approaches that obtained for continuous functions and once again the matrix C becomes diagonal. The goal of the matrix inversion is to minimize the errors due to finite aperture and finite sampling.

SUMMARY OF THE ALGORITHM IN SURADON

Loop over gathers:

Loop over x within each gather:
- get an input trace,
- extract x information for computing $g(x)$ from trace header,
- do forward temporal FFT (sign in transform is +1),
- store result in memory.

Loop over ω from $\omega_{\min}$ to $\omega_{\max}$:
- gather all x components for a given ω,
- solve system $BF = f$ for F using a complex form of Levinson recursion.

Loop over p:
- gather all ω for a given p,
- do inverse temporal FFT (sign in transform is -1),
- put p information in trace header,
- output trace in τ-p domain.

Suiradon has a similar 3 loop structure with the following changes. The loop bringing in the τ-p data and doing the forward temporal Fourier transform is over p instead of x. The information for p is extracted from the trace headers. The information for $g(x)$ must be supplied by the user. In the second loop, the system $BF = f$ is solved for f by straightforward matrix multiplication. The final loop doing the inverse temporal FFT would be over x instead of p. The output data is in the (time,space) domain.

ADDITIONAL CONSIDERATIONS

The least-squares formalism derived here assumes that $n_p \leq n_x$. Ideally, when $n_p \geq n_x$, the least-squares inverse should be computed as $F = B^\dagger (BB^\dagger)^{-1} f$. For

this formulation, the option to use Levinson recursion is lost. However, one can use standard matrix techniques to do the inversion. Once the decision is made to go to the cost of using standard matrix inversion methods, it is possible to expand the theory, for either $n_p \leq n_x$ or $n_p \geq n_x$, to include operators with spatial weights. For example, spatial aperture weights could be included in a more complicated definition of the transform. Spatially variant anti-alias filters could be used. The theory also expands to cover other transforms such as Fourier-Bessel transforms. Anderson (1988) studied this broader class of transforms and compared inversions computed by Gauss-Jordan elimination, singular value decomposition, and, for applicable Toeplitz systems, Levinson recursion with Simpson's sideways recursion. Singular value decomposition provided the most accurate and consistently stable result, but at the greatest expense. Because, the inverse matrices are independent of the data, they can be computed once, stored, and reused, whenever a regular geometry can be assumed. However, the disk space required to store an inverse matrix for each frequency can be large, and the corresponding input/output effort is significant. The regular-geometry assumption can be very limiting because even when the acquisition geometry is regular, the editing of noisy traces and variations in the mute zone can make the geometry appear irregular to this algorithm. It far preferable to use irregular geometry than to fit artificially dead data when computing the model data in the transform domain.

In practice, one can use the Levinson recursion approach with $n_p \geq n_x$ and prewhiten the inversion step to ensure stability. It is generally better to ensure that the basis functions of the model in transform space span all of the events in the data, with minimal aliasing, than to work with too small a value for n_p.

CONCLUSION

For regular increments in generalized slowness p (i.e., $p = p_{\min} + k \cdot \delta p$), transforms of the form $f(x,\omega) \equiv \sum_{k=0}^{n_p-1} F(p_k,\omega) e^{i\omega p_k g(x)}$ can be solved using a complex form of Levinson recursion. This general form allows the function $g(x)$ to be x for 2-D linear τ-p transforms or x^2 for parabolic transforms. Without giving up the Hermitian Toeplitz form required for rapid solution, $g(x)$ could be defined as a more general function of spatial position if a geophysical application demanded it.

ACKNOWLEDGMENTS

To a large extent, this paper represents more an exercise in learning the SU system, LaTeX , and how to become compatible with CWP than anything related to new or original research. Craig Artley and Jack Cohen provided indispensable help. Ken Larner and Andreas Rueger proofread the paper and provided useful comments. The author was employed by British Petroleum during the 1987-88 time period when he first derived the algorithms presented here. R.G. Keys, S.T. Hildebrand, and D.E. Johnston provided useful discussions. As the Mobil Visiting Scientist at the Colorado School of Mines, the author is currently working with the Center for Wave Phenom-

ena, the Reservoir Characterization Project, the Center for Geoscience Computing, and Mobil.

REFERENCES

Anderson, J. E., 1988, The general discrete Radon transform– recent advances which enhance its utility for geophysical applications: BP internal research report.

Bednar, J.B., 1988, personal communication...

Beylkin, G., 1987, The discrete Radon transform: IEEE Transactions of Acoustics, Speech, and Signal Processing, **35**, 162–172.

Chapman, C.H., 1981, Generalized Radon transforms and slant stacks: Geophysical Journal of the Royal Astronomical Society, **66**, 445–453.

Claerbout, J.F., 1985, Fundamentals of geophysical data processing: Blackwell Scientific Publications.

Darche, G., 1990, Spatial interpolation using a fast parabolic transform: SEG Expanded Abstracts 1990, 1647–1650.

Foster, D.J. and Mosher, C.C., 1990, Multiple suppression using curvilinear Radon transforms: SEG Expanded Abstracts 1990, 1759.

Foster, D.J. and Mosher, C.C., 1992, Suppression of multiple reflections using the Radon transform: Geophysics, **57**, NO. 3, (March 1992), 386–395.

Gulunay, N., 1990, F-X domain least-squares Tau-P and Tau-Q: SEG Expanded Abstracts 1990, 1607–1610.

Hampson, D., 1986, Inverse velocity stacking for multiple elimination: J. Can. Soc. Expl. Geophys., **22** , 44–55.

Hampson, D., 1987, The discrete Radon transform: a new tool for image enhancement and noise suppression: SEG Expanded Abstracts 1987, 141–143.

Johnston, D.E., 1990, Which multiple removal method should I use? SEG Expanded Abstracts 1990, 1750–1752.

Kostov, C., 1989, Finite-aperture slant-stack transforms: SEP 61, 261.

Kostov, C., 1990, Toeplitz structure in slant-stack inversion: SEG Expanded Abstracts 1990, 1618–1621.

Sullivan, M., Schneider, W.A., and Shurtleff, R.N., 1990, Issues and applications of the Radon transform for multiple elimination: SEG Expanded Abstracts 1990, 1755–1758.

Thorson, J.R., 1984, Velocity stack and slant stack inversion methods: PhD Thesis, Stanford University, May, 1984.

APPENDIX A: LEVINSON RECURSION WITH HERMITIAN TOEPLITZ SYSTEMS

Solve the system $RA = B$ where R is a Hermitian Toeplitz matrix, B is a known complex vector, and A is the complex solution vector to be determined.

As a part of the solution effort, we will find the solution to $RF = S$, where F is a complex spiking filter and S is a vector with a unit spike in location 0 and zeros everywhere else.

Levinson recursion for Toeplitz systems is discussed by Claerbout (1985). The critical differences worth noting in this derivation are which terms become complex conjugates for a Hermitian Toeplitz system.

Iteration 0:

Initialize v: $v_0 = 1$
Solve for the spiking filter: $f_0 = v_0/r_0$
Solve for the shaping filter: $a_0 = b_0/r_0$

Higher Iterations:

Each successive iteration is built up using the solution from the previous iteration. For example, here we will build the 3 x 3 spiking filter for iteration 2 assuming that the 2 x 2 results from iteration 1 are available as listed below.

$$\begin{bmatrix} r_0 & r_1 \\ r_1^* & r_0 \end{bmatrix} \begin{bmatrix} f_0 \\ f_1 \end{bmatrix} = \begin{bmatrix} v_1 \\ 0 \end{bmatrix}$$

$$\begin{bmatrix} r_0 & r_1 \\ r_1^* & r_0 \end{bmatrix} \begin{bmatrix} a_0 \\ a_1 \end{bmatrix} = \begin{bmatrix} b_0 \\ b_1 \end{bmatrix}$$

Note that subscript on v corresponds to the iteration number. Solve for c such that

$$\begin{bmatrix} r_0 & r_1 & r_2 \\ r_1^* & r_0 & r_1 \\ r_2^* & r_1^* & r_0 \end{bmatrix} \left\{ \begin{bmatrix} f_0 \\ f_1 \\ 0 \end{bmatrix} - c \begin{bmatrix} 0 \\ f_1^* \\ f_0^* \end{bmatrix} \right\} = \begin{bmatrix} v_2 \\ 0 \\ 0 \end{bmatrix}$$

Because we are working with a basis made up of spiking filters, we obtain a simple form after performing the matrix multiplication by R. The only terms that need to be computed are those for the top row and the bottom row.

$$\left\{ \begin{bmatrix} v_1 \\ 0 \\ e \end{bmatrix} - c \begin{bmatrix} e^* \\ 0 \\ v_1^* \end{bmatrix} \right\} = \begin{bmatrix} v_2 \\ 0 \\ 0 \end{bmatrix}$$

where

$$e = \sum_{k=0}^{N_{\text{iter}}-1} r^*_{N_{\text{iter}}-k} f_k$$

For this computation, the output value of v_2 is not important as long as it does not equal 0. If v_2 equals 0, then our system has become unstable and the recursion should stop. We only need to concentrate on the bottom row to estimate a value for c. Based on the computed value of c, one can compute new values for the spiking filter f and v_2.

$$e - cv^*_{N_{\text{iter}}-1} = 0$$

$$c = \frac{e}{v^*_{N_{\text{iter}}-1}}$$

$$(f_k)_{N_{\text{iter}}} = (f_k - cf^*_{N_{\text{iter}}-k})_{N_{\text{iter}}-1}$$

$$v_{N_{\text{iter}}} = v_{N_{\text{iter}}-1} - ce^*$$

At the end of this iteration we have the 3 x 3 spiking filter solution for

$$\begin{bmatrix} r_0 & r_1 & r_2 \\ r_1^* & r_0 & r_1 \\ r_2^* & r_1^* & r_0 \end{bmatrix} \begin{bmatrix} f_0 \\ f_1 \\ f_2 \end{bmatrix} = \begin{bmatrix} v_2 \\ 0 \\ 0 \end{bmatrix}$$

Now, update the shaping filter A for this iteration by solving

$$\begin{bmatrix} r_0 & r_1 & r_2 \\ r_1^* & r_0 & r_1 \\ r_2^* & r_1^* & r_0 \end{bmatrix} \left\{ \begin{bmatrix} a_0 \\ a_1 \\ 0 \end{bmatrix} - c \begin{bmatrix} f_2^* \\ f_1^* \\ f_0^* \end{bmatrix} \right\} = \begin{bmatrix} b_0 \\ b_1 \\ b_2 \end{bmatrix}$$

Once again, we are taking advantage of the fact that F is a spiking filter so that we only need to pay attention to the bottom row of R for this computation.

$$\sum_{k=0}^{N_{\text{iter}}-1} r^*_{N_{\text{iter}}-k} a_k - cv^*_{N_{\text{iter}}} = b_{N_{\text{iter}}}$$

After computing c, we can update A and move on to the next iteration.

$$(a_k)_{N_{\text{iter}}} = (a_k)_{N_{\text{iter}}-1} - cf^*_{N_{\text{iter}}-k}$$

After the last iteration, the vector F should be normalized based on the current value of v. This ensures that $RF = S$, if F is a desired output from this computation.

APPENDIX B: A SIMPLE PARABOLIC τ-P TRANSFORM EXAMPLE

A very simple example of the parabolic τ-p transform demonstrates the utility of the least-squares approach. Figure B-1 displays a CMP gather that has a small-amplitude primary event properly flattened by NMO. A larger-amplitude multiple event still contaminates the data. An ideal parabolic transform would reveal that these data are the sum of only two parabolic events. Figure B-2 displays the parabolic transform obtained by using the conjugate operator. Note that the events are smeared together. Figure B-3 shows the discrete Radon transform result obtained using **suradon**. The least-squares approach does a better job of separating the two events in transform space.

A production-oriented processing code for parabolic filtering would operate somewhat differently than using **suradon**, followed by a parabolic τ-p mute, and **suiradon**. In practice, the desired result is a section with no multiples, created by an algorithm that is easy to use. A seismic processor would probably prefer to supply the maximum and minimum move-out error in ms at a reference offset rather than the parabolic shape factors used in **suradon**. The move-out timing error of a parabola at a reference offset can be readily picked from CMP gather displays. A parabolic filtering module would take care to not fit dead traces or muted regions during design of the model parabolas. Such care typically requires separate transforms for multiple time windows within the mute zone. **Suradon** operates on all of the data in only one time window, does not check for dead traces, and does not preserve all of the trace header information. A production-oriented module would operate in reject-filter mode, doing the forward transform, inverse transforming the estimated multiples, and subtracting the estimated multiples from the input data. Generally, it is preferable to apply a reject filter in order to preserve as much of the original data character as possible than to depend on the quality of a forward and inverse parabolic τ-p transform for every aspect of the data. The one-module, reject-filter approach also makes it easy to avoid stability problems by using only a limited range of frequencies for the reject filter without explicitly band-pass filtering the data. Because the data are input and output in the same domain, with the same number of traces per gather, it is easy to preserve all of the trace header information. **Suradon** and **suiradon** serve as general-purpose tutorial codes illustrating the method.

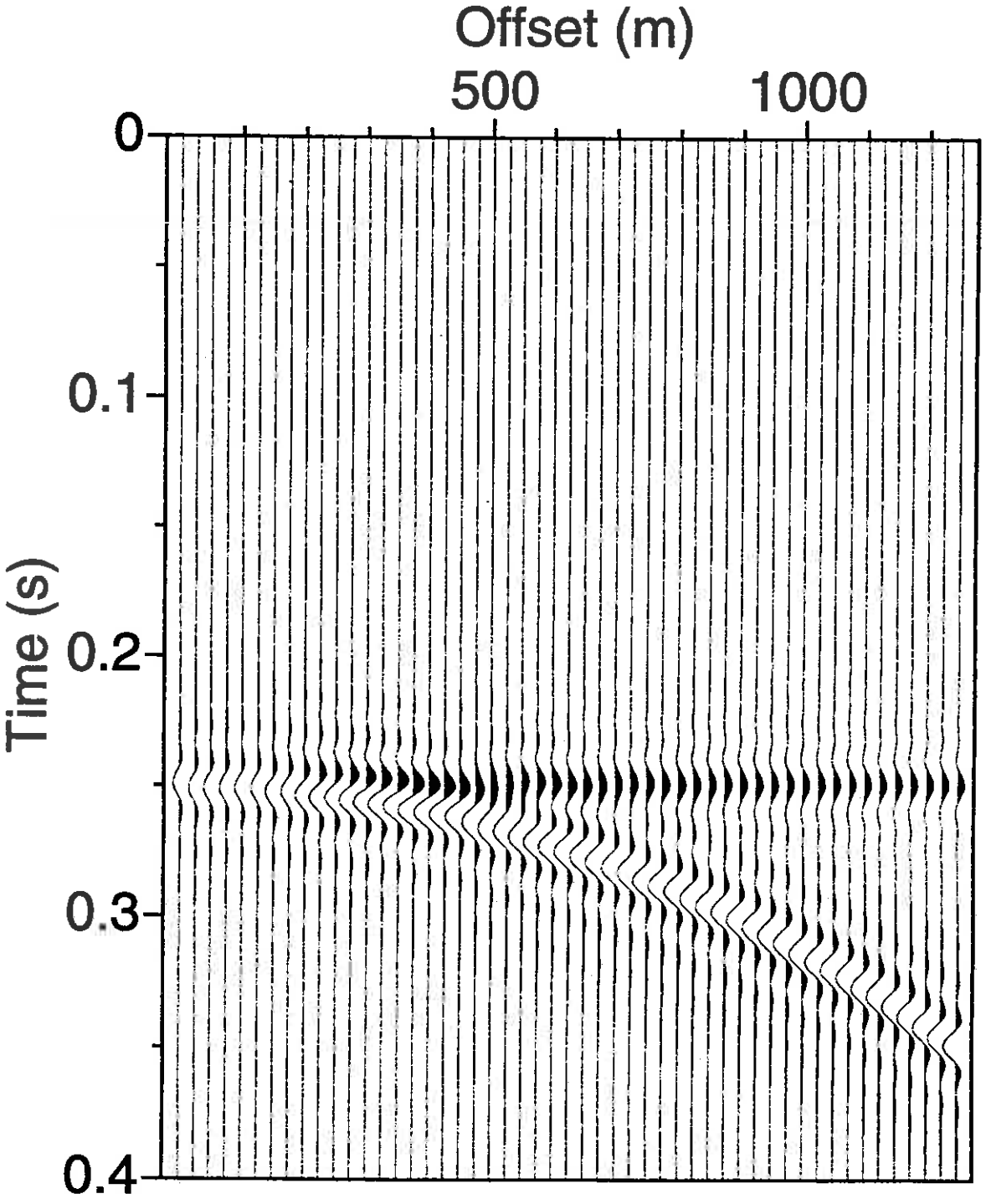

FIG. B-1. CMP gather with an aligned primary event (amplitude 1, parabola shape 0) and a multiple event (amplitude −2, parabola shape $64 \cdot 10^{-9}$ $(s/m)^2$) both at the same 0 offset intercept time of 0.25 s. A zero-phase band-pass filter 5/10 80/100 Hz has been applied to the data.

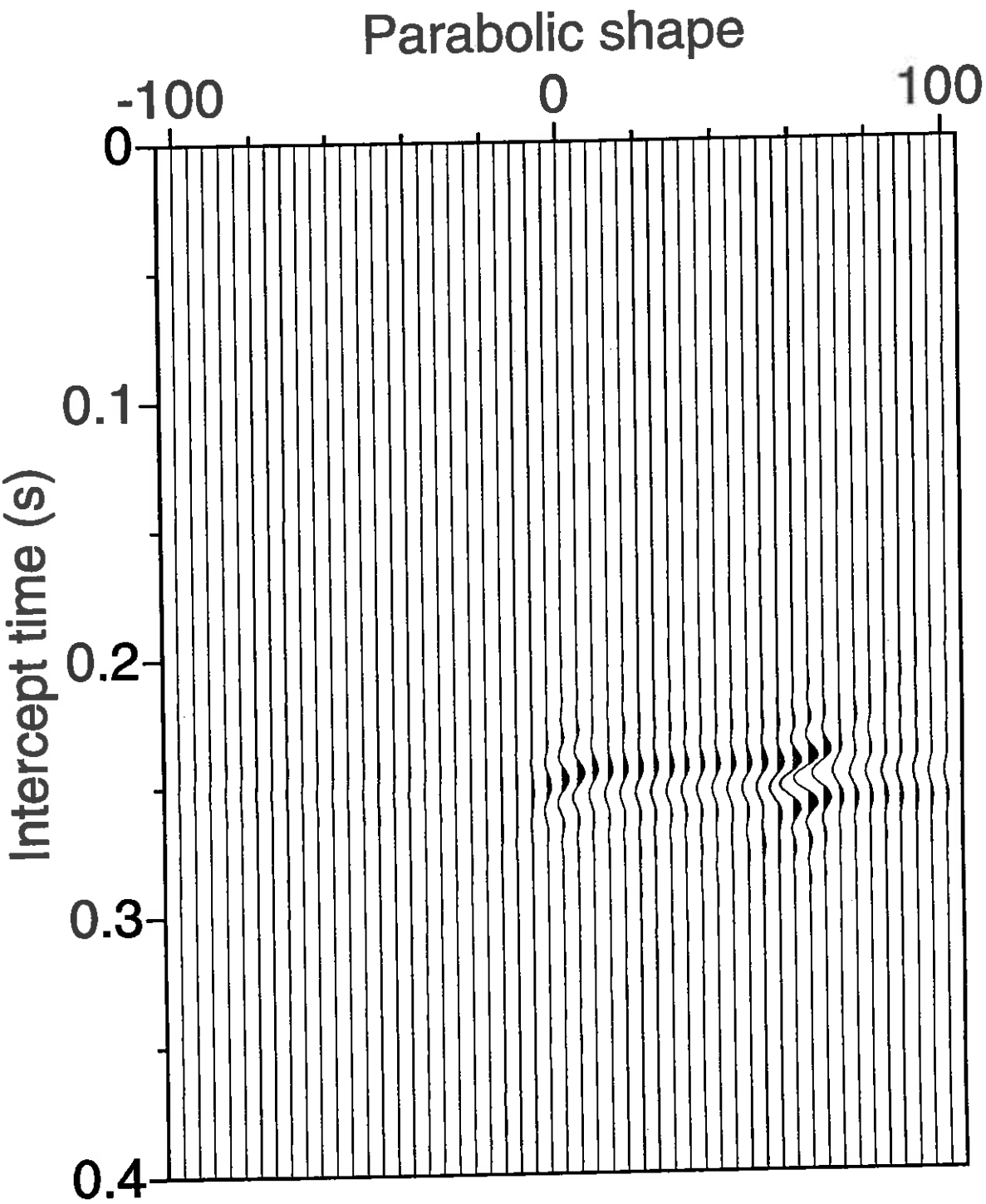

FIG. B-2. The conjugate method for computing the parabolic τ-p transform would compute $F = |\omega| B^\dagger f$. The scaling of the display covers up the fact that the overall gain of this result is incorrect. Compare the resolution of this result with that of the least-squares method. The horizontal axis labeled "parabolic shape" displays the parabolic p values, scaled by 10^9, in units of $(\mathrm{s/m})^2$.

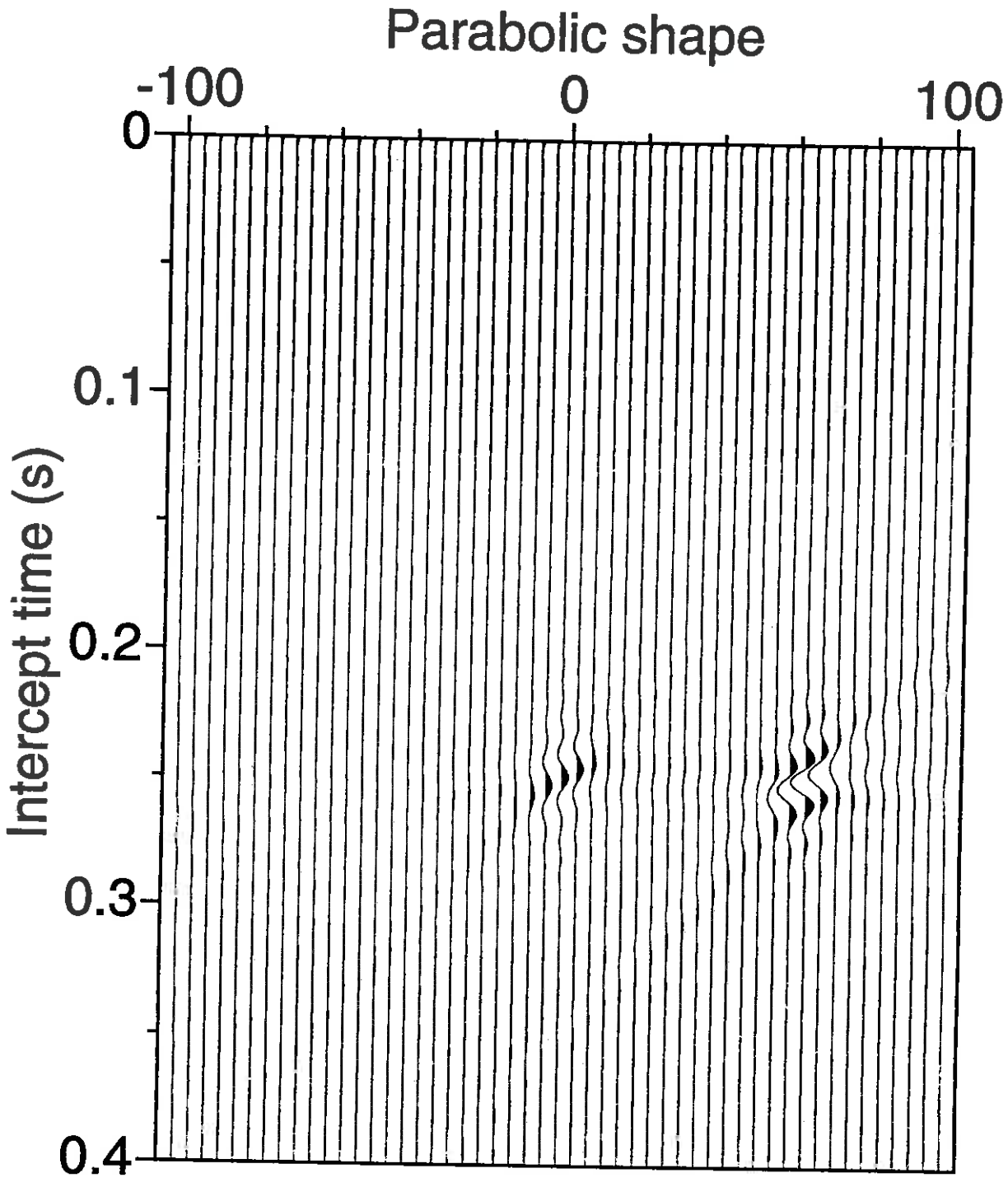

FIG. B-3. Using the least-squares approach for computing the transform provides better separation between the events in the parabolic τ-p domain. A perfect result would have a filtered amplitude of -2 at parabola shape $64 \cdot 10^{-9}$ $(\mathrm{s/m})^2$), a filtered amplitude of 1 at parabola shape 0 for intercept time 0.25 s, and zero values everywhere else. The horizontal axis labeled "parabolic shape", displays the parabolic p values, scaled by 10^9, in units of $(\mathrm{s/m})^2$.

Three-dimensional dip moveout for depth-variable velocity

Craig Artley, Patrick Blondel*,
Alexander M. Popovici*, and Matthias Schwab*

*Stanford Exploration Project
Stanford University
Standord, California 94305

Three-dimensional dip moveout for depth-variable velocity*

Craig Artley, Patrick Blondel†, Alexander M. Popovici†, and Matthias Schwab†

INTRODUCTION

Artley (1992) proposed a method for computing the 2-D dip-moveout (DMO) correction for media where the velocity is a function of depth (termed $v(z)$ *media*). The method first traces rays through the medium and then solves a system of equations that must be satisfied by the zero-offset ray and the two rays that make up the nonzero-offset path. Once these rays have been found, the time along the zero-offset ray and its emergence point are immediately known.

Here we extend the method to 3-D. In 2-D, rays were tabulated as three functions of the ray parameter p and the two-way time t along the ray. The functions computed by ray tracing were the horizontal distance ξ traveled by the ray, the two-way vertical time τ (stretched depth coordinate), and the propagation angle θ, measured with respect to the vertical. Since the velocity varies only with depth, exactly the same ray tables can be used for 3-D DMO. The ray parameter p is actually the magnitude of the vector formed by the x- and y-components of the slowness vector $\mathbf{p}$ at any point along the ray. Since the medium varies only with depth, $p = \sqrt{p_x^2 + p_y^2}$ is constant along the ray, just as in 2-D. Also, the azimuth angle that the horizontal component of $\mathbf{p}$ makes with the x-axis, $\phi = \tan^{-1}(p_y/p_x)$, is constant. At a given point along the ray, the z-component of $\mathbf{p}$ can be computed from the eikonal equation, $1/v^2 = p_x^2 + p_y^2 + p_z^2$, where v is the velocity of the medium at that point.

RAYPATH GEOMETRY

Figure 1 shows the source, geophone, and zero-offset rays in 3-D. As in 2-D, the rays must meet at the reflection point (x_r, y_r, z_r), but now the rays do not necessarily all lie in the same vertical plane. The total time t_{sg} along the nonzero-offset path is known, as are the source and receiver positions, and, thus, the source-receiver offset $2h$. Each ray is completely determined by its ray parameter, the azimuth angle the ray makes with the x-axis, and the time along the ray.

*Another version of this work appears in Stanford Exploration Project report **SEP-77**.

†Stanford Exploration Project, Stanford University, Stanford, California 94305

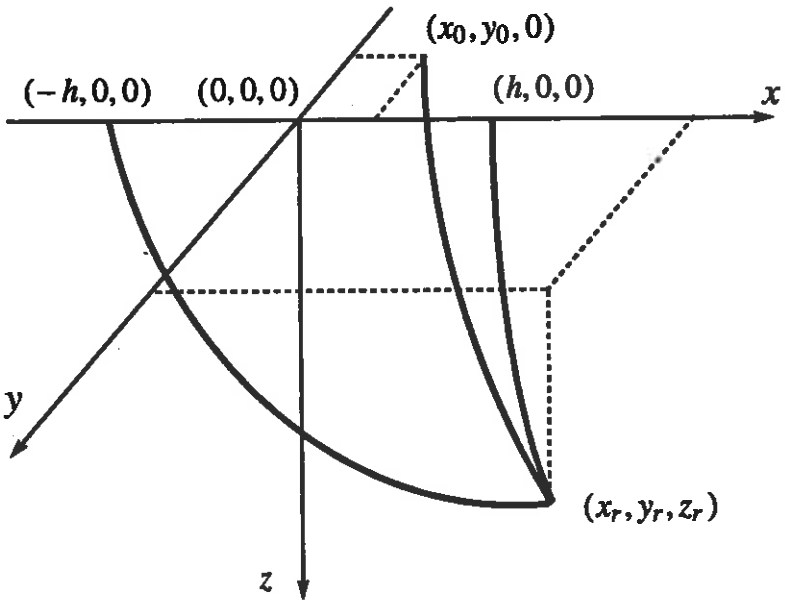

FIG. 1. Raypath geometry in 3-D. The source ray leaves the surface from $(-h, 0, 0)$, while the geophone ray leaves from $(h, 0, 0)$. The zero-offset ray leaves from zero-offset location $(x_0, y_0, 0)$. All three rays terminate at the reflection point (x_r, y_r, z_r).

The ray parameter p_0 of the zero-offset ray as well as the azimuth angle ϕ_0 (formed by the projection of the zero-offset ray onto the x-y plane and the x-axis) are taken to be known. The problem is then to find the ray parameter, p_s, azimuth angle, ϕ_s, and two-way time, t_s, for the source ray, as well as the corresponding quantities that determine the geophone ray (p_g, ϕ_g, and t_g). Additionally, the time t_0 along the zero-offset ray and the coordinates (x_0, y_0) must also be determined. Figure 2 is a map view of Figure 1, showing the definition of the azimuth angles. Note that, because the velocity of the medium varies only with depth, each ray is confined to a vertical plane.

SYSTEM OF EQUATIONS

The three rays (termed a *trio*) must satisfy several conditions. The first is that all three rays must terminate at the reflection point (x_r, y_r, z_r). Therefore, the tips of all three rays have the same x-coordinate,

$$x_r = \xi(p_s, t_s)\cos\phi_s - h \tag{1}$$
$$= \xi(p_g, t_g)\cos\phi_g + h \tag{2}$$
$$= \xi(p_0, t_0)\cos\phi_0 + x_0, \tag{3}$$

where, as seen in Figure 2, $\xi(p_s, t_s)$ is the projection onto the horizontal plane of the ray from the source to the reflection point, and so on for $\xi(p_g, t_g)$ and $\xi(p_0, t_0)$. Likewise, the rays have the same y-coordinate,

$$y_r = \xi(p_s, t_s)\sin\phi_s \tag{4}$$

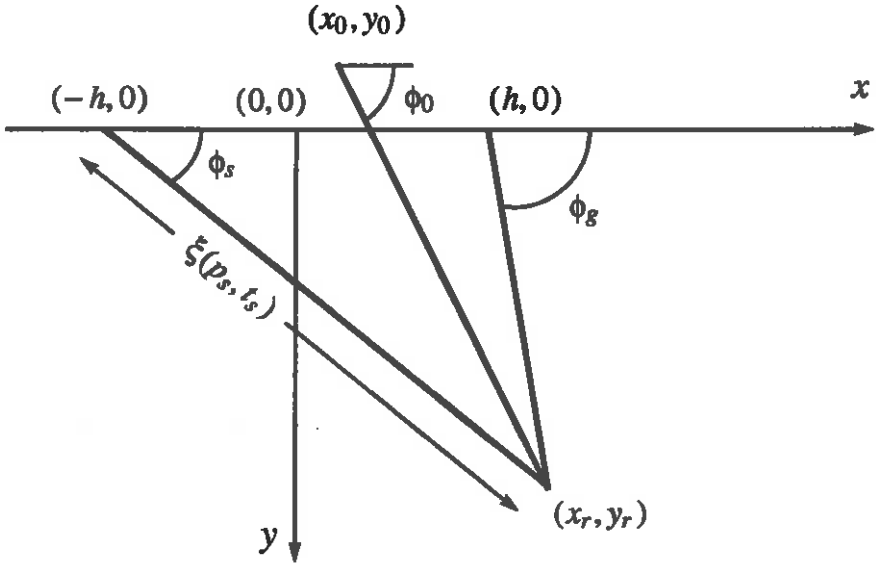

FIG. 2. Projection of the raypaths of Figure 1 onto the x-y plane.

$$= \xi(p_g, t_g) \sin \phi_g \tag{5}$$
$$= \xi(p_0, t_0) \sin \phi_0 + y_0. \tag{6}$$

Since they also have the same z-coordinate, the two-way vertical time for the three rays is the same:

$$\tau_r = \tau(p_s, t_s) \tag{7}$$
$$= \tau(p_g, t_g) \tag{8}$$
$$= \tau(p_0, t_0). \tag{9}$$

At the reflector, the zero-offset ray lies in the plane formed by the source and geophone rays. The zero-offset ray must also bisect the angle formed by these two rays, as shown in Figure 3. Since $\mathbf{p}_0$, $\mathbf{p}_s$, and $\mathbf{p}_g$ all have magnitude $1/v$, where v is the velocity at the reflection point, $\mathbf{p}_0$ is simply proportional to the vector sum of the slowness vectors of the source and geophone rays,

$$\mathbf{p}_0 = \lambda (\mathbf{p}_s + \mathbf{p}_g), \tag{10}$$

with

$$\lambda = \frac{\|\mathbf{p}_0\|}{\|\mathbf{p}_s + \mathbf{p}_g\|}. \tag{11}$$

Considering the z-component of equation (10) gives

$$p_{0z} = \lambda (p_{sz} + p_{gz}). \tag{12}$$

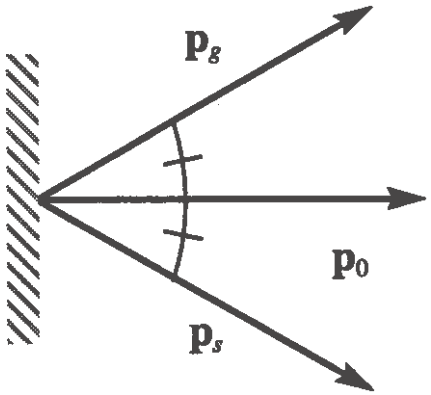

FIG. 3. Slowness vectors (tangents) at the reflection point. At the reflector, the zero-offset ray lies in the plane formed by the source and geophone rays.

Since $p_{0z} = \cos[\theta(p_0, t_0)]/v$, and similarly for p_{sz} and p_{gz}, this equation is equivalent to

$$\lambda = \frac{\cos[\theta(p_0, t_0)]}{\cos[\theta(p_s, t_s)] + \cos[\theta(p_g, t_g)]}, \tag{13}$$

where $\theta(p_0, t_0)$ is the propagation angle of the zero-offset ray, (and likewise for $\theta(p_s, t_s)$ and $\theta(p_g, t_g)$). (Recall that $\theta(p, t)$, like $\xi(p, t)$ and $\tau(p, t)$, is a tabulated function known from ray tracing.) We now use this expression for λ in the x-component of equation (10), giving

$$p_{0x} = \frac{\cos[\theta(p_0, t_0)]}{\cos[\theta(p_s, t_s)] + \cos[\theta(p_g, t_g)]} (p_{sx} + p_{gx}). \tag{14}$$

Similarly, the y-component of equation (10) yields

$$p_{0y} = \frac{\cos[\theta(p_0, t_0)]}{\cos[\theta(p_s, t_s)] + \cos[\theta(p_g, t_g)]} (p_{sy} + p_{gy}). \tag{15}$$

Finally, the nonzero-offset recording time t_{sg} is equal to one-half the sum of the *two-way* times along the source and geophone rays,

$$t_{sg} = \frac{1}{2}(t_s + t_g). \tag{16}$$

Eliminating the reflection point coordinates (x_r, y_r, and τ_r) from the preceding equations leaves a system of nine equations in nine unknowns,

$$0 = \xi(p_g, t_g)\cos\phi_g - \xi(p_0, t_0)\cos\phi_0 - x_0 + h \tag{17}$$

$$0 = \xi(p_g, t_g)\sin\phi_g - \xi(p_0, t_0)\sin\phi_0 - y_0 \tag{18}$$

$$0 = \xi(p_g, t_g)\cos\phi_g - \xi(p_s, t_s)\cos\phi_s + 2h \tag{19}$$

$$0 = \xi(p_g, t_g)\sin\phi_g - \xi(p_s, t_s)\sin\phi_s \tag{20}$$

$$0 = \tau(p_0, t_0) - \tau(p_s, t_s) \quad (21)$$
$$0 = \tau(p_0, t_0) - \tau(p_g, t_g) \quad (22)$$
$$0 = p_{0x}\{\cos[\theta(p_s, t_s)] + \cos[\theta(p_g, t_g)]\} - (p_{sx} + p_{gx})\cos[\theta(p_0, t_0)] \quad (23)$$
$$0 = p_{0y}\{\cos[\theta(p_s, t_s)] + \cos[\theta(p_g, t_g)]\} - (p_{sy} + p_{gy})\cos[\theta(p_0, t_0)] \quad (24)$$
$$0 = 2t_{sg} - (t_s + t_g)\,. \quad (25)$$

The known parameters of the system are t_{sg}, h, p_0, and ϕ_0, and the unknowns to be determined are p_s, p_g, ϕ_s, ϕ_g, t_s, t_g, t_0, x_0, and y_0.

Note that x_0 and y_0 appear (separately) in only the first two equations. Therefore, these equations can be removed from the system, and x_0 and y_0 can be computed after solving the remaining system. Furthermore, the last equation can be used to replace t_s by $2t_{sg} - t_g$ in the remaining equations. These simplifications reduce the system to six equations and six unknowns (where t_s is retained for notational simplicity):

$$0 = \xi(p_g, t_g)\cos\phi_g - \xi(p_s, t_s)\cos\phi_s + 2h \quad (26)$$
$$0 = \xi(p_g, t_g)\sin\phi_g - \xi(p_s, t_s)\sin\phi_s \quad (27)$$
$$0 = \tau(p_0, t_0) - \tau(p_s, t_s) \quad (28)$$
$$0 = \tau(p_0, t_0) - \tau(p_g, t_g) \quad (29)$$
$$0 = p_{0x}\{\cos[\theta(p_s, t_s)] + \cos[\theta(p_g, t_g)]\} - (p_{sx} + p_{gx})\cos[\theta(p_0, t_0)] \quad (30)$$
$$0 = p_{0y}\{\cos[\theta(p_s, t_s)] + \cos[\theta(p_g, t_g)]\} - (p_{sy} + p_{gy})\cos[\theta(p_0, t_0)]\,. \quad (31)$$

This system, like its 2-D counterpart, can be solved using Newton-Raphson iteration (e.g., Press et al., 1986). With the solution in hand, equations (17) and (18) are used to compute x_0 and y_0, the emergence point of the zero-offset ray. Then the 3-D DMO correction (x_0, y_0, t_0) corresponding to the specified value of p_0 and ϕ_0 is saved. The complete DMO operator is constructed by repeatedly solving the system for different values of p_0 and ϕ_0.

IMPLEMENTATION

We solve the system repeatedly while varying p_0 and ϕ_0, each time saving the kinematic DMO operator, $t_0(x_0, y_0)$. Since the method requires an initial guess to the solution at each step, we work radially outward by computing the operator for all p_0 while holding ϕ_0 constant, then moving to the next azimuth and repeating the process. At each new azimuth and $p_0 = 0$, we compute the initial guess by assuming constant velocity. After the solution is refined via Newton-Raphson iteration, we move to the next p_0 and repeat, using the solution at the previous p_0 as the trial solution. The algorithm is outlined below for fixed normal moveout (NMO) time t_n and source-receiver offset $2h$. $v_2(t)$ is the rms velocity function of the medium.

Computation of the DMO mapping:

Compute ray tables $\xi(p,t)$, $\tau(p,t)$, $\theta(p,t)$
Compute recording time via $t_{sg}^2 = t_n^2 + 4h^2/v_2^2(t_n)$
For all azimuths ϕ_0 *of zero-offset slope* {
    Compute trial solution to system for $p_0 = 0$,
        assuming $v = \text{const} = v_2(t_n)$
    For all magnitudes p_0 *of zero-offset slope* {
        Refine trial solution to system using
            Newton-Raphson iteration
        Save the DMO mapping $t_0(x_0, y_0)$
        Use final solution for this p_0 *as*
            trial solution for next p_0
    }
}

Rather than use p_s and ϕ_s as unknowns in the system, we choose instead to work directly with the components p_{sx} and p_{sy} and compute $p_s = \sqrt{p_{sx}^2 + p_{sy}^2}$, $\cos\phi_s = p_{sx}/p_s$, and $\sin\phi_s = p_{sy}/p_s$. We use analogous expressions for p_g and ϕ_g.

Figure 4 shows the DMO operator computed with this method for a medium with velocity $v(z) = 1.5 + 0.6\,z$ km/s, 1.5 km offset, and NMO time of 1.75 s. As shown by Perkins and French (1990), the crossline component "frowns", while the inline "smiles". The operator has been truncated to a maximum reflector dip of approximately 40 degrees for display purposes. The lower sheet of the complete operator described by Dietrich and Cohen (1992) would greatly complicate the figure.

CONCLUSION

We have extended Artley's (1992) method for computing the $v(z)$ DMO operator to work in 3-D. The 4×4 system in 2-D grows to 6×6 to describe the out-of-plane component of the operator. Simple tests with a constant velocity gradient show the scheme is feasible, and that the results are consistent with the analytical formulation of Dietrich and Cohen (1992).

ACKNOWLEDGMENTS

We began this work during Artley's visit to the Stanford Exploration Project during February, 1993. We are grateful to the sponsors of the Center for Wave Phenomena and the Stanford Exploration Project for making this collaboration possible.

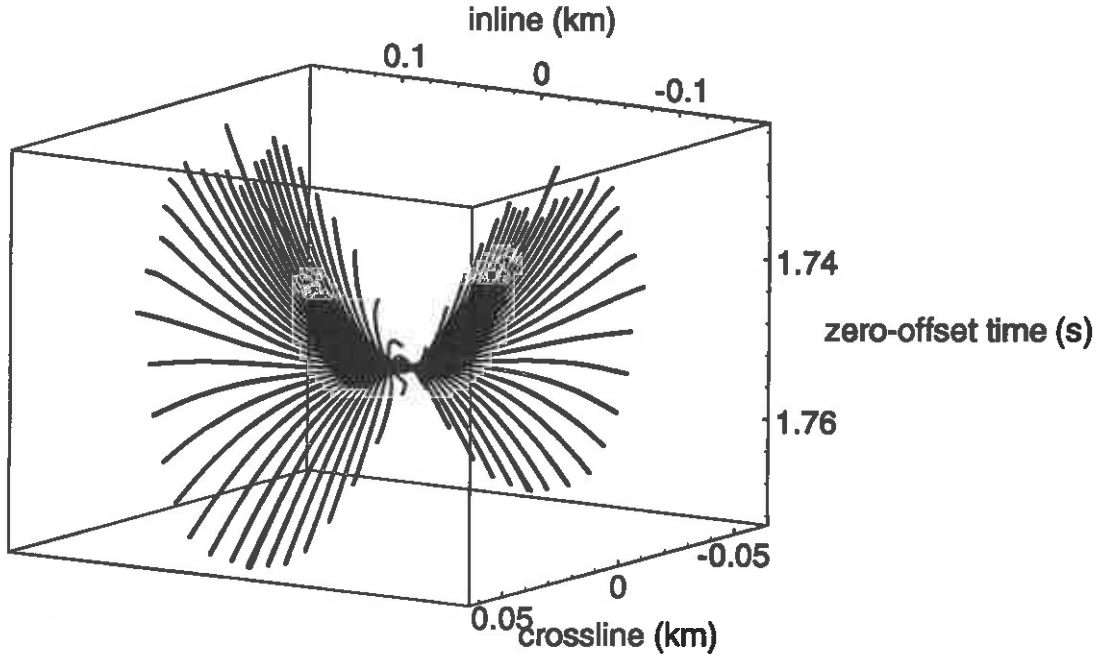

FIG. 4. DMO operator for 1.5 km offset and NMO time of 1.75 s for a medium with velocity $v(z) = 1.5 + 0.6\,z$ km/s. The lower sheet is not seen because the operator has been truncated for display purposes.

REFERENCES

Artley, C. T., 1992, Dip moveout processing for depth-variable velocity: M.S. thesis, Colorado School of Mines; also published as Center for Wave Phenomena report **CWP-115**.

Dietrich, M., and Cohen, J. K., 1992, 3-D migration to zero offset for a constant velocity gradient: an analytical formulation: *submitted for publication in* Geophysical Prospecting; also published as Center for Wave Phenomena report **CWP-113**.

Perkins, W. T., and French, W. S., 1990, 3-D migration to zero-offset for a constant velocity gradient: 60th Ann. Internat. Mtg., Soc. Expl. Geophys., Expanded Abstracts, 1354–1357.

Press, W. H., Flannery, B. P., Teukolsky, S. A., and Vetterling, W. T., 1986, Numerical recipes: Cambridge Univ. Press.

CWP-130

Expanded Abstract: Fundamentals of the discrete wavelet transform for seismic data processing

Jack K. Cohen and Tong Chen

Expanded Abstract: Fundamentals of the discrete wavelet transform for seismic data processing

Jack K. Cohen and Tong Chen

INTRODUCTION

The discrete wavelet transform has been an exciting topic of mathematical research for about 10 years now. Some of the early wavelet research had seismic applications explicitly in mind, but fields as diverse as quantum physics and voice coding have also provided insights leading to the development of the modern theory. Our purpose is to explain and illustrate what the wavelet transform can do to seismic data, thus providing the information necessary for researchers to assess its possible use in their areas of data processing.

This paper gives an application-oriented introduction to the one- and two-dimensional discrete wavelet transforms, including examples of wavelets, wavelet filters and their properties. We will make some suggestions about applications, but the main thrust of the paper is to provide the information necessary to assess the potential for use of wavelet methods in targeted areas of seismic processing. To set the stage for seismic applications, we give a detailed analysis of the effect of the wavelet transform on sloping reflections with a signal of given frequency band. This analysis reveals a semi-quantitative explanation of the well-known division of the two-dimensional wavelet transform into horizontal, vertical and diagonal emphasis panels. The result is simple and probably has been noted by other researchers, but we haven't found a prior reference for it. In any case, it provides an important insight for use of the two-dimensional wavelet transform in seismic processing.

Since the term "wavelet" is already used in seismology, there is potential for confusion with its differing use in the theory of the wavelet transform. In connection with the wavelet transform, this terminology is only loosely suggestive of seismic wavelets such as source signatures and propagating waveforms. The mathematical wavelets and the seismic wavelets *do* share some properties, notably the time-frequency localization discussed in the next paragraph. However, in the mathematical theory, the term *wavelet* is used in a technical sense. In particular, some of the mathematical wavelets don't look much like source signatures and the seismic wavelets commonly

used for modeling sources do not meet the technical criteria set down for the mathematical wavelets. Below, "wavelet" will always refer to the mathematical wavelets, not the seismic wavelets.

A seismic trace gives the time history of a geophone response. Its Fourier transform reveals the frequency content of this response. Often, what is really desired is the time *evolution* of the frequency response. For instance, a dominant feature of most seismic traces is the loss of high frequencies at later time. The wavelet transform of a trace provides a *simultaneous* display of its time-frequency content—therein lies a principal reason for its study. The short-time or windowed Fourier transform made popular by the work of Denis Gabor also localizes simultaneously in time and frequency, using a uniform time window for all frequencies. In contrast, the wavelet transform *adapts* the window according high frequencies the fine resolution they require and high frequencies the long windows needed to encompass them.

THE ONE-DIMENSIONAL DISCRETE WAVELET TRANSFORM

To get a feel for what happens to data under the discrete one-dimensional wavelet transform, consider the effect on a single data vector x of length $N = 2^n$ and sampling interval Δt. At the first stage, the wavelet transform splits this data into two sub-vectors a^1, d^1 each of length N/2 and sample interval $2\Delta t$. (Just how the sub-vectors are defined is immaterial for the moment.) The vector d^1 is retained as the first portion of the wavelet transform of x, while the splitting process is repeated on a^1 to produce a^2 and d^2. This process can be repeated until the n^{th} stage, when d^n and a^n each consist of a single point and the data vector x is replaced by the vectors d^1, d^2, ..., d^n, and a^n (see Figure 1). At each stage, the sum of lengths of the two

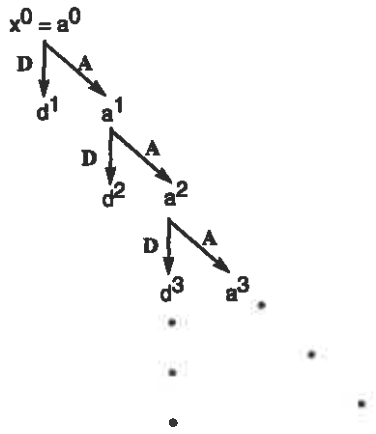

FIG. 1. 1D wavelet decomposition.

sub-vectors is the same as the length of the parent vector, thus the sum of the lengths of the d vectors plus the final single point a^n is the same as the length N of the original data. Since the x's play the role of the a's at the first stage, it is sometimes convenient to set $x = a^0$ as shown in Figure 1. In practice, the wavelet decomposition

is often carried out to fewer than n levels so that the final d and a contain more than a single datum.

As in Figure 1, denote the transformation from the parent a to the child a by **A** and the transformation from the parent a to the child d by **D**. The most important fact about the transformations **A** and **D** is that they are orthogonal. Thus, the decomposition of the data is a change of basis to an orthogonal basis—the *wavelet* basis. The **A** phase of the decomposition is essentially a "blurring" or *averaging* of the data at the previous stage. In frequency domain, this is equivalent to a low pass filter on the previous stage. The **D** phase of the decomposition is essentially the *difference* of the data at the previous stage and the averaged data at the current stage. In frequency domain, this is equivalent to a high pass filter on the previous stage. As we will see, the **A** and **D** operations are not "merely" averaging and differencing of adjacent data points, but these notions direct the intuition appropriately.

Since the **A** and **D** transformations are orthogonal, the inverse or reconstruction algorithm is well conditioned. It consists of applying transposed matrices to the current a and d vectors to climb the ladder in Figure 1 reconstructing the (previously discarded) parent a.

Wavelets and scaling functions

The function $\phi(t)$ underlying the **A** transformation is called the *scaling* function, and the function $\psi(t)$ underlying the **D** transformation is called the "mother" or "analyzing" wavelet. Scaling functions and analyzing wavelets occur in linked pairs. The mathematical theory constructs the wavelet $\psi(t)$ from a given scaling function $\phi(t)$. As already mentioned, the scaling functions $\phi(t)$ and analyzing wavelets $\psi(t)$ are localized in *both* time and frequency. While it is impossible for a given function $s(t)$ and its Fourier transform $\hat{s}(f)$ to simultaneously have finite (or "compact") support, it is not impossible for both of them to have negligible amplitude outside finite intervals in their respective domains (i.e., time t and frequency f). Scaling functions and analyzing wavelets used in practice have faster decay than $1/t$ in time and simultaneously have faster decay than $1/f$ in frequency.

The discrete wavelet transform provides a systematic mechanism for analysing data at different scales (octave by octave). Indeed, since the translation step 2^j is linked to the level (or octave), the high frequency events (j near 0) are treated with relatively small translation steps, so they get the fine resolution they require; while low frequency events ($j \gg 0$) get the larger time windows needed to encompass them. See Figure 2 for a schematic of the equal area tiling of the time-frequency plane by a wavelet basis.

Since the components of the wavelet transform are indexed by j—which gives the scale or frequency level and k—which gives the location, it follows that the wavelet transform simultaneously displays data in time-frequency domain. It also means that a one-dimensional array is, in a sense, transformed to two dimensions. This type of transformation should be compared and contrasted with the Gabor or short time

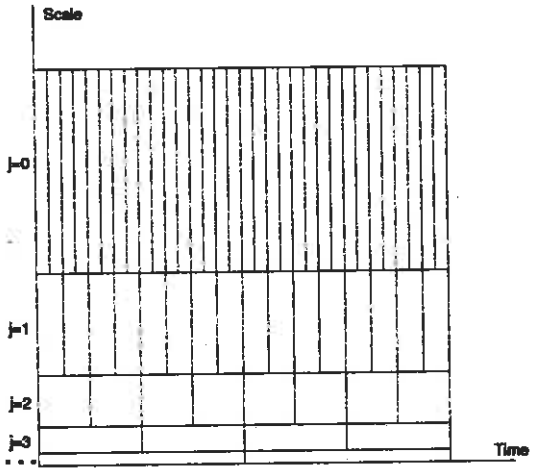

FIG. 2. Schematic equal area tiling of the time-frequency plane by wavelets.

Fourier transform. There again, time is transformed to time-frequency domain by windowing the time domain and Fourier transforming each window. But the Gabor transform does not adapt the frequency band to the temporal band as does the wavelet transform.

Recall that although the FFT is used algorithmically to compute the coefficients s_n of a function $s(t)$ in the Fourier basis, these coefficients are more fundamentally defined by the integration,

$$s_n = \frac{1}{T}\int_0^T s(t)e^{2\pi int/T}\,dt.$$

Analogously the coefficients c_{jk} of a function in the wavelet basis are algorithmically computed by the FWT outlined above, but are fundamentally defined by integrating the product of the function and the wavelet, as

$$c_{jk} = \int s(t)\psi_{jk}(t)\,dt. \tag{1}$$

Filters associated with scaling functions and analyzing wavelets

As has already been mentioned, the **A** operation is a low-pass filtering operation. This can be given concrete expression in terms of a filter m_0 associated with each scaling function $\phi(t)$ according to the fundamental relation,

$$\hat{\phi}(\xi) = m_0(\xi/2)\hat{\phi}(\xi/2). \tag{2}$$

As before, the notation, $\hat{\phi}$, is used for the Fourier transform of ϕ. Figure 3 shows the m_0 filter for a Meyer wavelet with fourth order smoothness (see appendix) for an explanation of the order n of a Meyer wavelet). Similarly, the **D** operation is a high-pass filter m_1 satisfying

$$\hat{\psi}(\xi) = m_1(\xi/2)\hat{\phi}(\xi/2). \tag{3}$$

Figure 4 shows the amplitude of the m_1 filter for the same Meyer wavelet. Notice that the scaling function is present on the right side of *both* equation (2) and equation (3). This is consistent with the previous averaged segment giving rise to both the next wavelet segment d^j and the next averaged segment a^j in Figure 1.

A remarkable feature of the low- and high-pass filters is their symmetry of their amplitudes in the quarter-period point as shown in Figure 5. For this reason, these filters are called "mirror filters" in the literature. These mirror filters also satisfy

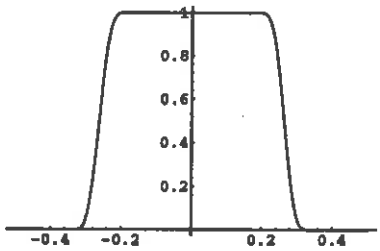

FIG. 3. Meyer m_0 low-pass filter with 4th order smoothness.

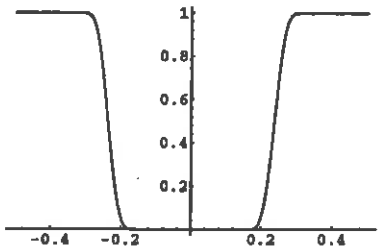

FIG. 4. Meyer m_1 high-pass filter with 4th order smoothness.

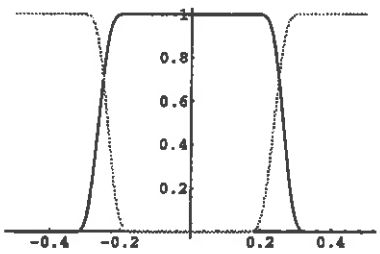

FIG. 5. Meyer m_0 and m_1 as mirror filters.

the "power conservation" law,

$$|m_0(\xi)|^2 + |m_1(\xi)|^2 = 1,$$

an equation that plays a crucial role in the mathematical development.

As in the example shown (Figure 5), the wavelet low/high-pass filters always overlap—they are not strictly low and high pass! The overlap means that bandpass

interpretations of wavelet filtering must always allow for an intrinsic amount of fuzziness near the boundary. The overlap can be lessened by the choice of wavelets, but it can't be totally eliminated.

Figures 6 and 7, respectively, show several members of the Daubechies, and Meyer families. In each case, the figure at the upper right may be regarded as the "typical" member of the family. .

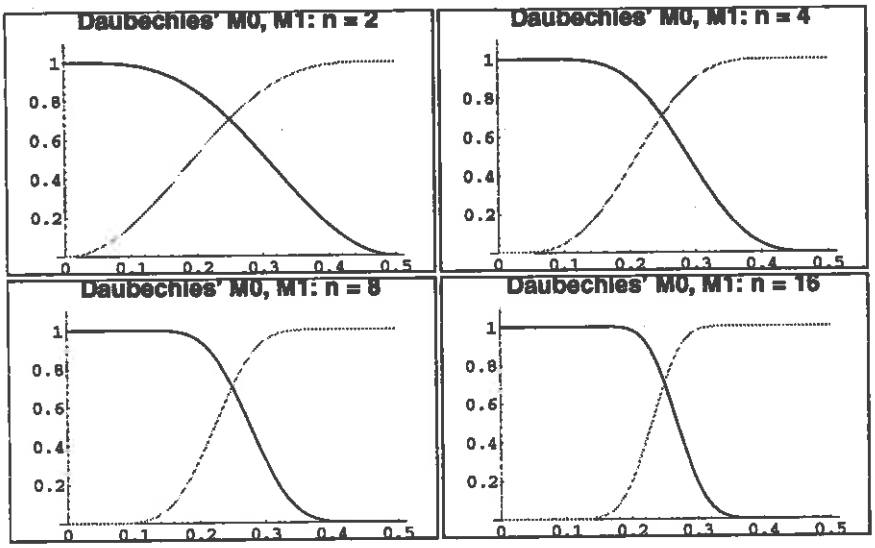

FIG. 6. Daubechies m0, m1 filters.

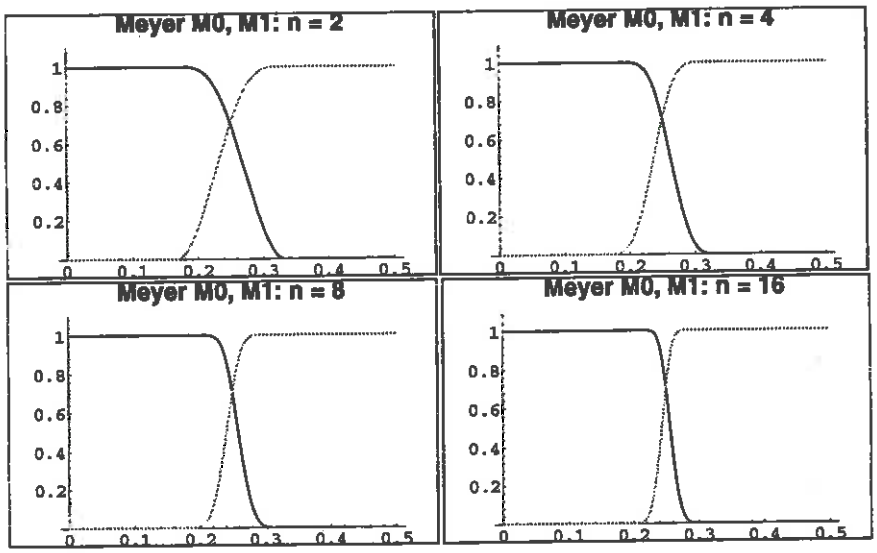

FIG. 7. Meyer m0, m1 filters.

Filtering with wavelets

Observe that after the high-pass operation **D**, the resulting data have the same doubled sampling interval as the averaged or blurred segment. How can its high frequencies be present with a halved Nyquist frequency? The answer is that the frequencies are "folded" over, just as if the data were aliased—see Figure 8. However, since *only* (well, *almost* only) the high frequencies are present in the **D** half-size segment, there is no confounding of information—that is, there is no true aliasing (well, *almost* none).

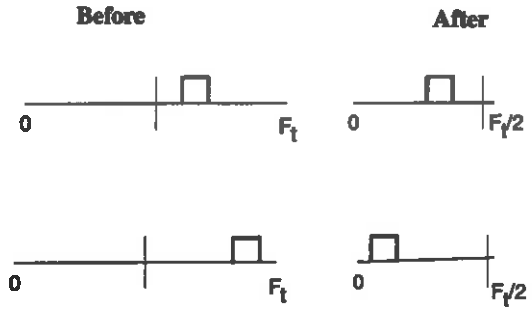

FIG. 8. Representation of frequencies in **D**.

The parenthetical comments in the previous sentence are again an acknowledgement of the inherent fuzziness of wavelet filtering operations. That is, the frequency overlap in the wavelet transform implies a degree of aliasing in the decomposition step. If the reconstruction algorithm is applied, then this aliasing is properly taken into account and the reconstruction is perfect. However, *most* applications will involve another operation interposed between decomposition and reconstruction (e.g. compression or migration). In such a case, the aliasing is not perfectly removed during reconstruction. With proper choice of wavelet, the aliasing distortion will be negligible for most applications.

Applications most suited to wavelet transform analysis are those that effectively use the simultaneous localization in time and frequency. The coefficients c_{jk} defined in equation (1) give a direct method for bringing this tool to bear on seismic data. In the theoretical form,

$$s(t) = \sum_{jk} c_{jk}\psi_{jk}(t),$$

of the wavelet transform decomposition, the effect of such an application could be summarized:

1. Localize in time and frequency by choosing a subset of the j's and k's.
2. Alter the c_{jk}'s in the chosen subset.

There are applications, notably data compression and filter design, where an octave is too gross a unit. One methodology for obtaining finer control in frequency

domain (at the expense of decreased temporal resolution) is to repeat the decomposition algorithm on one or more of the d vectors. This procedure is called forming *wavelet packets*, see Wickerhauser (1992), Daubechies (1992). Another methodology for overcoming the octave limitation is the use of the *continuous* wavelet transform, again, a good introduction is included in Daubechies (1992).

Finally, observe that everything said in this section applies without change to the case of spatial variations x and, indeed, there are sure to be interesting applications of the one-dimensional wavelet transform applied to the offset or midpoint variable of a seismic section. And, perhaps, the most interesting applications will involve more than one dimension, so turn now to a discussion of the two-dimensional wavelet transform.

THE TWO-DIMENSIONAL DISCRETE WAVELET TRANSFORM

The simplest way to obtain a wavelet basis for a two-dimensional space, say, t and x, is to multiply the one-dimensional bases:

$$\psi_{jj'kk'}(t,x) = \psi_{jk}(t)\psi_{j'k'}(x). \tag{4}$$

This is analogous to replacing the one-dimensional Fourier kernel $e^{i\omega t}$ with $e^{i\omega t}e^{-ikx}$ and does, indeed, provide a two-dimensional complete orthonormal basis in the wavelet case just as it does for Fourier transform. The disadvantage of this basis is the mixing of the scales j and j'. It turns out that it is possible to construct a basis using only a single scale j at the expense of having three wavelets (basis functions) at each j level. These three functions are

$$\begin{aligned} \psi^H_{jkk'}(t,x) &= \psi_{jk}(t)\phi_{jk'}(x), \\ \psi^V_{jkk'}(t,x) &= \phi_{jk}(t)\psi_{jk'}(x), \\ \psi^D_{jkk'}(t,x) &= \psi_{jk}(t)\psi_{jk'}(x). \end{aligned} \tag{5}$$

The averaging function at level j is

$$\phi_{jkk'}(t,x) = \phi_{jk}(t)\phi_{jk'}(x).$$

This is the basis used in the remainder of this paper and also in many of the existing applications of the two-dimensional wavelet transform.

It is convenient to think of the result of the wavelet transform with this basis as being displayed in four panels as in Figure 9. The **A** symbol for the averaged (in each direction) panel is the analog of the averaged portion occurring at each stage of the one dimensional transform. As indicated in this figure, the superscript symbols on the three wavelet portions of the basis stand for: **H**-*horizontal* emphasis panel, **V**-*vertical* emphasis panel and **D**-*diagonal* emphasis panel. The **V** panel is created by "averaging" in t and "differencing" in x. Hence a horizontal reflector would tend to be eliminated from the **V** panels. From such extreme examples, one can understand

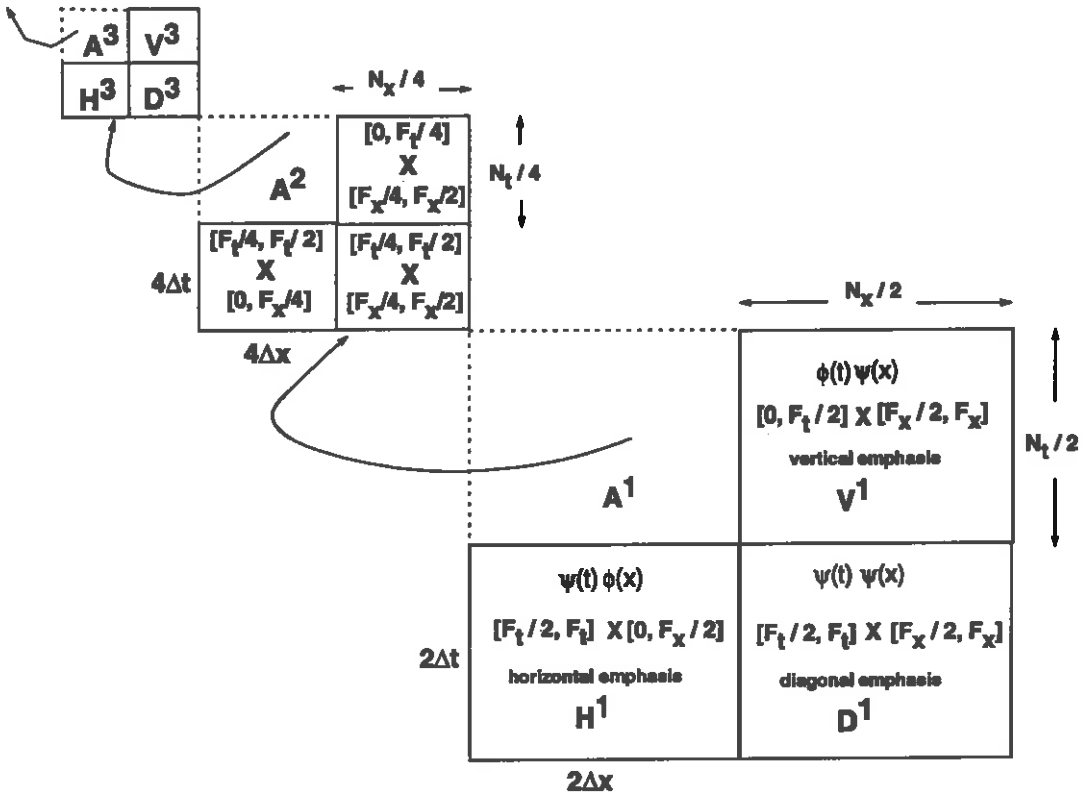

FIG. 9. 2D data decomposition.

the observation that **V** panel *does* emphasize steeper dip events, and analogously for the other panels.

A more precise analysis of the contents of the four panels in terms of dip angle is contained in the next section.

Just as in the one dimensional wavelet transform, "folding" occurs in the frequencies contained in each of the **H**, **V** and **D** panels. Specifically, the temporal frequencies are folded in **H**; the spatial frequencies are folded in **V** and both are folded in **D**. Again, this folding does not confound data (except for the filter overlaps), so should not be considered as true aliasing.

Analysis of sloping reflections

We give a detailed analysis of the effect of the discrete wavelet transform on sloping reflection planes with a signal of given frequency band. This leads to a semi-quantitative explanation of the known division of the two-dimensional wavelet transform into horizontal, vertical and diagonal emphasis panels and provides insight into the use of the two-dimensional wavelet transform in seismic processing. As an example of seismic processing using the wavelet transform, some simple examples of de-aliasing spatially aliased data are discussed.

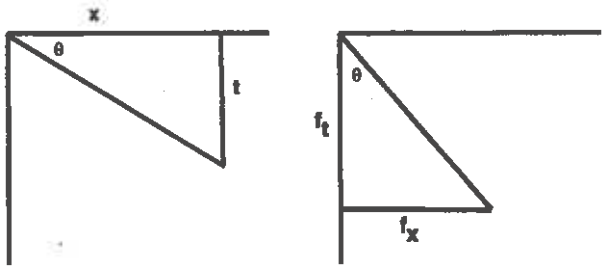

FIG. 10. A plane of time dip θ in space-time and in Fourier domain.

Consider the decomposition of the reflection data from a single dipping segment. Letting θ denote the *time* dip (or *apparent* dip or slope), the situation is shown in Figure 10. The plane is characterized by the equation $t = t_0 + x \tan\theta$ in space-time and by the equation

$$f_x = f_t \tan\theta \tag{6}$$

in Fourier domain. The latter result is established by taking the two-dimensional Fourier transform of $\delta(t - t_0 - x\tan\theta)$ using $2\pi f_t$ as the conjugate variable to t and $-2\pi f_x$ as the conjugate variable to x.

Seismic data are characterized by their frequency band in addition to their location in time-space. To include this vital aspect in the model, assume that the sampling interval in time is Δt, with associated Nyquist limit $F_t = 1/2\Delta t$, and similarly introduce Δx and $F_x = 1/2\Delta x$ in space. Suppose that the seismic signature along the sloping reflection has temporal band $[f^-, f^+]$. Equation (6) shows that the corresponding spatial band is $[f^-\tan\theta, f^+\tan\theta]$.

Figure 11 indicates that the use of the three-function wavelet basis of equation (5) divides the j^{th} octave in half in each direction, thus providing additional frequency localization. Even more important, the subdivision induced by this basis provides a degree of *dip localization*. As Figure 12 indicates, the angle

$$\theta_{HV} \stackrel{\text{def}}{=} \arctan\left(\frac{F_x}{F_t}\right) = \arctan\left(\frac{\Delta t}{\Delta x}\right), \tag{7}$$

approximately separates dips that appear in $\mathbf{H}$ from those that appear in $\mathbf{V}$. This condition is independent of the signal band limits and is also independent of the level j. This result gives analytic meaning to the notion that the $\mathbf{H}^j$ panels emphasize the horizontal aspects of the signal, while the $\mathbf{V}^j$ panels emphasize the vertical aspects of the signal.

Similarly, the angles θ_{Dmin} and θ_{Dmax} defined by

$$\theta_{Dmin} \stackrel{\text{def}}{=} \arctan\left(\frac{F_x}{2F_t}\right) = \arctan\left(\frac{\Delta t}{2\Delta x}\right), \tag{8}$$

$$\theta_{Dmax} \stackrel{\text{def}}{=} \arctan\left(\frac{2F_x}{F_t}\right) = \arctan\left(\frac{2\Delta t}{\Delta x}\right), \tag{9}$$

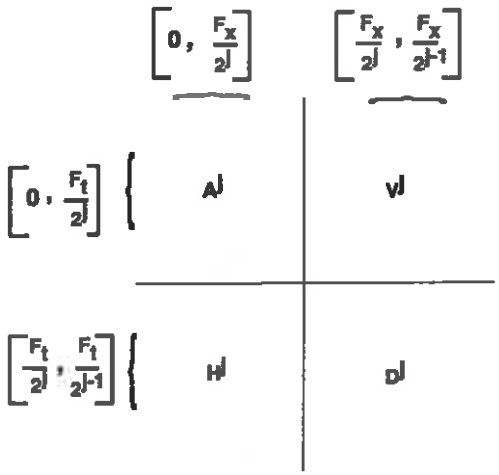

FIG. 11. Frequency content of level j panels.

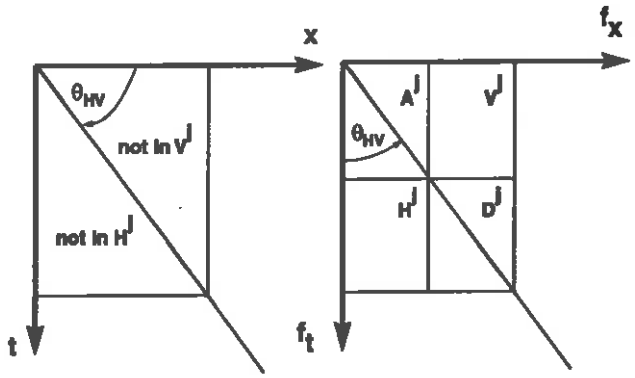

FIG. 12. Geometrical meaning of θ_{HV}.

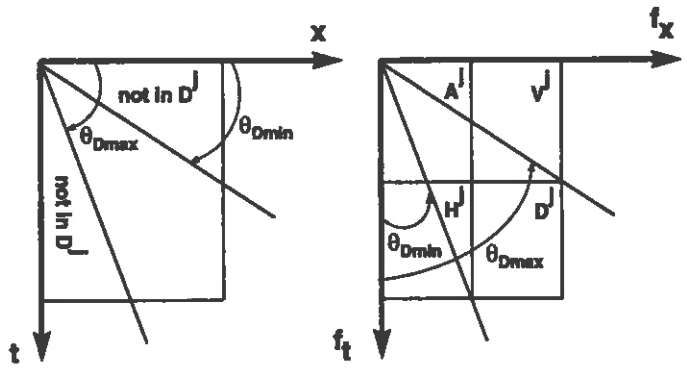

FIG. 13. Geometrical meaning of θ_{Dmin} and θ_{Dmax}.

and shown in Figure 13, approximately bound the dips that appear in the $\mathbf{D}^j$ panels.

Decomposition of sloping reflections

Set $F_t = F_x = 125\,\text{Hz}$ and set the signal band at 0–30 Hz throughout this section. These assumptions imply that the boundary angle for the **H** and **V** panels is

$$\theta_{HV} = \tan^{-1}(1) = 45°;$$

that the bounding angles for the **D** panels are

$$\theta_{Dmin} = \tan^{-1}(1/2) \approx 29°, \quad \theta_{Dmax} = \tan^{-1}(2) \approx 61°.$$

Figures 14 shows the predicted contents of the first level panels as a function of dip angle according to the restrictions implied by Figure 11 for the given signal band. The darker curve is the maximum value in the band and the lighter curve is the minimum. When the lighter curve lies above the darker curve, the band in that panel is approximately empty. Thus, for example, $\mathbf{D}^1$ and $\mathbf{H}^1$ are empty for all angles—this is a reflection of the fact that the maximum frequency $f^+ = 30\,\text{Hz}$, while half-Nyquist is 62.5 Hz. Moreover since these values are well separated, no visible leakage into these panels is expected for a reasonable wavelet. As the lower left panel of Figure 14 indicates, the inequalities developed earlier imply that the $\mathbf{V}^1$ panel remains (approximately) empty until an angle of about 64°.

Similarly, Figures 15 and 16 show the bandlimits predicted for levels two and three. Data with 30° dip and the 0–30 Hz signal band is shown in Figure 17

The paper compares these theoretical predictions against the results of the discrete wavelet decomposition of synthetic data using Daubechies 8 point wavelet ($_4D$). Here, consider just the results for the $\mathbf{H}^j$ panels at the first three levels. If the θ_{HV} angle bound was strict, then, for the case at hand, $\mathbf{H}^2$ would be empty. However, as Figure 15 indicates, the lower bound is only *slightly* higher than the upper bound (the precise values are $f^+_{H^2} = 30\,\text{Hz}$ and $f^-_{H^2} = 31.25\,\text{Hz}$), and so it is not too surprising

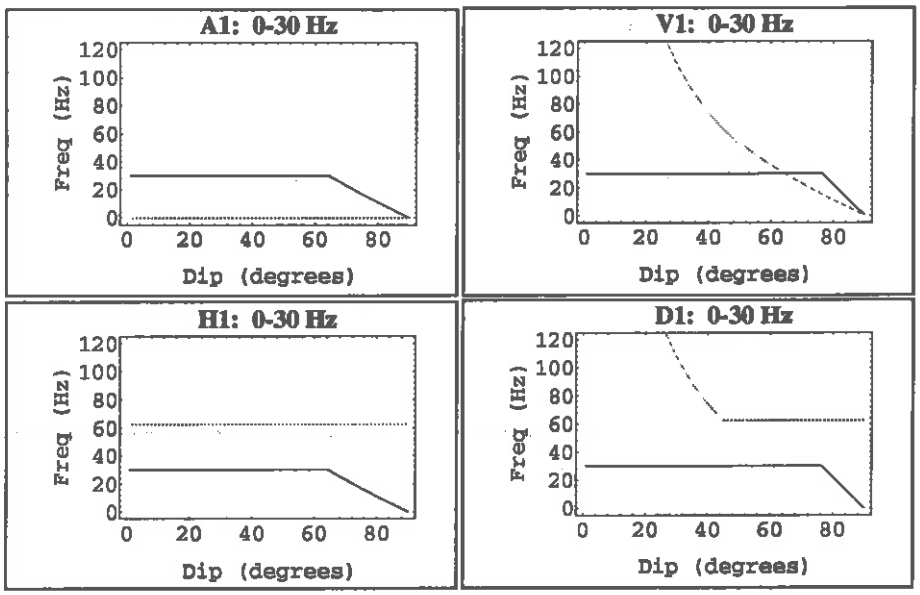

FIG. 14. Predicted first-level decomposition.

j	f^-_{Hj}	f^+_{Hj}
1	62.5	30.
2	31.25	30.
3	15.625	27.0633
4	7.8125	13.5316
5	3.90625	6.76582

Table 6. Theoretical frequency bounds for $\mathbf{H}^j$ for levels $j = 1$ to 5

that Figure 19 shows some "leakage" into $\mathbf{H}^2$ caused by the imprecision of wavelet filtering. Figure 16 and Table 6 indicate that $\mathbf{H}^3$ should contain a substantial amount of information relative to $\mathbf{H}^2$, and Figure 20 bears out this prediction. Figures 15 and 16 and Table 7 indicate that $\mathbf{D}^1$, $\mathbf{D}^2$ should be empty, while $\mathbf{D}^3$ contains significant information. Figures , and bear out this prediction.

Figure 21 shows the result of decomposition with a longer wavelet, the Daubechies 20 point wavelet. Since this wavelet has less overlap, the "leakage" is reduced. This bears out the idea that the overlap phenomena (the intrinsic wavelet aliasing) can be ameliorated by the choice of wavelet. However, using a longer wavelet is *not* a panacea—in particular, for operator compression, shortness of the wavelet is an overriding concern. On the other hand, it *is* important to fit the wavelet to the task and Meyer wavelets have markedly better filtering properties than the commonly used Daubechies wavelets.

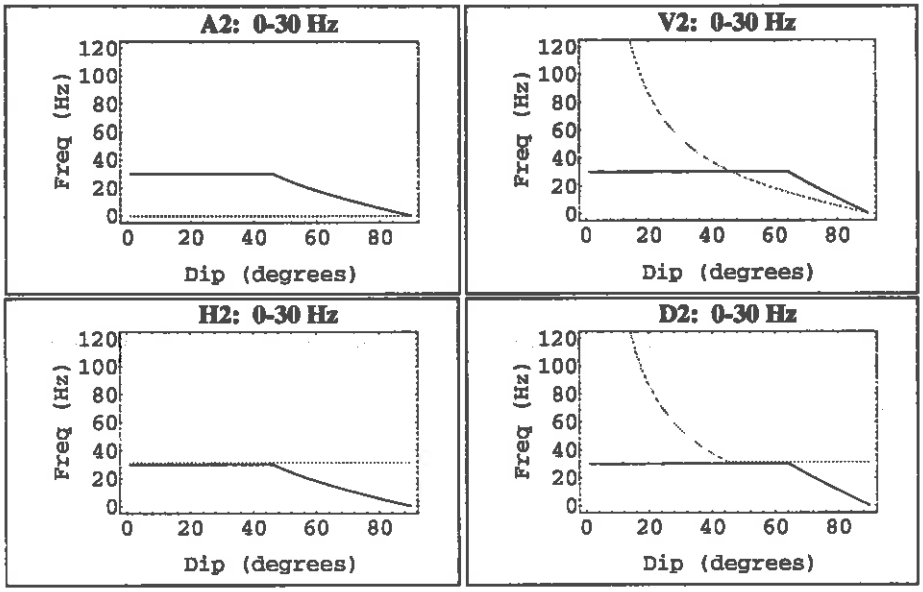

FIG. 15. Predicted second level decomposition.

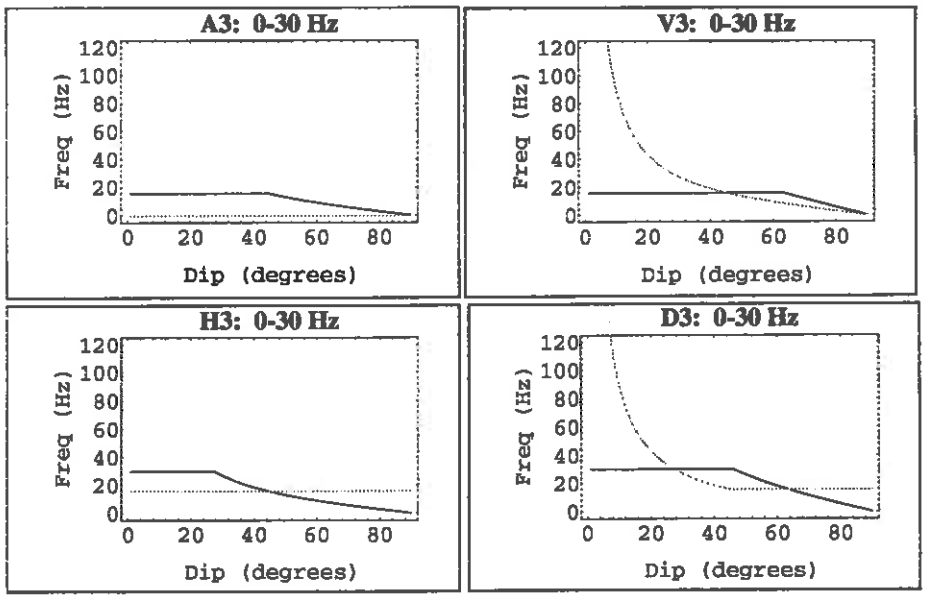

FIG. 16. Predicted third level decomposition.

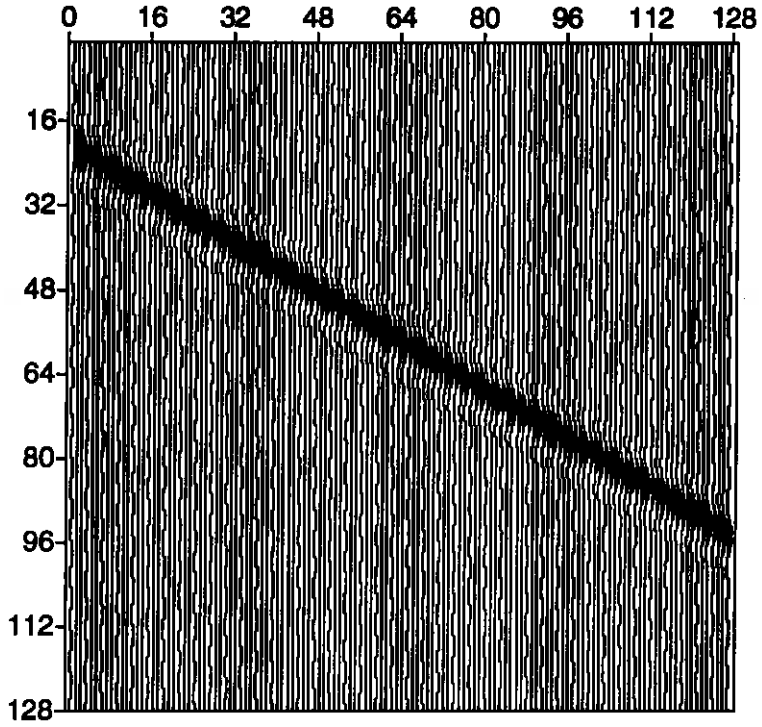

FIG. 17. 30° dip data with 0–30 Hz band.

j	f_{Dj}^{-}	f_{Dj}^{+}
1	108.253	30.
2	54.1266	30.
3	27.0633	30.
4	13.5316	15.625
5	6.76582	7.8125

Table 7. Theoretical frequency bounds for $\mathbf{D}^j$ for levels $j = 1$ to 5

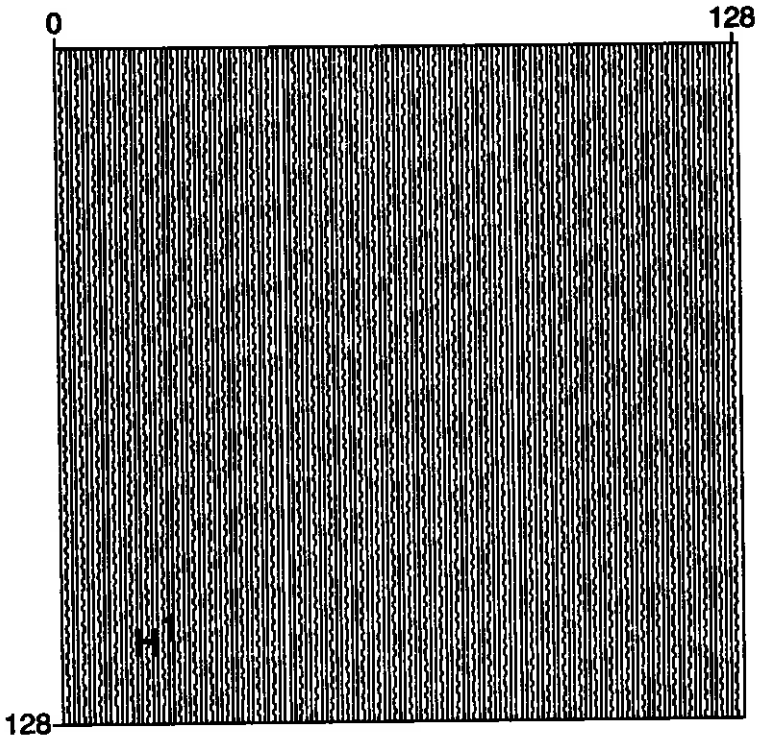

FIG. 18. Reconstructed H^1 panel for 30° dip data.

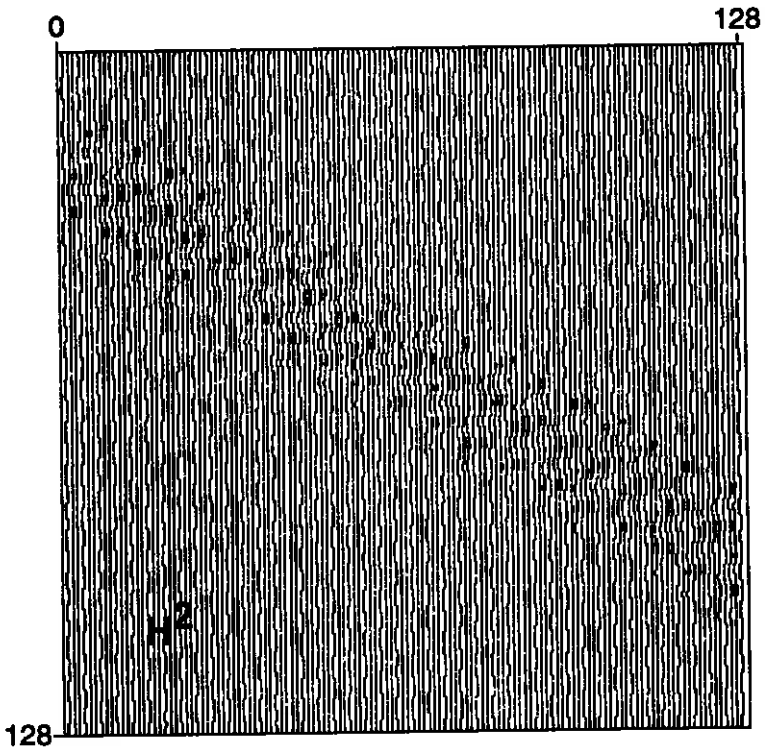

FIG. 19. Reconstructed H^2 panel for 30° dip data.

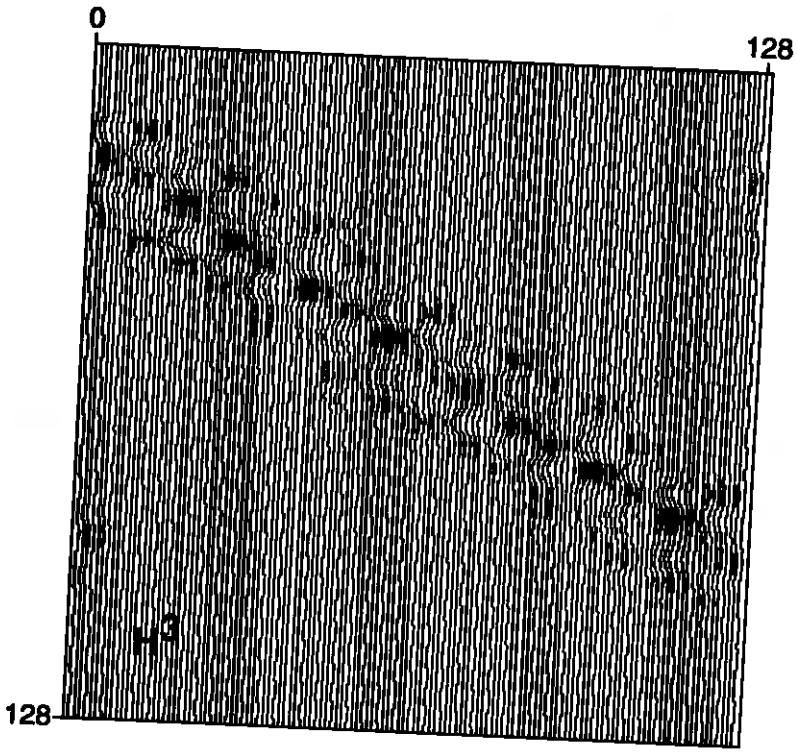

FIG. 20. Reconstructed $\mathbf{H}^3$ panel for 30° dip data.

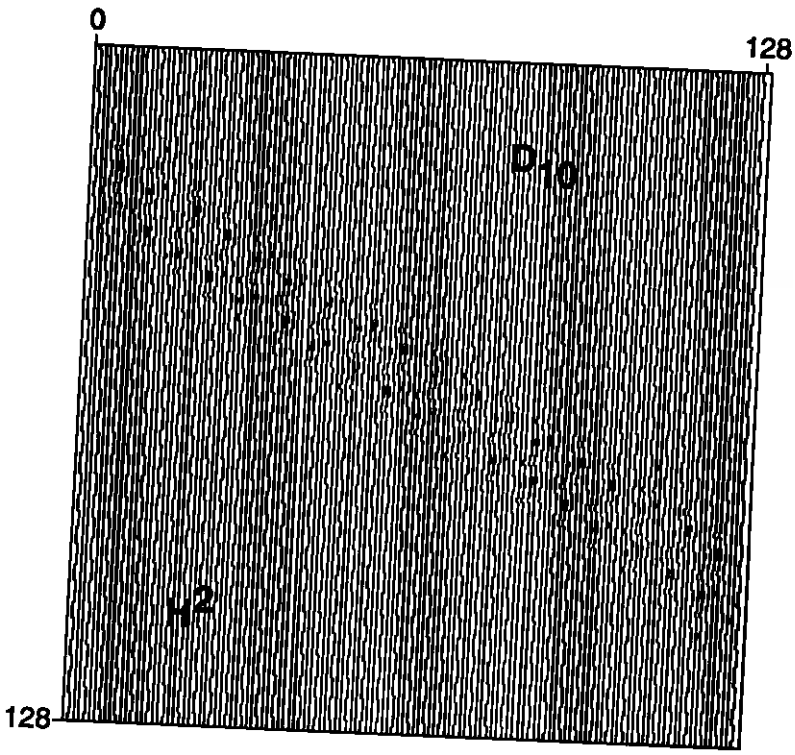

FIG. 21. Reconstructed $\mathbf{H}^2$ panel for 30° dip data with the $n = 10$ Daubechies wavelet.

Processing spatially aliased data

As an example of wavelet filtering some simple cases of spatial aliasing are treated using the properties of the three wavelet basis. A central problem is that filtering the panels near their boundaries will damage the overlap region causing aliasing distortion in the reconstruction process. One way to cope with this is to use a bandpass filters that avoid boundary regions. But if the wavelet used has a large overlap, it is impossible to find a pass band that removes the spatial aliasing while avoiding the overlap region.

A more fundamental way to obtain a satisfactory result is to use a wavelet with smaller overlap regions. Good results were obtained using the Meyer wavelet of order $n = 10$, which has very small overlap (cf. Figure 7).

Filtering with two-dimensional wavelets

The above discussion of spatial aliasing made a good test bed for demonstrating various aspects of the two-dimensional wavelet transform. These included exploiting the division into horizontal, vertical and diagonal panels implied by the basis given in equation (5) and controlling the intrinsic aliasing by choice of analyzing wavelet. However, the applications shown could have been done with pure Fourier methodology because the spatial-temporal localization of the wavelet basis wasn't brought to bear. A more suitable problem would be the treatment of spatial aliasing—or some other phenomenon—occuring in a local region of space-time, x-t, as well as a local region of the frequency plane, f_x-f_t.

That is, just as in the case of the one-dimensional transform, applications most suited to wavelet transform analysis are those that effectively use the simultaneous localization in data-domain and frequency-domain. The wavelet basis given in equation (5) implies the following theoretical expansion of the data:

$$s(t,x) = \sum_{jkk'} c^H_{jkk'} \psi^H_{jkk'}(t,x) + \sum_{jkk'} c^D_{jkk'} \psi^D_{jkk'}(t,x) + \sum_{jkk'} c^V_{jkk'} \psi^V_{jkk'}(t,x). \qquad (10)$$

Notice that in this "non-standard" two-dimensional basis, there is still only *one* frequency parameter (j). The natural two-dimensional product basis implied by equation (4) *would* afford separate localization in f_x and f_t, but this has been traded away in favor of the *dip localization* afforded by the use of the three basis functions, $\psi^H_{jkk'}$, $\psi^D_{jkk'}$ and $\psi^V_{jkk'}$ at level-j in place of the single function $\psi_{jkj'k'}(x,t) = \psi_{jk}(t)\psi_{j'k'}(x)$ appearing at level-j, j' in the product basis.

In the non-standard basis, frequency localization by octave (in both f_t and f_x) is attained by selecting j-values. Then selection of panel H, D or V further confines the frequency to a half-octave (in both f_t and f_x) and also confines the apparent dips. Within a panel, temporal localization is attained by selecting k-values and spatial localization is attained by selecting k'-values.

And, just as in one dimension, wavelet *packets* in t and/or x or the *continuous* wavelet transform in t and/or x may be superior tools for applications requiring finer

frequency control than stepping by octaves. Because of the greater continuity in variables such as offset or midpoint than in time, t-domain may more often require these refinements than x-domain.

ACKNOWLEDGEMENTS

Thanks to Gregory Beylkin, both for his patient theoretical support and for the use of his proprietary two-dimensional decomposition software. We thank Bee Bednar for sharing his knowledge and codes and John E. Anderson for helping us with his extensive knowledge of practical issues in seismic data processing. We also are grateful for important discussions with many others of our colleagues at the Colorado School of Mines, especially John W. Stockwell, Norman Bleistein, Ilya Tsvankin and Frank G. Hagin. We are also indebted to the excellent computing research facilities at the Center for Wave Phenomena and the Center for Geoscientific Computing which includes RS6000 workstations, the NeXT software environment, and the Center for Wave Phenomena Seismic Unix data processing environment.

REFERENCES

Alpert, B., 1992, Wavelets and other bases for fast numerical linear algebra: in Wavelets—A tutorial in theory and applications: Ed. Chui, C. K., Academic Press, Boston.

Beylkin, G., 1992, On the representation of operators in bases of compactly supported wavelets: SIAM Journal on Numerical Analysis, **6**, no. 6, 1716–1740.

Beylkin, G., Coifman, R., and Rokhlin, V. 1991, Fast wavelet transforms and numerical algorithms I: Comm. Pure and Appl. Math., **44**, 141–183.

Beylkin, G., Coifman, R., and Rokhlin, V. 1992, Wavelets and numerical analysis: in Wavelets and their applications, Ed. Ruskai, M. B., Jones and Bartlett, Boston.

Chun, J. H., and Jacewitz, C. A. 1981, Fundamentals of frequency domain migration: Geophysics, **46**, no. 5, 717–733.

Daubechies, I., 1992, Ten lectures on wavelets: SIAM, Philadelphia.

Gabor, D., 1946, Theory of Communication: J Inst. Elec. Eng. (London), **93**, 429–457.

Jawerth, B., and Sweldens, W. 1993, An overview of wavelet based multiresolution: Preprint, February 5, 1993.

Kleinert, F. 1992, Biorthogonal wavelets for fast matrix computations: Preprint, November 3, 1992.

Mallat, S. G., 1989a, A theory for multiresolution signal decomposition: The wavelet representation: IEEE Trans. Patt. Anal. Mach. Intell., **11**, no. 7, 674–693.

Mallat, S. G., 1989b, Multifrequency channel decomposition of images and wavelet models: IEEE Trans. Acoust. Speech Sig. Proc., **37**, no. 12, 2091–2110. Niitsuma, H., Tsuyuki, K., Asanuma, H., Discrimination of split shear-waves by wavelet transform: Canadian Geophysics., *to appear*.

Press, W. H., Teukolsky, S. A., Vetterling, W. T., Flannery, B. P., 1992, Numerical recipes in C, 2nd Edition: Cambridge University Press, New York.

Rioul, O., Vetterli, M., 1991, Wavelets and signal processing: IEEE Signal Proc., **8**, 14–38.

Wickerhauser, M. V., 1992, Acoustic signal processing with wavelet packets: in Wavelets—A tutorial in theory and applications: Ed. Chui, C. K., Academic Press, Boston.

Elimination of dispersion in finite-difference modeling and migration

Tong Fei

Elimination of dispersion in finite-difference modeling and migration

Tong Fei

ABSTRACT

Finite-difference acoustic-wave modeling and reverse-time depth migration based on the full wave equation are general approaches that can take into account arbitary variations in velocity and density, and can handle turning waves well. However, conventional finite-difference methods for solving the second-order acoustic-wave equation suffer from numerical dispersion if too few samples per wavelength are used. Here, I develop the *flux-corrected transport* (FCT) algorithm for the second-order acoustic-wave equation. Combining this FCT technique with the conventional finite-difference modeling and reverse-time wave extrapolation can ensure finite-difference solutions without numerical dispersion even with as few as five samples per dominant wavelength. Computed two-dimensional migration impulse responses and synthetic data show accurate imaging of positions of reflectors with greater than 90-degree dip, where velocity varies both laterally and vertically. Likewise, generated synthetic VSP seismograms show no indication of numerical dispersion.

INTRODUCTION

Since finite-difference modeling and migration is based on the full acoustic-wave equation without additional physical assumptions, the method potentially can address many issues, such as arbitrary velocity variation, turning waves, and multiple reflected waves.

Some finite-difference schemes for numerically solving the wave equation suffer from undesirable ripples, so-called *grid dispersion*, particularly near large gradients in wavefields or when too coarse a computation grid is used. Alford et al. (1974) and Kelly et al. (1976) have studied the grid dispersion existing in finite-difference methods. They concluded that the signals computed by finite-difference methods become strongly dispersed if the grid is too coarse. For eliminating the numerical dispersion, they state that at least 11 and 5.5 points per half-power wavelength must be used for the second-order and fourth-order finite-difference methods, respectively. Dablain (1986) also stated that the requirement of eliminating the dispersion is to

use 8 and 4 grid points to cover the Nyquist frequency for the second-order and fourth-order finite-difference methods, respectively. Both criteria, used by Alford and Kelly, and Dablain, are consistent. However, for data in which the embedded wavelet occupies, for example, two octaves, the dominant frequency is perhaps half of the reference frequency used by Kelly and Alford, and might be one-third or less of the Nyquist frequency used by Dablain. Thus, to satisfy the above requirement, about 18 to 20 points per dominant wavelength must be used for the second-order method, and 9 to 12 points per dominant wavelength for the fourth-order finite-difference method.

The flux-corrected transport (FCT) method developed by Boris and Book (1973) has been successfully applied in the solution of the continuity equation for acoustic media in circumstances involving large gradients and discontinuities, where conventional algorithms fail. This FCT technique has recently been implemented in acoustic problems for seismic applications (Fei, 1993). In that work, the second-order acoustic-wave equation is replaced by a set of first-order partial differential equations through a change of dependent variables. The FCT algorithm can treat strong gradients, shocks and impulses without the usual dispersively generated ripples, even for five or fewer points per dominant wavelength.

Here, I developed a FCT finite-difference algorithm that can be directly used with the second-order wave equation. This algorithm can also be applied to seismic modeling and migration with full consideration of variable velocity and density. It can image reflectors with a wide range of dips and generate synthetic seismograms with no numerical dispersions. It can also be used on a relatively coarse grid to achieve accuracy comparable to that of conventional finite-difference approaches on a finer grid.

THEORY

For velocity and density fields that are functions of space, the acoustic-wave equation is

$$\frac{1}{\rho}\frac{\partial^2 P}{\partial^2 t} = c^2\left[\frac{\partial}{\partial x}\left(\frac{1}{\rho}\frac{\partial P}{\partial x}\right) + \frac{\partial}{\partial y}\left(\frac{1}{\rho}\frac{\partial P}{\partial y}\right) + \frac{\partial}{\partial z}\left(\frac{1}{\rho}\frac{\partial P}{\partial z}\right)\right] + f(x,y,z,t), \qquad (1)$$

where $\rho = \rho(x,y,z)$ is density, $c = c(x,y,z)$ is wave velocity, and $f(x,y,z,t)$ is the source function.

The above wave equation for inhomogeneous media can be approximated by a second-order explicit conventional finite-difference scheme. However, this finite-difference discretization causes the phase speed to become a function of discretization interval, and generates undesirable numerical dispersion when the spatial grid is too coarse (that is, too few samples per wavelength are used). In order to eliminate this non-physical dispersion, a new FCT algorithm directly applied to the second-order wave equation can be applied.

The essential idea of FCT is the application of a corrective *diffusion* to a dispersive *transport* scheme, such as conventional second-order finite-difference schemes, localizing the diffusion to the regions where non-physical ripples tend to form. This diffusion is carried out in a conservative way; that is, whenever a portion of the wavefield is removed at one point, the same amount is added back in somewhere else, and, as a result, there is no net loss or gain of the quantity (e.g. pressure) to the system. But for a real problem, there is no priori information about where the dispersion might exist, so the FCT attempts to apply the diffusion everywhere (steps 2 and 4 in Appendix A). Once the solution is diffused, an oppositing *anti-diffusion* is introduced to cancel the diffusion wherever it is not needed (steps 3, 5 and 6 in Appendix A). Interaction of the conventional stage (or transport stage), and diffusion and anti-diffusion stages enables FCT algorithms to treat strong gradients, shocks, and wavefields on coarse grids, with almost none of the usual dispersively generated ripples.

With this flux-corrected transport technique, seismograms and depth migration images for spatially variable media are obtained at less computational effort than in conventional finite-difference methods, which require a finer grid and smaller time step to achieve comparable accuracy.

In the computer implementation, the absorbing boundary condition of Clayton and Engquist (1980) has been applied to the side boundaries and the lower boundary. Also, when doing the wave extrapolations, an expanding boundary (about the wavefield moving outward from the source) has been used in order to save the computational cost.

NUMERICAL EXAMPLES

The following gives sample results of tests of the new FCT algorithm on two-dimensional forward problems and reverse-time depth migration, and comparison with results obtained by a conventional finite-difference method. The reverse-time depth migration, which basically is the same as forward modeling, simply runs time backwards.

Wedge model

Here, I give comparisons of the FCT and the second-order conventional finite-difference results with the analytical results for a 90-degree wedge model. The time variation of the source function is $(t-0.1)e^{-\alpha(t-0.1)^2}$, where t is time, measured in s, and α=700 s^{-2}. Figure 1 shows the normalized source function and its power spectrum. The upper half-power frequency is 10 Hz, and the corresponding half-power wavelength is about 0.244 km for velocity v=2.438 km/s.

Figure 2a shows a model in which the velocity in a rectangular area is assumed to be zero, while outside that area, the velocity is a constant 2.438 km/s. The modeled area in the tests is 5.266×5.266 km^2, with upper left corner at the origin. The upper left corner of the rectangular is at (2.194 km, 3.510 km). A line source is located at

(2.633 km, 3.072 km), and three receivers, #1, #2 and #3, are located at (2.545 km, 3.159 km), (1.755 km, 3.072 km) and (2.018 km, 3.861 km), respectively. Figures 2a, 4a and 6a illustrate the geometry of the model, receiver locations and the spacing for tests involving three different sizes of spatial step.

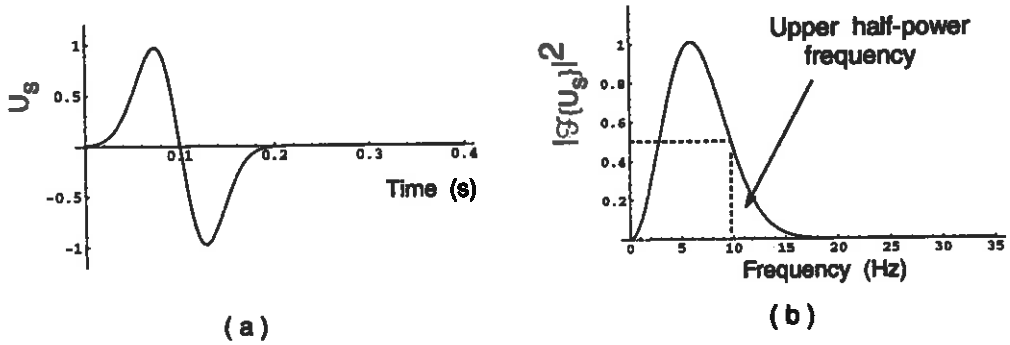

FIG. 1. (a) Normalized time response of the source function. (b) Normalized power spectrum of the source function.

For the fine grid, Δx=0.02194 km, the number of grid points G_0 per upper half-power wavelength is about 11. Figures 2b and 2c show wavefield snapshots at 1.026 s by the conventional finite-difference method and by the FCT method, respectively. Figure 3 shows the comparison of time responses by both methods with that obtained by the analytical solution at the three different receiver locations. The comparison indicates that both conventional method and the FCT method generate accurate solutions with no numerical dispersion.

On a medium-coarseness grid, Δx=0.04388 km, for which $G_0 \approx 5.5$, the wavefield snapshot obtained by the conventional finite-difference approach becomes dispersive (Figure 4b). As seen in Figures 4 and 5, an oscillatory tail has developed in solutions by the conventional finite-difference method. For the FCT method, the wavefield snapshot and time responses show no indication of numerical dispersion. However, the FCT method produces some distortion of waveform.

When the grid size becomes more coarse, Δx=0.08776 km, for which $G_0 \approx 2.7$, the oscillations in the conventional finite-difference solution increase significantly (Figure 6b, Figure 7a, 7c and 7e). The FCT technique, however, still generates a wavefield with no numerical dispersion (Figure 6c). Time responses at the three receiver locations also indicate that the FCT technique has eliminated numerical dispersion, even for $G_0 \approx 2.7$ (Figure 7b, 7d and 7f). However, the waveforms generated by the FCT method show considerable distortion, change of amplitudes, and, in places, apparent time errors. The most obvious waveform distortion (Figure 6) is a loss of resolution, much as would happen in an attenuating medium. As seen in Figure 6b, that distortion exists for the conventional finite-difference solution, as well. The loss of resolution is a limitation imposed by use of too coarse a grid, independent of whether or not FCT is used.

The comparison presented here demonstrates that the FCT technique can over-

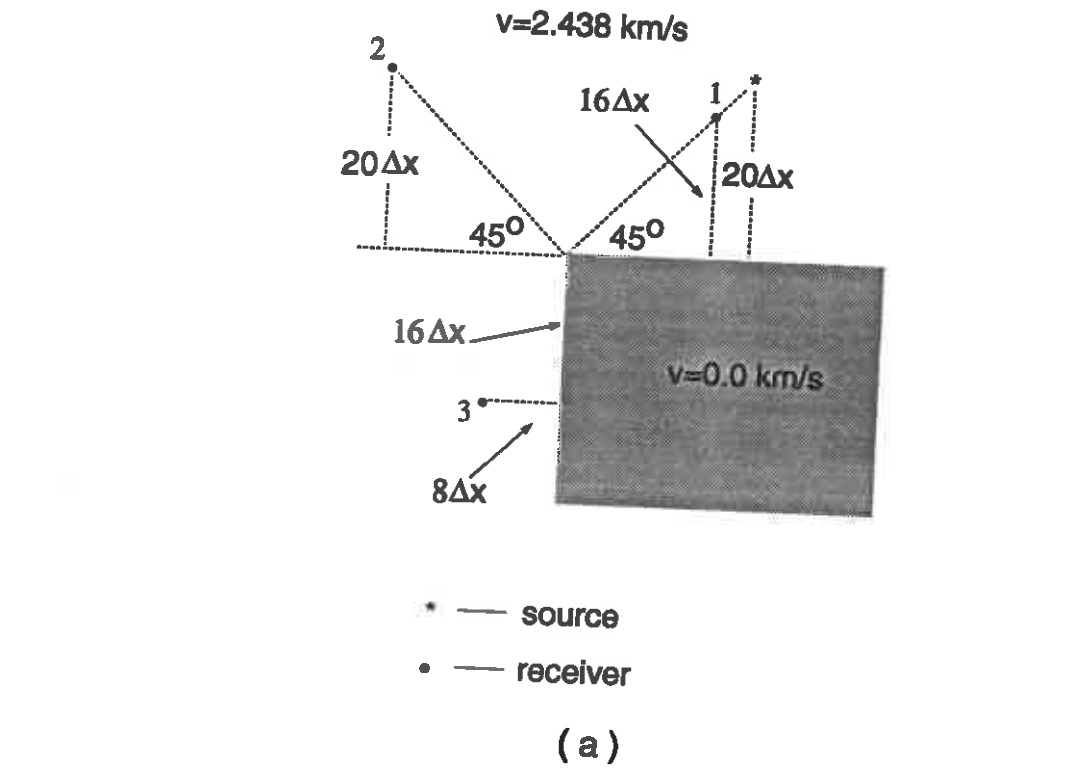

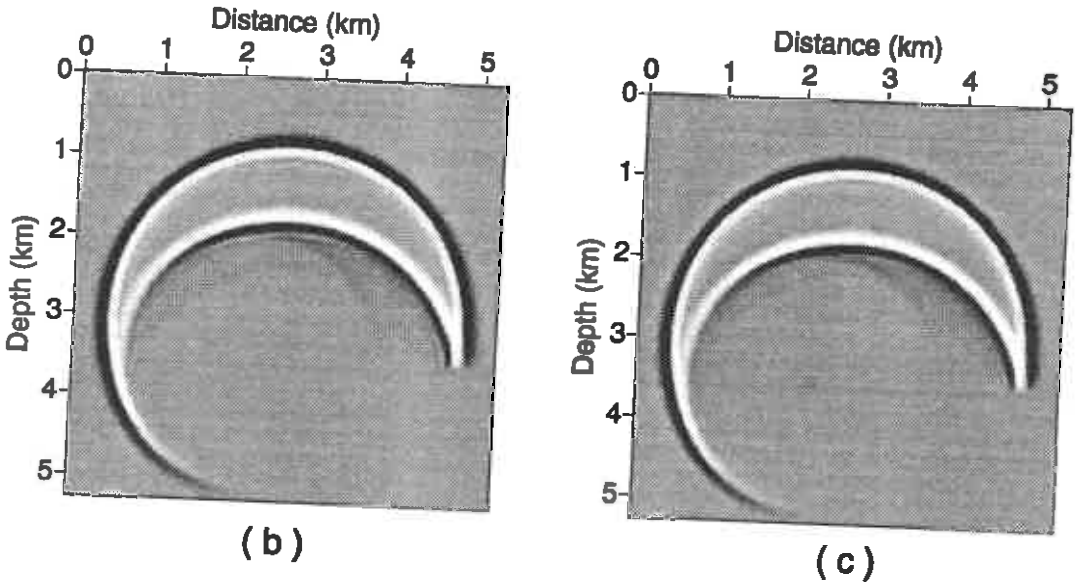

FIG. 2. Wavefield snapshot at 1.026 s on fine grid ($G_0 \approx 11$), Δx=0.02194 km. (a) Wedge model. (b) Conventional finite-difference solution. (c) The FCT solution.

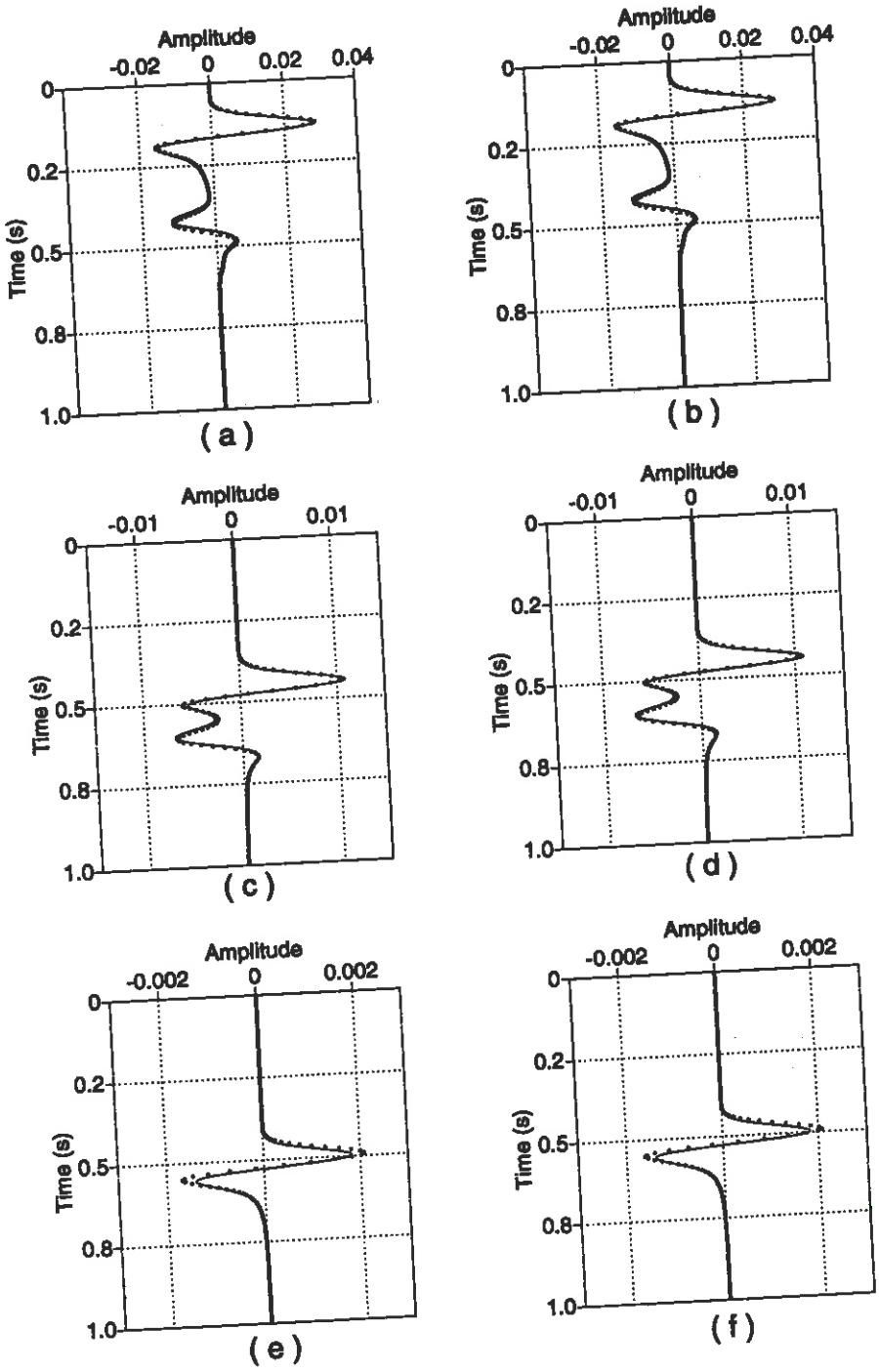

FIG. 3. Comparison of analytical solution (solid line) with conventional finite-difference solution and FCT solution ($\star$) on fine grid ($G_0 \approx 11$). (a), (c) and (e) are for the conventional finite-difference method. (b), (d) and (f) are for the FCT method. (a) and (b) are the solutions at receiver #1; (c) and (d) are the solutions at receiver #2; and (e) and (f) are the solutions at receiver #3.

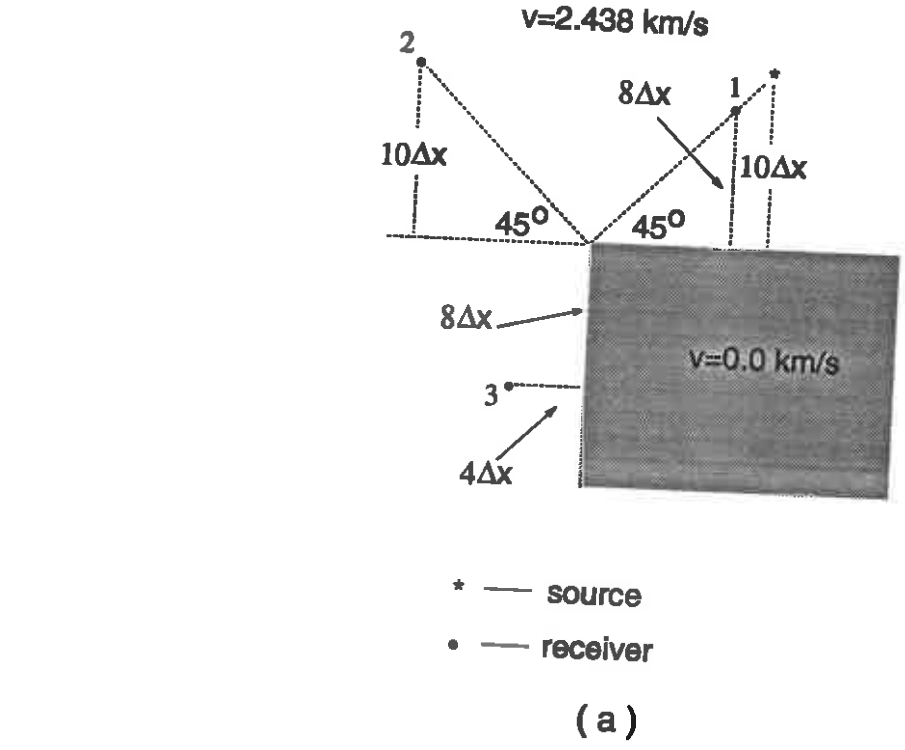

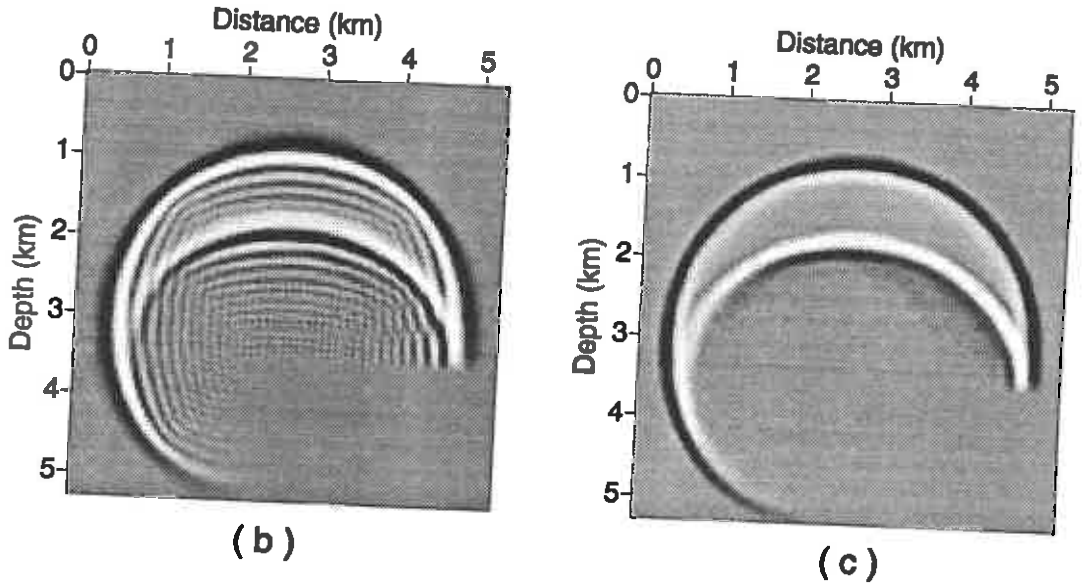

FIG. 4. Wavefield snapshot at 1.026 s on medium-coarseness grid ($G_0 \approx 5.5$), Δx=0.04388 km. (a) Wedge model. (b) Conventional finite-difference solution. (c) The FCT solution.

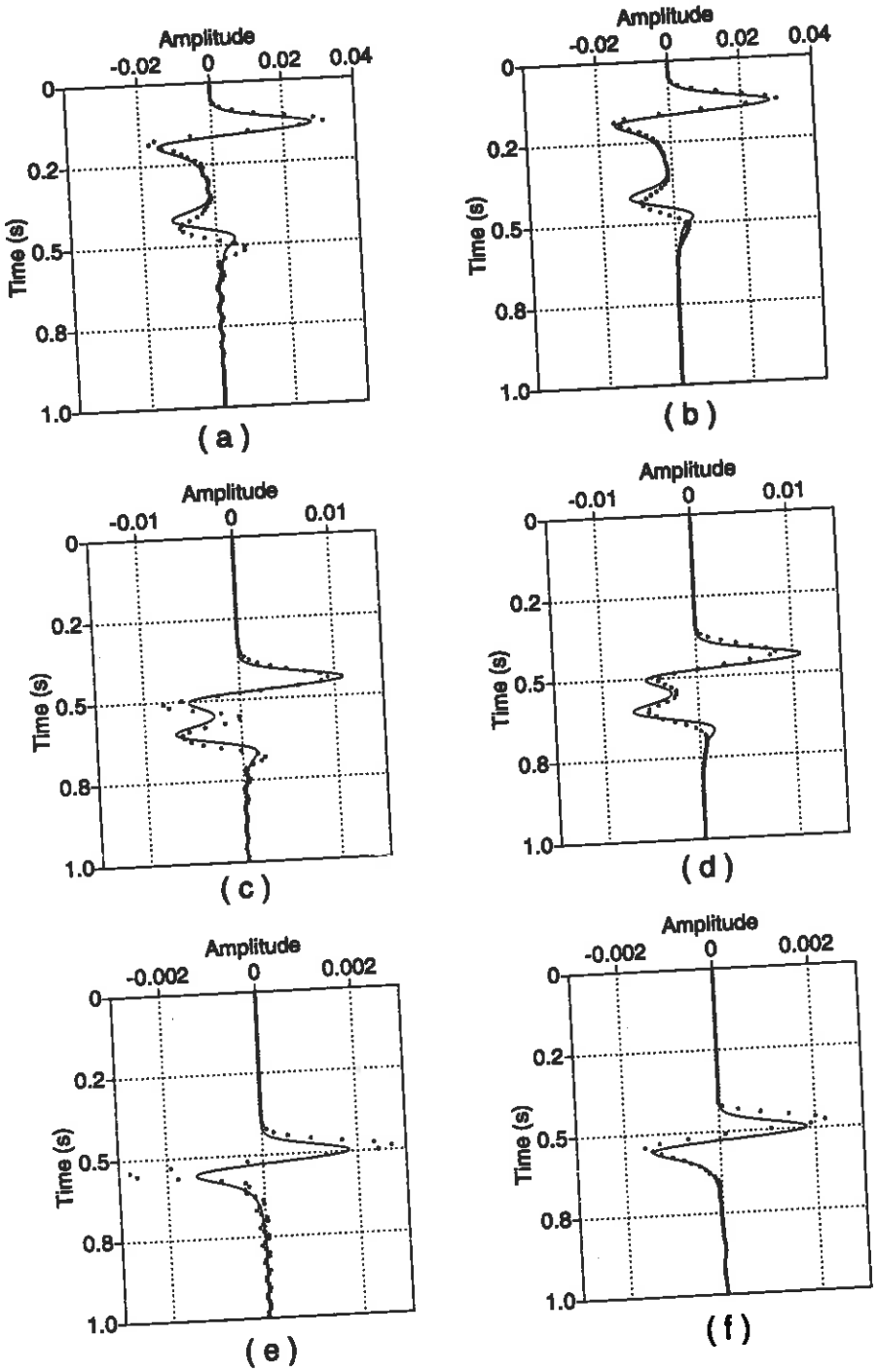

FIG. 5. Comparison of analytical solution (solid line) with conventional finite-difference solution and FCT solution ($\star$) on medium-coarseness grid ($G_0 \approx 5.5$). (a), (c) and (e) are for the conventional finite-difference method. (b), (d) and (f) are for the FCT method. (a) and (b) are the solutions at receiver #1; (c) and (d) are the solutions at receiver #2; and (e) and (f) are the solutions at receiver #3.

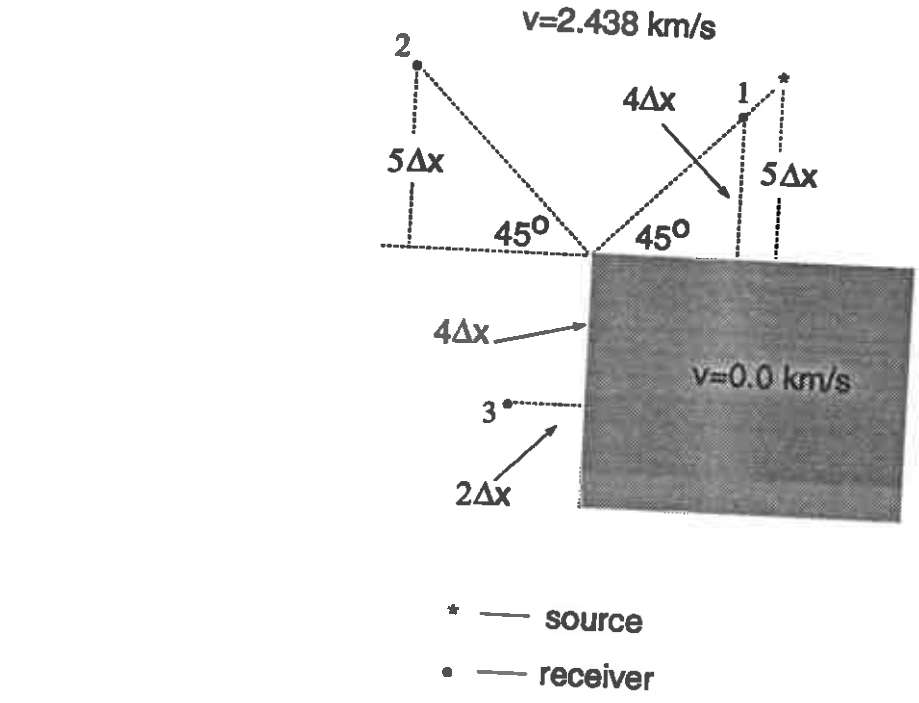

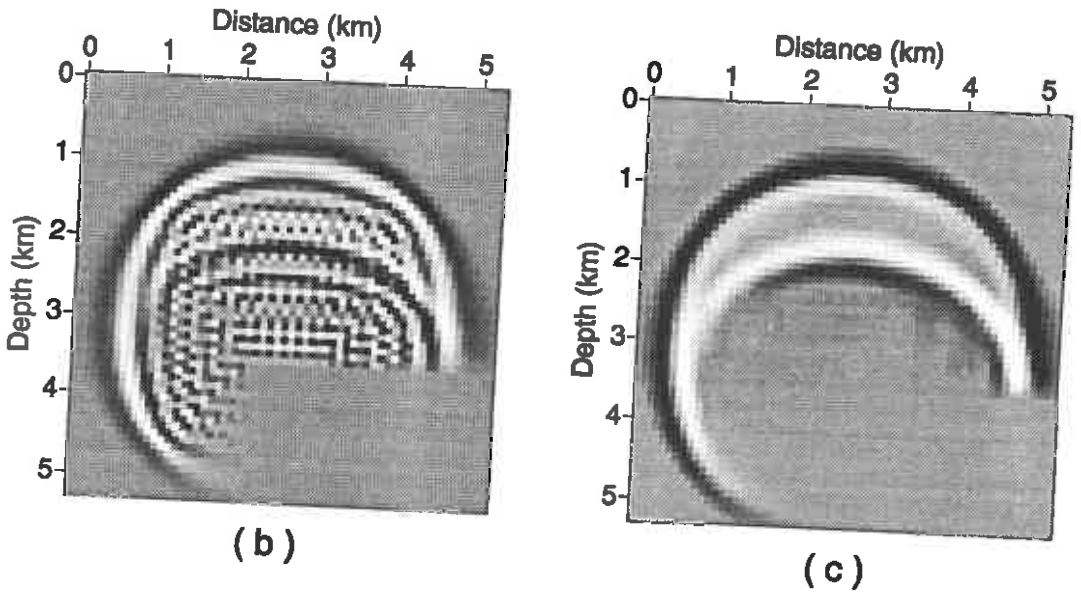

FIG. 6. Wavefield snapshot at 1.026 s on coarse grid ($G_0 \approx 2.7$), Δx=0.08776 km. (a) Wedge model. (b) Conventional finite-difference solution. (c) The FCT solution.

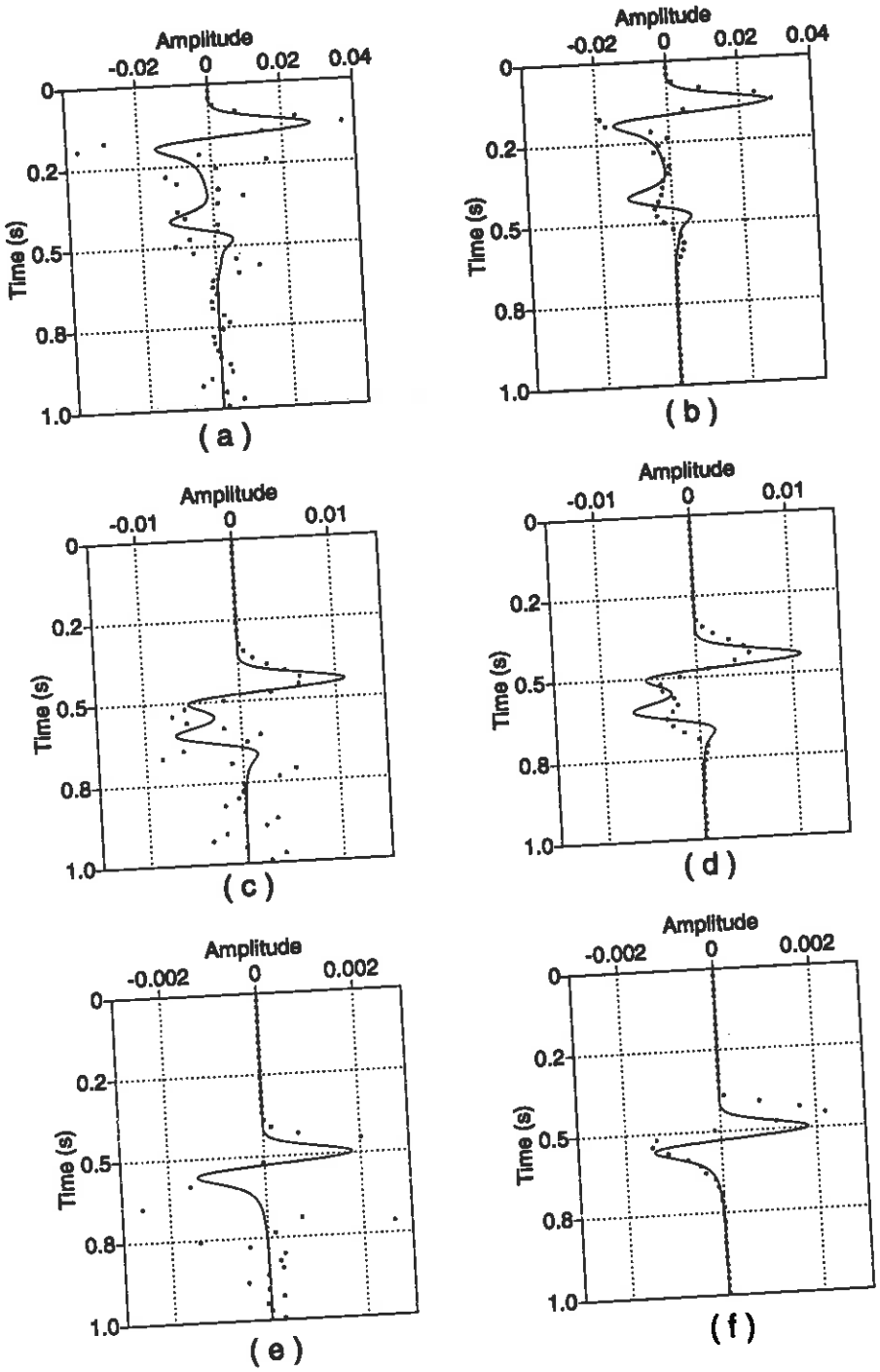

FIG. 7. Comparison of analytical solution (solid line) with conventional finite-difference solution and FCT solution ($\star$) on coarse grid ($G_0 \approx 2.7$). (a), (c) and (e) are for the conventional finite-difference method. (b), (d) and (f) are for the FCT method. (a) and (b) are the solutions at receiver #1; (c) and (d) are the solutions at receiver #2; and (e) and (f) are the solutions at receiver #3.

come the problem of numerical dispersion existing in finite-difference approach. As long as the grid in not too coarse, the FCT method can eliminate the dispersion without too severe a loss of resolution.

Two-dimensional impulse responses

Figure 8 shows the post-stack migration response of the FCT algorithm to three pulses in 2-D space, where velocity is a constant 2.0 km/s, and density is a constant. The pulses each consist of a single cycle of a sine wave (from one trough to its adjacent one), and, here, I use five samples per wavelength of the sinusoid pulse. The spatial steps Δx and Δz are 0.02 km, and the time step Δt is 6 ms, running backward. The three semi-circular reflectors seen in the figure are in the correct positions, with no indication of numerical dispersion. Theory predicts that the migration impulse response in two-dimensional space carries a 45-degree phase shift (Claerbout, 1985), so a symmetrical input pulse generates a phase-distorted migration response. The measured migration impulse response in this test (Figure 8) has about 50-degree phase shift.

For velocity changing both laterally and vertically, $c = 1.5 + 0.1x + 0.5z$ km/s, the post-stack migration response of the FCT algorithm to three impulses (five samples per wavelength of the sinusoid pulse, and $\Delta t = 2.6$ ms) is shown in Figure 9. Again, three semi-circular reflectors are in the correct positions, with no indication of numerical dispersion. Here the FCT method gives a good image for reflector dip beyond 90 degrees, but, the amplitudes beyond 90-degree appear weak. Note that due to the lateral velocity variation, the centers of the semi-circular reflectors are shifted to the right.

Salt-dome structure model

Figure 10 shows a reflector structure modeling the boundary of an overhanging salt dome with dip as large as 125 degrees. The input zero-offset time section for two different velocity models (Figure 11) was obtained by a Kirchhoff modeling program. For both sections, the wavelet is a symmetric Ricker wavelet with dominant frequency of 15 Hz. The first velocity model has a constant gradient in the vertical direction, and the second velocity model has a constant gradient in a direction intermediate to horizontal and vertical. Figures 12 and 15 show the results of FCT reverse-time depth migration applied to each of the zero-offset synthetic data sets in Figure 11. The spatial steps Δx and Δz in these tests are 0.012 km; the time step Δt is 1.7 ms for the constant vertical velocity gradient, and 1.5 ms for the diagonal-gradient case.

Figure 11a gives the synthetic data for velocity linearly increasing with depth, $c(z) = 1.5 + 0.9z$ km/s. The second-order FCT migrated section (Figure 12) shows accurate imaging of the dome structure, with no indication of grid dispersion. The broadening of deeper events is expected for the increase of velocity with depth. Second-order conventional finite-difference migration applied to the same zero-offset data with the same spacing has strong numerical dispersion (Figure 13). When I

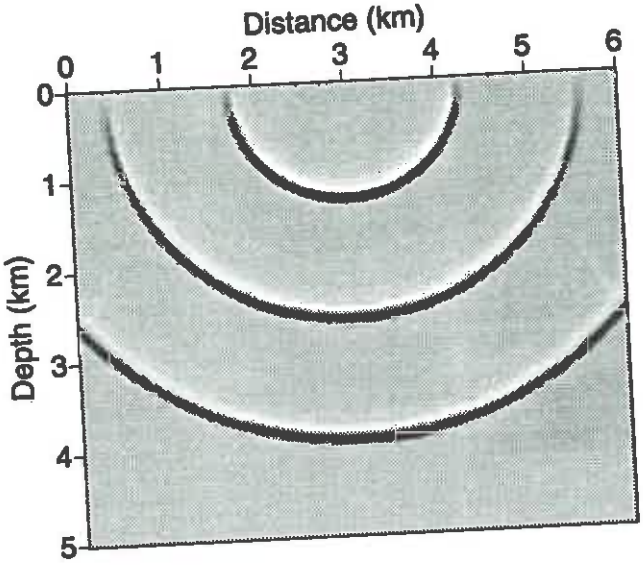

FIG. 8. Migration impulse responses by the flux-corrected transport method for a constant background velocity of 2.0 km/s and constant density.

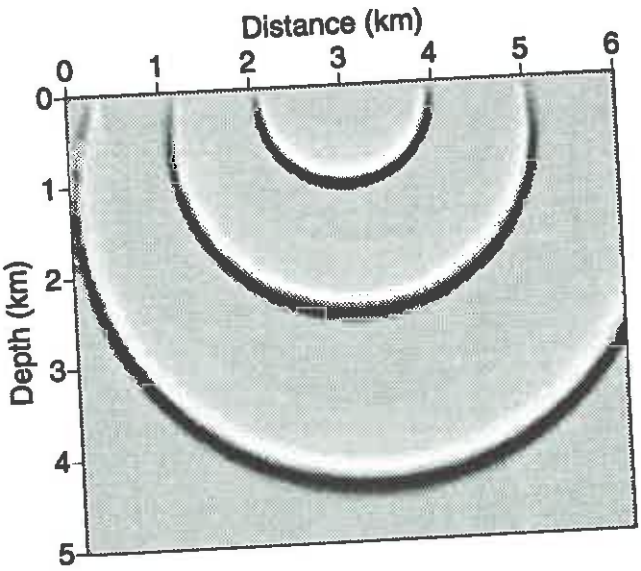

FIG. 9. Migration impulse response for velocity linearly increasing with depth and horizontal distance, $c = 1.5 + 0.1x + 0.5z$ km/s, and constant density.

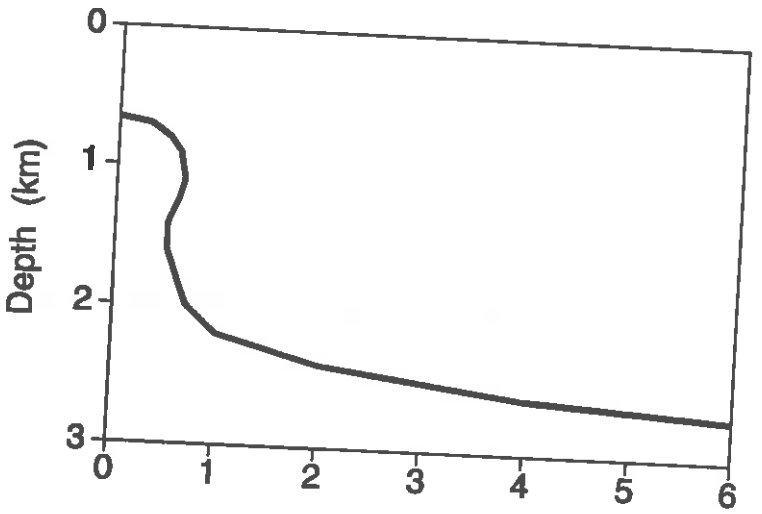

FIG. 10. Reflector model used to generate synthetic data in Figure 11 for the tests described in Figures 12 through 15.

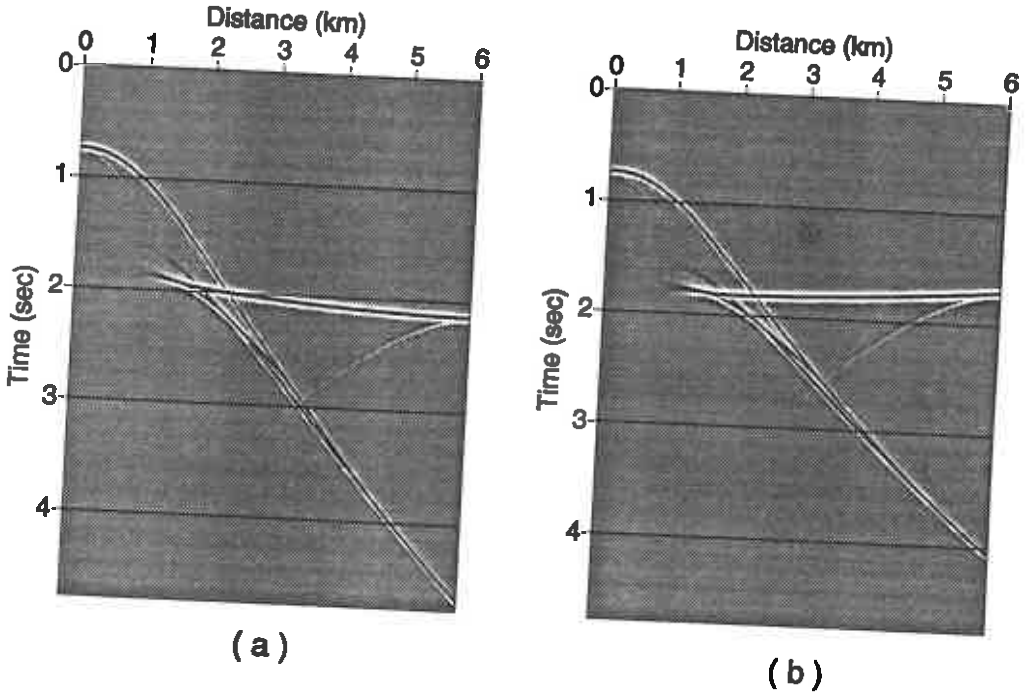

FIG. 11. Zero-offset synthetic time sections generated by Kirchhoff modeling for (a) velocity linearly increasing with depth, $c(z) = 1.5 + 0.9z$ km/s, and (b) velocity model with linear variation in (x, z), $c(x) = 1.5 + 0.1x + 0.9z$ km/s.

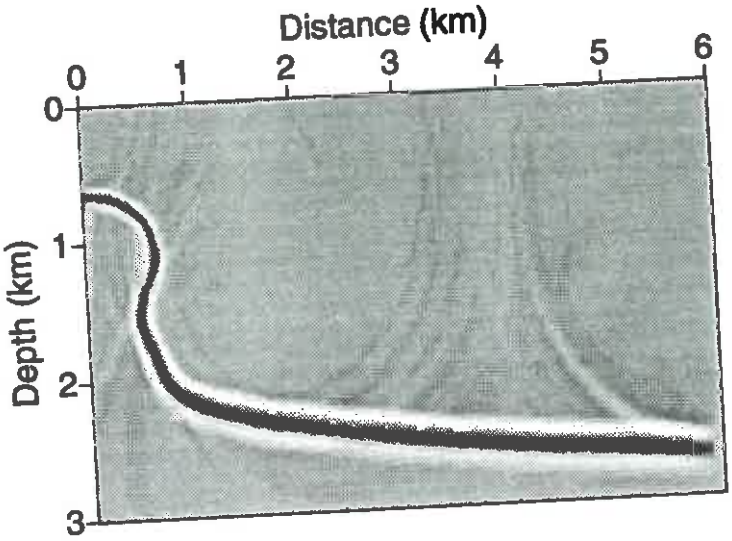

FIG. 12. FCT migration for velocity model $c(z) = 1.5 + 0.9z$ km/s, and constant density. $\Delta x = \Delta z = 0.012$ km.

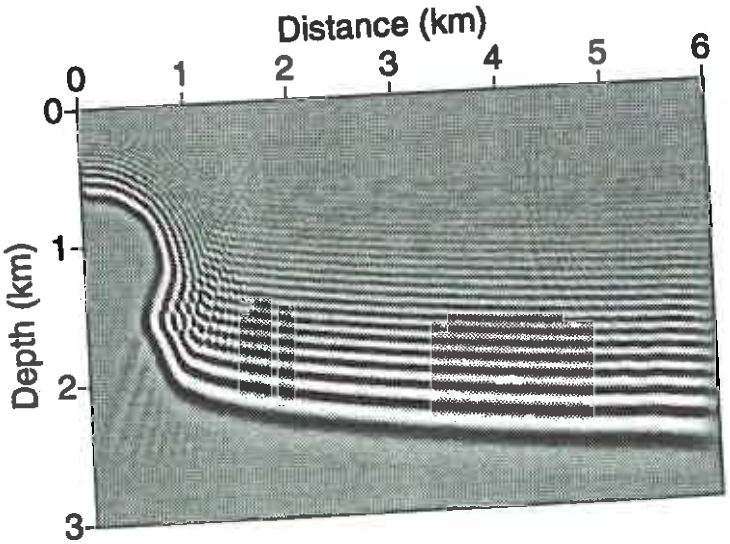

FIG. 13. Second-order conventional finite-difference migration for the same model and on the same grid as for the FCT migration in Figure 12.

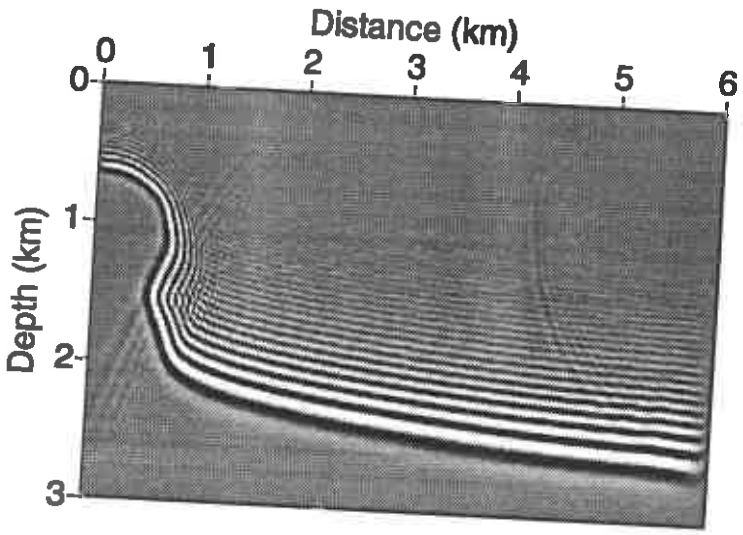

FIG. 14. Second-order conventional finite-difference migration for the same model as that for the FCT migration in Figure 12 and on the finer grid. Δx=Δz=0.008 km.

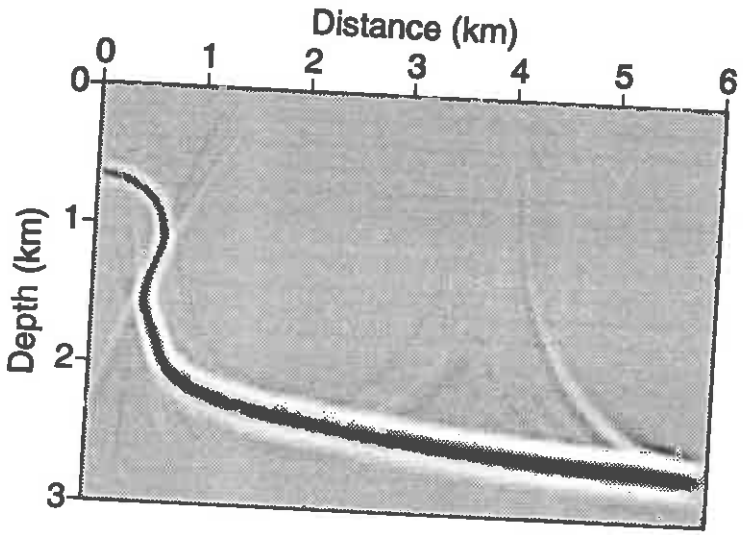

FIG. 15. FCT migration for velocity model $c(z) = 1.5 + 0.1x + 0.9z$ km/s, and constant density. $\Delta x = \Delta z = 0.012$ km.

reduce the grid size to 0.008 km, which has about the same computation cost as that for the FCT method on the coarser grid, the migrated section obtained by the conventional method still has strong numerical dispersion (Figure 14).

For the second model, wherein velocity varies both laterally and vertically, $c(x) = 1.5 + 0.1x + 0.9z$ km/s, again migration by the FCT method gives clear and correct reflector position for all dips with no numerical dispersion (Figure 15).

VSP data

Figure 16 shows a fault structure used for generating synthetic, acoustic VSP data. The velocity is 5.2 km/s in the first layer (shallow part), and 7.5 km/s in the second layer (deep part). The line source is located at $x = 0.666$ km on the surface and the receiver borehole is at $x = 3.75$ km.

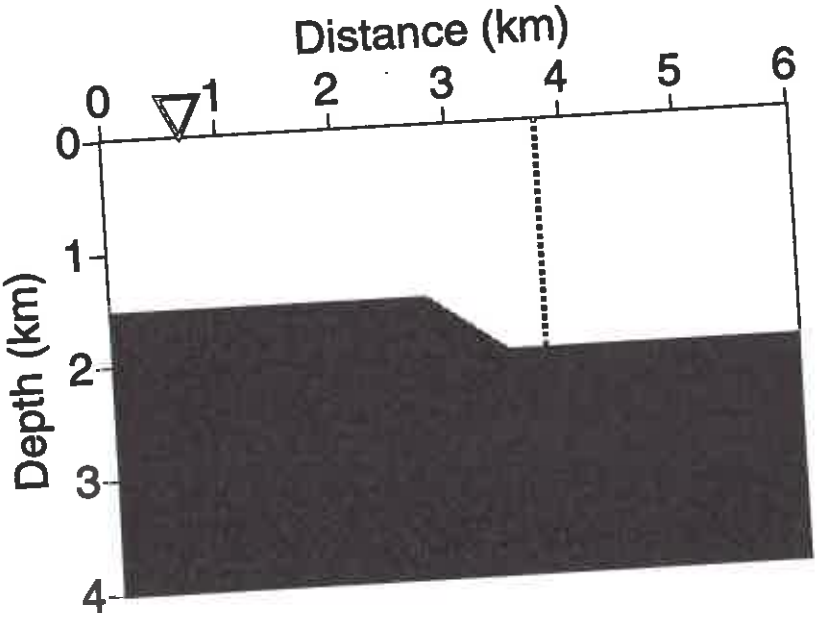

FIG. 16. Velocity model (fault model) used for generating synthetic VSP data.

Figure 17 gives synthetic VSP seismograms for the fault model in Figure 16. Figure 17a is generated by applying the zero-gradient reflection boundary condition on the surface and absorbing boundary condition on the side and lower boundaries. For the seismogram in Figure 17b, a zero-gradient reflection boundary condition is applied to all the boundaries. Figure 17a shows that only the direct arrival, reflection from the interface and the reflection from the surface can be clearly identified. Weak waves have been reflected from the sides or bottom. Figure 17c shows VSP data from the physical modeling of the same VSP and fault geometry. The physical model has dimension of 72×48 inch^2. In it, the upper layer (Lexan) has a P-wave velocity 5.2

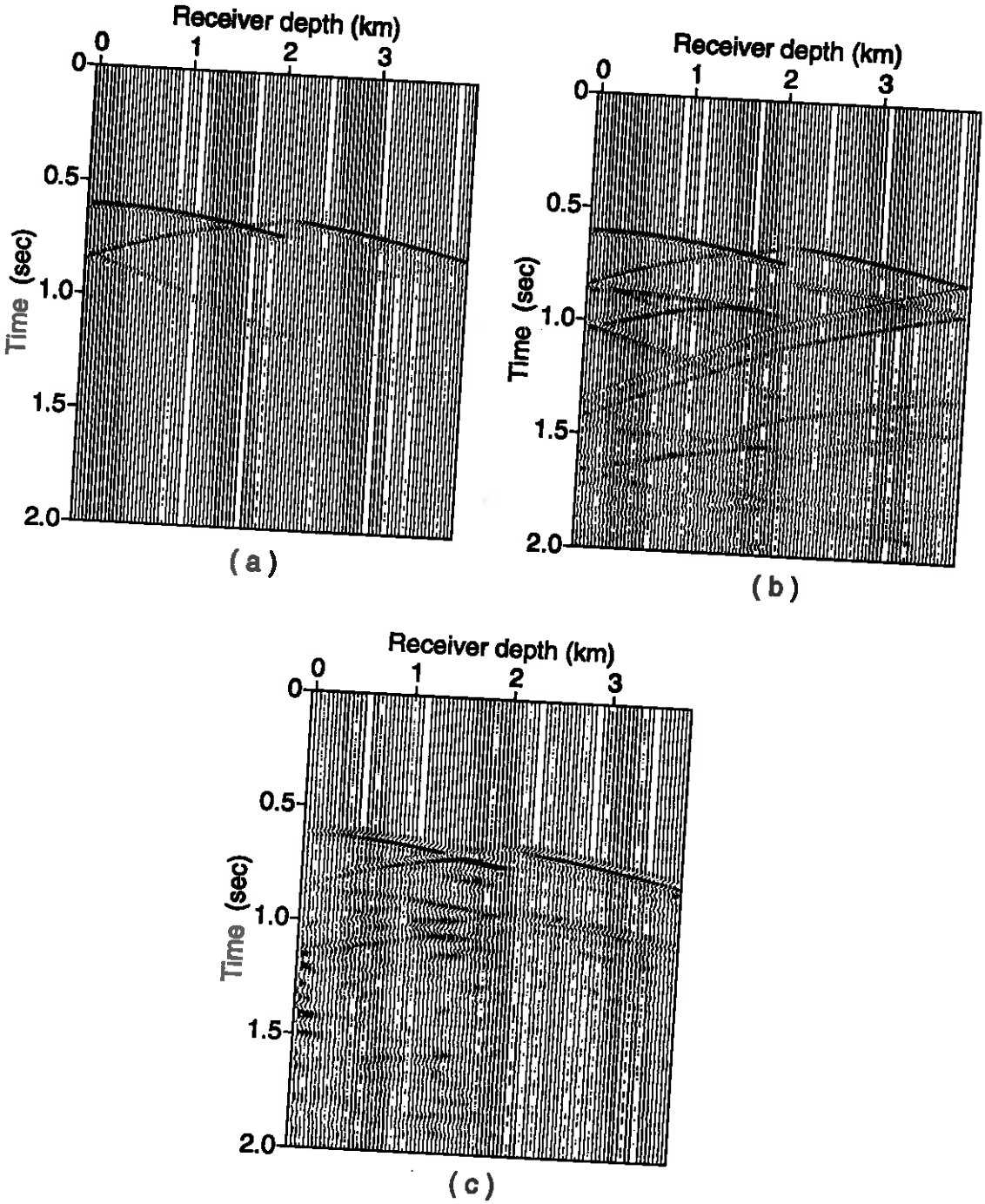

FIG. 17. VSP seismograms. (a) and (b) are synthetic seismograms generated by the FCT finite-difference method. (a) Zero-gradient boundary condition on surface and, absorbing boundary condition on side and lower boundaries; (b) zero-gradient condition on each boundary. (c) Physical modeling data.

km/s, and the lower layer (Plexiglass) has a higher P-wave velocity 7.2 km/s. A vertical-displacement source is located on the surface, 8 inches from the upper left corner, and the borehole containing vertical-displacement receivers is on the vertical line 45 inches from the left edge. The synthetic VSP data for reflection boundary conditions (Figure 17b) compares favorably with the physical modeling VSP data (Figure 17c). One source of difference will be that the physical-model data contain S-waves.

CONCLUSIONS

Too coarse a grid used in finite-difference wavefield extrapolation, causes both numerical dispersion and loss of resolution. The FCT method is effective in curing the dispersion problem; the resolution problem still remains. As we have seen, the FCT finite-difference modeling and reverse-time depth migration can handle arbitrary velocity and density fields. Although the additional FCT steps used for the second-order wave equation require about 1.8 times more computation than does the conventional finite-difference step, the FCT method offers the opportunity to use a coarse grid to obtain accuracy in wavefield extrapolation that is comparable to that obtained by conventional finite-difference methods on finer grid. From the comparison of the FCT technique for the second-order wave equation with that for the first-order wave equation (Fei, 1993), I conclude that both FCT algorithms have about the same computational cost. However, the advantage of the FCT method for the second-order wave equation is that the corrective stage can be easily embedded in existing finite-difference algorithms.

In any case, 2-D finite-difference reverse-time depth migration is still slower than other methods such as Gaussian beams. 3-D modeling and single-pass 3-D migration might offer more computational benefit for the reverse-time FCT approach; this remains to be investigated.

ACKNOWLEDGMENTS

Thanks to Professor Ken Larner for his suggestions and guidance. I also thank Professor John Scales for helpful discussions and comments. I appreciate the VSP group at Colorado School of Mines for providing the physical modeling data.

REFERENCES

Alford, R., Kelly, K., and Boore, D., 1974, Accuracy of finite-difference modeling of the acoustic wave equation: Geophysics, **39**, 834-842.

Boris, J., and Book, D., 1973, Flux-corrected transport. I. SHASTA, A fluid transport algorithm that works: J. Comput. Phys., **11**, 38-69.

Claerbout, J., 1985, Imaging of the earth's interior: Blackwell Scientific Publications, Inc.

Clayton, R., and Engquist, B., 1980, Absorbing side boundary conditions for wave equation migration: Geophysics, **45**, 895-904.

Dablain, M. A. 1986, The application of high-order differencing to the scalar wave equation: Geophysics, **51**, 54-66.

Fei, T., 1993, Seismic modeling and reverse-time depth by flux-corrected transport: **CWP-128**, Colorado School of Mines.

Kelly, K., Ward, R., Treitel, S., and Alford, R., 1976, Synthetic seismograms: a finite-difference approach: Geophysics, **41**, 2-27.

APPENDIX A: FLUX-CORRECTED TRANSPORT

The flux-corrected transport (FCT) method (Boris and Book, 1973) was developed primarily for solving the first-order continuity equation in hydrodynamics. In Appendix A of Fei (1993), I showed the prescription for applying the method to the first-order equations in acoustic wave propagation. For the second-order acoustic-wave equation, the *diffusive* and *anti-diffusive flux* are computed differently, and the FCT algorithm proceeds as follows.

1. Advance the solutions by a standard second-order finite-difference method and obtain $P^{n+1}_{i,j,k}$ at time level $n+1$ ($P^{n+1}_{i,j,k}$ is the value of P at the time sample $n+1$, x-coordinate sample i, y-coordinate sample j and z-coordinate sample k).

2. Compute *diffusive fluxes* at time level n :

$$
\begin{aligned}
Q^{\,n}_{x\,i+1/2,j,k} &= \eta_1(P^n_{i+1,j,k} - P^n_{i,j,k} - P^{n-1}_{i+1,j,k} + P^{n-1}_{i,j,k}) \quad 0 \le \eta_1 \le 1 \\
Q^{\,n}_{y\,i,j+1/2,k} &= \eta_1(P^n_{i,j+1,k} - P^n_{i,j,k} - P^{n-1}_{i,j+1,k} + P^{n-1}_{i,j,k}) \quad 0 \le \eta_1 \le 1 \\
Q^{\,n}_{z\,i,j,k+1/2} &= \eta_1(P^n_{i,j,k+1} - P^n_{i,j,k} - P^{n-1}_{i,j,k+1} + P^{n-1}_{i,j,k}) \quad 0 \le \eta_1 \le 1, \quad \text{(A-1)}
\end{aligned}
$$

   where η_1 is a coefficient that varies with position. In typical applications, η_1 might vary linearly, with values between 0.02 and 0.1. This function is empirically determined from a few numerical experiments by considering the amplitude treatment of events for small scale problems. Results are not critically sensitive to the choice of η_1 once it is close to a good value.

3. Compute diffusive fluxes at time level $n+1$, for use in step 6 below :

$$
\begin{aligned}
\tilde{Q}^{\,n+1}_{x\,i+1/2,j,k} &= \eta_2(P^{n+1}_{i+1,j,k} - P^{n+1}_{i,j,k} - P^n_{i+1,j,k} + P^n_{i,j,k}) \quad 0 \le \eta_2 \le 1 \\
\tilde{Q}^{\,n+1}_{y\,i,j+1/2,k} &= \eta_2(P^{n+1}_{i,j+1,k} - P^{n+1}_{i,j,k} - P^n_{i,j+1,k} + P^n_{i,j,k}) \quad 0 \le \eta_2 \le 1 \\
\tilde{Q}^{\,n+1}_{z\,i,j,k+1/2} &= \eta_2(P^{n+1}_{i,j,k+1} - P^{n+1}_{i,j,k} - P^n_{i,j,k+1} + P^n_{i,j,k}) \quad 0 \le \eta_2 \le 1, \quad \text{(A-2)}
\end{aligned}
$$

   with a similar choice of η_2 as for η_1 in step 2.

Dispersion elimination

4. Modify (i.e. *diffuse*) the solution P using Q_x, Q_y and Q_z; this process smooths the solution (also causes some loss of amplitude) and eliminates the dispersive ripples:

$$\begin{aligned} \tilde{P}^{n+1}_{i,j} = P^{n+1}_{i,j} \quad &+ \quad (Q^{n-1}_{x_{i+1/2,j,k}} - Q^{n-1}_{x_{i-1/2,j,k}}) \\ &+ \quad (Q^{n-1}_{y_{i,j+1/2,k}} - Q^{n-1}_{y_{i,j-1/2,k}}) \\ &+ \quad (Q^{n-1}_{z_{i,j,k+1/2}} - Q^{n-1}_{z_{i,j,k-1/2}}). \end{aligned} \tag{A-3}$$

5. Compute diffusive fluxes with the diffused $\tilde{P}^{n+1}$ and P^n:

$$\begin{aligned} X_{i+1/2,j,k} &= (\tilde{P}^{n+1}_{i+1,j,k} - P^n_{i+1,j,k}) - (\tilde{P}^{n+1}_{i,j,k} - P^n_{i,j,k}) \\ Y_{i,j+1/2,k} &= (\tilde{P}^{n+1}_{i,j+1,k} - P^n_{i,j+1,k}) - (\tilde{P}^{n+1}_{i,j,k} - P^n_{i,j,k}) \\ Z_{i,j,k+1/2} &= (\tilde{P}^{n+1}_{i,j,k+1} - P^n_{i,j,k+1}) - (\tilde{P}^{n+1}_{i,j,k} - P^n_{i,j,k}). \end{aligned} \tag{A-4}$$

6. *Anti-diffuse* the solution as follows, and obtain the corrected solution for P :

$$\begin{aligned} P^{n+1}_{i,j,k} = \tilde{P}^{n+1}_{i,j,k} \quad &- \quad (X^c_{i+1/2,j,k} - X^c_{i-1/2,j,k}) - (Y^c_{i,j+1/2,k} - Y^c_{i,j-1/2,k}) \\ &- \quad (Z^c_{i,j,k+1/2} - Z^c_{i,j,k-1/2}), \end{aligned} \tag{A-5}$$

where

$$\begin{aligned} X^c_{i+1/2,j,k} &= S_x \max\{0, \min[S_x X_{i-1/2,j,k}, \mathrm{abs}(\tilde{Q}^{n+1}_{x_{i+1/2,j,k}}), S_x X_{i+3/2,j,k}]\}, \\ Y^c_{i,j+1/2,k} &= S_y \max\{0, \min[S_y Y_{i,j-1/2,k}, \mathrm{abs}(\tilde{Q}^{n+1}_{y_{i,j+1/2,k}}), S_y Y_{i,j+3/2,k}]\}, \\ Z^c_{i,j,k+1/2} &= S_z \max\{0, \min[S_z Z_{i,j,k-1/2}, \mathrm{abs}(\tilde{Q}^{n+1}_{z_{i,j,k+1/2}}), S_z Z_{i,j,k+3/2}]\}, \\ S_x &= \mathrm{sign}\{\tilde{Q}^{n+1}_{x_{i+1/2,j,k}}\}, \\ S_y &= \mathrm{sign}\{\tilde{Q}^{n+1}_{y_{i,j+1/2,k}}\}, \\ S_z &= \mathrm{sign}\{\tilde{Q}^{n+1}_{z_{i,j,k+1/2}}\}. \end{aligned}$$

Seismic modeling in anistropic media

Tong Fei

Seismic modeling in anisotropic media

Tong Fei

ABSTRACT

Realistic modeling of elastic wave propagation in the Earth requires consideration of the inhomogeneity and, in some applications, anisotropy. Finite-difference modeling based on the full elastic-wave equation can take such factors into account.

Here, through a change of dependent variables, I first replace the second-order elastic wave equations by a set of first-order partial differential equations, which I then solve by finite-differences upgraded by the flux-corrected transport (FCT) method. Computed snapshots of the two-dimensional elastic wavefield and synthetic seismograms for inhomogeneous models of anisotropic media indicate that this method gives solutions without numerical dispersion even when as few as five samples per dominant wavelength are used.

INTRODUCTION

Finite-difference solutions to the wave equation are useful tools in wave extrapolation. The methods can address a full range of issues – arbitrary velocity variation, attenuation, turning waves, shear waves and anisotropy.

Finite-difference schemes for the wave equation often suffer from undesirable ripples, particularly near large gradients in wavefields or when too coarse a computation grid is used. Alford et al. (1974), Kelly et al. (1976) and Dablain (1986) have studied the numerical dispersion existing in finite-difference methods. To eliminate the grid dispersion in the second-order finite-difference method, Kelly and Alford stated that at least 11 points per upper half-power wavelength must be used, and Dablain concluded that 8 points per wavelength at Nyquist frequency must be used. Consistent with Kelly, Alford and Dablain's conclusions, Fei (1993b) expressed the computation accuracy in terms of number of points per *dominant* wavelength (typically about twice the upper half-power wavelength) and found that about 18 to 20 points per dominant wavelength must be used for the conventional second-order method. To reduce the computational requirements in finite-difference modeling and migration, Fei (1993a, 1993b) adapted the flux-corrected transport (FCT) method, developed by Boris and Book (1973) for solving the continuity equation in hydrodynamics, to

seismic applications for acoustic media. The FCT algorithm can treat strong gradients, shocks and impulses, without the usual dispersively generated ripples, even for five or fewer points per dominant wavelength. The method thus gains its efficiency because it requires fewer points per wavelength.

In seismic applications, acoustic media are not always applicable. Modeling of amplitude versus offset (AVO) behavior requires treatment of wave propagation in elastic media. Likewise, acoustic-wave modeling cannot yield any information about P- and S-wave conversion. Moreover, since isotropy is not a valid assumption for much of the Earth's subsurface, general seismic modeling and imaging techniques for anisotropic media needs to be developed. Here, I extended the FCT finite-difference modeling technique from acoustic media to elastic and anisotropic media.

THEORY

The key steps in deriving equations used for FCT modeling for acoustic media are given in Fei (1993a). For elastic media, the pattern is similar: (1) define new dependent variables, (2) form nine first-order, so-called *conservative*, equations in these variables, based on the original second-order elastic-wave equation, and (3) apply the FCT technique to the conservative equations.

Equations of motion for elastic media

For elastic media, the three general equations of motion are

$$\rho\frac{\partial^2 u_i}{\partial t^2} = f_i + \frac{\partial}{\partial x_j}\left(\sigma_{ij}\right) \qquad i = 1,2,3, \tag{1}$$

where x_1, x_2 and x_3 are the three Cartesian coordinates (later labeled x, y and z). u_i is the displacement vector, ρ is density, f_i is the source function, and σ_{ij} are the components of the stress tensor. By Hooke's law, the stress and strain tensors have the relation $\sigma_{ij} = c_{ijpq}e_{pq}$, where c_{ijpq} are the elastic coefficients. The most general inhomogeneous anisotropic medium is defined by 21 independent components in c_{ijpq}, each of which can vary independently over space. e_{pq} are the components of the strain tensor

$$e_{pq} \equiv \frac{1}{2}\left(\frac{\partial u_p}{\partial x_q} + \frac{\partial u_q}{\partial x_p}\right). \tag{2}$$

Since the strain tensor is symmetric, it has six independent components: e_{11}, e_{22}, e_{33}, e_{12}, e_{13} and e_{23}.

With new dependent variables defined as

$$v_i \equiv \rho\frac{\partial u_i}{\partial t} \qquad i = 1,2,3, \tag{3}$$

and considering the six independent components of strain tensor e_{pq} as the other six dependent variables, equations (1) and (2) can then be replaced by nine first-order partial differential equations. These nine new equations constitute a complete set of equations for doing wave extrapolation by the FCT method, for the most general inhomogeneous, anisotropic elastic media. These equations are

$$\frac{\partial v_i}{\partial t} = f_i + \frac{\partial}{\partial x_j}\left(c_{ijpq} e_{pq}\right) \qquad i = 1, 2, 3, \tag{4}$$

$$\frac{\partial e_{pq}}{\partial t} = \frac{\partial}{\partial x_q}\left(\frac{v_p}{2\rho}\right) + \frac{\partial}{\partial x_p}\left(\frac{v_q}{2\rho}\right) \qquad p, q = 1, 2, 3. \tag{5}$$

Note in definition (3) that the new dependent variables v_i have 90-degree phase shift relative to the variables u_i.

Where the elastic medium is assumed to be isotropic, the c_{ijpq} take the form

$$c_{ijpq} = \lambda \delta_{ij} \delta_{pq} + \mu(\delta_{ip}\delta_{jq} + \delta_{iq}\delta_{jp}), \tag{6}$$

where δ_{ij} is the Kronecker delta. Thus, when the medium is isotropic, c_{ijpq} involves only two independent coefficients, λ and μ, the *Lamé* coefficients. Using relation (6) in the three equations (4), gives

$$\frac{\partial v_i}{\partial t} = f_i + \frac{\partial}{\partial x_j}\left[\lambda \delta_{ij}(e_{11} + e_{22} + e_{33}) + 2\mu e_{ij}\right] \qquad i = 1, 2, 3. \tag{7}$$

With the P-wave velocity $\alpha = \sqrt{\frac{\lambda+2\mu}{\rho}}$ and S-wave velocity $\beta = \sqrt{\frac{\mu}{\rho}}$, equations (7) can be rewritten as

$$\frac{\partial v_i}{\partial t} = f_i + \frac{\partial}{\partial x_j}\left[\rho(\alpha^2 - 2\beta^2)\delta_{ij}(e_{11} + e_{22} + e_{33}) + 2\rho\beta^2 e_{ij}\right] \qquad i = 1, 2, 3. \tag{8}$$

With equations (8) and (5), wave extrapolation by the FCT technique can be accomplished for the most general inhomogeneous, isotropic medium.

The Earth's subsurface is seldom isotropic. In some applications, it is useful to consider the medium as transversely isotropy. Then, the strain and stress relation can be written as

$$\begin{aligned}
\sigma_{11} &= Ae_{11} + (A - 2N)e_{22} + Fe_{33}, \\
\sigma_{22} &= (A - 2N)e_{11} + Ae_{22} + Fe_{33}, \\
\sigma_{33} &= Fe_{11} + Fe_{22} + Ce_{33},
\end{aligned}$$

$$\begin{aligned}\sigma_{23} &= 2Le_{23},\\ \sigma_{13} &= 2Le_{13},\\ \sigma_{12} &= 2Ne_{12},\end{aligned} \tag{9}$$

where A, C, F, L and N are the five independent elastic coefficients that describe a general transversely isotropic isotropic medium, with axis of symmetry in the vertical (x_3) direction. With these strain and stress relations, the three equations of motion for transversely isotropic media, with vertical axis of symmetry, can be written as

$$\frac{\partial v_1}{\partial t} = f_1 + \frac{\partial}{\partial x_1}\Big[Ae_{11} + (A-2N)e_{22} + Fe_{33}\Big] + \frac{\partial}{\partial x_2}\Big[2Ne_{12}\Big] + \frac{\partial}{\partial x_3}\Big[2Le_{13}\Big], \tag{10}$$

$$\frac{\partial v_2}{\partial t} = f_2 + \frac{\partial}{\partial x_1}\Big[2Ne_{12}\Big] + \frac{\partial}{\partial x_2}\Big[(A-2N)e_{11} + Ae_{22} + Fe_{33}\Big] + \frac{\partial}{\partial x_3}\Big[2Le_{23}\Big], \tag{11}$$

$$\frac{\partial v_3}{\partial t} = f_3 + \frac{\partial}{\partial x_1}\Big[2Le_{13}\Big] + \frac{\partial}{\partial x_2}\Big[2Le_{23}\Big] + \frac{\partial}{\partial x_3}\Big[Fe_{11} + Fe_{22} + Ce_{33}\Big]. \tag{12}$$

Using Thomsen (1986) parameters for elastic anisotropic media, the relations between above elastic coefficients and Thomsen parameters are as follow,

$$\begin{aligned}\alpha_0 &= \sqrt{\frac{C}{\rho}},\\ \beta_0 &= \sqrt{\frac{L}{\rho}},\\ \varepsilon &= \frac{A-C}{2C},\\ \gamma &= \frac{N-L}{2L},\\ \delta &= \frac{(F+L)^2-(C-L)^2}{2C(C-L)},\end{aligned} \tag{13}$$

where α_0 is P-wave velocity parallel to the symmetry axis, β_0 is S-wave velocity parallel to that axis, and ε, γ and δ are three dimensionless anisotropy parameters. With these relations, we can convert between the two sets of parameters.

Three first-order equations, (10) through (12), and six others, equations (5) give a complete set of equations for doing wave extrapolation in general transversely isotropic media (with vertical axis of symmetry) by the FCT technique.

Flux-corrected transport

For the most general elastic media, the FCT technique is basically the same as that for acoustic media. Conceptually, the method consists of two major stages — a *transport* stage (Stage I), followed by an *anti-diffusive* or corrective stage (Stage II). Interaction of these two stages enables FCT algorithms to do the wavefield extrapolation with no numerical dispersion.

In the transport stage, a standard finite-difference method is used to advance the solution. In this stage, the amplitude ripples of numerical dispersion arise if too coarse a grid is used. Stage II is devoted to correcting the numerical dispersion introduced in Stage I. In Stage II, a corrective *diffusion* step is applied to the solutions obtained in Stage I, and then an oppositing *anti-diffusion* step is applied where the diffusion was not needed.

The difference between the elastic FCT and acoustic FCT algorithms is that for acoustic media, the FCT corrections need only apply to one dependent variable, while for elastic media, the FCT corrections should be applied to three dependent variables, v_1, v_2 and v_3. When v_1, v_2 and v_3 are corrected, e_{ij} can then be directly computed from equation (5). In Appendix A of Fei (1993a), the FCT procedures for solving the first-order acoustic-wave equations were given. The same procedures can be equally applied to the first-order elastic-wave equations. For wave propagation in acoustic media, Fei (1993b) also showed that the FCT method could be formulated to work directly on the second-order acoustic-wave equation, and that formulation should hold for the elastic-wave equations as well. However, I prefer working with the first-order elastic-wave equations, as described here, because coding should be easier and the strain tensor is obtained for free.

The promise of this flux-corrected transport technique is that for a given spatial grid size, accuracy of the finite-difference calculation is enhanced. Alternatively, one could do seismic modeling for spatially variable media at less computational effort than that in conventional finite-difference methods, which require a finer grid and smaller time-step to achieve comparable accuracy.

	acoustic medium	*elastic medium*
Transport Stage	1	3.6
Corrective Stage	1.5	4.5
Total	2.5	8.1

Table 8. Comparison of the relative cost of the FCT method for acoustic and elastic media.

Because of the increased complexity of the equations and increased number of dependent variables, the cost of conventional finite-difference solution to the elastic-wave equation is about 3.6 times the cost of finite-difference solution to the acoustic-wave equation. In the FCT method, added cost is required for the corrective stage. Fei

(1993a) stated that, for the acoustic problems, the corrective stage added about 1.5 times the cost of the finite-difference computation, making the full FCT method about 2.5 times the cost of the conventional finite-difference computation (for the same grid size). Satisfyingly, the cost of the corrective stage for each of the three dependent variables in the elastic-wave equation is identical to the cost of the corrective stage for the acoustic case. Therefore, whereas the cost of the conventional finite-difference modeling (i.e. the transport stage of the FCT method) for elastic media is about 3.6 times of that for acoustic media, for the full FCT method, the cost ratio is reduced to about 3.2.

The approximate relative costs are summarized in Table 1. Note in Table 1, that for elastic media the cost of the full FCT method is about 2.3 times that of conventional finite-difference modeling when the same grid size is used in both. However, just as for the acoustic case (Fei, 1993a), the cost of the FCT for 2-D elastic wave modeling will be about a sixteenth that for conventional finite-difference modeling because the FCT method can yield comparable accuracy on a coarser grid.

NUMERICAL EXAMPLES

I tested the FCT algorithm on two-dimensional forward problems for both homogeneous and inhomogeneous elastic, isotropic media, and on layered, transversely isotropic media. For each medium, P- and SV-waves, as well as SH-wave, are computed. In each of the tests, the spatial steps Δx and Δz are 0.02 km, and the time step Δt is chosen to satisfy a conventional stability condition.

Test results show that, as with acoustic media, for elastic media the FCT method can also generate wavefields without numerical dispersion, even for as few as five points per dominant wavelength.

Snapshots for isotropic media

Figures 1 and 2 show the snapshots at 0.64 s for two elastic isotropic media with a constant density 2.4 g/cm^3. The line source, with a 20-Hz Ricker wavelet assigned to force components f_1, f_2 and f_3, is located at (2.5 km, 2.5 km). For this source function, the corresponding points per dominant S-wavelength are about 4 to 6, depending on the velocity of the medium, while for P-wave, the points per dominant wavelength are about 8 to 10. Force components f_1 and f_3 are for generating the P- and SV-waves, while the force component f_2 is for generating the SH-wave. The directions of the force are indicated in Figure 1.

Figure 1, for a homogeneous medium, shows expected circular P- and S-waves with the wavefront at their correct positions. Figure 2 shows the wavefront behavior in an inhomogeneous medium with linear velocity variation. The P-wave velocity is $v_p = 1.5 + 0.1x + 0.5z$ km/s, and the S-wave velocity is $v_s = 1.0 + 0.1x + 0.4z$ km/s, where x is the lateral direction and z is depth. Note that the wavefronts of the P-, SV- and SH-waves in Figure 2 propagate faster in directions of increasing velocity.

Both figures show that applying the FCT method to elastic isotropic media generates wavefield snapshots with no numerical dispersion.

Material	α_0 (km/s)	β_0 (km/s)	ε	δ	γ	ρ (g/cm^3)
Sandstone-shale	3.009	1.654	0.013	-0.001	0.0035	2.34
Mesaverde-shale	3.749	2.621	0.128	0.078	0.1	2.92
Cotton Valley shale	4.721	2.89	0.135	0.205	0.18	2.64
Limestone-shale	3.306	1.819	0.134	0.0	0.156	2.44
Taylor sandstone	3.368	1.829	0.11	-0.035	0.255	2.5
Anisotropic-shale	2.745	1.508	0.103	-0.001	0.345	2.34
Anisotropic*	2.0	0.894	0.0	-0.241	0.4	2.4
Mesaverde clayshale	3.928	2.055	0.334	0.73	0.575	2.59
Gypsum-weathered material	1.911	0.795	1.161	-0.14	2.781	2.35

Table 9. Thomsen parameters for several materials (Thomsen, 1986). * Medium with Thomsen parameters designed here to test wavefront behavior for ε=0, and with relatively large δ and γ.

Snapshots for transversely isotropic media

Each of Figures 3 through 5 shows a set of nine wavefield snapshots for waves from a line source in a transversely isotropic medium, with vertical axis of symmetry and constant Thomsen parameters (Thomsen, 1986). Table 2 gives the values of the Thomsen parameters for the different materials tested here. For all cases, the same source function and location used for the examples in Figures 1 and 2 has been used here.

Figure 3 shows sets of snapshots for three media considered to be mildly anisotropic, sandstone-shale, Mesaverde shale and Cotton-Valley shale. Figure 4 gives the wavefield snapshots for limestone-shale, Taylor sandstone and anisotropic-shale. For these moderately anisotropic media, the weak triplication behavior can be seen in the SV-wavefronts. Figure 5 exhibits the wavefront behavior for examples of media with extreme anisotropy, a medium with α_0=2.0, β_0=0.894, ε=0.0, γ=0.4, δ=-0.241 and ρ=2.4 g/cm^3, Mesaverde clayshale and gypsum-weathered material. Strong triplications in the SV-wavefronts are evident.

Tested examples given here indicate that the FCT method also works well for seismic modeling in anisotropic media: the method generates wavefields with no indication of numerical dispersion.

Snapshots in a layered medium

Figure 6 shows a 2-D earth model with three layers. Each layer is homogeneous. The snapshots in Figures 7 through 9 have been generated at times t=0.48, 0.6, and

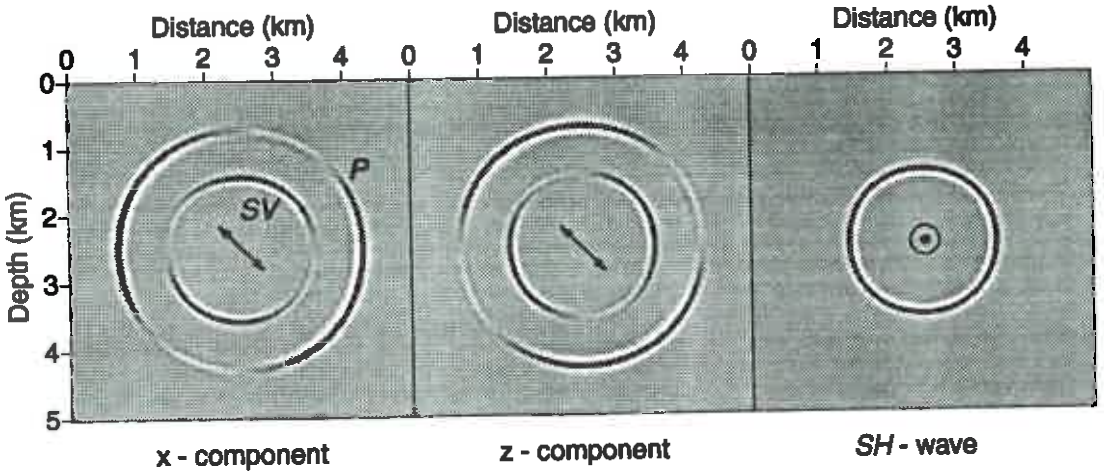

FIG. 1. Snapshots for a homogeneous elastic, isotropic medium with P-wave velocity of 3.0 km/s, and S-wave velocity of 1.8 km/s. The density is a constant, 2.4 g/cm^3.

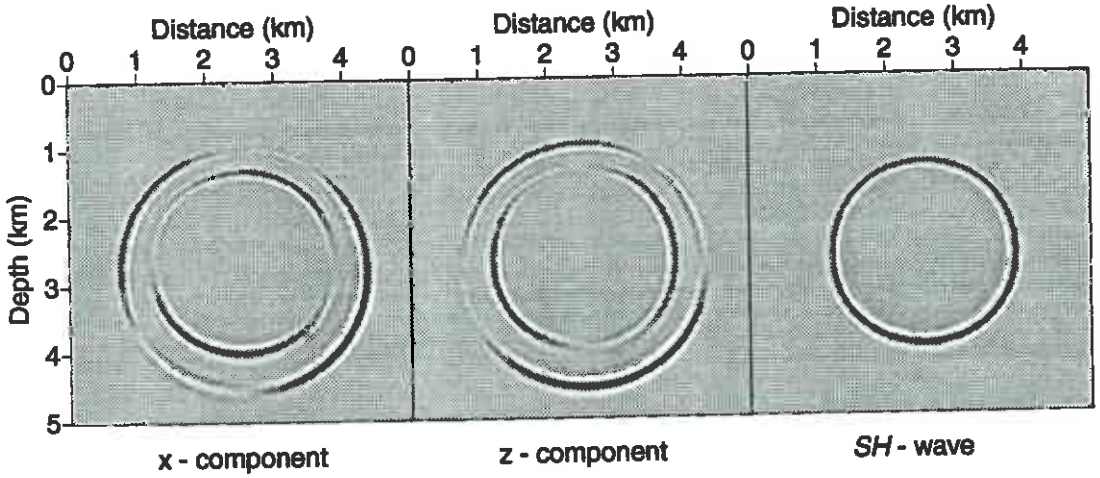

FIG. 2. Snapshots for an elastic isotropic medium with linear velocity variation. P-wave velocity is $v_p = 1.5+0.1x+0.5z$ km/s, and S-wave velocity $v_s = 1.0+0.1x+0.4z$. The density is a constant 2.4 g/cm^3.

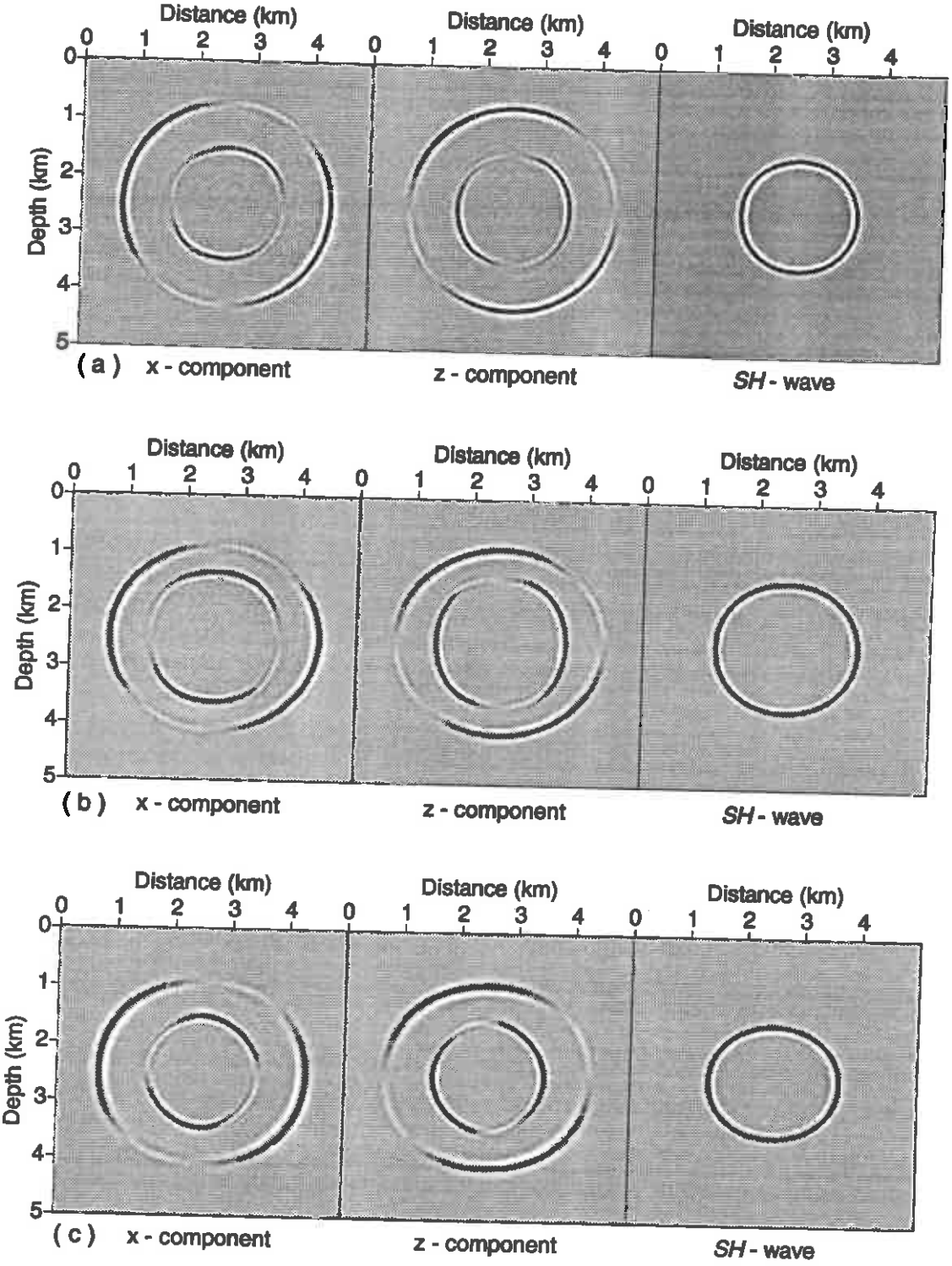

FIG. 3. Wavefield snapshots for (a) sandstone-shale; (b) Mesaverde shale; and (c) Cotton Valley shale.

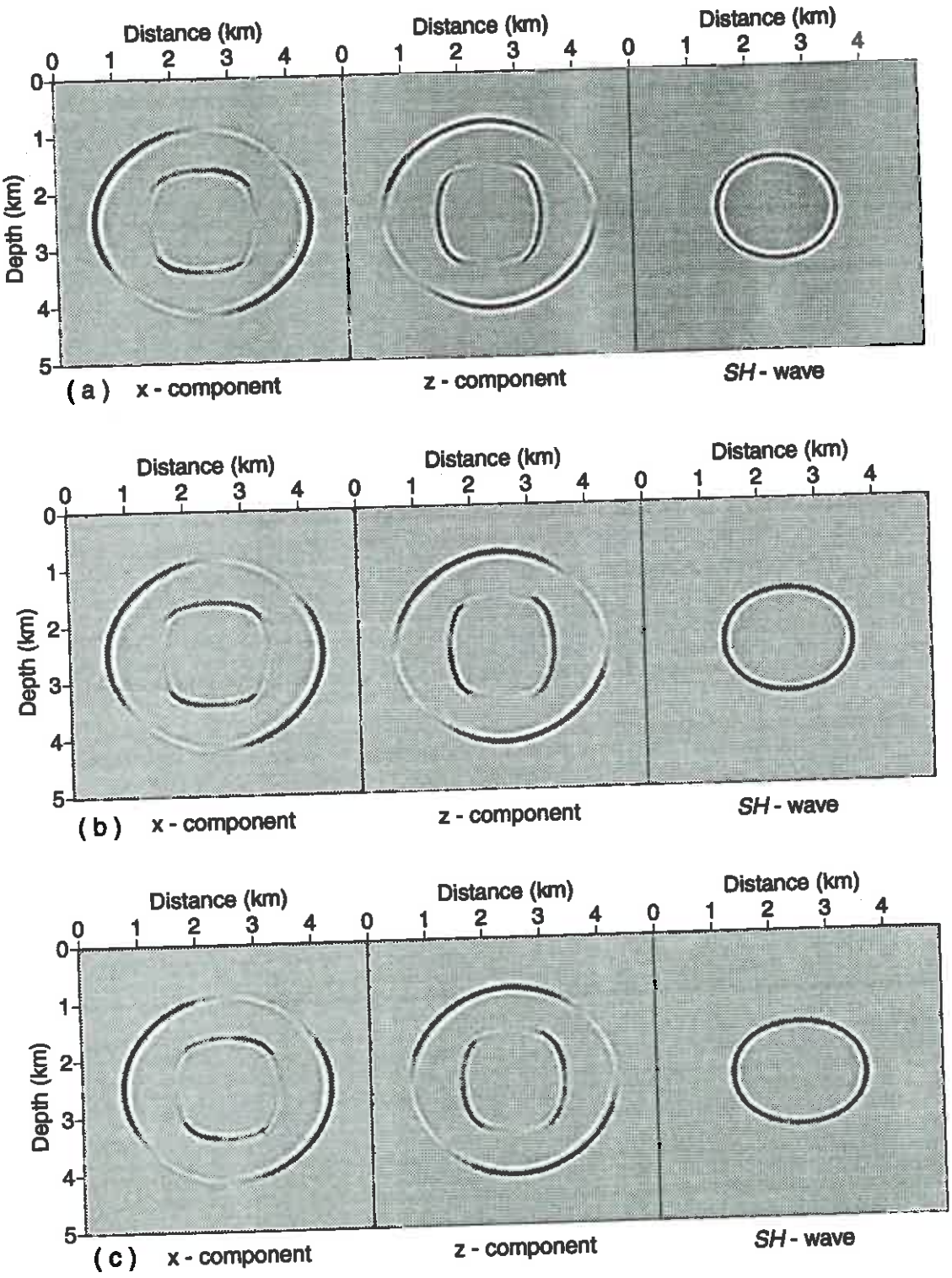

FIG. 4. Wavefield Snapshots for (a) limestone-shale; (b) Taylor sandstone; and (c) anisotropic shale.

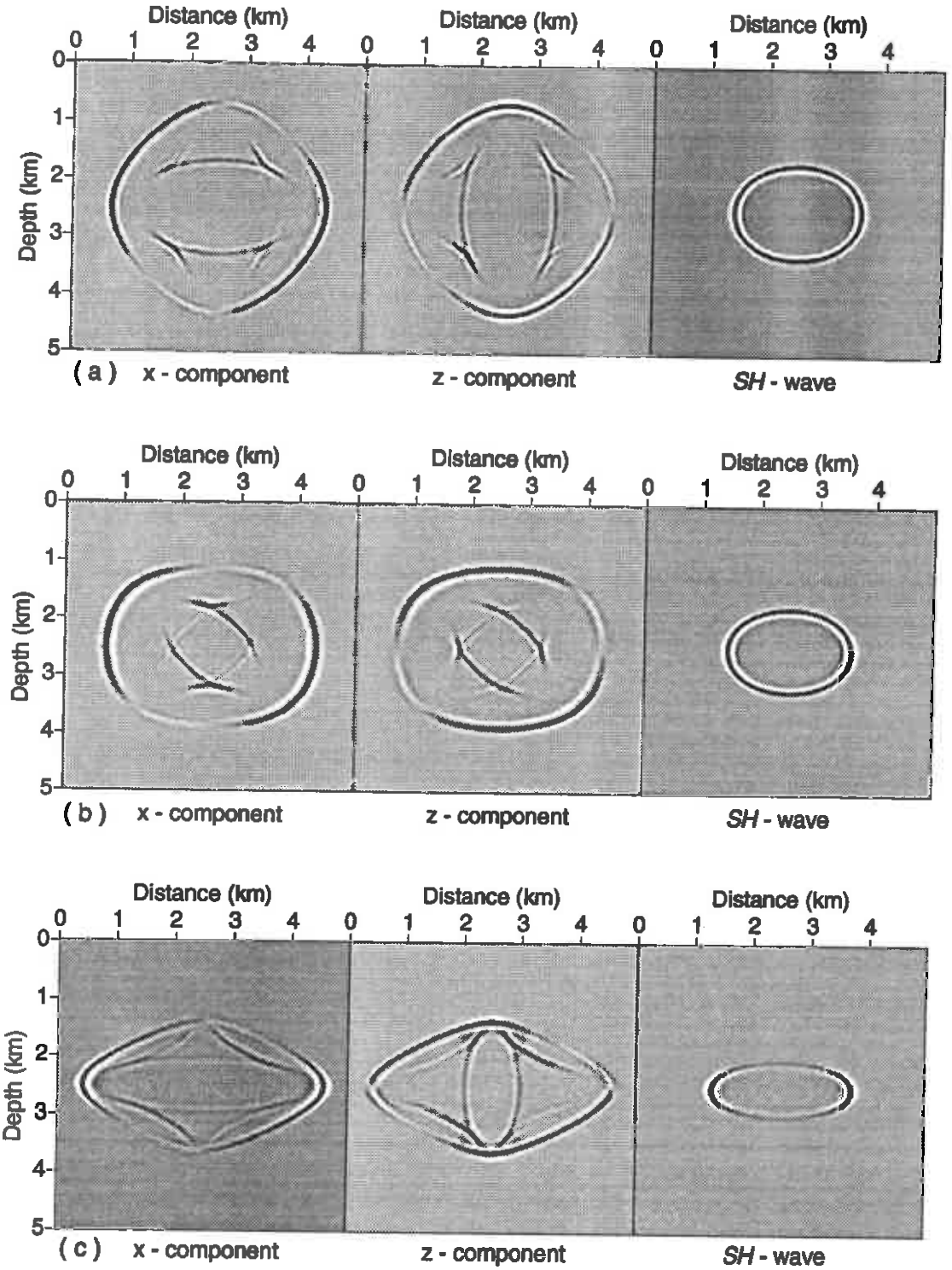

FIG. 5. Wavefield snapshots for media that are considered strongly anisotropic. (a) medium with α_0=2.0, β_0=0.894, ε=0.0, γ=0.4, δ=-0.241 and ρ=2.4 g/cm^3; (b) Mesaverde clayshale; and (c) gypsum-weathered shale.

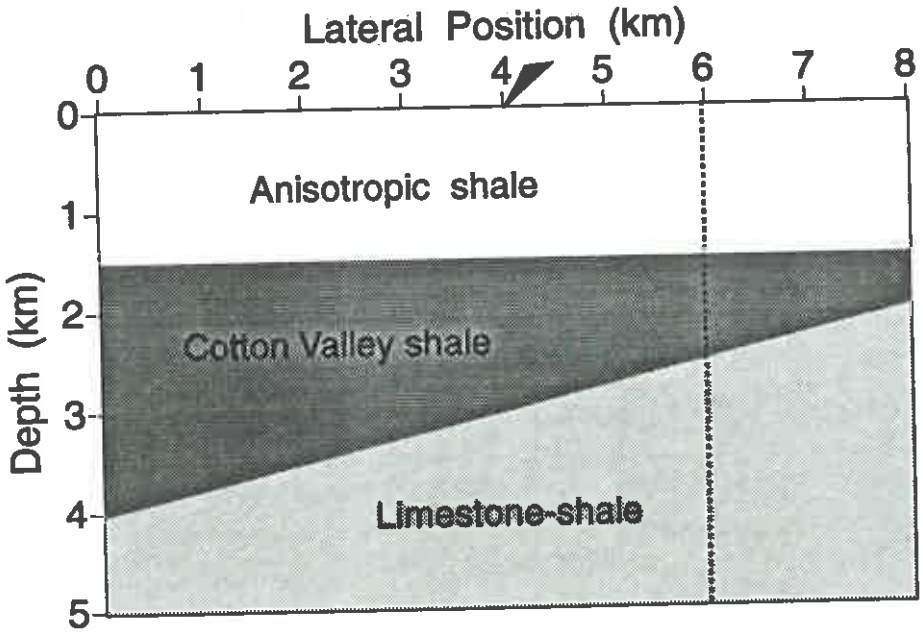

FIG. 6. Earth model used for generating the wavefield snapshots, synthetic surface reflection seismograms and VSP seismograms shown in Figures 7 through 12. The upper layer is anisotropic shale with low P- and S-wave velocities; the second layer is Cotton Valley shale, which has high velocities, and the third layer is limestone-shale with intermediate velocities. The dashed line is the borehole position.

0.84 s, respectively, with a line source (same as that used for the examples in Figures 1 and 2) located at (3.5 km, 0.8 km).

The snapshots show the evolution of the various (complicated) wavefields for this simple earth model. After the earliest of times, the P- and SV-waves intermingle fully, while the SH-wave propagation is much simpler.

Synthetic seismograms in a layered medium

Figures 10 to 12 show the synthetic surface reflection seismograms and VSP seismograms generated by the FCT method for the layered model in Figure 6. The vertical-displacement line source (20-Hz Ricker wavelet) is located on the surface, at lateral position 4 km (position of black triangle in Figure 6). Also, the source for generating the SH-wave (20-Hz Ricker wavelet) is given at the same location. The receiver line for recording the reflection seismograms is on the surface, and the receiver borehole for recording the VSP seismograms is at lateral position 6 km.

Figure 10a shows the in-line horizontal-motion of the surface reflection seismogram. From the figure, it is seen that both the reflection amplitudes and the phases change with offset. At small offset, hardly any reflection can be observed, because a vertical-displacement source is used. Figure 10b gives the in-line horizontal-motion of the VSP seismogram. The direct arrival in each layers, $\grave{P}$, $\grave{P}\grave{P}$ and $\grave{P}\grave{P}\grave{P}$, and the conversions of the P- and SV-waves at the interfaces, can be clearly identified.

Figure 11a shows the in-line vertical-motion of the surface reflection seismogram. Strong P-wave reflection, with phase changes versus offset, can be observed for all offsets. At small offset, the SV-wave reflection and the reflection from P- and SV-wave conversion cannot be observed. Figure 11b gives the in-line vertical-motion of the VSP seismogram. From this figure, again, we can clearly identify the direct arrival and the P- and SV-wave conversions.

For the SH-wave, the surface reflection seismogram and the VSP seismogram are given in Figure 12a and Figure 12b. Both figures indicate that the SH-wave behaves much simpler than do the P- and SV-waves.

CONCLUSIONS

The FCT seismic modeling applied to the first-order acoustic-wave equation can be applied equally well to the elastic anisotropic media. Rewriting of the elastic-wave equations gives a new set of the first-order partial differential equations, with no additional assumptions. These equations are then amenable to solution by the flux-corrected transport method. The FCT finite-difference modeling presented here was applied to 2-D problems with arbitrary elastic coefficients (or Thomsen parameters) and density fields. Tested results show no numerical dispersion, even when as few as five samples per dominant S-wavelength are used. For a given grid size, the cost of the full FCT method is about 2.3 times that of conventional finite difference modeling. However, the FCT method offers the opportunity to use a coarse grid to

obtain accuracy in wavefield extrapolation that is comparable to that obtained by conventional finite-difference methods, at less computation effort. Therefore, for 2-D problems, the FCT method will cost about a sixteenth of the cost of conventional finite-difference modeling.

Just as for acoustic case (Fei, 1993b), the FCT method can be applied directly to the second-order elastic-wave equations. Moreover, the FCT algorithms for solving first-order and second-order wave equations can both be applied to media with tilted axis of symmetry by rotating the whole set of system equations. The FCT for the first-order wave equations, as is done here, is easier to code. In contrast, an advantage of using the FCT directly for the second-order wave equation is that the corrective step can be readily implemented in existing conventional finite-difference algorithms.

ACKNOWLEDGMENTS

Thanks to Professor Ken Larner for the suggestions and guidance that he gave for this work.

REFERENCES

Alford, R., Kelly, K., and Boore, D., 1974, Accuracy of finite-difference modeling of the acoustic wave equation: Geophysics, **39**, 834-842.

Boris, J., and Book, D., 1973, Flux-corrected transport. I. SHASTA, A fluid transport algorithm that works: J. Comput. Phys., **11**, 38-69.

Clayton, R., and Engquist, B., 1980, Absorbing side boundary conditions for wave equation migration: Geophysics, **45**, 895-904.

Dablain, M. A. 1986, The application of high-order differencing to the scalar wave equation: Geophysics, **51**, 54-66.

Fei, T., 1993a, Seismic modeling and reverse-time depth by flux-corrected transport: **CWP-128**, Colorado School of Mines.

Fei, T., 1993b, Elimination of dispersion in finite-difference modeling and migration: **CWP** project review, this issue, Colorado School of Mines.

Kelly, K., Ward, R., Treitel, S., and Alford, R., 1976, Synthetic seismograms: a finite-difference approach: Geophysics, **41**, 2-27.

Thomsen, L., 1986, Weak elastic anisotropy: Geophysics, **51**, 1954-1966.

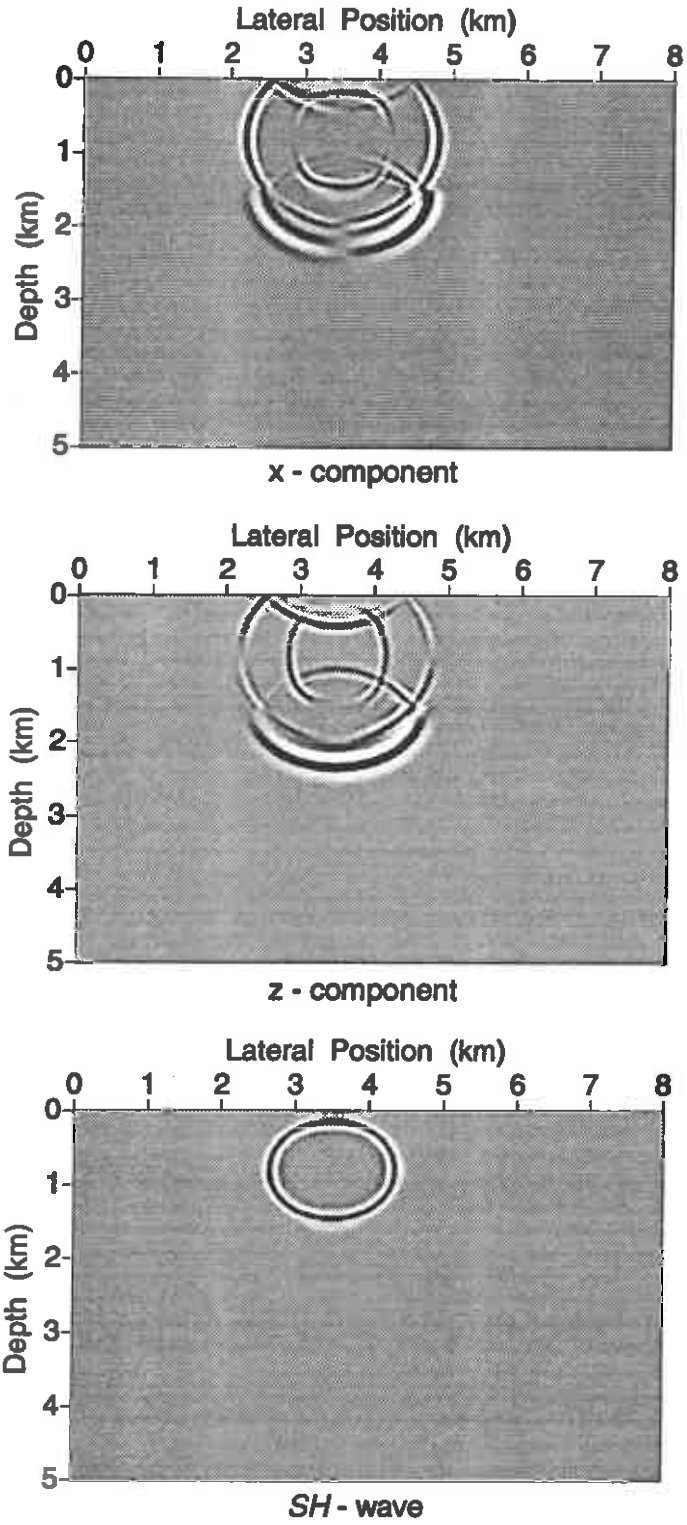

FIG. 7. Snapshots of x-, y-, and z-components at 0.48 s for the layered medium in Figure 6.

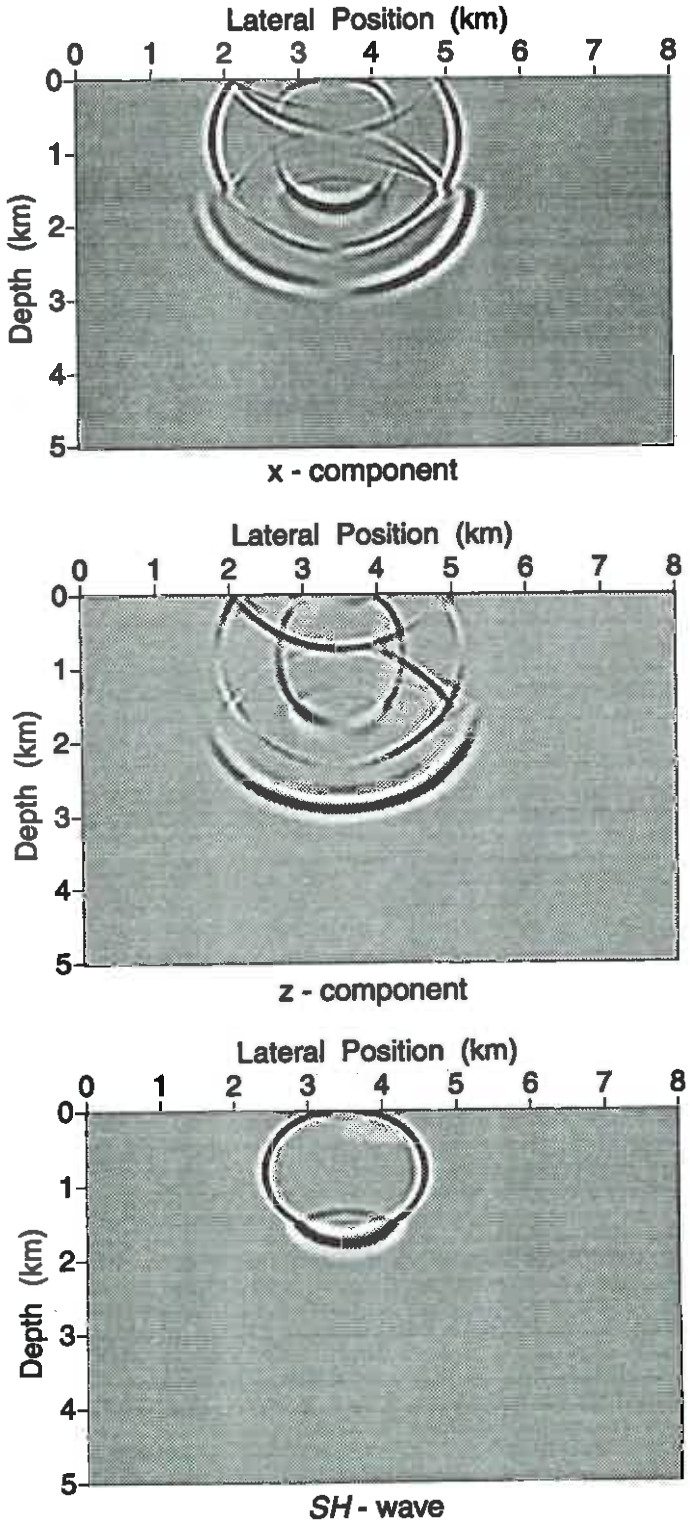

FIG. 8. Snapshots of x-, y-, and z-components at 0.6 s for the layered medium in Figure 6.

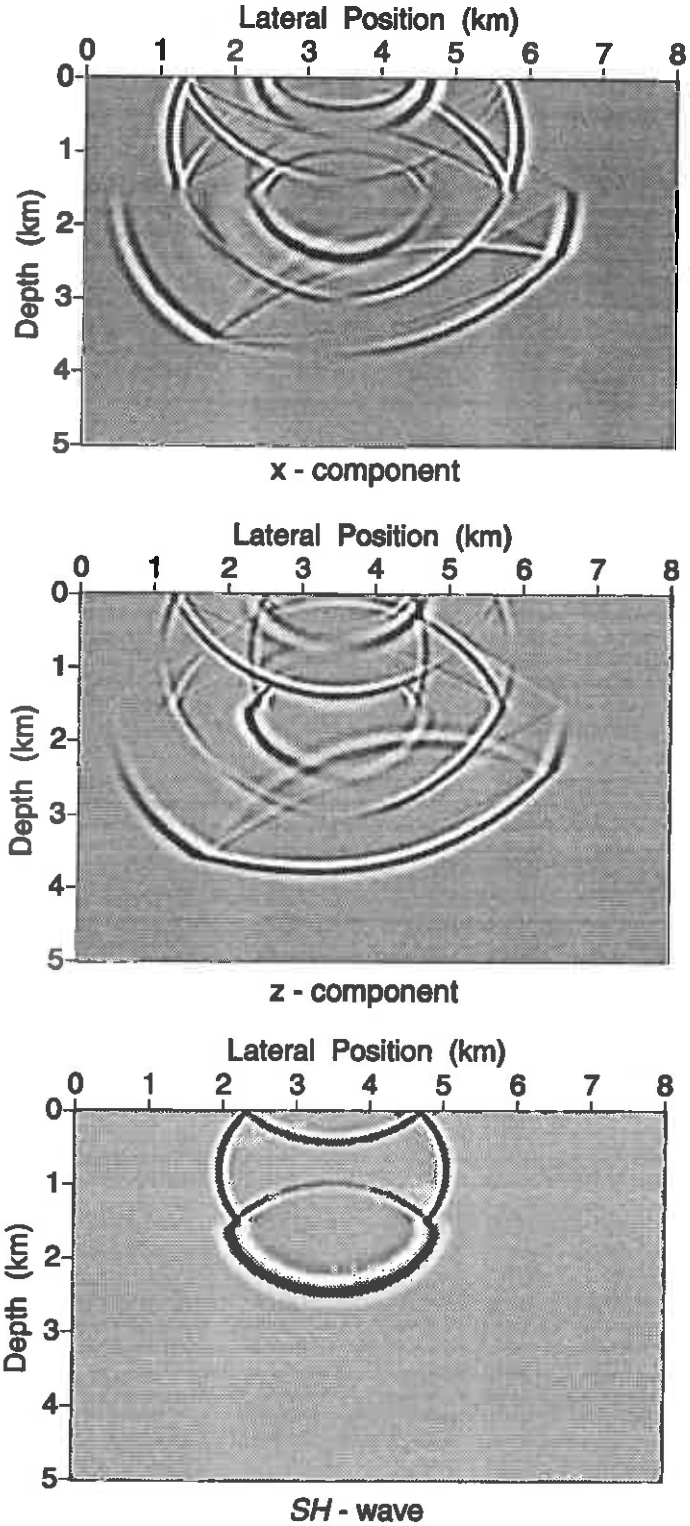

FIG. 9. Snapshots of x-, y-, and z-components at 0.84 s for the layered medium in Figure 6.

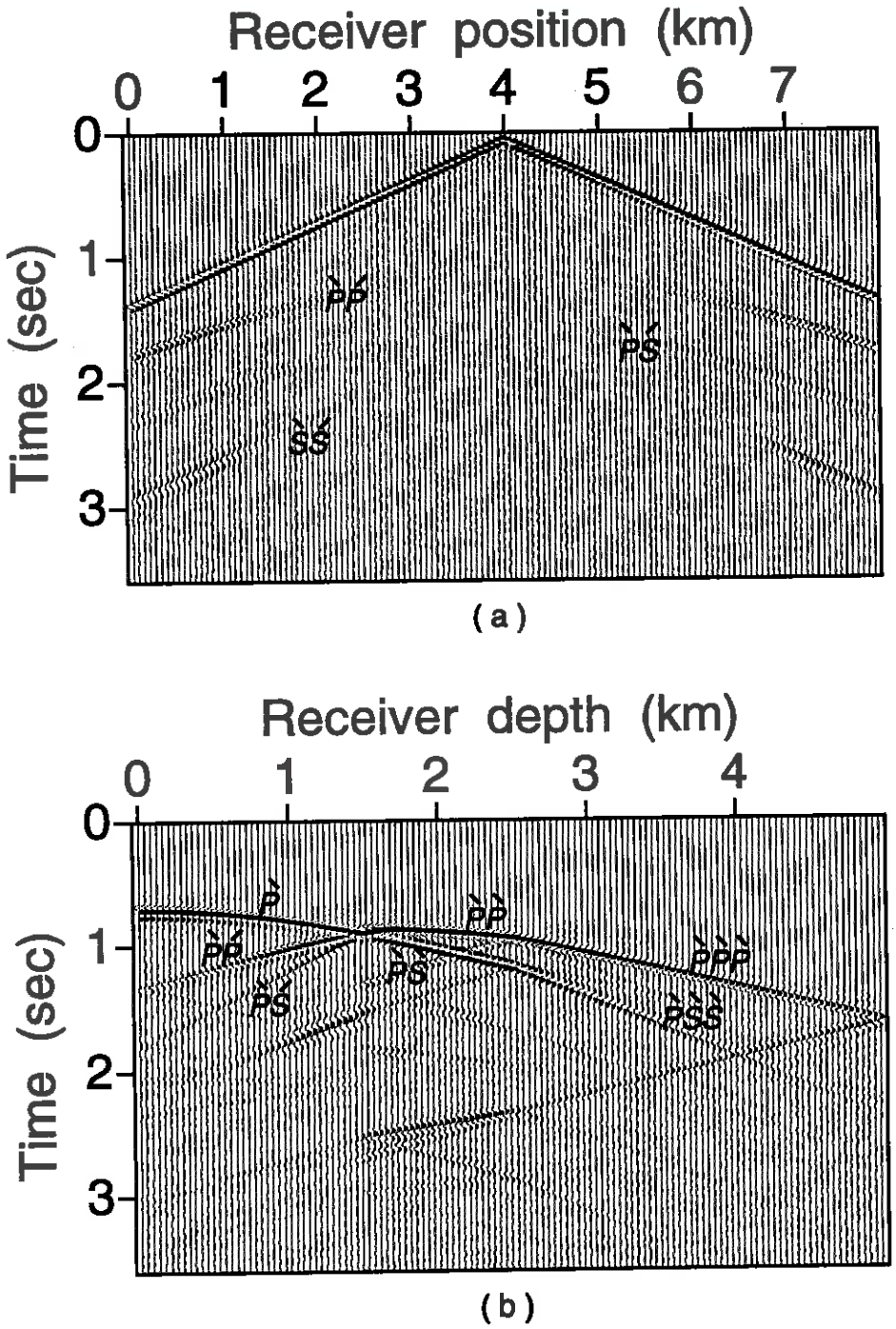

FIG. 10. In-line horizontal-motion seismograms for a vertical displacement source in the layered model of Figure 6. (a) Surface seismic reflection seismogram. (b) VSP seismogram.

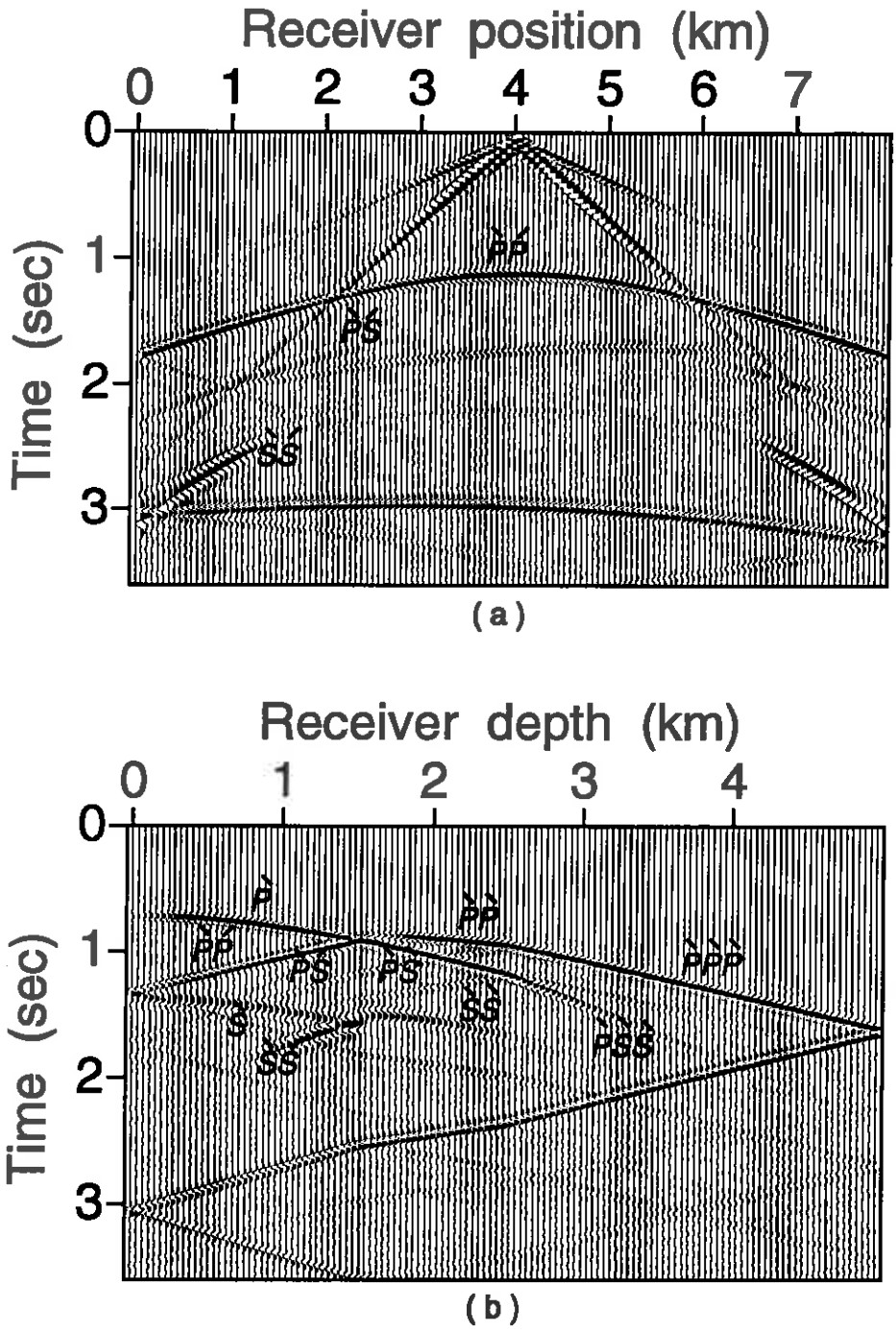

FIG. 11. In-line vertical-motion seismograms for a vertical displacement source in the layered model of Figure 6. (a) Surface seismic reflection seismogram. (b) VSP seismogram.

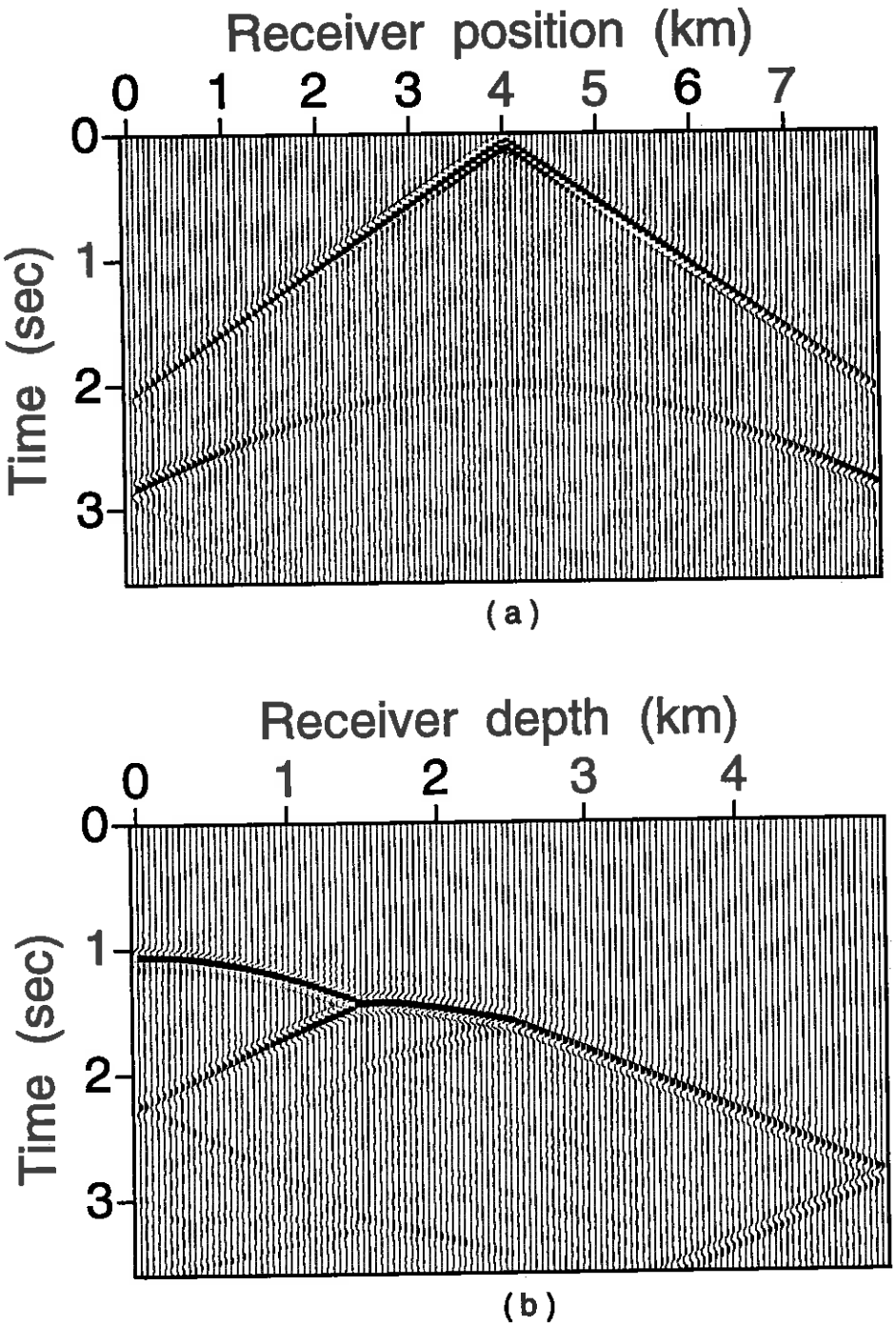

FIG. 12. *SH*-wave seismograms in the layered model of Figure 6. (a) Surface seismic reflection seismogram. (b) VSP seismogram.

A study on distributed genetic algorithms

Wenceslau Gouveia

A study on distributed genetic algorithms

Wenceslau Gouveia

ABSTRACT

Monte Carlo based global optimization methods, such as simulated annealing and genetic algorithms, are used in a wide variety of fields such as management science, computer science, engineering, applied earth sciences and VLSI design. Unlike most local search procedures, Monte Carlo techniques do not require any derivative information about the objective function, and are found to provide a robust search method for a broad spectrum of optimization problems. Genetic algorithms work simultaneously with a group of potential solutions and use stochastic processes to guide the search for an optimal result. This provides an efficient exchange of information among likely solutions, and allows the algorithm to rapidly assimilate and exploit the information gained to find better results, i.e., associated with lower values of the objective function, to the optimization problem.

Here I outline the theory of genetic algorithms. Then, I present the relatively new model of distributed genetic algorithms based on the paleontological theory of "punctuated equilibria" (Cohoon et al., 1987). This approach offers a conceptual modification to the traditional genetic algorithms by taking advantage of a number of populations (sets of likely solutions) evolving quasi-independently. I outline details of the implementation of this method on a cluster of net-connected workstations using PVM as a message-passing subroutine library. Optimization of a multimodal objective function and inversion of 1D acoustic seismic synthetic data are examples used to compare the relative performance of distributed genetic algorithms and conventional genetic algorithms.

INTRODUCTION

The problem of multi-parameter nonlinear optimization is common in many areas of science and engineering. Solving such a problem amounts to the difficult task of minimizing a nonlinear function in the presence of many local minima. This function, often called "objective" or "cost" function, is not necessarily analytic and must quantify the quality of the proposed solution.

It is well known that gradient-based optimization techniques may fail to provide

the correct result when the objective function is multimodal. If such a technique is applied to a given problem, it is necessary to rely that the initial estimate of the optimum answer is within the valley of the global minimum. Otherwise the method will get stuck in local minima. Since these techniques use local information about the objective function to improve initial estimates of the optimal solution they fall into the category of **local search optimization** methods.

Approaches to solving problems with multimodal objective functions are collectively called **global search optimization** methods. These techniques are designed to obtain the optimum answer of the problem by performing a wide search over the space of likely solutions. Exhaustive search is an example of such a technique. Here the objective function is evaluated at every possible solution and the best result is reported. Considering the extremely large number of possible answers to a typical nonlinear optimization problem, this method is useless in practice. The so-called Monte Carlo optimization techniques are another example of global search methods, where probabilistic transition rules are used to improve estimates of the solution toward the optimum result.

A relatively new Monte Carlo optimization procedure, the **genetic algorithm**, has been increasingly applied to a wide variety of multimodal optimization problems. This method, based on the work of Holland (1975) in the artificial intelligence field, works simultaneously with a group of potential solutions and uses stochastic processes to guide the search for the optimal result, in a way that proceeds from an analogy between function optimization and evolution theory. It thus provides an efficient exchange of information among likely solutions, and allows the algorithm to rapidly assimilate and exploit the information gained to update the current set of solutions toward better ones.

Cohoon, et al. (1987) have introduced an alternative formulation of genetic algorithms, motivated by the concept of "punctuated equilibria" and the desire to make effective use of a distributed-memory parallel computing system in complex optimization problems. This approach offers a conceptual modification to the traditional genetic algorithms by taking advantage of several groups of trial solutions that are processed quasi-independently.

After a brief introduction on the theory of genetic algorithms, I shall assess the characteristics of this new formulation, denoted from now on as **distributed genetic algorithms**, relative to conventional ones. In this evaluation, I use as examples optimization of a multimodal analytic objective function and inversion of 1D seismic data. Finally, I outline details of the implementation, where I used a cluster of net-connected workstations with the Parallel Virtual Machine (**PVM**) library [1] as the message-passing software.

[1] from Oak Ridge Laboratories

AN OVERVIEW ON GENETIC ALGORITHMS

This brief description on genetic algorithms follows closely the work of Scales, et al. (1992). For the interested reader, an extensive bibliography is currently available on the theory of genetic algorithms and its application to several fields (see, for example, Holland (1975), Goldberg (1987) and Whitley (1993)).

Genetic algorithms are designed with an analogy to the mechanics of natural selection and genetics, and are based on the principle of "survival of the fittest." Instead of acting on one possible solution of the optimization problem at a time, this procedure acts on a "population" of likely solutions. Essentially, a set of stochastic transition operators is applied to the current population, which favors the creation of new "individuals" (new possible solutions) that "perform better" than did their predecessors. In this context of optimization, better performers means that the objective function evaluated for those individuals has lower values than those of their competitors.

Although many different stochastic operators have been proposed to improve the performance of genetic algorithms (Muhlembein et al., 1991), they are closely related to the ones originally proposed by Holland. In this work I restrict this overview to these conventional operators, namely **selection**, **crossover** and **mutation**.

At this point it is useful to present some details on a common internal representation used by genetic algorithms for the individuals of a population, where each parameter of a trial solution is coded into a binary string. So, for example, if the current population consists of two possible solutions with three parameters each, as $(18, 28, 6)$ and $(16, 20, 3)$, and the required resolution requires a 5-bit string, a possible internal representation of this population would be $(10010, 11100, 00110)$ and $(10000, 10100, 00011)$. All the stochastic operators are then applied to these strings.

Many other types of coding are possible, each of which may have a different effect on the nature of the algorithm. Goldberg (1987) discusses a *gray* coding, which prevents that any two sequential decimal values are represented by binary strings that differs by more than one element. As an example, 7 and 8 are represented by (0111) and (1000) using standard binary coding and by (0100) and (1100) using gray coding. This is the coding scheme used in this work.

Selection

Selection of an individual from a population means an opportunity that is given to this individual to propagate its characteristics into the next generation. This stochastic procedure assigns the highest and lowest probability of selection to the best and worst individual of a population, respectively. How the probabilities of selection are allocated for the other individuals is dependent on the specific selection mechanism. In any case, better-performer individuals have always greater possibilities of being selected.

Typically a group of individuals is selected from the current population, forming a "population of parents." It is important not to overemphasize the fitness of an indi-

vidual in the selection process. Such overemphasis can lead to premature convergence to a local minimum. In the other hand, too little weight given to higher-performer individuals can result in unnecessarily slow convergence. This balance between exploration (global search) and exploitation (local search) is important in the global optimization process. I will address this issue later.

Crossover

From the population generated by the selection process, new individuals are generated by a mixing, or crossover, of the binary strings from two randomly paired parents. Each individual of the population is crossed over with a probability P_c and, as a consequence, some of the previously selected individuals may not have a chance to reproduce.

Figure 1a illustrates this process. In this example, the parents are the individuals $(10100, 11010, 11111)$ and $(11111, 00011, 00110)$. The crossover point, where the binary strings are cut and transposed, is also randomly chosen. After the crossover the new individuals are $(11100, 00010, 01111)$ and $(10111, 11011, 10110)$. Typically, the new individuals will replace the parents, however, in different implementations a criterion may be used to define whether the replacement will occur or not.

At this point a new set of potential solutions, whose features are mainly inherited from better performer individuals of the previous population, is generated. However, nonzero chances are also allocated for allowing poorer performer individuals to propagate their characteristics to future generations.

Mutation

This last stochastic operator randomly perturbs one parameter of an individual in the current population. This process is illustrated in Figure 1b. The objective here is to add diversity to the current population. Note that, in the absence of mutation, no individual generated by the crossover operator could ever acquire a new characteristic that was not already present in the population.

It is important to understand that as the mutation probability is increased, a larger degree of randomness is introduced in the optimization process. As a consequence, exploration of the model space becomes favored over exploitation of the information contained in the population.

Typically mutation probability is kept small ($\approx .001$). However in some advanced genetic implementations, the mutation probability starts from a high value (favouring exploration) and is slowly reduced (favoring exploitation) as the search goes on (Sen and Stoffa, 1992).

Although much progress has been made in the theoretical understanding of genetic algorithms, it is not yet known how to insure an optimal implementation for a given problem. The tuning of the genetic algorithm's free parameters, namely size of the population, crossover probability and mutation probability are rather *ad hoc*.

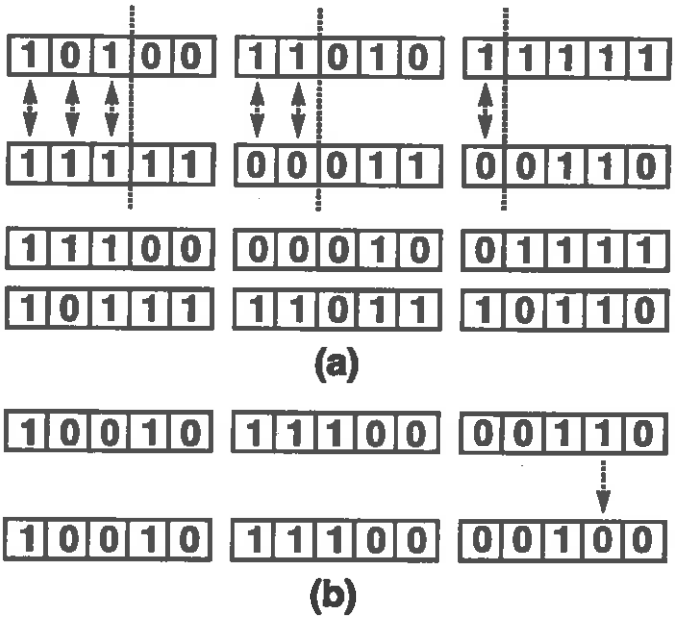

FIG. 1. Crossover (a) and mutation (b) operators.

A clearer theoretical framework is needed for a more thorough comprehension of the subject. This is an active topic of current research interest. Nevertheless, genetic algorithms have been applied to an increasing number of complex optimization problems with success.

Parallel implementation of genetic algorithms offers many possible alternatives. Since the objective-function evaluations at each potential solution of the problem are independent from each other, a high degree of parallelism can immediately be perceived. The application of the stochastic operators to the current population can also be done concurrently. Next, I discuss an alternative, *distributed* implementation of genetic algorithms presented in Cohoon, et al. (1987).

DISTRIBUTED GENETIC ALGORITHMS

According to the the theory of "punctuated equilibria," continued evolution can be obtained through introduction of previous stabilized individuals into new environments. As a consequence, new species would be generated since these individuals must adapt themselves to different conditions.

A possible model of a distributed genetic algorithm, inspired by this theory, evolves N subpopulations in parallel and disjointedly from each other during a given number of iterations (i.e., one evolution). Following that, is a phase during which some individuals migrate from one subpopulation to the others. As a consequence each subpopulation is augmented by a surplus of individuals and must select from among the new and old ones those that will survive to the next generation. This procedure is repeated for a prespecified number of evolutions. Typically, the number of individuals

within a subpopulation is kept constant during the whole optimization process.

The relationship of this strategy with the concept of "punctuated equilibria" is clear. Each subpopulation corresponds to a disjoint environment. By exchanging individuals among them new characteristics are added to those subpopulations, what propitiates different conditions for the evolution of possibly better-performer individuals.

This scheme is illustrated in Figure 2. Figure 2a shows isolated environments (cities) where the evolution of the individuals takes place, and likely paths that they may follow when migrating from one environment to the other. Figure 2b shows a possible implementation of this model on a distributed-memory computer system. All the initial individuals are generated in the master processor and randomly distributed among the worker processors, connected by a ring topology, forming the subpopulations. Each processor sends, using a selection criterion or just randomly, some individuals from its subpopulation to a neighbor processor, following the direction showed in Figure 2b. In this implementation each processor is an IBM RISC/6000 workstation model 530, and the connection is provided by a Token Ring network with nominal data transfer rate of 16 Mbit/s.

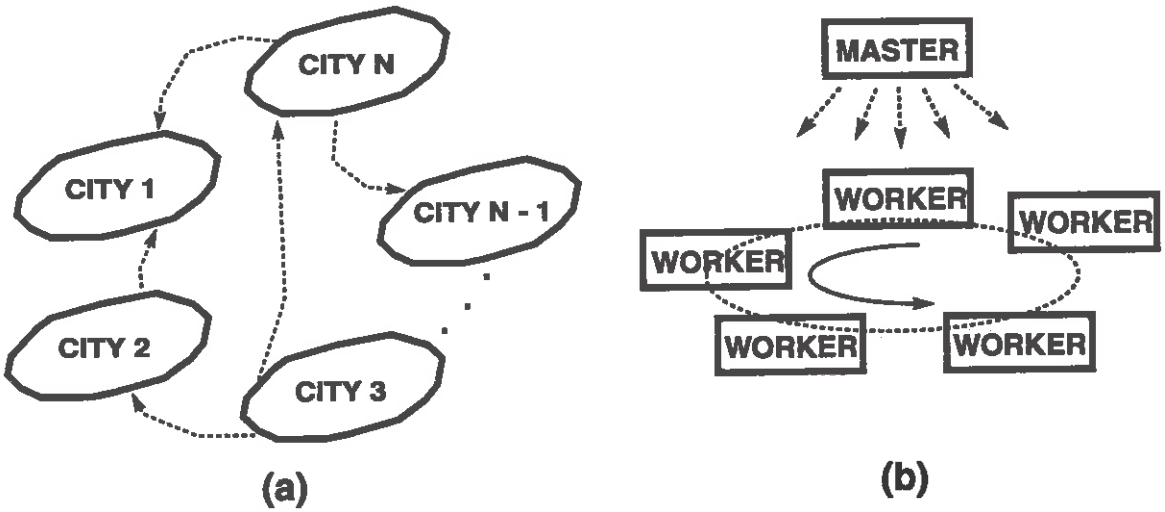

FIG. 2. Punctuated equilibria model (a) and a possible computer implementation (b).

Several parameters are necessary to execute a distributed genetic algorithm. Table 1 describes the most important ones.

Table 2 illustrates an example where four different sets of 50 randomly generated possible solutions are allocated to each one of the four processors. In each evolution, the stochastic operators are applied to the subpopulations, with the defined probabilities, until the objective function is evaluated 1000 times. Remember that at each iteration (selection + crossover + mutation) a new generation is produced, and the

performance of the new individuals should be computed. In this case with 50 individuals in a subpopulation, approximately 20 generations are formed in each evolution. In each generation approximately 60% of the individuals will attempt to produce new trial solutions due crossover. The .001 mutation probability implies that 1 among 1000 individuals, in average, will have its characteristics changed by this stochastic operator.

Subpopulation size (**SP**)	Number of individuals in each processor
Number of evolutions (**E**)	Number of exchanges among processors
Trials per evolution (**TE**)	Number of iterations without processor communication
Number of processors (**WP**)	Number of processors used in this execution
Probability of crossover (**Pc**)	Probability for crossover occurrence of two individuals
Probability of mutation (**Pm**)	Probability for mutation occurrence in a individual

Table 10. Important parameters for the distributed genetic algorithm.

Subpopulation size	50
Number of evolutions	10
Trials per evolution	1000
Number of processors	4
Probability of crossover	.6
Probability of mutation	.001

Table 11. Example of parameters for the distributed genetic algorithm.

After one evolution, 10% of the individuals (in this case 5) of each subpopulation are exchanged among the processors following the ring topology illustrated in Figure 2b. A new evolution starts and this process is repeated 10 times. To reproduce this experiment in terms of computational demand, using a sequential genetic algorithm, the following parameters would be used:

Subpopulation size	200
Number of evolutions	1
Trials per evolution	40000
Number of processors	1
Probability of crossover	.6
Probability of mutation	.001

Table 12. Required parameters for a sequential genetic algorithm applied in an experiment that is similar to that in Table 1, in terms of the total number of objective-function evaluations.

Due to the stochastic nature of the algorithm it is not guaranteed that the same amount of computations is performed in both cases. By tight control of the execution,

it would be possible to assure the same computational cost of the sequential and parallel versions, but this option is not provided in the current implementation.

It is claimed in the genetic algorithm literature (Cohoon et al., 1987, Whitley and Starkweather, 1990, Muhlembein et al., 1991, and Sen and Stoffa, 1992) that distributed genetic algorithms, based on the concept of "punctuated equilibria," not only provide a computational speedup [2] but also are able to perform a more efficient search over the space of solutions. By more efficient, I mean producing an equivalent result for the optimization problem with fewer evaluations of the objective function. Next, I make a comparative analysis among sequential and distributed genetic algorithms, with respect to computational speedup, and effectiveness of the search for the optimum solution.

A COMPARATIVE ANALYSIS OF SEQUENTIAL AND DISTRIBUTED GENETIC ALGORITHMS

In comparing of sequential and distributed genetic algorithms I will use two different objective functions. The first one, proposed in Torn and Zilinskas (1989), is defined by the following expression

$$R(x_1, x_2, ..., x_n) = n + \sum_{i=1}^{n} \Big[x_i^2 - cos(2\pi x_i) \Big]. \tag{1}$$

This function is highly multimodal. The global minimum is at $x_i = 0, i = 0, 1, ..., n$, giving $R(x_i) = 0$. Grid points with $x_i = 0$ except at one coordinate, where $x_j = 1$, give $R(x_i) = 1$, the "best" of all local minima. With increasing distance from the global minimum the objective function evaluated at local minimum becomes larger.

The second objective function is related to the geophysical inversion problem. The aim of inversion is the estimation of elastic properties of the subsurface whose modelled response matches observations within given tolerance. Therefore the objective function, used called the *misfit function* in this context, quantifies the difference between synthetic seismograms, obtained from the trial solution (subsurface model), and the observed seismograms. Several mathematical expressions for the misfit function are possible. In this paper, for the sake of simplicity, I will use the following definition

$$R(\mu) = \sum_{i=1}^{n} (So_i{}^2 - S_i(\mu)^2)^{\frac{1}{2}}. \tag{2}$$

Where So_i and $S_i(\mu)$ are the i^{th} sample of the observed and synthetic seismogram modeled for the geological profile μ respectively. n is the number of samples used

[2] Ratio of elapsed time for the sequential test to that for the distributed implementation

in the computation of the misfit function. I address here the problem of 1D seismic inversion, in order to reduce the computational demand of the problem as compared with that in 2D or 3D seismic inversion. However, the results obtained here could be extended to 2D and 3D situations.

I used the modeling algorithm described in Robinson (1967), which provides the complete reflectivity series (primaries and multiples), which will be used in the calculation of the objective function. For display purposes the reflectivity series is convolved with a finite-length wavelet.

First I assess the computational performance improvement provided by the distributed genetic algorithm. Then, I compare the effectiveness of the global search for the optimum solution performed by the two implementations, given the same amount of initial information.

Computational performance

Of the many possible ways to evaluate the performance gain provided by the distributed implementation, in this analysis I used equation [1] with dimensions $n = 20$ and $n = 400$ as the objective function, and the parameters shown in Table 4 for the distributed genetic algorithm. I selected these parameters in order to keep the product $(E).(TE).(WP)$ the same as in the correspondent sequential run. This assures that the parallel and sequential executions will perform approximately the same number of computations.

Experiment (Fig. 3)	SP	E	TE	WP
1 (Fig. 3a)	50,100,150,200	2	4K,8K,12K,16K	2...8
2 (Fig. 3b)	50,100,150,200	4	2K,4K,6K,8K	2...8
3 (Fig. 3c)	50,100,150,200	8	1K,2K,3K,4K	2...8
4 (Fig. 3d)	50,100,150,200	16	.5K,1K,1.5K,2K	2...8
5 (Fig. 3e)	50,100,150,200	16	.5K,1K,1.5K,2K	2...8

Table 13. Parameters used in the performance analysis of the distributed genetic algorithm.

Consider first the performance curves illustrated in Figures 3a-3d. Despite fluctuations due the stochastic nature of the algorithm, the performance curves are generally above the line of linear speedup. The exchange of individuals among processors may explain this super linear-speedup, since, as it adds new characteristics to each subpopulation, it can facilitate the task of the crossover operator to produce new individuals. The easier is this process, the bigger the number of new individuals produced in each generation.

As the optimization process advances, the population tends to reduce its diversity of information due the combination and selection of better-performer individuals. As a consequence, the generation of new trial solutions by the stochastic operators becomes

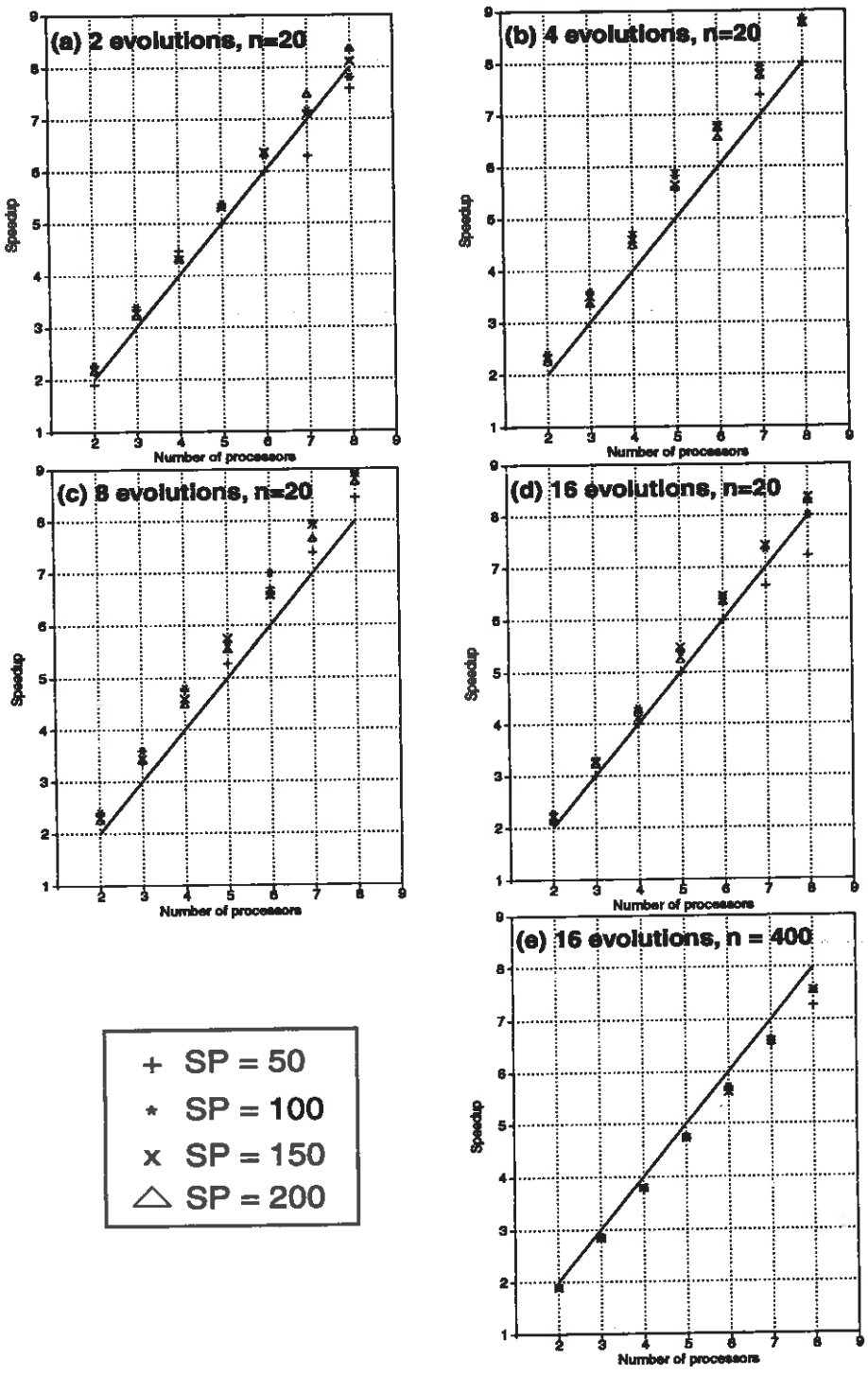

FIG. 3. Performance results of the distributed implementation. In each curve the total number of evaluations of the objective function is kept constant, and each symbol corresponds to different population sizes from 50 to 200 individuals.

increasingly more difficult. The distributed genetic algorithm seems to provide an effective way to overcome this lack of diversity.

Increasing the number of evolutions in the experiments has the purpose to raise the communication among processors, in order to identify a possible drop in the performance of the system. It is well known that the limitation on data transfer rate of the network is the main degrading factor of performance in distributed applications on a cluster of workstations. To impose a communication demand on the network 20 times higher than in the case illustrated in Figure 3d, I optimized equation [1] with $n = 400$. Performance curves are shown in Figure 3e. Although they are slightly below the linear-speedup line, no noticeable degradation can be observed in the performance of the system. These figures lead to the conclusion that distributed genetic algorithms are a suitable application for network computing systems.

We should keep in mind that these results depend on the parameters and the objective function used in the experiments. Different parameters and objective functions will produce other performance results. Besides, all these measures were performed in a controlled environment, where all the workstations and the network were in a low level of utilization. When the processors are shared by other applications, a more realistic situation, these figures will certainly change.

Optimization results

Here I compare the optimization results obtained from the sequential and distributed genetic algorithms. The total number of objective function evaluations, necessary to compute the optimum solution within a given error, will be the main measure for this analysis.

Consider first the optimization of equation [1] with $n = 20$. Each parameter can assume 1024 different values within the interval $[-5.12, 5.11]$. Thus, the size of the space of possible solutions is approximately $1.6\text{x}10^{60}$. As mentioned before, the minimum global is at $x_i = 0, i = 0, 1, ..., n$, giving $R(x_i) = 0$. The parameters used in single-processor, 6-processor and 8-processor runs are shown in Table 5. The objective function evaluated at the best solution (i.e., the error of the final result), the elapsed time of each experiment and the speedup provided by the distributed implementation are also presented. Figure 4 illustrates the performance of the best individual in the current population as a function of the number of iterations (evaluations of the objective function) for the three experiments.

The distributed version was more efficient in its search for the optimum solution than the sequential one, since an equivalent result was obtained with less computational effort (60000, 45600 and 45000 evaluations of the objective function for the single-processor, 6-processor and 8-processor runs, respectively).

The distributed implementation provides a better balance between exploitation and exploration over the space of possible solutions. The small subpopulations, when evolving in isolation, perform efficient local searches over several regions of the space

of solutions. The exchange of individuals among these subpopulations is responsible for the assimilation of global information.

The size of each subpopulation is a critical parameter in the distributed implementation. It should be tuned accordingly to the specific situation, and a number of trial experiments is always necessary.

Parameter	Sequential	Distributed 1	Distributed 2
SP	320	40	25
E	1	20	15
TE	60000	380	375
WP	1	6	8
Pc	0.6	0.6	0.6
Pm	0.001	0.001	0.001
Objective function	0.0414499	0.0373033	0.0186594
Elapsed time (s) : Speedup	188 : 1	20 : 9.4	16 : 11.7

Table 14. Parameters and results for the optimization of equation [1].

For the 1D seismic inversion problem (equation [2]), using an example similar to that of Scales, et al. (1992), I consider the simple situation of a five-layer acoustic model. The synthetic 1D reflectivity series plays the role of "observed" data. The trial models consists of 14 reflection coefficients each constrained to the interval of $[-1, 1]$. In this case, the size of the space of possible solutions is approximately $1.39\text{x}10^{42}$.

Table 6 gives parameters for the single-processor, 4-processor and 6-processor runs. Matches with the observed data are shown in Figure 5a. Figure 5b illustrates the performance of the best individual during the optimization, as a function of the number of iterations, for the three experiments. 40000 and 43200 iterations for the 4-processor and 6-processor runs, respectively, and 70000 for the sequential run were necessary to provide equivalent results, demonstrating, in this example, the superior performance of the parallel implementation.

Parameter	Sequential	Distributed 1	Distributed 2
SP	390	45	35
E	1	10	9
TE	70000	1000	800
WP	1	4	6
Pc	0.6	0.6	0.6
Pm	0.001	0.001	0.001
Objective function	0.0479291	0.0473291	0.0475291
Elapsed time (sec) : Speedup	237 : 1	24 : 9.8	19 : 12.5

Table 15. Parameters and results for the 1D acoustic seismic inversion.

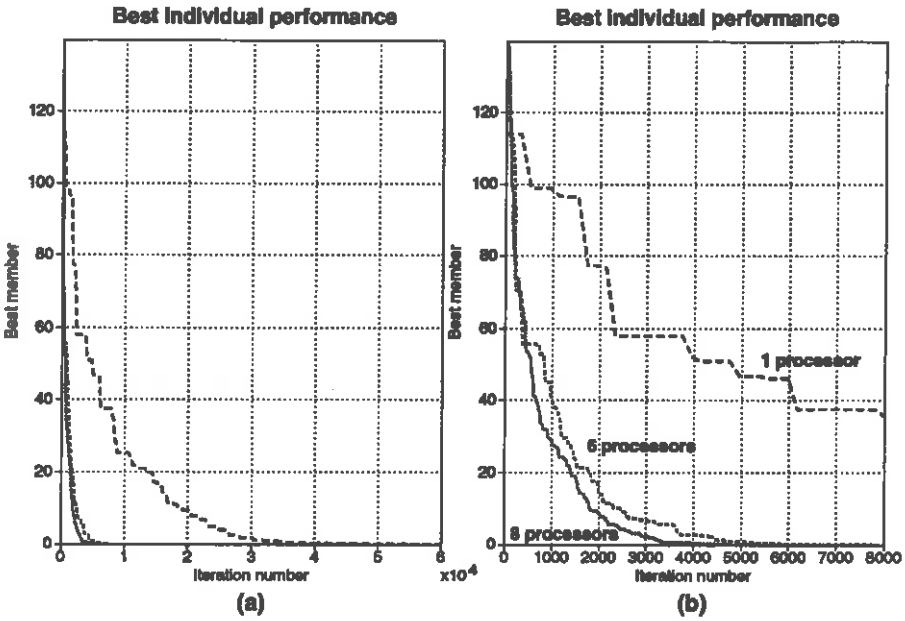

FIG. 4. (a) Performance of the best individual during the optimization of equation [1] using 1, 6 and 8 processors. For better visualization, (b) shows just the first 8000 iterations.

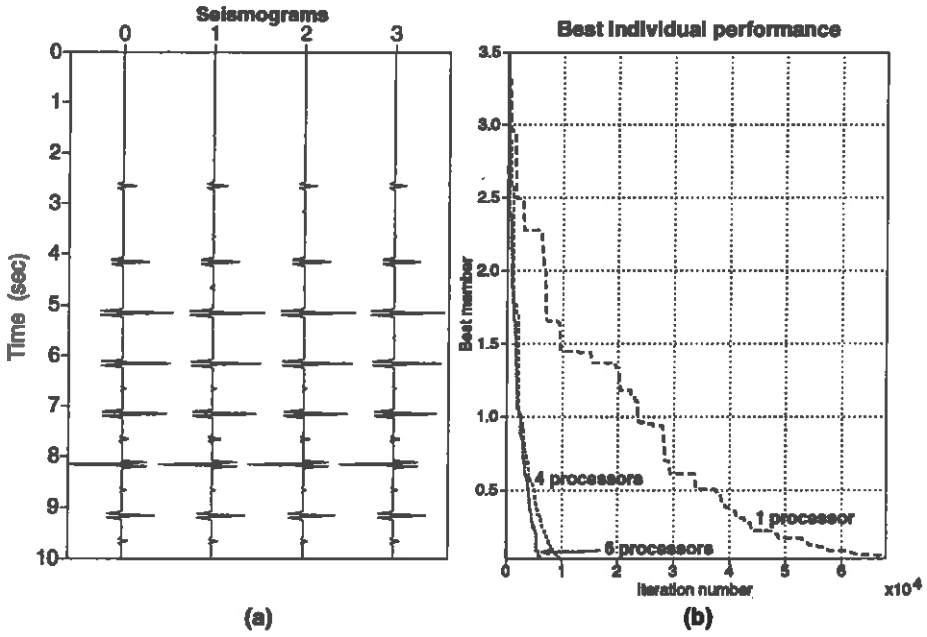

FIG. 5. Results obtained from the 1D seismic inversion. In (a) trace 0 is the "observed data," and traces 1, 2, and 3 were obtained from the 1, 4 and 6 processor runs respectively. (b) illustrates the performance of the best individual during the optimization for the three experiments.

IMPLEMENTATION DETAILS

As already mentioned the distributed genetic algorithm was implemented on a cluster of workstations IBM Risc/6000 model 530H, connected by a Token Ring network. All the synchronization and data transfer-routines were provided by the Parallel Virtual Machine (PVM) library.

Figure 2b illustrates the ring topology used in this implementation of the distributed genetic algorithm. All trial solutions are generated randomly at the host processor and spread over all the work processors. During the optimization process just the work processors communicate, for the exchange of individuals, until the objective function is evaluated a specified number of times (number of evolutions times the trials per evolution). Finally the work processors send their final solutions to the master processor, that chooses the best one.

The pseudo code for this implementation is outlined below.

```
/* Random generation of solutions and distribution among work processors */
MASTER: Random generation of possible solutions at the master processor
MASTER for: N work processors do
                MASTER send: subpopulation to each worker
                WORKER receive: subpopulation from the master
MASTER endfor;
/* Evolution and exchange of individuals */
WORKER for: Number of evolutions do
                WORKER for: Number of evaluations of the objective function do
                                WORKER: Evolve the population
                WORKER endfor;
                WORKER send: 10% of its subpopulation to neighbor processor
                WORKER receive: new individuals from neighbour processor
WORKER endfor;
/* Best solutions of each processor send to master */
WORKER send: best solution to the master
MASTER receive: receive best solution from each work processor
MASTER: select best solution of the optimization
```

Other topologies are possible. I also implemented a hypercube-type connection, wherein all the work processors receive the best individuals from all other processors involved in the optimization. At least for the examples tested, the ring topology seems to provide better results. A possible reason is that, in this case, the subpopulations are optimized more independently than in the hypercube implementation. This may result in a more efficient global search under the paradigm of "punctuated equilibria."

CONCLUSION

In this work I studied the distributed genetic algorithm, an alternative implementation of genetic algorithms based on the concept of "punctuated equilibria." Results provided by the distributed version, implemented on a cluster of net-connected workstations using PVM as a message-passing library, are encouraging. Not only the computational speedup is satisfactory but fewer iterations are necessary to obtain an equivalent answer than the one provided by the sequential genetic algorithm, indicating a better balance between exploration and exploitation of the space of potential solutions.

However it is worth mention that many parameters influence the performance of a genetic algorithm in an optimization problem, and some trial experiments are always necessary to estimate them. The already large set of required parameters is increased in the distributed implementation by the new parameters: The number of work processors, the size of the subpopulation, the number of solutions exchanged among the processors, and the number of evolutions necessary for a satisfactory answer.

Nevertheless, in a complex optimization procedure such geophysical inversion, the distributed implementation provides a much faster response time, which enables a more thorough inspection of the likely solutions of the problem. A convenient set of likely solutions can supply confidence bounds on the estimated parameters of the final optimal solution, which can be useful in further steps of data processing.

Further research on this subject will focus on the study of the applicability of genetic algorithms in 2D seismic full-waveform inverse problems. The multimodal character of the objective functions that arise in this problem overwhelms conventional optimization techniques, and efficient Monte Carlo methods may be a useful alternative.

ACKNOWLEDGMENTS

I thank John Scales and Ken Larner for their critical review of the paper, and Dr. John Grefenstette from the Naval Research Laboratory for sending me the source code of GENESIS, the sequential genetic algorithm which I used in my distributed implementation.

REFERENCES

Cohoon, P. C., Hegde, S. U., Martin, W. N., and Richards, D. S., 1987, Punctuated equilibria, a parallel genetic algorithm: Proc. Second Int. Conf. Genetic Algorithms and Their Applications, MA, 148-154.

Goldberg, D. E., 1989, Genetic algorithms in search, optimization and machine learning, Addison-Wesley, Reading, MA.

Holland, J. H., 1975, Adaptation in natural and artificial systems, University of Michigan Press, Ann Harbor, MI.

Muhlembein, H., Schomisch, M. and Born, J., 1991: Proc. Fourth Int. Conf. Genetic Algorithms and Their Applications, CA, 271-278.

Robinson, E. A., 1967, Multichannel time series analysis with digital computer programs, Holden-Day, Inc., SF.

Scales, J. A., Smith, M. L., and Fischer, T. L., 1992, Global optimization methods for multimodal inverse problems: Journal of Computational Physics, **103**, 248-268.

Sen M. K. and Stoffa, P. L., 1992, Rapid sampling of model space using genetic algorithms: examples from seismic waveform inversion: Geophysical Journal International, **108**, 281-292.

Torn, A. and Zilinskas, A., 1989, Global optimization: Lecture Notes in Computer Science, Springer, Berlin, **350**.

Whitley, D., 1993, A genetic algorithm tutorial: Technical Report CS-93-103, Colorado State University.

Whitley, D., and Starkweather, T., 1990, Genitor II: a distributed genetic algorithm: Journal of Experimental and Theoretical Artificial Intelligence, **2**, 189-214.

A Kirchhoff approach to seismic modeling and prestack depth migration

Zhenyue Liu

A Kirchhoff approach to seismic modeling and prestack depth migration

Zhenyue Liu

ABSTRACT

The Kirchhoff integral provides a robust method for implementing seismic modeling and prestack depth migration, which can handle lateral velocity variation and turning waves. With a little extra computation cost, the Kirchhoff-type migration can obtain multiple outputs that have the same phase but different amplitudes, compared with that of other migration methods. The ratio of these amplitudes is helpful in computing some quantities such as reflection angle.

Here, I develop a seismic modeling and prestack depth migration method based on the Kirchhoff integral, that handles both laterally variant velocity and a dip beyond 90 degrees. The method uses a finite-difference algorithm to calculate traveltimes and WKBJ amplitudes for the Kirchhoff integral. Compared to ray-tracing algorithms, the finite-difference algorithm gives an efficient implementation and single-valued quantities (first arrivals) on output. In my finite-difference algorithm, the upwind scheme is used to calculate traveltimes, and the Crank-Nicolson scheme is used to calculate amplitudes. Moreover, interpolation is applied to save computation cost.

The modeling and migration algorithms here require a smooth velocity function. I develop a velocity-smoothing technique based on damped least-squares to aid in obtaining a successful migration. This velocity-smoothing technique also can be used to improve results of other migration algorithms, such as Gaussian beam migration.

INTRODUCTION

Seismic modeling and migration play an important role in seismic data processing. To treat complex media, one needs prestack depth migration that can handle lateral velocity variation and reflector dips. Conventional techniques, such as the downward continuation of sources and geophones by finite difference (S-G finite-difference migration), are relatively slow and dip-limited. Compared to S-G finite-difference migration, the Kirchhoff integral implements prestack migration relatively efficiently and has no dip limitation.

Bleistein et al. (1987) derived the Kirchhoff integral method by using the WKBJ approximation. This method treats amplitude in migration in a WKBJ-consistent manner so that the output is the reflectivity function. Furthermore, Bleistein showed that one can design weights in the Kirchhoff integral to determine quantities such as the reflection angle, based on the stationary-phase principle. In Bleistein's integral formula, the integrand consists of traveltime, WKBJ amplitude, ray parameters, and so on. Two commonly used approaches to calculate traveltimes and the other quantities in the Kirchhoff integral are ray-tracing and finite-difference applied to the eikonal equation. The ray-tracing algorithm calculates traveltimes and amplitudes on each ray. Usually, the rays do not pass through output grid points, so we need to interpolate to obtain traveltimes and amplitudes at the grid locations. This interpolation is complicated when the raypaths have a caustic, and thus limits the efficiency of the ray-tracing algorithm. In contrast, the finite-difference algorithm calculates traveltimes and amplitudes directly at output grid locations. For caustics, the finite-difference algorithm calculates the first-arrival traveltime and the corresponding amplitudes.

Traveltimes satisfy the eikonal equation, and amplitude terms satisfy linear partial differential equations that depend on traveltime derivatives. Van Trier and Symes (1990) introduced a finite-difference scheme for solving this equation to obtain the traveltimes and traveltime derivatives. Pusey and Vidale (1991) used a similar, explicit scheme to solve for the WKBJ amplitudes. For the explicit scheme, one has to choose a small enough step size for a stability when the velocity function is varied. In this paper, I use the Crank-Nicolson scheme to solve for the amplitudes. Compared to the explicit scheme, the Crank-Nicolson scheme is second-order accurate and absolutely stable so that computation cost is made relatively small for variable velocity by choosing large step sizes.

Calculation cost of pointwise traveltimes and amplitudes by the above method would dominant the total calculation cost of the Kirchhoff integral method. For each source or receiver, the calculation cost depends on the number of grid points. To speed up the Kirchhoff integral method, I apply interpolation to avoid computation on the entire grid.

A smooth velocity function is required by most migration algorithms. A few methods for smoothing the model velocity have been developed in the past. The windowed-averaging method, for example, calculates a smooth velocity value at one point by averaging velocity values over a depth-midpoint window centered at this point. If the original velocity is discontinuous, it is easy to show that the smoothed velocity from the windowed-averaging method does not have the continuity of the first derivative. Consequently, this method is not effective when the velocity has a strong discontinuity. Here, I present a velocity-smoothing technique based on damped least-squares. The curvature of the raypath is a key factor in migration imaging. The smaller the curvature, the more stable the migration result. I derive a representation for the curvature that depends on first derivatives of velocity. A smooth velocity

function is sought that minimizes the weighted sum of (1) the deviation between the smooth velocity and the original one, and (2) the first derivatives of velocity with respect to spatial variables. I use the result that the reciprocal of the curvature of the raypath is proportional to the velocity gradient. Therefore, my method may remove migration artifacts by suppressing the curvature of the raypath. Moreover, this method allows local variation in the degree of smoothing allowed by using a window function, so that the velocity is smoothed more in rougher areas.

FINITE-DIFFERENCE ALGORITHM

The Kirchhoff integral method can be represented by

$$output = integral\{weight \cdot input\}.$$

For modeling problems, the input consists of velocity layers, and the output is seismic traces; for inversion problems, the input is seismic traces, the output is a structural image. Both require common quantities to be calculated. These quantities include (Bleistein, 1986):

τ	traveltime,
ϕ	propagation angle,
σ	running ray parameter,
β	incident angle from source or reciever,
$\partial\beta/\partial x$	geometrical spreading parameter.

For each source or receiver, the above quantities satisfy the follow eqations:

$$\left(\frac{\partial\tau}{\partial x}\right)^2 + \left(\frac{\partial\tau}{\partial z}\right)^2 = \frac{1}{v^2(x,z)}, \tag{1}$$

$$\sin\phi = v\frac{\partial\tau}{\partial x}, \tag{2}$$

$$\frac{\partial\sigma}{\partial x}\frac{\partial\tau}{\partial x} + \frac{\partial\sigma}{\partial z}\frac{\partial\tau}{\partial z} = 1, \tag{3}$$

$$\frac{\partial\beta}{\partial x}\frac{\partial\tau}{\partial x} + \frac{\partial\beta}{\partial z}\frac{\partial\tau}{\partial z} = 0, \tag{4}$$

$$\frac{\partial}{\partial z}\left(\frac{\partial\beta}{\partial x}\right) + \frac{\partial}{\partial x}\left[\mu(x,z)\frac{\partial\beta}{\partial x}\right] = 0, \tag{5}$$

where $v(x,z)$ is velocity and

$$\mu(x,z) = \frac{\partial\tau}{\partial x}\left[\frac{\partial\tau}{\partial z}\right]^{-1}.$$

Equation (1) is the eikonal equation. Equations (3) and (4) are derived by Pusey and Vidale (1991). Equation (5) follows from equation (3). Van Trier et al. (1990) used the efficient *upwind* scheme to solve this equation for traveltime and traveltime derivatives. However, computation in Cartesian coordinates requires that $\partial\tau/\partial z$ be positive, so turning waves cannot be handled. Computation in polar coordinates does not suffer this limitation. Let us introduce the coordinate transform

$$x = x_s + r\sin\theta, \qquad z = r\cos\theta.$$

In polar-coordinates, equations (1) through (5) become

$$\left(\frac{\partial\tau}{\partial r}\right)^2 + \frac{1}{r^2}\left(\frac{\partial\tau}{\partial\theta}\right)^2 = \frac{1}{v^2(r,\theta)}, \tag{6}$$

$$\sin(\phi-\theta) = \frac{v}{r}\frac{\partial\tau}{\partial\theta}, \tag{7}$$

$$\frac{\partial\sigma}{\partial r}\frac{\partial\tau}{\partial r} + \frac{1}{r^2}\frac{\partial\sigma}{\partial\theta}\frac{\partial\tau}{\partial\theta} = 1, \tag{8}$$

$$\frac{\partial\beta}{\partial r}\frac{\partial\tau}{\partial r} + \frac{1}{r^2}\frac{\partial\beta}{\partial\theta}\frac{\partial\tau}{\partial\theta} = 0, \tag{9}$$

$$\frac{\partial}{\partial r}\left(\frac{\partial\beta}{\partial\theta}\right) + \frac{\partial}{\partial\theta}\left[\mu(r,\theta)\frac{\partial\beta}{\partial\theta}\right] = 0, \tag{10}$$

where

$$\mu(r,\theta) = \frac{\partial\tau}{\partial\theta}\left[r^2\frac{\partial\tau}{\partial r}\right]^{-1}.$$

Although more computation is required in polar-coordinates, the boundary conditions are more easily treated and, more importantly, we can handle turning waves.

The coefficient μ of equation (10) is inside the differential operator. If an error exists in numerical computation of μ, the solution of equation (10) may suffer. Instead of solving equation (10), I use an approximate formula

$$\frac{\partial\beta}{\partial\theta} = \frac{v_0 r}{\sigma}\cos(\theta-\phi), \tag{11}$$

where v_0 is the velocity value at the source position. Formula (11), derived in Appendix A, is exact for linear velocity. When velocity is strongly nonlinear, the geometry-spreading factor based on formula (11) is not accurate. However, not only the geometry-spreading factor but also the finite difference algorithm, which requires that $\partial\tau/\partial r$ be positive, suffers from strong-nonlinear velocity . The smoothing technique in this paper will produce a sufficiently smooth velocity to solve these two problems.

Crank-Nicolson scheme

Van Trier et al. (1990) gives an upwind finite-difference scheme for solving equation (6). Also that scheme yields derivative values for use in equation (7). Pusey and Vidale (1991) use a similar scheme to solve equation (8). Those upwind schemes are explicit. Therefore, one has to choose a small enough step size for stability when the velocity function is varied. In this paper, the Crank-Nicolson scheme is applied to equations (8) and (9). Compared to the explicit scheme, the Crank Nicolson scheme is second-order accurate and absolutely stable so that computation cost is made relatively small for variable velocity by choosing large steps.

Let

$$p = \frac{\partial \tau}{\partial r}, \qquad q = \frac{1}{r^2}\frac{\partial \tau}{\partial \theta}.$$

With the Crank-Nicolson approximation, equation (8) becomes

$$\frac{\sigma_i^{j+1} - \sigma_i^j}{2\Delta r}(p_i^{j+1} + p_i^j) + \frac{q_i^{j+1} + q_i^j}{8\Delta\theta}(\sigma_{i+1}^{j+1} - \sigma_{i-1}^{j+1} + \sigma_{i+1}^j - \sigma_{i-1}^j) = 1, \qquad (12)$$

and equation (9) becomes

$$\frac{\beta_i^{j+1} - \beta_i^j}{2\Delta r}(p_i^{j+1} + p_i^j) + \frac{q_i^{j+1} + q_i^j}{8\Delta\theta}(\beta_{i+1}^{j+1} - \beta_{i-1}^{j+1} + \beta_{i+1}^j - \beta_{i-1}^j) = 0, \qquad (13)$$

where j is the index of r, i is the index of θ, and Δr and $\Delta\theta$ define the grid cell sizes.

For each j, equations (12) and (13) are tridiagonal systems that can be solved relatively efficiently.

INTERPOLATION TECHNIQUE

Calculation cost of pointwise traveltimes and amplitudes by the above method would dominant the total calculation cost of the Kirchhoff integral method. For each source or receiver, the calculation cost depends on the number of grid points. To speed up the Kirchhoff integral method, I apply interpolation at two stages so as to avoid computation on the entire grid.

One stage is the interpolation between the sources or receivers: I calculate traveltimes and amplitudes only at selected sources or receivers, and then interpolate traveltimes and amplitudes at the other sources or receivers. Suppose that the traveltime functions $\tau(x, z; x_{s_1})$ and $\tau(x, z; x_{s_2})$ from two sources x_{s_1} and x_{s_2} have been calculated. I interpolate a traveltime function from source x_s $(x_{s_1} < x_s < x_{s_2})$ by

$$\tau(x, z, x_s) = \lambda\tau(x + x_{s_2} - x_s, z; x_{s_2}) + (1 - \lambda)\tau(x + x_{s_1} - x_s, z; x_{s_1}), \qquad (14)$$

where $\lambda = (x_s - x_{s_1})/(x_{s_2} - x_{s_1})$. When the velocity is only depth-dependent, this linear interpolation is exact because the traveltime is invariant for parallel movement; i.e., for any h,

$$\tau(x + h, z; x_s + h) = \tau(x, z; x_s).$$

For a general velocity function $v(x,z)$, the interpolation error depends on $\partial v/\partial x$. Reducing this error is one motivation for smoothing the velocity.

The other interpolation is between grid points. To save computation, I use a relatively coarse grid in the traveltime and amplitude calculation. Then, to preserve resolution, I use a finer grid for migration output with traveltimes and amplitudes calculated by bilinear interpolation.

VELOCITY SMOOTHING

A smooth velocity function is required by most migration algorithms. Before a smoothing technique is selected, it is essential to know how smoothness of velocity affects migration results.

Numerous migration algorithms are based on ray theory (high-frequency assumption). The smaller the curvature or the larger the radius of curvature, the better is the quality of the raypath. Generally, a large curvature increases the sensitivity of a raypath to the incident angle from the source, resulting in sparse raypath coverage. In addition, a large curvature may cause troubles in the imaging process. In Gaussian beam migration, for example, traveltime at one point in the vicinity of a central ray are calculated by projecting this point onto the ray and then by using the Taylor series expansion. If the curvature of the ray is too large, the projecting point is not unique and also the Taylor series expansion is inaccurate, so that a poor migration result may suffer from the inaccurate calculation of the traveltimes. For another example, the finite-difference method in this paper will fail if, at any point of the raypath, there is more than a 90-degree difference between the ray direction and the direction from the source position to this point. Therefore, control of the curvature of the raypath is necessary. From Dohr (1985, p. 23), the curvature κ can be represented by

$$\kappa \equiv \frac{1}{R} = -\frac{\partial v}{\partial x}\frac{\cos\theta}{v} + \frac{\partial v}{\partial z}\frac{\sin\theta}{v}, \tag{15}$$

where R is the radius of the curvature, v is the velocity, and θ is the propagation angle. Equation (15) shows that the first derivatives dominate the curvature of the ray. Based on this characteristic, I used the damped least-squares method to calculate a smooth velocity that has suppressed the first derivatives and, therefore, reduced the raypath curvature. Use of a smooth velocity function is also required in the WKBJ approximation and in the interpolation for traveltimes.

Let $v(x,z)$ be the original velocity; then a smooth velocity $v_s(x,z)$ is determined by

$$\int (\bar{v}_s(x,z) - v(x,z))^2\,dx + \alpha_x^2 \int w(x,z)\left(\frac{\partial \bar{v}_s}{\partial x}\right)^2 dx = \min, \tag{16}$$

$$\int (v_s(x,z) - \bar{v}_s(x,z))^2\,dz + \alpha_z^2 \int w(x,z)\left(\frac{\partial v_s}{\partial z}\right)^2 dz = \min, \tag{17}$$

where α_x, α_z are the *smoothing parameters* and $w(x,z)$ is a window function. The window function, ranging from 0 to 1, allows local variation in the degree of smoothing desired. Roughness of the original velocity function is usually not uniform, so one can design a window function such that velocity is smoothed more in rougher areas.

Equation (16) smooths the original velocity along the x-direction, from which $\bar{v}_s(x,z)$ is obtained; equation (17) smooths $\bar{v}_s(x,z)$ along the z-direction to get the smoothed velocity $v_s(x,z)$. In the wavenumber domain and for $w(x,z) \equiv 1$, the smooth velocity can be determined by

$$V_s(k_x,k_z) = \frac{V(k_x,k_z)}{(1+\alpha_x^2 k_x^2)(1+\alpha_z^2 k_z^2)}, \tag{18}$$

where V_s and V are the Fourier transforms of v_s and v respectively. Therefore, large-wavenumber components are suppressed. In discretization, equation (18) becomes

$$V_s(k_x,k_z) = \frac{V(k_x,k_z)}{(1+4(\alpha_x/\Delta x)^2\sin^2(k_x\Delta x/2))\,(1+4(\alpha_z/\Delta z)^2\sin^2(k_z\Delta z/2))}, \tag{19}$$

where Δx and Δz define the grid-cell sizes. A proof of formula (18) and formula (19) is in Appendix B. I define the unit of the smoothing parameters by

$$\alpha_x = \Delta x/2, \qquad \alpha_z = \Delta z/2.$$

For such smothing parameters, the Nyquist-wavenumber components in x and z directions, respectively, reduce by 1/2, i.e.,

$$V_s(2/\Delta x, 2/\Delta z) = \frac{1}{4}V(2/\Delta x, 2/\Delta z).$$

The larger the values of α_x and α_z, the smoother will be $v_s(x,z)$ and the larger will be the difference between $v(x,z)$ and $v_s(x,z)$. The following formula may be used to measure the difference between $v(x,z)$ and $v_s(x,z)$:

$$\epsilon^2(z) = \frac{\int\int_0^z (v_s(x,z') - v(x,z'))^2 dz'dx}{\int\int_0^z v(x,z')^2 dz'dx}. \tag{20}$$

Based on my experience,if $\epsilon(z)$ is greater than 0.1, the smoothing parameters are too large—the velocity is oversmoothed.

COMPUTER IMPLEMENTATION

I applied the modeling and migration method to synthetic models. Also, I tested the effect of velocity smoothing on the Kirchhoff migration of this paper and Gaussian beam migration.

Synthetic Data

The first model shown in Figure 1a, consists of five reflectors, each with a dipping and horizontal segment. Dips for the dipping segments range from 30 to 90 degrees in 15-degree increments. The velocity function consists of a linear function, $v(z) = 1.5+z$ km/s, plus a lateral variation that is $\cos(\frac{\pi}{2}(x-1.5))$ multiplied by a depth-dependent function, as shown in Figure 1b. The maximum lateral variation is 12 percent at $z = 1$ km. With the model and the velocity function, I generated two data sets: zero-offset and an offset of 1000 m. Figures 2 and 3 show the modeling data and inversion results for the two offsets. Because of the lateral variation in velocity, even horizontal reflectors give curve events in the data. After migration, all reflectors, horizontal through vertical, are imaged to their correct positions, for both the zero- and nonzero-offset data. Figure 4 shows Gaussian beam migration result by using the same zero-offset data. While both our method and Gaussian beam migration did well, the Gaussian beam migration used 17 minutes on the IBM Risk System/6000, and our method used 7 minutes, even though I used the prestack algorithm for the zero-offset data.

The second example is on turning-wave migration. The model shown in Figure 5 is a single reflector, with a segment beyond 90 degrees. The velocity function is the same as in the first example, shown in Figure 1b. With the model and the velocity function, I generated a data set with an offset of 500 m, shown in Figure 6a. After migration, the reflector is imaged to its correct position shown in Figure 6b, even for the segment beyound 90-degrees. This result shows that my method can handle lateral variation in velocity and turning waves.

Smoothing test

The velocity model shown in Figure 7 consists of six constant-velocity layers and the input zero-offset data for migration shown in Figure 8 were generated with this model by the CSHOT program(Docherty, 1987).

Different smoothed velocity functions are used in Gaussian-beam migration that is implemented by Hale's program (1992). Figure 9 shows the data migrated with the unsmoothed velocity in Figure 7. The migration result is poor: low resolution and migration artifacts are in the first three reflectors, and the last two reflectors are almost invisible. Figure 10 shows the data migrated with a smoothed velocity (smoothing parameters $\alpha_x = \alpha_z = 2.5$). While it is much better than Figure 9, there are still some artifacts. Figure 11, showing the data migrated with a more smoothed velocity (smoothing parameter $\alpha_x = \alpha_z = 5$), gives an improved structural image. If too large smoothing parameters ($\alpha_x = \alpha_z = 20$) are used, the migration result, shown in Figure 12, deteriorates. One can see that the corners of the third reflector have become too sharp, and the bottom reflector is no longer flat. Figure 13 shows the data migrated with the smoothed velocity by the windowed averaging method. The window size is selected so that the difference between the smoothed velocity and the original one is about the same as that in Figure 11. Both the damped least-squares

and the windowed averaging method improve structural images through smoothing the velocity, but the former looks a little better than the latter. There is incoherence on the vicinity of the right intersection between the first and the second interface in Figure 13 compared to Figure 11. The selected parts are shown in Figure 14. From this result, one may conclude that if the differences between the smoothed velocities and the original one are the same, the damped least-squares method smooths velocity a little more effectively, therefore, gives a slightly better result.

The velocity in Figure 7 has strong lateral variation. For this unsmoothed velocity, the finite difference algorithm for the eikonal equation 6 will break down because $\partial\tau/\partial z$ may not positive. Therefore, in order to implement the Kirchhoff migration of this paper, the smoothed velocity is required. The least smoothing parameters for this requirement are $\alpha_x = \alpha_z = 14$. Since the velocity is slightly oversmoothed, the bottom reflector is not very flat. Furthermore, like other Kirchhoff migration methods, the discontinuities in the bottom event of Figure 8 make strong diffraction smiles in Figure 10 since large apertures are used. In contrast, Gaussian beam migration does not suffer this problem.

Figure 16 shows the differences between the smoothed velocities and the original one, which is calculated by using formula (20). The larger the smoothing parameters, the larger the difference. This difference may help to choose suitable smoothing parameters. For example, the difference for $\alpha_x = \alpha_z = 20$ is greater than 0.1 from which I conclude that the velocity is oversmoothed and then reject these smoothing parameters.

CONCLUSION

The Kirchhoff integral provides a powerful tool for modeling and migration. In this paper, a finite-difference algorithm is used to calculate traveltimes and amplitudes. With the help of interpolation, this method can be efficiently implemented. The result on the synthetic data shows that this method can handle lateral variation in velocity and turning waves. One limitation is that the Kirchhoff method cannot efficiently deal with caustics in the Green's functions of the integration operator and multiple-arrival times. Another is that this method needs a sufficiently smooth velocity function. When velocity has a strong lateral variation, the eikonal equation cannot be solved by this method. This difficulty may be solved through using smoothed velocity.

ACKNOWLEDGMENTS

Thanks to Dr. Ken Larner for his critical reading of the first drafts of this paper. Thanks to Dr. Norman Bleistein for his help and guidance on this paper.

REFERENCES

Bleistein, N., 1986, Two and one-half dimensional in-plane wave propagation: Geophys. Prosp., **34**, 686-703.

Bleistein, N., Cohen, J., and Hagin, F., 1987, Two and one-half dimensional Born inversion with an arbitrary reference: Geophys., **52**, 26-36.

Docherty, P. C., 1987, Ray theoretical modeling, migration, and inversion in the two-and-one-half-dimensional layered acoustic media: Center for wave phenomena Research Report, CWP-051.

Dohr, G., 1985, Seismic shear waves (part A: theory): Geophysical Press, London—Amersterdam.

Hale, D, Computational aspects of Gaussian beam migration: CWP Review, 1992.

Pusey, L., and Vidale, J., 1991, Accurate-difference calculation of WKBJ traveltimes and amplitudes: 1991 SEG expanded abstracts, p. 1513.

van Trier, J., and Symes, W., 1990, Upwind finite-difference calculation of seismic traveltimes: 1990 SEG expanded abstracts, p. 1000.

APPENDIX A: GEOMETRIC-SPREADING FACTOR FOR LINEAR VELOCITY

Firstly, I assume that the velocity is

$$v(z) = v_0 + az.$$

Following from formulas in Bleistein (1986), I find

$$x - x_s = \frac{v_0}{a \sin\beta}(\cos\beta - \cos\phi), \tag{A-1}$$

and

$$\sigma = \frac{v_0^2(\cos\beta - \cos\phi)}{a \sin^2\beta}. \tag{A-2}$$

From Snell's law

$$\frac{\sin\beta}{v_0} = \frac{\sin\phi}{v(z)},$$

I have

$$\frac{d\phi}{d\beta} = \frac{v(z)\cos\beta}{v_0 \cos\phi}. \tag{A-3}$$

By using the Snell's law and equation (A-1), I obtain

$$x - x_s = \frac{v_0}{a}\cot\beta - \frac{v(z)}{a}\cot\phi. \tag{A-4}$$

Taking the derivative with respect to β and using equation (A-3) gives

$$\frac{\partial x}{\partial \beta} = -\frac{v_0}{a\sin^2\beta} + \frac{v(z)}{a\sin^2\phi}\frac{d\phi}{d\beta} = -\frac{v_0}{a\sin^2\beta} + \frac{v^2(z)\cos\beta}{av_0\sin^2\phi\cos\phi} = \frac{v_0(\cos\beta - \cos\phi)}{a\sin^2\beta\cos\phi}.$$

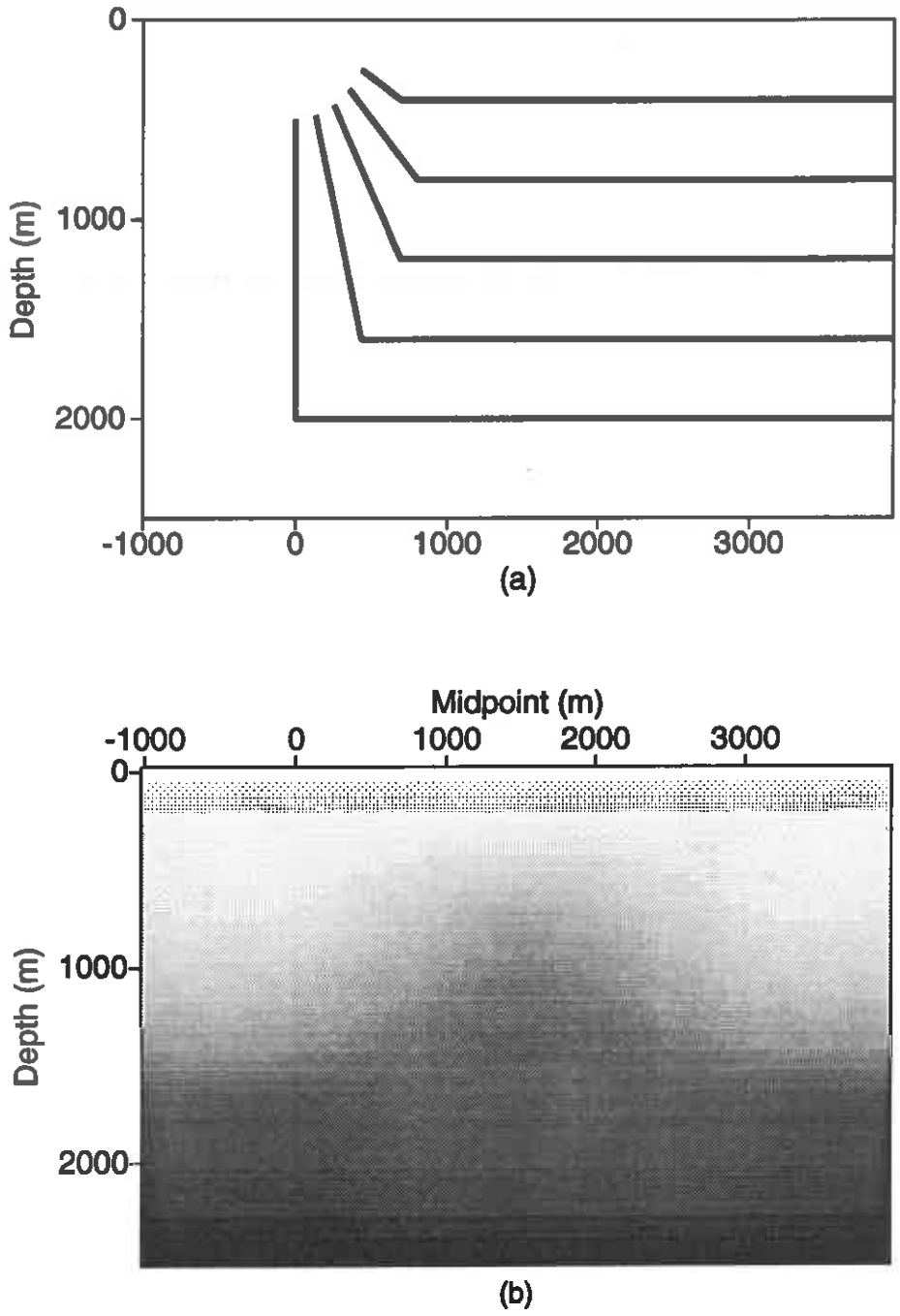

FIG. 1. (a) Subsurface structural model used to generate synthetic seismic traces. (b) Velocity model. The darker shading denotes higher velocity.

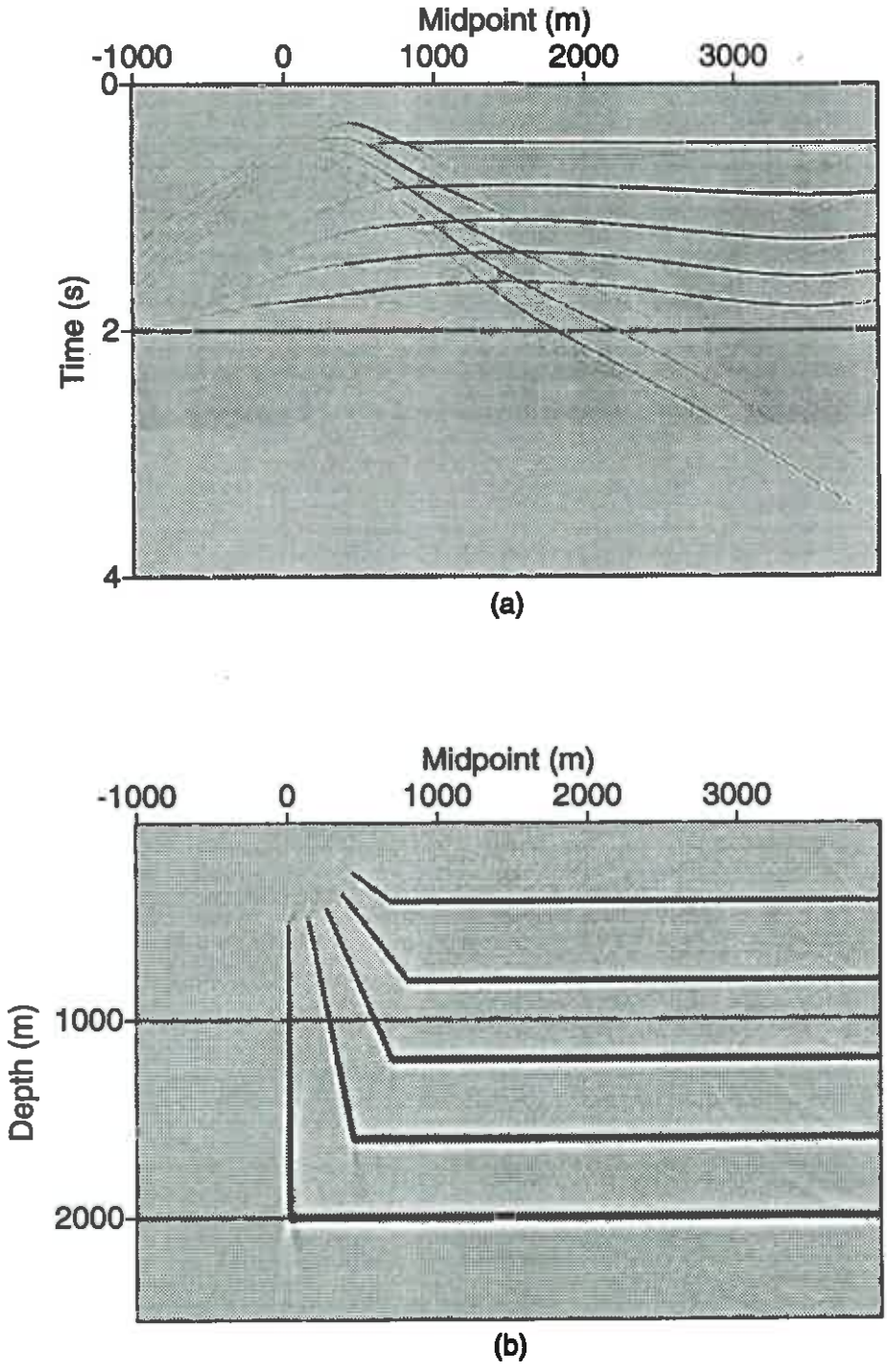

FIG. 2. (a) Zero-offset data for the model in Figure 1. (b) The Kirchhoff migration of the data in (a), with velocity model in Figure 1b.

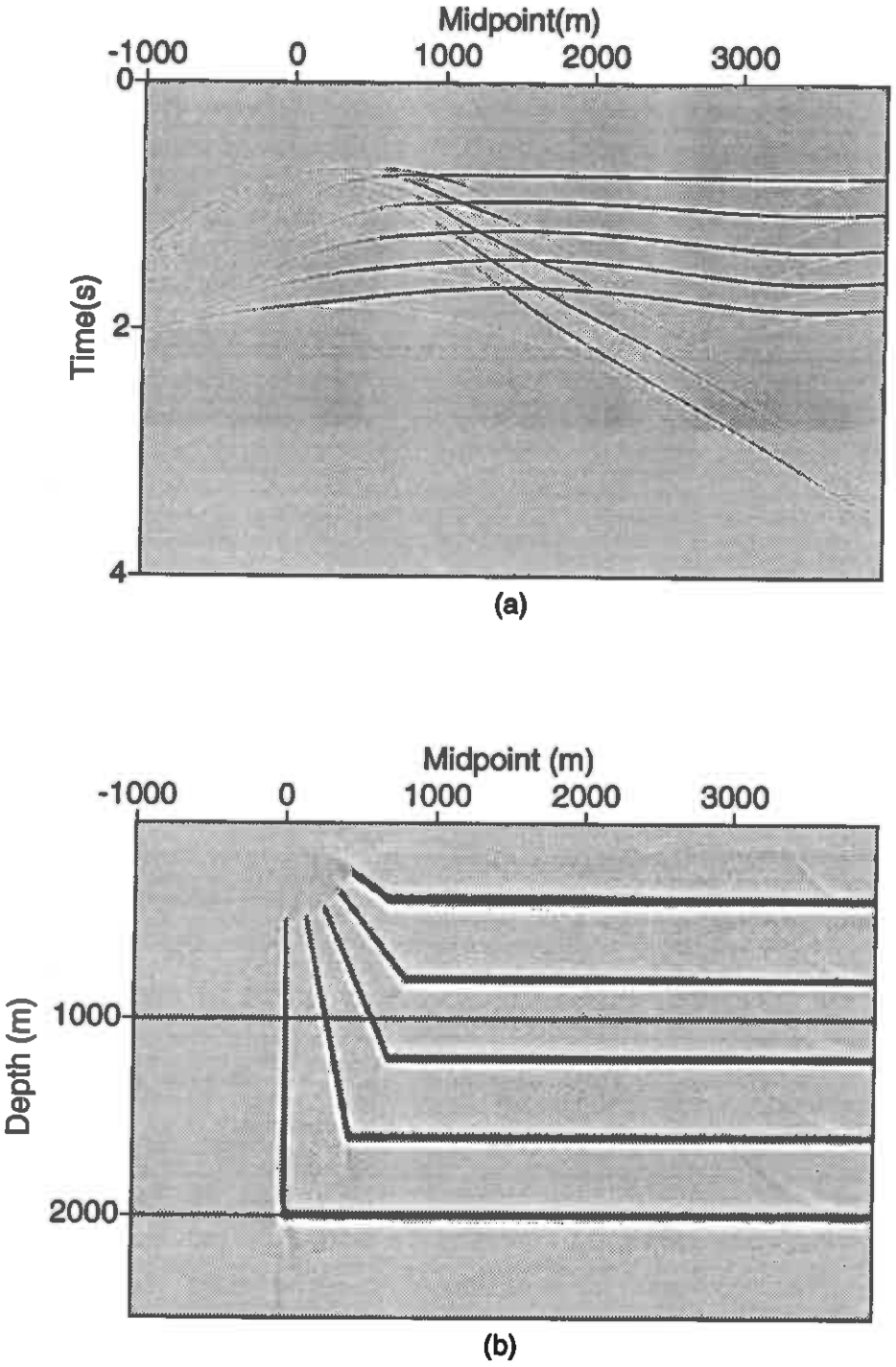

FIG. 3. (a) Nonzero-offset data (offset=1000 m) for the model in Figure 1. (b) The Kirchhoff migration of the data in (a), with velocity model in Figure 1b.

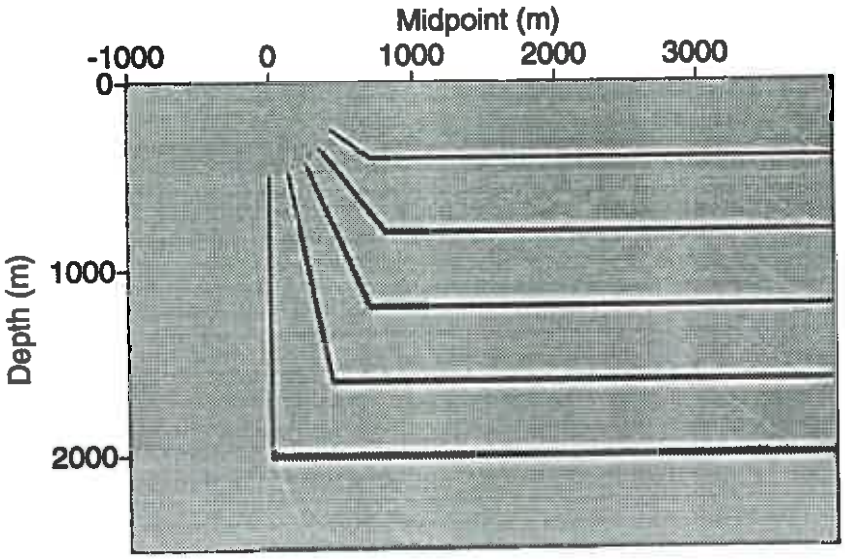

FIG. 4. Gaussian-beam migration of the data in Figure 2a.

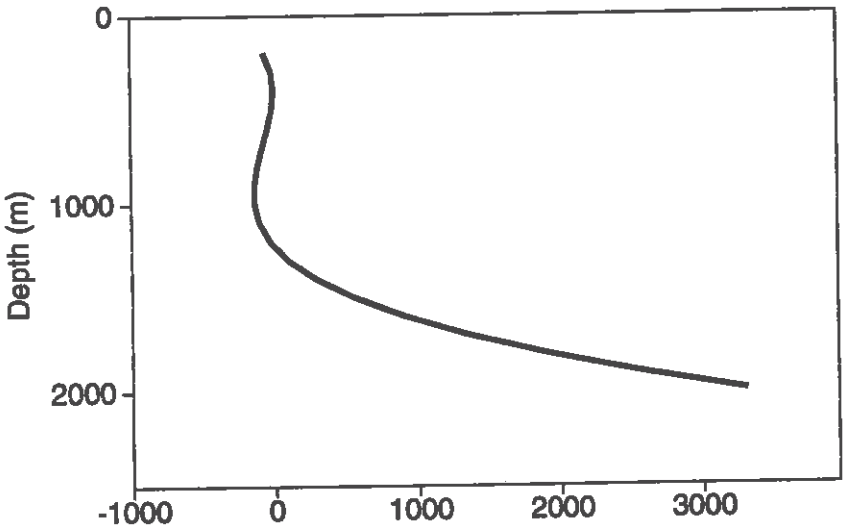

FIG. 5. Subsurface structural model used to generate turning waves.

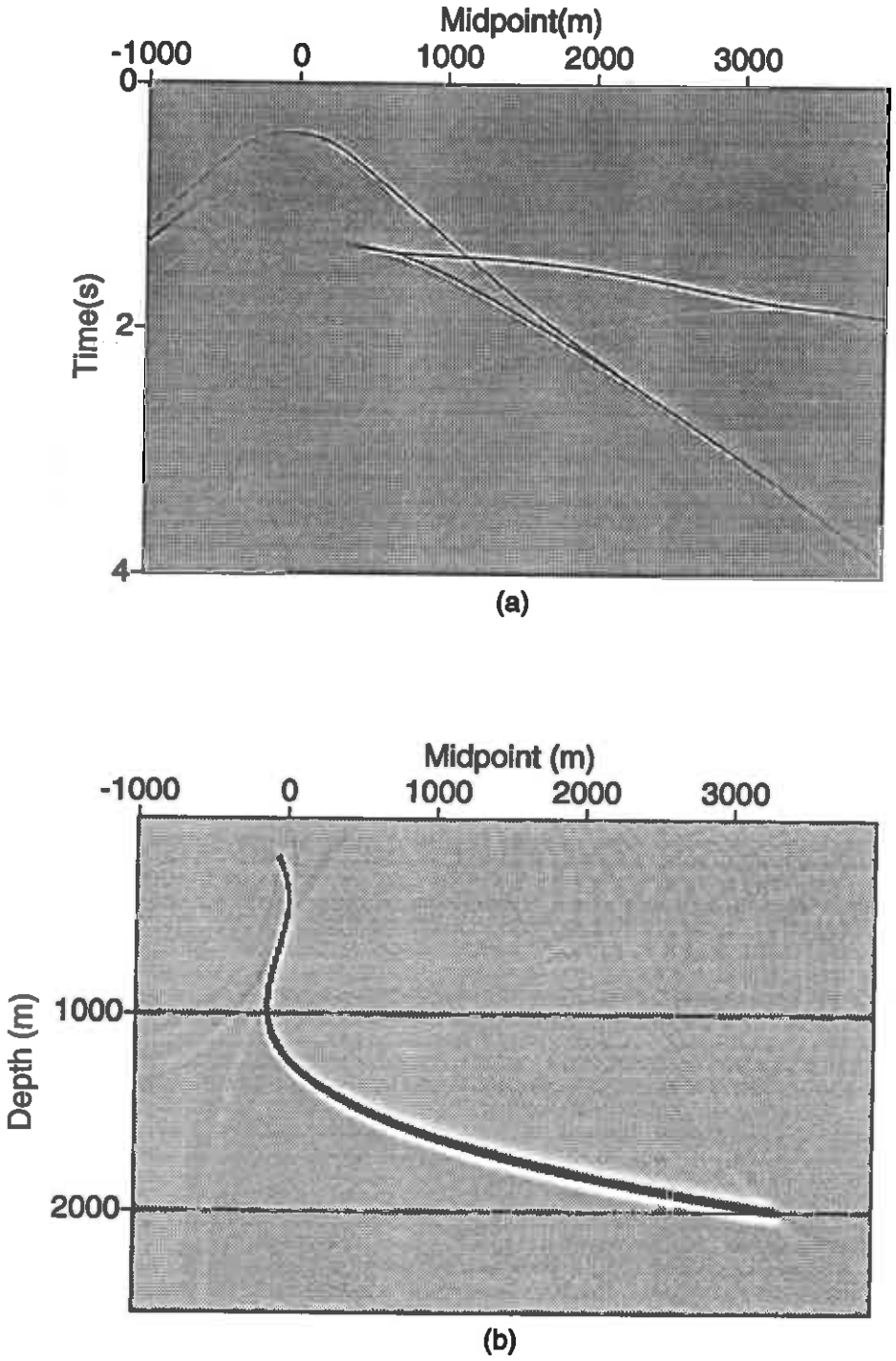

FIG. 6. (a) Data (offset=500 m) for the model in Figure 5. (b) The Kirchhoff migration of the data in (a), with velocity model in Figure 1b.

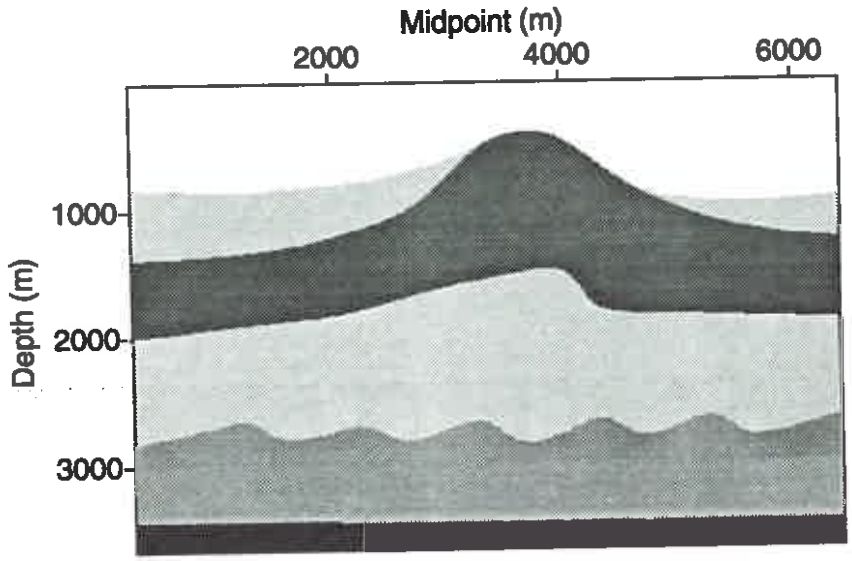

FIG. 7. True velocity model in smoothing test. The darker shading denotes higher velocity.

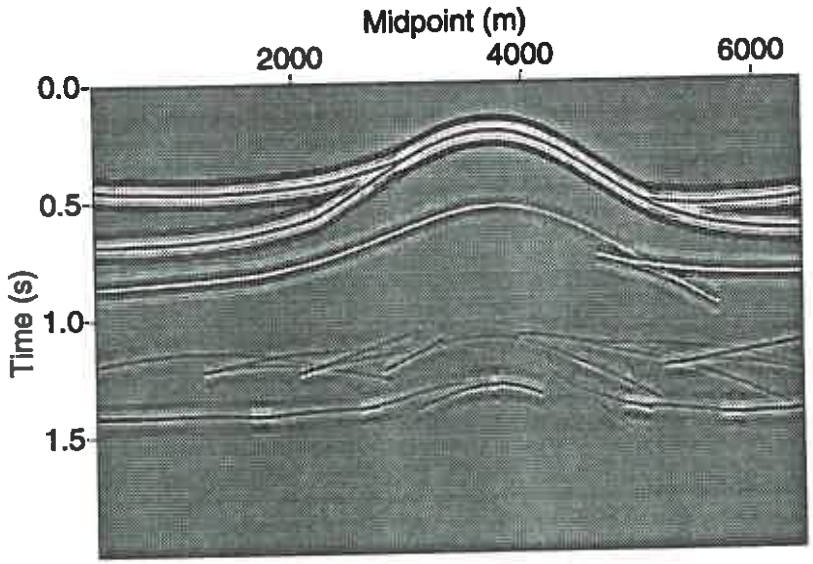

FIG. 8. Zero-offset synthetic data generated with the velocity model in Figure 7.

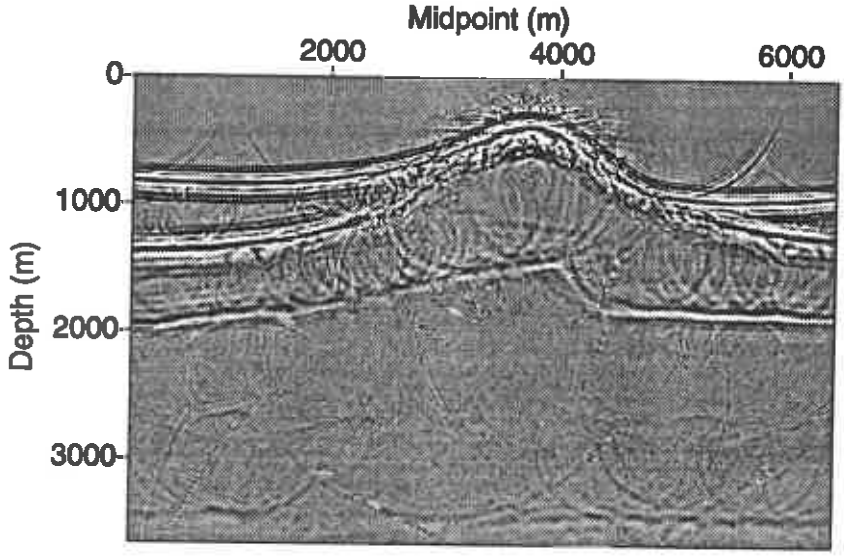

FIG. 9. Gaussian beam migration with the unsmoothed velocity model in Figure 8.

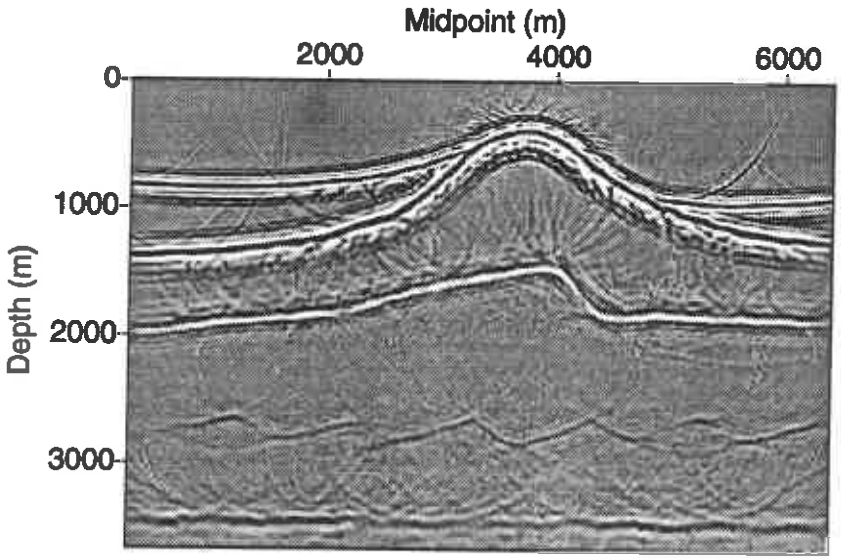

FIG. 10. Gaussian beam migration with a smoothed velocity model. The smoothing parameters $\alpha_x = \alpha_z = 2.5$. The velocity is undersmoothed.

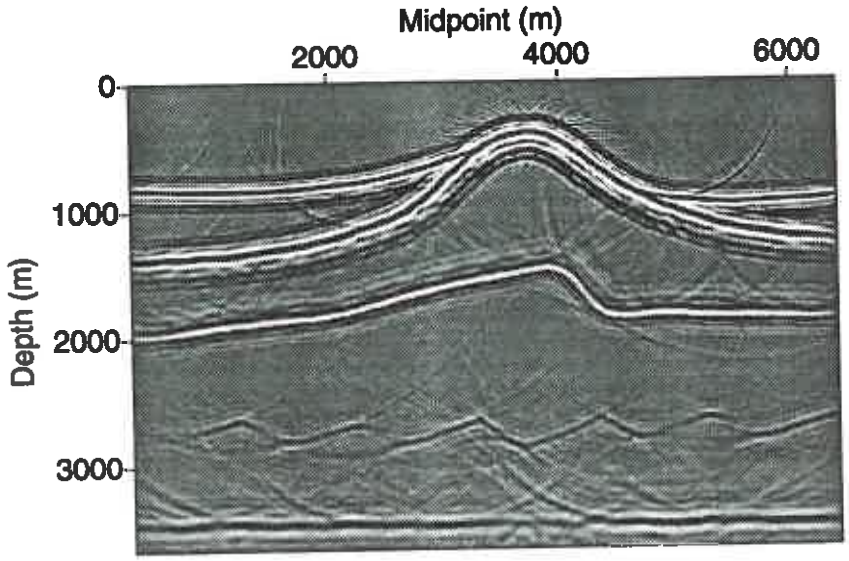

FIG. 11. Gaussian beam migration with a smoothed velocity model. The smoothing parameters $\alpha_x = \alpha_z = 5$.

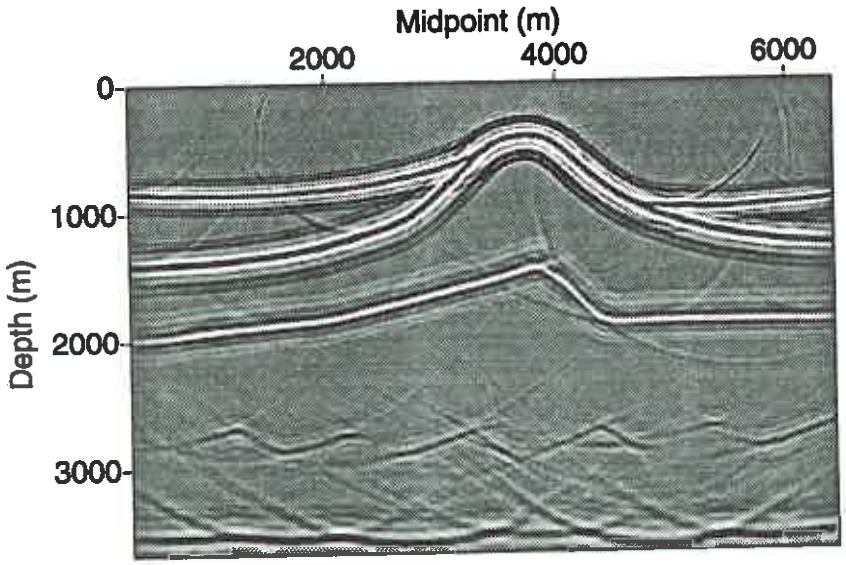

FIG. 12. Gaussian beam migration with a smoothed velocity model. The smoothing parameters $\alpha_x = \alpha_z = 20$. The velocity is oversmoothed.

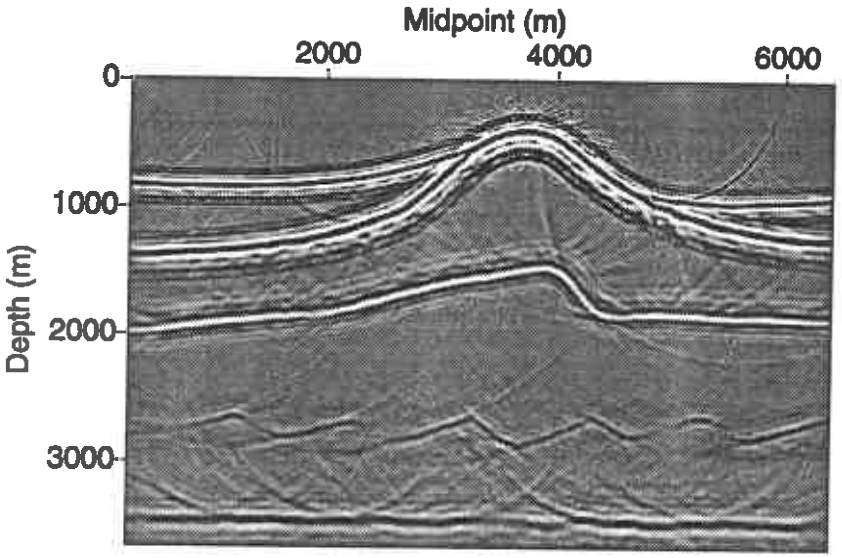

FIG. 13. Gaussian beam migration with a smoothed velocity model. The velocity is smoothed by the windowed averaging with the window size of 9 points.

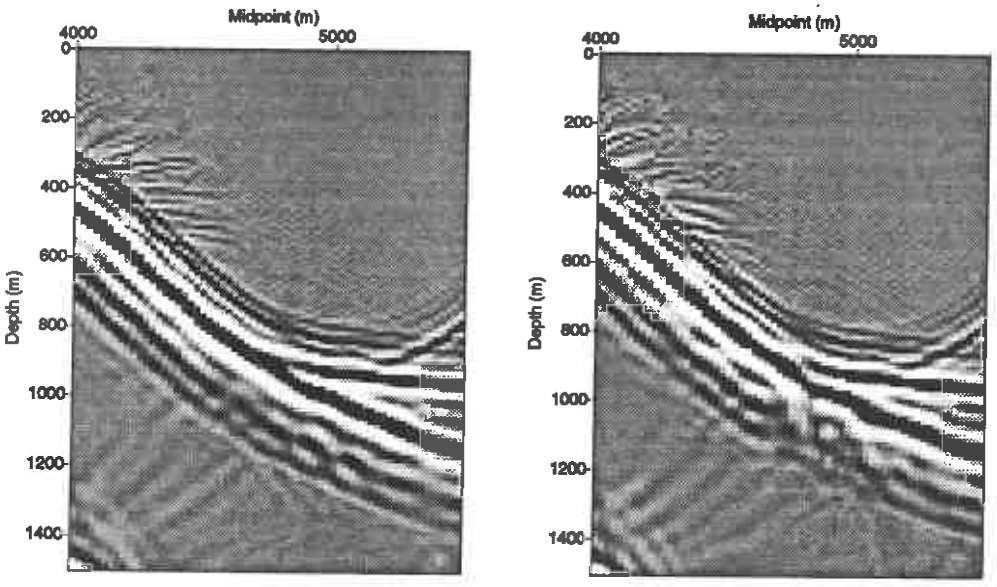

FIG. 14. Selection form Figure 11 and Figure 13. The left one is from Figure 11 and the right one is from Figure 13.

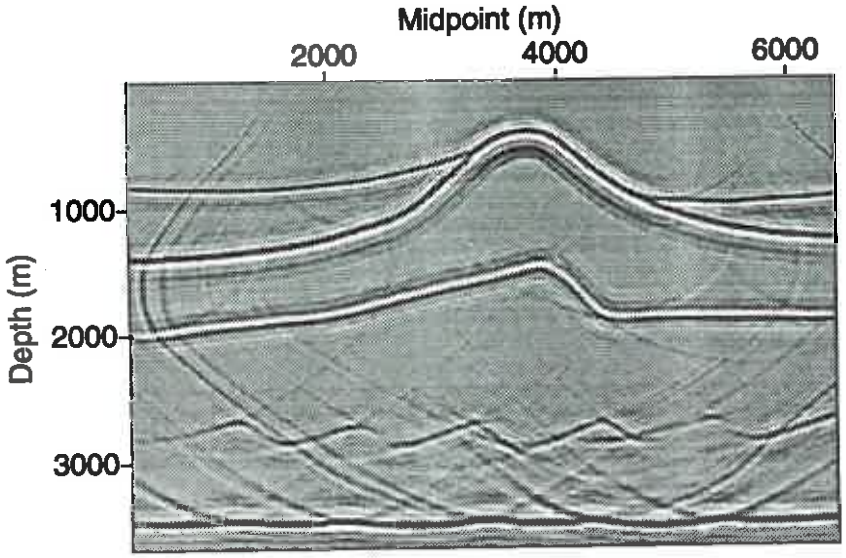

FIG. 15. Kirchhoff migration with a smoothed velocity model. The smoothing parameters $\alpha_x = \alpha_z = 14$. The velocity is slightly oversmoothed.

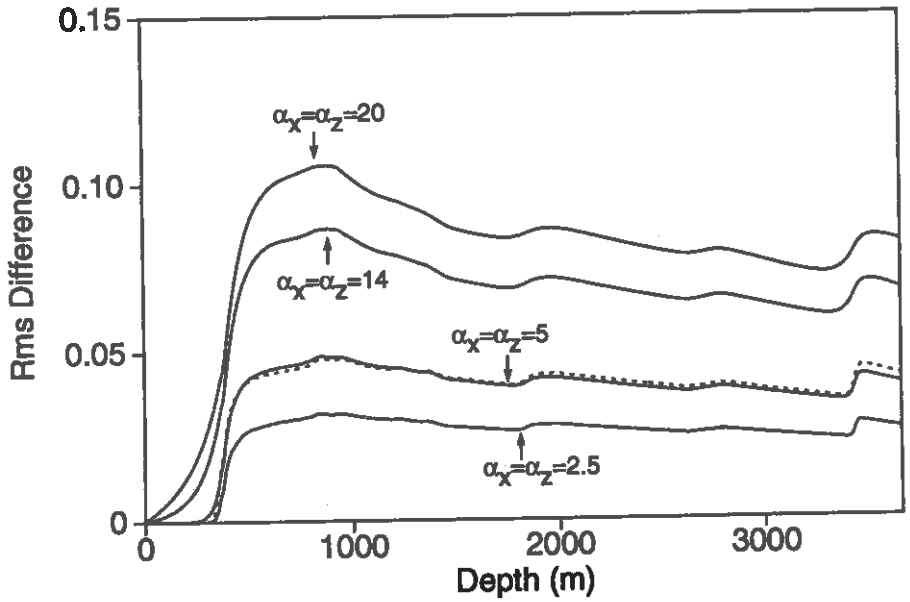

FIG. 16. The relative rms-differences between smoothed velocities and the true velocity. Four solid curves denote the smoothed velocities by the damped least-squares. The dashed curve denotes the smoothed velocity by the windowed averaging.

Therefore,

$$\frac{\partial x}{\partial \beta} = \frac{\sigma}{v_0 \cos\phi}; \tag{A-5}$$

i.e.,

$$\frac{\partial \beta}{\partial x} = \frac{v_0 \cos\phi}{\sigma}. \tag{A-6}$$

From equation (4),

$$\frac{\partial \beta}{\partial z} = -\frac{\partial \beta}{\partial x}\frac{\partial \tau}{\partial x}\left[\frac{\partial \tau}{\partial z}\right]^{-1} = -\frac{\partial \beta}{\partial x}\tan\phi$$

The above formula and the chain rule for partial differentiation give

$$\frac{\partial \beta}{\partial \theta} = \frac{\partial \beta}{\partial x}\frac{\partial x}{\partial \theta} + \frac{\partial \beta}{\partial z}\frac{\partial z}{\partial \theta} = \frac{\partial \beta}{\partial x}(r\cos\theta + r\sin\theta\tan\phi) = \frac{r\cos(\theta-\phi)}{\cos\phi}. \tag{A-7}$$

Finally, substituting equation (A-6) into (A-7), I obtain

$$\frac{\partial \beta}{\partial \theta} = \frac{r v_0}{\sigma}\cos(\theta-\phi). \tag{A-8}$$

When the velocity is a linear function of x and z, there is a rotational transformation around the point $(x_s, 0)$ such that the velocity is a linear function of z in the new coordinate system. Also it is easy to show that equation (A-8) is invariant under the rotational transformation.

APPENDIX B: SMOOTHING IN WAVENUMBER

By using the Euler's formula from the calculus of variations, we change (16) into a differential equation for $\bar{v}_s(x,z)$:

$$\bar{v}_s(x,z) - v(x,z) - \alpha_x^2 \frac{\partial^2 \bar{v}_s}{\partial x^2} = 0. \tag{B-1}$$

Taking the Fourier transforms with respect to x and z gives the solution in the wavenumber domain

$$\bar{v}_s(k_x,k_z) = v(k_x,k_z)/(1+\alpha_x^2 k_x^2).$$

Similarly,

$$v_s(k_x,k_z) = \bar{v}_s(k_x,k_z)/(1+\alpha_z^2 k_z^2).$$

So

$$v_s(k_x,k_z) = \frac{v(k_x,k_z)}{(1+\alpha_x^2 k_x^2)(1+\alpha_z^2 k_z^2)}. \tag{B-2}$$

In discretization, the second derivative can be approximated by

$$\frac{\partial^2 \bar{v}_s}{\partial x^2} \approx \frac{\bar{v}_s(x+\Delta x,z) - 2\bar{v}_s(x,z) + \bar{v}_s(x-\Delta x,z)}{(\Delta x)^2}$$

whose Fourier transform with respect to x is

$$\frac{4\sin^2(k_x\Delta x/2)}{(\Delta x)^2}\,\bar{v}_s(k_x,z).$$

Using this formula and taking the Fourier transforms with respect to x and z in (B-1) give the solution in the wavenumber domain

$$\bar{v}_s(k_x,k_z)=\frac{v(k_x,k_z)}{1+4(\alpha_x/\Delta x)^2\sin^2(k_x\Delta x/2)}.$$

Similarly,

$$v_s(k_x,k_z)=\frac{\bar{v}_s(k_x,k_z)}{1+4(\alpha_z/\Delta z)^2\sin^2(k_z\Delta z/2)}.$$

So

$$v_s(k_x,k_z)=\frac{v(k_x,k_z)}{(1+4(\alpha_x/\Delta x)^2\sin^2(k_x\Delta x/2))\,(1+4(\alpha_z/\Delta z)^2\sin^2(k_z\Delta z/2))}. \quad \text{(B-3)}$$

CWP-135

Velocity analysis by perturbation

Zhenyue Liu and Norman Bleistein

Velocity analysis by perturbation

Zhenyue Liu and Norman Bleistein

ABSTRACT

Prestack depth migration provides a powerful tool for doing velocity analysis in complex media. Both prominent approaches to velocity analysis—depth-focusing analysis and residual-curvature analysis, rely on approximate formulas in order to estimate velocity errors. Generally, these formulas are derived under the assumptions of horizontal reflector, lateral velocity homogeneity, or small offset. Therefore, the conventional methods for updating velocity lack sufficient computational efficiency when velocity has large, lateral variations.

Here, using a perturbation method, we derive an analytic relationship between residual moveout and residual velocity. In our derivation, we impose no limitation on offset, dip, or velocity distribution. Based on this formula, we revise the residual-curvature-analysis method for velocity estimation that involves recursion and iteration. Furthermore, this formula provides the sensitivity and error estimation for migration-based velocity analysis, which is helpful in explaining the reliability of the estimated velocity.

INTRODUCTION

Prestack depth migration that can handle dipping reflectors and lateral velocity variations is robust in imaging complex structures. In order to process data by this method, one often needs to have a more accurate velocity model than may be obtained from simple velocity-analysis methods, such as normal moveout. Meanwhile, prestack depth migration itself is an attractive tool for doing velocity analysis because of its high sensitivity to the velocity model. Two approaches to migration velocity analysis have been developed: depth-focusing analysis (DFA) and residual-curvature analysis (RCA). Depth-focusing analysis is based on using stacking power to measure velocity error. Residual-curvature analysis is based on residual moveout to measure velocity error.

Migration velocity analysis must address two issues to succeed: (1) how to establish a criterion for knowing if a migration velocity is acceptable; (2) how to update the velocity, if it is unacceptable. In DFA, a migration velocity is acceptable if the difference between migration depth and focusing depth is zero. In RCA, a migration

velocity is acceptable if the difference between imaged depths from different offsets is zero. Quantitatively, these differences can be used to update the velocity. To date, a variety of updating formulas have been developed. These formulas degrade with increasing complexity of media (lateral velocity variation and reflector dip), because of rough approximations used to estimate velocity. Although iteration generally is helpful in obtaining a more accurate velocity, a good approximation not only reduces iteration steps but guarantees the convergence. The conventional formulas for updating velocity were derived under one or more assumptions as follows:

(i) lateral velocity homogeneity;

(ii) small offset;

(iii) horizontal reflector.

In DFA, all three assumptions are used (MacKay and Abma, in 1992). In RCA, the assumptions vary with migration types. For common-shot migration or common-receiver migration, Al-Yahya's formula (1989) used all three assumptions. Lee and Zhang (1992) developed a formula that replaces assumption (iii) by the assumption of small dip. For Common-offset migration, Deregowski's formula (1990) used the first two conditions. [This was proven by Liu and Bleistein (1992).] Both DFA and RCA use assumptions (i) and (ii). Under the assumption of a small offset, the residual moveout can be approximated by a hyperbola or a parabola. However, this approximation is poor when the velocity has an obvious lateral variation.

Conventional approaches, such as DFA and RCA, inspect information on each midpoint individually. This may not be reliable when conflicting events exist because velocity estimation will depend on which event is used. Furthermore, the conventional approaches estimate the stacking velocities that are assumed to equal the rms velocities, and then convert the rms velocities into the interval velocities by Dix' equation or other methods. The stacking velocity is very sensitive to the lateral variation in velocity. When the velocity is laterally variant, the stacking velocity may be very different from the rms velocity.

Because of limitations, conventional approaches to velocity analysis cannot handle complex media (such as the model for Marmousi data). To overcome these limitations, some geophysicists used a macro-model method for estimating the interval velocity directly . A macro-model consists of velocities and velocity interfaces. An initial macro-model is determined from conventional techniques; the macro-model is updated iteratively by using depth-focusing, residual-curvature analysis, or both. The whole process may be accomplished with interpretation based on geological knowledge. The present macro-model method has two significant drawbacks. The first one is that velocity distribution is assumed to be constant in layers. In fact, velocity may vary within a block. The second one is that no efficient formula is used to update velocity. The criterion used now for updating velocity is only qualitative, which results in inaccuracy and inefficiency in velocity estimates.

In this paper, we present a new method for velocity analysis that revises the RCA method. Based on perturbation theory, we derive a quantitative relationship between

residual moveout and error of velocity that is valid for any offset, dip and velocity distribution. A similar formula was proposed by Lafond et al. (1993). However, that formula is restricted to constant-velocity layers. In contrast, our formula can handle any parameterization of velocity. To apply this formula, it is necessary to calculate some quantities that depend on the specular source-receiver pairs for each image point. Here, we use multiple outputs of Kirchhoff migration to determine these quantities efficiently.

Although prestack migration has superior advantages to deal with complex media, its weaknesses should be considered in application. Besides the costly computation, complexity of medium may degrade the effectiveness of the prestack migration method. Here, we discuss the sensitivity of migration-based velocity analysis, and show what factors affect the sensitivity, so that we may estimate the velocity error involved in the velocity analysis. Furthermore, this sensitivity analysis provides an indicator of when *a priori* geological knowledge is necessary for estimating reasonable velocities.

VELOCITY ESTIMATION

If an incorrect velocity is used in prestack migration, the imaged depths from different offsets at a common-image-gather will differ from each other. In this situation, a residual moveout is observed in migrated data. The principle of velocity analysis is to correct the velocity so that the imaged depths at each common-image-gather are close to for each other. For this purpose, one needs a quantitative relationship between the residual moveout and the velocity error. Here, we use the perturbation method to derive the representation for the residual moveout.

We denote by X a 2-D vector, $X = (x, z)$. Let x_s be the source position and x_r be the receiver position on the surface. For any point X below the surface, $\tau_s(x_s, X)$ or $\tau_r(X, x_r)$, respectively, denote traveltimes from x_s to X, or X to x_r.

Suppose we know the total reflection travetime function $T(y, h)$ (therefore, $\partial T/\partial y$) that depends on midpoint y and half-offset h. Given a velocity function $v(x, z)$, then, for each h, the reflector is determined by

$$\tau_s(x_s, X) + \tau_r(X, x_r) = T(y, h), \tag{1}$$

$$\frac{\partial \tau_s}{\partial y} + \frac{\partial \tau_r}{\partial y} = \frac{\partial T}{\partial y}, \tag{2}$$

where $X \equiv (x, z)$ is the point on the reflector. The reflector is related to offset; for a fixed image location x, the imaged depth z can be computed that is a function of h. If $v(x, z)$ equals the true velocity, then the imaged depth z is independent of offset h; otherwise—for incorrect velocity—z varies with offset h. Consequently, the imaged depth provides information on velocity.

Suppose that the velocity distribution v is characterized by a parameter λ,

$$v = v(\lambda; X).$$

For example, when $v(x,z) = v_0 + ax + bz$, λ is either v_0, a, or b.

For a fixed image location x, we differentiate equation (1) with respect to λ. Noticing that y and z are functions of λ, then

$$\left[\frac{\partial \tau_s}{\partial y} + \frac{\partial \tau_r}{\partial y}\right]\frac{dy}{d\lambda} + \left[\frac{\partial \tau_s}{\partial \lambda} + \frac{\partial \tau_r}{\partial \lambda}\right] + \left[\frac{\partial \tau_s}{\partial z} + \frac{\partial \tau_r}{\partial z}\right]\frac{dz}{d\lambda} = \frac{\partial T}{\partial y}\frac{dy}{d\lambda}. \tag{3}$$

By using equation (2), the first term of the left side in equation (2) is balanced by the right-hand term. Therefore,

$$\left[\frac{\partial \tau_s}{\partial z} + \frac{\partial \tau_r}{\partial z}\right]\frac{dz}{d\lambda} = -\frac{\partial \tau_s}{\partial \lambda} - \frac{\partial \tau_r}{\partial \lambda}.$$

From

$$\frac{\partial \tau_s}{\partial z} = \frac{\cos\theta_s}{v}, \qquad \frac{\partial \tau_r}{\partial z} = \frac{\cos\theta_r}{v},$$

where θ_s or θ_r are angels between the raypath from the source or the receiver, and the vertical at X, we have that

$$\frac{\cos\theta_s + \cos\theta_s}{v}\frac{dz}{d\lambda} = -\frac{\partial \tau_s}{\partial \lambda} - \frac{\partial \tau_r}{\partial \lambda}.$$

That is,

$$\frac{dz}{d\lambda} = g(x,h), \tag{4}$$

where,

$$g(x,h) = -\left[\frac{\partial \tau_s}{\partial \lambda} + \frac{\partial \tau_r}{\partial \lambda}\right]\frac{v(\lambda;X)}{\cos\theta_s + \cos\theta_r}. \tag{5}$$

Suppose that the true parameter is λ^* and the true depth is z^*. If there is a small perturbation $\Delta\lambda = \lambda^* - \lambda$ between the true parameter and the parameter used in migration, then the imaged depth will have a corresponding perturbation $\Delta z(x,h) \approx z^* - z(x,h)$. From equation (4), Δz can be represented by

$$\Delta z = g(x,h)\Delta\lambda. \tag{6}$$

Equation (6) is true for an arbitrary velocity distribution, any dipping reflector, and any offset, which is significantly different from the limited result of conventional RCA.

When the velocity distribution is characterized by multiple parameters, $\hat{\lambda} = (\lambda_1, \lambda_2, ..., \lambda_n)^T$, the imaged-depth perturbation will be affected by the perturbations of all these parameters. Therefore, equation (6) is modified by

$$\Delta z(x,h) = \sum_{i=1}^{n}\frac{\partial z}{\partial \lambda_i}\Delta\lambda_i = \sum_{i=1}^{n} g_i(x,h)\Delta\lambda_i, \tag{7}$$

where

$$g_i(x,h) = -\left[\frac{\partial \tau_s}{\partial \lambda_i} + \frac{\partial \tau_r}{\partial \lambda_i}\right] \frac{v(\hat{\lambda};X)}{\cos\theta_s + \cos\theta_r}. \tag{8}$$

If we could solve for $\Delta\hat{\lambda}$, the true parameters can be estimated by

$$\hat{\lambda}^* = \hat{\lambda} + \Delta\hat{\lambda}.$$

Notice that the left side of equation (7) involves the unknown z^*, so it is necessary to remove z^* in this equation. The true depth can be approximately replaced by the corrected imaged depth $z + \Delta z$,

$$z^* \approx z(x,h) + \Delta z(x,h) = z(x,h) + \sum_{i=1}^{n} g_i(x,h)\Delta\lambda_i.$$

Because z^* is independent of offset, the corrected imaged-depths from different offsets should be close to for each other. Suppose that there are offsets h_1, h_2, ..., h_m, and image locations x_1, x_2, ..., x_K, then

$$z_j^{(k)} + \Delta\hat{z}^{(k)} = z_j^{(k)} + \sum_{i=1}^{n} g_{ij}^{(k)}\Delta\lambda_i,$$

where

$$z_j^{(k)} = z(x_k, h_j),$$

$$\Delta\hat{z}^{(k)} = \Delta z(x_k, h_j),$$

$$g_{ij}^{(k)} = g_i(x_k, h_j).$$

We seek $\Delta\lambda_i$'s such that the corrected imaged depths have the minimum variance; i.e.,

$$\sum_{k=1}^{K}\sum_{j=1}^{m}\left(z_j^{(k)} + \Delta z_j^{(k)} - \overline{\hat{z}^{(k)} + \Delta\hat{z}^{(k)}}\right)^2 = \min, \tag{9}$$

where

$$\hat{z}^{(k)} = (z_1^{(k)}, z_2^{(k)}, ..., z_m^{(k)})^T,$$

$$\Delta\hat{z}^{(k)} = (\Delta z_1^{(k)}, \Delta z_2^{(k)}, ..., \Delta z_m^{(k)})^T.$$

Here we use the overline to denote the mean value of a vector over the offset index. For example,

$$\overline{\hat{z}^{(k)}} = \frac{1}{m}\sum_{j=1}^{m} z_j^{(k)}.$$

Indroduce the matrix and vector,

$$A^{(k)} \equiv [a_{il}^{(k)}]_{n\times n}, \qquad \hat{b}^{(k)} \equiv (b_1^{(k)}, b_2^{(k)}, ..., b_n^{(k)})^T,$$

where

$$a_{il}^{(k)} = \sum_{j=1}^{m} \left(g_{ij}^{(k)} - \overline{\hat{g}_i^{(k)}} \right) \left(g_{lj}^{(k)} - \overline{\hat{g}_l^{(k)}} \right),$$

$$b_i^{(k)} = \sum_{j=1}^{m} \left(g_{ij}^{(k)} - \overline{\hat{g}_i^{(k)}} \right) \left(z_j^{(k)} - \overline{\hat{z}^{(k)}} \right),$$

$$\hat{g}_i^{(k)} = (g_{i1}^{(k)}, g_{i2}^{(k)}, ..., g_{in}^{(k)})^T;$$

then, as shown in Appendix A, the solution of equation (9) must satisfy the linear equation,

$$\left[\sum_{k=1}^{K} A^{(k)} \right] \Delta\hat{\lambda} = -\sum_{k=1}^{K} \hat{b}^{(k)}. \tag{10}$$

Specifically, if there is only one parameter to be determined, equation (10) will have an explicit solution

$$\Delta\lambda = -\frac{\sum_{k=1}^{K} \sum_{j=1}^{m} \left(g_j^{(k)} - \overline{\hat{g}^{(k)}} \right) \left(\hat{z}_j^{(k)} - \overline{\hat{z}^{(k)}} \right)}{\sum_{k=1}^{K} \sum_{j=1}^{m} \left(g_j^{(k)} - \overline{\hat{g}^{(k)}} \right)^2}, \tag{11}$$

where

$$g_j^{(k)} = g(x_k, h_j),$$

and

$$\hat{g}^{(k)} = (g_1^{(k)}, g_2^{(k)}, ..., g_m^{(k)})^T.$$

If the corrected imaged-depths are not close enough to each other, we implement iteration to obtain more accurate parameters. The iteration stops when the variance achieves a given accuracy.

Calculation of the function g_i

The function $g_i(y, h)$ involves the derivatives of traveltimes with respect to the parameter λ. In the eikonal equation,

$$\left(\frac{\partial\tau}{\partial x} \right)^2 + \left(\frac{\partial\tau}{\partial z} \right)^2 = \frac{1}{v^2(x,z)},$$

if we take the derivative with respect λ, then

$$\frac{\partial\mu}{\partial x}\frac{\partial\tau}{\partial x} + \frac{\partial\mu}{\partial z}\frac{\partial\tau}{\partial z} = \frac{1}{2}\frac{\partial}{\partial\lambda}\left(\frac{1}{v^2(x,z)} \right), \tag{12}$$

where

$$\mu = \frac{\partial\tau}{\partial\lambda}.$$

For each source or receiver, $\partial\tau/\partial\lambda$ is determined by solving equation (12). Therefore, given an imaged point (x, z) and a specular source-receiver pair x_s and x_r, we can

calculate g_i from formula (8). However, there is not an explicit formula to represent the specular source-receiver pair from the imaged point for a complex medium. To solve this problem, here, we use the Kirchhoff integral to calculate g_i. In the Kirchhoff summation, we calculate two inversion outputs which have two different amplitudes. One is the original amplitude; the other is the original one multiplied by the quantity g_i. Thus, the ratio of the amplitudes of the two outputs will give g_i at the specular source-receiver position according to the stationary-phase principle, without requiring knowledge of the specular source-receiver pair. This is the same technique as was used to determine the angle of reflection in Kirchhoff inversion. [See Bleisten et al. (1987).]

Parameterization of Velocity

Although equation (7) holds for any velocity distribution, the solution will be underdetermined if too many unknown parameters are involved. Consequently, it is essential to characterize the velocity distribution by choosing appropriate parameters. Conventionally, one assumes that a velocity model consists of the construction of the macro-model (constant velocities and velocity interfaces). The interfaces divide the whole model into a number of blocks. Here, we replace constant velocity in one block by a linear function that is characterized by three parameters:

$$\lambda_1 + \lambda_2(z - z_0) + \lambda_3(x - x_0),$$

where (x_0, z_0) is a reference point. Thus, the velocity distribution is written in a form of

$$v(x, z) = v_0(x, z) + \lambda_1 + \lambda_2(z - z_0) + \lambda_3(x - x_0), \tag{13}$$

where v_0 is a background velocity.

An imaged depth only depends on the velocity above it, except for turning rays. Therefore, a recursive algorithm is possible to determine velocity in an individual block. We start from the block nearest surface. In each block, iteration is used to calculate velocity parameters. Given an initial guess for λ_i's, common-offset depth migration is implemented to obtain imaged depths and $g_i(x, h)$ in equation (8) for each midpoint and each offset. Equation (10) will give a correction of the parameters. Then by using the updated parameters as initial guess, we correct the velocity again until convergence is achieved. After velocity analysis in one block, we migrate data with the correct velocity, and then pick the block interface from the imaged structure. When we finish determining velocity and velocity interface in one block, we will repeat the same procedure to the next block.

SENSITIVITY OF MIGRATION VELOCITY ANALYSIS

Velocity analysis by prestack migration uses the difference between the imaged depths from different offsets to correct the velocities, which is represented by equation (10). If the variance defined by (9) is zero, we conclude that the velocity is correct. However, one cannot obtain exactly zero variance. Many factors result in

a non-zero variance: noise in the input data, nonacoustic properties, and inaccurate description of velocity distribution, so on. Even the variance is apparently zero, it is actually not zero because of the errors in picking the imaged depths. The imaged depths in the variance are picked on the migration output, so that the position error in imaged depths is controlled by the resolution of the migration output, which, in turn, depends on wavelength, among other things.

Quantitatively, the matrices in equation (10) that depend on the functions, g_i, can be used to describe the sensitivity of the velocity error $\Delta\lambda$ to the variance error. Here, we will derive analytical representations for the simplest cases. For simplicity, we assume that the velocity $v(x,z)$ consists of a constant background velocity v_0 and a perturbation that is a linear function of depth in one block. Moreover, we assume that the upper boundary of the block is a horizontal line, $z = d$; i.e.,

$$v(x,z) = v_0 + \alpha(\lambda_1 + \lambda_2(z - z_0)), \tag{14}$$

where $\alpha = 0$ for $z < d$ and $\alpha = 1$ for $z > d$. The initial guesses are

$$\lambda_1 = \lambda_2 = 0.$$

Suppose that the true parameters are λ_1^* and λ_2^*, and the reflector is a horizontal segment at a depth z^*. As shown in Appendix B, we obtain the representations for the g_i's in equation (8)

$$g_1(x,h) = \frac{h^2 + z^2}{z^2}\frac{z - d}{v_0}, \tag{15}$$

$$g_2(x,h) = \frac{h^2 + z^2}{z^2}\frac{(z - z_0)^2 - (d - z_0)^2}{2v_0}. \tag{16}$$

From the above two equations, we conclude that

$$g_2(x,h) = \frac{(z - z_0)^2 - (d - z_0)^2}{2(z - d)} g_1(x,h).$$

This means that the coefficients in equation (8) are proportional for all image locations and all offsets, so that we cannot solve for λ_1 and λ_2 separately. Thus, we have a conclusion: *The parameters λ_1 and λ_2 cannot be determined at the same time if only one reflector segment is used in the velocity-analysis process.*

This conclusion shows that one should avoid solving for λ_1 and λ_2 at the same time unless well-separated reflector segments are used for velocity analysis.

If the parameter λ_2 is given (i.e., $\Delta\lambda_2 = 0$), then equation (8) is simplified to

$$\Delta z(x,h) = \left(\frac{h^2}{z^2} + 1\right)\frac{z - d}{v_0}\Delta\lambda_1. \tag{17}$$

When $\Delta\lambda_1$ is small, $z(x,h) \approx z^*$. Therefore, for any different two half-offsets h_2 and h_1 ($h_2 > h_1$), the difference of imaged depths from these two offsets are

$$z(x,h_2) - z(x,h_1) = \left[\frac{h_2^2}{(z^*)^2} - \frac{h_1^2}{(z^*)^2}\right]\frac{z^* - d}{v_0}\Delta\lambda_1.$$

i.e.,

$$\delta z(x, h_1, h_2) \equiv z(x, h_2) - z(x, h_1) = \frac{(h_2^2 - h_1^2)(z^* - d)}{(z^*)^2 v_0} \Delta\lambda_1. \tag{18}$$

Equation (18) shows that the error in λ_1 is proportional to the thickness of the block layer, which is consistent with results in the paper of Liu and Bleistein (1990). When there is a thin layer, the velocity estimation will become unreliable, so that migration-based velocity analysis cannot handle thin layers.

Similarly, if the parameter λ_1 is given (i.e., $\Delta\lambda_1 = 0$), then

$$\delta z(x, h_1, h_2) = \frac{(h_2^2 - h_1^2)(z^* - d)(z^* + d - 2z_0)}{2(z^*)^2 v_0} \Delta\lambda_2. \tag{19}$$

Equation (19) shows that the error in λ_2 is determined not only by the thickness of the block layer but by the difference between the central depth of the block layer and the reference depth z_0.

We have two kinds of the depth errors: Δz and δz. The former is the difference between the true depth and the imaged depth, which reflects migration error due to the velocity error; the latter is the difference between the imaged depths from different offsets, which results in the velocity error in velocity analysis. The ratio of these two depth errors is given by equations (17) and (18),

$$\gamma \equiv \frac{\Delta z(x, h)}{\delta z(x, h_1, h_2)} = \frac{h^2 + (z^*)^2}{(h_2^2 - h_1^2)}. \tag{20}$$

The ratio γ indicates the migration error due to the resolution in migration output. Equation (20) shows that γ increases as the depth increases.

For a general case, we do not have analytical representations for the g_i's. But we can calculate the g_i's numerically from which to estimate the velocity error. In fact, if there is only one parameter, equation (11) gives an explicit error estimation,

$$|\Delta\lambda| \leq \left[\frac{\sum_{k=1}^{K} \sum_{j=1}^{m} \left(\hat{z}_j^{(k)} - \overline{\hat{z}^{(k)}} \right)^2}{\sum_{k=1}^{K} \sum_{j=1}^{m} \left(g_j^{(k)} - \overline{\hat{g}^{(k)}} \right)^2} \right]^{1/2}, \tag{21}$$

where the Cauchy-Schwarz inequality is used.

COMPUTER IMPLEMENTATION

We applied our velocity analysis technique to synthetic data. The prestack migration is implemented by Liu's program (1993). The velocity model shown in Figure 1 consists of linear velocity functions and interfaces. Synthetic seismic traces are generated from this model, with 5 offsets ranging from 100 meters to 900 meters. Two of the common offset gathers are shown in Figure 3.

The velocity analysis process is outlined as follows:

In the first layer, the initial guess of velocity is 1500 m/s. With two iterations, the velocity is 2017 m/s. The true value is 2000 m/s.

In the second layer, we assume that velocity has the form $v(z) = 2017 + \lambda(z - 500)$ m/s, which guarantees a continuous velocity across the first interface. The initial guess is $\lambda = 0$. With two iterations, the velocity is

$$v(z) = 2017 + 1.035(z - 500) = 1500 + 1.035z \text{ m/s}.$$

The true velocity is $v(z) = 1500 + 1.0z$ m/s.

In the left third layer, we assume that velocity has the form $v(x, z) = 1000 + 1.5z + \lambda x$ m/s. The initial guess is $\lambda = 0$. With one iteration, the velocity is $v(x, z) = 1000 + 1.5z - 0.1x$ m/s. The true velocity is $v(x, z) = 1000 + 1.5z - 0.2x$ m/s. Despite the error in lateral variation, the stopping criterion is met since the difference of the imaged depths is apparently zero. Therefore, iteration ceases.

In the right third layer, we assume that velocity has the form $v(z) = 2535 + \lambda(z - 1000)$ m/s. The initial guess is $\lambda = 1.035$. With one iteration, the velocity is

$$v(z) = 2535 + 1.55(z - 1000) = 985 + 1.55z \text{ m/s}.$$

The true velocity is $v(z) = 1000 + 1.5z$ m/s.

In the fourth layer, the velocity is a constant. The initial guess is $v = 4000$. With one iteration, the velocity is 3586 m/s. The true velocity is $v = 3500$ m/s.

After velocity analysis, we obtain the velocity model shown in Figure 2. With this velocity model, we implement migration, and the result is shown in Figure 5 which is close to the migration result with the true velocity, shown in Figure 4.

Also, we test the computation of g_1 in the first layer. The numerical g_1 is computed from the ratio of the amplitudes in the Kirchhoff migration outputs. Then we compare the numerical g_1 with the true value calculated in equation (17). In our test, $v_0 = 500$ m/s and $d = 0$. The result listed in Table 1 shows that our numerical value of g_1 is accurate for all offsets.

Table 16. Test for g_1. The unit of offset and depth is m/s.

Offset	Imaged depth	Numerical g_1	True g_1
100	370	0.249	0.251
300	360	0.278	0.282
500	330	0.345	0.346
700	290	0.476	0.475
900	210	0.773	0.783

CONCLUSION

Velocity analysis by prestack migration can handle complex media for which conventional approaches lack the efficiency in updating velocity. The perturbation method is used here to derive an analytical relationship between the residual moveout and the error in the background velocity. This method is not limited by offset, dip, or velocity distribution. Based on that, we can estimate velocity efficiently. Furthermore, this relationship helps us to estimate the velocity error from the data resolution. This velocity analysis technique also can be generalized to 3D and to converted waves.

REFERENCES

Al-Yahya, K., 1989, Velocity analysis by iterative profile migration: Geophysics, **54**, 718-729.

Bleistein, N., Cohen, J., and Hagin, F., 1987, Two and one-half dimensional Born inversion with an arbitrary reference: Geophysics, **52**, 26-36.

Deregowski, S. M., 1990, Common-offset migrations and velocity analysis: First Break, **8**, 6, 225-234.

Lafond, C. F., and Levander, A. R., 1993, Migration moveout analysis and depth focusing: Geophysics, **58**, 91-100.

Lee, W. and Zhang, L., 1992, Residual shot profile migration: Geophysics, **57**, 815-822.

Liu, Z, 1993, A Kirchhoff approach to seismic modeling and prestack depth migration: CWP Project Review, 1993.

Liu, Z., and Bleistein, N., 1991, Velocity analysis by inversion: 1991 SEG expanded abstracts, p. 1230.

Liu, Z. and Bleistein, N., 1992, Velocity analysis by residual moveout: 1992 SEG expanded abstracts, p. 1034.

MacKay, S., and Abma, R., 1992, Imaging and velocity estimation with depth-focusing analysis: Geophysics, **57**, 1608-1622.

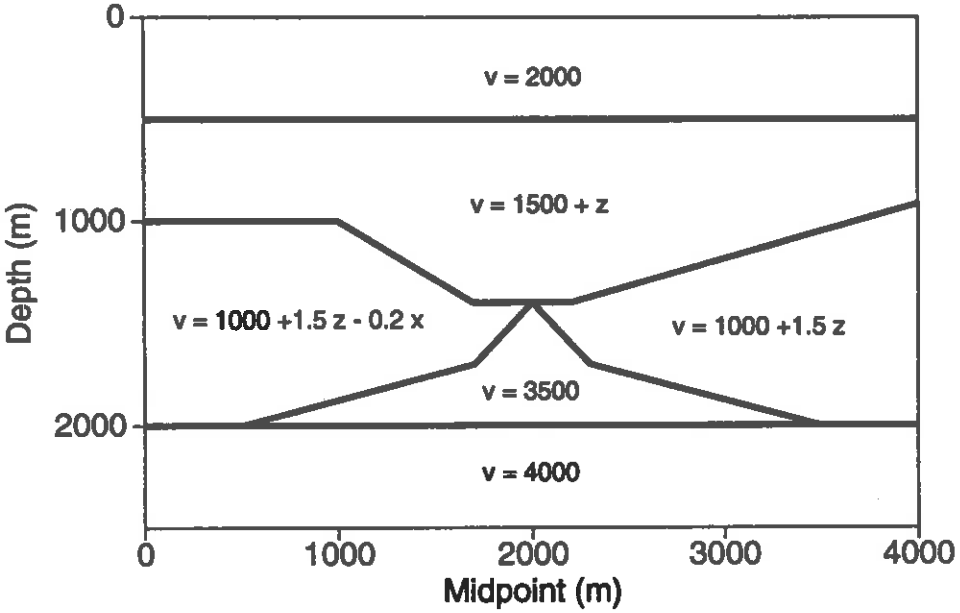

FIG. 1. The true velocity model. The velocity unit is m/s.

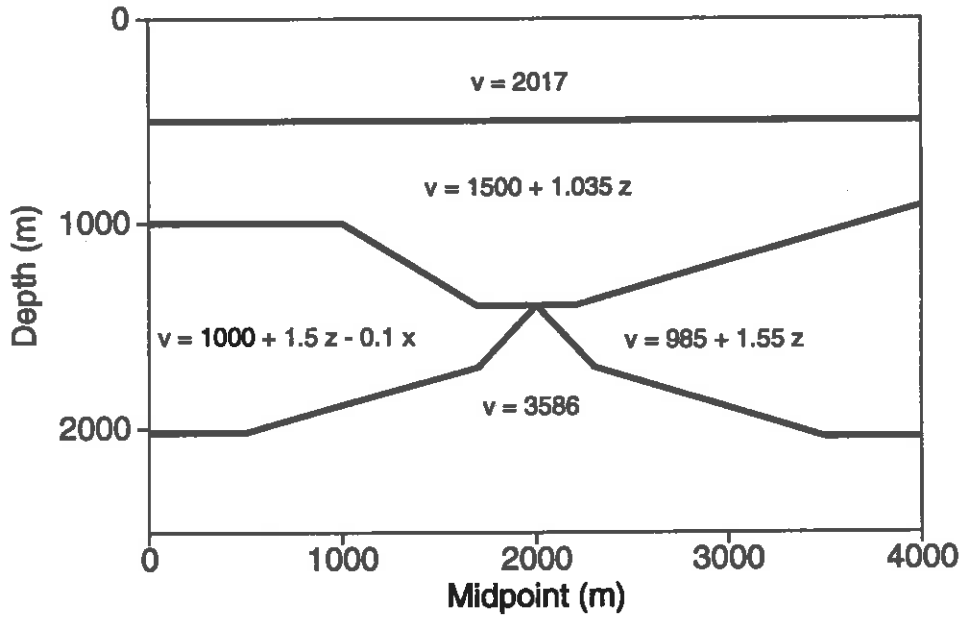

FIG. 2. The velocity model from velocity analysis. The velocity unit is m/s.

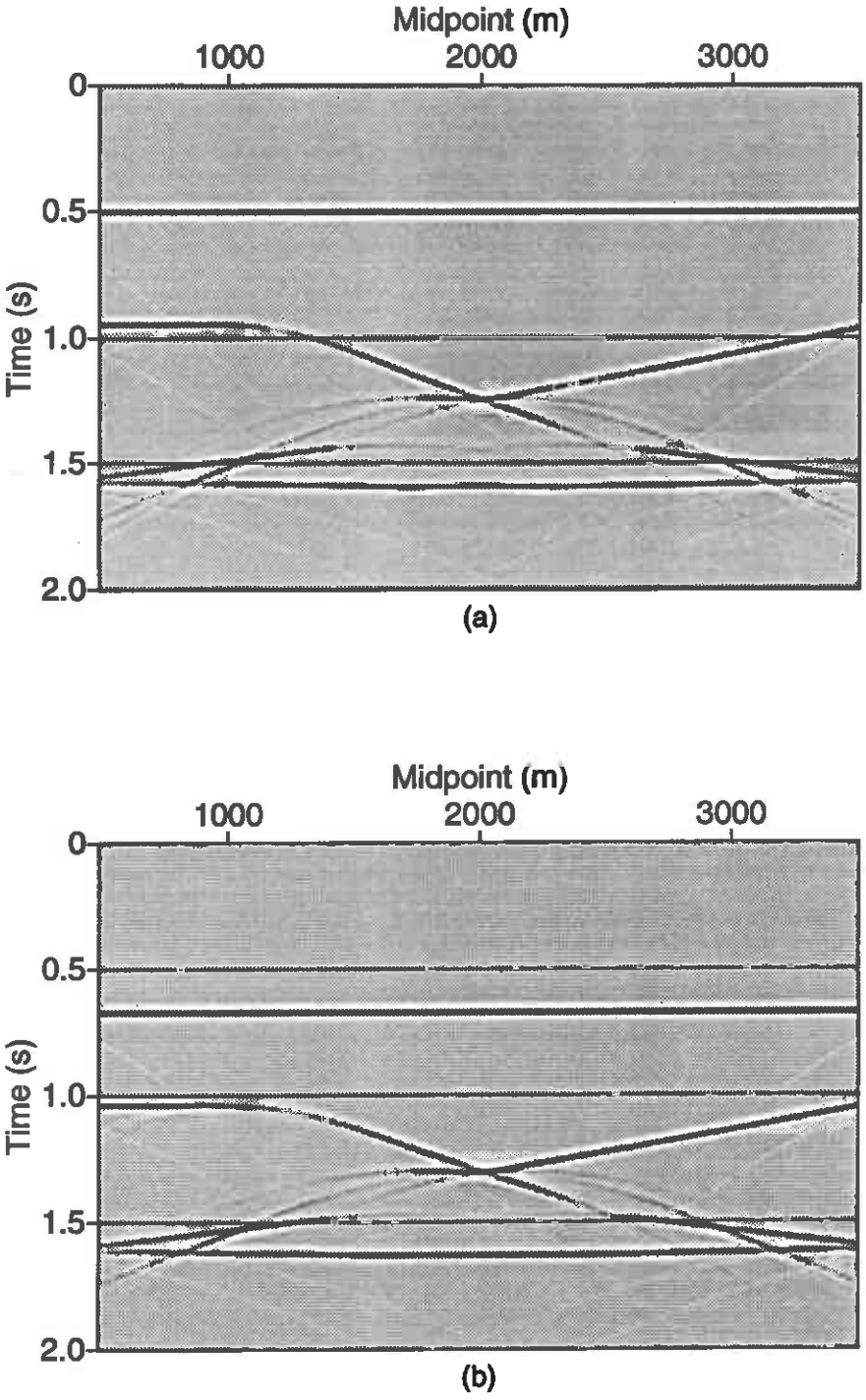

FIG. 3. Synthetic data: (a) with offset of 100 meters and (b) with offset of 900 meters.

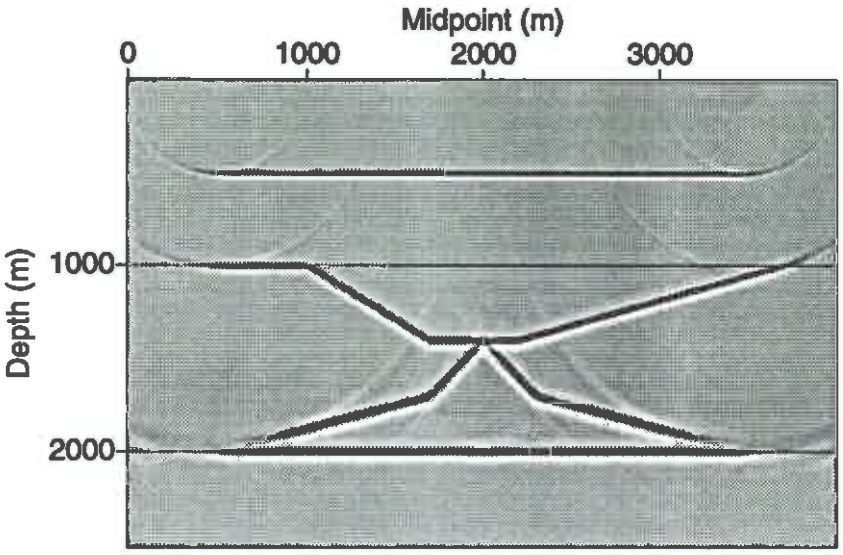

FIG. 4. Prestack migration with the true velocity model in Figure 1. The offset is 100 meters.

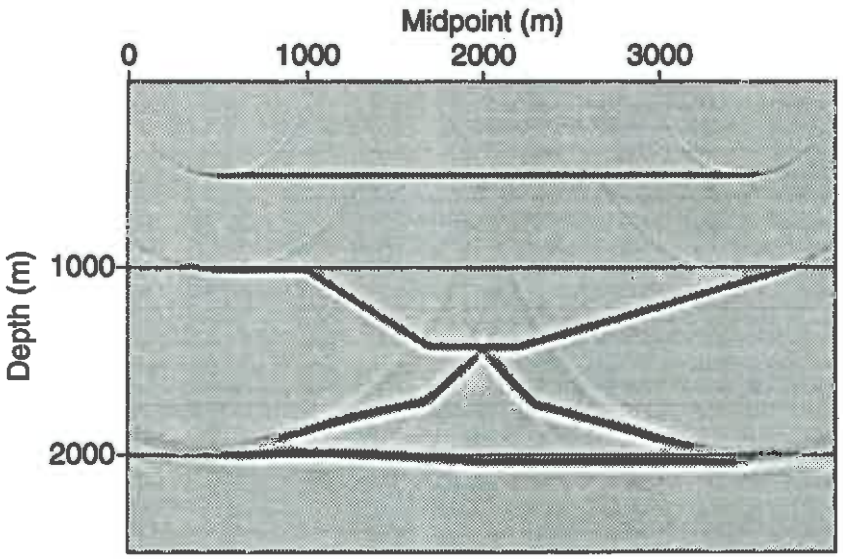

FIG. 5. Prestack migration with the velocity model in Figure 2. The offset is 100 meters.

DERIVATION OF EQUATIONS (10)

By using the matrix and vector notations on page 5 and 6, we have

$$\begin{aligned}\overline{\Delta\hat{z}^{(k)}} &= \frac{1}{m}\sum_{j=1}^{m}\Delta z_j^{(k)} \\ &= \frac{1}{m}\sum_{j=1}^{m}\sum_{i=1}^{n} g_{ij}^{(k)}\Delta\lambda_i \\ &= \sum_{i=1}^{n}\left(\Delta\lambda_i\frac{1}{m}\sum_{j=1}^{m} g_{ij}^{(k)}\right) \\ &= \sum_{i=1}^{n}\left(\Delta\lambda_i\overline{\hat{g}_i^{(k)}}\right), \end{aligned} \tag{22}$$

and

$$\begin{aligned} z_j^{(k)} + \Delta z_j^{(k)} - \overline{\hat{z}^{(k)} + \Delta\hat{z}^{(k)}} &= z_j^{(k)} - \overline{\hat{z}^{(k)}} + \Delta z_j^{(k)} - \overline{\Delta\hat{z}^{(k)}} \\ &= z_j^{(k)} - \overline{\hat{z}^{(k)}} + \sum_{i=1}^{n}\Delta\lambda_i\left(g_{ij}^{(k)} - \overline{\hat{g}_i^{(k)}}\right). \end{aligned} \tag{23}$$

Define a function

$$f(\Delta\hat{\lambda}) \equiv \sum_{k=1}^{K}\sum_{j=1}^{m}\left(z_j^{(k)} + \Delta z_j^{(k)} - \overline{\hat{z}^{(k)} + \Delta\hat{z}^{(k)}}\right)^2.$$

Thus, finding the minimum of $f(\Delta\hat{\lambda})$ is equivalent to that its gradient with respect to $\Delta\hat{\lambda}$ equal $\hat{0}$, i.e.,

$$\frac{\partial f(\Delta\hat{\lambda})}{\partial\Delta\lambda_l} = 0 \qquad l = 1, 2, ..., n. \tag{24}$$

By using equation (23),

$$f(\Delta\hat{\lambda}) = \sum_{k=1}^{K}\sum_{j=1}^{m}\left[z_j^{(k)} - \overline{\hat{z}^{(k)}} + \sum_{i=1}^{n}\Delta\lambda_i\left(g_{ij}^{(k)} - \overline{\hat{g}_i^{(k)}}\right)\right]^2.$$

So,

$$\begin{aligned}\frac{\partial f(\Delta\hat{\lambda})}{\partial\Delta\lambda_l} &= 2\sum_{k=1}^{K}\sum_{j=1}^{m}\left[z_j^{(k)} - \overline{\hat{z}^{(k)}} + \sum_{i=1}^{n}\Delta\lambda_i\left(g_{ij}^{(k)} - \overline{\hat{g}_i^{(k)}}\right)\right]\left(g_{lj}^{(k)} - \overline{\hat{g}_l^{(k)}}\right) \\ &= 2\sum_{k=1}^{K}\sum_{j=1}^{m}\left(z_j^{(k)} - \overline{\hat{z}^{(k)}}\right)\left(g_{lj}^{(k)} - \overline{\hat{g}_l^{(k)}}\right) \\ &\quad +2\sum_{k=1}^{K}\sum_{j=1}^{m}\sum_{i=1}^{n}\Delta\lambda_i\left(g_{ij}^{(k)} - \overline{\hat{g}_i^{(k)}}\right)\left(g_{lj}^{(k)} - \overline{\hat{g}_l^{(k)}}\right). \end{aligned} \tag{25}$$

The conditions (24) imply that

$$\sum_{k=1}^{K}\sum_{j=1}^{m}\sum_{i=1}^{n}\Delta\lambda_i\left(g_{ij}^{(k)}-\overline{\hat{g}_i^{(k)}}\right)\left(g_{lj}^{(k)}-\overline{\hat{g}_l^{(k)}}\right)=-\sum_{k=1}^{K}\sum_{j=1}^{m}\left(z_j^{(k)}-\overline{\hat{z}^{(k)}}\right)\left(g_{lj}^{(k)}-\overline{\hat{g}_l^{(k)}}\right);$$

i.e.,

$$\left[\sum_{k=1}^{K}A^{(k)}\right]\Delta\hat{\lambda}=-\sum_{k=1}^{K}\hat{b}^{(k)}. \tag{26}$$

This completes the verification that the solution of equation (10) provides the minimum of the left side in (9).

DERIVATION OF EQUATIONS (14) AND (15)

The solution of equation (12) can be represented by

$$\frac{\partial\tau}{\partial\lambda}=\int_L\frac{\partial}{\partial\lambda}\left(\frac{1}{v(x,z)}\right)dl=-\int_L v^{-2}(x,z)\frac{\partial v(x,z)}{\partial\lambda}dl, \tag{27}$$

where L is the raypath. Here, to simplify notations, we suppose that all derivatives with respect to λ are evaluated at $\lambda_1=\lambda_2=0$. When the background velocity is a constant v_0 as in (13), equation (27) becomes

$$\frac{\partial\tau}{\partial\lambda}=-\frac{1}{\cos\theta}\int_0^z v_0^{-2}\frac{\partial v(x,z')}{\partial\lambda}dz', \tag{28}$$

where θ is the angel between the raypath and the vertical. For the velocity function in equation (14), if $z>d$, then

$$\frac{\partial v(x,z')}{\partial\lambda_1}=1,$$

and

$$\frac{\partial v(x,z')}{\partial\lambda_2}=z'-z_0;$$

if $z<d$, then

$$\frac{\partial v(x,z')}{\partial\lambda_1}=\frac{\partial v(x,z')}{\partial\lambda_2}=0.$$

Therefore,

$$\frac{\partial\tau}{\partial\lambda_1}=-\frac{1}{\cos\theta}\int_d^z\frac{1}{v_0^2}dz'=-\frac{1}{\cos\theta}\frac{z-d}{v_0^2}, \tag{29}$$

and

$$\frac{\partial\tau}{\partial\lambda_2}=-\frac{1}{\cos\theta}\int_d^z\frac{z'-z_0}{v_0^2}dz'=-\frac{1}{\cos\theta}\frac{(z-z_0)^2-(d-z_0)^2}{2v_0^2}. \tag{30}$$

Because the reflector is horizontal, the raypaths from the source and the receiver are symmetric. We have

$$\cos\theta_s = \cos\theta_r = \frac{z}{\sqrt{z^2+h^2}},$$

Substituting the above formula and equations (29) and (30) into equation (8), we obtain

$$g_1(x,h) = \frac{h^2+z^2}{z^2}\frac{z-d}{v_0},$$

and

$$g_2(x,h) = \frac{h^2+z^2}{z^2}\frac{(z-z_0)^2-(d-z_0)^2}{2v_0}.$$

This completes the verifications of equations (15) and (16).

Application of dynamic ray tracing in triangulated subsurface models

Andreas Rüeger

Application of dynamic ray tracing in triangulated subsurface models

Andreas Rüger

ABSTRACT

Hale and Cohen (1991) developed software to generate two-dimensional computer models of complex geology. Their method uses a triangulation technique designed to support efficient and accurate computation of seismic wavefields for models of the earth's interior. Subsequently, Hale (1991) used this triangulation approach to perform dynamic ray tracing and create synthetic seismograms based on the method of Gaussian beams. Here, I extend this methodology to allow an increased variety of ray-theoretical experiments. Specifically, it is now possible to define a reflection and transmission sequence for each interface and to incorporate attenuation and density variations. In addition, I have added an option to perform Fresnel-volume ray tracing (Červený and Soares, 1992). Corrections for reflection and transmission losses at interfaces, and for two-and-one-half dimensional (2.5-D) spreading are included. However, despite these enhancements, difficulties remain in attempts to compute accurate synthetic seismograms if strong lateral velocity inhomogeneities are present. Several examples of computations of high-frequency seismograms based on the method of Gaussian beams are provided to emphasize the advantages and disadvantages of the proposed modeling method. The new features are illustrated for both surface and vertical seismic profiling (VSP) acquisition geometries.

INTRODUCTION

New triangulation methods for representing subsurface models in computers have helped to overcome limitations inherent to previous computer models of the earth's interior. A mesh of triangles can flexibly characterize complex subsurface models that can, for example, include velocity lenses and overhanging dome structures. Additionally, Hale and Cohen (1991) designed spatial data structures that contain the *adjacency topology* (Weiler, 1988) of the model, so that computing time is not wasted in searching for the triangles and model parameters in the vicinity of any arbitrary point in the model.

The combination of *dynamic ray tracing* (Červený, 1985) and the triangulation

technique is very promising. Dynamic ray tracing is an important extension of the classical kinematic ray tracing. It provides useful dynamic properties such as geometrical spreading and wavefront curvature information along the rays. Hale (1991) took advantage of the dynamic ray tracing results to generate synthetic seismograms based on the method of Gaussian beams (Červený, et al., 1982).

The purpose of this project is to enhance the usefulness of Gaussian beam ray tracing in triangulated subsurface media and to discuss its current limitations.

In the era of high-speed computing, forward modeling based on ray-theoretical methods competes with finite-difference approaches (e.g., Fei, 1993). The latter allows specification of model parameters such as the seismic velocity at each point in the gridded model. If the grid spacing is chosen fine enough, the accuracy of the calculated synthetic seismograms is very good. A synthetic section generated with a finite-difference method provides all types of seismic events simultaneously. This often makes it difficult to identify reflections from interfaces of interest. Moreover, the computing speed of finite-difference methods is about two orders of magnitude slower than for ray tracing experiments. This significantly reduces the application of finite-difference methods as an interpretation tool.

	FLEXIBILITY	DIAGNOSTIC	ACCURACY	SPEED
FD	10	5	9	3
oldTRI	6	7	5	10
newTRI	8	9	7	9

poor excellent

1 2 3 4 5 6 7 8 9 10

Table 17. A comparison of finite-difference methods (**FD**), Hale's Gaussian beam modeling package (old**TRI**) and its extension (new**TRI**), which is introduced in this paper. Details are given in the text.

If certain requirements are met, ray-theoretical techniques and, in particular, the dynamic ray tracing method do have a future in seismic modeling. Several criteria may be established to compare the performance of either method (see Table 17). Here, based on my experience, I assign grades from 1 to 10 to the performance of

finite difference methods (**FD**), Hale's Gaussian beam modeling package (old**TRI**) and its extension (new**TRI**), which I introduce in this paper.

- **Flexibility :** The first criterion assesses the model complexity and the variety of ray modes that can be traced. I have added an option to specify a constant attenuation factor and density for each geologic block, i.e., for each area bounded by interfaces. Moreover, the software now allows the introduction of a broader class of raypaths. That is, as shown in Figure 1, interfaces no longer are limited to being either reflectors or transmitters of seismic energy, but now can be both, in a specified sequence. This generalization broadens the applicability of the modeling. For example, it is now possible to include multiples.

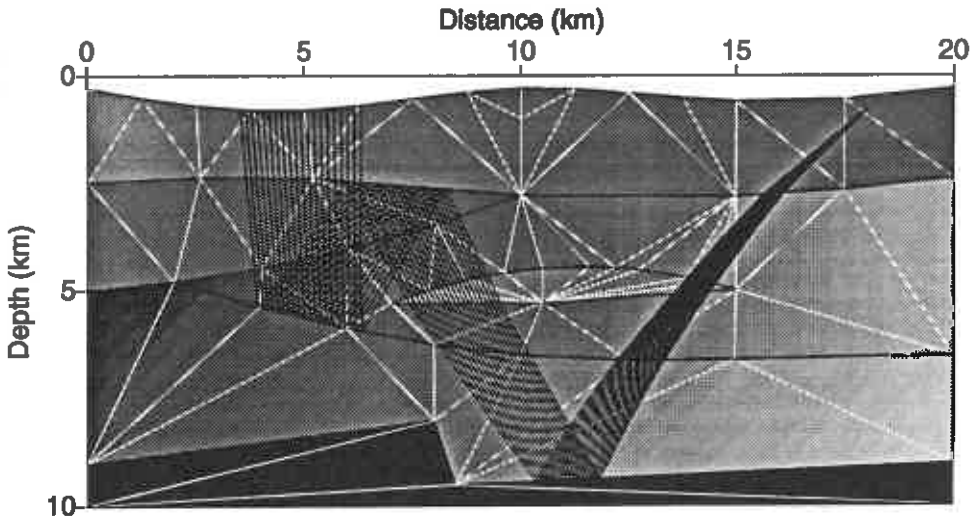

FIG. 1. Ray tracing in a complex subsurface model. This model includes sharp-edged interfaces and lens-type structures. Lithological interfaces are represented by black lines. The shading denotes the seismic velocity field. Also shown as black lines are raypaths corresponding to one type of interface multiple. The white lines are edges of auxiliary triangles used in the model building.

- **Diagnostics :** The second criterion evaluates the capability of the method to act as a tool for interpretation and for understanding of wave propagation in complex structures. Several new options have been included and will be presented in this paper. One of the new features, called *physical ray tracing* or *Fresnel-volume ray tracing* (Červený and Soares, 1992), may be used to study the resolution and the validity conditions of the ray method.

- **Accuracy :** Third, accurate seismograms have to be computed. The computation of the reflection and transmission losses at interfaces as well as correction for 2.5-D amplitude spreading improve the accuracy of the Gaussian beam ray tracing. However, problems remain when dealing with significant inhomogeneities

in the model. Some limitations are intrinsic to ray methods; others are specific to the Gaussian beam approach. Both are discussed later in this paper.

- **Speed :** The fourth criterion, computational aspects, underlines one of the big advantages of ray methods. The new options of the ray-tracing package such as the computation of the out-of-plane spreading, energy partitioning at interfaces, and attenuation, can be performed while still maintaining the attractive feature of computational efficiency with limited computer storage requirements.

Modeling using the Gaussian beam method is only one possible application of the dynamic ray-traced data generated along rays. Alternative methods (e.g., the paraxial method) can also use these data to create synthetic seismograms. The new modifications such as the tracing of multiples, computation of out-of-plane spreading, or reflection and transmission correction are evaluated independently of the Gaussian beam procedure. To understand better the advantages and disadvantages of Gaussian beam ray tracing, the new options are illustrated for both surface and VSP acquisition geometries. A comparison with VSP data obtained in a physical modeling laboratory supports benefits of the ray-theoretical modeling.

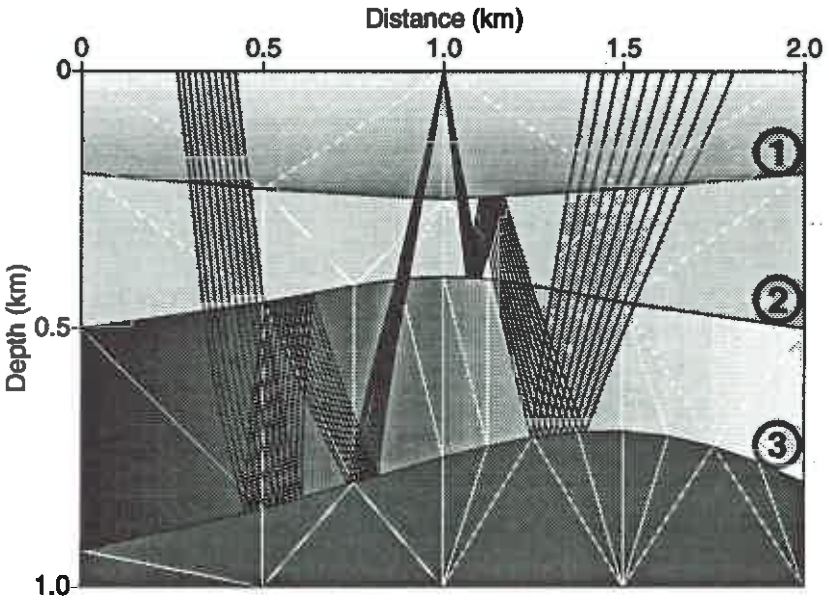

FIG. 2. Raypaths for two different families of multiples. Interfaces of interest are labeled. The shading of the different layers indicates that the seismic wave velocity varies with both depth and lateral position.

IMPROVEMENTS IN THE MODEL REPRESENTATION

Reflection and Transmission Sequences

Hale (1991) demonstrated how complicated models such as salt domes can be triangulated for efficient ray tracing. His version of the modeling code was designed to generate reflections from only a single selected reflector in any given run of the program. The approach presented here is more dynamic. The generation of multiple raypaths, for example, requires a certain flexibility in the definition of the interfaces. Previously, any given interface could either reflect or transmit seismic energy, but not both; this definition of interfaces did not allow one to trace multiples. As illustrated in Figure 2, to obtain selected multiples, a sequence of reflections and transmissions has to be defined at each interface of interest. I have installed this new feature in the ray-tracing code. For each reflector, a *reflecting sequence* can now be defined by the user of this modeling software.

The two different families of multiples in Figure 2 have been created by instructions similar to those in other SU command shells. To generate the multiple raypath between interface **2** and **3** shown on the left side of the figure, the shell parameter statements are the following:

```
refseq=2,0,1,0 \      # refl./transm. sequence for interface 2
refseq=3,1,1 \        # refl./transm. sequence for interface 3
```

The first number after the equality sign denotes the interface; the following numbers signify the sequence of reflections and transmissions at this interface: "0" denotes transmission, "1" reflection. If no reflection sequence is defined for a reflector, the interface is considered to be only transmitting. In the above case, the first hit on interface **2** will lead to a transmission of the seismic energy and the second arrival generates a reflection. Finally, the ray propagates towards the surface. For the type of multiple displayed on the right side of Figure 2, the following statements are used:

```
refseq=1,0,1,0 \      # refl./transm. sequence for interface 1
refseq=2,1,0,0 \      # refl./transm. sequence for interface 2
refseq=3,1 \          # refl./transm. sequence for interface 3
```

Attenuation and Density

I have not changed the original specification of the velocity field characterized by a linear gradient in reciprocal velocity-squared (so-called *sloth*). Additionally, the user may now assign a constant attenuation and density value to each geologic block bounded by interfaces. The implementation of noncausal absorption is made efficient

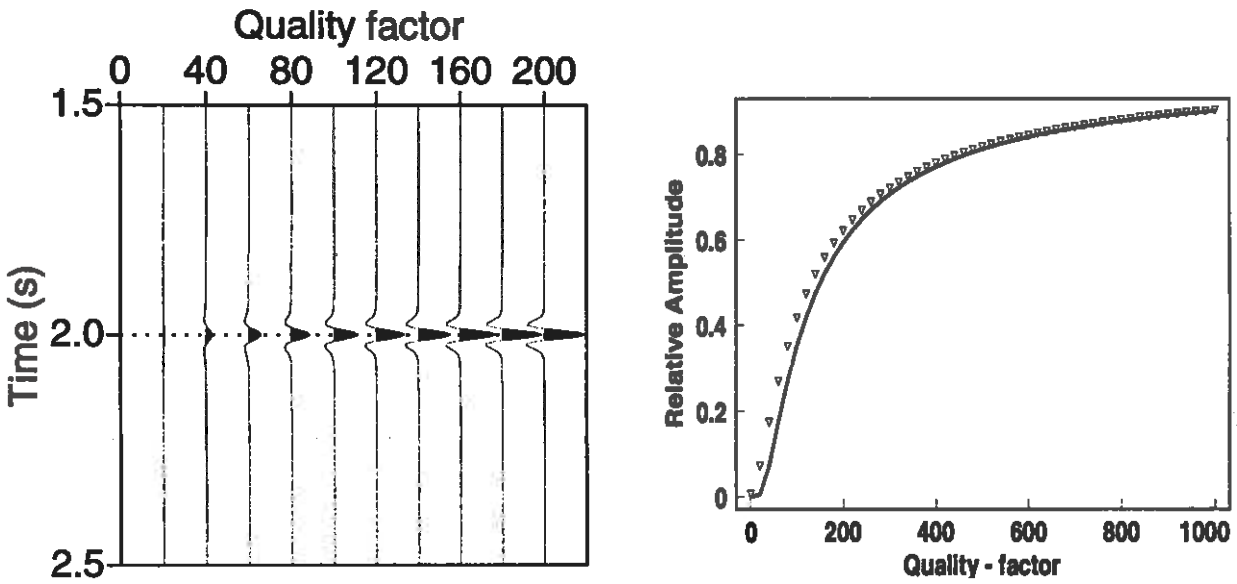

FIG. 3. Synthetic seismograms displayed as a function of quality factor Q. The receiver is situated in a homogeneous medium, 5 km from a point source. Velocity of the medium is 2.5 km/s. Only the noncausal attenuation effect is evaluated. The solid line in the right diagram represents analytically computed solutions; the triangles denote modeled results.

by introducing a complex velocity using the *Debye approximation* (Müller, 1983).

$$\frac{1}{v} \doteq \frac{1}{v_{real}} \cdot (1 + \frac{i}{2Q}),$$

where v_{real} is the specified real-valued seismic velocity, and Q is the familiar quality factor for dissipative wave propagation. For ω denoting radial frequency and s, the monotonically increasing arclength along the ray, the amplitude decay A_{decay} due to attenuation is given by

$$A_{decay} = \exp\left(-\omega \int_{s_0}^{s} \frac{1}{2Qv_{real}} ds\right) = \exp(-\omega t^*)$$

For a constant Q in each triangle, the global absorption factor t^*

$$t^* = \int_{s_0}^{s} \frac{1}{2Qv_{real}} ds = \sum_{i=1}^{i=N} \frac{t_i}{2Q_i}$$

can be obtained as a simple by-product of the ray tracing. Here, N is the number of triangles traversed; Q_i and t_i are the quality factor and the traveltime within the i-th triangle. The efficiency of the noncausal treatment in dissipative models is essentially the same as in perfectly elastic models. Figure 3 is a display of the seismic response of a homogeneous, absorbing medium with $v_{\text{real}} = 2.5\,\text{km/s}$. The receiver is situated

5 km from the source. Each trace corresponds to a different value of quality factor Q. The right diagram shows the amplitude at the dominant frequency versus Q. The solid line represents the analytically computed values, the triangle symbols denote results computed by the Gaussian beam modeling. The values are normalized by setting the amplitude for the perfectly elastic medium to unity. Note that the accuracy increases with decreasing absorption in the medium. However, even for small values of Q, the comparison is satisfactory.

Multiplication by A_{decay} in the frequency domain yields noncausal results. I implemented a correction proposed by Červený (1987) to approximately simulate causal absorption (see Figure 4). For decreasing Q, one recognizes a similar decay in amplitude as in the noncausal case, but also a delay of the causal signal towards larger traveltime. A more detailed examination shows that the signals broaden and become slightly asymmetric. The computational cost of including causal attenuation is significantly higher than for the noncausal case; therefore, the causal feature is optional.

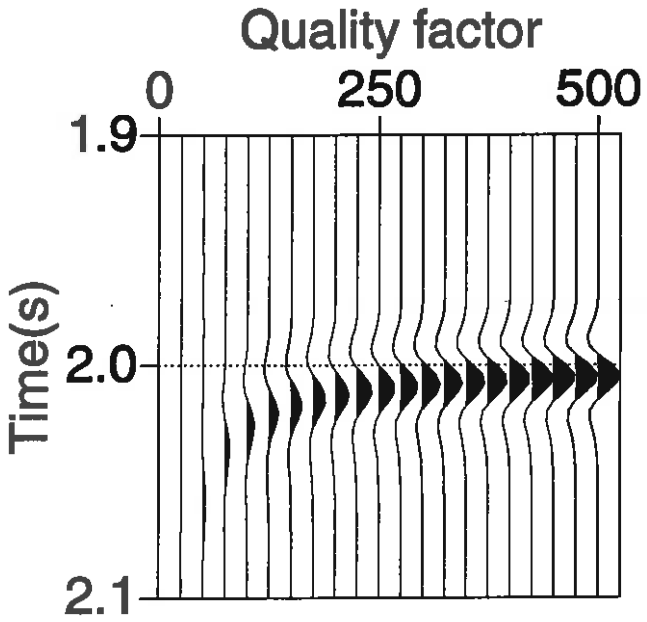

FIG. 4. Synthetic seismograms displayed as a function of quality factor Q. The receiver is situated in a homogeneous medium, 5 km from a point source. Velocity of the medium is 2.5 km/s. Causal absorption is included.

GAUSSIAN BEAM MODELING AS AN INTERPRETATION TOOL

VSP Modeling Experiment

Recordings from VSP experiments are routinely used to improve the estimation of subsurface properties close to a well. VSP data sets are often more difficult to interpret than are surface data. While the latter bear a certain similarity to actual subsurface structure, the patterns in VSP sections are quite different from the actual configuration in the subsurface. Generation of VSP synthetic data helps to overcome this interpretation problem by providing a tool to help identify events on recorded VSP seismic sections and to check the validity of existing imaging software.

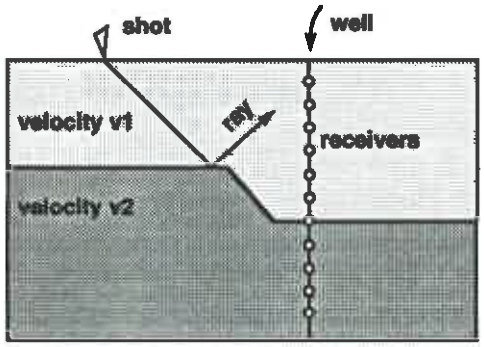

FIG. 5. Fault-model VSP experiment with one shot-point. The generated seismic wavefield is recorded by geophones in a well. Figures 9 and 10 show synthetic data and physical-modeling data for this model.

The software described in this paper can be used to generate data for VSP experiments. Consider the fault model shown in Figure 5. This model was used by Jaramillo (1993) of the VSP research group at CSM both to analyze the quality of the generated synthetic and physical model data and to use the modeling software as an interpretation tool for the Yucca Mountain Project. The ray-tracing code provides an additional source of model data.

Figure 6 shows one family of rays generated by the modeling software. Two reflections are considered in the ray propagation: the first is at the left boundary of the model, and the second at the hanging wall. The rays finally are recorded by receivers in the borehole.

If the left boundary of the model is labeled **1**, the fault **2**, and the borehole **3**, the UNIX command shell for this experiment contains the lines:

```
refseq=1,1 \      # refl./transm. sequence for the left boundary
refseq=2,1 \      # refl./transm. sequence for the fault
refseq=3,-1 \     # refl./transm./stop  sequence for the borehole
```

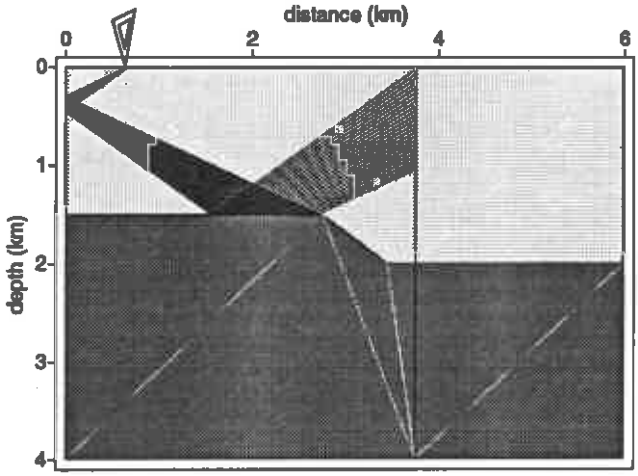

FIG. 6. One family of rays generated by the modeling program. The event is recorded by receivers in the vertical borehole. The corresponding reflection in the synthetic seismic section in Figure 9 is labeled **i**.

I have previously introduced the designations, "1" for reflection, "0" for transmission; here, I introduce "-1" to denote the stopping of the ray. Thus, the first intersection of the raypath with the borehole terminates the tracing of this ray. Information including the traveltime, corresponding amplitude, and index of the stopping interface are stored in a file. By default, the rays are stopped at the boundaries of the model. Only rays with the correct stopping index will contribute to the events on the seismic section and, optionally, will be displayed. Another feature allows one to select only direct arrivals or only primaries. These new enhancements proved to be helpful in the Yucca Mountain Project.

The synthetic seismic response for the specific event shown in Figure 6 is labeled as event **i** in Figure 9. This reflection can also be identified in the recorded p-wave physical modeling data (Figure 10). In Figures 7 and 8, a series of ray families is displayed for the same geometry. The letter labels on the models in Figures 7 and 8 correspond to the events in Figure 9. In this form, one can conveniently compare the synthetic section and the physical modeling data, and identify individual events.

The modeling software now allows tracing of all rays of interest. It is possible to specify reflections from the vertical and horizontal boundaries of the model, features that are recorded in physical modeling experiments; multiples can be conveniently defined, and rays may also be traced across the borehole before they encounter the receiver line a second time and are recorded (see events **g** and **h**).

Differences in Figures 9 and 10 can be attributed to a number of factors. Among them is the fact that the ray-trace code presently generates only acoustic events, whereas the physical model is 2-D elastic. The entire experiment, including the building of the model, the tracing of nine different ray modes, and the generation of

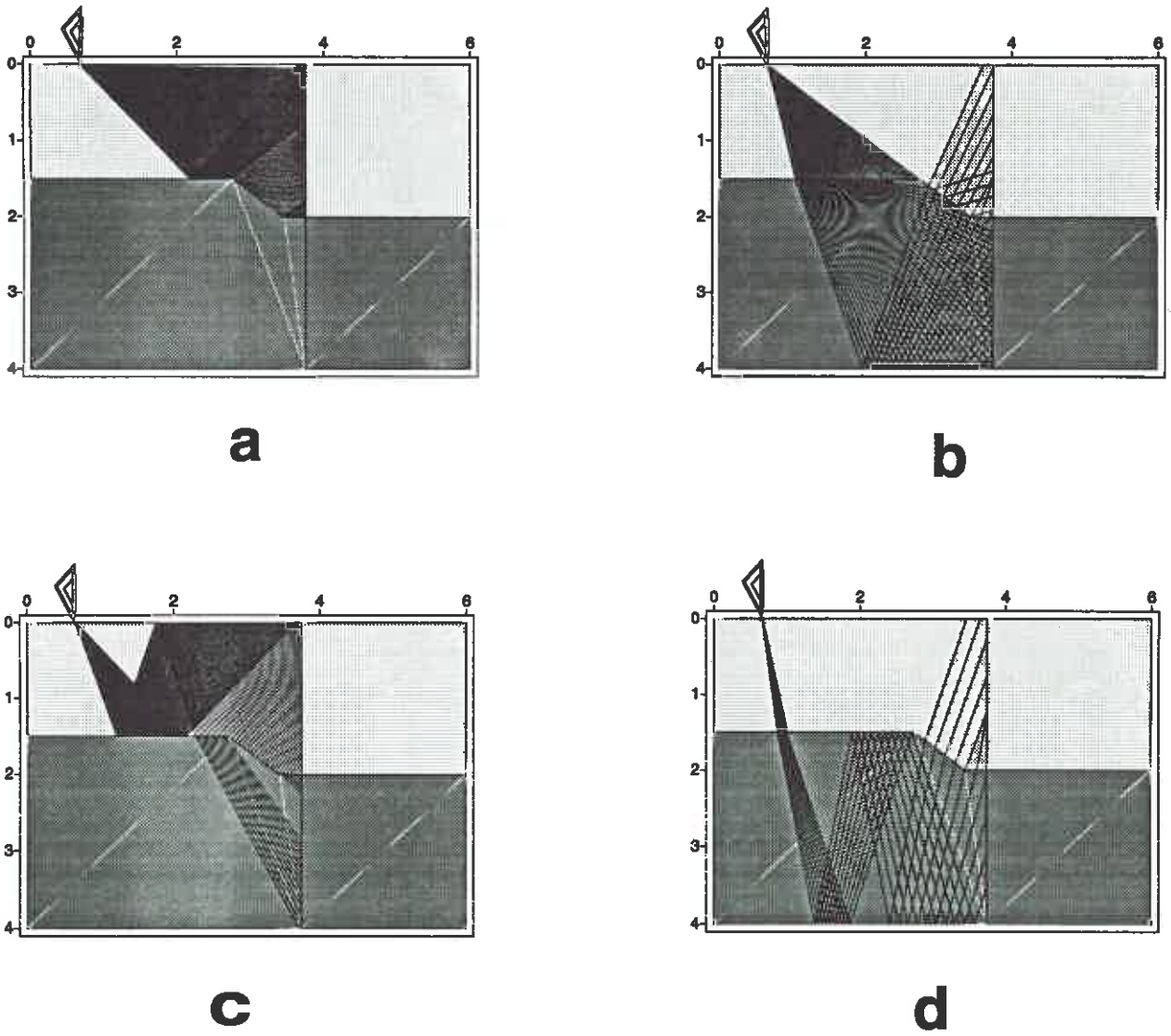

FIG. 7. Four different ray types are shown. In example **a**, both direct arrivals and primaries from the foot wall and the hanging wall are present. **b** displays bottom reflections and direct arrivals, **c** surface multiples and **d** bottom multiples. The corresponding seismic events are labeled accordingly in the seismic section. Note that although the ray density at the source is identical in each figure, the ray coverage at the borehole is different.

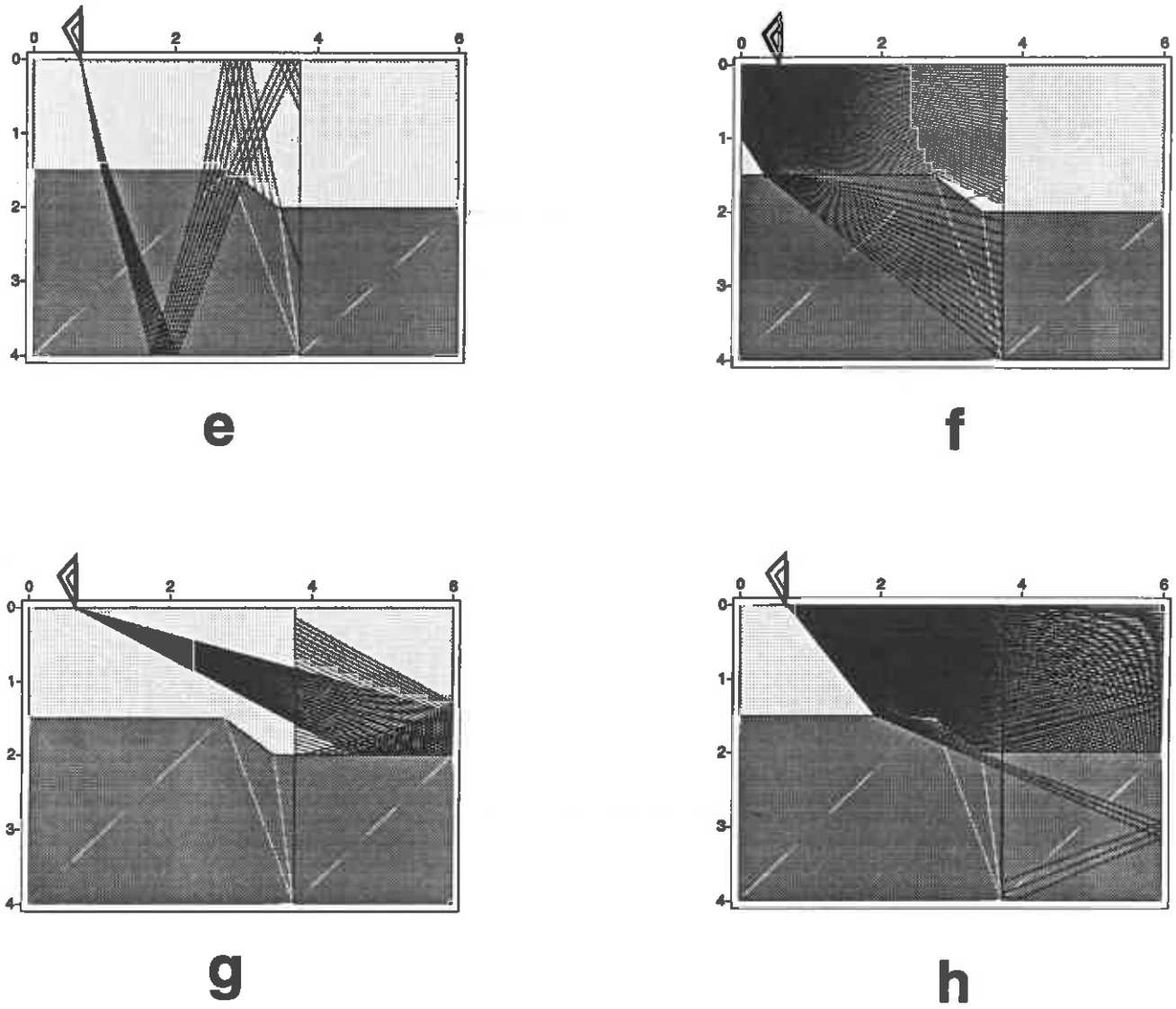

FIG. 8. The modeling software allows tracing of raypaths that reflect from the sides of the model and that cross the borehole. Rays that are reflected back from the boundary of the model, and pass the receiver line a second time are finally recorded by the geophones in the borehole (see events **g** and **h** in Figure 9). As can be seen in **e** and **f**, rays with overcritical incidence are not transmitted.

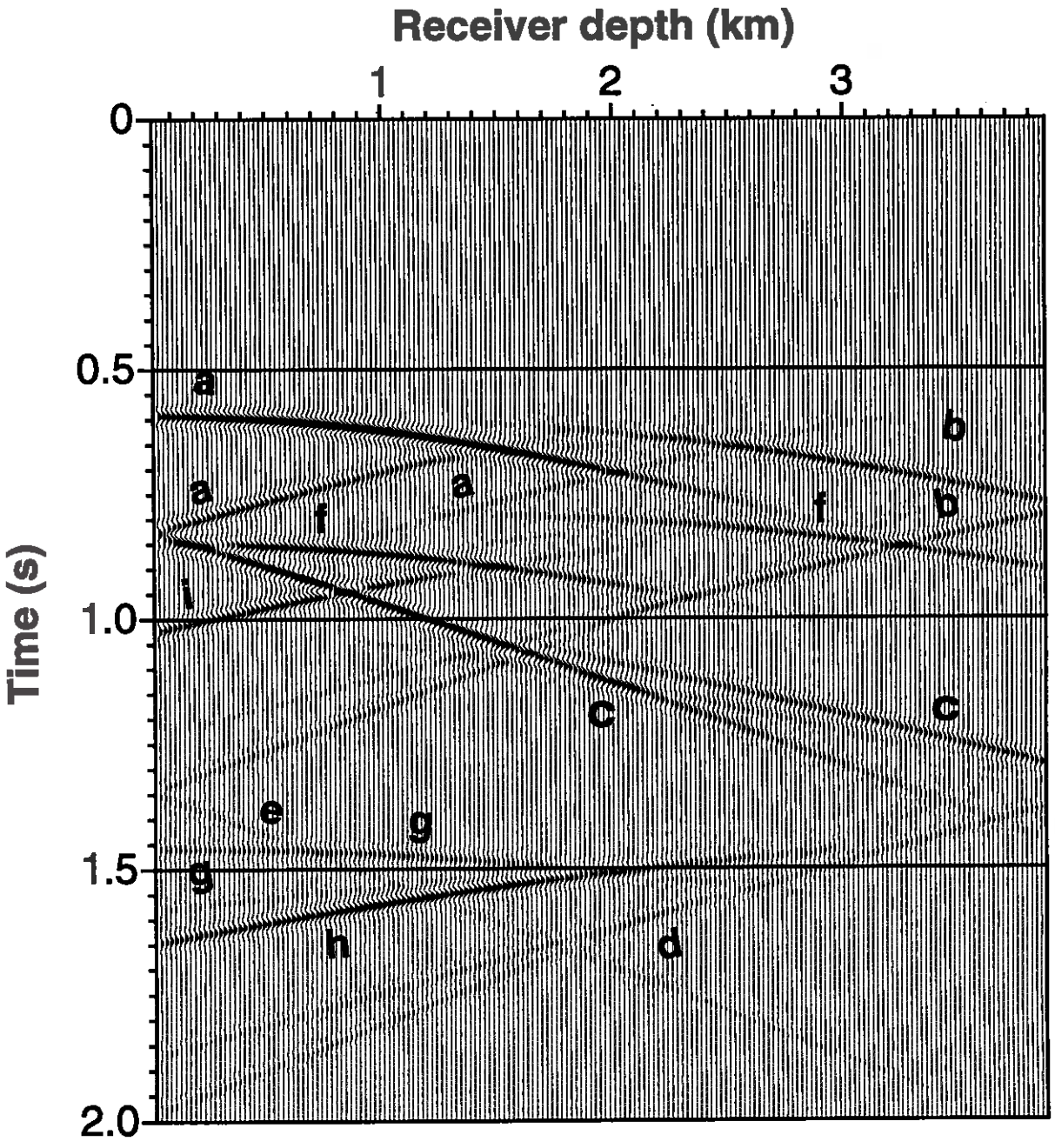

FIG. 9. Synthetic data generated by the extended version of Hale's acoustic modeling program. The ray families presented in the previous two figures generate seismic responses that are labeled accordingly here.

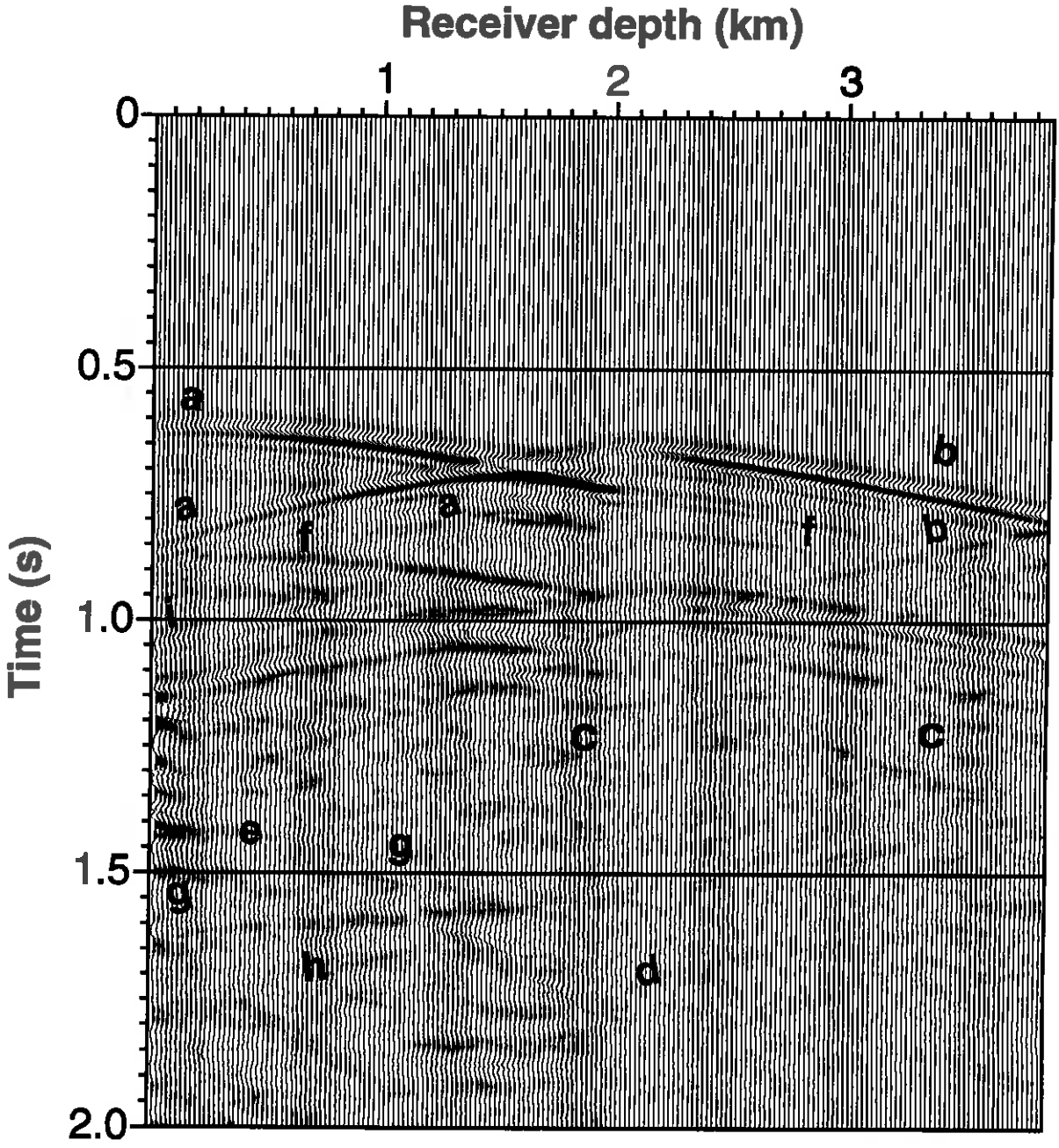

FIG. 10. The physical modeling data set after applying a waveform filter to obtain the p-wave contribution to the data. Comparison with the synthetic section helps identify the majority of the dominant coherent events.

the synthetic seismic sections took 23 s of CPU time on an IBM RS6000 workstation.

Fresnel-Volume Ray Tracing

The term *Fresnel-volume* was introduced by Kravtsov and Orlov (1980) to generalize the concept of Fresnel-zones. These authors suggested that rays be considered as physical objects rather than volumeless trajectories. Stated differently, all points within a region in the vicinity of the ray, the Fresnel-volume, influence the wave propagation associated with this ray. As illustrated in Figure 11, a point F belongs to the

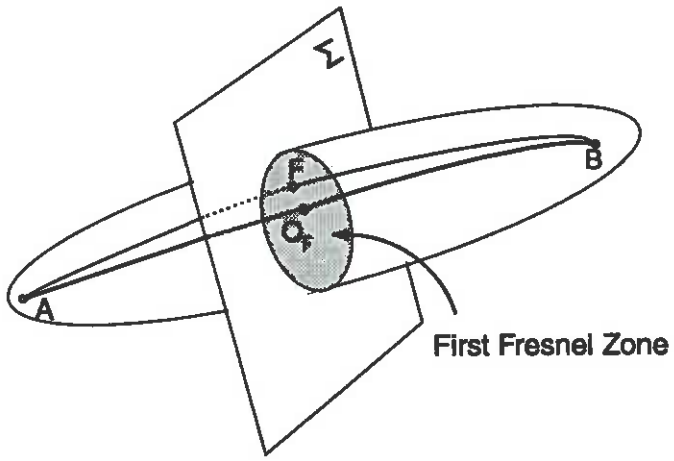

FIG. 11. The Fresnel-volume for a ray from A to B. The point O_F marks the intersection of the ray with the plane Σ. Points such as F influence the wavefield along the ray if the *Fresnel condition* (1) is satisfied (see also Červený and Soares [1992]).

Fresnel-volume of the ray from A to B, if the *Fresnel condition* (1) is satisfied (see also Červený and Soares [1992]), that is

$$|\tau(F,A) + \tau(F,B) - \tau(B,A)| \leq \frac{1}{2}T. \tag{1}$$

Here, T denotes the dominant period of the signal, and $\tau(F,A)$, $\tau(F,B)$ and $\tau(B,A)$ are the traveltimes from F to A, F to B and B to A, respectively. Fresnel-volumes depend on the velocity field close to the ray as well as on the dominant frequency of the signal.

I used recent work by Červený and Soares (1992) to supplement the dynamic ray tracing routine with an option to compute the two-dimensional paraxial approximation of the Fresnel-zone. This may be performed efficiently and accurately by using the elements of the ray propagator matrix, which are evaluated in the dynamic ray tracing.

Fresnel-volume ray tracing (or *physical ray tracing*) offers several applications for the field of exploration geophysics. For example, study of the resolution of the seismic method can be extended to complicated media, and the validity conditions of ray methods can be stated explicitly in terms of the radius of the Fresnel-zone at any point along a specified raypath (see Kravtsov and Orlov, 1980). In Figure 12, the plot of the Fresnel-volume (actually, Fresnel area, for these 2-D models) for a signal frequency of 5 Hz indicates that the ray-theoretical assumptions are violated because the edges of the fault and the velocity lens intersect with the Fresnel-volume. The wavefield along the ray is, in this sense, obstructed. The wavefield recorded at the receiver is influenced by the zone covered by this Fresnel-volume and not only by the line traced by the classical ray.

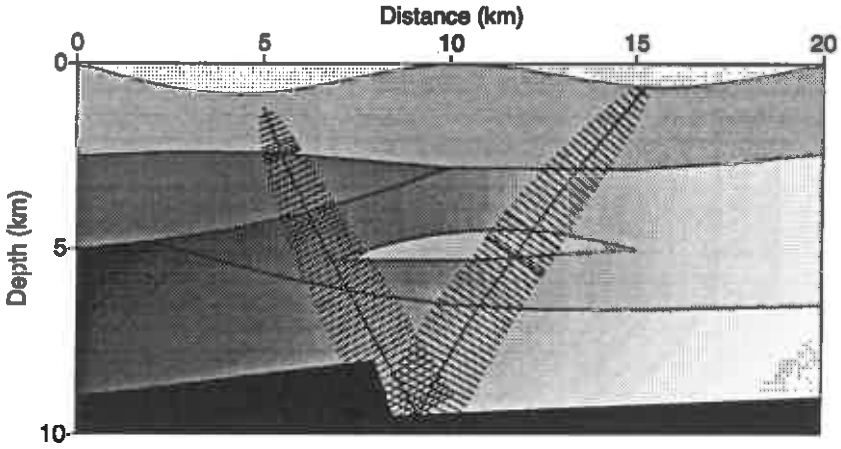

FIG. 12. The Fresnel-volume for a ray traveling through an inhomogeneous medium. A signal frequency of 5 Hz is considered. Interaction of the Fresnel-volume and the edges of the lens and the fault indicate a violation of the ray-theoretical assumptions.

ACCURACY OF THE MODELING

Two-and-one-half Dimensional Spreading

I included a computationally simple procedure to correct for geometrical spreading for a point source in the medium. Previously, the Gaussian beam modeling yielded amplitudes for a line source with a cylindrical wave expansion. I used the three-dimensional dynamic ray-tracing equation to derive the necessary amplitude correction. Consider variations of the properties of the medium to be restricted to the (x_1, x_3)-plane, with no variations in the x_2-direction allowed. This situation is referred to as being *two-and-one-half dimensional* (Bleistein, 1986).

The factor that multiplies the original two-dimensional solution is proportional to

$$\left(\int_{s_0}^{s} v\, ds\right)^{-\frac{1}{2}} = (\sigma - \sigma_0)^{-\frac{1}{2}},$$

where σ is a running parameter of units [length^2/time], and s is the arclength increasing from s_0 to s along the ray. Figure 13 emphasizes the difference in amplitude decay for homogeneous 2-D and 2.5-D media. To help see the spreading behavior, the 10 traces of each seismic section are summed and displayed below. The amplitude decay is proportional to $r^{-\frac{1}{2}}$ for the line source and r^{-1} for the point source, where r is the distance traveled.

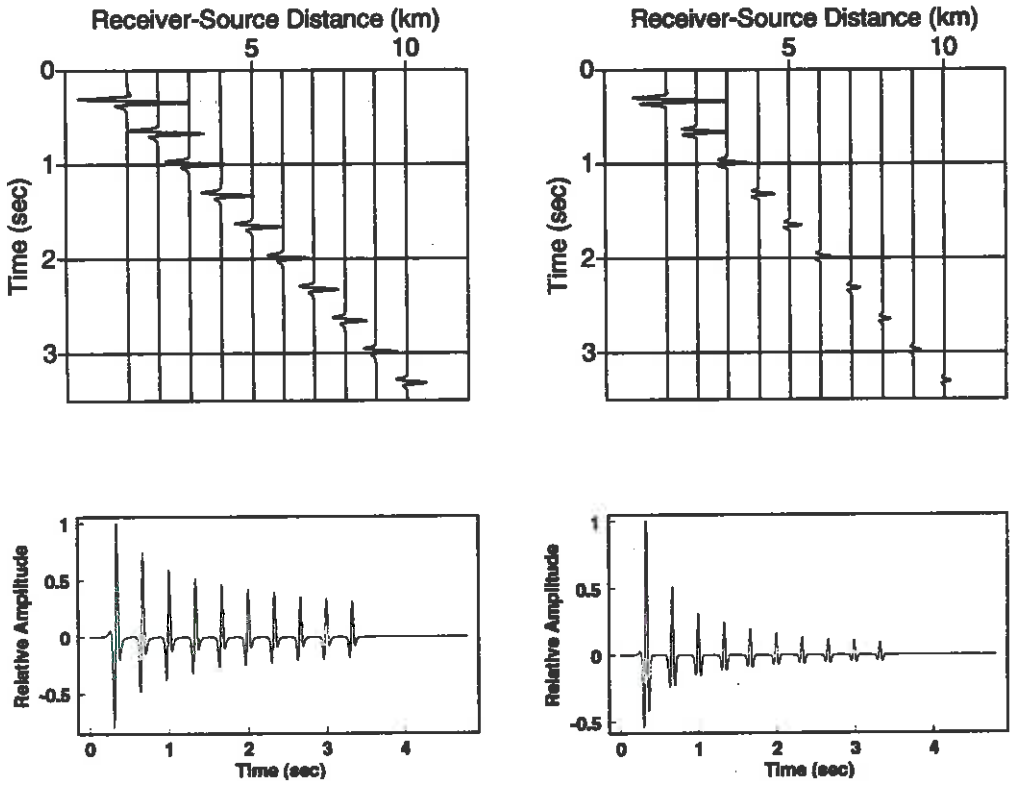

FIG. 13. Seismic sections generated by Gaussian beam modeling in homogeneous media. The right side simulates the energy spreading due to a point source; the left time section shows the response due to a line source. Below, the seismic traces of each section are added to better visualize the difference in amplitude decay.

Reflection and Transmission

Hale (1991) traced rays through models containing velocity discontinuities. One example is the model shown in Figure 14. If a ray impinges on a boundary dividing two media with different velocities or densities, one must account for reflection and transmission at boundaries in order to properly calculate the wavefield amplitude. While Hale implemented a correction for the influence of discontinuities on geometrical spreading, the loss of energy reflected by impedance discontinuities was

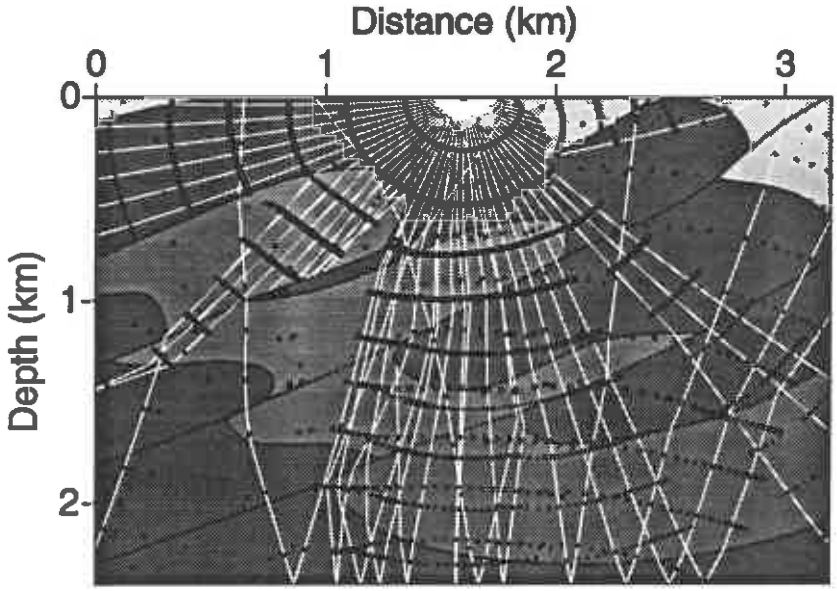

FIG. 14. Rays and wavefronts for an overthrust model. Rays are plotted as white lines, and wavefronts as black symbols. Data acquired for this model need to be corrected for reflection and transmission losses.

not included. I modified the program to compute the necessary correction factor A_{RT} along the ray:

$$A_{RT} = \sum_{i=1}^{N} R_i \sqrt{(v_i^- / v_i^+)} \sqrt{(\cos\alpha_i^+ / \cos\alpha_i^-)} \qquad (2)$$

A corresponding expression for two-dimensional elastic media has been derived by Červený and Pšenčík (1984). The summation is over all interfaces encountered by the ray. At the i-th interface, this expression involves the reflection or transmission coefficient R_i for acoustic pressure waves, which can be evaluated by assuming the continuity of both pressure and the normal component of particle velocity across an interface (Brekhovskikh, 1960). The meaning of the other quantities in equation (2) is sketched in Figure 15. If the ray is reflected back from interface Σ_i, the two square-roots yield unity because both the velocities and the angles of incident and reflected ray are identical. The additional computing time required for evaluating the reflection and transmission correction is negligible.

Difficulties with the Gaussian Beam Approach

So far, the majority of issues addressed in this paper involved the tracing of the rays and the computation of helpful information such as out-of-plane spreading or reflection and transmission losses. These quantities and the results of kinematic and dynamic ray tracing are evaluated at the ray ends and stored in a file. Several methods have been proposed to use these data to generate synthetic seismograms, among them are the *paraxial method* (e.g. Beydoun and Keho, 1987) and the Gaussian beam

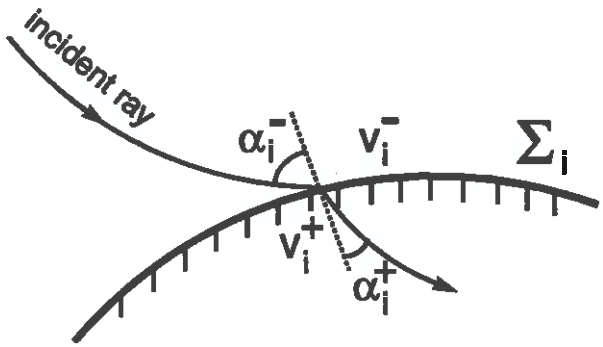

FIG. 15. Sketch of the quantities involved in the transmission of a ray at interface Σ_i. The incidence angle is α_i^-,and the refraction angle is α_i^+. The velocity is discontinuous, jumping from v_i^- to v_i^+ across the interface.

method (GBM) (e.g., Červený, et al, 1982). Both of these methods share the advantage that time-consuming two-point ray tracing is not required. In the paraxial method, the seismic response at a receiver is calculated by extrapolating the information provided by the nearest ray. The GBM uses a weighted sum of information of all rays in the vicinity of the receiver. Although this procedure is computationally more difficult and less efficient, it offers the advantage that the results are regular, even in regions where the conventional ray methods fail (e.g. caustics or shadow zones). These situations are extensively discussed in the literature (e.g. Weber, 1988; Kästner and Fritsche, 1988; Müller, 1984), and several examples of computations of GBM results are shown. None of these references, however, provides examples of using the GBM in models of significant complexity, such as in Figure 14, nor do they consider reflections from more than one target. To improve our understanding of the difficulties that influence the Gaussian beam solutions for models with strong inhomogeneities, a quick review of the Gaussian beam summation approach is necessary.

Gaussian beams represent high-frequency asymptotic solutions of the wave equation. These solutions are concentrated close to rays. Similar to the classical ray methods, where the source wavefield is expanded into rays, in the GBM the source field is expanded into Gaussian beams. Several degrees of freedom are available to achieve an accurate expansion:

- the number of beams used in the expansion
- the width of each beam
- the phase-front curvature of each beam.

Phase-front curvature, i.e., the second derivative of traveltime evaluated at the ray, and beam width may vary from beam to beam and can be specified at an arbitrary point along the ray. The width and the number of beams determine the beam coverage

in the area of interest. Since the wave equation is linear, synthetic seismograms may be computed at any point P in the medium as a weighted sum over all beams.

$$u(P) = \int_{\phi} \Phi(\phi)\ u_{\phi}(P)\ d\phi, \tag{3}$$

where $u(P)$ is the solution at the receiver, and $u_{\phi}(P)$ is the solution of the beam with take-off angle ϕ, evaluated at P. The common procedure for estimating the complex-valued weighting function $\Phi(\phi)$ is to compare integral (3) with the exact solution of the wave equation in homogeneous media for frequency $\omega \to \infty$ (Červený, et al, 1982). Additionally, it is assumed that, at the source, the phase-front curvature and the width of the beam are the same for all take-off angles or, as shown by Müller (1984), vary linearly as a function of ϕ. For simplicity, the curvature of the phase

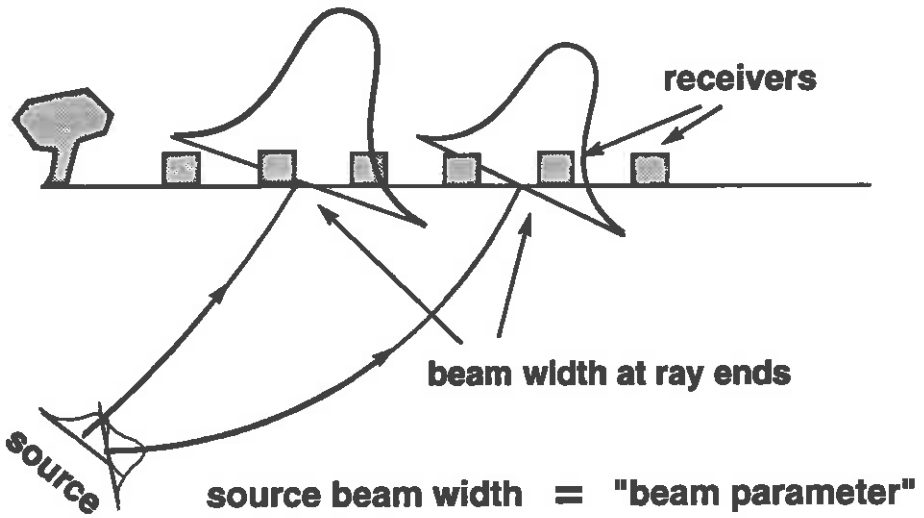

FIG. 16. Sketch to illustrate the meaning of *beam parameter* and *beam width at ray end*. Note that the rays are the support of the beams and that the amplitude of a beam decreases exponentionally away from the ray. The response at the receivers is obtained as a weighted sum over the beams.

front of the beam is set to zero at the source; i.e., phase-fronts are planar at the source. The introduction of beams with plane phase-fronts at the source does not include any error; however, that choice reduces the variety of possible expansions of a wavefield into Gaussian beams. The only beam parameter left to be specified is the beam width at the source (see Figure 16).

To illustrate difficulties inherent to the GBM, a simple experiment is sketched in Figure 17. Rays are traced from a single shotpoint and are reflected from an interface at the depth of 2.5 km. Synthetic seismograms for various choices of beam parameter are shown in Figure 18. Note that the choice of beam parameter has influence on the

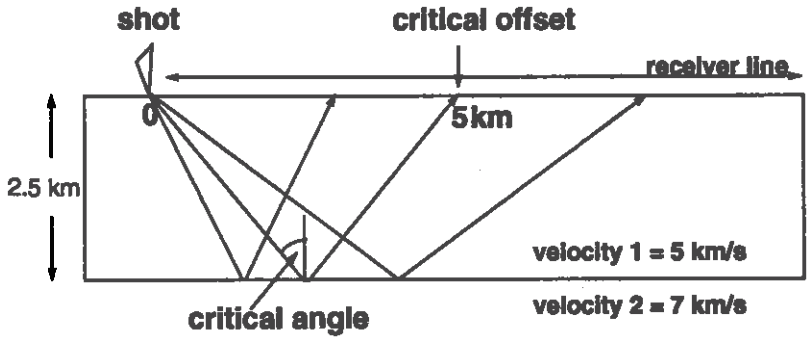

FIG. 17. Geometry of an experiment to show the dependence of the GBM results on the choice of beam parameter. Seismic sections for various beam parameters are displayed in Figure 18.

generated time sections. Even in this simple model, a poor choice of beam parameter yields spurious arrivals and abnormal amplitude behavior (see Figures 18a and 18d).

This phenomenon may be understood better by considering Figure 19. The diagram shows the dominant frequency beam widths at the ray ends as a function of source-to-receiver offset. The wrong choice of beam parameter yields beam widths that are too broad at the ray ends. For an initial beam width of 0.1 km, the width of the beams at the ray ends even exceeds the horizontal dimensions of the model. This leads to spurious arrivals because the influence of the beam is not limited to the vicinity of its emerging point.

There is an additional problem in tracing beams through models such as the one in Figure 14. Hale (1991) generated a synthetic midpoint gather for a shotpoint at 1.6 km. This result is shown in Figure 20a. Negative and positive offset represent the interchange of source and receiver positions. Reciprocity requires that trace amplitudes be independent of this interchange. The asymmetry suggests that the created dataset is not accurate. Hale supposed two reasons for the failure. First, the missing correction for reflection and transmission on the amplitudes, and second, the violation of the beam assumption. The latter requires the model parameters to vary smoothly relative to the width of the beam (e.g., White, et al., 1987). At an interface, for example, the width of the beam has to be significantly smaller than the radius of curvature of the interface. Figure 20b displays the result of the common midpoint gather after correcting for the energy loss due to reflection and transmission. The asymmetry is still very strong, and one cannot recognize any obvious improvement. I evaluated the beam width at the surface for a source located at a horizontal distance of 1.6 km (see Figure 21). The range of beam widths exceeds the dimensions of the model by about one order of magnitude! This indicates that beams attached to rays

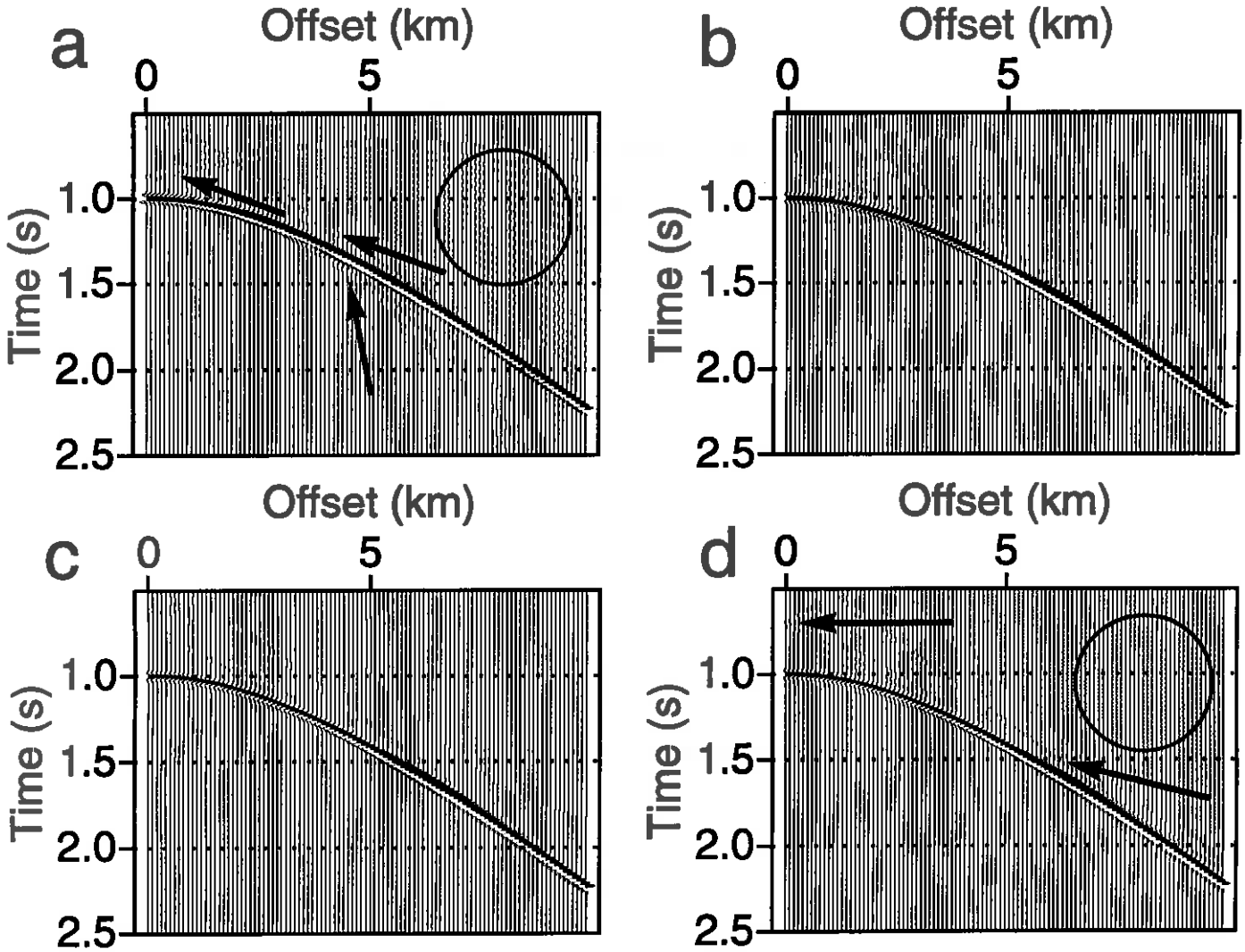

FIG. 18. Seismic sections computed for the experiment sketched in Figure 17. The choice of beam parameter is the following: (a) 0.1 km; (b) 1.0 km; (c) 2.0 km; (d) 5.0 km. The arrows indicate spurious arrivals. Close examination of the encircled areas show artifacts due to the broad beams.

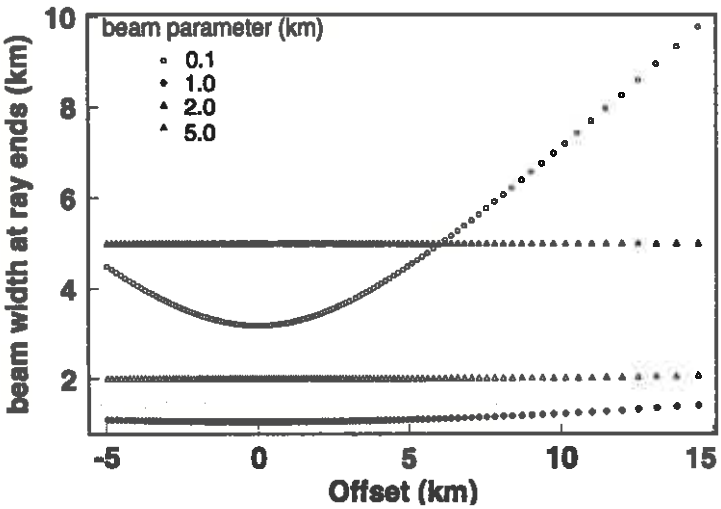

FIG. 19. A more detailed analysis of the results obtained in the experiment sketched in Figure 17 allows a better understanding of some of the difficulties of Gaussian beam modeling. The diagram displays plots the dominant frequency beam width at the receiver as a function of offset. Each symbol denotes a different choice of initial beam width at the source.

do not provide an accurate description of the wavefield. Moreover, I was unable to choose *any* beam parameter that gave acceptable beam widths at the surface.

Increasing the complexity of the model requires a more careful examination of the width of the beam. The beam parameter must be chosen such that the beam remains as narrow as possible along the ray. Both the location at which to assign this parameter (e.g., at the source or at the ray ends) and its optimum value have been investigated by various authors (Weber, 1988; Müller, 1984; Červený, 1985). The results, however, were satisfactory only for models with minor inhomogeneities (Kästner and Fritzsche, 1988).

APPLICATION OF GAUSSIAN BEAM MODELING

I suggest a compromise between the rigorous validity conditions of the beam methods and the practical application of beam modeling. Three criteria should be carefully examined when modeling seismic responses in complex media:

- The beam width should not exceed the natural length-scale of the problem.
- Each receiver should receive contributions from several beams.
- The modeling should yield stable results for small variations of the "optimal" beam parameter.

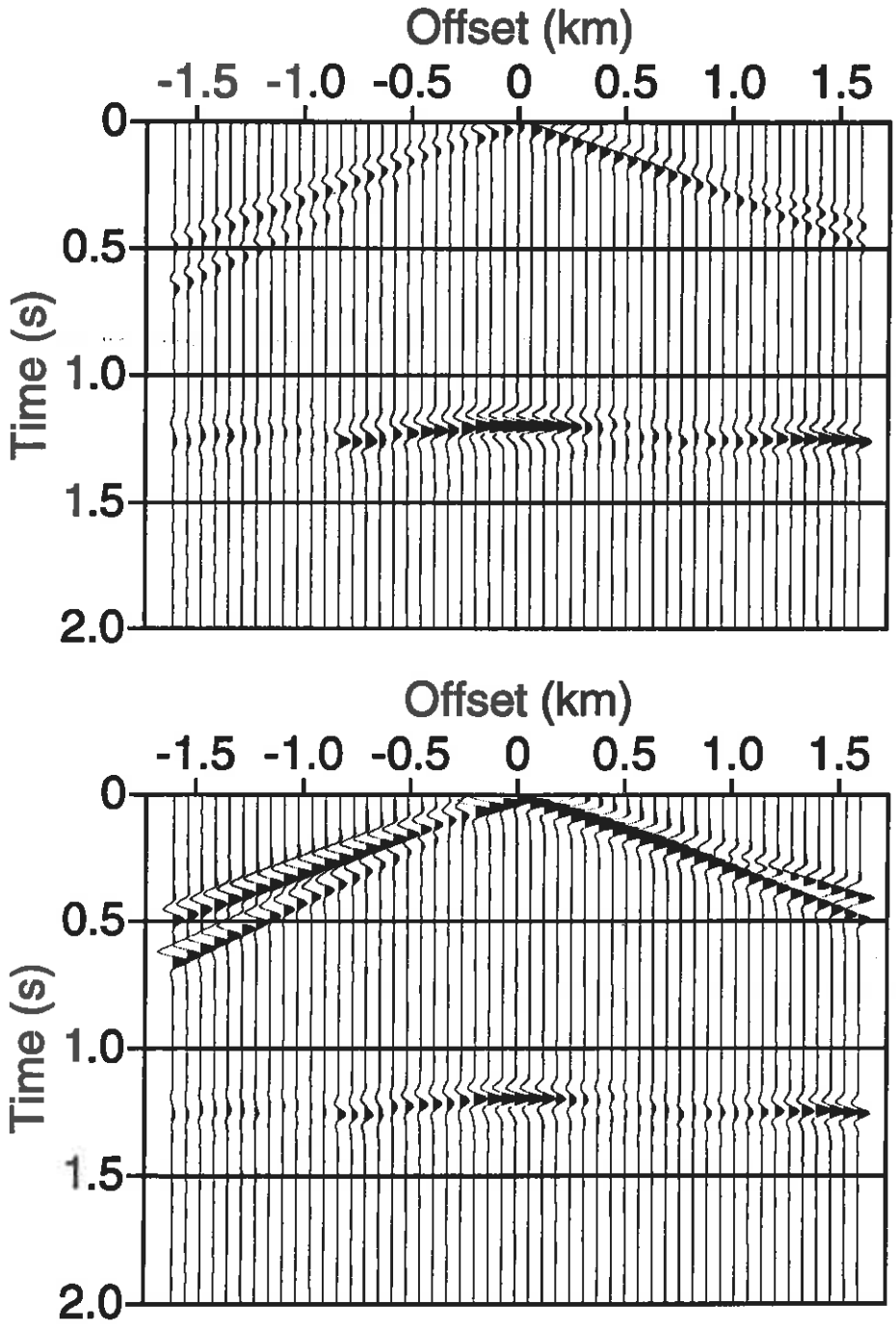

FIG. 20. Common midpoint gathers for the model shown in Figure 14. The midpoint is situated at 1.6 km offset. Asymmetry suggests that the data generated are not accurate. In (a), the correction for transmission and reflection of seismic energy at velocity discontinuities is not included. After taking into account reflection and transmission losses (b), amplitudes are changed, but the asymmetry remains.

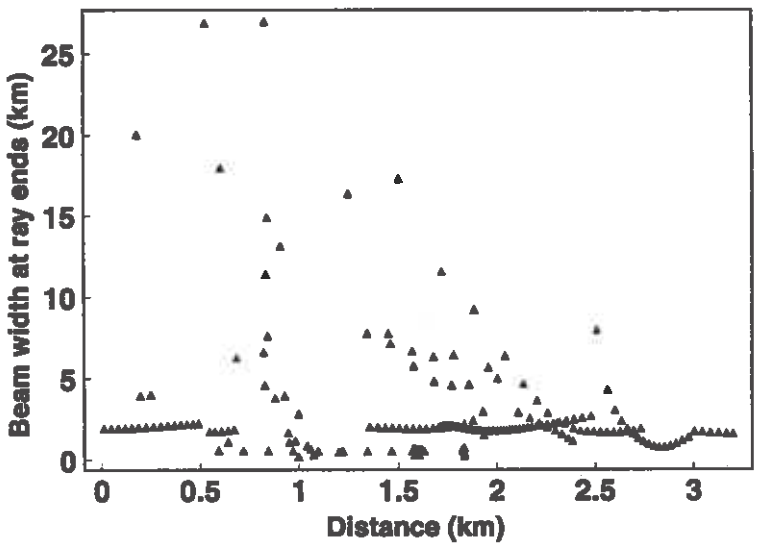

FIG. 21. Analysis of the dominant frequency beam widths at the ray end indicates the violation of the beam assumptions for the overthrust model (Figure 14). Several beam widths exceed the horizontal dimension of the model by about one order of magnitude.

Even a simple plot of the beam width at the ray ends can help to decide if the beam approach is appropriate. Figure 22 shows rays traced in a salt dome model. The area of inapplicability of the Gaussian beam method can be identified in Figure 23. The arrivals at receiver positions between 0 to 1.5 km correspond to turned rays. Positions in that range, according to my experience, also show unstable results for classical ray tracing. It is possible, however, to generate accurate seismograms in the range of receiver positions from 1.5 to 4 km.

I supplemented the modeling code with an option to display beam-width information at the ray ends. Both statistical data such as the average beam width, and graphical information similar to those in Figures 21 and 23 are computed. This information helps identify regions of inapplicability of beam modeling and find an appropriate beam parameter. The default beam parameter is the one that yields the minimum average beam width at the ray ends.

To reduce the spurious arrivals due to the influence of beams that are too broad, I added an option to limit the range of extrapolation away from the ray ends. Moreover, a warning is given if too few beams contribute to a receiver. Experiments indicate that the modeling, including the testing of various beam parameters, can be performed more efficiently than by conventional ray tracing with the CShot package (Docherty, 1987).

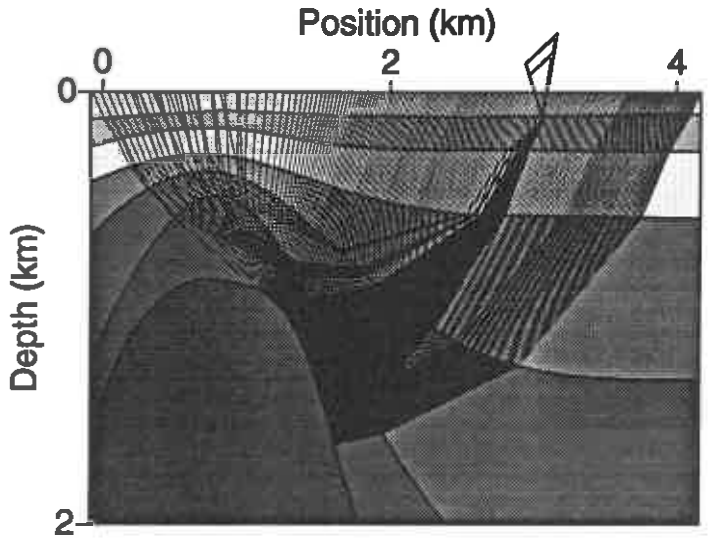

FIG. 22. Rays traced in a salt dome model. The source is situated at 3.2 km horizontal position. Near-critical rays emerge in the region of 0 to 1.5 km and yield extremely broad beam widths. The rays reflected from the dome, however, behave well.

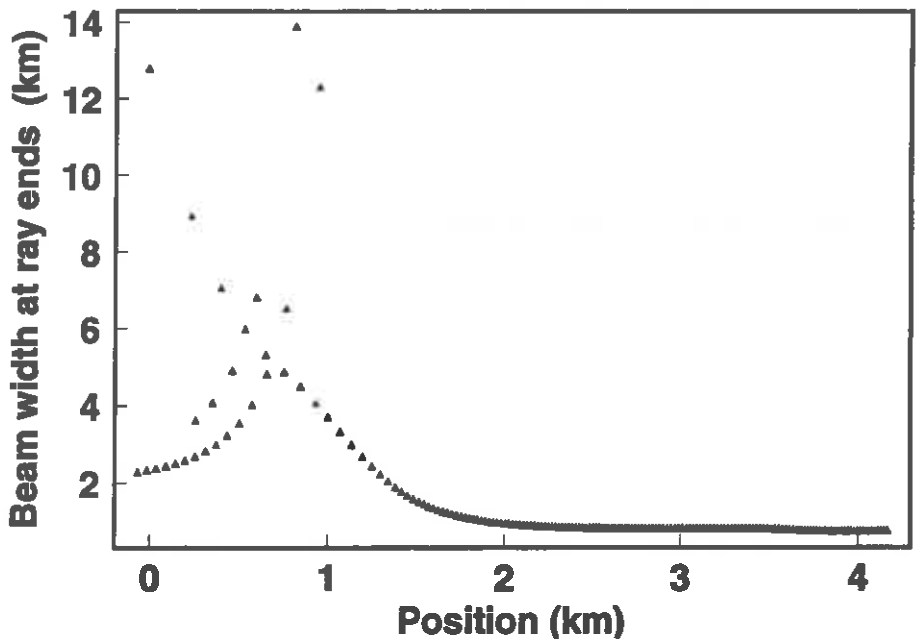

FIG. 23. Analysis of the dominant frequency beam width at the ray ends in Figure 22. Data acquired in the region beyond the horizontal position of 1.5 km will yield accurate results.

FUTURE WORK

Two approaches may help to improve the performance of Gaussian beam modeling:

- A more sophisticated choice of beam parameter has to be developed. The optimal choice of beam parameter is certainly dependent on the properties of the medium encountered by the individual rays. It might be necessary to specify a different phase-front curvature and beam width at proper chosen locations along each ray, that is, as a function of ϕ. In addition, we should consider a weighting function that varies with ϕ; that is, $\Phi(\phi)$ in equation (3) must be evaluated.
- Smoothing of the velocity field could reduce the spreading problem of the beams. This approach is motivated by the good performance of the Gaussian beam migration procedure (e.g., Hale, 1992; Hill, 1990) where the model velocities are smoothed.

The GBM should be used for modeling of seismic wavefields in models with significant inhomogeneities only when we can achieve a focusing of the beams along the ray. Then, an extension of the GBM modeling code to elastic media would be worthwhile. The required changes are not difficult. The more involved extension to three-dimensional models and an interactive procedure for the modeling could then be considered.

As long as these improvements cannot be realized, the GBM should be restricted to models with weak inhomogeneities. This constraint is similar to those in conventional ray tracing. However, the GBM provides an explicit means of checking the applicability of the method by providing beam-width information.

Modeling using the GBM is only one possible application of the dynamic ray-traced data generated along rays. Alternative methods (e.g., the paraxial method) can also use these data to create synthetic seismograms. The new modifications such as the tracing of multiples, computation of out-of-plane spreading, or reflection and transmission correction are evaluated independently of the Gaussian beam procedure.

CONCLUSION

Several new implementations improve the flexibility and accuracy of Gaussian beam modeling in triangulated subsurface media. The influence of energy partitioning at interfaces, 3-D spreading in a 2-D model, and attenuation on the seismic amplitudes and phases can be simulated efficiently. An option to perform Fresnel-volume ray tracing helps in the study of the resolution of seismic signals and indicates the validity region of ray-theoretical methods. The modifications can be used while maintaining the attractive feature of computational speed and limited computer storage.

The theory of beam modeling is accurate and efficient if models with weak inhomogeneities are considered. To help choose an appropriate beam parameter, I included

a code to statistically analyze the beam widths at the ray ends and to compute an "optimal" beam parameter.

The GBM, as currently developed, cannot properly handle models of high complexity. The limitations are similar to those of classical ray theory. However, the GBM provides an explicit means of checking the applicability of the method by providing beam-width information. A test of the beam widths can identify regions where difficulties might be expected.

ACKNOWLEDGMENTS

I thank the VSP group at the Colorado School of Mines for providing the physical modeling data set. Special thanks to Dr. Klimes in Prague for helpful discussions.

REFERENCES

Ben-Menahem, A. and Beydoun, W.B., 1985, Range of validity of seismic ray and beam methods in general inhomogeneous media — General Theory: Geophys. J. R. astr. Soc., **82**, 207–234.

Beydoun, W. and Keho, T., 1987, The paraxial ray method: Geophysics, **52**, 1639–1653.

Bleistein, N., 1984, Mathematical methods for wave phenomena: Academic Press Inc., New York.

Bleistein, N., 1986, Two-and-one-half dimensional in-plane wave propagation: Geophysical Prospecting, **34**, 686–703.

Brekhovskikh, L. M., 1960, Waves in layered media: Academic Press Inc., New York.

Červený, V., Popov, M.M., Pšenčík, I., 1982, Computation of wave fields in inhomogeneous media — Gaussian beam approach: Geophys. J. R. astr. Soc., **70**, 109–128.

Červený, V., and Pšenčík, I., 1984, Gaussian beams in elastic 2-D laterally varying layered structures: Geophys. J. R. astr. Soc., **78**, 65–91.

Červený, V. and Soares, J., 1992, Fresnel volume ray tracing: Geophysics, **57**, 902–915.

Červený, V., 1985, The application of raytracing to the numerical modeling of seismic wavefields in complex structures. In: Handbook of Geophysical Exploration. Section I, Seismic Exploration Vol. 15 A, Seismic shear waves. Geophysical Press, London, p. 1–124.

Červený, V., 1987, Ray methods for three-dimensional seismic modelling: Petroleum industry course, Trondheim, Norway.

Docherty, P., 1987, Two-and-one-half dimensional common shot modeling: Center for Wave Phenomena Research Report, **CWP-050**, Colorado School of Mines, Golden, CO.

Fei, T., 1993, Elimination of dispersion in finite-difference modeling and migration: This report.

Hale, D., and Cohen, J. K., 1991, Triangulated models of the Earth's subsurface: Center for Wave Phenomena Report, **CWP-107**, Colorado School of Mines, Golden, CO.

Hale, D., 1991, Dynamic ray tracing in triangulated subsurface models: Center for Wave Phenomena Report, **CWP-107**, Colorado School of Mines,Golden, CO.

Hale, D., 1992, Migration by the Kirchhoff, slant stack, and Gaussian beam methods: Center for Wave Phenomena Report, **CWP-121**, Colorado School of Mines,Golden, CO.

Hill, N. R., 1990, Gaussian beam migration: Geophysics, **55**, 1416–1428.

Jaramillo, H. H., 1993, Modeling and imaging of computational and physical VSP data: M.S. Thesis #7302, Colorado School of Mines, Golden, CO.

Kästner, U. and Fritzsche, M., 1988, Synthetische Gauss-Beam Seismogramme in dreidimensionalen Medien: Diplomarbeit, Geophysikalisches Institut der Universität Karlsruhe, Germany.

Kravtsov, Y. and Orlov, Y., 1990, Geometrical optics in inhomogeneous media: Springer Verlag, New York.

Müller, G., 1983, Rheological properties and velocity dispersion of a medium with power-law dependence of Q on frequency: Geophys. J. R. astr. Soc., **54**, 20–29.

Müller, G., 1984, Efficient calculations of Gaussian beam seismograms for two-dimensional inhomogeneous media: Geophys. J. R. astr. Soc., **79**, 153–166.

Weber, M., 1988, Computation of body-wave seismograms in absorbing 2-D media using the Gaussian beam method: comparison with exact methods, Geophys. J. R. astr. Soc., **92**, 9–24.

Weiler, K., 1988, The radial edge structure: a topological representation for non-manifold geometric boundary modeling, *in* Wozny, M. J., McLaughlin, H. W., and Encarnacao, J. L., Eds., Geometric modeling for CAD applications: Elsevier Science Publishers B. V., 3–36.

White, B. S., Norris, A., Bayliss, A., Burridge, R., 1987, Some remarks on the Gaussian beam summation method: Geophys. J. R. astr. Soc., **89**, 579–636.

Inverse calculations with realistic *a priori* information

John A. Scales, Boyi Ou, and Albert Tarantola*

*Institut de Physique du Globe de Paris

Inverse calculations with realistic *a priori* information

John A. Scales, Boyi Ou and Albert Tarantola *

ABSTRACT

In order to estimate quantitatively the confidence that one can place in the solution of an inverse calculation, it is necessary to know both the statistics of the data and the distribution of physically reasonable models.

In the first place, we need to know the statistics of the data even to be able to define what we mean by "fitting the data." If we are too optimistic about these uncertainties, it may be impossible to find a model which does fit. If we are too pessimistic, then too many models will fit the observations.

We also need to characterize the distribution of feasible models since it is easy to construct unrealistic models which nevertheless fit the data quite well. For example, a highly heterogeneous, isotropic model may fit the data as well as a relatively homogeneous anisotropic one. If we say that the heterogeneous, isotropic model is unrealistic or has artifacts, then we are using prior information to assign it a small significance.

We describe preliminary research aimed at characterizing this *a priori* information. Our goals are to compute approximations to the probability density function of seismic data without making any restrictive assumptions, and to construct distributions on the space of feasible models which take into account the expertise of interpreters, geologists, reservoir engineers, etc. At present, we are a long way from completing those goals and can provide only the barest outline of how things will go. Therefore this report should be taken as being decidedly provisional.

* *Institut de Physique du Globe de Paris*

EMS

g the

foot,

nber of
nto 100
bins of
diumum
from 50
depend
number
acy.

This is
poses, is
already
ne series
ensional
reduces
process
nd-order
pairwise
s for our
or more
(6) gives
rkovian?

adequate
ving the
check to
check by
esis that

study
riving
rucial
re it is
bles of
s fails
ve the
ıption
en we

linary
3) and
ndom
at for
ponds
by

ticular
pecify

In that
andom-
urely a

by in-
e of ρ_M
d max-
models
ılation.
ampling
to how

. What
, Equa-
gements
lifferent
ecomes
ing the
data, I
bability

(3)

vertical
$(D|I)$ is

(4)

$)_1$ to be

(5)

(6)

(7)

$)_1 D_2$,the
owledge
ve make
ll be the

equivalent

ng, goals: the
odels conform
ple, we could
ı a region of
sis, we might
s of constant,
ces are good
S sense. The
with artifacts
earth should
uite well that
d constantly
of sequences
sence of salt
, and so on.
on but how.

f constraints
phy we may
en layers on
common to
erpreted as,
ble range of
ot explicitly
on that the
commonly
e difference
on amongst
regularized

of the opti-
samples of
even slight
rious prob-
olem is not
ı we could
em is that
implicitly

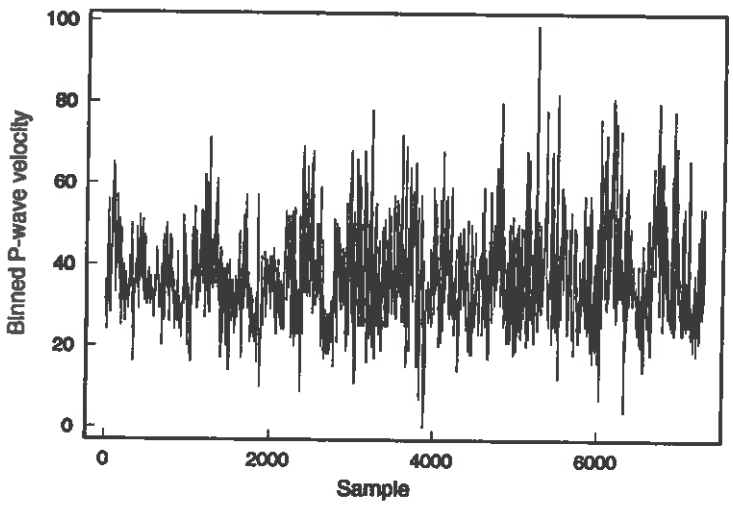

FIG. 4. The "binned" version of the log using 100 bins. This version of the log is reasonably close to the log shown in Figure (3).

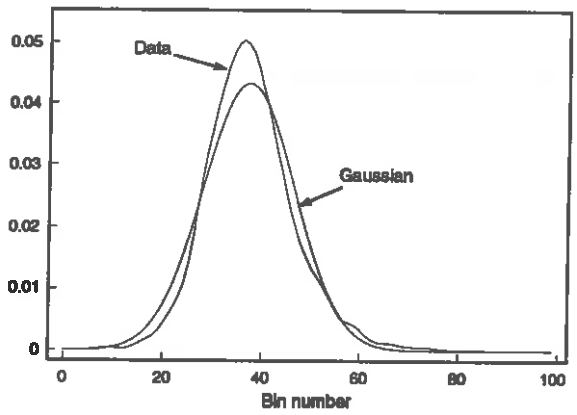

FIG. 5. Probability density function estimated from the smoothed histogram of values appearing in the log using 100 bins. This is overlain by a Gaussian having the same mean and standard deviation.

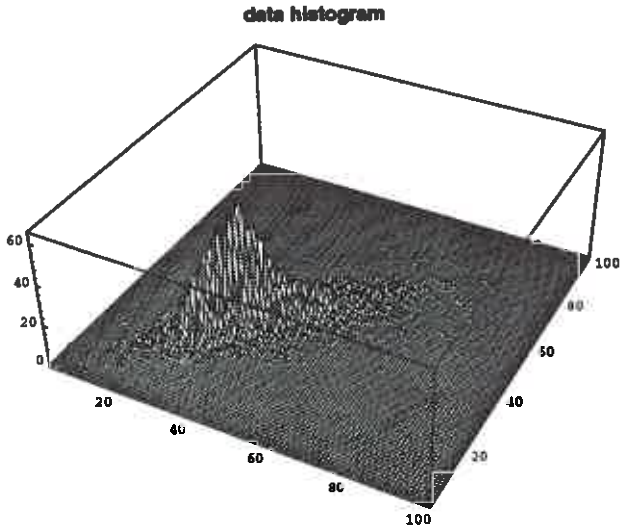

FIG. 6. Histogram of pairwise transitions from bin i to bin j.

the data and pseudo-random realization are drawn from the same distribution.[6]

Wheel of Fortune

The pseudo-random realizations of the log are computed in the following way. First, looking at Figure (6), we observe that for any bin value j, a slice through this surface for constant j is a 1-D histogram giving the relative probability of making a transition from j to any of the bins. What we do is make a weighted *roulette wheel* for each j based upon these 1-D histograms. In other words for each j there will be a roulette wheel with, in this case 100, sectors, one for each of the bins. The size of the i-th sector will be in proportion to the transition probability $j - i$ from the 2-D histogram. The idea is this: if we are at a particular site on the log and the current value of the binned P-wave velocity is j, then by spinning the roulette wheel associated with j, we will select a transition with exactly the probability required by the observed statistics. So we simply start at one end of the log and select a bin at random. From then on we fill out the log by selecting the appropriate roulette wheel, spinning it, and putting the resulting sample in the next site on the log.

There are many other ways of generating psuedo-random realizations based on these histograms. For example, on a much simpler problem of lithology estimation, Doyen and Guidish (1992) suggest doing a kind of Monte Carlo optimization using an objective function that is the difference between the observed data histogram and a histogram computed for a model chosen by randomly perturbing some initial model. But in our case, due to the multi-modality of the histograms, as evidenced in Figure (6), it is not clear that this sort of optimization would achieve reasonable extrema. This is especially true given the fact that a log with 8000 samples drawn from

[6]Most any statistics text will have a discussion of the Kolmogorov-Smirnov and related Chi-squared tests. The code we used implementing the K-S test is from Press *et al.* (1986).

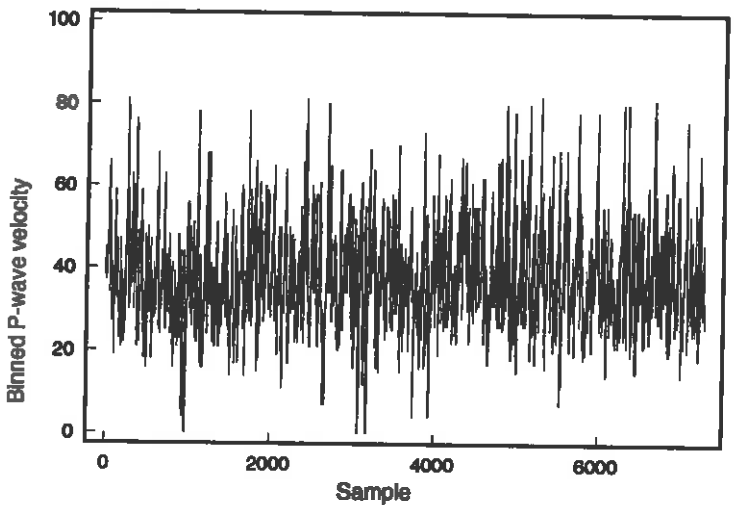

FIG. 7. Pseudo-random log generated according to the second-order statistics of the observed log.

100 bins represents a sample in a model space containing 100^{8000} points! In addition, there is a vast literature in geostatistics which treats this issue. (For example, see Journal and Huijbregts (1978).) We plan to take advantage of as much of this work as we can.

Figure (7) shows an example of a pseudo-random log generated according to the roulette-wheel method outlined above. Its histogram of pair-wise transitions is shown in Figure (8) and would seem to provide a relatively good match of that shown in Figure (6). The RMS difference between these two histograms is shown in Figure (9).

The pseudo-random log seems to capture some of the "texture" of the real data reasonably well. In order to quantify this similarity we ran a two-sample Kolmogorov-Smirnov test on the data, the null-hypothesis being that both samples are drawn from the same distribution. The K-S statistic returns a very small value (.006) for the resulting probability, indicating a very low probability for the null hypothesis.

To make a more systematic look at this phenomenon, we generated a suite of 100 pseudo-random logs according to our prescription. Figure (10) shows very little systematic trend in the values of the K-S statistic. Presumably, if we can consistently generate logs with a high value of the K-S statistic, then we can be reasonably certain that we have captured the essence of the data. In the absence of this, the only solution would appear to be to estimate the higher order statistics of the data; i.e., the *polyspectra*. For example, the third-order cumulant of a stationary process, which is a function of two lags s_1 and s_2, is given by

$$C(s_1, s_2) = E[\{X_t - \mu_x\}\{X_{t+s_1} - \mu_x\}\{X_{t+s_2} - \mu_x\}] \tag{8}$$

where $\mu_x = E[X_t]$ (Priestley, 1989). The bi-spectrum is the Fourier transform of this cumulant. A rigorous test for Gaussianity could then be based on testing the null

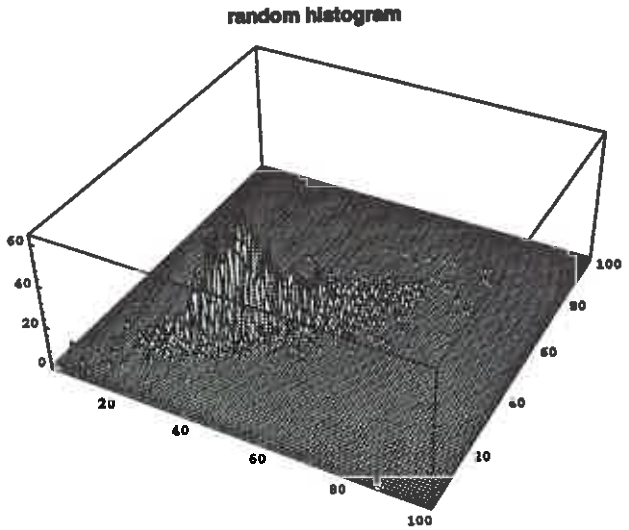

FIG. 8. Histogram of pairwise transitions from bin i to bin j in the pseudo-random log

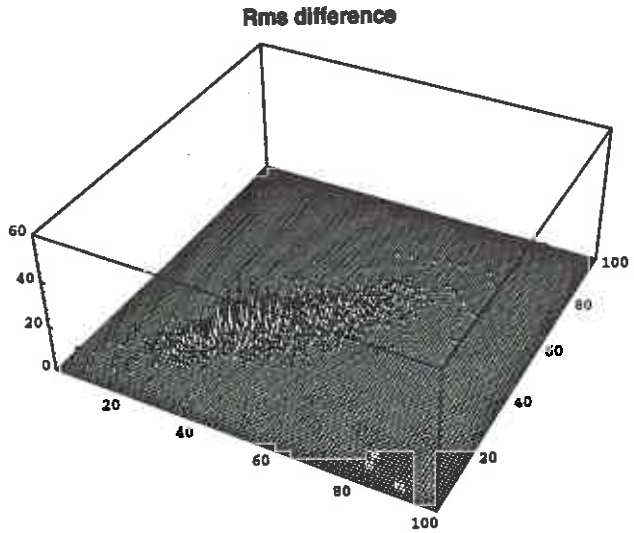

FIG. 9. RMS difference between the data histogram and that of the pseudo-random log.

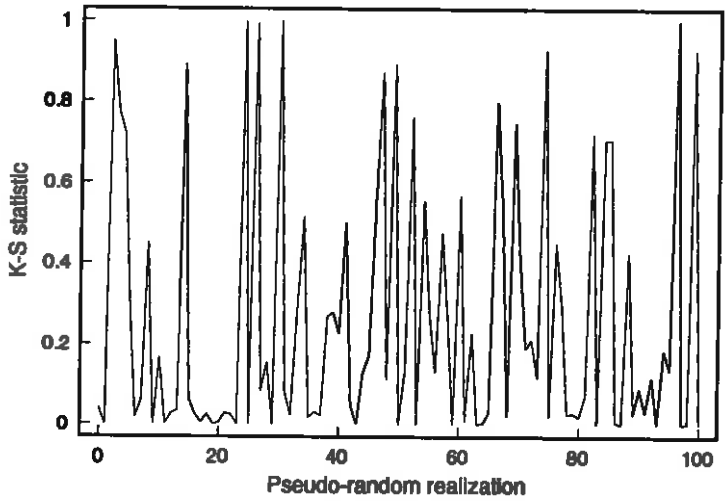

FIG. 10. Kolmogorov-Smirnov statistic for 100 pseudo-random realizations of the log.

hypothesis that the bi-spectrum is zero at all frequencies. The test statistic would be constructed from estimates of the bi-spectrum over a grid of frequencies, as described in Priestley (1989).

CONCLUSIONS

We have shown some very preliminary work aimed at, on the one hand, estimating statistics of seismic data in a very general way, in particular without resorting to any parametric models; and on the other hand, we have begun to consider what sorts of realistic *a priori* information we might be able to use in a seismic inverse calculation. We believe that the latter will require seismologists to work in close cooperation with stratigraphers, geostatisticians, reservoir engineers, and others who have expertise that can be brought to bear on the Earth models we are attempting to construct from seismic data. Once we have constructed these more realistic Bayesian priors we are faced with the daunting task of sampling a high-dimensional, almost certainly multimodal posterior probability density on the space of models. However, recent work on Monte Carlo methods such as genetic algorithms leave us optimistic that such sampling can be done provided the dimensionality of the spaces is not too large. And here, realistic prior information will be important not only to limit the search to models which are *a priori* likely but also to allow us to generate parsimonious parameterizations, or Earth models, so as to mitigate the "curse of dimensionality", which seems to affect all global sampling methods.

ACKNOWLEDGEMENTS

This research was begun while the first author, then still employed by Amoco Production Company, was a visitor at the *Institut de Physique du Globe de Paris.*

He wishes to express his sincere thanks to his friends and colleagues in Paris for their warm hospitality and for providing such a stimulating working environment, and to Amoco for making this visit possible.

REFERENCES

Doyen, P.M., and Guidish, T.M., 1992, Seismic discrimination of lithology: a Bayesian approach: preprint.

Duijndam, A.J.W., 1987, Detailed Bayesian inversion of seismic data: PhD thesis, Technical University of Delft.

Fischer, K.H., and Hertz, J.A., 1991, Spin glasses: Cambridge University Press.

Godfrey, R., Muir, F., and Rocca, F., 1980, Modeling seismic impedance with Markov chains: Geophysics, **45**, 1351-1372.

Hermann, G.T., 1985, Application of maximum entropy and Bayesian optimization methods to image reconstruction from projections, *in* Smith, C. R., and Grandy, W. T., Jr., Eds., Maximum-entropy and Bayesian methods in inverse problems: Reidel.

Jaynes, E.T., 1985, Where do we go from here?, *in* Smith, C. R., and Grandy, W. T., Jr., Eds., Maximum-entropy and Bayesian methods in inverse problems: Reidel.

Jeffreys, R.C., 1983, The logic of decision: University of Chicago.

Journal, A. and Huijbregts, Ch., 1978, Mining geostatistics: Academic Press.

Koch, M., 1993, Simultaneous inversion for 3-D crustal structure and hypocentres including direct, refracted and reflected phases–I. Development, validation and optimal regularization of the method: Geophysical Journal, **112**, 385-412.

Mosegaard, K., and Tarantola, A., 1993, Monte Carlo sampling of probabilities: Nature (submitted).

Press, W.H., Flannery, B.P., Teukolsky, S.A., and Vetterling, W.T., 1986, Numerical recipes: Cambridge.

Priestley, M.B., 1988, Non-linear and non-stationary time series analysis: Academic.

Priestley, M.B., 1981, Spectral analysis and time series, 2 vols.: Academic.

Pugachev, V.S., 1965, Theory of random functions and its application to control problems: Pergamon.

Scales, J.A., Docherty, P.C., and Gersztenkorn, A., 1990, Regularization of nonlinear inverse problems–imaging the near-surface weathering layer: Inverse Problems, **6**, 115-131.

Scales, J.A., Smith, M.L., and Fischer, T.L., 1992, Global optimization methods for multimodal inverse problems: Journal of Computational Physics, **102**, 258-268.

Tarantola, A., 1987, Inverse problem theory–methods for data fitting and model parameter estimation: Elsevier.

Walden, A.T., 1985, Non-Gaussian reflectivity, entropy, and deconvolution: Geophysics, **50**, 2862-2888.

Walden, A.T. and Hosken, J.W.J., An investigation of the spectral properties of primary reflection coefficients: Geophysical Prospecting, **33**, 400–435.

Zhdanov, M.S., 1988, Integral transforms in geophysics: Springer.

Zhdanov, M.S., 1993, Lecture notes on inversion theory (in preparation).

APPENDIX A: THE BAYESIAN POSTERIOR PROBABILTY DENSITY

As we have argued, the posterior probability density on the space of models must be the product of two terms: a term which involves the *a priori* probability on the space of models and a term which measures the extent of data fit

$$\sigma(\mathbf{d}) = \rho(\mathbf{m})\ L(\mathbf{m}). \tag{A-1}$$

L is called the likelihood function and depends implicitly on the data.

We now show how Equation (A-1) follows logically from Bayes' theorem provided we generalize our notion of "data" to allow for the possibility that the data might be specified by probability distributions (Tarantola (1987), Chapter 1). To do so we make use of an idea due to Jeffreys (1983) (see also, Duijndam (1987)). We begin by using the notation common amongst Bayesians, then we show how this relates to the more standard inverse-theoretic notation in Tarantola (1987).

In this approach we assume that we have some prior joint distribution $p_0(\mathbf{m}, \mathbf{d})$. Further, we suppose that as the result of some observation, the marginal pdf of $\mathbf{d}$ changes to $p_1(\mathbf{d})$. We regard $p_1(\mathbf{d})$ as being the "data" in the sense that we often know the data only as a distribution, not exact numbers. In the special case where the data are exactly known, $p_1(\mathbf{d})$ reduces to a delta function $\delta(\mathbf{d} - \mathbf{d}_{obs})$.

How do we use this new information in the solution of the inverse problem? The answer is based upon the following assumption: **whereas the information on d has changed as a result of the experiment, there is no reason to think that the conditional degree of belief of m on d has.** I.e.,

$$p_1(\mathbf{m}|\mathbf{d}) = p_0(\mathbf{m}|\mathbf{d}). \tag{A-2}$$

From this one can derive the posterior marginal $p_1(\mathbf{m})$:

$$p_1(\mathbf{m}) \equiv \int_D p_1(\mathbf{m}, \mathbf{d})\ d\mathbf{d} \tag{A-3}$$

$$= \int_D p_1(\mathbf{m}|\mathbf{d}) p_1(\mathbf{d})\ d\mathbf{d} \tag{A-4}$$

$$= \int_D p_0(\mathbf{m}|\mathbf{d}) p_1(\mathbf{d})\, d\mathbf{d} \tag{A-5}$$

$$= \int_D \frac{p_0(\mathbf{d}|\mathbf{m}) p_0(\mathbf{m})}{p_0(\mathbf{d})} p_1(\mathbf{d})\, d\mathbf{d} \tag{A-6}$$

$$= p_0(\mathbf{m}) \int_D \frac{p_0(\mathbf{d}|\mathbf{m})}{p_0(\mathbf{d})} p_1(\mathbf{d})\, d\mathbf{d}, \tag{A-7}$$

where D denotes the data space.

Switching now to the inverse-theoretic notation, let us regard $p_0(\mathbf{d})$ as being the noninformative prior distribution on data $\mu_D(\mathbf{d})$: this is what we know about the data **before** we've actually done this particular experiment. Further, we identify $p_1(\mathbf{m})$ as the posterior distribution on the space of models, $p_1(\mathbf{d})$ as the data errors, $p_0(\mathbf{m})$ as the prior distribution on the space of models, and $p_0(\mathbf{d}|\mathbf{m})$ as the modeling errors:

$$\begin{aligned} p_1(\mathbf{m}) &\equiv \sigma(\mathbf{m}) \\ p_1(\mathbf{d}) &\equiv \rho_D(\mathbf{d}) \\ p_0(\mathbf{m}) &\equiv \rho_M(\mathbf{m}) \\ p_0(\mathbf{d}|\mathbf{m}) &\equiv \Theta(\mathbf{d}|\mathbf{m}), \end{aligned}$$

then we arrive at precisely Equation (1.65) of Tarantola (1987)

$$\sigma(\mathbf{m}) = \rho_M(\mathbf{m}) \int_D \frac{\rho_D(\mathbf{d})\Theta(\mathbf{d}|\mathbf{m})}{\mu_D(\mathbf{d})}\, d\mathbf{d} \tag{A-8}$$

An important special case occurs when the modeling errors are negligible, i.e., we have a perfect theory. Then the conditional distribution $\Theta(\mathbf{d}|\mathbf{m})$ reduces to a delta function $\delta(\mathbf{d} - g(\mathbf{m}))$ where g is the forward operator. Then the posterior is simply

$$\sigma(\mathbf{m}) = \rho_M(\mathbf{m}) \left[\frac{\rho_D(\mathbf{d})}{\mu_D(\mathbf{d})}\right]_{\mathbf{d}=g(\mathbf{m})} \tag{A-9}$$

2.5D full wave-form modeling

John W. Stockwell

2.5-D full-waveform modeling

John W. Stockwell, Jr.

ABSTRACT

The need for modeling 3-D seismic data in a 2-D setting has motivated investigators to create so-called 2.5-D modeling methods. One such method proposed by Liner (1991) involves the use of an approximate 2.5-D wave operator for constant-density media.

The traveltimes and amplitudes predicted by WKBJ analysis of the Liner 2.5-D wave equation match those predicted by Bleistein's 2.5-D ray-theoretic development for both constant and piecewise constant wavespeed models. However, WKBJ analysis indicates that the Liner 2.5-D variable wavespeed equation will have a maximum amplitude error of $\pm 35\%$ (compared with the $+250\%$ error obtained by using the ordinary 2-D wave equation) in a linear $c(z)$ model where the wavespeed doubles or halves from the beginning to the end of a raypath. The WKBJ series results suggest a modification to the Liner equation that may reduce this error.

Construction of 2.5-D wave equations for variable density (acoustic) problems also follows from the WKBJ analysis.

INTRODUCTION

The recording of seismic data along a line on the Earth's surface is still a widely used technique. The earth model implied by such a dimensionally-constrained recording geometry is a 3-D model with only 2 dimensions of parameter variability, Bleistein (1986). Consequently, there is a need for modeling seismic data in problems with 2-D parameter variability, but yielding waves having full 3-D amplitude behavior. This need has motivated investigators (Deregowski and Brown 1983, Ursin 1978, Hubral 1978, and Newman 1973) to consider 2-D models scaled by an out-of-plane geometric spreading factor to make the amplitudes approximate 3-D amplitudes.

Bleistein (1986) shows how to describe such 2.5-D modeling in a unified manner using the methods of high-frequency asymptotics. In particular, Bleistein develops the ray-theoretic implications of 2.5-D modeling for both constant and variable-density acoustic problems. Bleistein also characterizes the effects of the 2.5-D assumption on the Fourier-like integrals that form the basis of many migration algorithms.

A different approach was taken by Liner (1991), who attempted to create a "2.5-D wave equation" by using the constant wavespeed Green's function as trial solution to the 2-D wave equation. The resulting equation has the general form of a damped wave equation with a damping coefficient that varies both in space and time. This equation also contains an additional term containing no derivatives.

The advantage of the Liner approach is that it promises to make *full-waveform* modeling in 2.5 dimensions possible. Because numerical implementation of the Liner equation has yielded encouraging results (Bording and Liner 1992 and Bording and Liner 1993), further analysis of this equation is warranted. Therefore, the topic of this paper will be a test of Liner's 2.5-D wave equation against the 2.5-D ray theoretic results of Bleistein via a WKBJ series method. A WKBJ -based extension of the Liner equation to variable-density (acoustic) problems is presented here, as well.

THE CONCEPT OF A 2.5-D WAVE EQUATION

To approximately describe 3-D wave propagation in a 2-D setting, a reasonable approach might be to construct a damped wave equation

$$\left[\nabla^2 - \gamma(\boldsymbol{x},t)\frac{\partial}{\partial t} - \frac{1}{c^2}\frac{\partial^2}{\partial t^2}\right] U(\boldsymbol{x},t) = 0$$

with a spatially and temporally-varying damping coefficient $\gamma(\boldsymbol{x},t)$ to correct the amplitudes for the effect of out-of-plane geometric spreading. (Here $\boldsymbol{x} \equiv (x,z)$ and ∇^2 is the 2-D Laplacian operator.) Such a "2.5-D wave equation" will probably not be an exact result, but may be best described as an *asymptotic wave operator*. That is, it would be an approximate wave operator having the same asymptotic behavior as the 3-D wave equation for a select collection of models and/or frequency ranges.

The use of approximate wave operators in geophysics has a long tradition. The most notable examples involve the use of the parabolic approximations to the Helmholtz equation (see Claerbout 1970 for exploration geophysics applications; see Tappert 1977 and Hill 1986 for examples of ocean acoustics applications).

THE LINER 2.5-D WAVE OPERATOR

Here is a brief outline of the method that Liner (1991) used to construct a 2.5-D asymptotic wave operator. Liner reasoned that in a constant wavespeed medium, the "2.5-D Green's function" is just the in-plane representation of the 3-D Green's function:

$$G_{2.5D} = \frac{\delta(t - r/c)}{4\pi r},$$

with $r = \sqrt{x^2 + z^2}$ being just the range for the case $y = 0$. The ideal problem to be solved would be to find $\mathcal{L}$ such that

$$\mathcal{L}G_{2.5D} = -\delta(t)\delta(\boldsymbol{x}),$$

where $\boldsymbol{x} \equiv (x, z)$. Then $\mathcal{L}$ would be the "exact 2.5-D operator". Note that the Green's function must also satisfy the homogeneous equation

$$\mathcal{L}G_{2.5D} = 0 \tag{1}$$

for $(\boldsymbol{x}, t) \neq (\mathbf{0}, \mathbf{0})$.

Because Liner did not intend to use the operator in the vicinity of the source, he chose to try to construct a nontrivial wave operator that satisfies (1) using the homogeneous 2-D wave equation as starting point. Liner's method was to substitute $G_{2.5D}$ as a trial solution into the homogeneous 2-D wave equation to yield

$$\left[\nabla^2 - \frac{1}{c^2}\frac{d^2}{dt^2}\right] G_{2.5D}(\boldsymbol{x}, t) = -\frac{\delta'(t - r/c)}{4c\pi r^2} - \frac{\delta(t - r/c)}{4\pi r^3}. \tag{2}$$

The two remainder terms on the right result because $G_{2.5D}$ is not a solution to the 2-D wave equation. Liner proposed the following formula

$$\left[\nabla^2 - \frac{1}{c^2}\left\{\frac{d^2}{dt^2} + \frac{c}{r}\frac{d}{dt} + \frac{c^2}{r^2}\right\}\right] U(\boldsymbol{x}, t) = 0, \tag{3}$$

which is just the homogeneous 2-D wave equation with 2 additional terms, to account for the remainder terms in equation (2). Note, while $G_{2.5D}$ is a solution to equation (3), it cannot be assumed to be the *Green's function* of this equation.

Equation (3) is a constant wavespeed equation. To handle variable wavespeed problems, Liner proposed the following formula:

$$\left[\nabla^2 - \frac{1}{c^2}\left\{\frac{d^2}{dt^2} + \frac{1}{t}\frac{d}{dt} + \frac{1}{t^2}\right\}\right] U(\boldsymbol{x}, t) = 0. \tag{4}$$

Liner justified choosing this form by noting that in equation (3) the factors of c/r and c^2/r^2 are, respectively, $1/\tau$, and $1/\tau^2$, where τ is traveltime. Because the signals typically recorded in geophysical investigations have considerably shorter duration than the observed traveltimes, Liner assumed that $t \approx \tau$, where t is absolute time.

For future reference, equations (3) and (4) will be called, respectively, the "r-equation" and the "t-equation", reflecting the respective r and t dependence of the coefficients of these equations. Note that the t-equation reduces to the r-equation for constant wavespeed media under the assumption of $t \approx \tau$.

Testing the r-equation with WKBJ Asymptotics

If the Liner 2.5-D wave equation is to be considered useful, its solution must match the solutions predicted by other methods of solving the 2.5-D modeling problem. The paper by Bleistein (1986) outlines a ray-theoretic WKBJ asymptotic-based solution to the 2.5-D modeling problem. By deriving the eikonal and transport equations associated with Liner's 2.5-D wave equations, it is possible to make a direct comparison of the high-frequency behavior of these equations with the Bleistein's 2.5-D ray theory.

All standard 2-D and 3-D ray theoretic results that follow are taken from Bleistein (1984) section 8.2, while 2.5-D ray theoretic results are taken from Bleistein (1986). Paralleling the standard development of ray theory, the r-equation is Fourier transformed in time to yield the Helmholtz-like or reduced form

$$\left[\nabla^2 + \frac{\omega^2}{c^2} + \frac{i\omega}{rc} - \frac{1}{r^2c^2}\right] u(\boldsymbol{x},\omega) = 0. \tag{5}$$

The WKBJ series

$$u(\boldsymbol{x},\omega) \sim \sum_{n=0}^{\infty} \frac{A_n(\boldsymbol{x})}{(i\omega)^n} \exp[i\omega\tau(\boldsymbol{x})],$$

is substituted into (5). Here $\tau(\boldsymbol{x})$ is the traveltime and $A_n(\boldsymbol{x})$ is the n^{th} order amplitude function.

The result is a series in powers of $i\omega$

$$\begin{aligned} 0 \;=\; e^{i\omega\tau(\boldsymbol{x})} \sum_{n=0}^{\infty} \Bigg[& \frac{A_n}{(i\omega)^{n-2}} \left((\nabla\tau)^2 - \frac{1}{c^2} \right) \\ & + \frac{1}{(i\omega)^{n-1}} \left(2\nabla\tau \cdot \nabla A_n + A_n \nabla^2 \tau + \frac{A_n}{rc} \right) \\ & + \frac{1}{(i\omega)^n} \left(\nabla^2 A_n - \frac{A_n}{r^2c^2} \right) \Bigg] \end{aligned} \tag{6}$$

Only the $n = 0$ and $n = 1$ terms of this series are of immediate interest.

The $n = 0$ term of the series is $O(\omega^2)$. Setting the coefficient of this first term equal to 0 yields the 2-D eikonal equation

$$(\nabla\tau)^2 - \frac{1}{c^2} = 0. \tag{7}$$

This result agrees with the eikonal equation in the 2.5-D ray theoretic formulation.

The $n = 1$ term is $O(\omega^1)$. Setting the coefficient of this term equal to 0 yields the (first) transport equation

$$2\nabla A_0 \cdot \nabla\tau + A_0 \nabla^2 \tau + \frac{A_0}{cr} = 0. \tag{8}$$

This equation is just the standard 2-D transport equation with an extra term, A_0/cr.

If this new transport equation describes the 3-D in-plane geometric spreading that the 2.5-D model requires, then it is reasonable that it would have the form of a 2-D transport equation with an extra term to account for the out-of-plane component of geometric spreading.

Just such a transport equation may be deduced from Bleistein's 2.5-D ray theoretic development. From standard ray theory

$$\nabla\tau = \frac{\partial \boldsymbol{x}}{\partial\sigma} \qquad \text{and} \qquad \frac{d\tau}{d\sigma} = \frac{1}{c^2}. \tag{9}$$

Here σ is a running parameter along a ray, representing a quantity with units of [length]^2/[time] and is related to the traveltime τ through the second expression above. The standard transport equation (either 2-D or 3-D)

$$2\nabla A_0 \cdot \nabla\tau + A_0\nabla^2\tau = 0, \tag{10}$$

may be rewritten as

$$\frac{dA_0^2}{d\sigma} = -A_0^2\nabla^2\tau, \tag{11}$$

by multiplying equation (10) by A_0 and by using the first relation in (9).

Another important result from ray theory is that

$$\nabla^2 A_0 = \frac{d}{d\sigma}\{\log[J_{3D}]\} \qquad \text{where} \qquad J_{3D} \equiv \frac{\partial(x_1, x_2, x_3)}{\partial(\sigma, \alpha, \beta)}.$$

Here J_{3D} is the 3-D ray Jacobian and α and β are parameters that label the ray by its initial direction.

For the special case of $x_2 = 0$ and $c(\boldsymbol{x}) = c(x_1, x_3)$—the 2.5-D assumption—$J_{3D}$ becomes σJ_{2D} and equation (11) becomes

$$\nabla^2 A_0 = \frac{d}{d\sigma}\{\log[\sigma J_{2D}]\} \qquad \text{where} \qquad J_{2D} \equiv \frac{\partial(x_1, x_3)}{\partial(\sigma, \beta)}.$$

Thus,

$$\nabla^2 A_0 = \frac{1}{\sigma} + \frac{d}{d\sigma}\{\log[J_{2D}]\} = \frac{1}{\sigma} + \nabla_{2D}^2 A_0, \tag{12}$$

where ∇_{2D}^2 is the 2-D in-plane Laplacian. This implies that equation (10) becomes

$$2\nabla A_0 \cdot \nabla\tau + A_0\nabla^2\tau + \frac{A_0}{\sigma} = 0 \tag{13}$$

for 2.5-D. Because the out-of-plane component of the gradient of τ is zero, i.e. $\partial\tau/\partial x_2 = 0$, when (13) is evaluated in the $x_2 = 0$ plane, ∇ and ∇^2 are the 2-D gradient and Laplacian operators, respectively. For constant wavespeed media, $\sigma = c^2\tau$ and $\tau = r/c$, meaning that this equation reduces to (8) for the case of constant wavespeed.

This shows that the high-frequency behavior of the r-equation, as expressed by leading order WKBJ (ray theoretic) analysis, agrees with Bleistein's 2.5-D ray theory both in traveltime and amplitude.

Progressing wave analysis of the t-equation

The WKBJ analysis of the r-equation in the previous section yields eikonal and transport equations that reduce to forms consistent with the expectations of a 2.5-D theory assuming constant wavespeed. However, the t-equation is of greater interest,

because it is intended for use in variable wavespeed problems. This equation is not as easy to analyze with the WKBJ method as the r-equation because the time variability of the coefficients makes forming the temporal Fourier transform more difficult. (This is not impossible, if divisions by it are interpreted as integrations in ω, see Liner and Stockwell, 1993).

There is an alternate asymptotic method called the progressing wave formalism, Lewis (1964), (compare with Červený, Molotkov, and Pšenčík, 1977) that can be used to conduct a WKBJ -like analysis in the time domain. This method uses the trial solution

$$U(\boldsymbol{x},t) \sim \sum_{n=0}^{\infty} A_n(\boldsymbol{x}) S_n\Big(t-\tau(\boldsymbol{x})\Big),$$

where each S_{n-1} is the derivative of each S_n. Substituting the series into equation (3) to yield

$$\begin{aligned} 0 \;=\; \sum_{n=0}^{\infty}\Big[& W_{n-2}A_n(\boldsymbol{x})\left((\nabla\tau)^2-\frac{1}{c^2}\right) \\ & +W_{n-1}\left(2\nabla\tau\cdot\nabla A_n + A_n\nabla^2\tau+\frac{A_n}{c^2 t}\right) \\ & +W_n\left(\nabla^2 A_n-\frac{A_n}{c^2t^2}\right)\Big]. \end{aligned}$$

(Here the substitution $W_n \equiv (-1)^n S_n$ has been made to emphasize the similarity of this result with equation (6).) The coefficients of each term of a given order in n are set to zero individually because W_k of different order in k cannot be assumed to cancel each other.

As with the WKBJ analysis, the coefficients of the $n=0$ and $n=1$ terms of the series are of immediate interest. The coefficient of the $n=0$ term yields the same eikonal equation as seen in the WKBJ analysis (see equation (7)).

The coefficient of the WKBJ or the progressing waveform analysis of the t-equation yields a first transport equation of the form

$$2\nabla A_0\cdot\nabla\tau + A_0\nabla^2\tau + \frac{A_0}{c^2 t} = 0. \tag{14}$$

Under the assumption that the propagating waveforms have short time histories, τ may be substituted for t in equation (14).

Amplitude comparisons

The eikonal equation associated with the t-equation is the same 2-D eikonal equation that is implied by Bleistein's 2.5-D ray theory, meaning that the t-equation predicts the same traveltimes as Bleistein's 2.5-D ray theory, for high-frequency data. Comparing the amplitudes predicted by the t-equation with Bleistein's 2.5-D theory requires that the transport equation (14) be solved.

Equation (14) may be rewritten as a differential equation in σ

$$\frac{dA_0^2}{d\sigma} = -\frac{A_0^2}{c^2\tau} - A_0^2 \frac{d}{d\sigma}\{\log[J_{2D}]\},$$

as was equation (12). Here $c^2\tau$ replaces the σ in equation (12). Dividing by A_0^2 and integrating with respect to σ gives

$$\int_{\sigma_0}^{\sigma} \frac{1}{A_0^2}\frac{dA_0^2}{d\sigma'}d\sigma' = -\int_{\sigma_0}^{\sigma} \frac{d\sigma'}{c^2(\boldsymbol{x}(\tau'))\tau'} - \int_{\sigma_0}^{\sigma} \frac{d}{d\sigma'}\{\log[J_{2D}]\}\, d\sigma'.$$

Simplifying, yields

$$\log A_0^2(\sigma) - \log A_0^2(\sigma_0) = -\int_{\sigma_0}^{\sigma} \frac{d\sigma'}{c^2(\boldsymbol{x}(\tau'))\tau'} - \log[J_{2D}(\sigma)] + \log[J_{2D}(\sigma_0)]. \qquad (15)$$

To solve equation (15) for A_0 it is necessary to integrate

$$Q = \int_{\sigma_0}^{\sigma} \frac{d\sigma'}{c^2(\boldsymbol{x}(\tau'))\tau'},$$

where σ' and τ' are dummy integration variables. Recall from equation (9) that

$$d\sigma' = c^2(\boldsymbol{x}(\tau'))d\tau'.$$

Using this in equation (15) gives

$$Q = \int_{\tau(\sigma_0)}^{\tau(\sigma)} \frac{c^2(\boldsymbol{x}(\tau'))d\tau'}{c^2(\boldsymbol{x}(\tau'))\tau'} = \int_{\tau(\sigma_0)}^{\tau(\sigma)} \frac{d\tau'}{\tau'} = \log[\tau(\sigma)] - \log[\tau(\sigma_0)]. \qquad (16)$$

Substituting equation (16) into equation (15) yields

$$\begin{aligned}\log A_0^2(\sigma) - \log A_0^2(\sigma_0) \;=\; & -\log[\tau(\sigma)] + \log[\tau(\sigma_0)] \\ & -\log[J_{2D}(\sigma)] + \log[J_{2D}(\sigma_0)]. \qquad (17)\end{aligned}$$

Absorbing all of the parts in equation (17) that depend on σ_0 into a constant and solving for $A_0(\sigma)$, yields the result

$$A_0^{\text{Liner}}(\sigma) = \text{const}\, \frac{1}{\sqrt{\tau J_{2D}}}.$$

The corresponding result from Bleistein (1986) is

$$A_0^{\text{Bleistein}}(\sigma) = \frac{1}{4\pi\sqrt{\sigma J_{2D}}}.$$

For a medium with constant wavespeed c_0, the transport equation associated with the t-equation is the same as that for the standard scalar wave equation, because

$\sigma = c_0^2\tau$ in that case. If, however, the wavespeed profile is smoothly varying, beginning as a constant value c_0, then the t-equation result must be the same as Bleistein's result for the constant wavespeed part, meaning that a factor of $1/c_0$ must be present in the constant multiplier.

Therefore, the high-frequency amplitude function for Liner's equation is

$$A_0^{\text{Liner}}(\sigma) = \frac{1}{4\pi\sqrt{c_0^2\,\tau J_{2D}(\sigma)}},$$

where c_0 is the wavespeed at the beginning of the ray path in a smoothly varying medium.

Because the leading order terms of the WKBJ series are the same for the Liner equation as for the standard wave equation, the same 2.5-D form of the WKBJ Green's function is implied in both cases. This means that, to leading order, the transmission and reflection effects across boundaries will be described by the same asymptotic representation. Thus, as long as the high-frequency condition is honored, the Liner equation can be expected to describe wave propagation in piecewise constant wavespeed media with the same degree of accuracy as the standard wave equation, provided that $t \approx \tau$.

However, the t-equation will not describe the amplitudes exactly in smoothly varying media, even if $t \approx \tau$ because the out-of-plane spreading factor $1/c_0\sqrt{\tau}$ is not the same as $1/\sqrt{\sigma}$,

AMPLITUDE ERROR ESTIMATES

The maximum and minimum error estimates for a medium with the linear wavespeed profile of the form $c(z) = c_0(1 \pm \eta z)$ are given by the ratio

$$\frac{A_0^{\text{Bleistein}}}{A_0^{\text{Liner}}} = \sqrt{\frac{c_0^2\tau}{\sigma}}$$

Bleistein (1986) gives analytic expressions for σ and τ in the special case of $c(z)$ media

$$\tau = \int_{\xi_3}^{z} \frac{dz'}{c^2(z')\sqrt{1/c^2(z') - \sin^2\beta/c^2(\xi_3)}}$$

and

$$\sigma = \int_{\xi_3}^{z} \frac{dz'}{\sqrt{1/c^2(z') - \sin^2\beta/c^2(\xi_3)}}. \tag{18}$$

Here, ξ_3 and z represent the initial and final x_3-positions on the ray, respectively, with z' being the dummy integration variable. The parameter β is explicitly defined to be the initial ray take-off angle, measured from the vertical. Therefore it is possible to

directly compare the Bleistein's 2.5-D amplitudes with the high frequency asymptotic amplitudes of the t-equation for the simple linear profile $c(z) \equiv c_0(1 + \eta z)$.

The ratio of the 2.5-D amplitudes to the t-equation amplitudes is given by

$$\frac{A^{\text{Bleistein}}}{A^{\text{Liner}}} = \sqrt{\frac{c^2\tau}{|\sigma|}}.$$

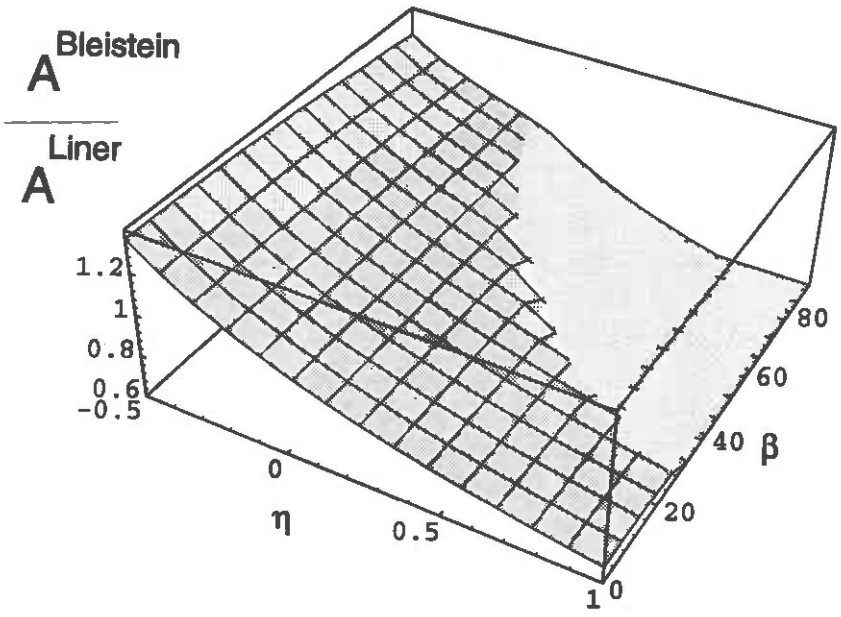

FIG. 1. Ratio of Bleistein's 2.5-D amplitudes vs. WKBJ amplitudes for the t-equation.

For the model being considered, this ratio is independent of the reference wavespeed c_0, meaning that we may arbitrarily fix the depth to $z = 1$. Then η will represent the fractional change in wavespeed with depth from its initial value of c_0 at $z = 0$, to its final value at $z = 1$. For example, $\eta = -0.5$ and $\eta = 1.0$ imply wavespeeds of $c_0/2$ and $2c_0$ at $z = 1$, respectively.

Figure 1 shows a estimate of this amplitude ratio for $-0.5 \leq \eta \leq 1.0$ and $0 \leq \beta \leq 90$ degrees, computed using *Mathematica*™. (The zone that is blank represents, η, β combinations for which no rays exist.) The amplitude ratio shows that the t-equation overestimates the amplitude when the wavespeed decreases with depth (i.e. when $\eta < 0$) and underestimates the amplitude when the wavespeed increases (i.e. when $\eta > 0$). The maximum size of the error in amplitude is about $\mp 35\%$ in each respective case of halving or doubling the wavespeed from the reference value. From Figure 1 it is apparent that the Liner equation is most acceptable in models where the amplitude change is described by $|\eta| \leq 0.2$, implying amplitude errors $\leq 10\%$.

PROPOSED MODIFICATIONS OF THE T-EQUATION

The t-equation is useful for modeling constant density media with a range of constant, piecewise constant, and weakly-varying wavespeed profiles. However, insight gained from considering the WKBJ analysis can be used to propose extensions of this equation to more general problems.

The following symbolic form

$$\left[\nabla^2 - \frac{1}{\sigma}\frac{\partial}{\partial t} - \frac{1}{c^2}\frac{\partial^2}{\partial t^2}\right] U(\boldsymbol{x},t) = 0 \tag{19}$$

would have equation (13) as its transport equation. (Remarkably, this choice of wave equation yields a WKBJ series that agrees to *all orders* with the WKBJ series implied by Bleistein's 2.5-D theory.) Note that there is no term corresponding to the last term in the t-equation in (19).

The practicality of implementing (19) may be questionable, because an estimate of σ is needed. Recall that $\sigma = \int^{\tau} c^2(\tau')d\tau'$, meaning that σ is a quantity that can be derived in the most general application only by tracing rays to all points in the medium—not practical for this application. Clearly, an approximation is needed. One approximation is to take $\sigma_n \approx c^2(x,z)n\Delta t$, which is just the $c^2\tau$ approximation (with $t \approx \tau$) that is built into the Liner equation. More sophisticated approximations could be made by assuming a general form of a $c(z)$ profile as an "average medium" and using equation (18) to estimate σ.

Extension to variable density

Bleistein (1986), section 5, develops 2.5-D ray theory for the variable density (acoustic) wave equation

$$\rho(\boldsymbol{x})\nabla\cdot\left(\frac{\nabla U(\boldsymbol{x},t)}{\rho(\boldsymbol{x})}\right) - \frac{1}{c^2(\boldsymbol{x})}\frac{\partial^2 U(\boldsymbol{x},t)}{\partial t^2} = 0. \tag{20}$$

Here, $\boldsymbol{x} \equiv (x_1, x_2, x_3)$ and $\rho(\boldsymbol{x})$ is the density function for the medium. Equation (20) is Fourier transformed with respect to time and the WKBJ series

$$u(\boldsymbol{x},\omega) \sim \sum_{n=0}^{\infty} \frac{B_n(\boldsymbol{x})}{(i\omega)^n}\exp[i\omega\tau(\boldsymbol{x})],$$

is substituted to yield the series

$$\begin{aligned} 0 \;=\; e^{i\omega\tau(\boldsymbol{x})}\sum_{n=0}^{\infty}\Bigg[& \frac{B_n}{(i\omega)^{n-2}}\left((\nabla\tau)^2 - \frac{1}{c^2}\right) \\ & + \frac{1}{(i\omega)^{n-1}}\left(2\nabla\tau\cdot\nabla B_n + B_n\rho\nabla\left(\frac{1}{\rho}\right) + B_n\nabla^2\tau\right) \\ & + \frac{1}{(i\omega)^n}\left(\nabla^2 B_n\right)\Bigg]. \end{aligned}$$

As before the coefficients of the $n = 0$ and $n = 1$ terms are of greatest interest.

The $n = 0$ term yields the same 2-D eikonal equation as seen in other parts of this paper, while the $n = 1$ term yields the first transport equation

$$2\nabla\tau \cdot \nabla B_0 + B_0\rho\nabla\left(\frac{1}{\rho}\right) + B_0\nabla^2\tau = 0. \tag{21}$$

Dividing equation (21) by $\rho^{1/2}$ it is possible to obtain the simplified form

$$2\nabla\left(\frac{B_0}{\rho^{1/2}}\right) \cdot \nabla\tau + \frac{B_0}{\rho^{1/2}}\nabla^2\tau = 0. \tag{22}$$

Comparing equation (22) with (10), it is apparent that the quantity $B_0\rho^{-1/2}$ satisfies the standard transport equation, meaning that

$$B_0(\boldsymbol{x}) = \text{const } A(\boldsymbol{x})\sqrt{\rho(\boldsymbol{x})}.$$

If the same initial datum for A is given at a point $\boldsymbol{x}_0$ for B, then the initial values of B and A would have to agree, meaning that

$$B(\boldsymbol{x}_0)\sqrt{\rho(\boldsymbol{x}_0)} = A(\boldsymbol{x}_0)\sqrt{\rho(\boldsymbol{x}_0)}$$

at $\boldsymbol{x}_0$, implying that

$$B(\boldsymbol{x}) = A(\boldsymbol{x})\sqrt{\frac{\rho(\boldsymbol{x})}{\rho(\boldsymbol{x}_0)}},$$

for the general position $\boldsymbol{x}$. The only difference between constant density amplitudes and variable density amplitudes is the additional factor of $\sqrt{\rho(\boldsymbol{x})/\rho(\boldsymbol{x}_0)}$.

The amplitude function for 2.5-D models variable density acoustic problem is given by Bleistein as

$$B = \frac{1}{4\pi}\sqrt{\frac{\rho(\boldsymbol{x}(\sigma,\beta))}{\rho(\boldsymbol{\xi})\,\sigma J_{2D}}}.$$

Here, $\rho(\boldsymbol{\xi})$ is the density at some initial position $\boldsymbol{\xi}$ and σ is the running parameter along the ray.

It is apparent that variable density does not affect the value of the out-of-plane spreading coefficient. It is possible to write the transport equation implied by the variable-density 2.5-D theory as

$$2\nabla\left(\frac{B_0}{\rho^{1/2}}\right) \cdot \nabla\tau + \frac{B_0}{\rho^{1/2}}\nabla^2\tau + \frac{B_0}{\rho^{1/2}\sigma} = 0,$$

or multiplying through by $\rho^{1/2}$,

$$2\nabla(B_0) \cdot \nabla\tau + B_0\rho\nabla\left(\frac{1}{\rho}\right) + B_0\nabla^2\tau + \frac{B_0}{\sigma} = 0.$$

Damped wave operators of the form

$$\rho(\boldsymbol{x})\nabla\cdot\left(\frac{\nabla U(\boldsymbol{x},t)}{\rho(\boldsymbol{x})}\right)-\gamma(\boldsymbol{x},t)\frac{dU(\boldsymbol{x},t)}{dt}-\frac{1}{c^2(\boldsymbol{x})}\frac{d^2U(\boldsymbol{x},t)}{dt^2}=0$$

will yield eikonal and transport equations compatible with the 2.5-D theory for the acoustic wave equation. It follows that the 2.5-D variable-density wave equation corresponding to Liner's t-equation is

$$\rho(\boldsymbol{x})\nabla\cdot\left(\frac{\nabla U(\boldsymbol{x},t)}{\rho(\boldsymbol{x})}\right)-\frac{1}{c^2}\left\{\frac{d^2}{dt^2}+\frac{1}{t}\frac{d}{dt}+\frac{1}{t^2}\right\}U(\boldsymbol{x},t)=0.$$

Similarly,

$$\rho(\boldsymbol{x})\nabla\cdot\left(\frac{\nabla U(\boldsymbol{x},t)}{\rho(\boldsymbol{x})}\right)-\frac{1}{\sigma}\frac{dU(\boldsymbol{x},t)}{dt}-\frac{1}{c^2}\frac{d^2U(\boldsymbol{x},t)}{dt^2}=0.$$

is the symbolic form that corresponds to equation (19).

CONCLUSIONS

Analysis of the 2.5-D wave equation of Liner (1991) using a WKBJ series method shows that the traveltimes and amplitudes predicted by Liner's equation match those of predicted by Bleistein's 2.5-D ray theory for constant and piecewise-constant wavespeed media.

However, for media with smoothly varying wavespeed profiles the WKBJ analysis reveals that the transport equation associated with the Liner wave equation is not the same as that implied by Bleistein's 2.5-D theory. For a linear $c(z)$ wavespeed profile whose wavespeed halves or doubles from the beginning to the end of a ray path, the amplitude error resulting from this mismatch will be $\mp 35\%$. For models with turning rays, the total amplitude error will tend to be less, because the overestimation of amplitude in one direction will be offset by an underestimation of amplitude as the ray travels in the opposite direction. In either case, the Liner 2.5-D equation will still yield amplitudes that are far more realistic than the 2-D wave equation. For the linear $c(z)$ model discussed above, the corresponding amplitudes for the 2-D wave equation will be 250% too large.

The WKBJ analysis provides a method for creating an alternate asymptotic wave operator that resembles the Liner equation, but that is matched more closely to Bleistein's 2.5-D ray theory in predicted amplitude behavior. However, there may be little advantage in implementing this alternate scheme because of the difficulty of estimating the parameter σ.

The WKBJ method also may be applied to create 2.5-D wave operators for variable-density (acoustic) problems. As of this date, these new operators have yet to be tested numerically.

ACKNOWLEDGMENTS

Many thanks to Jack Cohen, Tong Chen, and Norman Bleistein for reviewing this manuscript.

REFERENCES

Bleistein, N., 1984, Mathematical Methods for Wave Phenomena: Academic Press.

Bleistein, N, 1986, Two-And-One-Half Dimensional In-Plane Wave Propagation: Geoph. Prosp., **34** , 686-703.

Bleistein, N., Cohen J. K., and Hagin, F. G. 1987, Two and one half dimensional Born inversion with an arbitrary reference Geophysics, **52** , 26-36.

Bording, R. P. and Liner, C. L., 1992, Acoustic Wave Equation Modeling: The two and one half dimension stability condition, SIAM Texas-Oklahoma Section Meeting.

Bording, R. P. and Liner, C. L., 1993, Some numerical aspects of the 2.5-dimensional wave equation, SEG international meeting abstracts.

Červený, V., Molotkov, I. A., and Pšenčík, I. 1977, Ray Methods in Seismology, Univerzita Karlova, Prague.

Deregowski, S. M. and Brown, S. M. 1983, A theory of acoustic diffractors applied to 2-D models, Geophysical Prospecting, **31**, 293-333.

Hill, R. J. 1986, Wider-angle parabolic wave equation, Journal of the Acoustical Society of America, **79** (5), 1406-1409.

Hubral, P. 1978, Discussion on: "Wavefront curvature in a layered medium" (Bjørn Ursin), Geophysics, **48**, 1551-1552.

Liner, C. L. 1991, Short Note: Theory of a 2.5-D acoustic wave equation for constant density media: Geophysics, **56**, 2114-2117

Liner, C. L. and Stockwell, Jr. J. W., 1993, Some analytical aspects of the 2.5-dimensional wave equation, SEG international meeting abstracts.

Lewis, R. M. 1964, The Progressing Wave Formalism *in* Proceedings of the Symposium on Quasi-Optics, Polytechnic Institute of Brooklyn, June 8,9,10 1964, 74-103.

Newman, P. 1973, Divergence effects in a layered earth, Geophysics **38**, 481-488.

Tappert, F. D. 1977, The parabolic approximation method *in* Wave Propagation and Underwater Acoustics, edited by, Keller, J. B. and Papadakis, J. S., Springer-Verlag, Berlin, 224-287.

Ursin, B. 1983, Wavefront curvature in a layered medium, Geophysics **43**, 1011-1013.

Analytic description of dip moveout in anisotropic media

Ilya Tsvankin

Analytic description of dip moveout in anisotropic media

I. Tsvankin

ABSTRACT

Dip-moveout (DMO) processing is usually based on the cosine-of-dip correction for moveout velocity valid for homogeneous, isotropic media. Some recently developed DMO algorithms allow for a velocity gradient above the reflector, but still ignore anisotropy.

While there is little doubt that anisotropy may seriously distort most processing and interpretation steps (e.g., migration), the character of the influence of anisotropy on DMO is not clear. Numerical studies of moveout velocities of reflections from dipping boundaries beneath transversely isotropic media (Levin, 1990; Larner, 1993) have shown no apparent correlation between the conventional measures of anisotropy and errors in DMO correction. Here, I present an analytic treatment of normal moveout velocities valid for a wide range of homogeneous anisotropic models including transverse isotropy with a tilted symmetry axis and symmetry planes in orthorhombic media. NMO velocity for a dipping reflector is shown to be a relatively simple function of phase velocity and its first two derivatives taken at the dip angle.

In the case of weak transverse isotropy, the exact expression for NMO velocity is transformed into a concise DMO formula, which gives an adequate explanation for the existing numerical results. The errors in isotropic DMO correction turn out to be dependent primarily on the difference between Thomsen parameters ϵ and δ. For the most common case, $\epsilon - \delta > 0$, the cosine-of-dip corrected moveout velocity remains significantly larger than the moveout velocity for a horizontal reflector. DMO errors at a dip of 45° may exceed 25%, even for weak anisotropy. By comparing analytically-derived NMO velocities with moveout velocities calculated on finite spreads, I analyze the magnitude of nonhyperbolic moveout as a function of reflector dip.

For transversely isotropic media with a constant vertical velocity gradient and typical (positive) values of the difference $\epsilon - \delta$, inhomogeneity tends to reduce (sometimes significantly) the dip-moveout error that anisotropy induces in conventional constant-velocity DMO.

The formula for NMO velocity derived in the paper provides a basis for building dip-moveout algorithms in anisotropic media. It can also be used to overcome the ambiguity in the inversion of reflection moveouts for anisotropic parameters by including dip-dependence of moveout velocities in the inversion procedure.

INTRODUCTION

Conventional methods of seismic processing and interpretation are designed for isotropic velocity fields and, therefore, are subject to error when velocity is angle-dependent. It has been shown that elastic anisotropy may seriously distort the results of velocity analysis, normal moveout (NMO) correction, migration, amplitude-versus-offset (AVO) analysis etc. (Banik, 1984; Thomsen, 1986; Winterstein and Paulsson, 1990; Tsvankin and Thomsen, 1992, Larner and Cohen, 1993, among others). Apparently, dip moveout processing cannot be an exception because existing algorithms rely on the behavior of moveout velocity with reflector dip established for isotropic models (Levin, 1971):

$$V_{nmo}(\phi) = V_{nmo}(0)/\cos\phi, \tag{1}$$

where ϕ is the dip angle. For homogeneous isotropic media reflection moveout is purely hyperbolic, and equation (1) is exact for any spread length.

It is well known that anisotropy may distort the normal (short-spread) moveout velocity for horizontal reflectors as well as enhance deviations from hyperbolic moveout (Banik, 1984; Thomsen, 1986; Tsvankin and Thomsen, 1992, 1993a). Therefore, it is natural to expect formula (1) to become inaccurate in the presence of anisotropy.

Levin (1990) modeled reflection moveout for dipping reflectors beneath homogeneous transversely isotropic media with two different orientations of the axis of symmetry. He showed that if the axis is perpendicular to the reflector, isotropic DMO formula (1) holds with good accuracy. However, if the symmetry axis is kept vertical, the error of equation (1) for one of the models in Levin's study (the shale-limestone) reaches almost 40% at 60° dip. For the other three media used by Levin the errors were relatively small, although one of the models (Cotton Valley shale) may be considered even more "anisotropic" with respect to P-waves than the shale-limestone. Indeed, Thomsen anisotropic parameters ϵ and δ for the shale-limestone are $\epsilon = 0.134$, $\delta = 0$, while for Cotton Valley shale $\epsilon = 0.135$, $\delta = 0.205$. Small errors for the other two models (Pierre shale and Berea sandstone) are not surprising since both are characterized by very weak P-wave anisotropy. It is also important to mention that Levin has not found noticeable nonhyperbolic moveout on CMP gathers with spread length equal to the distance from the CMP to the reflector.

Recently, it has been recognized that depth-variable velocity may have a significant impact on dip-moveout processing. However, existing DMO algorithms built for depth-variable velocity fields still ignore anisotropy (e.g., Hale and Artley, 1993).

The combined influence of anisotropy and inhomogeneity on DMO has been studied by Larner (1993), who has performed calculations similar to those of Levin (1990) but for "factorized" transversely isotropic models with a vertical velocity gradient ("factorized" means that the ratios of the elastic constants are independent of spatial position). The main conclusion of that work is that the DMO errors remain very close to those found by Levin, provided isotropic DMO correction takes the velocity gradient into account.

Thus, the existing numerical results show no simple correlation between DMO errors and the "degree of anisotropy." Evidently, further insight into the problem requires analytic description of dip moveout in anisotropic media. Byun (1982) and Uren et al. (1990b) derived analytic expressions for normal moveout velocity from dipping reflectors in elliptically anisotropic models. Uren et al. (1990b) also showed that for elliptical anisotropy reflection moveout remains hyperbolic irrespective of the orientation of the elliptical axes. However, elliptical anisotropy is just a special case of transverse isotropy that is hardly typical for real rocks (Thomsen, 1986). Byun (1984) obtained an analytic expression for normal moveout velocity in general transversely isotropic media by applying a local elliptical fit to the wavefront. The results discussed below show that Byun's formula deviates from the exact NMO velocity for non-elliptical models.

Here, I derive a formula for normal moveout velocity valid for many anisotropic models of practical importance. This expression is convenient to use because it involves just phase velocity and its two first derivatives taken at the dip angle; calculation of group velocity and group angle is not necessary. For weak transverse isotropy with a vertical symmetry axis, this exact expression for NMO velocity is transformed into a simple function of Thomsen parameters ϵ and δ. The exact and weak-anisotropy expressions for NMO velocity are then compared with the moveout velocity calculated from $t^2 - x^2$ curves on conventional short spreads in order to verify analytic solutions and estimate the influence of nonhyperbolic moveout. For values of ϵ and δ believed to be typical for real rocks, the DMO-corrected moveout velocity remains significantly higher than the NMO velocity for a horizontal reflector. Finally, Larner's (1993) ray-tracing algorithm is used to analyze the combined influence of anisotropy and vertical velocity gradient on the isotropic constant-velocity DMO correction.

NORMAL MOVEOUT VELOCITY IN ANISOTROPIC MEDIA

Let us consider a common-midpoint (CMP) gather over a homogeneous anisotropic medium; the CMP line is perpendicular to the strike of the reflector (Figure 1). The only assumption made about anisotropy at this stage is that phase and group velocity vectors do not deviate from the sagittal (incidence) plane, i.e., the sagittal plane is a plane of symmetry. For instance, the present treatment is valid for any plane containing the symmetry axis in transversely isotropic media (plus the isotropy plane), as well as for symmetry planes in orthorhombic media.

Out-of-plane phenomena cannot be neglected if the sagittal plane lies outside symmetry planes in azimuthally anisotropic media; still, the formula derived below remains a good approximation if azimuthal anisotropy is weak. Azimuthally anisotropic models with orthorhombic symmetry caused by a combination of thin horizontal layering and vertical fracture systems with a low fracture density seem to be typical for sedimentary basins (Leary et al., 1990). Such media are characterized by relatively weak azimuthal anisotropy and more pronounced velocity variations in vertical planes. It is likely that for models of this type the normal-moveout equation discussed here would be acceptable even outside symmetry planes.

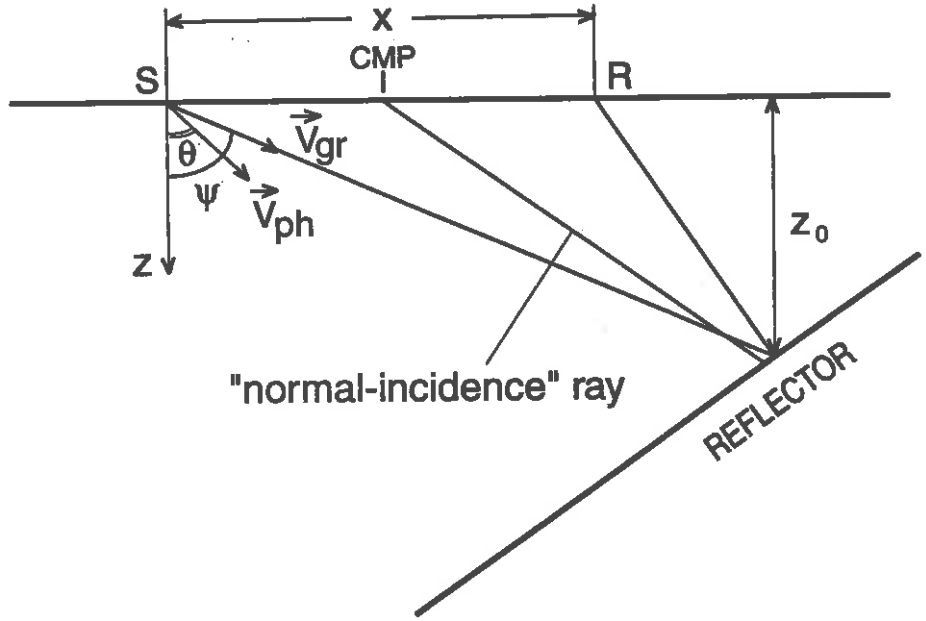

FIG. 1. Common-midpoint gather over a homogeneous anisotropic medium. $\vec{V}_{gr}$ and $\vec{V}_{ph}$ are the group and phase velocity vectors respectively. For brevity, henceforth in the text $\vec{V}_{ph}$ is referred to just as $\vec{V}$.

Our goal is to find an analytic expression for the normal moveout velocity in the CMP geometry (Figure 1):

$$V_{nmo}^2(\phi) = \lim_{x \to 0} \frac{dx^2}{dt^2}. \tag{2}$$

The NMO velocity for CMP gathers over horizontally homogeneous isotropic or anisotropic media may be written as (Larner, 1993)

$$V_{nmo}^2(\phi) = \frac{1}{t_0} \frac{dx}{dp}, \tag{3}$$

where x is the source-receiver offset, t_0 is the two-way traveltime along the "normal-incidence" ray (the normal-incidence ray corresponds to the zero-offset reflection [$x =$

0] but is not necessarily perpendicular to the reflector in the presence of anisotropy), and p is the ray parameter. The derivative should be taken at $x = 0$.

Ignoring the displacement of the reflection point at small offsets, we can use z_0 (Figure 1) as the depth of the normal-incidence reflection point. The offset x then becomes

$$x = 2z_0 \left(\tan\psi - \tan\psi_n\right),$$

where ψ is the group angle with the vertical (z) axis and ψ_n is the angle between vertical and the normal-incidence ray. Now equation (3) can be rewritten as

$$V^2_{nmo}(\phi) = \frac{2z_0}{t_0}\frac{d\tan\psi}{dp}. \tag{4}$$

In order to evaluate equation (4), we use the general relation between group and phase velocities in anisotropic media (Berryman, 1979)

$$\vec{V}_{gr} = \frac{\partial(kV)}{\partial k_x}\vec{x} + \frac{\partial(kV)}{\partial k_y}\vec{y} + \frac{\partial(kV)}{\partial k_z}\vec{z},$$

where $\vec{k}$ is the the wave vector, V_{gr} and V are the group and phase velocities respectively. If the incidence (vertical) plane $[x, z]$ is a plane of symmetry, group- and phase-velocity vectors for CMP reflections remain in the vertical plane and depend only on the in-plane phase angle θ (we measure θ from the z axis, see Figure 1). Therefore, group velocity may be represented as

$$\vec{V}_{gr} = (V\sin\theta + \frac{dV}{d\theta}\cos\theta)\vec{x} + (V\cos\theta - \frac{dV}{d\theta}\sin\theta)\vec{z}. \tag{5}$$

Note that the vertical axis is not necessarily an axis of symmetry. From equation (5), the group angle ψ is given by

$$\tan\psi = \frac{\tan\theta + \frac{1}{V}\frac{dV}{d\theta}}{1 - \frac{\tan\theta}{V}\frac{dV}{d\theta}}. \tag{6}$$

The derivative $\frac{d\tan\psi}{dp}$ in (4) may be written as

$$\frac{d\tan\psi}{dp} = \frac{d\tan\psi}{d\theta}\frac{d\theta}{dp}.$$

Using equation (6) we find

$$\frac{d\tan\psi}{d\theta} = \frac{1 + \frac{1}{V}\frac{d^2V}{d\theta^2}}{\cos^2\theta(1 - \frac{\tan\theta}{V}\frac{dV}{d\theta})^2}.$$

Since $p = \sin\theta/V$,

$$\frac{d\theta}{dp} = \frac{V}{\cos\theta(1 - \frac{\tan\theta}{V}\frac{dV}{d\theta})},$$

and

$$\frac{d\tan\psi}{dp} = \frac{V\left(1 + \frac{1}{V}\frac{d^2V}{d\theta^2}\right)}{[\cos\theta(1 - \frac{\tan\theta}{V}\frac{dV}{d\theta})]^3}. \tag{7}$$

The vertical distance from the normal-incidence reflection point to the surface is given by

$$z_0 = \frac{1}{2} V_{gr}(\psi)\, t_0 \cos\psi.$$

Using expression (5) for group velocity yields

$$z_0 = \frac{1}{2} V t_0 \cos\theta(1 - \frac{\tan\theta}{V}\frac{dV}{d\theta}). \tag{8}$$

Now (7,8) are substituted into equation (4) for NMO velocity:

$$V^2_{nmo}(\phi) = \frac{V^2(\theta)}{\cos^2\theta} \frac{1 + \frac{1}{V}\frac{d^2V}{d\theta^2}}{\left(1 - \frac{\tan\theta}{V}\frac{dV}{d\theta}\right)^2}.$$

Since the phase angle θ for the normal-incidence ray is equal to the dip angle ϕ, we finally obtain

$$V_{nmo}(\phi) = \frac{V(\phi)}{\cos\phi} \frac{\sqrt{1 + \frac{1}{V(\phi)}\frac{d^2V}{d\theta^2}}}{1 - \frac{\tan\phi}{V(\phi)}\frac{dV}{d\theta}}, \tag{9}$$

where the derivatives should be evaluated at the angle ϕ.

Equation (9) is valid for NMO velocity of P and S-waves in symmetry planes of arbitrary anisotropic media. Difficulties in application of formula (9) can be expected only in anomalous areas near shear-wave singularities and cusps, where the group-velocity function is multi-valued. This expression is relatively simple to use because it does not involve components of the group-velocity vector of the normal-incidence ray (note that the angle between the normal-incidence ray and vertical is generally different from ϕ). For example, it can be used in symmetry planes of orthorhombic media just by substituting the appropriate phase velocity function and its derivatives.

Apparently, the result of the conventional isotropic dip-moveout correction

$$V_{corr}(\phi) = V_{nmo}(\phi)\cos\phi \tag{10}$$

may be far different from the NMO velocity for a horizontal reflector $V_{nmo}(0)$, if anisotropy is present. Below, I examine the behavior of the normal moveout velocity and performance of the isotropic DMO correction for transversely isotropic media.

TRANSVERSE ISOTROPY WITH A TILTED AXIS OF SYMMETRY

Levin (1990) showed numerically that the isotropic P-wave DMO correction remains accurate in the case when the symmetry axis is perpendicular to the reflector. Equation (9) gives a clear analytic explanation for this result. If the reflector's normal coincides with the symmetry direction, then $\frac{dV}{d\theta}$ at the dip angle is zero, and formula (9) reduces to

$$V_{nmo}(\phi) = \frac{V(\phi)}{\cos\phi}\sqrt{1+\frac{1}{V(\phi)}\frac{d^2V}{d\theta^2}}\,. \tag{11}$$

The values of $V(\phi)$ and $\frac{d^2V}{d\theta^2}$ at any dip correspond to the symmetry direction and, therefore, are independent of ϕ. Hence, equation (11) coincides with the isotropic equation (1)

$$V_{nmo}(\phi) = V_{nmo}(0)/\cos\phi\,.$$

This means that the isotropic DMO correction holds if the symmetry axis is perpendicular to the reflector. However, this result is derived for normal (zero-spread) moveout velocities rather than for moveout velocities measured on finite spreads. If the medium above the reflector is homogeneous and isotropic, reflection moveout on CMP gathers is purely hyperbolic, and equation (1) is exact irrespective of the maximum offset. In the presence of anisotropy, moveout is generally nonhyperbolic (Tsvankin and Thomsen, 1992, 1993a), and (1) may become inaccurate with increasing spread length. Although the spreads used by Levin (1990) are rather short (equal to the normal distance to the relector), his results for the models with the symmetry axis perpendicular to the reflector show small errors in formula (1) indicative of the influence of nonhyperbolic moveout on the moveout velocity.

While dip-dependence of the NMO velocity is not distorted by the anisotropy when the symmetry axis is perpendicular to the reflector, the value of $V_{nmo}(0)$ is not the same as the NMO velocity for isotropic media. The P-wave V_{nmo} velocity depends on the anisotropic parameter δ, which is responsible for P-wave velocity near the symmetry axis (Thomsen, 1986); this will be discussed in more detail below.

Application of formula (9) remains straightforward in a more general case when the symmetry axis is tilted at an arbitrary angle. Phase velocity in transversely isotropic

media is usually expressed through the angle between the phase-velocity vector and the symmetry axis. The formula for the P-wave phase velocity in standard notation (using the elastic coefficients c_{ij} and density ρ) can be found, for instance, in White (1983):

$$\begin{aligned} 2\rho V^2(\theta) &= (c_{11}+c_{44})\sin^2\theta + (c_{33}+c_{44})\cos^2\theta \\ &+ \{[(c_{11}-c_{44})\sin^2\theta - (c_{33}-c_{44})\cos^2\theta]^2 \\ &+ 4(c_{13}+c_{44})^2\sin^2\theta\cos^2\theta\}^{1/2}. \end{aligned} \tag{12}$$

To get the SV-wave velocity, the plus sign in front of the radical should be replaced with a minus. Thomsen (1986) gives analogous formulas in his notation, and transforms them into much simpler expressions for weakly anisotropic media. In order to use any of these velocity equations in the calculation of the NMO velocity (9), they should be evaluated at the angle between the symmetry axis and the reflector's normal.

TRANSVERSE ISOTROPY WITH A VERTICAL AXIS OF SYMMETRY

Levin (1990) points out that the two orientations of the symmetry axis most likely to be encountered in practice include a vertical axis and an axis normal to reflectors. In the previous section it was proved that in the latter case dip-dependence of normal moveout velocity remains the same as in isotropic media. Therefore, although formula (9) allows for rather general anisotropy, in the following I concentrate on transversely isotropic media with a vertical symmetry axis, or vertical transverse isotropy (VTI).

VTI will be characterized by the vertical P- and S-waves velocities ($V_{P0}=\sqrt{c_{33}/\rho}$ and $V_{S0}=\sqrt{c_{44}/\rho}$), and anisotropic parameters ϵ, δ, and γ, as suggested by Thomsen (1986):

$$\epsilon = \frac{c_{11}-c_{33}}{2c_{33}}, \tag{13}$$

$$\delta = \frac{(c_{13}+c_{44})^2-(c_{33}-c_{44})^2}{2c_{33}(c_{33}-c_{44})}, \tag{14}$$

$$\gamma = \frac{c_{66}-c_{44}}{2c_{44}}. \tag{15}$$

P- and SV-waves propagation is fully described by four parameters: V_{P0}, V_{S0}, ϵ, and δ.

The SH-wave slowness surface and wavefront are elliptical with the phase velocity given (exactly) by

$$V_{SH}(\theta) = V_{S0}\sqrt{1 + 2\gamma \sin^2\theta}. \tag{16}$$

Special cases: comparison with previous results

In this section, formula (9) is compared with analytic expressions for the normal moveout velocity from a horizontal reflector beneath VTI media (Hake et al., 1984; Thomsen, 1986), and from dipping reflectors beneath elliptically anisotropic media (Byun, 1982; Uren et al., 1990b). Formula (9) and the P-wave moveout velocity computed from $t^2 - x^2$ curves are also compared with analytically-based calculations for general transverse isotropy presented by Byun (1984).

In the case of a horizontal reflector ($\phi = 0$), equation (9) reduces to

$$V_{nmo}(0) = V(0)\sqrt{1 + \frac{1}{V(0)}\frac{d^2V}{d\theta^2}}.$$

Using equation (12) to evaluate the second derivative of phase velocity and substituting expression (14) for δ, we find for the P-wave

$$V_{nmo}(0)\,(P) = V(0)\sqrt{1 + 2\delta}, \tag{17}$$

which coincides with Thomsen's (1986) result. When the symmetry axis is perpendicular to a dipping reflector, the P-wave NMO velocity is given just by (17) and the cosine-of-dip factor (equation (1)). Similarly, we get the known expression for the zero-dip NMO velocity of the SV-wave.

For elliptical anisotropy,

$$V(\theta) = \sqrt{V_1^2 \cos^2\theta + V_2^2 \sin^2\theta}.$$

The NMO velocity (9) then becomes

$$V_{nmo}(\phi) = \frac{V_2}{\cos\phi}\sqrt{\cos^2\phi + \frac{V_2^2}{V_1^2}\sin^2\phi}. \tag{18}$$

Equation (18) agrees with the normal-moveout formulas of Byun (1982) and Uren et al. (1990b). In elliptically anisotropic media, reflection moveout remains purely hyperbolic irrespective of reflector dip or the orientation of the elliptical axes (Uren et al., 1990).

In VTI media, equations for elliptical anisotropy are strictly valid only for the SH-wave. If the SH-wave phase velocity is parametrized by γ (16), formula (18) yields

$$V_{nmo}(\phi)\,(SH) = \frac{V_{S0}\sqrt{1+2\gamma}}{\cos\phi}\sqrt{1+2\gamma\sin^2\phi}\,. \tag{19}$$

Since for the SH-wave $V_{nmo}(0) = V_{S0}\sqrt{1+2\gamma}$, (19) may be represented as

$$V_{nmo}(\phi)\,(SH) = \frac{V_{nmo}(0)}{\cos\phi}\,\frac{V_{SH}(\phi)}{V_{S0}}\,, \tag{20}$$

$V_{SH}(\phi)$ is the SH-wave's phase velocity at the dip angle. Therefore, for elliptical anisotropy the error of the cosine-of-dip DMO correction is directly determined by phase velocity variations, i.e., the error is given just by the phase velocity at the dip angle divided by the vertical velocity.

Below I demonstrate that the formula for elliptical anisotropy may lead to significant errors in the P-wave NMO velocity even for "almost" elliptically anisotropic models.

Byun (1984) generalized his elliptical normal-moveout formula for arbitrary transverse isotropy by applying a local elliptical fit to the wavefront. The resulting expression for the normal moveout velocity involves the group velocity and group angle of the normal-incidence ray. The moveout velocity multiplied with the cosine of the angle ψ_n between the normal-incidence ray and vertical ("emergence angle" in Byun's paper) Byun calls the "diffractor velocity." Figure 2 shows the P-wave moveout velocity for the limestone-sandstone model used in Byun's study with his normalization. The dotted curve is the analytic NMO velocity computed from formula (9); the solid curve is the moveout velocity recovered directly from traveltimes ($t^2 - x^2$ curves) calculated by a ray-tracing code over a spread of 1500 m. The distance from the CMP to the reflector in the traveltime calculations on this and all subsequent plots (except for Figure 13) is 3000 m (for a description of the algorithm used to calculate traveltimes, see Larner, 1993).

Figure 2 was designed to reproduce the result in Figure 6a in Byun's (1984) paper. However, the moveout velocities in Figure 2 are substantially higher than those computed by Byun; a similar discrepancy was found for the second model used in Byun's work. Since the analytic and numerical results in Figure 2 are close to each other (a small difference between the two curves will be explained below), it seems that Byun's formula deviates (at least for these two models) from the exact V_{nmo} for non-elliptical media.

We can only speculate about the reason of this inaccuracy. One of the assumptions made by Byun in his derivation is that V_{nmo} for VTI media can be found by fitting an ellipse with vertical and horizontal axes to the wavefront. It is possible that the correct moveout velocity at non-zero dips is given by a tilted fitted ellipse, even though

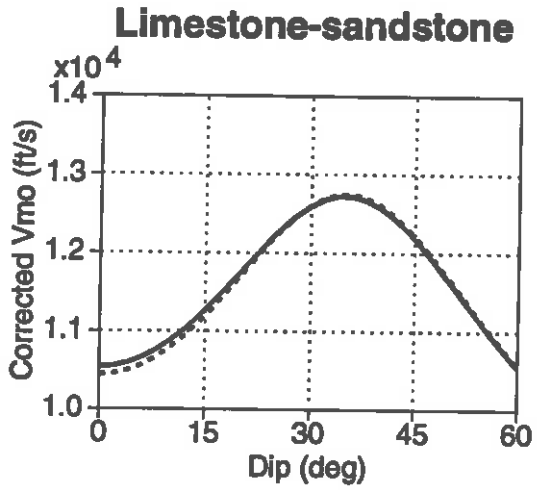

FIG. 2. P-wave moveout velocity calculated from formula (9) (dotted curve) and from traveltimes (solid curve) for the limestone-sandstone model from Byun (1984). Both curves are converted into the "diffractor velocities" as suggested by Byun. Model parameters are V_{P0}=10483 ft/s, V_{S0}=5753 ft/s, ϵ=0.183, $\delta = -0.004$.

the symmetry axis is vertical. However, this is no more than a tentative conclusion; the nature of the above discrepancy needs further investigation.

How many parameters determine the P-wave DMO signature?

This important question has to be answered before starting a systematic study of the behavior of NMO velocities in transversely isotropic media. In conventional notation, the P-wave phase velocity (12) is a function of four elastic coefficients: c_{11}, c_{33}, c_{13}, and c_{44}. This might lead one to believe that dip-dependence of the P-wave V_{nmo} is also determined by four variables.

However, it is possible to cut down on the number of parameters by switching to Thomsen (1986) notation. First, note that V_{P0} is just a scaling coefficient for the P-wave phase velocity, if $V_{P0}/V_{S0}, \epsilon$, and δ are kept constant. Therefore, V_{P0} does not change the dependence of the P-wave normal moveout velocity V_{nmo} on the dip angle ϕ. This conclusion is illustrated by Figure 3, which proves that the normalized P-wave NMO velocity $V_{nmo}(\phi)/V_{nmo}(0)$ is independent of the vertical velocity V_{P0}. The moveout velocity in Figure 3 is multiplied with $\cos\phi$, as it is conventionally done in the isotropic DMO correction.

Another parameter that can be eliminated from the P-wave dip-moveout problem is the shear-wave vertical velocity V_{S0} (or the ratio V_{P0}/V_{S0}). Although the P-wave phase velocity formally depends on four Thomsen parameters (V_{P0}, V_{S0}, ϵ, and δ), the contribution of V_{S0} is practically negligible.

Indeed, in the weak anisotropy approximation, the P-wave phase velocity is a

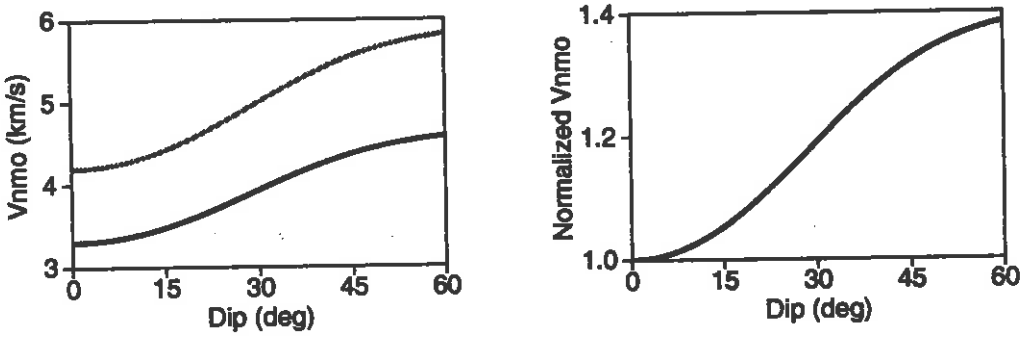

FIG. 3. Influence of V_{P0} on the cosine-of-dip corrected P-wave normal moveout velocity calculated from formula (9). The black curve corresponds to the shale-limestone model with V_{P0}=3.306 km/s, V_{S0}=1.819 km/s, ϵ=0.134, δ=0. The gray curve is for the model with V_{P0}=4.200 km/s, and the same V_{P0}/V_{S0}, ϵ, and δ.
The curves on the right plot are normalized by the NMO velocity for a horizontal reflector $V_{nmo}(0)$.

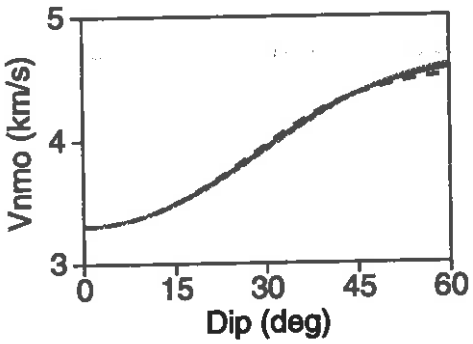

FIG. 4. Influence of V_{S0} on the cosine-of-dip corrected P-wave normal moveout velocity calculated from formula (9). The solid curve corresponds to the shale-limestone model with V_{P0}=3.306 km/s, V_{S0}=1.819 km/s, ϵ=0.134, δ=0. The other two curves are for the models with the same V_{P0}, ϵ, and δ, but with V_{S0}=1.300 km/s (gray) and V_{S0}=2.300 km/s (dashed).

function just of V_{P0} and the anisotropic coefficients ϵ and δ (Thomsen, 1986). If anisotropy is not weak, Thomsen's velocity equation becomes inaccurate, but the P-wave phase velocity remains practically independent of V_{S0} (Tsvankin and Thomsen, 1993b). Hence, even for a wide range of V_{S0}, the corresponding variations in the P-wave normal moveout velocity are extremely small, as is supported by the result in Figure 4.

Thus, in VTI media dip-dependence of the P-wave NMO velocity is a function of just two anisotropic coefficients ϵ and δ. More than that, in the next two sections I show that the angular behavior of the NMO velocity is primarily determined by a particular combination of these parameters, i.e., by the difference $\epsilon - \delta$. If the symmetry axis is inclined, the NMO velocity is also dependent on the tilt angle.

Weak-anisotropy approximation for normal moveout velocity

A convenient way to understand the influence of anisotropy on normal moveout velocity is to use the weak-anisotropy approximation (WAA). Although WAA is no substitute for exact equations (such as formula [9]) in DMO correction, it can provide us with simple analytic relations elucidating the dependence of the NMO velocity on the parameters ϵ and δ.

In the case of weak anisotropy ($\epsilon \ll 1$, $\delta \ll 1$), phase velocities of P- and SV-waves can be significantly simplified by retaining only the terms linear in δ and ϵ. The P-wave phase velocity linearized in ϵ and δ is given by (Thomsen, 1986)

$$V_P(\theta) = V_{P0}\,(1 + \delta \sin^2\theta \cos^2\theta + \epsilon \sin^4\theta)\,. \tag{21}$$

The derivatives of (21) needed in the expression for NMO velocity (9) are then

$$\frac{dV_P(\theta)}{d\theta} = V_{P0} \sin 2\theta\,(\delta \cos 2\theta + 2\epsilon \sin^2\theta)\,,$$

$$\frac{dV_P^2(\theta)}{d\theta^2} = 2V_{P0}\,[\delta \cos 4\theta + 2\epsilon \sin^2\theta(1 + 2\cos 2\theta)]\,.$$

After substitution of the above weak-anisotropy equations into (9) and further linearization in ϵ and δ, we get

$$V_{nmo}(\phi) = \frac{V_P(\phi)}{\cos\phi}\,[1 + \delta + 2(\epsilon - \delta)\sin^2\phi(1 + 2\cos^2\phi)]\,. \tag{22}$$

$V_P(\phi)$ is the phase velocity given by (21). In the isotropic DMO correction, multiplication of $V_{nmo}(\phi)$ with $\cos\phi$ is supposed to convert the moveout velocity at dip ϕ into the moveout velocity for a horizontal reflector. Hence, the anisotropy-induced DMO error is given by

$$\frac{V_{nmo}(\phi)\cos\phi}{V_{nmo}(0)} = \frac{V_P(\phi)}{V_{P0}}\left[1 + 2(\epsilon - \delta)\sin^2\phi(1 + 2\cos^2\phi)\right]. \qquad (23)$$

The structure of equation (23) suggests that the P-wave dip-moveout error in transversely isotropic media has two major components, which may be called the "elliptical error" and "non-elliptical error." Indeed, for elliptical anisotropy $\epsilon = \delta$, and the error is determined just by angular variations in the P-wave phase velocity. This result has already been discussed in the previous section (18,20). The second, "non-elliptical" component of the DMO error is the term containing the difference $\epsilon - \delta$. Comparison of the two terms shows that even for relatively small values of $\epsilon - \delta$, the second term usually makes a significant contribution to the total error, especially at mild dips (up to 45°). For typical values of the anisotropic coefficients, the difference $\epsilon - \delta$ determines, to a large degree, the angular behavior of the P-wave NMO velocity. This conclusion is supported by exact numerical calculations in the next section.

Now we can explain the puzzling difference between the DMO signatures for the models of Cotton Valley shale and the shale-limestone (Levin, 1990; Larner, 1993). For Cotton Valley shale ($\epsilon = 0.135$, δ=0.205), the P-wave phase velocity increases with angle, while $\epsilon - \delta$ is negative. As a result, the two components of the DMO error in (23) almost cancel each other, and the accuracy of the isotropic DMO correction is quite satifactory.

Figure 5 shows the comparison between the moveout velocity calculated directly from traveltimes ($t^2 - x^2$ curves) over a spread of 3000 m, the exact NMO velocity (9), and the weak-anisotropy normal-moveout approximation (22). All three curves for Cotton Valley shale display only small variations in the corrected moveout velocity with angle, confirming the conclusion about the validity of isotropic DMO for this particular model. Though Cotton Valley shale has a large value of δ, the weak-anisotropy result is close to the exact NMO velocity (the difference is less than 1.5%).

For the shale-limestone ($\epsilon = 0.134$, δ=0), the increase in the P-wave phase velocity is supplemented by a positive value of $\epsilon - \delta$. This combination leads to a pronounced increase in the cosine-of-dip corrected moveout velocity with dip angle. Note that the accuracy of the weak-anisotropy approximation for the shale-limestone is very high. A systematic comparison between the weak-anisotropy approximation and the exact NMO velocity is presented in the next section.

Formula (9) can also be transformed into the weak-anisotropy approximation for the SV-wave normal moveout velocity. Using the WAA expression for the SV-wave phase velocity (Thomsen, 1986), we obtain

$$V_{nmo}(\phi)\,(SV) = \frac{V_{SV}(\phi)}{\cos\phi}\left[1 + \sigma - 2\sigma\sin^2\phi(1 + 2\cos^2\phi)\right], \qquad (24)$$

where σ is the effective parameter introduced by Tsvankin and Thomsen (1992) to describe SV-wave propagation:

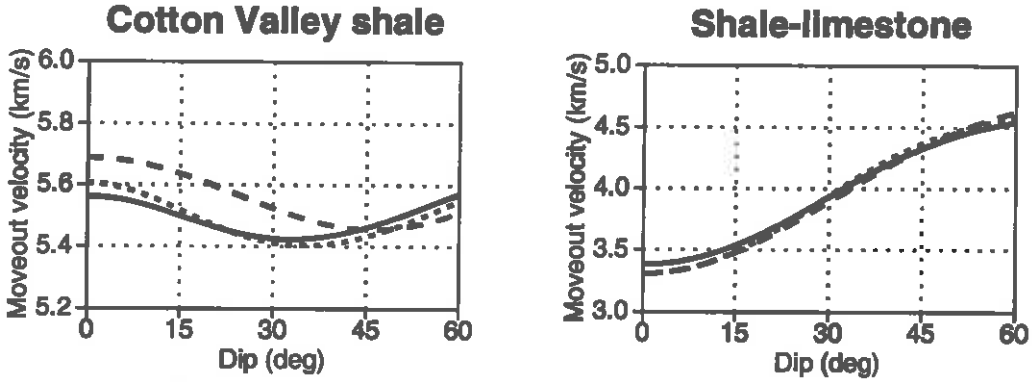

FIG. 5. Cosine-of-dip corrected P-wave moveout velocity for Cotton Valley shale and the shale-limestone. The solid curve is the moveout velocity calculated from the traveltimes on a spread of 3000 m; the dotted curve is the exact NMO velocity computed from formula (9); the dashed curve is the weak-anisotropy approximation (22).
Parameters of Cotton Valley shale are V_{P0}=4.721 km/s, V_{S0}=2.890 km/s, ϵ=0.135, δ=0.205.

$$\sigma = \left(\frac{V_{P0}}{V_{S0}}\right)^2 (\epsilon - \delta).$$

Hence, the DMO signature for the SV-wave is mostly determined by just one anisotropic parameter - σ.

Equations (22) and (24) can be easily rewritten for the more general case of transverse isotropy with a tilted axis of symmetry..

Dip-moveout signature for P-waves

Before doing a systematic analysis for vertical transverse isotropy, it is worthwhile to explain the difference between the moveout velocities calculated directly from traveltimes ($t^2 - x^2$ curves), and exact NMO velocities in Figures 2 and 5. The moveout velocities calculated from traveltimes coincide with those computed by Levin (1990) for the same parameters, thus proving the accuracy of the numerical algorithm. Since the moveout velocity was determined from a least-squares fit to $t^2 - x^2$ curves on a finite spread length, it could have been distorted by nonhyperbolic moveout, while the analytic NMO velocity describes purely hyperbolic moveout on very short spreads. To check out this possibility, Figure 5 is reproduced in Figure 6, but with the moveout velocity calculated on a much shorter spread (1000 m instead of 3000 m), reduced to just 1/3 of the distance from the CMP to the reflector. Now the moveout velocity recovered from the traveltimes (solid curve) practically coincides with the analytic

solution for the NMO velocity (dotted curve). Therefore, the analytic and numerical results are in agreement with each other.

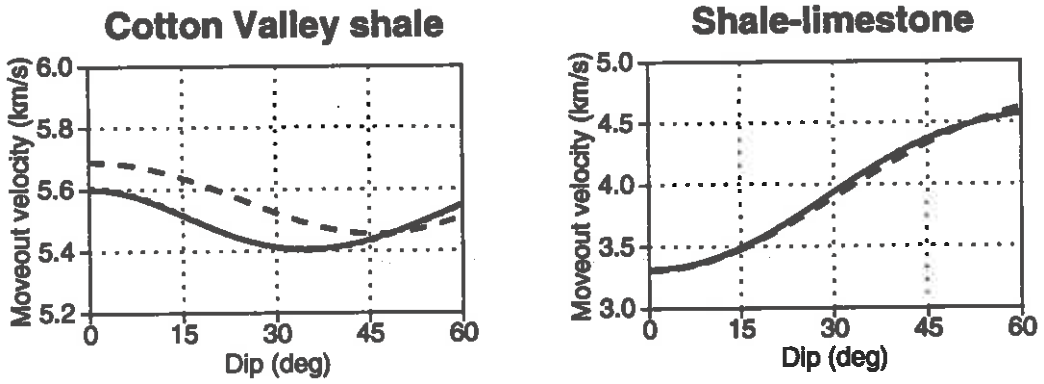

FIG. 6. Same as Figure 5, but the spread length used to calculate the moveout velocity from $t^2 - x^2$ curves (solid curve) is 1000 m instead of 3000 m.
The analytic curves of the exact NMO velocity (dotted) and the weak-anisotropy approximation (dashed) have not been changed.

Since the two models studied above exhibit such a different behavior of the P-wave NMO velocity, it is important to find out what can be expected for transversely isotropic media that are likely to be encountered in the subsurface. Existing laboratory and field data indicate that in most cases $\epsilon > \delta$ (Thomsen, 1986; Tsvankin and Thomsen, 1992). For instance, $\epsilon \geq \delta$ for transversely isotropic media due to thin bedding of isotropic layers (Berryman, 1979). Also, the value of ϵ is almost always positive (Thomsen, 1986). This means that the cosine-of-dip corrected moveout velocity in transversely isotropic media is usually higher than the moveout velocity for a horizontal reflector (see formula [23]). Hence, the behavior of the corrected moveout velocity for the shale-limestone model may be typical for subsurface formations.

Rather than examine specific transversely isotropic models published in the literature, I present a systematic analysis of the P-wave DMO signatures for transversely isotropic media parametrized by ϵ and δ. Since the weak-anisotropy approximation suggests the difference $\epsilon - \delta$ as the most influential parameter in the DMO correction, I generate four suites of plots for $\epsilon - \delta = -0.1$, 0, 0.1, and 0.2 (Figures 7–10). The choice of the values of $\epsilon - \delta$ is explained above; although $\epsilon - \delta$ is believed to be predominantly positive, the value of -0.1 is included for completeness. Each plot contains the same three curves as Figures 5 and 6: the moveout velocity calculated from $t^2 - x^2$ curves on the spread 3000 m long (solid), the exact analytic normal moveout velocity computed from equation (9) (dotted), and the weak-anisotropy approximation for V_{nmo} given by equation (22) (dashed). Comparison between the first two curves makes it possible to estimate the influence of nonhyperbolic moveout on the moveout velocity for the typical spread length equal to the distance from the CMP

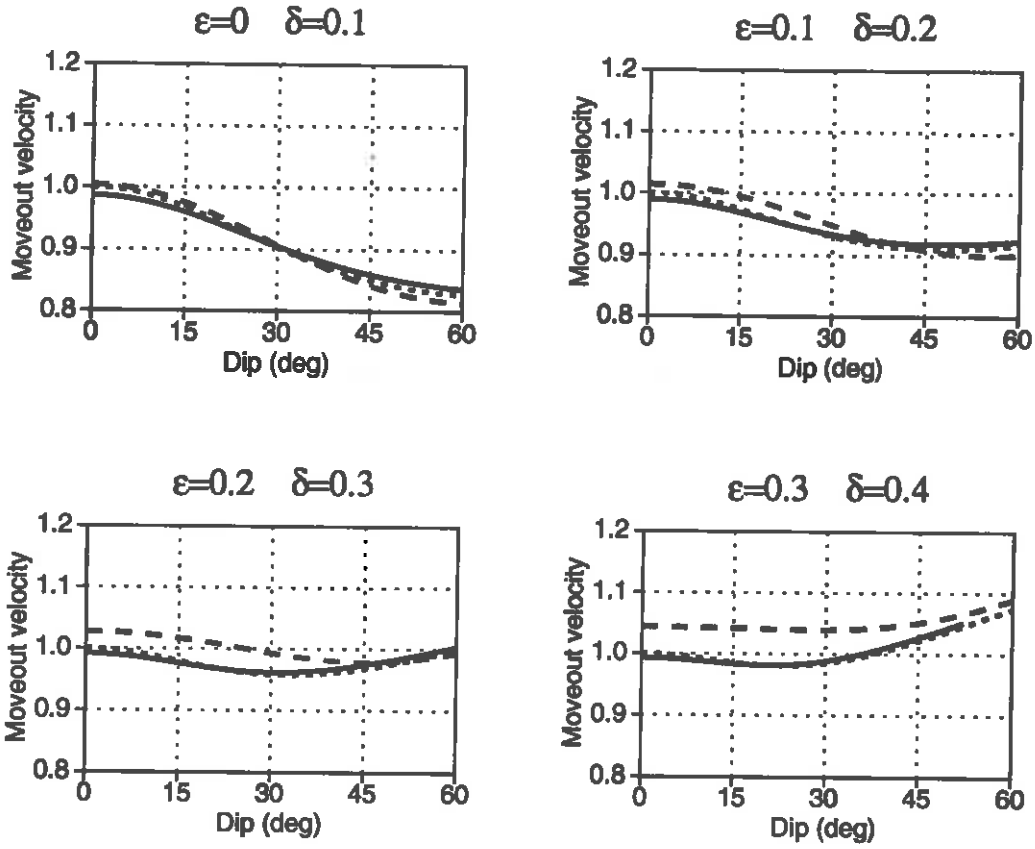

FIG. 7. Cosine-of-dip corrected P-wave moveout velocity for models with $\epsilon - \delta = -0.1$. The solid curve is the moveout velocity calculated from $t^2 - x^2$ curves on a spread length of 3000 m; the dotted curve is the exact NMO velocity from formula (9); and the dashed curve is the weak-anisotropy approximation from formula (22). The solid curve for $\epsilon = 0.3$, $\delta = 0.4$ stops around 52° because the algorithm used to calculate traveltimes broke down at steep dips.

to the reflector. The difference between the second and third curves shows the error of the weak-anisotropy approximation. The vertical P-wave velocity V_{P0} is adjusted so that on each plot the exact $V_{nmo}(0) = 1$.

First, I examine dip-dependence of the cosine-of-dip corrected moveout velocity using the exact analytic expression (9) (dotted curve). Later on, I discuss the accuracy of the weak-anisotropy approximation and the influence of nonhyperbolic moveout.

The whole suite of plots in Figures 7–10 proves that the P-wave DMO signature is controlled, to a significant degree (although not entirely), by the difference $\epsilon - \delta$. In spite of certain variations from one pair of ϵ, δ to another, the behavior of the moveout velocity is similar for all curves with fixed $\epsilon - \delta$, especially for moderate anisotropies $|\epsilon| < 0.2$, $|\delta| < 0.2$. The dominant role of $\epsilon - \delta$ is particularly pronounced for the most typical case $\epsilon - \delta > 0$ (Figures 9, 10). It is interesting that on most of the

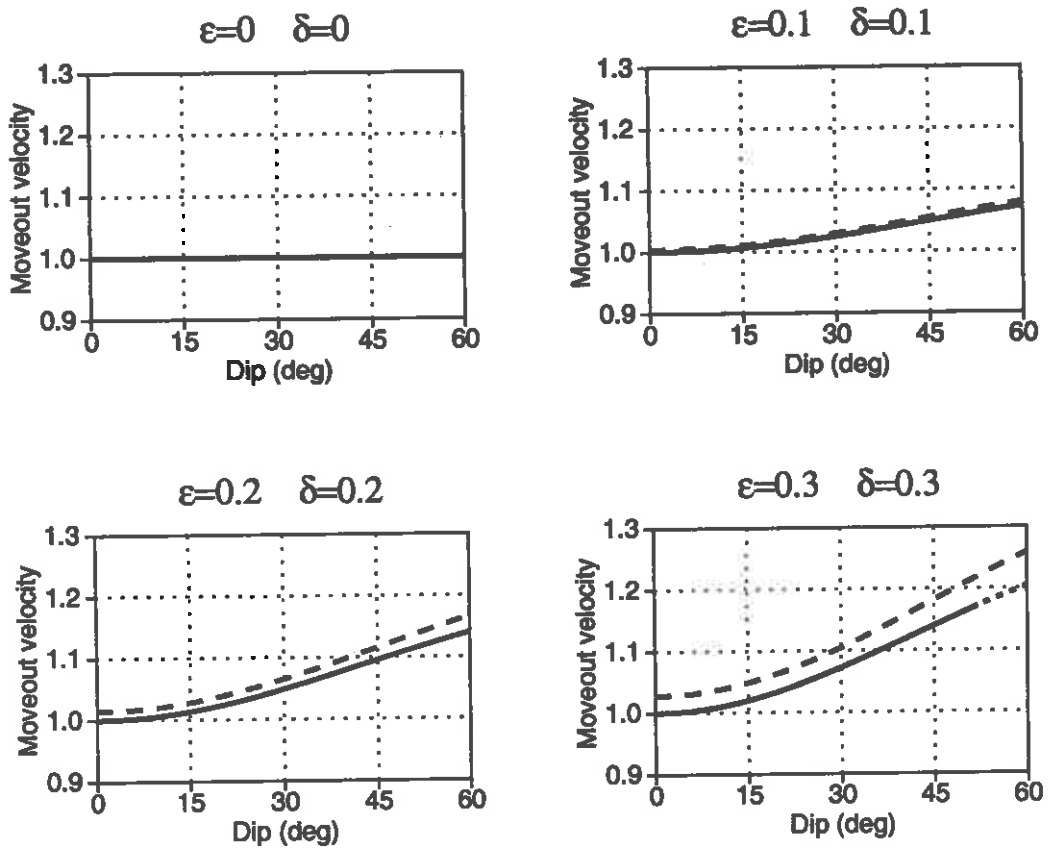

FIG. 8. Cosine-of-dip corrected P-wave moveout velocity for models with $\epsilon - \delta = 0$ (elliptical anisotropy).

plots the exact NMO velocity shows even less dependence on a specific combination of ϵ and δ for a fixed $\epsilon - \delta$, than does the weak-anisotropy result (for instance, see Figure 10).

When $\epsilon - \delta = -0.1$ (Figure 7), the cosine-of-dip corrected moveout velocity decreases with dip (for mild dips), as predicted by the weak-anisotropy approximation. This trend becomes less pronounced with increasing ϵ and δ due to a more significant increase in the phase velocity with angle (formula [23]). Note that for a fixed negative $\epsilon - \delta$, isotropic DMO becomes more accurate (i.e., the curves are closer to unity) with increasing anisotropies ϵ and δ. On the whole, the error in isotropic DMO, determined by the amplitude of the angular variations in the corrected moveout velocity, is relatively small (the "Cotton Valley shale" case).

For elliptically anisotropic models ($\epsilon - \delta = 0$, Figure 8), the anisotropy-induced distortions of DMO are entirely determined by the amplitude of the phase-velocity variations with angle. The DMO error for elliptical anisotropy is moderate: the difference between the corrected moveout velocity and the zero-dip V_{nmo} for $\phi < 60°$,

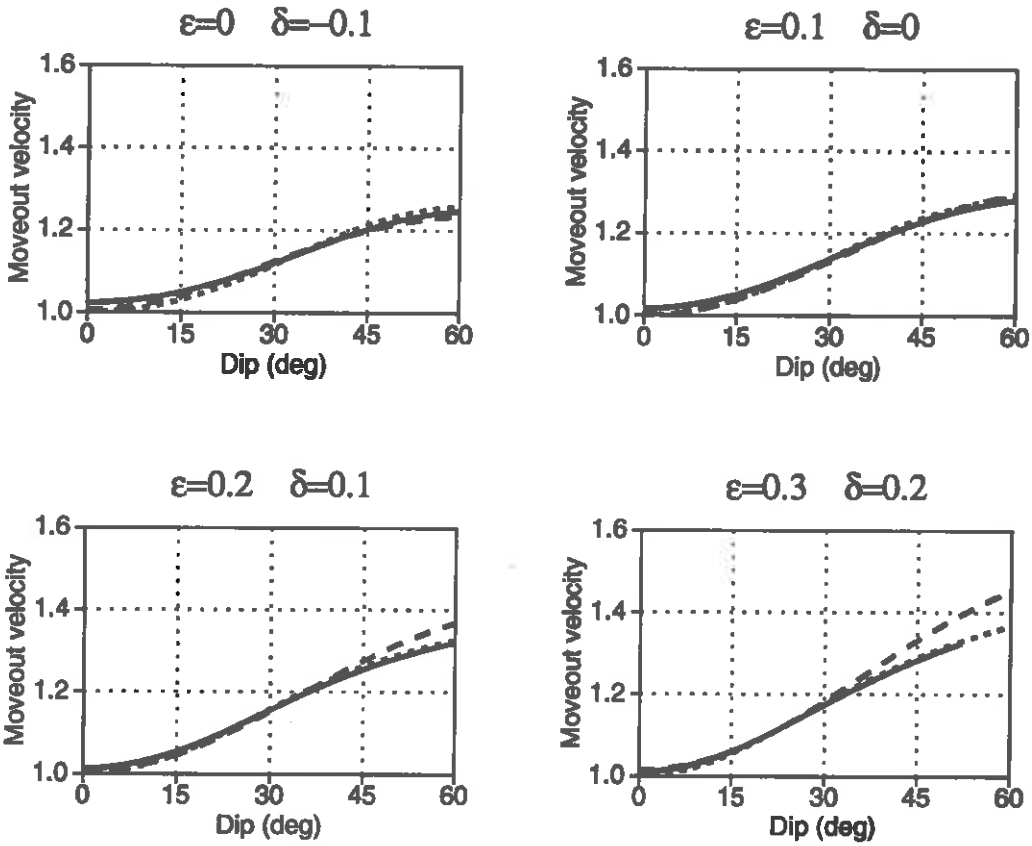

FIG. 9. Cosine-of-dip corrected P-wave moveout velocity for models with $\epsilon - \delta$ =0.1.

$|\epsilon| < 0.2$, $|\delta| < 0.2$ is less than 15%. The DMO correction is, of course, perfect for the isotropic case, $\epsilon = \delta = 0$.

If $\epsilon - \delta$ is positive (the most common case, Figures 9 and 10), the anisotropy causes a pronounced increase in the cosine-of-dip corrected moveout velocity with dip angle. Even for relatively small $\epsilon - \delta = 0.1$, the dip-moveout error reaches 25% at 45° dip and 30-35% at a dip of 60° ("the shale-limestone" case). For $\epsilon - \delta = 0.2$ (Figure 10), the corrected moveout velocity at 60° dip is consistently about 60% higher than the zero-dip moveout velocity! A remarkable feature of models with positive $\epsilon - \delta$ is a very weak dependence of the exact NMO velocity on ϵ and δ for a fixed difference $\epsilon - \delta$.

Thus, for typical VTI media, with positive $\epsilon - \delta$, the isotropic DMO correction severely understates moveout velocities at dips exceeding 20° to 30°, even when the anisotropy is weak.

The weak-anisotropy approximation for the normal moveout velocity given by equation (22) remains sufficiently accurate in the most important range of small and

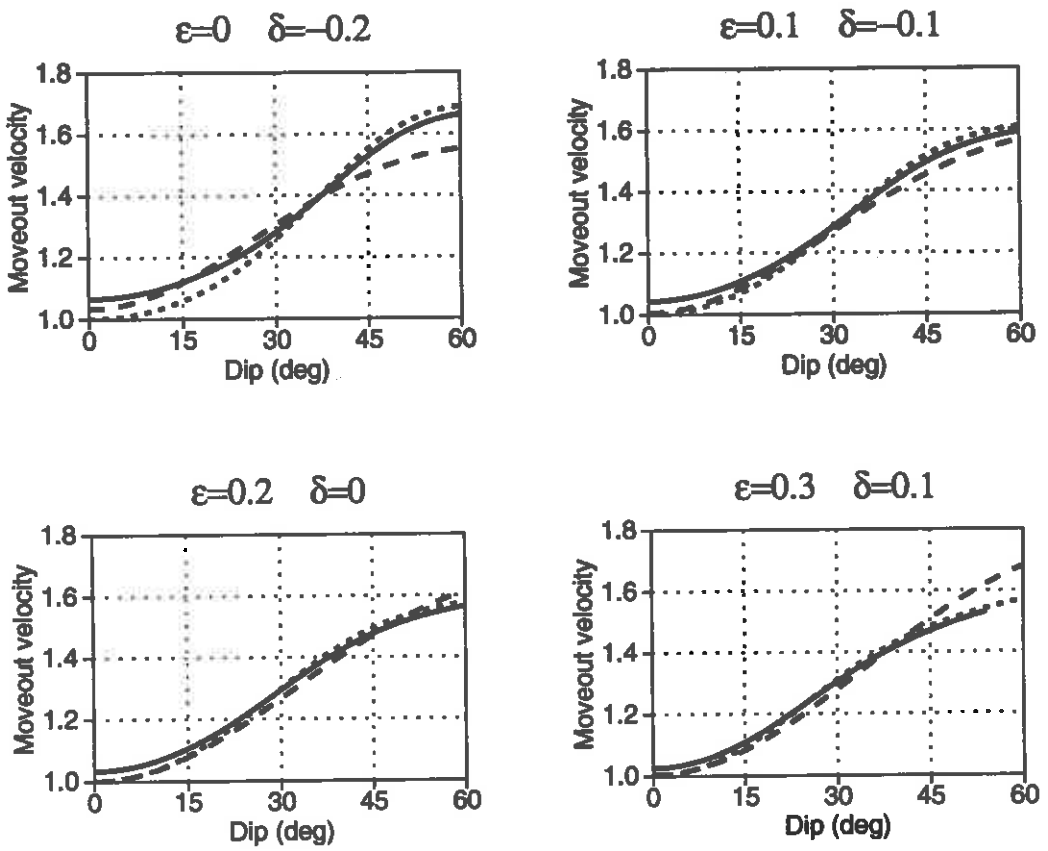

FIG. 10. Cosine-of-dip corrected P-wave moveout velocity for models with $\epsilon - \delta$=0.2.

moderate values of ϵ and δ. The error of the weak-anisotropy result (as compared with the exact NMO velocity) does not exceed 5% for $|\epsilon| \leq 0.2$, $|\delta| \leq 0.2$ (the only exception is the model with $\epsilon = 0$, $\delta = -0.2$).

The above suite of plots also presents a comprehensive picture of the moveout-velocity distortions at various dips caused by nonhyperbolic moveout. The influence of nonhyperbolic moveout manifests itself through the difference between the moveout velocity, calculated from $t^2 - x^2$ curves, and the exact NMO velocity. It is well known that deviations from hyperbolic moveout rapidly increase with spread length; this trend may be enhanced by anisotropy (Tsvankin and Thomsen, 1992, 1993a). For a maximum offset-to-depth ratio of 1, used in my calculations, the contribution of nonhyperbolic moveout to the moveout velocity is not significant, but the difference between the NMO and finite-spread velocities is clearly visible on some of the plots.

For small dips, the distortions of the moveout velocity due to deviations from hyperbolic moveout are in good agreement with the analytic results by Tsvankin and Thomsen (1992, 1993a), who gave a description of nonhyperbolic moveout for

horizontal reflectors using the quartic Taylor series term for $t^2 - x^2$ curves. For the P-wave, the influence of nonhyperbolic moveout is proportional to the absolute value of $\epsilon - \delta$; if $\epsilon - \delta$ is fixed, nonhyperbolic moveout is more pronounced for smaller δ. The analytic analysis also shows that the P-wave moveout velocity measured on finite spreads is larger than the NMO velocity if $\epsilon - \delta > 0$, and smaller than V_{nmo} if $\epsilon - \delta < 0$. Evidently, for elliptical anisotropy ($\epsilon = \delta$) the moveout is purely hyperbolic, and the dotted and solid curves fully coincide with each other. The validity of these conclusions is clearly seen in Figures 7–10.

The observed differences between the NMO velocity and the finite-spread moveout velocity seem to contradict the results by Levin (1990) and Larner (1993), who have not noticed visible deviations of their moveout curves from hyperbolae for the same spread length. However, this is an apparent discrepancy. Tsvankin and Thomsen (1992, 1993a) show that for spread lengths close to the depth of the reflector, the best-fit hyperbola is very close to the actual moveout curve although the moveout velocity of this hyperbola may be different by several first percent from the NMO velocity.

It is interesting that the difference between the moveout velocity on a finite spread and the NMO velocity changes sign with increasing dip (i.e., the solid and dotted lines cross), but the influence of nonhyperbolic moveout for steep reflectors is typically smaller than for zero dip. I conclude that if $|\epsilon - \delta|$ <0.15-0.2, nonhyperbolic moveout does not seriously distort the P-wave moveout velocity on short spreads, common for CMP acquisition design, even if dips are relatively large.

DMO FOR TRANSVERSELY ISOTROPIC MEDIA WITH VERTICAL VELOCITY GRADIENT

The above analysis is valid for homogeneous transversely isotropic models. Larner (1993) has studied the P-wave dip-moveout error for factorized VTI media with a constant gradient in vertical velocity. In terms of Thomsen notation used here, the velocity V_{P0} in factorized transversely isotropic media varies with position, while the V_{P0}/V_{S0} ratio and the anisotropic coefficients ϵ and δ remain constant. The four models used in Larner's work have the same anisotropic parameters and root-mean-square (RMS) vertical velocity down to the reflector as the models in Levin's (1990) study. One of the interesting results reported by Larner is that for the shale-limestone model with a typical value of the velocity gradient, constant-velocity DMO gives a higher accuracy than does V(z) DMO (both DMO corrections ignore anisotropy). Comparison of the moveout velocities for homogeneous and inhomogeneous shale-limestone suggests that inhomogeneity can compensate (to a certain degree) the DMO distortions caused by the anisotropy.

The results obtained in the previous section indicate that the DMO signature for the homogeneous shale-limestone may be considered typical for a wide range of VTI models. To verify whether the "compensation effect," found by Larner, is typical for inhomogeneous VTI media, I carry out the same calculations as in the previous

section, but for factorized transversely isotropic media with a vertical velocity gradient of 0.6 s^{-1} (Figure 11). The moveout velocity is calculated from $t^2 - x^2$ curves using Larner's (1993) ray-tracing program; the only change made in the code was the parameterization of VTI media in terms of ϵ and δ.

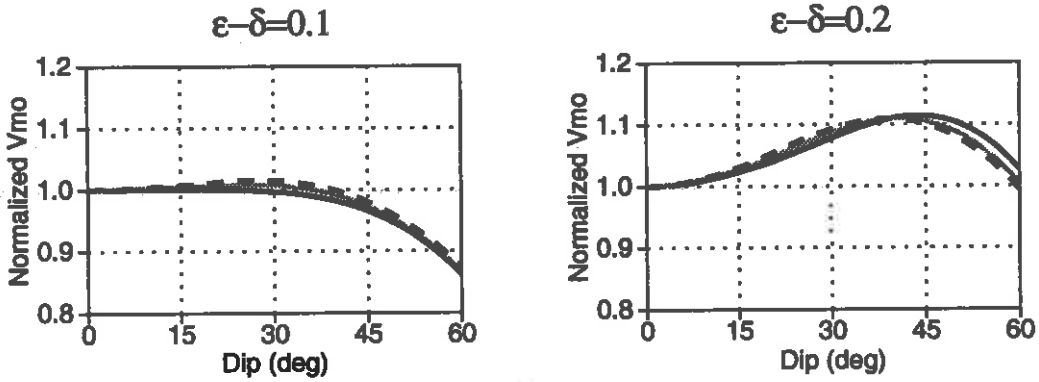

FIG. 11. Cosine-of-dip corrected P-wave moveout velocity for VTI models with a velocity gradient of 0.6 s^{-1}. The curves are normalized by the moveout velocity for a horizontal reflector. Each curve corresponds to a different pair of ϵ, δ. On the left plot, ϵ=0, $\delta = -0.1$ (black curve); ϵ=0.1, δ=0 (gray curve); ϵ=0.2, δ=0.1 (dashed curve). On the right plot, ϵ=0.1, $\delta = -0.1$ (black curve); ϵ=0.2, δ=0 (gray curve); ϵ=0.3, δ=0.1 (dashed curve). The distance from the CMP to the reflector and the spread length are 3000 m; the RMS vertical velocity down to 3000 m is 3500 m/s.

Comparison of Figure 11 with Figures 9 and 10 shows that for typical positive values of $\epsilon - \delta$, angular variations of the cosine-of-dip corrected moveout velocity are substantially suppressed by the velocity gradient. When velocity increases with depth, small-offset reflections from dipping interfaces travel more close to vertical than in a homogeneous medium. This makes the "effective dip" of the reflector smaller and reduces the increase in the moveout velocity with dip angle, both in isotropic and anisotropic media. For $\epsilon - \delta$=0.1, the influence of vertical velocity variations even leads to "overcorrection" in constant-velocity DMO, making the cosine-of-dip corrected moveout velocity decrease with dip angle.

Note that we do not make a distinction between the true dip angle and the apparent dip often used in constant-velocity DMO process (Larner, 1993). In homogeneous media, the two dips are usually close to each other; the dip-angle error in inhomogeneous media depends on the relative spatial position of dipping reflectors and a horizontal reflector, and will not be discussed here.

Figure 11 is reproduced in Figure 12, but with the DMO correction that honors inhomogeneity (V(z) DMO, Larner, 1993). Although the DMO error caused by the anisotropy is somewhat smaller than in homogeneous media with the same ϵ and δ (Figures 9 and 10), it is much larger than the error of the simplest cosine-of-dip correction (Figure 11). Therefore, consistent with Larner's results for the shale-limestone

model, for typical factorized transversely isotropic models the DMO correction that ignores both anisotropy and inhomogeneity is often more accurate than the correction that honors inhomogeneity but ignores anisotropy.

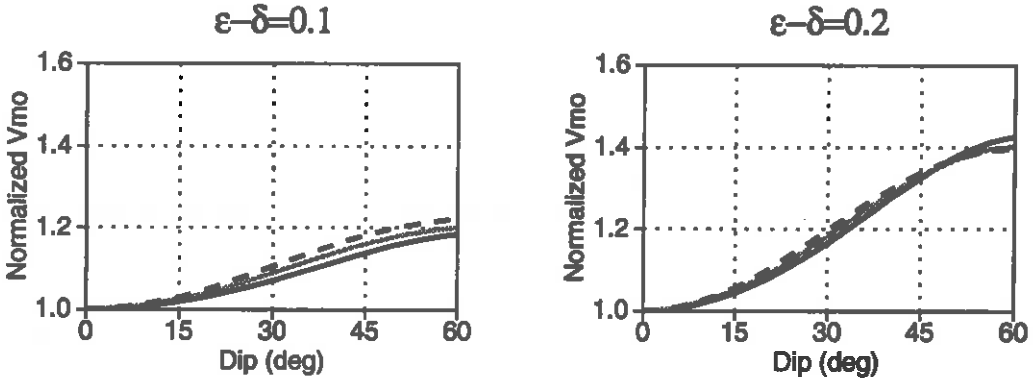

FIG. 12. P-wave moveout velocity after V(z) DMO correction. All parameters are the same as in Figure 11.

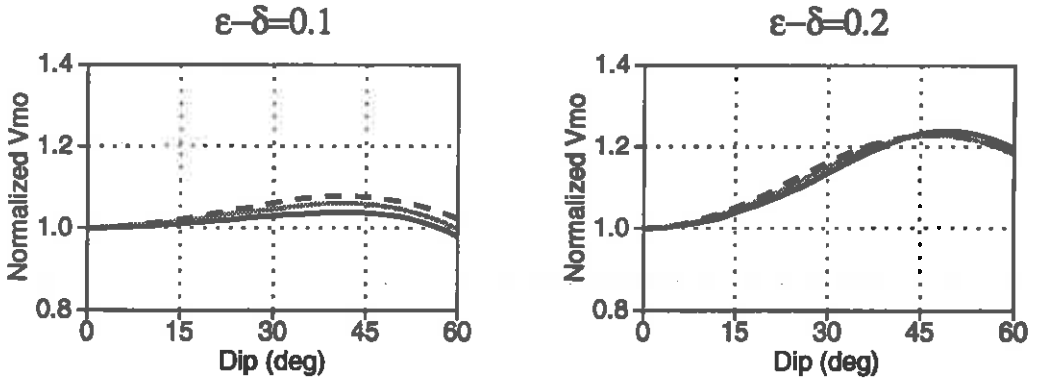

FIG. 13. Cosine-of-dip corrected P-wave moveout velocity for the same elastic parameters as in Figure 11, but for a more shallow reflector: the distance from the CMP to the reflector and the spread length are 1500 m.

Another important conclusion from Figures 11 and 12 is that in factorized vertically inhomogeneous VTI media the P-wave moveout velocity is still primarily controlled by the difference between ϵ and δ, rather than by the individual values of these parameters. However, in V(z) media, dip-dependence of the moveout velocity is also a function of the velocity gradient, the RMS vertical velocity, and the depth of the reflector. As illustrated by Figure 13, for more shallow reflectors the influence of the velocity gradient is less pronounced, and the corrected moveout velocity is closer to the result for a homogeneous medium. It is interesting that for the rather

typical model parameters used in Figure 13, the anisotropy and inhomogeneity practically cancel each other's influence, and constant-velocity DMO yields almost an ideal correction.

DISCUSSION AND CONCLUSIONS

In the presence of anisotropy, dip-dependence of moveout velocity deviates from the cosine-of-dip function, thus leading to errors in isotropic DMO correction. Here, I have presented an analytic expression for normal moveout velocity valid in the case when the incidence (sagittal) plane coincides with one of the symmetry planes of a homogeneous anisotropic medium. This formula can be used for P- and S-wave NMO velocities in many anisotropic models of practical importance, including transverse isotropy with a tilted symmetry axis, and symmetry planes in orthorhombic media.

Further insight into the problem is provided by the simple dip-moveout formula for weak transverse isotropy derived from the exact NMO expression. This weak-anisotropy approximation for the P-wave normal-moveout velocity is sufficiently accurate in a wide range of small and moderate values of ϵ and δ. The error of the weak-anisotropy result usually does not exceed 5% for $|\epsilon| \leq 0.2$, $|\delta| \leq 0.2$. The analytic solutions give a clear explanation for existing numerical results for transversely isotropic media, such as Levin's (1990) conclusion that the isotropic DMO correction remains valid when the symmetry axis is perpendicular to the reflector.

Dip-dependence of the P-wave moveout velocity for transverse isotropy with a vertical symmetry axis is shown to be a function of only two parameters – ϵ and δ. More than that, the P-wave DMO signature is controlled, to a significant degree, by the difference $\epsilon - \delta$. The systematic study of VTI media parameterized by ϵ and δ proves that for $\epsilon - \delta > 0$ (the most common case), the cosine-of-dip corrected moveout velocity remains significantly larger than the moveout velocity for a horizontal reflector. Even for relatively small $\epsilon - \delta = 0.1$ and $\epsilon \leq 0.2$, the error of conventional isotropic DMO reaches 25% at 45° dip and exceeds 30% at a dip of 60°. For $\epsilon - \delta = 0.2$ (also a feasible value), the cosine-of-dip corrected moveout velocity at 60° dip is almost 60% higher than the zero-dip moveout velocity!

The analytic study of NMO velocities was supplemented by calculations of the P-wave moveout velocity from reflection $t^2 - x^2$ curves on short-spread CMP gathers, typical for CMP acquisition design. Comparison between the analytic NMO velocity and the moveout velocity calculated on finite spreads makes it possible to analyze the magnitude of nonhyperbolic moveout as a function of reflector dip. The difference between the two velocities changes sign with increasing dip but usually is smaller for steep dips than for a horizontal reflector. If $|\epsilon - \delta| < 0.15$-$0.2$, nonhyperbolic moveout does not seriously distort the P-wave moveout velocity on short spreads, even for steep reflectors.

Significant errors of conventional DMO correction for typical transversely isotropic models mean that it is imperative to develop dip-moveout algorithms for anisotropic

media. Uren et al. (1990a) have generalized Gardner DMO for elliptically anisotropic models; however, the elliptical P-wave DMO correction becomes inaccurate even for "almost" elliptically anisotropic models. The formula for NMO velocity, derived here, can provide a basis for building DMO algorithms for general transversely isotropic and even orthorhombic media.

One of the major problems in developing dip-moveout processing (as well as migration, amplitude-versus-offset algorithms, etc.) in anisotropic media is to recover anisotropic parameters with sufficient accuracy. For VTI media, the parameter δ can be determined using the P-wave NMO velocity from a horizontal reflector and the true vertical velocity (such as from check shot or VSP data). However, the proper DMO correction also requires knowledge of the parameter ϵ, which cannot be recovered from short-spread P-wave data alone. If the vertical P- and/or S-velocities (or reflector depth) are known, both ϵ and δ can be determined from the P- and SV-wave NMO velocities. Tsvankin and Thomsen (1992, 1993b) show that it is possible to find all four anisotropic parameters governing P-SV propagation ($V_{P0}, V_{S0}, \epsilon, \delta$) from the combination of long-spread P- and SV-traveltimes. Since ϵ is directly related to the horizontal velocity, it can also be determined from head-wave velocities or results of cross-hole tomography.

Another way to overcome the ambiguity in the inversion for anisotropic parameters is to include dip moveout itself in the inversion procedure. High sensitivity of the P-wave normal moveout velocity to $\epsilon - \delta$ can be used to find ϵ from the NMO velocity of a reflection from a dipping interface by means of equation (9), provided δ has already been determined. Since the true dip angle ϕ is usually also unknown, the analytic expression for the NMO velocity should be used along with the equation for the apparent dip on the zero-offset section. This combination provides two simultaneous equations to be solved for ϵ and ϕ. More than that, normal moveout velocites for two distinctive dips and the NMO velocity for a horizontal reflector are sufficient to recover all three parameters governing P-wave propagation: V_{P0}, ϵ, and δ. Certainly, this kind of inversion would be much more dificult to carry out in $V(z)$ media. These ideas will be explored further in a sequel paper.

For transversely isotropic media with a linear velocity gradient and typical (positive) values of the difference $\epsilon - \delta$, inhomogeneity tends to reduce (sometimes significantly) dip-moveout error that anisotropy induces in conventional constant-velocity DMO. Therefore, if a medium is not only anisotropic, but also has a vertical velocity gradient, constant-velocity isotropic DMO can perform better than can be expected from the results for homogeneous anisotropic media.

ACKNOWLEDGMENTS

I am grateful to Ken Larner for many helpful discussions, for use of his ray-tracing code, and for his review of the paper. I would also like to thank John Anderson (Mobil) for his useful insight into the character of DMO performance.

REFERENCES

Banik, N.C., 1984, Velocity anisotropy of shales and depth estimation in the North Sea basin: Geophysics, **49**, 1411-1419.

Berryman, J.G., 1979, Long-wave elastic anisotropy in transversely isotropic media: Geophysics, **44**, 896-917.

Byun, B., 1982, Seismic parameters for media with elliptical velocity dependencies: Geophysics, **47**, 1621-1626.

Byun, B., 1984, Seismic parameters for transversely isotropic media: Geophysics, **49**, 1908-1914.

Hale, D., and Artley, C., 1993, Squeezing dip moveout for depth-variable velocity: Geophysics, **58**, 257-264.

Leary, P.C., Crampin, S., and McEvilly, T.V., 1990, Seismic fracture anisotropy in the Earth's crust: An overview: J. Geophys. Res., **95**, B7, 11,105-11,114.

Levin, F.K., 1971, Apparent velocity from dipping interface reflections: Geophysics, **36**, 510-516.

Levin, F.K., 1990, Reflection from a dipping plane - Transversely isotropic solid: Geophysics, **55**, 851-855.

Larner, K., 1993, Dip-moveout error in transversely isotropic media with linear velocity variation in depth: Geophysics, in press.

Larner, K., and Cohen, J.K., 1993, Migration error in transversely isotropic media with linear velocity variation in depth: Geophysics, in press.

Thomsen, L., 1986, Weak elastic anisotropy: Geophysics, **51**, 1954-1966.

Tsvankin, I.D., and Thomsen, L.A., 1992, Nonhyperbolic reflection moveout and the inverse problem for transversely isotropic media: SEG Annual Mtg. Expanded Abstracts, 1348-1351.

Tsvankin, I.D., and Thomsen, L.A., 1993a, Nonhyperbolic reflection moveout in anisotropic media: Geophysics, submitted.

Tsvankin, I.D., and Thomsen, L.A., 1993b, Inversion of reflection traveltimes for transverse isotropy: Geophysics, submitted.

Uren, N.F., Gardner, G.N.F., and McDonald, J.A., 1990a, Dip moveout in anisotropic media: Geophysics, **55**, 863-867.

Uren, N.F., Gardner, G.N.F., and McDonald, J.A., 1990b, Normal moveout in anisotropic media: Geophysics, **55**, 1634-1636.

White, J.E., 1983, Underground sound: Application of sound waves: Elsevier, 253 p.

Winterstein, D.F., and Paulsson, B.N.P., 1990, Velocity anisotropy in shale determined from cross-hole seismic and vertical seismic profile data: Geophysics, **55**, 470-479.

Body-wave radiation patterns and AVO in anisotropic media

Ilya Tsvankin

Body-wave radiation patterns and AVO in anisotropic media

I. Tsvankin

ABSTRACT

It is well known that the angular dependence of reflection coefficients may be significantly distorted in the presence of elastic anisotropy. However, the influence of anisotropy on amplitude-versus-offset analysis (AVO) is not limited to reflection coefficients. AVO signatures in anisotropic media are also distorted by the redistribution of energy along the wavefront of the wave travelling down to the reflector and back up to the surface. Significant anisotropy above the target horizon may be rather typical of sand-shale sequences commonly considered in AVO analysis. Unless properly corrected for, propagation phenomena in anisotropic media may seriously distort the character of AVO anomalies.

Here, I examine the influence of P- and S-wave radiation patterns on AVO in the most common anisotropic model – transversely isotropic media. A concise analytic solution, obtained in the weak-anisotropy approximation, provides a convenient way to estimate the impact of the distortions of the radiation patterns on AVO results. It is shown that the shape of the P-wave radiation pattern in the range of angles most important to AVO analysis ($0-45°$) is mostly dependent on the difference between Thomsen parameters ϵ and δ. For models with $\epsilon - \delta > 0$ (the most common case), the P-wave amplitude may drop substantially over the first $25° - 45°$ from vertical, even if the anisotropy is relatively weak. The distortions of the SV-wave radiation pattern are usually much more significant than those for the P-wave.

The anisotropic directivity factor for the incident wave may be of equal or greater importance for AVO than the influence of anisotropy on the reflection coefficient. Therefore, interpretation of AVO anomalies in the presence of anisotropy requires an integrated approach that takes into account not only the reflection coefficient but also the wave propagation above the reflector.

INTRODUCTION

It has been shown in the literature that elastic anisotropy may significantly distort the angular dependence of reflection coefficients (e.g., Keith and Crampin, 1977;

Banik, 1987; Wright, 1987). Banik (1987) and Thomsen (1993) developed analytic approximations for the reflection coefficient at a boundary between two transversely isotropic media. Yet another substantial distortion of the amplitude-versus-offset (AVO) signature in anisotropic media is associated with the wave propagation above the reflector.

The real goal of AVO is to perform reflection coefficient-versus-angle analysis rather than study directly amplitude-versus-offset dependence. Hence, correction for the angular amplitude variation caused by the wave phenomena above the reflector is an essential component of AVO technology. This correction is well understood for isotropic models; in the ray approximation, it involves primarily source directivity, energy divergence, reflection and transmission coefficients along the raypath, and attenuation losses (Duren, 1992).

If the velocity above the reflector is angle–dependent, the behavior of body-wave amplitudes becomes much more complicated, and the isotropic correction breaks down. The presence of anisotropic layers above the target horizon may be quite typical for sand-shale sequences commonly considered in AVO analysis. While reservoir sands can be expected to exhibit very weak anisotropy (if any), shale formations are often characterized by strong transverse isotropy (White et al., 1983; Banik, 1984; Winterstein and Paulsson, 1990).

Tsvankin and Chesnokov (1990a; hereafter referred to as Paper I) gave a description of point-source radiation patterns in azimuthally isotropic and orthorhombic media. They showed that the most powerful factor that modifies the distribution of energy along the wavefront is focusing and defocusing of energy, usually associated with maxima and minima, respectively, in the angle-dependent velocity. Further discussion of radiation patterns in different anisotropic models can be found in Ben-Menahem et al. (1991) and Gajewski (1993). A numerical example illustrating the influence of the distortion of P-wave radiation patterns on AVO was presented by Samec and Blangy (1992).

The main goal of this paper is to study the influence of the distortions of body-wave radiation patterns in anisotropic media on amplitude-versus-offset analysis. The existing solutions for point-source radiation in anisotropic models require numerical evaluation and do not provide easy analytic insight into the problem. Here, I present a concise weak-anisotropy approximation for radiation patterns in transversely isotropic media, which relates the distortions of point-source radiation to Thomsen parameters ϵ, δ (for the P- and SV-wave), and γ (for the SH-wave). The analytic solution is compared with results of numerical modeling based on the technique suggested in Paper I. The analytic and numerical methods are used to study radiation patterns in the range of angles most important for AVO analysis and compare the influence of anisotropy on two principal components of AVO signature, i.e., on the wave propagation above the reflector and reflection coefficients.

GENERAL ANALYSIS FOR TRANSVERSE ISOTROPY

Far-field point-source radiation in isotropic homogeneous non-attenuating media is determined just by the source directivity factor and spherical divergence of amplitude (Aki and Richards, 1980). The far-field approximation for source radiation in anisotropic media, derived in Paper I by means of the stationary-phase method, is a much more complicated function, which depends on the shape of the slowness surface. The most significant distortion of radiation patterns in anisotropic media is caused by the phenomena defined in Paper I as "focusing" and "defocusing" of energy. Energy increases (focuses) in parts of the wavefront with high concentration of group-velocity vectors of elementary plane waves (which comprise point-source radiation). Conversely, defocusing corresponds to areas with low concentration of group-velocity vectors. Often (but not always), focusing takes place near velocity maxima, while defocusing is often associated with velocity minima.

The stationary-phase approximation was used in Paper I only for qualitative estimates. Quantitative analysis of radiation patterns in Paper I was performed by a numerical technique based on plane-wave decomposition of point-source radiation with subsequent evaluation of Fourier-Bessel integrals in the frequency domain. This numerical method involves an approximate treatment of azimuthal anisotropy; however, it is exact for azimuthally isotropic media. Here, the stationary-phase solution for radiation patterns from Paper I is transformed into a much simpler expression valid for weak transverse isotropy. The accuracy of the weak-anisotropy formula is checked by comparison with radiation patterns generated by the numerical plane-wave decomposition technique.

I consider a simple model of a horizontal reflector below a transversely isotropic medium with a vertical symmetry axis (VTI) (Figure 1). Transverse isotropy will be described by the vertical velocities of P- and S-waves (V_{P0} and V_{S0}) and three dimensionless anisotropic parameters (ϵ, δ, and γ) introduced by Thomsen (1986).

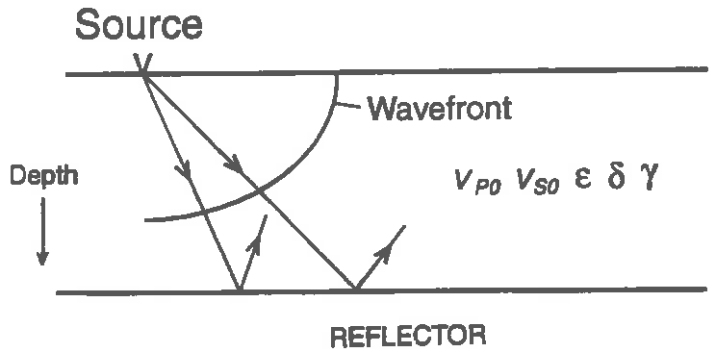

FIG. 1. Reflection from the bottom of a transversely isotropic layer. The redistribution of energy along the wavefront of the incident wave may distort the AVO response.

It is important to mention that the radiation patterns in this paper are derived as

a function of the phase angle with the symmetry axis; therefore, the analytic developments below can be easily applied not only for VTI media, but also for transverse isotropy with any orientation of the axis of symmetry.

Derivation of the weak-anisotropy approximation for point-source radiation is given in Appendix A. The far-field radiation pattern from a point force for weak transverse isotropy ($\epsilon \ll 1, \delta \ll 1, \gamma \ll 1$) is shown to be

$$U(R,\theta) = \frac{F_u}{4\pi\rho V^2(\theta) R} \frac{1}{\sqrt{\frac{\sin\psi}{\sin\theta}\left(1+\frac{1}{V}\frac{d^2V}{d\theta^2}\right)}}, \tag{1}$$

where U is the absolute value of the displacement, θ is the phase angle measured from vertical, V is the phase velocity, ρ is the density, $R = \sqrt{z^2+r^2}$ (z is the receiver depth, r is the horizontal source-receiver offset). The source term F_u is the projection of the force on the displacement (polarization) vector. Expression (1) should be evaluated at the phase angle θ, corresponding to a given ray (group-velocity) angle $\psi = \tan^{-1}(r/z)$ of the incident wave; note that at velocity maxima or minima the phase and group velocity vectors coincide with each other.

Formula (1) clearly shows the way anisotropy distorts point-source radiation in anisotropic media. The term $F_u/(4\pi\rho V^2 R)$ formally coincides with the well-known expression for the far-field point-force radiation in isotropic media (Aki and Richards, 1980). However, phase velocity in equation (1) is angle-dependent, and the term $V^2(\theta)$ reflects direct influence of velocity variations on the radiation pattern. Since body-wave polarizations are dependent on the elastic constants, the source term F_u may also be distorted by anisotropy. Also, the expression should be evaluated at the phase direction, which is generally different from the source-receiver direction due to the presence of anisotropy.

The term under the radical represents the pure contribution of anisotropy to the radiation pattern. As shown in Paper I, the second derivative of phase velocity is responsible for the focusing and defocusing phenomena discussed above.

The distinction between the source term and the rest of formula (1) is very important. While F_u is itself distorted by anisotropy, the existence of a pure "medium" term means that the redistribution of energy along the wavefront happens not only in the source layer, but also in any other anisotropic layer along the raypath.

Apparently, in the absence of anisotropy equation (1) reduces to the expression for isotropic media given in Aki and Richards (1980). If the anisotropy is not weak, formula (1) cannot be expected to be quantitatively accurate but it is still useful for qualitative estimates. Asymptotic expression (1) is used below to study the influence of transverse isotropy on the AVO response for P-, SV-, and SH-waves.

P-WAVE RADIATION PATTERNS AND AVO

The issue of P-wave AVO is of particular importance because P-waves constitute the overwhelming majority of all seismic data being acquired in the oil industry. The P-wave phase-velocity function for weak transverse isotropy ($\delta \ll 1$, $\epsilon \ll 1$) is given by (Thomsen, 1986)

$$V_P(\theta) = V_{P0}\left(1 + \delta \sin^2\theta \cos^2\theta + \epsilon \sin^4\theta\right). \tag{2}$$

Equation (2) is fully linearized in the anisotropies ϵ and δ. Differentiating (2) yields

$$\frac{dV_P(\theta)}{d\theta} = V_{P0} \sin 2\theta \left(\delta \cos 2\theta + 2\epsilon \sin^2\theta\right), \tag{3}$$

$$\frac{dV_P^2(\theta)}{d\theta^2} = 2V_{P0}\left[\delta \cos 4\theta + 2\epsilon \sin^2\theta(1 + 2\cos 2\theta)\right]. \tag{4}$$

Also, for weak anisotropy

$$\sin\psi = \sin\theta\left\{1 + \cos^2\theta[2\delta + 4(\epsilon - \delta)\sin^2\theta]\right\}.$$

Substituting the above equations into formula (1) and further linearizing in δ and ϵ, we obtain a concise approximation for the P-wave radiation pattern,

$$U_P(R,\theta) = \frac{F_u}{4\pi\rho V_{P0}^2 R}\left[1 - 2\delta - 2(\epsilon - \delta)\sin^2 2\theta + \delta \sin^2\theta\right]. \tag{5}$$

The weak-anisotropy approximation (5) is more accurate at velocity maxima and minima than in areas of rapid velocity changes. At velocity extrema $\frac{dV_P}{d\theta} = 0$, phase and group angles are equal to each other, and many terms quadratic in the parameters ϵ and δ drop out from the original stationary-phase formula (A-4), thus increasing the accuracy of the weak-anisotropy approximation.

The polarization of the P-wave excited by a point source in a homogeneous anisotropic medium is usually close to the isotropic direction (Paper I). This means that the source directivity factor F_u has almost the same influence on the P-wave radiation pattern, as it has in isotropic media. However, for more complex sources such as explosions or dislocations, the source term becomes a function of phase velocity and, therefore, may have a significant influence on the angular amplitude distribution (Tsvankin and Chesnokov, 1990b).

The P-wave phase velocity always has an extremum in the symmetry (vertical) direction. According to formula (5), for $\theta = 0$ the anisotropic correction factor reduces to $1 - 2\delta$. Thus, the focusing (or defocusing) of the P-wave energy at vertical incidence depends on just one anisotropic coefficient – δ, the parameter responsible

for near-vertical P-wave propagation. If $\delta < 0$, the velocity function has a maximum at $\theta = 0°$, and the amplitude at vertical incidence decreases due to the defocusing; conversely, if $\delta > 0$, a velocity minimum leads to lower amplitudes at $\theta = 0°$. It should be emphasized that the velocity maximum or minimum in the symmetry direction is the only "3-dimensional" extremum in transversely isotropic media: phase velocity increases (or decreases) away from the symmetry axis in all directions, not just in the incidence plane. Therefore, the focusing (or defocusing) of energy in the symmetry direction is more pronounced than for any other velocity extremum with the same value of $dV^2/d\theta^2$.

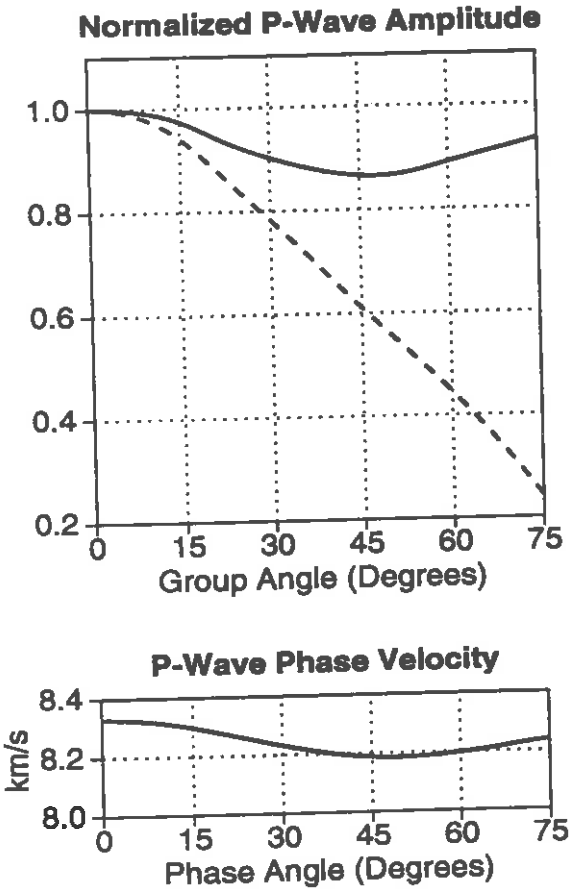

FIG. 2. Angular dependence of the P-wave amplitude and phase velocity in transversely isotropic olivine. The model parameters are: V_{P0}=8.328 km/s, V_{S0}=4.606 km/s, $\delta = -0.059$, $\epsilon = -0.008$. The wave is excited by a vertical point force. The source-receiver distance is constant. The dashed curve is the uncorrected amplitude; the solid curve is the amplitude after the correction for the source directivity used in isotropic models. Both curves are normalized by the vertical-incidence amplitude.

Equation (5) shows that the lowest order anisotropic correction to the radiation pattern in the range of angles used in AVO ($0° - 45°$) is determined by the difference

$\epsilon - \delta$. For elliptical anisotropy ($\epsilon = \delta$), the term $2(\epsilon - \delta)\sin^2 2\theta$ vanishes, and the anisotropic correction factor does not change much between 0° and 45°, unless δ is relatively large.

If $\epsilon - \delta > 0$ (the most common case), transverse isotropy causes the P-wave amplitude to decrease away from vertical. Figure 2 shows the amplitudes of the P-wave excited by a point vertical force in a model of transversely isotropic olivine with $\epsilon - \delta = 0.051$. The amplitudes were picked from seismograms generated by the numerical technique based on evaluation of Fourier-Bessel integrals (Paper I).

The solid curve in Figure 2 shows the amplitude after the standard correction for the source directivity used in isotropic media (just $1/\cos\psi$ in this case). If the medium were isotropic, this correction would make the amplitude independent of angle. Due to the influence of anisotropy, the amplitude at a group angle of 45° remains 13.5% lower than at vertical incidence. For the model in Figure 2, the P-wave phase velocity has a maximum at $\theta = 0°$ and a minimum near $\theta = 49°$. Thus, due to the focusing of energy at vertical incidence and the defocusing near $45 - 50°$, the P-wave amplitude decreases away from vertical. Although a distortion of 13.5% over a 45° interval does not seem significant, it occurs in a medium with less than 2% maximum variation in the P-wave phase velocity!

For the model of transversely isotropic olivine, the difference between the weak anisotropy approximation (5) and the result obtained by the numerical technique developed in Paper I is essentially within the error of the numerical method (Figure 3).

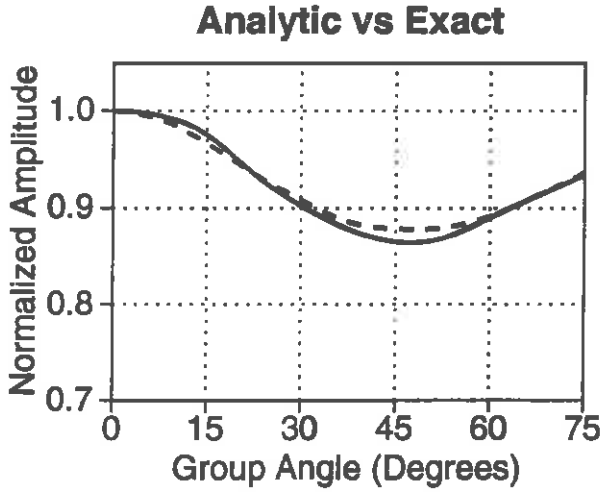

FIG. 3. Comparison between analytic approximation (5) (dotted curve) and the exact P-wave amplitude (solid curve, same as in Figure 2) for the model from Figure 2. Both curves are corrected for the isotropic directivity factor and normalized by the vertical-incidence amplitude.

The above model represents a weakly anisotropic medium with small negative

$\delta = -0.059$ and $\epsilon \approx 0$. While both positive and negative values of δ are plausible, ϵ is almost always positive (Thomsen, 1986). Formula (5) shows that if $\delta < 0$, the decrease in the P-wave amplitude becomes more pronounced with increasing ϵ and decreasing δ. The example in Figure 2, corresponding to $\epsilon \approx 0$, has been chosen to illustrate the minimum distortions of the P-wave radiation pattern for a typical negative δ.

The dependence of the amplitude distortions on the anisotropic parameters for $\delta < 0$ is related to the position of the velocity minimum. The locations of the minima and/or maxima of the velocity function are determined by the zeroes of $\frac{dV_P}{d\theta}$, given by formula (3). Obviously, the velocity function always has minimum or maximum at vertical incidence and at $\theta = 90°$. An "intermediate" extremum between 0° and 90° occurs if at some θ_i

$$\sin^2\theta_i = \frac{\delta}{2(\delta - \epsilon)} \tag{6}$$

From (6) it follows that this extremum exists only if

$$\begin{cases} \delta > 0 \\ \delta > 2\epsilon \end{cases} \tag{7}$$

or

$$\begin{cases} \delta < 0 \\ \delta < 2\epsilon \end{cases} \tag{8}$$

Furthermore, from (6) it is easy to deduce that the extremum is located at angles between 0° and 45° only if δ and ϵ have opposite signs.

With increasing ϵ and decreasing δ ($\epsilon > 0$, $\delta < 0$), the P-wave phase-velocity minimum moves closer to vertical (formula [6]), and the defocusing of energy determined by the second derivative of the velocity function (formula [4]) becomes more pronounced and spreads over a wider range of angles. It is important to mention that the maximum of energy defocusing in this case is shifted from the velocity minimum towards larger angles because $\frac{dV_P^2}{d\theta^2}$ continues to increase even beyond the velocity minimum. As a result, even for weakly anisotropic models with $\delta < 0$ ($|\delta| \leq 0.1$, $|\epsilon| \leq 0.1$), the P-wave amplitude may drop by 30% and more from 0° to 45° (Figure 4; plots on the left).

Thus, for negative δ the corrected P-wave amplitude typically decreases with angle because ϵ is predominantly positive, and $\epsilon - \delta > 0$. In addition, the term $\delta \sin^2\theta$ in (5) is also negative.

If δ is positive, the anisotropy causes either an increase or a decrease in P-wave amplitude with angle depending on the difference $\epsilon - \delta$. For elliptical anisotropy ($\epsilon = \delta$), the P-wave amplitude is governed by the term $\delta \sin^2\theta$ in (5) and, therefore, slowly increases away from vertical.

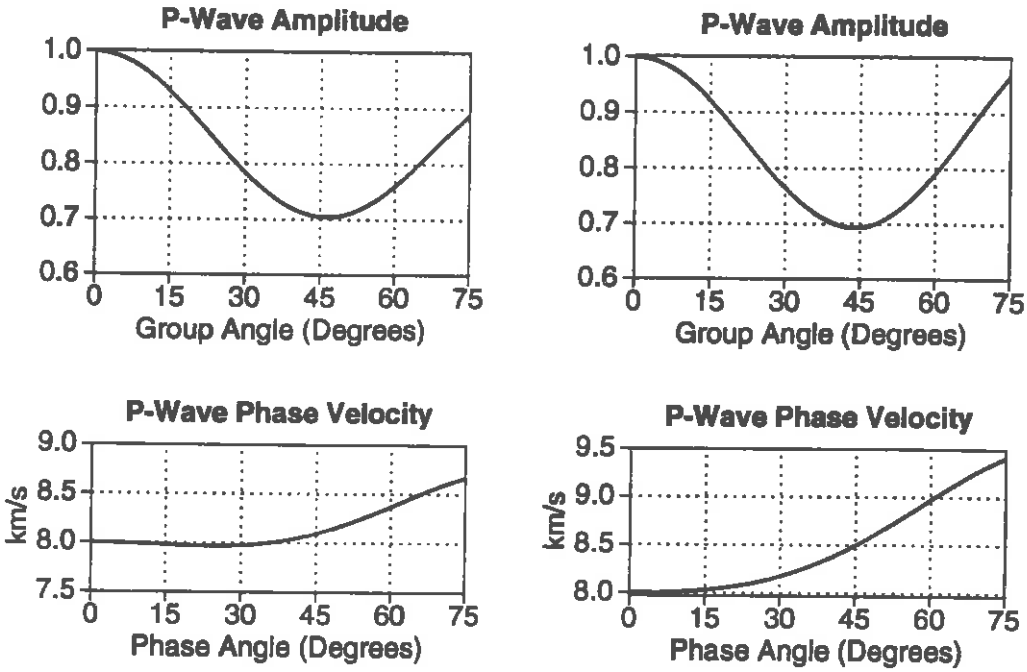

FIG. 4. Angular dependence of the P-wave amplitude and phase velocity for two models with the same $\epsilon - \delta = 0.15$ and V_{P0}=8 km/s. The plots on the left are for ϵ=0.1, $\delta = -0.05$; the plots on the right are for ϵ=0.2, δ=0.05. The computations were made in the weak-anisotropy approximation. The amplitude curves are corrected for the isotropic directivity factor and normalized by the vertical-incidence amplitude.

According to the existing data, typically $\epsilon > \delta$ (Thomsen, 1986; Tsvankin and Thomsen, 1992). For instance, $\epsilon \geq \delta$ for transverse isotropy caused by thin bedding of isotropic layers (Berryman, 1979). If $\epsilon > \delta$, the anisotropy usually leads to a decrease in the P-wave amplitude with angle due to the term $-2(\epsilon - \delta)\sin^2 2\theta$, unless $\delta \gg \epsilon - \delta$. Although there are no velocity minima between 0° and 90° for $\epsilon > \delta > 0$, the second derivative of the phase-velocity function usually increases with angle θ. Since V_P and $(\sin\psi/\sin\theta)$ in formula (1) also grow with angle, the P-wave amplitude decreases away from vertical (Figure 4; plots on the right).

From the results for $\delta < 0$ (e.g. Figure 2), one might get the impression that the P-wave amplitude anomalies represent an amplified version of the phase-velocity function. However, this is not necessarily the case because the P-wave amplitude behavior is mostly determined by the difference $\epsilon - \delta$, rather than by the individual values of the anisotropic coefficients. Two distinctly different phase-velocity functions in Figure 4 correspond to models with the same $\epsilon - \delta$ and, therefore, yield similar amplitude curves.

How do the distortions of the radiation pattern compare with the influence of anisotropy on the reflection coefficient? Thomsen (1993) gives the following approx-

imation for the P-wave reflection coefficient in the limit of weak transverse isotropy, and small velocity and density contrasts at the reflector:

$$R(\theta) = R_{isot}(\theta) + R_{anis}(\theta)\,, \tag{9}$$

where $R_{isot}(\theta)$ is the reflection coefficient in the absence of anisotropy ($\epsilon = 0$, $\delta = 0$) and

$$R_{anis}(\theta) = \frac{1}{2}(\delta_1 - \delta)\sin^2\theta + \frac{1}{2}(\delta - \delta_1 + \epsilon - \epsilon_1)\sin^2\theta\tan^2\theta\,. \tag{10}$$

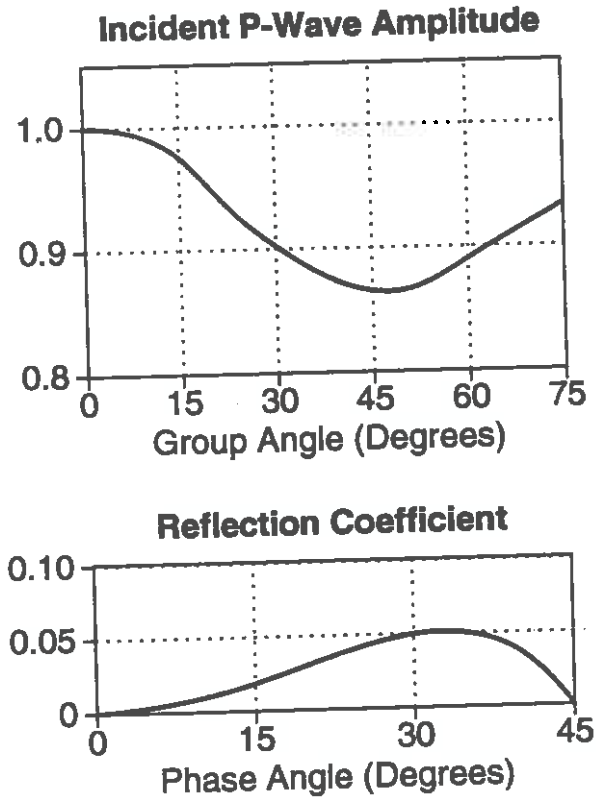

FIG. 5. Comparison of the influence of anisotropy on the P-wave radiation pattern and on the reflection coefficient. The transversely isotropic model from Figure 2 overlies an isotropic medium with the normal-incidence reflection coefficient $R(0) = 0.1$. (Top) The exact amplitude of the incident wave corrected for the isotropic directivity factor. (Bottom) The angular variation in the reflection coefficient caused by anisotropy (calculated from Thomsen's equation as $R_{anis}(\theta)/R(0)$).

Subscript 1 refers to the medium below the reflector. Suppose beneath the transversely isotropic medium from Figure 2 is an isotropic medium, and the normal-incidence reflection coefficient has a typical value of 0.1. From equations (9) and

(10), we find that the anisotropy-induced variations in the reflection coefficient are limited to 5% as compared with 13.5% distortions of the radiation pattern (Figure 5). This means that in this case the redistribution of energy above the reflector causes more pronounced angular amplitude variations than does the influence of anisotropy on the reflection coefficient.

Obviously, this comparison cannot be regarded as general. The angular variations in the reflection coefficient depend on the difference in the anisotropic parameters above and below the reflector, while the radiation pattern is entirely determined by the properties of the incidence medium. Also, the influence of anisotropy on the reflection coefficient becomes more pronounced for very weak reflectors. However, it is clear that the two phenomena are often of the same order of magnitude.

In isotropic AVO analysis, the presence of gas is often identified by an increase in the P-wave reflection coefficient with angle. If the medium above the reflector is transversely isotropic with $\epsilon - \delta > 0$, the amplitude may substantially decrease away from vertical due to propagation phenomena above the reflector and, therefore, cancel out or even reverse the increase in the reflection coefficient.

S-WAVE RADIATION PATTERNS AND AVO

The phase velocity of the SV-wave in transversely isotropic media is mostly determined by a single anisotropic parameter $\sigma = \frac{V_{P0}^2}{V_{S0}^2}(\epsilon - \delta)$ (Tsvankin and Thomsen, 1992; Thomsen 1986). In the weak-anisotropy approximation, the SV-wave phase velocity is given by

$$V_{SV}(\theta) = V_{S0}\,(1 + \sigma \sin^2\theta \cos^2\theta)\,. \tag{11}$$

Note that formula (11) can be obtained from the P-wave phase velocity (equation [2]) by replacing δ with σ and setting $\epsilon = 0$. Since the radiation pattern in the weak-anisotropy approximation (1) is a function of phase velocity (except for the source term F_u), the SV-wave radiation pattern can be easily derived from P-wave formula (5) by making the same substitutions ($\delta = \sigma$, $\epsilon = 0$):

$$U_{SV}(R,\theta) = \frac{F_u}{4\pi\rho V_{S0}^2 R}\,[1 - 2\sigma + 2\sigma \sin^2 2\theta + \sigma \sin^2\theta]\,. \tag{12}$$

In addition to maxima or minima at $\theta = 0°$ and $\theta = 90°$, the SV-wave phase velocity function has an extremum near 45° (unless $\epsilon = \delta$, and V_{SV} is constant). In the most common case of positive σ ($\epsilon > \delta$), the SV-wave phase velocity has a minimum at vertical incidence followed by a maximum near 45° (exactly as for the P-wave when $\epsilon = 0$, $\delta > 0$). As shown by formula (12) and the analysis in the previous section, this leads to an increase in the incident wave amplitude with angle. An important difference, however, is that σ is usually much bigger than δ due to the contribution of the squared velocity ratio. It is also noteworthy that the term F_u

is usually much more distorted by transverse isotropy for the SV-wave than for the P-wave.

Figure 6 shows the angular variation in the SV-wave amplitude for the model from Figure 2, which has $\sigma > 0$. As in Figure 2, the amplitudes were calculated using the technique described in Paper I. It is interesting that due to the influence of anisotropy even the raw amplitudes of the SV-wave grow with incidence angle, although the angle between the force and the polarization vector increases as the receiver moves away from vertical. After the isotropic correction for the source directivity, the amplitude at 45° is more than 60% higher than at vertical incidence.

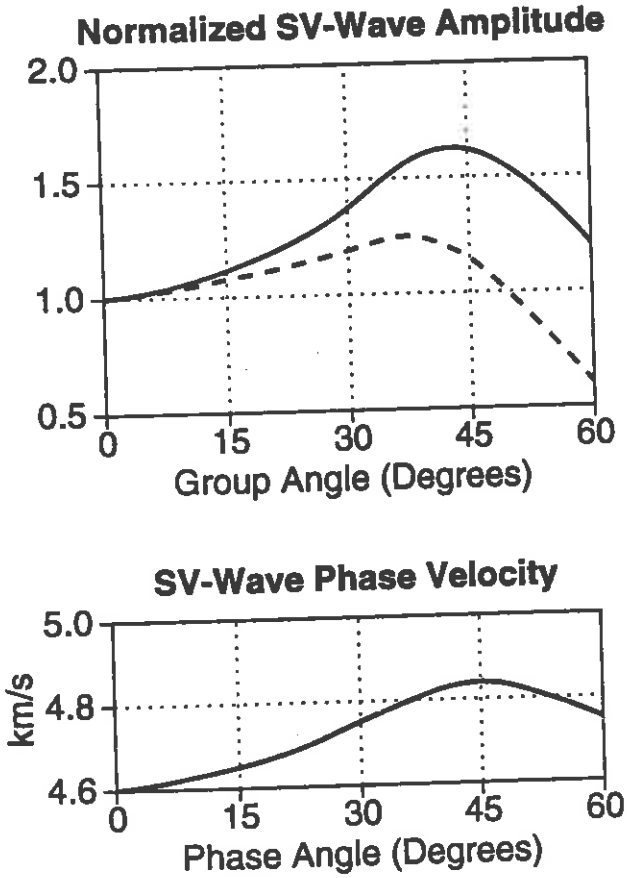

FIG. 6. Angular dependence of the SV-wave amplitude and phase velocity in transversely isotropic olivine (model from Figure 2, $\sigma = 0.168$). The wave is excited by a horizontal point force. The source-receiver distance is constant. The dashed curve is the uncorrected amplitude; the solid curve is the amplitude after the correction for the source directivity used in isotropic models. Both curves are normalized by the vertical-incidence amplitude.

In spite of a relatively high value of σ ($\sigma = 0.168$), the weak anisotropy approximation (12) (not shown on the plot) accurately predicts the magnitude of the amplitude

increase between 0° and 45°.

The SV-wave velocity anisotropy (i.e., the maximum variation in velocity) for the model from Figure 6 is only about 5%. Thus, the combination of the velocity extrema of opposite sign at 0° and near 45° causes strong distortions of the SV-wave radiation pattern, even for only moderate velocity variations. The SV-wave velocity anisotropy of about 10% leads to drastic distortions of the radiation pattern (see Paper I).

The SH-wave slowness surface in a homogeneous transversely isotropic medium is elliptical, and the phase velocity is given (exactly) by

$$V_{SH}(\theta) = V_{S0}\sqrt{1 + 2\gamma \sin^2\theta}\,.$$

Thus, the results we obtained for the P-wave for the case of elliptical anisotropy ($\epsilon = \delta$) apply to the SH-wave, if $\epsilon = \delta$ is replaced by γ. If γ is positive (which is usually the case; see Thomsen, 1986), the defocusing of energy at vertical incidence leads to an increase in the SH-wave amplitude with angle. However, for weak and moderate anisotropy this increase is not substantial.

DISCUSSION AND CONCLUSIONS

Since the conventional methods used to compensate for propagation phenomena in AVO analysis are based on the assumption of isotropy, the influence of anisotropy on the wave propagation to and from the reflector may have a direct influence on the character of AVO anomalies.

Here, the relation between P- and S-waves' radiation patterns and AVO response has been analyzed for transversely isotropic models. A concise analytic solution, obtained in the weak-anisotropy approximation, relates the angular dependence of body-wave amplitudes to the anisotropic parameters. Combined with the Thomsen (1993) appproximation for the reflection coefficients in transversely isotropic media, this solution provides a framework for a comprehensive qualitative analysis of the influence of transverse isotropy on AVO.

The shape of the P-wave radiation pattern in the range of angles most important to AVO analysis ($0-45°$) is mostly dependent on the difference between the parameters ϵ and δ. For models with $\epsilon - \delta > 0$, transverse isotropy causes the P-wave amplitude to drop by 30% and more over the first 45° from the vertical, even if the anisotropy is relatively weak. These results prove that application of the elliptical-anisotropy approximation (ϵ=δ) to P-wave's amplitudes may lead to serious errors even if the medium is relatively close to elliptical.

The redistribution of energy along the wavefront is even more significant for the SV-wave than for the P-wave. For the typical case, $\epsilon > \delta$ ($\sigma > 0$), and just 5% SV-velocity anisotropy, the SV-wave amplitude increases by over 60% between 0° and 45°.

The results obtained here can be easily applied to transversely isotropic media with a tilted symmetry axis. The distortions of radiation patterns in more complicated anisotropic models (e.g., orthorhombic) may be substantially reinforced by azimuthal velocity variations (Paper I) and shear-wave singularities.

The distortions of radiation patterns may be of greater importance to AVO analysis than the influence of anisotropy on the reflection coefficient, especially for strong reflectors or small differences in the anisotropic coefficients across the reflector.

Therefore, accurate interpretation of AVO anomalies in anisotropic media is impossible without a proper correction for the influence of anisotropy on the wave propagation above the reflector. It is also clear that this correction should be included in any algorithm designed to use reflection coefficients to invert for anisotropy.

An approximate correction for simple models like the one considered in this work can be made by using asymptotic expressions for radiation patterns such as those discussed in this paper or presented by Ben-Menahem et al. (1991) or Gajewski (1993). However, the redistribution of energy along the wavefront may occur not only in the source layer but also in any anisotropic layer between the reflector and the surface. The correction for more complicated, realistic models requires application of numerical methods capable of allowing for anisotropy in wave propagation through layered media.

Still, the greatest challenge in correcting AVO signatures for anisotropy is to determine anisotropic parameters with sufficient accuracy. The lowest-order correction to the reflection coefficient depends just on the value of δ above and below the reflector. For VTI media, δ can be determined in a straightforward way from the P-wave moveout velocity and the true vertical velocity. However, the lowest-order term in the angular dependence of the P-wave radiation pattern contains the difference $\epsilon - \delta$. Therefore, correction for propagation phenomena requires knowledge of the parameter ϵ, which is much more difficult to obtain. Some ways to recover ϵ are discussed by Tsvankin (1993).

ACKNOWLEDGMENTS

I wish to thank L. Thomsen (Amoco) for useful discussions. Reviews by K. Larner, L. Deng, and T. Tjan were helpful in improving the manuscript. I am grateful to C. Artley for his help with software problems.

REFERENCES

Aki, K., and Richards, P.G., 1980, Quantitative seismology: theory and methods: W.N. Freeman & Co., San Francisco.

Banik, N.C., 1987, An effective parameter in transversely isotropic media: Geophysics, **52**, 1654-1664.

Ben-Menahem, A., Gibson Jr., R.L., and Sena, A.G., 1991, Green's tensor and radiation patterns of point sources in general anisotropic inhomogeneous elastic media: Geophys. J. Int., **107**, 297-308.

Berryman, J.G., 1979, Long-wave elastic anisotropy in transversely isotropic media: Geophysics, **44**, 896-917.

Duren, R.E., 1992, Range-equation weights for AVO: Geophysics, **57**, 1203-1208.

Gajewski, D., 1993, Radiation from point sources in general anisotropic media: Geophys. J. Int., in press.

Keith, C.M., and Crampin, S., 1977, Seismic body waves in anisotropic media: Reflection and refraction at a plane interface: Geophys. J. R. Astr. Soc., **49**, 181-208.

Samec, P., and Blangy, J.P., 1992, Viscoelastic attenuation, anisotropy, and AVO: Geophysics, **57**, 441-450.

Thomsen, L., 1986, Weak elastic anisotropy: Geophysics, **51**, 1954-1966.

Thomsen, L., 1993, Weak anisotropic reflections: Offset Dependent Reflectivity (Ed. M. Backus), in press.

Tsvankin, I. 1993, Analytic description of dip moveout in anisotropic media: CWP Project Review-93 (this volume), Colorado School of Mines.

Tsvankin, I.D., and Chesnokov, E.M., 1990a, Synthesis of body-wave seismograms from point sources in anisotropic media: J. Geophys. Res., **95**(B7), 11317-11331.

Tsvankin, I., and Chesnokov, E., 1990b, Synthetic waveforms and polarizations at the free surface of an anisotropic halfspace: Geophys. J. Int., **101**, 497-505.

Tsvankin, I.D., and Thomsen, L.A., 1992, Nonhyperbolic reflection moveout and the inverse problem for transversely isotropic media: SEG Annual Mtg. Expanded Abstracts, 1348-1351.

White, J.E., Martineau-Nicoletis, L., and Monash, C., 1983, Measured anisotropy in Pierre shale: Geophys. Prosp., **31**, 709-725.

Winterstein, D.F., and Paulsson, B.N.P., 1990, Velocity anisotropy in shale determined from cross-hole seismic and vertical seismic profile data: Geophysics, **55**, 470-479.

Wright, J., 1987, The effects of transverse isotropy on reflection amplitude vs offset: Geophysics, **52**, 564-567.

APPENDIX A: WEAK-ANISOTROPY APPROXIMATION FOR RADIATION PATTERNS IN TRANSVERSELY ISOTROPIC MEDIA

In Paper I, point-source radiation in homogeneous arbitrary-anisotropic media was decomposed into a Weyl-type integral over plane waves. The displacement from a point force in the frequency domain was shown to be

$$\vec{U} = \frac{i\omega}{(2\pi)^2} \sum_{\nu=1}^{3} \int_{-\infty}^{+\infty} \int_{-\infty}^{+\infty} \vec{U}_{pl}\, e^{-i\omega(m_1 x_1 + m_2 x_2 + m_{3\nu} x_3)}\, dm_1 dm_2\,, \qquad \text{(A-1)}$$

with the plane-wave displacement $\vec{U}_{pl}$ given by

$$\vec{U}_{pl} = Res \left[\frac{1}{D(m_3)} G^{ad} \vec{F} \right]_{m_{3\nu}} \qquad \text{(A-2)}$$

The source is located at origin of a Cartesian coordinate system. The summation over ν corresponds to three possible wave types (P- and two S-waves); $\vec{m}$ is the slowness vector, $G_{ik} = c_{ijkl} m_j m_l - \rho \delta_{ik}$ is the Green-Christoffel matrix, G^{ad} is the adjoint matrix of G, $m_{3\nu}$ (the vertical slownesses of the plane waves) are roots of $D(m_3) = det\, G$, $\vec{F}$ is the point-force vector, and $i = \sqrt{-1}$. To obtain the solution in the time domain, (A-1) should be convolved with the source pulse.

It is convenient to represent (A-1) in the polar coordinates ($m_1 = m_0 \cos\phi, m_2 = m_0 \sin\phi$):

$$\vec{U} = \frac{i\omega}{(2\pi)^2} \sum_{\nu=1}^{3} \int_{0}^{+\infty} \int_{0}^{2\pi} \vec{U}_{pl}\, e^{-i\omega(m_0 r \cos(\phi-\alpha) + m_{3\nu} z)}\, m_0 dm_0 d\phi\,, \qquad \text{(A-3)}$$

where $x_1 = r\cos\alpha$, $x_2 = r\sin\alpha$, $x_3 = z$.

In Paper I, the far-field radiation pattern was derived from (A-1) by means of the stationary-phase approximation. For vertical transverse isotropy, the stationary-phase solution for the ν–th wave (for brevity, henceforth I omit the superscript ν) is represented by

$$|\vec{U}| = \frac{|\vec{U}|_{pl}}{2\pi V} \frac{\sin\theta \left(\frac{\cos\theta}{V} + \frac{d(1/V)}{d\theta} \sin\theta \right)}{\sqrt{\frac{r\sin\theta}{V} \frac{d^2\Phi}{d\theta^2}}}\,, \qquad \text{(A-4)}$$

$$\begin{aligned} \frac{d^2\Phi}{d\theta^2} &= (r\sin\theta + z\cos\theta)\Big[\frac{1}{V} - \frac{d^2(1/V)}{d\theta^2} \\ &\quad + \frac{2}{V} \left(\frac{r\cos\theta - z\sin\theta}{r\sin\theta + z\cos\theta} \right)^2 \Big], \end{aligned} \qquad \text{(A-5)}$$

where Φ is the phase function in the integral for source radiation (A-3), θ is the phase angle measured from the vertical (z) axis, V is the phase velocity. Expression (A-4) should be evaluated at the phase angle θ, corresponding to a given ray (group velocity) angle ψ determined by the receiver position ($\tan\psi = r/z$).

Here, the general solution for transverse isotropy (A-4) is transformed into a much simpler weak-anisotropy approximation. The derivation is given for P-waves only; the radiation patterns of S-waves are obtained in a similar way.

In the following, it is assumed that the source and receiver are located in the $[x_1, x_3]$ plane; in this case, at the stationary-phase point $\phi = \alpha = 0$. As a preliminary step, $|\vec{U}_{pl}|$ (formula [A-2]) should be represented as a function of the P-wave slowness vector. The non-zero components of the Green-Christoffel matrix in the plane $[x_1, x_3]$ are

$$G_{11} = c_{11}m_0^2 + c_{44}m_3^2 - \rho\,, \tag{A-6}$$

$$G_{22} = c_{66}m_0^2 + c_{44}m_3^2 - \rho\,, \tag{A-7}$$

$$G_{33} = c_{44}m_0^2 + c_{33}m_3^2 - \rho\,, \tag{A-8}$$

$$G_{13} = G_{31} = m_0 m_3 (c_{13} + c_{44})\,. \tag{A-9}$$

The determinant of G is

$$D = det\, G = G_{22}\,(G_{11}G_{33} - G_{13}^2)\,.$$

The vertical slownesses of the P- and SV-waves are the roots of the polynomial $G_{11}G_{33} - G_{13}^2$, while the solutions of $G_{22} = 0$ give the vertical slownesses for the SH-wave. Since the P-wave displacement vector lies in the $[x_1, x_3]$ plane, formula (A-2) for the P-wave becomes

$$U_{pl\,1} = R\,(F_1 G_{33} - F_3 G_{13})\,, \tag{A-10}$$

$$U_{pl\,3} = R\,(F_3 G_{11} - F_1 G_{13})\,, \tag{A-11}$$

with

$$R = \frac{m_3 - m_{3P}}{det\, G}\bigg|_{m_{3P}} = \frac{1}{2c_{33}c_{44}m_{3P}(m_{3P}^2 - m_{3SV}^2)}\,. \tag{A-12}$$

m_{3P} and m_{3SV} are the vertical slownesses for the P- and SV-waves. m_{3SV} is given by

$$m_{3SV}^2 = \frac{(c_{11}m_0^2 - \rho)(c_{44}m_0^2 - \rho)}{c_{33}c_{44}m_{3P}^2} \tag{A-13}$$

Taking into account that for m_{3P} $G_{11}G_{33} - G_{13}^2 = 0$, we find from (A-10) and (A-11):

$$|\vec{U}_{pl}| = RF_u\,(G_{11} + G_{33})\,, \tag{A-14}$$

where F_u is the projection of the point force on the plane-wave displacement vector $\vec{U}_{pl}$. Substutuing R from (A-12) and (A-13), G_{11} from (A-6) and G_{33} from (A-8) into (A-14) yields

$$|\vec{U}_{pl}| = \frac{F_u m_{3P}}{2} \frac{m_0^2(c_{11}+c_{44}) + m_{3P}^2(c_{33}+c_{44}) - 2\rho}{m_{3P}^4 c_{33}c_{44} - (c_{11}m_0^2 - \rho)(c_{44}m_0^2 - \rho)}. \tag{A-15}$$

Equation (A-15) is valid for general transverse isotropy. At this point, we substitute $\epsilon = (c_{11} - c_{33})/(2c_{33})$, $m_0 = \frac{\sin\theta}{V}$, and $m_{3P} = \frac{\cos\theta}{V}$, and introduce the weak-anisotropy approximation for the P-wave phase velocity (Thomsen, 1986)

$$V_P(\theta) = V_{P0}\left(1 + \delta \sin^2\theta \cos^2\theta + \epsilon \sin^4\theta\right). \tag{A-16}$$

Formula (A-16) along with the expressions for ϵ, m_0, and m_{3P} can be used to transform (A-15) for weak transverse isotropy. Linearization in δ and ϵ, after tedious but straightforward algebra, gives

$$|\vec{U}_{pl}| = \frac{F_u}{2V\rho\cos\theta}\left[1 + 2\sin^2\theta(\delta\cos 2\theta + 2\epsilon\sin^2\theta)\right]. \tag{A-17}$$

The next step is to obtain the weak-anisotropy approximation for $\frac{d^2\Phi}{d\theta^2}$ (A-5). Expressing r and z through the source-receiver distance R ($r = R\sin\psi$, $z = R\cos\psi$), we find

$$r\sin\theta + z\cos\theta = R\cos(\psi - \theta), \tag{A-18}$$

and

$$\frac{r\cos\theta - z\sin\theta}{r\sin\theta + z\cos\theta} = \frac{\tan\psi - \tan\theta}{1 + \tan\psi\tan\theta} \tag{A-19}$$

The weak-anisotropy approximation for the group angle ψ is (Thomsen, 1986)

$$\tan\psi = \tan\theta\left[1 + 2\delta + 4(\epsilon - \delta)\sin^2\theta\right]. \tag{A-20}$$

Using equations (A-18), (A-19), and (A-20), and dropping the terms quadratic in ϵ and δ from equation (A-5), we get

$$\frac{d^2\Phi}{d\theta^2} = \frac{R}{V}\left(1 + \frac{1}{V}\frac{d^2V}{d\theta^2}\right). \tag{A-21}$$

Substituting the phase-velocity function (A-16) into the numerator of equation (A-4) yields

$$\left(\frac{\cos\theta}{V} + \frac{d(1/V)}{d\theta}\sin\theta\right) = \frac{\cos\theta}{V}\left[1 - 2\sin^2\theta(\delta\cos 2\theta + 2\epsilon\sin^2\theta)\right]. \qquad \text{(A-22)}$$

Finally, formulas (A-17), (A-21), and (A-22) are substituted into the original stationary-phase expression (A-4):

$$|\vec{U}| = \frac{F_u}{4\pi\rho V^2 R}\,\frac{1}{\sqrt{\frac{\sin\psi}{\sin\theta}\left(1 + \frac{1}{V}\frac{d^2V}{d\theta^2}\right)}}. \qquad \text{(A-23)}$$

Equation (A-23) can be fully linearized in the anisotropies ϵ and δ. However, expression (A-23) is a useful intermediate result because analogous derivations lead to the same formula for S-waves. Fully linearized expressions for each wave (P, SV, SH) are discussed in the main text.

2-D depth migration in transversely isotropic media using explicit operators

Omar Uzcategui

2-D depth migration in transversely isotropic media using explicit operators

Omar Uzcategui

ABSTRACT

Stable, explicit depth-extrapolation filters can be used to propagate plane waves corresponding to the qP and qSV (quasi-P and quasi-SV propagation) modes for transversely isotropic media in which the axis of symmetry is vertical (VTI). Here, I discuss and compare results of two different methods for obtaining the filters. The first, a modified Taylor series method, is used to calculate N-coefficients of a finite-length filter such that the Taylor expansion around vertical propagation matches the spatial Fourier transform of the downward continuation operator for VTI media. Second, a least-squares method is used to calculate the filter coefficients such that the amplitude and phase departures from the ideal response of the downward continuation operator for VTI media are minimized over a range of frequencies and propagation angles. In both methods, the amplitude response of the filter is forced to be less than unity in the evanescent region and close to unity in the propagation region in order to achieve stability.

In general, as exemplified in the cases studied here, the constrained least-squares method produced filters with accurate wavefield extrapolation for a wider range of propagation angles than that obtained for the modified Taylor series method. In both methods, the maximum angle that can be accurately propagated depends on the ratio of frequency to vertical phase velocity (f/V_v), and on the length of the filter. However, for a fixed length and for a given ratio f/V_v, the maximum angle propagated with accuracy depends on the elastic constants of the medium. The accuracy of the filters degrades as the degree of anisotropy becomes more extreme. For anisotropic media that are almost elliptical, the filters are quite accurate.

INTRODUCTION

Explicit filters (Holberg, 1988; Hale, 1991a) are a useful tool in the extrapolation of seismic wavefields for depth migration in isotropic media. Explicit filtering is attractive because it can be implemented efficiently on pipelined and parallel computers. In addition, explicit methods can be easily extended for 3-D depth migration

in isotropic, heterogenous media (Hale, 1991b). For transversely isotropic media, explicit depth-extrapolation filters can be obtained following the same steps as in the isotropic case but with special considerations for the anisotropic nature of the phase velocity.

The modified Taylor series method used by Hale (1991a) for isotropic media can be adapted for VTI media, but now considering that the horizontal wavenumber and the phase velocity are functions of the propagation angle. The basic idea is to find a filter in frequency-midpoint ($\omega - x$) space such that its spatial Fourier transform matches (in the propagation region) that of the downward continuation operator for TI media. To ensure attenuation of the evanescent energy, some degrees of freedom in the filter are used to force amplitude values to be less than unity in the evanescent region.

Holberg (1988) obtained explicit depth-extrapolation filters for isotropic media by minimizing the squared error of amplitude and phase of the filter in a given range of propagation angles with the vertical ($0 \leq \theta \leq \theta_{max}$). For VTI media I follow the same approach, but now take into account the theoretical expression of the downward-continuation operator for VTI media. To get stability for angles greater than θ_{max} and in the evanescent region, I introduce a penalty function that grows for amplitude values of the filter greater than unity. I then use a conjugate gradient algorithm to minimize the resulting function.

FILTER DESIGN

The theoretical downward-continuation operator for VTI media can be obtained from the equations of motion for elastic plane waves propagating in the vertical (x, z) plane (Kitchenside, 1991). The match is done only in the propagation region; the filter must attenuate the energy in the evanescent region. For a particular frequency ω in the propagation region, the spatial Fourier transform of the filter $W(k_x, \omega)$ must approximate

$$D\left[k_x(\theta)\right] = exp\left\{ i\frac{\Delta z}{\Delta x}\left[\left(\frac{\omega \Delta x}{V_p(\theta)}\right)^2 - k_x^2(\theta)\right]^{\frac{1}{2}}\right\}, \tag{1}$$

where $D\left[k_x(\theta)\right]$ is the exact downward-continuation operator for the medium, Δz and Δx are the vertical and horizontal sampling intervals, and $V_p(\theta)$ and $k_x(\theta)$ are the phase velocity and the horizontal wavenumber for a given propagation mode (qP or qSV), evaluated at the propagation angle θ. $k_x(\theta)$ is related to the phase velocity by

$$\frac{k_x(\theta)}{\Delta x} = \frac{\omega \sin(\theta)}{V_p(\theta)}, \tag{2}$$

$W(k_x, \omega)$ can be written as

$$W(k_x,\omega) = \sum_{l=0}^{(N-1)/2} (2-\delta_{l0}) h_l(\omega) cos(k_x l), \tag{3}$$

where δ_{l0} is the Kronecker delta function, $h_l(\omega)$ are complex coefficients of the filter, and N is the number of coefficients. Because $W(k_x,\omega)$ is symmetric in k_x, only $(N+1)/2$ different coefficients $h_l(\omega)$ are needed to determine the filter response.

In the modified Taylor series method (Hale, 1991a), the filter coefficients $h_l(\omega)$ are obtained by matching the filter's Taylor expansion around $\theta = 0$ with that of the downward-continuation operator. In particular, because the filter is symmetric and we want this filter to be exact for vertical propagation, we would match the first $(N+1)/2$ even derivatives at $\theta = 0$. However, to obtain attenuation in the evanescent region, we must try to match fewer than $(N+1)/2$ derivatives and let the remaining degrees of freedom in the filter be used to ensure that the amplitude of the filter is less than unity in that region ($|W(k_x,\omega)| \leq 1$). Following Hale (1991a), the filter coefficients are represented as a sum of M weighted basis functions:

$$h_l(\omega) = \sum_{m=0}^{M-1} c_m(\omega) b_{ml}, \tag{4}$$

where the basis function b_{ml} is given by

$$b_{ml} = (2-\delta_{m0}) \cos(\frac{2\pi ml}{N}). \tag{5}$$

The problem is now to determine M complex weights $c_m(\omega)$. To achieve stability, the number M of weights must be less than the number $(N+1)/2$ of filter coefficients, so only the first M derivatives of the Fourier transform of the filter are matched with those of the downward-continuation operator for VTI media. The remaining $(N+1)/2 - M$ degrees of freedom are used to ensure stability.

The Fourier transform of the extrapolation filter will be now

$$W(k_x,\omega) = \sum_{m=0}^{M-1} c_m(\omega) B_m[k_x(\theta)] \simeq D[k_x(\theta)] \tag{6}$$

where $B_m[k_x(\theta)]$ is given by

$$B_m[k_x(\theta)] = (2-\delta_{m0}) \sum_{l=0}^{(N-1)/2} (2-\delta_{l0}) \cos(\frac{2\pi ml}{N}) \cos[k_x(\theta) l]. \tag{7}$$

The basic difference between this Fourier transform of the basis function $B_m[k_x(\theta)]$ and that given by Hale (1991) for isotropic media is that in this case (VTI media) the horizontal wavenumber k_x also depends on θ through $V_p(\theta)$ (see equation (2)).

In equation (6), M terms in the Taylor series expansion around $\theta = 0$ for the filter $W(k_x, \omega)$ are matched with those terms corresponding to the Taylor series expansion of the downward continuation operator $D(k_x)$. These Taylor series expansions are given by

$$W[k_x(\theta), \omega)] \simeq \sum_{m=0}^{M-1} c_m(\omega) \left[B_m(0) + \frac{B_m^2(0)\theta^2}{2!} + \frac{B_m^4(0)\theta^4}{4!} + ... \frac{B_m^{2M}(0)\theta^{2M}}{(2M)!} \right]$$

$$D[k_x(\theta)] \simeq D(0) + \frac{D^2(0)\theta^2}{2!} + \frac{D^4(0)\theta^4}{4!} + ... \frac{D^{2M}(0)\theta^{2M}}{(2M)!},$$

where $D^{(2l)}(0)$ and $B_m^{(2l)}(0)$ are the $2l^{th}$ derivatives of the downward continuation operator and basis functions respectively, evaluated at $\theta = 0$. Matching of these Taylor expansions gives a linear system of equations for the coefficients $c_m(\omega)$

$$\sum_{m=0}^{M-1} c_m(\omega) B_m^{(2l)}(0) = D^{(2l)}(0) \quad l = 0, 1, ..M, \tag{8}$$

$$B_m^{(2l)}(0) = (2 - \delta_{m0}) \sum_{n=0}^{(N-1)/2} \cos(\frac{2\pi mn}{N}) \cos[nk_x(\theta)]^{(2l)}(0), \tag{9}$$

where $\cos[nk_x(\theta)]^{2l}(0)$ is the $2l^{th}$ derivative of $\cos[nk_x(\theta)]$ evaluated at $\theta = 0$. This system of equations is solved for $c_m(\omega)$, and equation (4) is used to calculate the final filter coefficients $h_l(\omega)$.

For the least-squares method, the match of the Fourier transform of the filter with the downward-extrapolation operator is done over a range of propagation angles ($\theta = 0, .., \theta_{max}$). Following Holberg (1988), we do the matching by minimizing the sum of the square errors in the amplitude and phase response of the filter,

$$J(\omega) = \int_{\theta=0}^{\theta=\theta_{max}} (\delta^2 + \alpha^2) dk_x \tag{10}$$

subject to the constraints

$$|W(k_x, \omega)| < 1.0 \ \ for \ \ |k_x| > \frac{\omega sin(\theta_{max})}{V_p(\theta_{max})}. \tag{11}$$

Here, α is the amplitude error of the filter, given by $\alpha = 1.0 - |W(k_x, \omega)|$, and δ is the phase error of the filter given by $\delta = k_z \Delta z - tan^{-1} \frac{Im(W(k_x,\omega))}{Re(W(k_x,\omega))}$.

Constraint (11) was incorporated into the least-squares problem (10) by adding to the error function $J(\omega)$ a penalty function that is proportional to the square of the amplitude error when the amplitude of the filter exceeds unity. I then use for the minimization the IMSL subroutine *NCONG*, which solves a non-linear least-squares problem using a conjugate-gradient algorithm.

FILTER ACCURACY FOR A SINGLE FREQUENCY

Taylor series method

For the Taylor series method we can see from equation (8) that the degree to which the filter would approach the downward-continuation operator depends on the number M of terms used in the Taylor expansion. Long filters will use more terms, so they better approximate the $D(k_x)$ operator than do short filters. However, for VTI media the downward-continuation operator is also a function of the phase velocity, whose variations with respect to the propagation angle θ changes from one medium to another. For media with smooth variation of $V_p(\theta)$ with respect to θ, the Taylor expansion of $V_p(\theta)$ would be a good representation of $V_p(\theta)$ itself, and only a few terms in (8) would be used. For strongly anisotropic media with large variations of $V_p(\theta)$, more terms would be needed in equation (8).

The downward-continuation operator is a complex exponential (see equation (1)) of unity magnitude in the propagation region ($0° \leq \theta \leq 90°$). The Taylor series expansion would be a good representation of $D(k_x)$ when its amplitude is equal to one and its phase is equal to the phase of $D(k_x)$. Figure 1 shows the amplitude for the Taylor series expansion of the downward continuation operator as a function of the propagation angle, for several VTI media. The vertical phase velocities and anisotropy parameters for these media are given in Table 1, with the same notation given by Thomsen (1986). The number of terms in the expansion was 19, $\Delta z/\Delta x = 1$ and, for all the cases shown, the ratio $\omega\Delta x/V_p(0)$ (normalized frequency in radians) is constant and equal to 1.86. This ratio was kept constant because the downward-continuation operator is basically a function of $\omega\Delta x/V_p(\theta)$. If I had fixed ω the ratio, $\omega\Delta x/V_p(0)$ would change with $V_p(0)$ for the different media and thus the comparison would not be fair. From Table 1, we see for example, that a ratio of $\omega\Delta x/V_p(0)$ of 1.86 for the Taylor sandstone with $\Delta x = 10$ m, corresponds to a frequency of 27 Hz for the q-SV propagation mode and 50 Hz for the q-P mode.

Figure 1 shows that for the first two media (Berea and Lance sandstones), the amplitude of the Taylor expansion for the q-P and q-SV modes matches the amplitude of $D(k_x)$ in the range 0 to 60°. Similar fits, not shown here, are obtained for the phase response. For the other two media (Taylor sandstone and Cotton Valley shale) the Taylor expansion can approximate the amplitude of $D(k_x)$ only in the range 0 to 50°. A filter designed to match these Taylor expressions could propagate waveforms accurately only until a maximum of 60° (Berea and Lance sandstones) and 50° (Taylor sandstone and Cotton Valley shale). Even when the length of the filter and the ratio $\omega\Delta x/V_p(0)$ is the same for all the media in Figure 1, the maximum angle that can be accurately propagated by the filter is different for each medium. That is not the case for isotropic media, where, for a given length of the filter, this maximum angle of propagation is limited only by the ratio $\omega\Delta x/V_p(0)$ (Hale, 1991a). The curves in Figures 1 through 3 all pertain to a single normalized frequency. Similar curves result for other normalized frequencies, but the dip limit for acceptable accuracy becomes more restricted as normalized frequency increases.

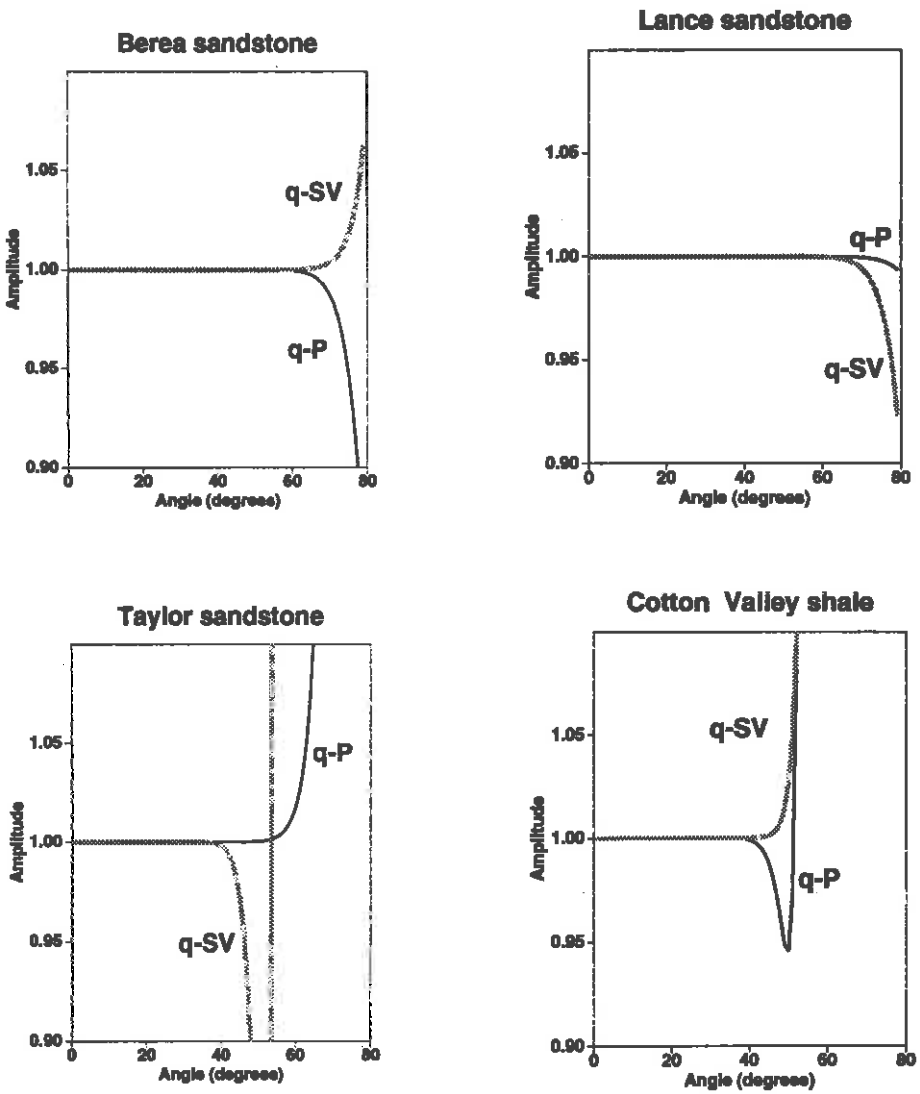

FIG. 1. Amplitude of Taylor expansions for the downward-continuation operators of several VTI media, and for both qP and qSV propagation modes. The number of terms in the expansion is N=19, and a normalized frequency of 1.86 radians is used. The Berea and Lance sandstones can be considered as weakly anisotropic. Taylor sandstone and Cotton Valley shale are moderately anisotropic.

Medium	α_0 km/s	β_0 km/s	ϵ	δ
Berea sandstone	4.206	2.664	0.002	0.020
Lance sandstone	5.029	2.987	-0.005	-0.015
Taylor sandstone	3.368	1.829	0.110	-0.035
Cotton Valley shale	4.721	2.890	0.135	0.205
Mesaverde clayshale (a)	3.928	2.055	0.334	0.730
Mesaverde clayshale (b)	3.794	2.074	0.189	0.204
Gypsum-weathered	1.911	0.795	1.161	-0.140

Table 18. Vertical phase velocities (P-wave α_0 and S-wave β_0) and anisotropy parameters (ϵ and δ) for several VTI media, in the notation of Thomsen (1986).

According to Thomsen (1986), a medium can be considered as weakly anisotropic if the values of the anisotropy parameters ϵ and δ are small with respect to unity. On this basis, the Berea and Lance sandstones can be considered as weakly anisotropic, and the Taylor sandstone and Cotton Valley shale moderately anisotropic. Figure 2 shows amplitude responses for two media that are highly anisotropic; the Mesaverde clayshale (a) and the weathered gypsum both have high values of ϵ and δ (see Table 1). For the same length of filter and ratio $\omega\Delta x/V_p(0)$ used in Figure 1, the filters can propagate accurately to a maximum angle of only 25° for both the qP and qSV modes in the Mesaverde clayshale (a), and to 35° and 20° for the qP and qSV modes, respectively, in the weathered gypsum.

Figures 1 and 2 showed just the Taylor series expansions of the downward-continuation operator for several VTI media and for a given $\omega\Delta x/V_p(0)$. To obtain the filter coefficients $h_l(\omega)$ in the modified Taylor series method, these Taylor series expansions are used in the right-hand side of equation (8) and that system of equations is solved for the coefficients $c_m(\omega)$ to get finally $h_l(\omega)$ using equation (4). Figure 3 shows detailed amplitude spectra of filters in the propagation region ($\theta \leq 90°$) obtained from the Taylor series expansions shown in Figures 1 and 2 for the Taylor sandstone and the weathered gypsum. The amplitude scale displays only values close to unity to show the stability in the propagation region. Note that the maximum angle accurately propagated in Figures 1 and 2 is larger than the angle shown in Figure 3. The filters designed by the modified Taylor series method must not only match the Taylor expansions but also attenuate the energy in the evanescent region. Therefore, some degrees of freedom have been used to obtain attenuation, so the designed filter cannot match exactly the Taylor series expansions. Figure 4 shows amplitude spectra of the filters in Figure 3, now as a function of normalized wavenumber (in cycles) rather than dip; 0.5 cycles corresponds to Nyquist wavenumber ($\pi/\Delta x$). The amplitude scale has been increased to show attenuation in the evanescent region. Normalized wavenumbers greater than 0.2 and 0.18 correspond to evanescent waves for

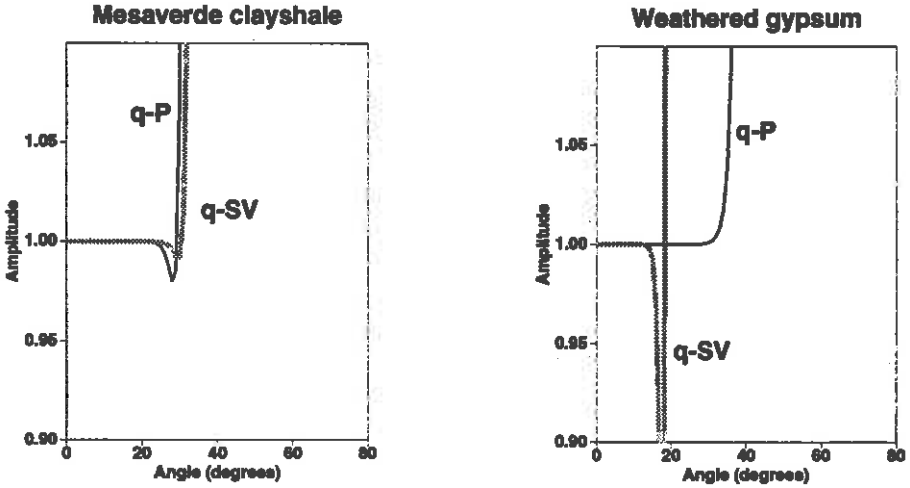

FIG. 2. Amplitude of Taylor expansions for the downward-continuation operators of the Mesaverde clayshale (a), and weathered gypsum, and for both qP and qSV propagation modes. The number of terms in the expansion is N=19, and a normalized frequency of 1.86 radians is used. The media shown in this figure can be considered as strongly anisotropic.

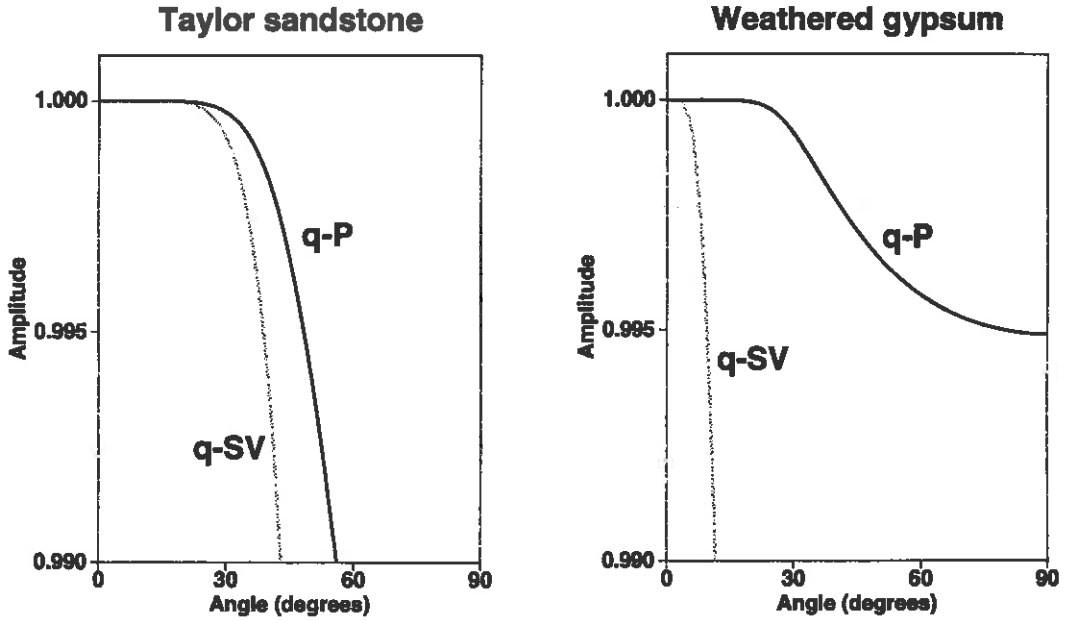

FIG. 3. Detailed amplitude response in the propagation region for qP and qSV, 19-coefficient filters obtained from the Taylor expansions of Figures 1 and 2. The normalized frequency is 1.86 radians.

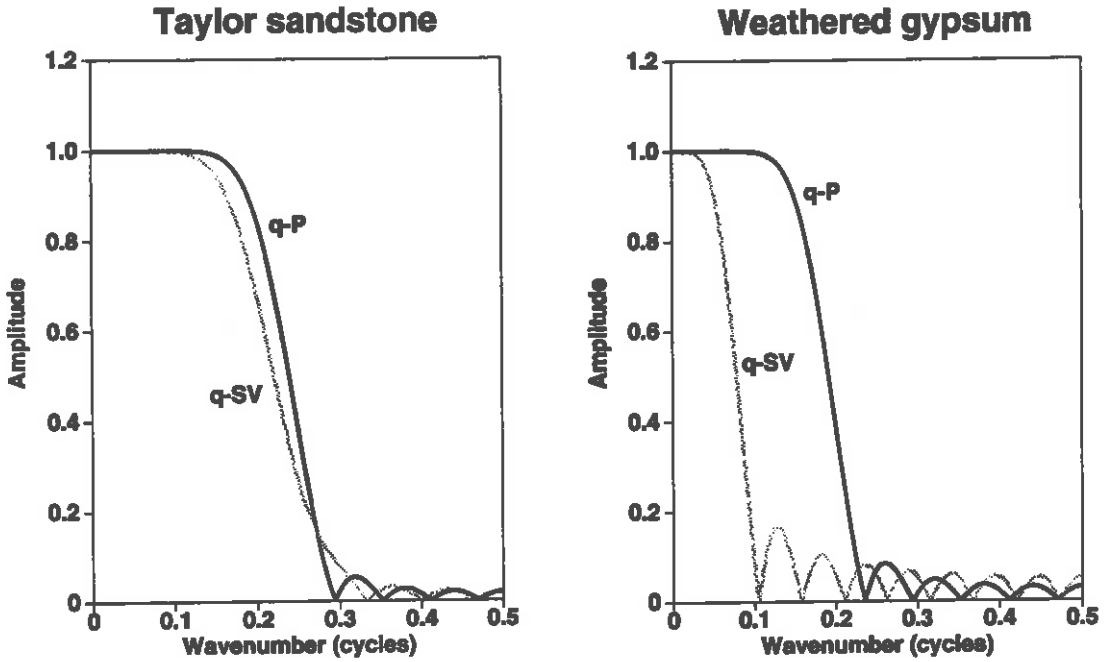

FIG. 4. Amplitude response for the same filters in Figure 3 but now evaluated as a function of wavenumber. Wavenumbers greater than 0.2 correspond to the evanescent region.

the Taylor sandstone and weathered gypsum respectively. The small amplitudes in the evanescent region show that both extrapolators are clearly stable in the evanescent region.

Least-squares method

The filter accuracy in the least-squares method will also depend on the number of coefficients used, but now, we match the filter response with the exact downward continuation operator and not with its Taylor series expansion, as we did in the Taylor series method. This approach will avoid the progressively more poorer fit of the theoretical operator by the Taylor series expansion for increasing propagation angles. However, the amplitude spectrum of a filter designed by least-squares methods has an oscillatory character, as seen in Figure 5, with amplitude values greater than unity for some wavenumbers. As demonstrated by Holberg (1988), the magnitude of these oscillations is reduced by restricting the range of propagation angles for which the fit is done. This introduces a new parameter (absent in the Taylor series method) in the design of the filter— the maximum design angle (θ_{max} in equation (10)).

Figure 5 shows amplitude spectra as a function of dip (left) and as a function of wavenumber (right) for filters obtained using the least-squares method, for the Taylor sandstone and for the same normalized frequency used in Figures 1 and 2.

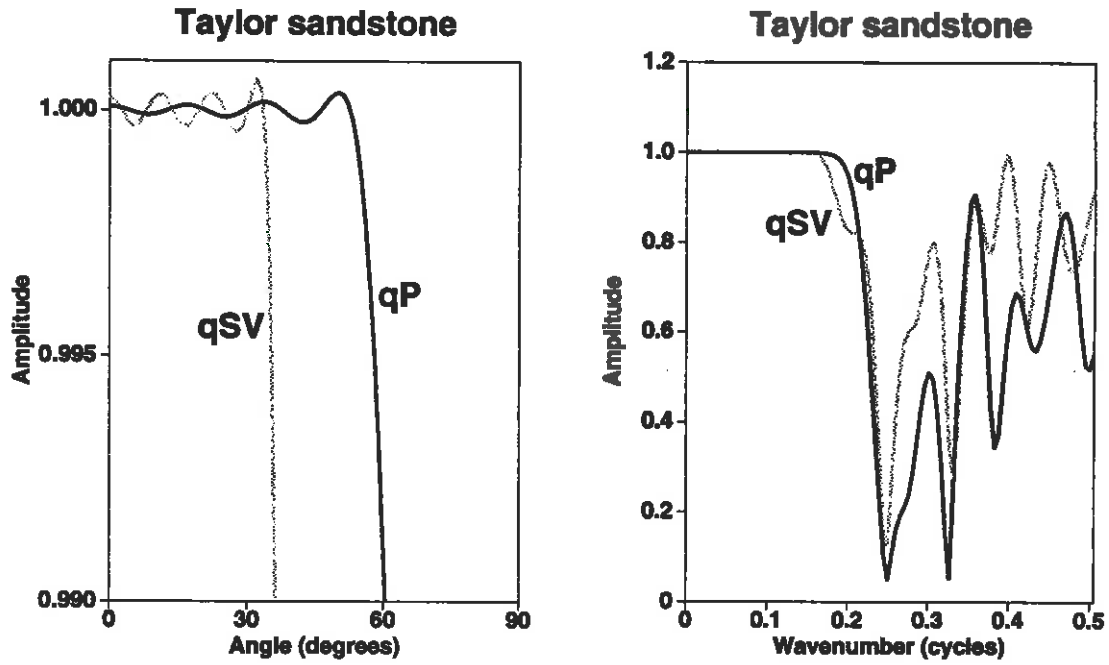

FIG. 5. Detailed amplitude response in the propagation region (left), and amplitude as a function of wavenumber (right) for qP and qSV 19-coefficient filter obtained using the least-squares method. The normalized frequency is 1.86 radians.

The maximum design angles were $\theta_{max} = 60°$ and $35°$ for the qP and qSV mode, respectively. Note the ripples in the propagation region seen in the detailed amplitude spectrum. Although some of these amplitude values are greater than unity, they do not exceed 1.001, which guarantees the application of this filter for about one thousand steps of downward extrapolation with a maximum error of approximately $e \simeq 2.71$. Both extrapolators (qP and qSV) are stable, and attenuate the energy in the evanescent region.

For a given length of filter, there will be a maximum design angle (θ_{max}) in the least-squares method beyond which accuracy and stability are lost. The maximum allowed design angle increases somewhat as filter length increases. Here, an accurate and stable filter is one having a maximum absolute amplitude error of no more than 0.001 in the region $\theta \leq \theta_{max}$, and amplitude values less than unity for $\theta_{max} < \theta \leq 90°$ and in the evanescent region. An N-coefficient filter cannot achieve both goals (accuracy and stability) for θ_{max} close to 90° because there are not enough degrees of freedom to satisfy both conditions. The maximum design angles in Figure 5 were obtained after several tests with differents θ_{max}, beginning with a high initial value of θ_{max} and reducing this value until an accurate and stable filter is found.

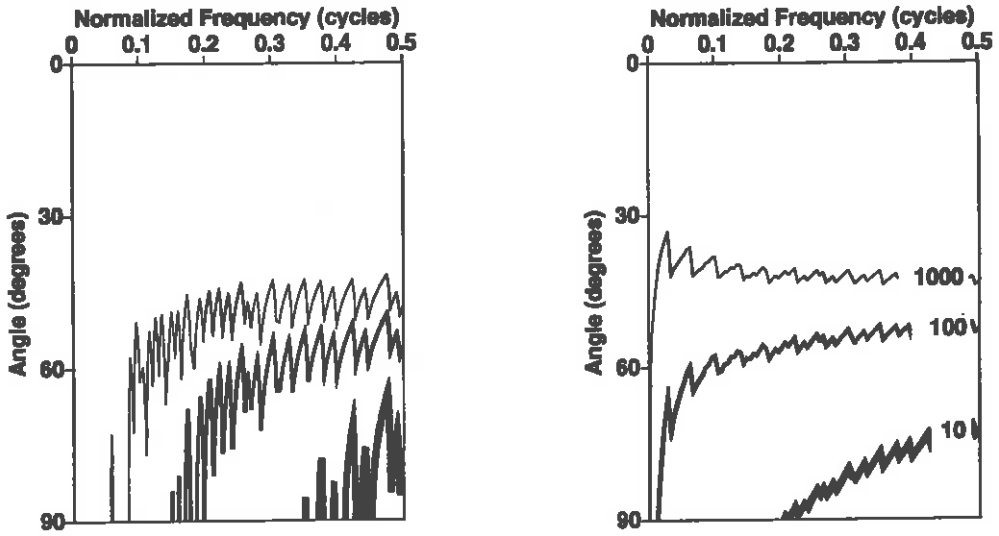

FIG. 6. Contours of amplitude error (left) and phase error (right) for the qP mode in the Taylor sandstone. The 39-coefficient filter was computed by the modified Taylor series method. For the amplitude error, contour levels are -1/1000 (thin), -1/100 (medium), and -1/10 (thick) for each step of depth extrapolation. The phase errors are labeled with the number of extrapolation steps required to accumulate one-half cycle of phase error.

ACCURACY FOR A RANGE OF FREQUENCIES

In a real application, several filters are obtained to propagate a range of frequencies. Figure 6 shows the amplitude and phase errors for the Taylor sandstone using a 39-coefficient filter based on the modified Taylor series method. The errors are shown as a function of normalized frequency $f\Delta x/V_p(0)$ in cycles, and propagation angle in degrees. The thin, medium, and thick contours correspond, respectively, to amplitude errors of $-1/1000$, $-1/100$, and $-1/10$. The amplitude error was calculated as the difference $\mid W \mid -1.0$, so negative values in the error indicate amplitude values in the filter less than unity. An amplitude error of $-1/1000$ corresponds to a filter amplitude of 0.999; after 1000 steps of downward extrapolation with this error, the amplitude of the initial waveform extrapolated will be $(0.999)^{1000} \simeq 0.4$ times the initial amplitude. Phase errors are labeled with the number of steps of downward extrapolation needed to accumulate an error of one-half cycle (π radians). Figure 6 shows that the Taylor sandstone's filter will attenuate waves propagating at about 45° by a factor of 0.4, and with one-half cycle of phase error after 1000 steps of downward extrapolation.

Figure 7 shows the corresponding errors for a 39-coefficient filter and the Taylor

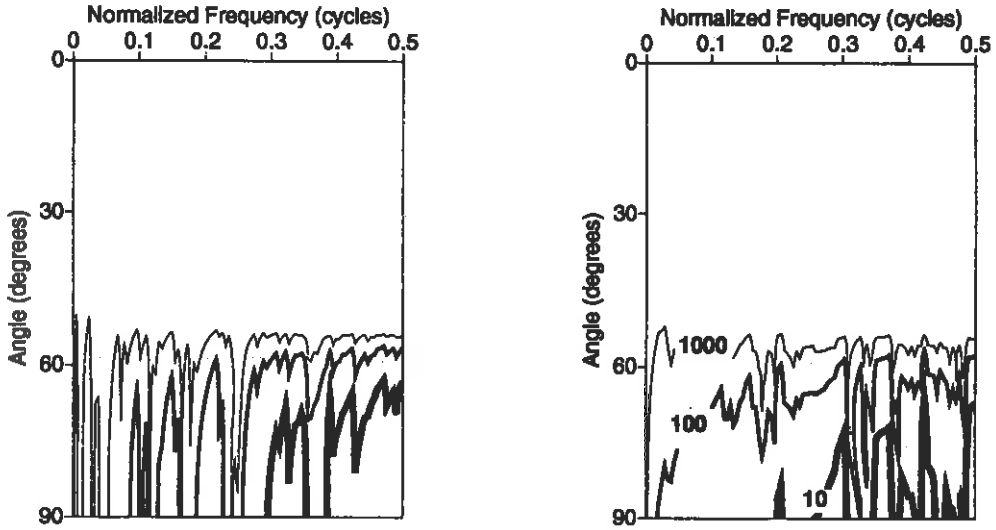

FIG. 7. Amplitude error contours (left) and phase error contours (right) for the qP mode in the Taylor sandstone (39-coefficient filter; least-squares method).

sandstone, now using the least-squares method. After 1000 steps of downward extrapolation, seismic waves propagating at more than 60° will accumulate error that is comparable to errors for waves propagating at only 45° in Figure 6. Thus, for the same number of filter coefficients, almost 15° has been gained through use of the least-squares approach.

Figures 8 and 9 compare amplitude and phase errors of a 39-coefficient filter for the qP mode in the weathered gypsum using the Taylor series and least-squares methods. The design angle used in the least-squares method was 30°. Note the small increase ($\simeq 5°$) in the range of angles for accurate propagation when the least-squares method is used. Figures 10 and 11 show the corresponding errors for the qSV propagation mode in the Taylor sandstone. The design angle used in the least-squares method was 35°. Comparing with Figures 6 and 7, we see that for a given medium (Taylor sandstone), the range of angles for accurate propagation is better for the qP than for the qSV mode. Note in Figure 10 the irregular error in amplitude and phase produced by the Taylor-series filter; however, for the least-squares filter, the error is uniform for angles less than the design angle ($\theta_{max} = 35°$) and very irregular beyond this region, where there is no control over the phase and amplitude of the filter. Figure 12 shows the amplitude and phase errors for the qSV propagation mode in the weathered gypsum using the Taylor series method. For this medium, errors in both amplitude and phase are large for very small propagation angles. The result for the least-squares

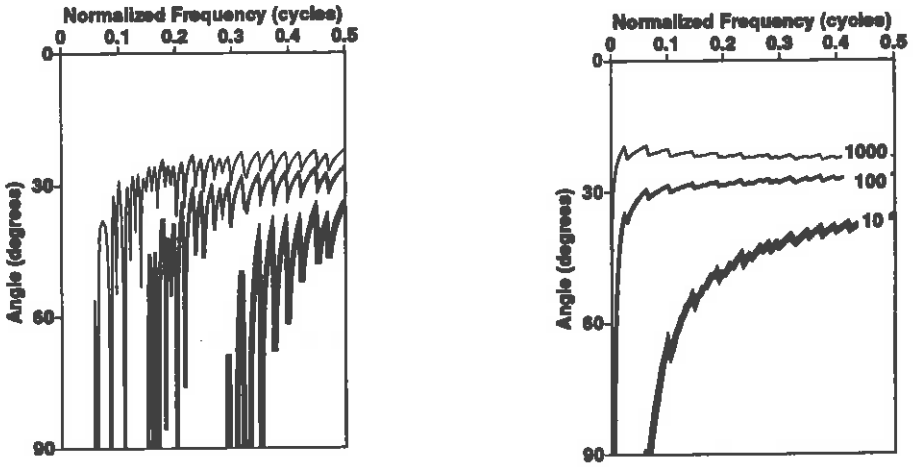

FIG. 8. Amplitude error contours (left) and phase error contours (right) for the qP mode in the weathered gypsum (39-coefficient filter; Taylor series method).

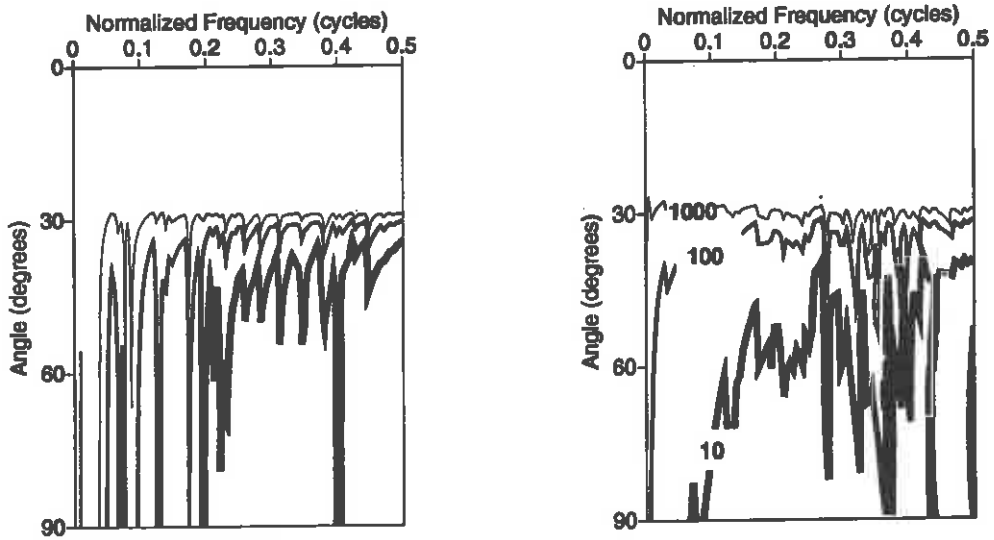

FIG. 9. Amplitude error contours (left) and phase error contours (right) for the qP mode in the weathered gypsum (39-coefficient filter; least-squares method).

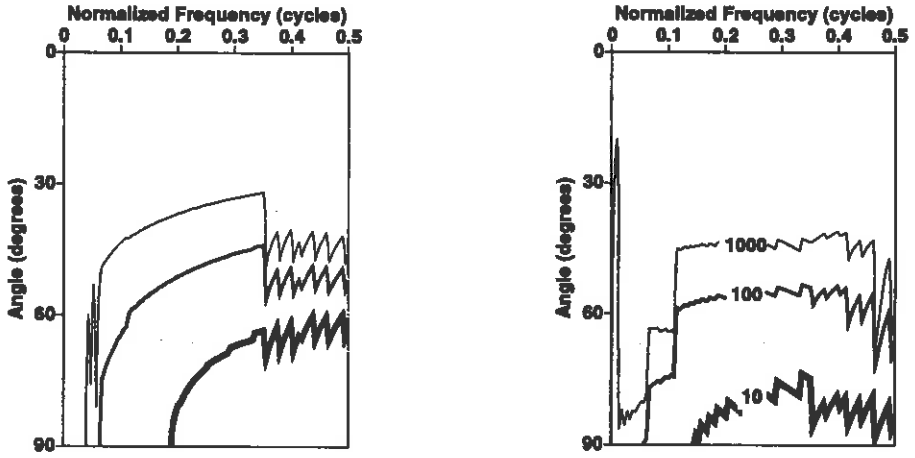

FIG. 10. Amplitude error contours (left) and phase error contours (right) for the qSV mode in the Taylor sandstone (39-coefficient filter; Taylor series method).

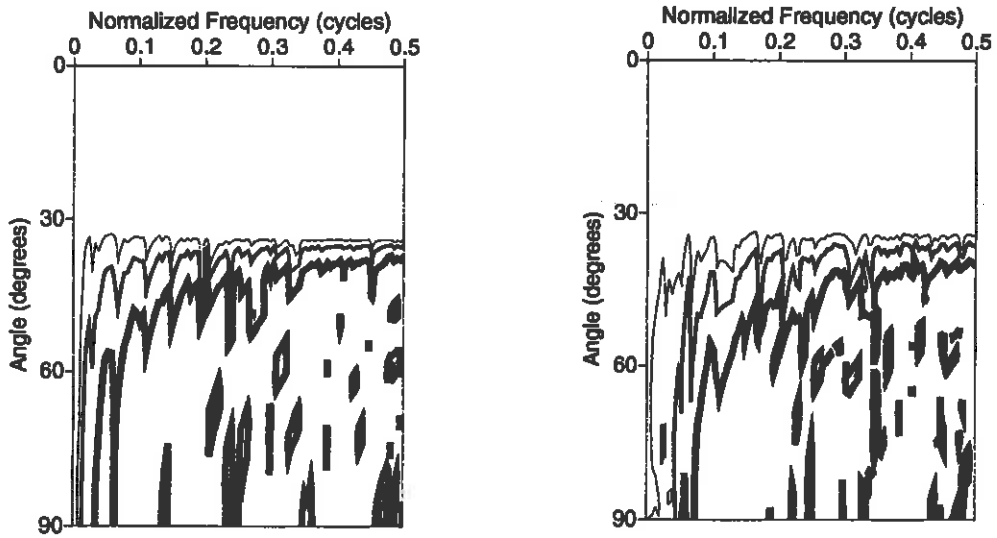

FIG. 11. Amplitude error contours (left) and phase error contours (right) for the qSV mode in Taylor sandstone (39-coefficient filter; least-squares method).

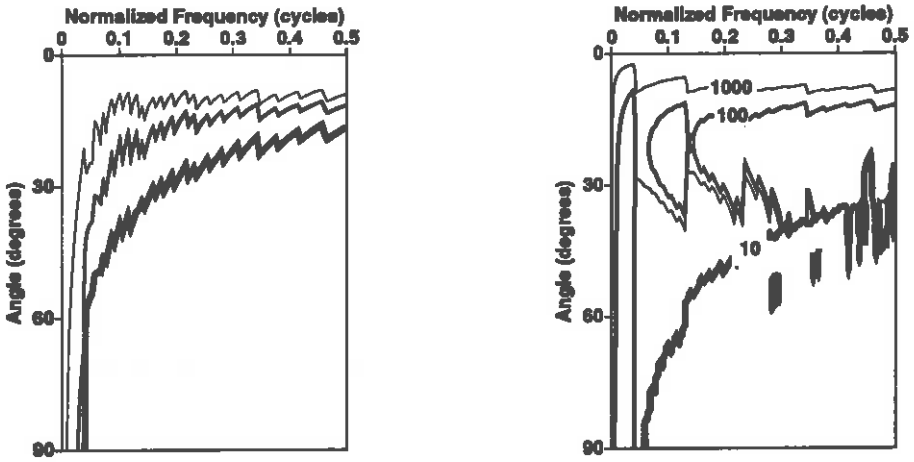

FIG. 12. Amplitude error contours (left) and phase error contours (right) for the qSV mode in the weathered gypsum (39-coefficient filter; Taylor series method). Only low propagation angles have small errors in amplitude. The phase error is large for almost all the propagation angles.

method (not shown here) is no better. Moreover, use of filters with more than 39 coefficients in both methods is of little help.

MIGRATION IMPULSE RESPONSES

The performance of the operators can also be illustrated by study of migration impulse responses. The same migration program used by Hale (1991) for isotropic media was used here to calculate the migration impulse responses for the qP and qSV propagation modes. This same program can be used because in migration by explicit filtering, the downward continuation process is performed by space-variant convolution of the data with the explicit filters (Holberg, 1988). The convolution process is the same for both isotropic and VTI media; we need only change the filter coefficients.

Figure 13 shows qP impulse responses for the Taylor sandstone using the modified Taylor series method (left) and the least-squares method (right). In both tests, spatial sampling intervals $\Delta x = \Delta z = 10$ m, and the time sampling interval $\Delta t = 10$ ms; therefore, the Nyquist frequency is 50 Hz. The normalized frequency varies from 0 to 0.3 cycles. A trajectory of the theoretical impulse response (shown in the figures as a thin solid line) was calculated using the theoretical group velocity and ray angle (Thomsen, 1986) for this medium. Note that the large dips are more severely attenuated by the modified Taylor series filter than by the least-squares filter. Although steep events (corresponding to high propagation angles) are attenuated for

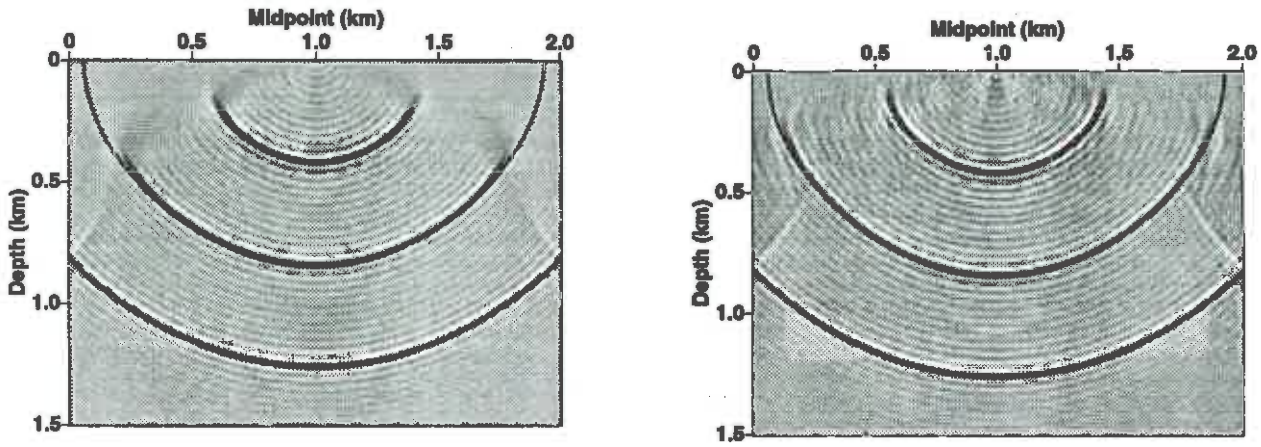

FIG. 13. Impulse responses of migration via N=39-coefficient explicit extrapolators for the qP propagation mode in the Taylor sandstone. Modified Taylor series (left) and least-squares (right) methods.

both filters, the fit with the theoretical impulse response is good for a wide range of angles.

Figure 14 shows qP impulse responses for the weathered gypsum, using the modified Taylor series method (left) and the least-squares method (right). The highest dip present in this response is lower than that obtained for the qP Taylor sandstone filter (compare with Figure 13). This basically reflects the behavior of the amplitude error shown in the Figures 8 and 9, where wavefield components with dips greater than 30° are propagated with large negative errors corresponding to amplitude values less than unity. Therefore, these components will be attenuated.

Figures 15 and 16 show qSV impulses for the Taylor sandstone and Mesaverde clayshale (b) (almost elliptical material; Thomsen, 1986), respectively. Both responses were calculated using 39-coefficient filters derived by the least-squares method. Note the attenuation at large dips for the Taylor sandstone. However, for the Mesaverde clayshale (b), steep events can be propagated accurately. Even when the number of coefficients is the same in both media, more accurate propagation is obtained for the almost elliptical material.

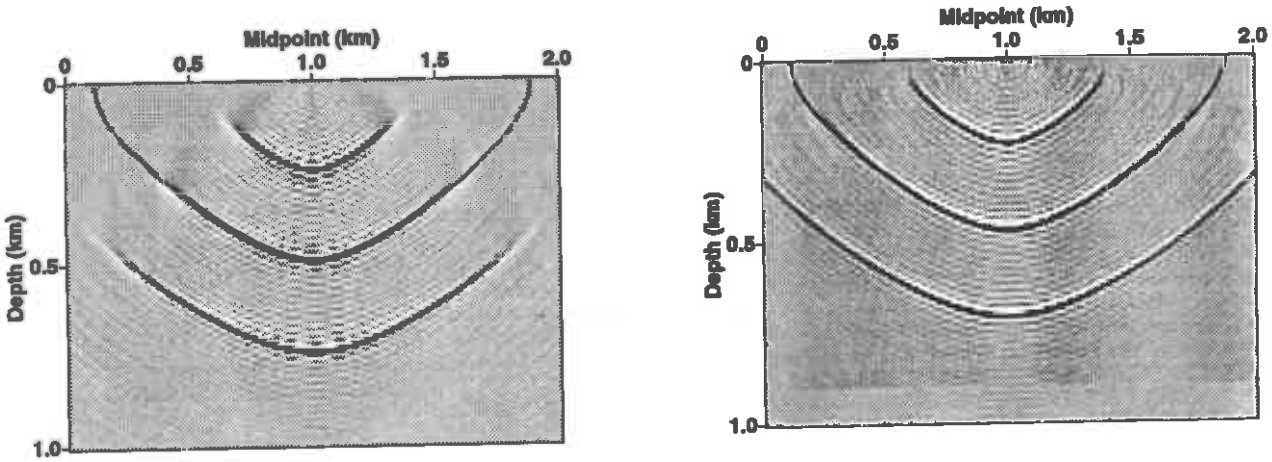

FIG. 14. Impulse responses of migration via N=39-coefficient explicit extrapolators for the qP propagation mode in the weathered gypsum. Modified Taylor series (left) and least-squares (right) methods.

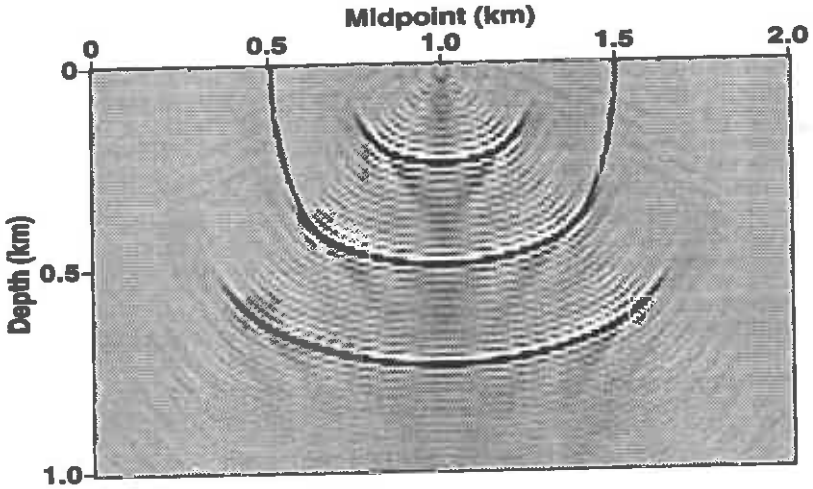

FIG. 15. Migration impulse responses via N=39-coefficient, explicit extrapolators for qSV waves in the Taylor sandstone. Least-squares method.

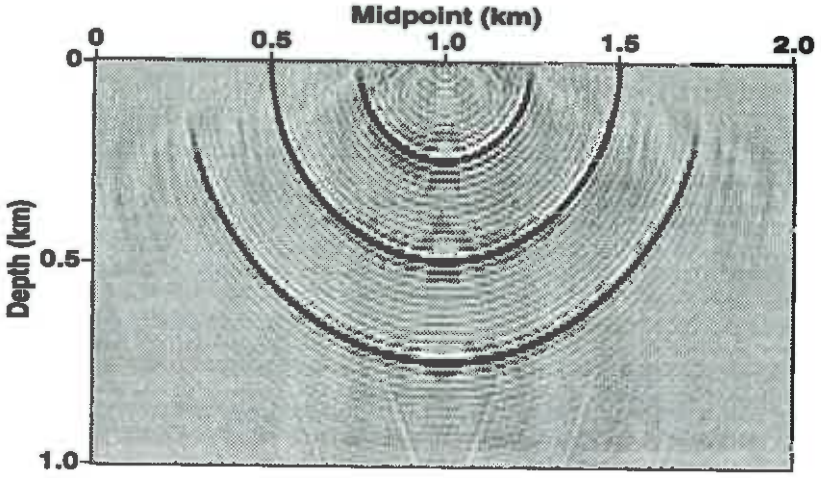

FIG. 16. Migration impulse responses via N=39-coefficient, explicit extrapolators for qSV waves in the Mesaverde clayshale(b). Least-squares method.

CONCLUSION

Explicit depth-extrapolation filters for VTI media can be derived either by a generalization of the modified Taylor series method or by a least-squares method initially developed for isotropic media.

Clearly, the results shown here are limited to the few models used, and also pertain to just VTI media. A similar approach for transversely isotropic media with a tilted axis of symmetry can be developed if the theoretical downward-continuation operator for such media is used in the equations developed here. In a qualitative way, the results in this paper show that the accuracy in the extrapolators (for a constant filter-length and normalized frequency) is a function of the elastic properties in the medium. In particular, more-accurate filters are obtained for weakly than for strongly anisotropic media. This result can be related to the behavior of the downward-continuation operator in the medium. Weakly anisotropic media need fewer filter coefficients than do strongly anisotropic media to produce a good representation of the downward-continuation operator. However, further analysis is neccesary to study the role of the anisotropy parameters (ϵ and δ) in the accuracy of the extrapolators. In particular, the fact that highly-accurate filters were obtained for almost elliptical anisotropic media ($\epsilon - \delta \simeq 0$) could be an indication that the accuracy of the filters would be a function of this difference.

The examples presented also show that the constrained least-squares method produced filters with accurate extrapolation for a wider range of propagation angles than that obtained for the modified Taylor series method. Again, the accuracy in both methods degrades as the degree of anisotropy becomes more extreme. For weakly

and moderately anisotropic media, the accuracy of the filters in doing downward extrapolation is comparable to that obtained by Hale (1991a) and by Holberg (1988) for isotropic media. Some alternative approach to improve the accuracy of the operators for strongly anisotropic media might be suggested once a quantitative analysis of the influence of ϵ and δ on the accuracy of the filters is performed.

ACKNOWLEDGMENTS

The author thanks INTEVEP, Venezuela, for its financial support. Thanks also to Professor Ken Larner and Ilya Tsvankin for their critical review of this paper.

REFERENCES

Claerbout, J. F., 1985, Imaging the earth's interior: Blackwell Scientific Publications, Inc.

Hale, I. D., 1991a, Stable explicit depth extrapolation of seismic wavefields: Geophysics, **56**, 1770–1777.

Hale, I. D., 1991b, 3-D depth migration via McClellan transformations: Geophysics, **56**, 1778–1785.

Holberg, O., 1988, Toward optimum one-way wave propagation: Geophys. Prosp., **36**, 99–114.

Kitchenside, P. W., 1991, Phase shift-based migration for transverse isotropy: 61 th Ann. Internat. Mtg., Soc. Expl. Geophys., Expanded Abstracts, 993–946

Thomsen, L., 1986, Weak elastic anisotropy: Geophysics, **51**, 1954–1966

Uren, N. F., Gardner G. H. F., and McDonald, J. A., 1990, The migrator's equation for anisotropic media: Geophysics, **55**, 1429–1434.

Migration by analytic continuation through a variable background medium

Michael S. Zhdanov and Timo Tjan

Migration by analytic continuation through a variable background medium

Michael Zhdanov and Timo Tjan

ABSTRACT

Conventional migration of wavefields is based on depth extrapolation of the upgoing field in reverse time. This extrapolation provides us with a means to determine the positions of reflectors and diffraction points and, therefore, to produce an image of a geological cross section. However, conventional depth extrapolation allows us to restore only some transformation of the field in the subsurface rather than the true field. For example, this approach rules out the proper imaging of multiple reflections. Meanwhile, there is reason to expect that a different reconstruction of the seismic wavefield — reconstruction by analytic continuation — can yield a more comprehensive image of a medium. An exact depth extrapolation based on analytic continuation could contribute to the restoration of the true process of seismic wave propagation in a medium. In this case, multiples do not "pass" the layers where they have been formed and, hence, they cannot generate any fictitious reflecting boundaries. Here, we describe a method for doing migration of seismic wavefields in the frequency domain by analytic continuation through a medium with vertically variable velocity. Some preliminary experiments have been carried out and they show that the method works well in the case that we have multiples from a horizontal layer.

INTRODUCTION

The conventional procedure for the migration of wavefields is based on the depth extrapolation of the upgoing field in reverse time. However, this extrapolation restores only a transformation of the field in the subsurface rather than the true field. Also, one-way field extrapolation cannot reconstruct correct amplitudes of the seismic waves (Larner et al., 1981; Kosloff and Baysal 1982). In some situations it is worthwhile to restore the true distribution of the total seismic wavefield in the subsurface. This restoration can be accomplished by the method of analytic continuation. The method of analytic continuation is based on restoration of the field distribution in the lower halfspace with given background velocity from the known values of the field on the earth's surface. It is related to the analytical theory of the functions of real or

complex variables, but in this paper we discuss only the straightforward implementation needed for the solution of the migration problem. Some aspects of this problem have been discussed in earlier papers published by Kosloff and Baysal (1982) and by Zhdanov and Matusevich (1984). A more detailed introduction to this subject can be found in Zhdanov (1988) and Zhdanov, et al. (1988). Here, we focus on the method of migration by analytic continuation in a layered medium with vertically variable velocity.

FORMULATION OF THE PROBLEM

The method of analytic continuation can be formulated as a boundary value problem for the wavefield. Suppose the seismic field u, and its normal derivative are given on the surface of the layered half-space with the given vertical profile of the velocity variations (practical ways to determine the boundary values u^1 will be discussed later):

$$u(x,y,0,\omega) = u^0(x,y,\omega), \tag{1}$$

$$\frac{\partial}{\partial z}u(x,y,z,\omega)\Big|_{z=0} = u^1(x,y,\omega). \tag{2}$$

Reconstruction of the field $u(x,y,z,\omega)$ is required inside all layers in the earth. The solution of this problem can be divided into two stages:

1. continuation of the seismic field into a given layer with a depth-dependent velocity based on the equation

$$\nabla^2 u(x,y,z,\omega) + \frac{\omega^2}{V_\alpha^2(z)}u(x,y,z,\omega) = 0, \quad h_{\alpha-1} \le z \le h_\alpha, \tag{3}$$

   where h_α means the depth to the bottom of layer α.

2. recalculation of the field and its normal derivative from one side of the interface to the other by applying the proper boundary conditions on interfaces.

$$u(x,y,h_\alpha - 0,\omega) = u(x,y,h_\alpha + 0,\omega), \tag{4}$$

   and

$$V_\alpha(z)\frac{\partial}{\partial z}u(x,y,z,\omega)\Big|_{h_\alpha-0} = V_{\alpha+1}(z)\frac{\partial}{\partial z}u(x,y,z,\omega)\Big|_{h_\alpha+0} \tag{5}$$

Therefore, the solution of the stated problem comes down to continuation of the field within the limits of one given layer.

WAVEFIELD IN THE FREQUENCY-WAVENUMBER DOMAIN

We can present the field $u(x, y, z, \omega)$ in the form of the Fourier transform by space variables x, y

$$u(k_x, k_y, z, \omega) = \int_{-\infty}^{+\infty} \int_{-\infty}^{+\infty} u(x, y, z, \omega) e^{-i(k_x x + k_y y)} dx dy. \tag{6}$$

In the frequency-wavenumber domain, equation (3) can be written as

$$Lu(k_x, k_y, z, \omega) = 0, \tag{7}$$

where L is the one-dimensional Helmholtz operator

$$L \equiv \frac{\partial^2}{\partial z^2} + \frac{\omega^2}{C^2(z)},$$

and

$$\frac{1}{C^2(z)} = \frac{1}{V^2(z)} \left\{ 1 - V^2(z) \left[\left(\frac{k_x}{\omega} \right)^2 + \left(\frac{k_y}{\omega} \right)^2 \right] \right\}.$$

Note that C is a function of the vertical coordinate z and the space k_x, k_y and time ω frequencies:

$$C = C(k_x, k_y, z, \omega),$$

but, for the purposes of solving the differential equation in z, we write it as $C(z)$. Correspondingly, boundary conditions (1) and (2) will take the form

$$u(k_x, k_y, 0, \omega) = u^0(k_x, k_y, \omega), \quad u'(k_x, k_y, 0, \omega) = u^1(k_x, k_y, \omega), \tag{8}$$

where prime denotes the vertical derivative.

Our goal is to determine u everywhere inside the first layer, where the function $C(z)$ is a continuous function of depth, from the given values of u^0 and u^1 on the earth's surface. To solve this problem we apply the one-dimensional Green's theorem and corresponding Green's function.

SOLUTION OF THE BOUNDARY VALUE PROBLEM

Applying Green's theorem in one dimension to the first layer (Bleistein, 1984) gives

$$\int_0^{h_1} [u(z) Lg(z, \zeta) - g(z, \zeta) Lu(z)] \, dz = u(z) g'(z, \zeta) \Big|_0^{h_1} - g(z, \zeta) u'(z) \Big|_0^{h_1}. \tag{9}$$

Here, $u(z) = u(k_x, k_y, z, \omega)$ and $g(z, \zeta) = g(k_x, k_y, z, \zeta, \omega)$ is the Green's function that satisfies the equation

$$Lg(k_x, k_y, z, \zeta, \omega) = -\delta(z - \zeta). \tag{10}$$

Substituting equations (7) and (10) into (9) gives

$$u(\zeta) = g(z,\zeta)u'(z)\Big|_0^{h_1} - u(z)g'(z,\zeta)\Big|_0^{h_1}. \tag{11}$$

We now have two key issues. The first is how to determine the Green's function. This problem can be solved using the high-frequency asymptotic (WKBJ) approximation for the Green's function (Bleistein, 1984). The corresponding expressions for the Green's function are given in Appendix A.

The second key issue is how to determine the values of the field u on the bottom of the layer $z = h_1$ in equation (11). Evidently we can solve the boundary value problem (the recalculation of the field u inside the earth), if we know the field's values on the bottom of layer $z = h_1$. But we only have the recorded data u on the earth's surface $z = 0$. To overcome this difficulty we apply a special method of transformation of the right-hand side in (11), given at the bottom of the layer, to its surface. As shown in Appendix A, we can express the field values at $z = h_1$ in terms of the values at the earth's surface by decomposing the Green's function into the multiplication of two functions that depend on z and ζ separately, and by using Green's theorem (9) once again. A detailed mathematical explanation of this transformation is given in Appendix A.

Following this procedure, we have from equation (11) the following expressions for the analytic continuation of the wavefield into the first layer:

$$u(\zeta) = u^0\sqrt{\frac{C(\zeta)}{C(0)}}\cos\left[\omega\phi(\zeta)\right] + u^1\frac{\sqrt{C(\zeta)C(0)}}{\omega}\sin\left[\omega\phi(\zeta)\right], \tag{12}$$

where

$$\phi(\zeta) = \int_0^\zeta \frac{d\xi}{C(\xi)}.$$

In the same way, we can obtain an expression for the vertical derivative of the field inside the first layer:

$$u'(\zeta) = u^0\frac{-\omega}{\sqrt{C(\zeta)C(0)}}\sin\left[\omega\phi(\zeta)\right] + u^1\sqrt{\frac{C(0)}{C(\zeta)}}\cos\left[\omega\phi(\zeta)\right]. \tag{13}$$

The last result can be applied to the wavefield continuation from the top of the α layer to depth ζ within this layer:

$$u(\zeta) = u(h_{\alpha-1})\sqrt{\frac{C_\alpha(\zeta)}{C_\alpha(h_{\alpha-1})}}\cos[\omega\phi_\alpha(\zeta)] + u'(h_{\alpha-1})\frac{\sqrt{C_\alpha(\zeta)C_\alpha(h_{\alpha-1})}}{\omega}\sin[\omega\phi_\alpha(\zeta)], \tag{14}$$

$$u'(\zeta) = u(h_{\alpha-1})\frac{-\omega}{\sqrt{C_\alpha(\zeta)C_\alpha(h_{\alpha-1})}}\sin[\omega\phi_\alpha(\zeta)] + u'(h_{\alpha-1})\sqrt{\frac{C_\alpha(h_{\alpha-1})}{C_\alpha(\zeta)}}\cos[\omega\phi_\alpha(\zeta)], \tag{15}$$

where

$$\phi_\alpha(\zeta) = \int_{h_{\alpha-1}}^{\zeta} \frac{d\xi}{C_\alpha(\xi)}. \tag{16}$$

Thus, using formulae (12) through (16) and boundary conditions (8), (4) and (5) we can analytically continue the wavefield u from the surface of the earth through a variable background medium to any internal point of the earth's interior (as long as $C^2(z) > 0$, see Appendix A).

For analytic continuation of zero-offset seismic data, we apply to equations (12) and (14) the inverse Fourier transform from the frequency-wavenumber domain, (k_x, k_y, ω) to the time-space domain (x, y, t):

$$u(x,y,z,t) = \frac{1}{8\pi^3} \int_{-\infty}^{+\infty} \int_{-\infty}^{+\infty} \int_{-\infty}^{+\infty} u(k_x, k_y, z, \omega) e^{i(k_x x + k_y y - \omega t)} dk_x\, dk_y\, d\omega. \tag{17}$$

BOUNDARY CONDITIONS

In practice, only one of the functions u^0 or u^1 can be recorded on the earth's surface. Computation of the remaining field requires an additional geophysical assumption.

Here, we consider two possible models for the boundary conditions. One is based on the so-called *free surface conditions* wherein the vertical derivative of the wavefield on the surface of the solid earth is equal to zero:

$$u^1(x, y, \omega) = 0. \tag{18}$$

Relations (12) and (14) are then

$$u(\zeta) = u^0 \sqrt{\frac{C(\zeta)}{C(0)}} \cos[\omega\phi(\zeta)], \tag{19}$$

and

$$u'(\zeta) = u^0 \frac{-\omega}{\sqrt{C(\zeta)C(0)}} \sin[\omega\phi(\zeta)]. \tag{20}$$

Another model has been discussed by Kosloff and Baysal (1983). They suggest that the velocity $V(z) = V(0) =$ constant in some vicinity of the surface and that the recorded wavefield consists of upgoing waves only. In this case, the general solution of equation (7) in the vicinity of $z = 0$ takes the form

$$u(k_x, k_y, \zeta, \omega) = u^+(k_x, k_y, \omega) \exp\left[i\omega \frac{\zeta}{C(0)}\right] + u^-(k_x, k_y, \omega) \exp\left[-i\omega \frac{\zeta}{C(0)}\right]. \tag{21}$$

Because we consider only the upgoing wavefield at the surface, we delete the first term in this equation, giving

$$u(k_x, k_y, \zeta, \omega) = u^-(k_x, k_y, \omega) \exp\left[-i\omega \frac{\zeta}{C(0)}\right]. \tag{22}$$

Now we can calculate the vertical derivative of the wavefield at the earth's surface:

$$u^1(k_x, k_y, \omega) = -\frac{i\omega}{C(0)} u^0(k_x, k_y, \omega). \tag{23}$$

Substituting (23) into (12) and (13) , we have for the first layer,

$$u(\zeta) = u^0 \sqrt{\frac{C(\zeta)}{C(0)}} \exp\left[-i\omega\phi(\zeta)\right], \tag{24}$$

$$u'(\zeta) = u^0 \frac{-i\omega}{\sqrt{C(\zeta)C(0)}} \exp\left[-i\omega\phi(\zeta)\right]. \tag{25}$$

PHASE-SHIFT MIGRATION

Let us now compare the obtained results with corresponding expressions in conventional migration approaches. In traditional migration algorithms, it is assumed that the value h_1 goes to infinity. The reason for this assumption is that the boundaries of the layers with the strong velocity contrasts can generate the multiple reflections that involve both upgoing and downgoing waves; but the conventional migration algorithms are based on the exploding-reflector concept, which cannot deal with the multiple reflections and which considers only upgoing fields (Claerbout, 1985). In this assumption, taking into consideration the radiation condition from (11), we have

$$u(\zeta) = u(0)\tilde{g}'(0,\zeta) - \tilde{g}(0,\zeta)u'(0). \tag{26}$$

Note, here we use the complex conjugated Green's function $\tilde{g}(\omega) = g(-\omega)$ because in this section we would like to consider only upgoing waves.

In the case under consideration, we can modify the Green's function in such a way that on the earth's surface it is equal to zero. To see this, let us introduce the auxiliary function q,

$$q(z,\zeta) = -\frac{\sqrt{C(\zeta)C(z)}}{2i\omega} \exp\Big[-i\omega\left[\phi(\zeta) + \phi(z)\right]\Big]. \tag{27}$$

Everywhere in the lower half-space the function $q(z)$ is the high-frequency asymptotic solution of the Helmholtz equation

$$Lq(z) = 0, \tag{28}$$

satisfying the radiation condition at infinity. Therefore, we can rewrite equation (26) in the form:

$$u(\zeta) = u(0)\left[\tilde{g}'(0,\zeta) + q'(0,\zeta)\right] - \left[\tilde{g}(0,\zeta) + q(0,\zeta)\right]u'(0). \tag{29}$$

However, according to the definition (27),

$$q(0,\zeta) = -\tilde{g}(0,\zeta), q'(0,\zeta) = \tilde{g}'(0,\zeta). \tag{30}$$

Thus, we have

$$u(\zeta) = 2u(0)\tilde{g}'(0,\zeta) = u(0)\sqrt{\frac{C(\zeta)}{C(0)}}\exp\left[-i\omega\phi(\zeta)\right]. \tag{31}$$

Formula (31) presents exactly Gazdag's phase-shift method (Gazdag, 1978) for depth extrapolation of a seismic wavefield in the wavenumber-frequency (k_x, k_y, ω) domain. For migration of zero-offset seismic data, we apply to (31) the inverse Fourier transform (19) from frequency-wavenumber (k_x, k_y, ω) to time-space domain (x, y, t)

$$u(x,y,z,t) = \frac{1}{8\pi^3}\int_{-\infty}^{+\infty}\int_{-\infty}^{+\infty}\int_{-\infty}^{+\infty} u(k_x,k_y,0,\omega\sqrt{\frac{C(z)}{C(0)}}e^{-i\omega\phi(z)}e^{i(k_x x+k_y y-\omega t)}dk_x\,dk_y\,d\omega. \tag{32}$$

According to the exploding-reflector concept, the subsurface image I_m, based on the migration transformation, is obtained by setting $t = 0$ in equation (32),

$$I_m(x,z) = u(x,z,0) =$$

$$\frac{1}{8\pi^3}\int_{-\infty}^{+\infty}\int_{-\infty}^{+\infty}\int_{-\infty}^{+\infty} u(k_x,k_y,0,\omega)\sqrt{\frac{C(z)}{C(0)}}e^{i[k_x x+k_y y-\omega\phi(z)]}dk_x\,dk_y\,d\omega. \tag{33}$$

This result is a direct formulation of Gazdag's phase-shift migration method (Gazdag, 1978).

Let us now return from the phase-shift depth extrapolation formula (31) to the basic formula (26), and compare the latter with the general formula for analytic continuation (11). The main difference between them is that the formula for analytic continuation (11) takes into consideration both upgoing and downgoing waves and, therefore, accounts for the multiple reflections that are produced by strong velocity contrasts. This is achieved by calculating the wavefield in equation (11) along the two surfaces: $z = 0$ and $z = h_1$ (but we should remember that as a result of mathematical transformation, the integration over the plane $z = h_1$ is reduced to the integration over the surface of the earth $z = 0$). Conventional migration ignores the multiples, thus, possibly resulting in the reconstruction of false reflectors in the migrated image (we will discuss this question in detail later).

However, note that (31) and (24) are the same formula! This means that the initial step of analytic continuation in the model suggested by Kosloff and Baysal (1983) is the same as phase-shift depth extrapolation. As soon as we cross the first strong velocity boundary, however, we have to apply the boundary conditions (4) and (5), and then to extrapolate the field using formulae (14) and (15). From the physical

point of view, this means that we take into consideration the multiples generated at the first strong velocity boundary, and at subsequent ones, as well.

Thus, we can combine conventional methods of depth extrapolation (if we wish to ignore the multiples in some depth interval) with analytic continuation through the structures with the strong velocity contrasts. In this way, we aid the efficiency of analytic continuation. For media with continuously changing velocity $V(z)$ (i.e., $h_1 \to \infty$), analytic continuation [equation (24)] with the boundary condition (23) is identical to Gazdag's depth extrapolation (31).

MIGRATION OF TIME SECTIONS BY ANALYTIC CONTINUATION

It is important to recognize that in the general case analytic continuation is an ill-posed problem; that is, errors in the initial data can increase significantly during the continuation process. This follows from the behavior of the evanescent waves, which are given by the exponentially varying solutions of the wave equation. The evanescent waves are usually defined by the condition

$$k_x^2 + k_y^2 > \frac{\omega^2}{V^2(z)}. \tag{34}$$

The simplest way to overcome this difficulty is to eliminate the evanescent energy when implementing the analytic continuation algorithm (Kosloff and Baysal 1983). Moreover in this paper we use the high-frequency asymptotic approximation for the Green's function, which is only valid when

$$C^2(z) > 0 \tag{35}$$

or

$$k_x^2 + k_y^2 < \frac{\omega^2}{V^2(z)} \tag{36}$$

Thus, as in the case of conventional depth extrapolation, by using the analytic continuation algorithm, we eliminate the evanescent waves. The subsurface image then can be obtained based on the space-time structure analysis of the earth's total seismic wavefield. Consider the situation of a reflector on which a reflected wave is produced at the moment of direct wave arrival. Interference of the waves results in an increase (or decrease) of the amplitude of the total field at the reflection points in comparison with that of the surrounding points. This fact makes possible the use of analytic continuation for imaging of the earth's interior. We can restore the wavefield at each point of the section at the moment of direct-wave arrival. Then the locations of anomalous amplitudes of the field will show the location of the reflectors and the diffraction objects. We call this procedure *migration by analytic continuation.* This method of obtaining a migrated section (subsurface image $I_a(x, y, z)$) from time sections can be expressed mathematically by the formula

$$I_a(x, y, z) = \int_{-\infty}^{+\infty} \delta\left[t - \tau(x, y, z)\right] u(x, y, z, t)\, dt, \tag{37}$$

where $\tau(x,y,z)$ is the time of arrival of the direct wave at the point (x,y,z) and $u(x,y,z,t)$ is the analytically continued seismic wavefield; and $\delta(t)$ is the Dirac delta function.

Thus, substituting equation (14) into (17) and then into (37) we get

$$I_a(x,y,z) = \frac{1}{8\pi^3}\int_{-\infty}^{+\infty}\int_{-\infty}^{+\infty}\int_{-\infty}^{+\infty}\left\{u(h_{\alpha-1})\sqrt{\frac{C_\alpha(\zeta)}{C_\alpha(h_{\alpha-1})}}\cos\left[\omega\phi_\alpha(\zeta)\right]+\right.$$

$$\left.u'(h_{\alpha-1})\frac{\sqrt{C_\alpha(\zeta)C_\alpha(h_{\alpha-1})}}{\omega}\sin\left[\omega\phi_\alpha(\zeta)\right]\right\}e^{i[k_x x+k_y y-\omega\tau(x,y,z)]}dk_x\,dk_y\,d\omega, \qquad (38)$$

which describes imaging based on the analytic continuation migration.

ELIMINATION OF MULTIPLE REFLECTIONS

The problem of multiple elimination has been extensively studied in a number of publications (see, for example, Anstey and Newman, 1967; Kennett, 1974; Verschuur et al., 1980 and Verschuur et al., 1992) However, in most of the published papers, only surface-related multiple elimination have been discussed. Migration by analytic continuation provides an opportunity to eliminate the multiples that are produced by the (perfectly) reflecting free surface, as well as by the strong velocity contrasts in the lower parts of the section. Consider for the sake of simplicity the two-layered model shown in Figure 1. A line source is located in the lower layer. Conventional migration based on the depth extrapolation of the upgoing field fails to recognize multiple reflections shown in the right figure of Figure 1 for what they are. As a result they will give rise to fictitious reflecting boundaries in the migrated section. During migration, multiple waves produced in the top layer and presented in the observed field, "pass" into the lower layer where, in reality, they cannot penetrate. In contrast, depth extrapolation of the total field based on analytic continuation will restore the true process of wave propagation. Multiples are understood as such and hence, cannot generate any fictitious reflecting boundaries.

Figure 2 shows snapshots of the analytically continued wavefield at specified moments in time. Input consisted of the data shown at the right of Figure 1. At the latest time shown (150ms), m is a multiple reflection from within the shallow layer. As time decreases, the spatial structure of the calculated wavefield is simplified substantially and is free of multiple waves for times 50ms and less

Figure 3 shows a two layer model with a free surface and corresponding zero-offset data. Performing conventional phase-shift migration and migration by analytic continuation resulted in Figure 4. Conventional migration shows the false reflector caused by the presence of the multiple reflections. Migration by analytic continuation gives the correct image of the section. However the primary also gets weaker (twice as weak, where the multiple gets 20 times as weak). This is caused by interference of the upgoing and downgoing wavefield and the imaging condition (imaging at t=τ).

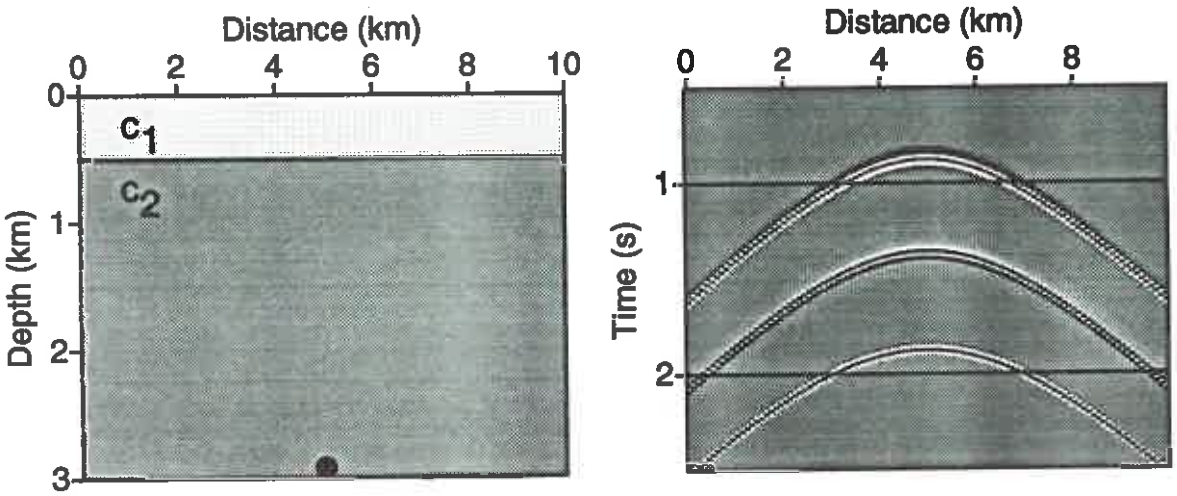

FIG. 1. (left) Point source in half-space beneath surface layer. (right) Synthetic zero-offset data, including two multiples.

Conventional phase-shift migration considers only the upgoing wavefield and images at t=0.

As a final example Figures 5 and 6 show the modeling and migrated results of a three layered model with a free surface and a syncline below the first layer. The multiple has become weaker (5 times as weak) because most energy has been migrated to the position of the primary. However again, the syncline and the primary of the flat interface get weaker as well after migration (twice as weak).

CONCLUSIONS

Migration by analytic continuation allows reconstruction of the true distribution of the seismic waves inside the earth. Implementation of this method is no more complicated than that of conventional migration (Stolt or Gazdag) in the frequency-wavenumber domain. The developed method can be applied to geological models with strong velocity contrasts. The method treats not only those multiple reflections related to the perfectly reflecting free surface, but also those from strong velocity boundaries within the subsurface. The quality of the multiples treatment by this migration technique will, of course, be degraded by the errors in the estimation of the acoustic-impedance discontinuities and location of the interfaces, that produce the multiples. This problem is of fundamental importance to the method and requires further study.

ACKNOWLEDGMENTS

We thank Ken Larner, Norman Bleistein and Jack Cohen for their helpful discussions and comments.

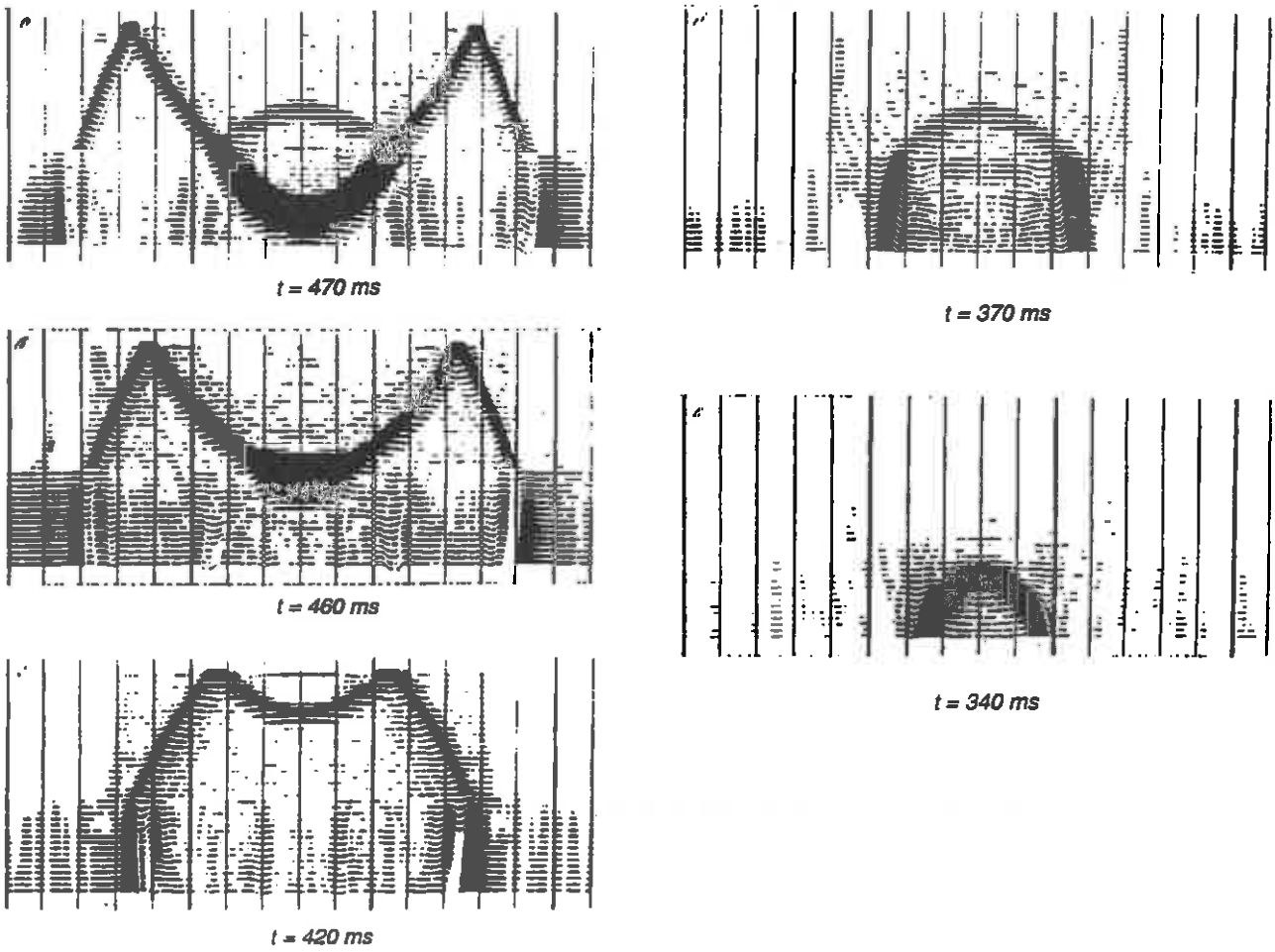

FIG. 2. Snapshots of the analytically continuated wavefield at different moments of time.

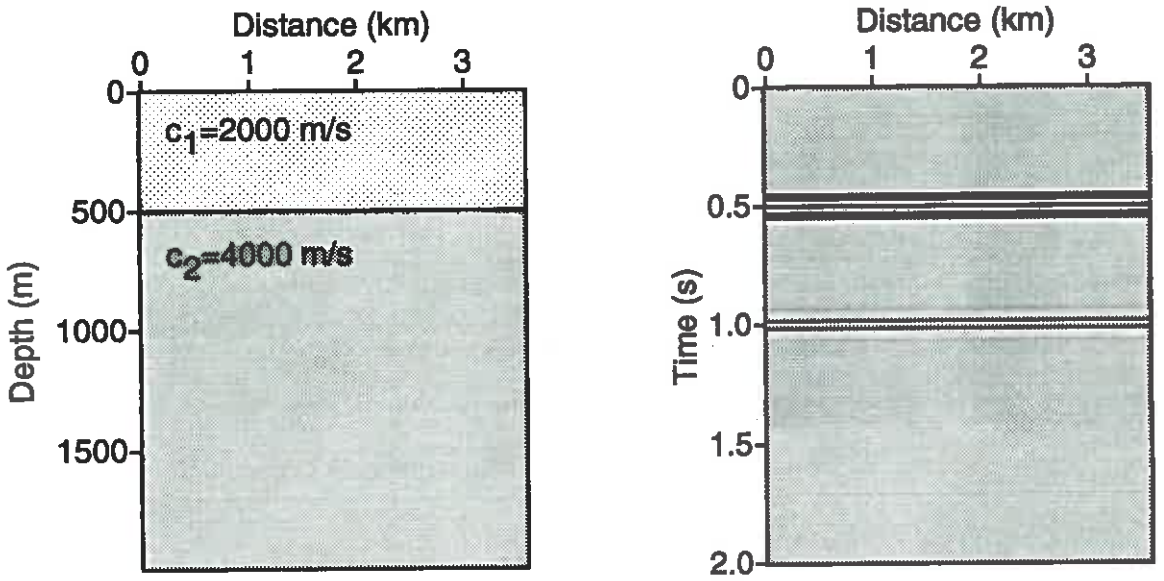

FIG. 3. (left) Simple two layer model with a free surface. (right) Zero-offset data obtained from a simulated seismic reflection experiment containing a primary and one multiple reflection

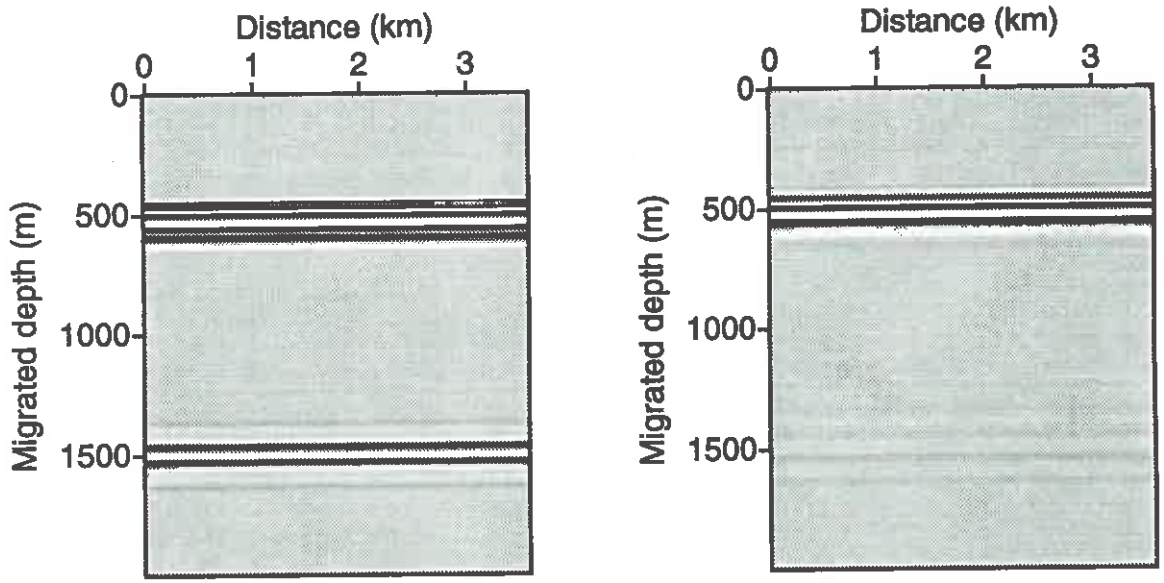

FIG. 4. (left) Depth-migrated data using conventional Gazdag migration. (right) Depth-migrated data using migration by analytic continuation.

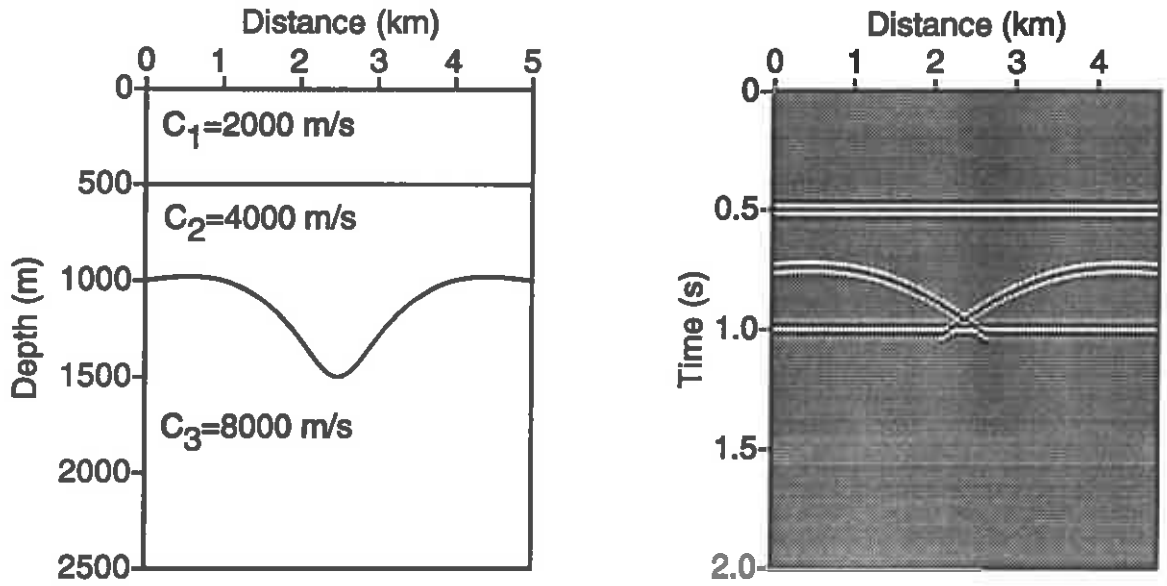

FIG. 5. (left) Three layer model with a free surface and a syncline below the first layer. (right) Zero-offset data obtained from a simulated seismic reflection experiment containing the primaries and one multiple reflection

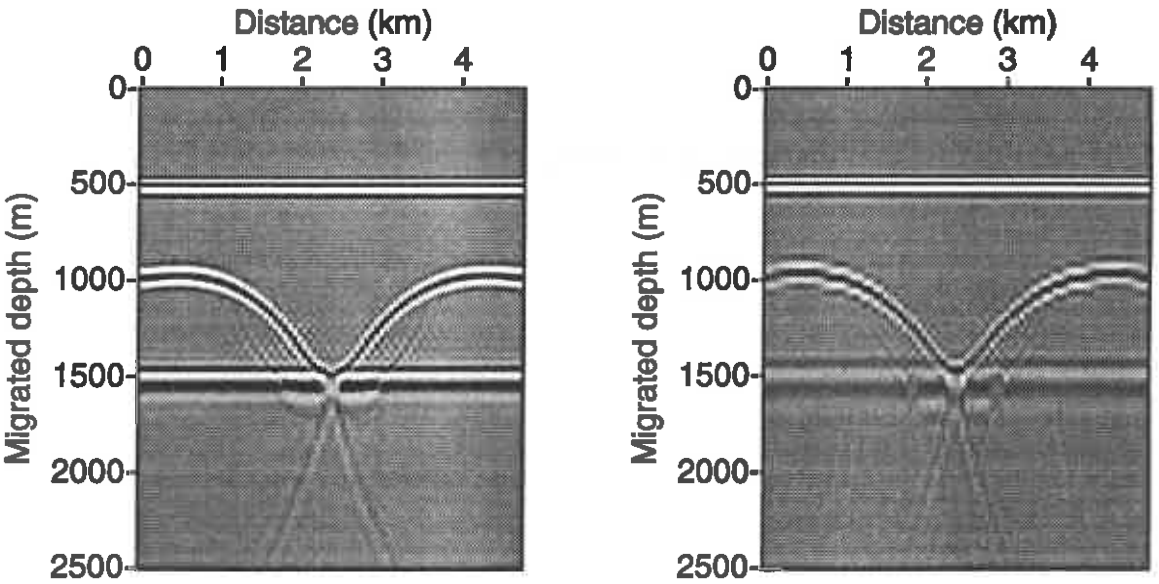

FIG. 6. (left) Depth-migrated data using conventional Gazdag migration. (right) Depth-migrated data using migration by analytic continuation.

REFERENCES

Anstey, N. A., and Newman, P., 1967, Part I: The sectional auto-correlogram; Part II: The sectional retro-correlogram: Geophys. Prosp., **14**, 391–426.

Bleistein, N., 1984, Mathematical methods for wave phenomena: Academic Press Inc.

Claerbout, J. F., 1985, Imaging the Earth's interior: Blackwell Scientific Publications, Oxford.

Gazdag, J., 1978, Wave equation migration with the phase-shift method: Geophysics, **43**, 1342–1351.

Kennett, B. L. N., 1979, On suppression of surface multiples on seismic records: Geophys. Prosp., **27**, 584-600.

Kosloff, D. D., and Baysal, E., 1982, Migration with the full acoustic wave equation: Geophysics, **48**, 677–687.

Larner, K., Hatton, L., Gibson, B., and Hsu I., 1981, Depth migration of imaged time sections: Geophysics, **46**, 734–750.

Tikhonov, A. N., and Arsenin, V. Ya. 1977, Solutions of ill-posed problems: John Wiley & Sons, New York, Toronto, London.

Verschuur, D. J., Berkhout, A. J., and Wapenaar, C. P. A., 1989, Wavelet estimation by prestack multiple elimination: 59th Ann. Int. SEG Mtg., Expanded Abstracts, 1129–1132.

Verschuur, D. J., 1992, Surface-related multiple elimination in terms of Huygens' sources: Jour. of Seis. Explor., **1**, 1, 49–60.

Zhdanov, M. S., and Matusevich, V. Yu., 1984, Restoration of the spatial pattern of wave propagation in an elastic medium. Ann. Geophys. **2**, 1, 1–16.

Zhdanov, M. S., 1988, Integral transforms in geophysics: Springer-Verlag, Berlin, Heidelberg, New York.

Zhdanov, M. S., Matusevich, V. Yu., and Frenkel, M. A., 1988, Seismic and electromagnetic migration: Nauka, Moscow.

APPENDIX A: 1-D GREEN'S FUNCTION IN THE SOLUTION OF THE BOUNDARY VALUE PROBLEM

In the simplest case, when $V(z) = V =$ constant and correspondingly, $C(z) = C =$ constant, the Green's function can be expressed in the form

$$g(z,\zeta) = -\frac{C}{2i\omega}\exp\left[\pm\frac{i\omega}{C}(z-\zeta)\right], \tag{A-1}$$

where we use the + sign for $z > \zeta$ and the − sign for $z < \zeta$. In the general case of variable $V(z)$ and $C(z)$, it is difficult to construct the direct analytical solution for the

Green's function. However, we can effectively use the high-frequency asymptotic solution (the so-called WKBJ approximation), which in the case of the one-dimensional Green's function can be written following Bleistein (1984) as

$$g(z,\zeta) \sim -\frac{\sqrt{C(\zeta)C(z)}}{2i\omega} \exp\left[\pm i\omega \int_{\zeta}^{z} \frac{d\xi}{C(\xi)}\right], \tag{A-2}$$

where, as in equation(A-1), we use the sign + for $z > \zeta$ and the sign − for $z < \zeta$. For constant velocity equation, (A-2) reduces to (A-1). Note that for the construction of WKBJ approximation we have to neglect the evanescent waves so that according to (35) and (36), we assume that

$$C^2(z) > 0.$$

Now, if we know the field's values at the bottom of layer $z = h_1$, we can use equation (11) to solve the boundary value problem — recalculation of the field u inside the earth. To overcome this difficulty, let us represent the Green's function $g(h_1,\zeta)$ in the form

$$g(h_1,\zeta) \sim a(h_1)b(\zeta), \tag{A-3}$$

where

$$a(z) = -\frac{\sqrt{C(z)}}{2i\omega} \exp\left[i\omega \int_{0}^{z} \frac{d\xi}{C(\xi)}\right], \tag{A-4}$$

and

$$b(\zeta) = \sqrt{C(\zeta)} \exp\left[-i\omega \int_{0}^{\zeta} \frac{d\xi}{C(\xi)}\right]. \tag{A-5}$$

Everywhere inside the first layer the function $a(z)$ is the high-frequency asymptotic solution of the Helmholtz equation

$$La(z) = 0. \tag{A-6}$$

Therefore, from Green's theorem (9), we have

$$u(h_1)g'(h_1,\zeta) - g(h_1,\zeta)u'(h_1) = u(0)a'(0)b(\zeta) - a(0)b(\zeta)u'(0). \tag{A-7}$$

Substituting (A-7) into (11) we have

$$u(\zeta) = -u(0)\left[a'(0)b(\zeta) - g'(0,\zeta)\right] + u'(0)\left[a(0)b(\zeta) - g(0,\zeta)\right]. \tag{A-8}$$

According to (A-2), (A-4) and (A-5)

$$g(0,\zeta) \sim -\frac{\sqrt{C(\zeta)C(0)}}{2i\omega} \exp\left[i\omega\phi(\zeta)\right], \tag{A-9}$$

and

$$a(0)b(\zeta) \sim -\frac{\sqrt{C(\zeta)C(0)}}{2i\omega} \exp\left[-i\omega\phi(\zeta)\right], \tag{A-10}$$

where

$$\phi(\zeta) = \int_0^{\zeta} \frac{d\xi}{C(\xi)}. \tag{A-11}$$

The leading order terms for $g'(0,\zeta)$ and $a'(0)b(\zeta)$ are

$$g'(0,\zeta) \sim \frac{1}{2}\sqrt{\frac{C(\zeta)}{C(0)}} \exp\left[i\omega\phi(\zeta)\right], \tag{A-12}$$

and

$$a'(0)b(\zeta) \sim -\frac{1}{2}\sqrt{\frac{C(\zeta)}{C(0)}} \exp\left[-i\omega\phi(\zeta)\right]. \tag{A-13}$$

Substituting equations (A-9), (A-10), (A-12) and (A-13) into (A-8), and taking into consideration the boundary conditions (8) we obtain

$$u(\zeta) = u^0\sqrt{\frac{C(\zeta)}{C(0)}} \cos\left[\omega\phi(\zeta)\right] + u^1\frac{\sqrt{C(\zeta)C(0)}}{\omega} \sin\left[\omega\phi(\zeta)\right]. \tag{A-14}$$

In the same way, we can calculate the vertical field derivative inside the first layer:

$$u'(\zeta) = u^0\frac{-\omega}{\sqrt{C(\zeta)C(0)}} \sin\left[\omega\phi(\zeta)\right] + u^1\sqrt{\frac{C(0)}{C(\zeta)}} \cos\left[\omega\phi(\zeta)\right]. \tag{A-15}$$

Thus, using the formulae (A-14) and (A-15) together with (14) and (15) and boundary conditions (8), (4) and (5), we can analytically continue the wave field u from the surface of the earth through a variable background medium to any internal point of the earth's interior.

CWP-136

— Expanded Abstract —
Tutorial: Regularization in inversion theory

Michael S. Zhdanov

Tutorial: Regularization in inversion theory, Expanded Abstract

Michael Zhdanov

ABSTRACT

Inversion of geophysical data is complicated by the fact that geophysical data are invariably contaminated by noise and are acquired at a limited number of observation points. Moreover, mathematical models are usually complicated, and yet at the same time are also simplifications of the true geophysical phenomena. As a result, the solutions are ambiguous and error-prone. The principal questions arising in geophysical inverse problems are the existence, uniqueness, and stability of the solution. Methods of solution can be based on linearized and nonlinear inversion techniques, and include different approaches, such as least-squares, gradient type (including steepest-descent and conjugate-gradient) and others. A central point of this tutorial is the application of so called "regularizing" algorithms for the solution of ill-posed inverse geophysical problems. These algorithms can use *a priori* geologic and geophysical information about the earth's subsurface to reduce the ambiguity and increase the stability of solution.

The important role of "regularizing" algorithms in the solution of ill-posed inverse seismic problems has been investigated in recent works of Koch (1992) and Sun and Shuster (1992). In mathematics we have a classical definition of the ill- posed problem: *a problem is ill-posed, according to Hadamard (1902), if the solution is not unique or if it is not a continuous function of the data (i.e., if to a small perturbation of data there corresponds an arbitrarily large perturbation of the solution).*

Unfortunately, from the point of view of the classical theory, all geophysical inverse problems are ill-posed, because their solutions are either non-unique or unstable. However, geophysicists solve this problem and obtain geologically reasonable results in one of two ways. The first is based on intuitive estimation of the possible solutions and selection of a geologically adequate model by the interpreter. The second way is based on the application of different types of regularization algorithms, which allow automatic selection of the proper solution by the computer using *a priori* geologic and geophysical information about earth structure.

The most consistent approach to the construction of regularization algorithms has been developed in the works of Tikhonov (1977, 1987) (see also Zhdanov, 1988,

Zhdanov et al. 1988). This approach gives a solid basis for construction of effective inversion algorithms for different applications. In usual way, describe the seismic inverse problem by the operator equation:

$$Am = d,\ m \in M,\ d \in D, \tag{1}$$

where D is the space of seismic data and M is the space of the parameters of seismic models; A is the operator of the forward problem that calculates the proper seismic data $d \in D$ for given model $m \in M$.

The main idea of the regularization method consists of the approximation of the ill-posed problem (1) by the family of well-posed problems

$$A_\lambda m = d,\ m \in M,\ d \in D, \tag{2}$$

depending on a scalar parameter λ called the *regularization parameter*. The regularization must be such that as λ vanishes, the procedures in the family should approach the accurate procedure A.

It is important to emphasize that regularization doesn't necessary mean the "smoothing" of the solution. The main basis for regularization is an implementation of *a priori* information in the inversion procedure. The more information we have about the seismic model, the more stable is the inversion. This information is used for the construction of the "regularized family" of well-posed problems (2).

The main goal of this paper is to present an overview of the methods of regularized solution of inverse problems based on the ideas of Tikhonov regularization, and to show different forms of their applications in both linear and nonlinear inversion techniques.

The foundations of regularization theory reviewed here include: 1) formulation of well-posed and ill-posed problems, 2) definition of the sensitivity and resolution of geophysical methods, 3) development of regularizing operators and stabilizing functionals, 4) introduction of the Tikhonov parametric functional, and 5) elaboration principles for determining of the regularization parameter.

I describe basic methods of the solution of the linear inverse problem using regularization, paying special attention to the discussion of regularization in the Backus-Gilbert method. I also discuss the main methods for regularizing the solution of nonlinear inverse problems. Finally, I describe regularization methods in wave-form inversion and travel-time inversion.

REFERENCES

Koch M., 1992, Optimal regularization of the linear seismic inverse problem: Geophysical Inversion, Society for Industrial and Applied Mathematics, Philadelphia, 183-244.

Sun Y. and Shuster G., 1992, Hierarchic optimizations for smoothing and cooperative inversion: 62nd Ann. Internat. Mtg., Soc. Expl. Geophys., Expanded Abstracts, 745-748.

Tikhonov, A.N., and Arsenin, V.Ya., 1977, Solutions of ill-posed problems: John Wiley & Sons, New York, Toronto, London.

Tikhonov, A.N., and Goncharsky A.V., 1987, Ill-posed problems in the natural sciences, MIR, Moscow, 303 p.

Zhdanov, M.S., 1988, Integral transforms in geophysics: Springer-Verlag, Berlin, Heidelberg, New York 367 p.

Zhdanov, M.S., Matusevich, V.Yu., and Frenkel, M.A., 1988, Seismic and electromagnetic migration: Nauka, Moscow, 327 p.

The Students and Faculty of the

Center for Wave Phenomena

Spring 1993

The Faculty

John E. Anderson
Visiting Scientist

John is Mobil's Visiting Scientist with the Geophysics Department at CSM for 1993-4. John received his B.Sc. in Physics from the University of Oklahoma in 1975 and an M.Sc. in Physics from Baylor in 1977. He was part of Cities Service's Geophysical Research Group from 1977 to 1983 in Tulsa. He spent one year in Houston with CGG working on VSP modeling and air gun characterization. From 1984-8, John spent 4 years as part of SOHIO/BP's Borehole Geophysics Group working on VSP, full-wave sonic, cross-well, and reservoir characterization problems. The past five years he has worked and consulted on wavelet processing, migration, DMP, and noise removal problems for Mobil in Dallas. He is part of Mobil's current effort to interact more closely with research going on at the Colorado School of Mines.

Norman Bleistein
Co-principal Investigator

Norm received a Ph.D. in 1965 from the Courant Institute of Mathematical Sciences at New York University. He spent three years as an assistant professor at MIT and fourteen years at Denver University before moving to the Colorado School of Mines. He has been on sabbatical for the past academic year during which he traveled to China where he taught a short course at Shandong University, and lectured at other Chinese institutions. He continues research in asymptotic analysis of seismic processing, writing a book on seismic inversion, and revising an earlier book for a second edition.

Jack K. Cohen
Co-principal Investigator

Jack received his Ph.D. from the Courant Institute of Mathematical Sciences at New York University. He was a professor of mathematics at Denver University before coming to CSM. His research interests are in seismic applications. In conjunction with the new Center for Geoscience Computing (CGC) that is partially supported by IBM, he has developed a workstation version of the Seisimic Unix Processing Line (SU).

Ken Larner
Co-principal Investigator

Ken has been the Charles Henry Green Professor of Exploration Geophysics at the Colorado School of Mines since August 1988. After receiving a Ph.D. in geophysics from MIT in 1970, he joined Western Geophysical Company where he became vice president for geophysical research 1979. The recipient of the Conrad Schlumberger Award of the EAEG, he was Spring 1988 SEG Distinguished lecturer and SEG president for 1988-89. He received the President's Award for CSM Outstanding Educator in 1992.

John A. Scales
Co-principal Investigator

John received a Ph.D. in physics at the University of Colorado in 1984. He worked as a research scientist for Amoco Production Company before joining CWP. His current projects involve full-waveform inversion of 2-D seismic data on a massively parallel computer and the incorporation of realistic prior information into the framework of statistical inference.

John Stockwell
Research Associate

As research associate, John manages the CWP public domain software which includes the maintenance and development of new software for the SU (Seismic Unix) package. He is the administrator of CWP's network of 29 NeXT workstations. John's research interests include acoustic and elastic modeling/inversion and wavelet transforms. He is coauthoring a textbook on seismic inversion with Jack Cohen and Norm Bleistein and is an adjunct instructor this semester in the Department of Mathematical and Computer Sciences.

Ilya D. Tsvankin
Associate Research Professor

Ilya received both his M.Sc. and Ph.D. in geophysics from Moscow State University. For the past two years, he has been a consultant to the Geophysical Research Department at Amoco Production Company, Tulsa. He has also served as deputy chief of the laboratory, "Geophysics of Anistropic Media" at the Institute of the Earth, Moscow. His current research topic is seismic modeling and inversion in anisotropic media, dealing with such problems as extension of amplitude-versus-offset (AVO) analysis and other methods of seismic exploration to anisotropic models.

Michael S. Zhdanov
Visiting Associate Professor

Michael is from the Institute of the Physics of the Earth, USSR Academy of Sciences and the Gubkin State University. He has been head of the Department of Deep Electromagnetic Study Insitute of Terrestrial Magnetism and Radiowave Propgation, USSR Academy of Sciences, and the Head of the Troitsk Branch of the Institute of the Physics of the Earth. He is a professor of geophysics at the Moscow Gubkin State University. During his tenure at CWP, Michael is pursuing research on seismic migration by analytic continuation and inversion methods. He is currently revising and translating a book on seismic and electromagnetic migration.

The Students

Mohammed Alfaraj

Degree program: Ph.D., Geophysics
Home country: Saudi Arabia

Mohammed has been an employee of ARAMCO since 1984. He earned a B.Sc. in electrical engineering at the University of Wisconsin-Milwaukee and an M.Sc. in geophysics at CSM. Mohammed's research interest is dip moveout and processing of mode-converted seismic data.

Tariq Alkhalifah

Degree program: M.Sc., Geophysics
Home country: Saudi Arabia

Tariq has been an employee of KACST, Saudi Arabia. He earned a B.Sc. at the University of Petroleum and Minerals. Tariq's M.Sc. thesis research is in seismic anisotropy as it affects raypaths in inhomogeneous media.

Craig Artley

Degree program: Ph.D., Geophysics
Home country: United States

Craig received his B.Sc. in geophysics from Texas A&M University, and an M.Sc. in geophysics at CSM last fall. He has worked summers in the research organizations of Western Geophysical, Exxon, and ARCO Oil and Gas. His research interests span seismic imaging and geophysical computing.

Tong Chen

Degree program: Ph.D., Mathematics
Home country: People's Republic of China

Tong earned a B.Sc. in electrical engineering from the University of Science and Technology of China. His research interests are the applications of wavelet analysis and parallel computing in seismic processing.

Hongling Deng

Degree program: Ph.D., Mathematics
Home country: People's Republic of China

"Lydia" earned an M.Sc. in mathematics at CSM and is continuing for a Ph.D. She holds a B.Sc. in electrical engineering with a specialty in signal processing from the University of Science and Technology of China. Her current research interest is computational seismology.

Tong Fei

Degree program: Ph.D., Mathematics
Home country: People's Republic of China

Tong Fei earned an M.Sc. in geophysics from the University of Alaska Fairbanks where he also earned a B.Sc. in physical oceanography, and an M.Sc. in ocean engineering. His research interests are seismic modeling and migration for flux-corrected transport for 2-D and 3-D acoustic and elastic anisotropic media. He is also interested in wave equation traveltime inversion and phase fluid motion in porous media.

Wenceslau Gouveia

Degree program: Ph.D., Geophysics
Home country: Brazil

Wenceslau's holds both a B.Sc. and an M.Sc. degree in electrical engineering from the Catholic University at Rio de Janeiro. Wenceslau has been employed as an industry specialist in geophysics for the Petroleum Center, IBM Brazil where his work related to computing on RISC workstations and vector machines. His current research interests are seismic processing and parallel computing.

Zhenyue Liu

Degree program: Ph.D., Mathematics
Home country: People's Republic of China

Zhenyue earned a B.Sc. in mathematics from Heilongjiannng University and an M.Sc. in mathematics from Harbin Institute of Technology in China, where he also taught mathematics. His current research interests are inversion and velocity analysis.

Boyi Ou

Degree program: Ph.D., Geophysics
Home country: People's Republic of China

Boyi recently earned a B.Sc. degree from Nanjing University. From August 1991 to August 1992 he worked in the Research Institute of Geophysical Prospecting for Petroleum. His current research interest is seismic data processing.

Andreas Rüeger

Degree program: M.Sc., Geophysics
Home country: Germany

Andreas is a recipient of the Fulbright Scholarship and earned a B.Sc. in geophysics from the University of Karlsruhe, Germany. He has participated in projects in Tansania, Kenya and Greenland. His M.Sc. thesis research is in dynamic ray tracing.

Timo Tjan

Degree program: M.Sc., Geophysics
Home country: The Netherlands

Timo recently earned an engineering degree from the Department of Applied Physics at the Delft University of Technology. His current research interest is analytic continuation migration.

Omar Uzcategui

Degree program: Ph.D., Geophysics
Home country: Venezuela

Omar earned a Licentiate in physics at the Universidad de Los Andes and an M.Sc. in geophysics at the Universidad Central de Venezuela. He has been employed in Venezuela by Intevep. His current research areas are inversion and migration for anisotropic media.

Meng Xu

Degree program: M.Sc., Mathematics
Home country: People's Republic of China

Meng recently earned a B.Sc. in modern applied physics at Qinghua University, Beijing. His current research interest is wavelet transform and applications processing.

Sponsors Mailing List: Technical Contacts

The Center for Wave Phenomena gratefully acknowledges the support of the companies listed here. We provide this list as a convenience to the sponsors.

Advance Geophysical Corp.
Mr. S. Rutt Bridges
7409 S. Alton Ct., Suite 100
Englewood, CO 80112

Amerada Hess Corporation
Dr. J. Bee Bednar
Geophysical Computer Applications
P.O. Box 2040
Tulsa, Oklahoma 74102

Amoco Production Company
Dr. Samuel H. Gray
Research Center
P.O. Box 3385
Tulsa, OK 74102

ARAMCO
Dr. Richard D. Chimblo
Geophysical Research & Development
Saudi ARAMCO, Rm. X-3480
Dhahran 31311
Saudi Arabia

ARCO Explor. & Prod. Technology
Dr. Dennis Corrigan
2300 West Plano Parkway
Plano, TX 75075

BP Exploration Inc.
Dr. Bruce G. Secrest
BP/Statoil Alliance (Trondheim)
P.O. Box 4587
Houston, TX 77210

Bureau of Geophysical Prospecting
Mr. Xu Dakun
P.O. Box 11
Zhuo Zhou City, Hebei Province
People's Republic of China

Compagnie Générale de Géophysique
Mrs. Laurence Boissy
6, rue Galvani
91341 Massy Cedex
France

Chevron Petroleum Technology
Dr. Clint W. Frasier
Exploration Products & Services Department
P.O. Box 446
La Habra, CA 90633

Conoco, Inc.
Dr. Doug Hanson
Exploration Research Division
P.O. Box 1267
Ponca City, OK 74603

Elf Aquitaine
Dr. Marc Verprat
CSTJF Avenue Larribau
64018 Pau Cedex
France

Exxon Production Research Company
Dr. William A. Schneider, Jr.
Subsurface Imaging Division
P.O. Box 2189
Houston, TX 77252-2189

GECO-PRAKLA
Mr. Andrew Pieprzak
1325 Dairy Ashford
Houston, TX 77077

Halliburton Geophysical Services, Inc.
Dr. Laurent J. Meister
5151 San Felipe
Houston, TX 77056

IBM Corporation
Dr. Thomas R. Morgan
Engineering/Petroleum Studies
Neighborhood Road
Kingston, NY 12301

Marathon Oil Company
Dr. Randy S. McKnight
Geoscience Technology Department
P.O. Box 269
Littleton, CO 80160

Mobil Research and Develop. Corp.
Dr. Stanley J. Laster
Geophysical Research
P.O. Box 819047
Dallas, TX 75381

Oryx Energy Company
Dr. Joong H. Chun
P.O. Box 830936
Richardson, TX 75083-0936

Shell Development Company
Dr. Philip Ensign
Geophysics Research
Bellaire Research Center
P. O. Box 481
Houston, TX 77001

STATOIL
Dr. Terje Dahl
Den norske stats olijeselskap a.s.
Postuttak
N-7004 Trondheim
Norway

Texaco, USA
Dr. Brian Sumner
Exploration Research
P.O. Box 770070
Houston, TX 77215-0070

UNOCAL
Dr. Robert D. Mager
Seismic Research & Applications
LaPalma Center
P.O. Box 68076
Anaheim, CA 92807

Western Geophysical
Dr. Wendell Wiggins
Research and Development
P.O. Box 2469
Houston, TX 77252

INDEX

amplitude versus offset, 355
anisotropy, 327, 355
    Gaussian beam, 57
    migration, 63
asymptotics, WKBJ, 311
AVO, 355

Bayesian inference, 293

common-image-gather, 243
converted waves, 5
    DMO, 5
    TZO, 5
Crank-Nicolson scheme, 218

Daubechies, 138
depth-focusing analysis, 241
dip moveout, 123, 327
DMO, 123, 327
    converted waves, 5
    3-D, 123
    variable velocity, 123
    anisotropy, and, 327

eikonal equation, 218

filter, 135, 136

Gaussian beam
    anisotropy, 87
    migration, 217
genetic algorithms, 200

Hermitian Toeplitz systems, 109

inverse problems, 199, 291, 417

Kirchhoff intergral, 217

Levinson recursion, 109

marco-model, 242
Meyer, 138
migration, 217, 377
    anisotropic media, 378
    anisotropy, 33
    explicit operators, 377
    Gaussian beam, 217
    Kirchhoff, 243
    prestack depth, 217, 241
    analytic continuation, 399
    phase shift, 399
modeling, 261, 311
    Gaussian beam, 261
    Kirchhoff, 217
Monte Carlo, 200
multiples, 399

parabolic transform, 109
parallel computing, 200
prior information, 292

radiation pattern, 355
radon transform, 109
ray tracing, dynamic, 261
    Fresnel-volume, 274
regularization, 417
residual moveout, 241
    velocity, 241
    curvature analysis, 241

suradon, 109

tau-p, linear 2-D, 109
triangulated models, 261
transformation to zero offset, 5
TZO, 5
    converted waves, 5

velocity analysis, 241
    gradient, 327
    smoothing, 217

wave equation, 2.5-D, 312
    variable-density, 322
wave propagation, 311
    2.5-D, 311
wavelet transform aliasing, 138
wavelets, 133